



HAL
open science

Tribology of PA66 or fiber-reinforced composite / steel contact under grease lubrication

Takeshi Kunishima

► **To cite this version:**

Takeshi Kunishima. Tribology of PA66 or fiber-reinforced composite / steel contact under grease lubrication. Other. Université de Lyon, 2021. English. NNT : 2021LYSEC020 . tel-03562238

HAL Id: tel-03562238

<https://theses.hal.science/tel-03562238>

Submitted on 8 Feb 2022

HAL is a multi-disciplinary open access archive for the deposit and dissemination of scientific research documents, whether they are published or not. The documents may come from teaching and research institutions in France or abroad, or from public or private research centers.

L'archive ouverte pluridisciplinaire **HAL**, est destinée au dépôt et à la diffusion de documents scientifiques de niveau recherche, publiés ou non, émanant des établissements d'enseignement et de recherche français ou étrangers, des laboratoires publics ou privés.



N°d'ordre NNT : 2021LYSEC20

**THESE de DOCTORAT DE L'UNIVERSITE DE LYON
opérée au sein de l'Ecole Centrale de Lyon**

**Ecole Doctorale N° 34
Ecole Doctorale Matériaux de Lyon**

**Spécialité de doctorat :
Génie des matériaux**

**Soutenue le 1^{er} juin 2021, par :
Takeshi KUNISHIMA**

**TRIBOLOGY OF PA66 OR FIBER-REINFORCED COMPOSITE
/ STEEL CONTACT UNDER GREASE LUBRICATION
TRIBOLOGIE DU CONTACT PA66 AVEC OU SANS FIBRES DE RENFORT
/ ACIER AVEC LUBRIFICATION À LA GRAISSE**

Devant le jury composé de :

Koshi ADACHI	Professeur, Tohoku University, Japan	Président de jury
Mitjan KALIN	Professeur, University of Ljubljana, Slovenia	Rapporteur
Fabrice VILLE	Professeur, INSA de Lyon, France	Rapporteur
Agnès FABRE	Maître de conférences, ENSAM Aix-en-Provence, France	Examinatrice
Clotilde MINFRAY	Maître de conférences, ECL, France	Examinatrice
Philippe KAPSA	Directeur de recherche émérite au CNRS, ECL, France	Directeur de thèse
Vincent FRIDRICI	Maître de conférences, ECL, France	Co-directeur de thèse
Setsuo NAGAI	JTEKT CORPORATION, Japan	Membre invité

ACKNOWLEDGEMENTS

This study was conducted at the Laboratoire de Tribologie et Dynamique des Systèmes (LTDS) in France as a collaborative research work with JTEKT Corporation in Japan. During three years, from June 2018 to June 2021, it was filled with wonderful experiences and opportunities to meet many extraordinary people. I completed this work and immensely grew as a person thanks to the encounter with those to whom I wish to express my feelings of gratitude hereafter.

First, I wish to express my sincere gratitude to Prof. Philippe Kapsa (LTDS), my PhD thesis supervisor, for giving me the basics of research and supporting me during the entire thesis work. Since we met in WTC Beijing in 2017, his professional guidance backed by his long career in tribology enabled me to observe the experimental outputs from the basic principles.

I am deeply grateful to Associate Prof. Vincent Fridrici (LTDS, Ecole Centrale de Lyon), my co-supervisor of the PhD thesis. Since we met in WTC Beijing in 2017, he generously received me from Japan and allowed me into his team. His thoughtful support continuously enabled me to concentrate on my research, and his insightful feedback and comments on my outputs always created the right path. His open-minded attitude taught me many things. During my three years of PhD work, he gave me uncountable suggestions and professional guidance for my work. He also patiently and critically proofread the countless manuscript of papers and theses.

I would like to offer my special thanks to Prof. Koshi Adachi (Tohoku University, Japan). He graciously advised me to conduct a PhD work in LTDS, and kindly introduced me to Prof. Philippe Kapsa and Associate Prof. Vincent Fridrici in WTC, Beijing. Without his kind cooperation and guidance, our collaboration with the LTDS would not have begun. In addition, he kindly became the president of the jury of my PhD thesis and passionately reviewed the thesis.

In my company, my deepest appreciation goes to Mr. Kazunori Hayashida (executive officer in R&D headquarters in JTEKT) and Mr. Hirokazu Arai (former General Manager in the material research development in JTEKT). They gave me a wonderful opportunity to study in a foreign country and strived to adjust my company to achieve it. To satisfy their expectations, I would like to return my special experience to future JTEKT. I also appreciate my supervisor, Mr. Takanori Kurokawa (General Manager in the Organic Material Laboratory at JTEKT). His technical comments as a dedicated researcher of plastic material and polymer gears, despite his busy schedule, helped improve the quality of my PhD work. He frequently called me on the phone and heard concerns about my life. Mr. Setsuo Nagai (Group Manager in group 1 in the Organic Material Laboratory at JTEKT) frequently encouraged me as my direct supervisor and occasionally kindly offered his concern about the coronavirus situation in France while he was busy every day. Mr. Tomoyasu Kada (JTEKT) kindly attended to me when I first visited the LTDS and offered me much assistance, particularly on the administrative procedure before and after I began my PhD life in France, and offered me great support for communication in French.

I would like to express my gratitude to all the colleagues in our research team in LTDS for their generous help. In particular, I would like to thank Mr. Gaëtan Bouvard (LTDS) for his technical support in the experiments. Without his help, my experiments could not have been performed within an acceptable period. Whenever I had problems with the tribometer, he stopped his own work and came to help. He also kindly designed sample holders for the sliding tests. I would also like to thank Dr. Jean-Christophe Abry (LTDS). In each technical meeting, he kindly provided me with valuable feedback as an experienced researcher based on his long career in the tribology field and knowledge on the tribology of fiber composites. Dr. Gaylord Guillonneau (LTDS) passionately shared much time in the micro-indentation hardness measurement, and he co-authored my paper. Mr. Thomas Malhomme

(LTDS) kindly offered me much support for optical microscope observations and interferometry measurements.

I would also like to express my gratitude to all colleagues outside our research team in the laboratory for their kind help. I would like to acknowledge Associate Prof. Clotilde Minfray (LTDS, Ecole Central de Lyon). Her remarkable experience in the field of tribochemistry provided me insights into my results. Dr. Jules Galipaud (LTDS) provided me with a high level of technical support in the XPS analysis to detect tribofilm formation. They kindly took part in the co-authoring of my paper, and without their special knowledge, which is dedicated to tribochemistry, the value of my research work would not be so great. Ms. Sophie Pavan (LTDS) kindly offered her help with the micro-indentation measurements. Mr. Didier Roux (LTDS) kindly machined my testing samples many times. Dr. Julien Fontaine (LTDS) kindly visited my company in Japan to discuss and allowed me to attend the ElyT workshop. Ms. H el ene Schoch (LTDS) kindly helped me to manage administrative tasks. In addition, I would like to express my gratitude to Mr. Laurent Dupuy and Ms. Delphine Pavon in SCIENCE ET SURFACE who kindly conducted the ToF-SIMS analysis. Their knowledge was truly helpful for the clarification of tribochemistry on the sliding surface.

Without significant help from my colleagues in material research development in JTEKT Corporation, I would not have completed my PhD work with high quality. Mr. Yasuharu Nagai (JTEKT) had technical discussions with me on the tribology of composite and polymer gear many times, and he took part in the co-authoring of several of my papers. Mr. Koji Kimura (JTEKT) gave me much support in the preparation of test samples through his professional technique of twin-screw extrusion and injection molding. Mr. Kazuki Nobetani (JTEKT), Mr. Junya Matsuyama (JTEKT), and Ms. Ayumi Odagiri (my former colleague in JTEKT) cooperated with me in the preparation and evaluation of test samples and for the chemical analysis. Mr. Toshiyuki Baba (JTEKT) also gave me technical advice based on his career in research on fiber-reinforced composites and chemical analysis. I would like to thank all of the extraordinary members of my research group (group 1 in the Organic Material Laboratory). In addition, Mr. Kazunori Miyake (group manager in Group 2 in the Organic Material Laboratory at JTEKT) and Ms. Kanako Takahara (JTEKT) frequently spared time and kindly gave me much helpful technical advice on the grease and tribology of polymers. Mr. Chikara Nakajima (JTEKT) helped me with the optical microscope observation of the metallic structure and provided me with knowledge of the heat treatment of steel. Dr. Masahiro Suzuki (General Manager in the Tribology Laboratory at JTEKT) gave me useful feedback on the results of tribochemistry, which was based on his professional experience as a PhD researcher in the field of tribology. Mr. Kazuhisa Kitamura (Group Manager in the Analysis and Evaluation Group at JTEKT) kindly hosted the luncheon meeting at WTC Beijing in 2017 when we first met Prof. Philippe Kapsa and Prof. Vincent Fridrici. Mr. Katsuhiko Kizawa (General Manager in Material Research Development in JTEKT) gave me insightful findings not only on the knowledge of material research, which is based on his career as a researcher of steel material and heat treatment technology, but also on several non-scientific topics (geopolitics, management, etc.) based on his special experience in the USA.

I would like to express my greatest appreciation to the PhD students at LTDS. Despite being far away from my country, I could keep up my mental stability and motivation with the assistance of many associates. I was fortunate to have such good LTDS mates. In particular, Mr. Tadashi Oshio gave me useful advice as a PhD student from a Japanese company, which was the same scenario I was in. I would also like to express my gratitude to his family. Dr. Yuta Muramoto also gave me great advice on my PhD study and French life, including the French language, as a preceding PhD candidate in the same research group. Dr. Haohao Ding also gave me some advice as a preceding PhD candidate in the same research group, and his PhD thesis with great quality inspired me to improve my own. Ms. Vilayvone

Saisnith frequently came to talk to me as a PhD student in the same research group and kindly offered me great assistance when I had difficulty with French. In addition, I would like to express my gratitude to all my LTDS colleagues, including Mr. Amaury Guillermin, Dr. Mayssa Al Kharboutly, Ms. Nasrya Kossoko, Mr. Valentin Salinas, Dr. Yun Long, Ms. Mariana de Souza, Mr. Kohei Mitsuzuka, Mr. Pradeep Mohanasundaram, Mr. Kazuki Ozawa, Dr. Adrien Pyskir, Dr. Laura Jay, Ms. Na Qiao, Ms. Rexhina Shyti, Ms. Meriem Ayadh, and all other PhD students.

Furthermore, I cannot say complete my PhD work without saying gratitude to my colleagues in JTEKT. I would like to thank Mr. Hirofumi Kuwabara (former General Manager in the Research Planning Department at JTEKT) who motivated me to study not only the research of the material and tribology but also wider range field of knowledge, and kindly offered concern during the *confinement* caused by Covid-19. Mr. Yuji Yoshizawa (JTEKT) gave me much support for the administrative procedure in my PhD study and negotiated with the Human Resources Department in my company to establish a good research environment. Dr. Tohru Onozaki (General Manager in the Data Analytics Department at JTEKT) gave me great advice based on his career as a PhD researcher in my company. I would like to express my gratitude to my colleagues in Human Resources Development, including Mr. Michiyuki Sugiyama (JTEKT), Ms. Keiko Hanatani (JTEKT), and Ms. Chihiro Komatsu (JTEKT). In particular, Ms. Maho Hiraiwa (JTEKT) and Ms. Naoko Suzuki (JTEKT) spared much time on daily administrative work, including the settlement of my expenses during my stay in Lyon. Mr. Yuki Sato (JTEKT), Ms. Kumiko Goto (JTEKT), and Mr. Takuya Wada (JTEKT) provided administrative support to the staff of the Human Resources Department at JTEKT Europe, Irigny, France. I also would like to thank Mr. Hiroshi Ii (former President at JTEKT Europe) and Mr. Hiroaki Ueda (President at JTEKT Europe). Mr. Ryo Nakano (JTEKT) and Takeshi Yamamoto (JTEKT) gave me some advice on the patent on my PhD study as a staff member in the Intellectual Property Department. Mr. Tomohiro Nakade (JTEKT) kindly provided valuable information on the PhD study in a foreign country as a PhD candidate in Europe. Mr. Atsumune Nagatani (JTEKT) kindly offered the latest information on the EPS and shared great experience in France. Mr. Tomohiko Haruyama (JTEKT) usually gave me thoughtful opinions on the various field, and kindly attended my PhD defense and gave me some questions. All my colleagues at the Automobile Components Headquarters at JTEKT kindly provided me with technical information on the worm reducer and EPS.

In addition, I would like to express my appreciation to the people in the plastic material and grease company who kindly provided raw material, evaluation material, and technical information. Without their support, I would not have completed my PhD study with high quality. I would also like to thank Ms. Atsuko Onuma of Service Expat 69000. She frequently offered support for daily life in Lyon, including applying for the residence card or driver's license in France, and accompanying us when my family went to the clinic.

Finally, I am grateful to my parents, younger sisters, my grandfather, and grandmother for their consistent, uncountable, and invaluable affection from my birth up until today. Finally, I am deeply grateful to my wife Misako and my son, Ryo.

Takeshi Kunishima

June 1st, 2021

ABSTRACT

Engineering plastics are widely used for sliding components including worm wheel in worm reducer used in the automotive electric power steering (EPS). To apply the EPS to much larger vehicles or downsize the worm reducer, the developments of polymer material and design of the worm reducer which can ensure good durability and lower friction are requested.

This study clarified the tribological properties of unreinforced and fiber-reinforced PA66 in contact with steel counterpart under grease lubrication to improve the tribological properties of polymer sliding components. Various sliding tests were conducted in a contact geometry which simulated that of the EPS worm reducer; PA66 or composite ring specimens were in contact with fixed four steel cylinders under mainly grease lubrication. Wear or creep resistances of glass fiber (GF)-reinforced PA66 composite were related to the typical sliding surface damage (peeled off fibers and PA66 scratching) and surface mechanical properties, and GF orientation influenced the wear resistance of the composite and steel. In addition, steel hardness influenced the tribological properties. The influence of temperature on the tribological properties of unreinforced or GF-reinforced PA66 under boundary lubrication with grease was also studied when considering the temperature dependence of the mechanical properties on the sliding surface of PA66 and the tribochemical reaction to zinc carboxylate additives in grease. The friction mechanism of the contact between PA66 or GF-reinforced composite and a steel under PAO8 oil or grease lubrication was discussed by focusing on various parameters including the normal load (contact pressure), sliding speed, temperature, and hardness of the steel counterpart. To explain the friction coefficient obtained under different test conditions, the theoretical minimum oil film thickness under oil lubrication was calculated using the equation of the soft elastic hydrodynamic lubrication regime, considering the contributions of the oil film and lubricated solid/solid contact to the friction coefficient. Subsequently, the differences in the friction behavior between PAO8 oil and grease lubrication were investigated.

The effect of the composite composition on the tribological properties was also investigated to aid in the development of a composite with optimal tribological properties. As important parameters of the compositions of GF composite, the types of GFs (GF surface treatment agent and GF diameter) and PA66 molecular mass were deeply studied. Particularly, as a way to increase the PA66 molecular mass of the fiber composite, reactive extrusion using poly-carbodiimide composite was used, and reactive extrusion mechanism and mechanical properties of glass or aramid fibers-reinforced PA66 with added carbodiimide were clarified. In addition to GF composite, the tribological mechanism of carbon fiber-reinforced PA66 composite was investigated under both dry and grease lubricated conditions. The effects of the PA66 molecular mass, the hardness of the counterpart steel, and the temperature on the tribological properties were studied under grease lubrication and compared to unreinforced and GF-reinforced PA66. In addition, the effect of the water absorption of GF-reinforced PA66 on the tribological properties was investigated.

The analysis of all these experimental results can provide guidelines for the selection of polymer-based material and for the design of optimal parts for the industrial application.

Keywords, PA66, glass fibers, carbon fibers, aramid fibers, PAO8 oil, grease, lubrication, wear, creep, friction, soft EHL, carbodiimide, worm wheel, EPS

RESUME

Les plastiques techniques sont largement utilisés dans la fabrication de pièces de frottement, dont les engrenages à denture hélicoïdale des réducteurs à vis sans fin utilisés dans les systèmes de direction assistée électrique (EPS) des véhicules automobiles. Pour étendre ce dispositif aux véhicules plus puissants ou pour réduire la taille de ces réducteurs, le développement de matériaux polymères et d'un design de réducteurs garantissant une bonne durabilité et un frottement réduit est nécessaire.

Cette étude a permis de comprendre les propriétés tribologiques du PA66 et de composites à base de PA66 renforcés de fibres en contact avec un contre-corps en acier sous lubrification à la graisse afin d'améliorer les propriétés tribologiques des composants en polymère. Les essais de frottement ont été réalisés avec une géométrie de contact simulant celle du réducteur ; les bagues composites étant en contact avec quatre cylindres fixes en acier avec une lubrification principalement à la graisse. Les résistances à l'usure ou au fluage du composite PA66 renforcé de fibres de verre étaient liées à un endommagement de surface caractéristique (arrachement des fibres et rayures du PA66) ainsi qu'aux propriétés mécaniques de la surface. L'orientation des fibres de verre influençait la résistance à l'usure du composite et de l'acier. De plus, la dureté de l'acier a influencé les propriétés tribologiques. L'influence de la température sur les propriétés tribologiques du PA66 non renforcé ou renforcé de fibres de verre dans le cas d'une lubrification limitée avec de la graisse a également été étudiée en considérant les effets de la température sur les propriétés mécaniques de surface du PA66 et sur la réaction tribochimique des additifs de carboxylate de zinc dans la graisse. Le mécanisme de frottement du contact entre le PA66 ou le composite renforcé de fibres de verre et l'acier sous lubrification à l'huile PAO8 ou à la graisse a été examiné en se concentrant sur divers paramètres dont la charge normale (pression de contact), la vitesse de glissement, la température et la dureté du contre-corps en acier. Afin d'expliquer le coefficient de frottement obtenu sous les différentes conditions d'essai, l'épaisseur minimale théorique du film d'huile en lubrification à l'huile a été calculée selon l'équation du régime de lubrification élasto-hydrodynamique souple en considérant les contributions du film d'huile et du contact solide/solide lubrifié sur le coefficient de frottement. Ensuite, les différences de comportements au frottement entre la lubrification à l'huile PAO8 et à la graisse ont été analysées.

L'effet de la composition du composite sur les propriétés tribologiques a également été étudié pour aider au développement d'un composite aux propriétés tribologiques optimales. Identifiés comme des paramètres importants de la composition des composites renforcés de fibres de verre, les types de fibres (traitement de surface et diamètre) et la masse moléculaire du PA66 ont été étudiés en détails. En particulier, l'extrusion réactive du composite avec le poly-carbodiimide a été utilisée comme moyen d'augmenter la masse moléculaire du PA66 dans le composite. Le mécanisme d'extrusion réactive et les propriétés mécaniques du PA66 renforcé de fibres de verre ou d'aramide avec ajout de carbodiimide ont été précisés. En plus du composite avec fibres de verre, le mécanisme tribologique du composite PA66 renforcé de fibres de carbone a également été étudié en frottement sec et en lubrification à la graisse. Les effets de la masse moléculaire du PA66, de la dureté du contre-corps en acier et de la température sur les propriétés tribologiques ont été étudiés avec lubrification à la graisse et comparés au cas du PA66 non renforcé et renforcé de fibres de verre. De plus, l'effet de l'absorption d'eau par le PA66 renforcé de fibres de verre sur les propriétés tribologiques a été étudié.

L'analyse de tous ces résultats expérimentaux peut fournir des lignes directrices pour la sélection de matériaux à base de polymères et pour la conception de pièces optimales pour l'application industrielle.

Mots-clés, PA66, fibres de verre, fibres de carbone, fibres d'aramide, huile PAO8, graisse, lubrification, usure, fluage, frottement, EHL souple, carbodiimide, roue à vis sans fin, EPS

CONTENTS

INTRODUCTION.....	1
CHAPTER I: ANALYSIS OF THE CONTACT AND BIBLIOGRAPHY SURVEY.....	7
1. Introduction	11
2. Worm reducer of automobile electric power steering (EPS)	11
2.1 General application of polymer sliding parts.....	11
2.2 Electric power steering systems in automobiles.....	12
2.3 Contact form of the worm reducer	13
2.4 Polymer worm wheel.....	15
2.5 Metallic worm shaft	17
2.6 Grease	18
2.7 Requirements for downsizing and high-power driving of worm reducer	20
3. Polymer and composite material	22
3.1 Polyamide (PA)	22
3.1.1 Types of polyamides.....	23
3.1.2 Polyamide 66 (PA66)	25
3.1.3 Molecular mass of polyamides	25
3.1.4 Hygroscopicity of polyamides	28
3.2 Reinforcement fibers.....	29
3.2.1 Glass fibers (GFs).....	30
3.2.2 Carbon fibers (CFs)	32
3.2.3 Aramid fibers (AFs).....	35
3.3 Additives	36
3.3.1 Solid lubricants.....	36
3.3.2 Molecular chain extender and carbodiimide compounds	37
3.4 Impact modifier	38
4. Metallic materials	39
5. Lubrication oil and grease.....	41
5.1 Characteristics of grease	41
5.2 Low friction additives.....	41
5.2.1 Oiliness improvers.....	41
5.2.2 Solid lubricants.....	42
5.2.3 Anti-wear agents.....	42
5.2.4 Friction modifiers.....	42
5.2.5 Extreme-pressure additives	42
5.3 Effect of lubrication on the tribology of polymers and composites.....	42
6. Effects of different parameters on tribological behavior of polymer on steel contacts	44

6.1	Basic mechanism of friction and wear	44
6.2	Effects of temperature	45
6.3	Effects of contact pressure.....	46
6.4	Effects of sliding velocity	48
7.	Lubricative theories and tribology of polymer materials under oil or grease lubricated conditions ...	48
7.1	Elastohydrodynamic lubrication (EHL) theories.....	48
7.2	Lubrication regime	51
7.3	Estimation of the oil film formation under grease lubrication and comparison with oil lubrication	53
8.	Conclusions	58
CHAPTER II: EXPERIMENTAL METHODS AND MATERIALS UNDER INVESTIGATION.....		59
1.	Introduction	63
2.	Evaluated materials.....	63
2.1	PA66 and reinforcement fibers	63
2.1.1	Preparation for unreinforced PA66 and glass fiber-reinforced composite.....	64
2.1.2	Preparation for carbon fiber-reinforced PA66.....	70
2.1.3	Preparation for aramid fiber-reinforced PA66.....	70
2.1.4	Preparation for the test specimens.....	71
2.1.5	Water absorption	75
2.2	Steel material	76
2.3	Lubricants (grease and oil).....	80
2.3.1	Urea grease	80
2.3.2	Barium complex grease.....	81
2.3.3	PAO8 oil.....	81
3.	Analysis of the sample before tests	82
3.1	Image analysis of fiber orientation on the composite sliding surface	82
3.2	Measurements of viscosity number.....	83
3.3	Measurements of molecular mass.....	83
3.3.1	GF-reinforced PA66 composite with added poly-carbodiimide	83
3.3.2	AF-reinforced PA66 composite with added poly-carbodiimide	83
3.4	FT-IR measurements of PA66 with added carbodiimide compounds	83
3.5	Measurements of fiber length distribution inside the tensile test specimens	85
3.6	Observation of fiber orientation inside the tensile test specimens.....	85
4.	Experimental set-ups and testing conditions.....	86
4.1	Tensile and Charpy impact tests	86
4.2	Sliding test at LTDS	88
4.2.1	Presentation of the tribometer and samples geometry	88

4.2.2	Tests conditions.....	90
4.2.3	Quantification of damage	93
4.3	Sliding test at JTEKT.....	94
4.4	Micro indentation measurement.....	95
4.5	Nano indentation measurement.....	96
5.	Analysis methods after sliding tests.....	96
5.1	Optical microscopy.....	96
5.2	SEM and EDX.....	96
5.3	Interferometry	97
5.4	XPS	97
5.5	ToF-SIMS.....	97
6.	Conclusions	98

CHAPTER III: BASIC TRIBOLOGICAL BEHAVIOR OF GF-REINFORCED PA66 IN CONTACT WITH CARBON STEEL UNDER HIGH CONTACT PRESSURE AND GREASE LUBRICATION.....99

1.	Introduction	101
2.	Detailed tribological behavior of the contact and damage of the GF-reinforced composite and unreinforced PA66	101
2.1	Sliding test results and observation of samples after test	101
2.2	Change over time of the sliding surface and reason of height decrease (contribution of wear and creep).....	106
2.3	Effect of fiber orientation and change in the surface mechanical properties.....	111
2.4	The difference of the tribological properties in unreinforced PA66 and GF-reinforced PA66 composite	116
3.	The effect of fiber orientation on the wear behavior of steel counterpart and composite	118
3.1	Wear behavior of counterpart steel and effect of the fiber orientation in the composite ring..	118
3.2	Effect of the fiber exposure on the sliding surface	120
4.	Contribution of each parameter to the increase of friction and damage.....	123
5.	Effects of the hardness of the steel counterpart	128
6.	Conclusions	130

CHAPTER IV: EFFECTS OF TEMPERATURE AND ADDITION OF ZINC CARBOXYLATE TO GREASE ON THE TRIBOLOGICAL PROPERTIES OF PA66 IN CONTACT WITH CARBON STEEL.....133

1.	Introduction	135
2.	Effects of adding zinc carboxylate to grease under test conditions with sliding heat generation using GF-reinforced PA66	136
3.	Temperature dependence of the tribological properties and effects of adding zinc carboxylate to grease.....	138

3.1	Temperature dependence of the tribological properties under 1 s stopping condition using GF-reinforced PA66.....	138
3.2	Temperature dependence of the tribological properties under test conditions at stable temperature using GF-reinforced PA66	139
3.3	Relationship between the mechanical properties and tribological properties, and effect of the tribochemistry.....	143
3.4	The temperature dependence and effect of the zinc carboxylate on the wear resistance of steel counterpart.....	145
3.5	The effect of the intermittent duration of sliding on the tribological properties	146
4.	Identification of the tribofilm on the surface of steel and composite at 80°C	148
4.1	Tribofilm analysis on the steel cylinder.....	148
4.1.1	SEM observation and EDX analysis	148
4.1.2	XPS analysis	151
4.1.3	ToF-SIMS analysis	153
4.2	Tribofilm analysis on the GF-reinforced PA66 composite	156
4.2.1	SEM observation and EDX analysis	156
4.2.2	XPS analysis	158
4.2.3	ToF-SIMS analysis.....	160
4.3	Tribochemical reaction on the sliding surface	160
5.	Contribution and roles of tribofilm on the tribological properties.....	161
6.	Temperature dependence on tribofilm formation.....	164
7.	Effects of adding zinc carboxylate to grease on the tribological properties of unreinforced PA66	165
8.	Conclusions	169

CHAPTER V: FRICTION MECHANISM OF UNREINFORCED AND GF-REINFORCED PA66 IN CONTACT WITH STEEL UNDER PAO8 OIL OR GREASE LUBRICATION.....

1.	Introduction	173
2.	Friction mechanism under PAO8 oil lubrication	175
2.1	Effect of ring surface roughness, sliding speed, and temperature on friction coefficient	175
2.2	Oil film thickness estimated based on lubrication regime.....	178
2.3	Development of Λ -friction coefficient master curve.....	182
2.4	Effect of normal load (contact pressure) on friction coefficient	183
2.5	Effect of steel counterpart hardness on friction coefficient	185
2.6	Effect of GF reinforcement on friction coefficient	187
3.	Friction mechanism under grease lubrication	192
3.1	Difference of the friction mechanism between PAO8 oil lubrication and grease without zinc carboxylate lubrication	192
3.2	Effect of addition of zinc carboxylate to grease under various test conditions	196

4. Conclusions	204
----------------------	-----

CHAPTER VI: EFFECTS OF GF PROPERTIES AND POLYMER MOLECULAR MASS ON THE MECHANICAL AND TRIBOLOGICAL PROPERTIES OF A PA66-BASED COMPOSITE.....207

1. Introduction	209
2. Effects of the interfacial shear strength between the GFs and PA66 on the mechanical and tribological properties.....	210
2.1 Effect of the interfacial shear strength on the mechanical properties	210
2.2 Effect of the interfacial shear strength on the tribological properties.....	211
2.3 Effect of the GF orientation on the sliding surface with different GF surface treatment agents	216
2.4 Estimation of the interfacial shear strength based on Kelly-Tyson model.....	217
3. Effects of the PA66 molecular mass on the mechanical and tribological properties.....	221
3.1 Effect of the PA66 molecular mass on the wear and creep resistance of GF composite	221
3.2 Effect of the PA66 molecular mass on the wear resistance of steel counterpart	225
3.3 Effect of the PA66 molecular mass on the fiber orientation on the sliding surface of GF composite ring specimen.....	225
3.4 Mechanism of the improvement in the tribological properties of GF composite with the increase in the PA66 molecular mass.....	226
4. Effects of GF diameter on the mechanical and tribological properties	230
4.1 Effect of GF diameter on the tensile mechanical properties	230
4.2 Effect of GF diameter on the wear and creep resistance of the composite.....	230
4.3 Effect of GF diameter on the wear resistance of steel counterpart.....	234
5. Conclusions	241

CHAPTER VII: REACTIVE EXTRUSION MECHANISM, MECHANICAL AND TRIBOLOGICAL BEHAVIOR OF FIBER- REINFORCED PA66 WITH ADDED CARBODIIMIDE.....243

1. Introduction	245
2. Effects of the structure surrounding the carbodiimide group on the reaction velocity and mechanism	247
3. Effects of the carbodiimide feeding position in the twin screw extruder and the amount of added carbodiimide	248
4. Wear resistance of GF composite with added carbodiimide	250
5. Wear resistance of AF composite with added carbodiimide	252
6. Toughness of PA66-GF-carbodiimide with added olefin polymer.....	254
7. Conclusions	256

CHAPTER VIII: COMPARISON OF THE TRIBOLOGICAL PROPERTIES OF CARBON/GLASS FIBER-REINFORCED PA66-BASED COMPOSITES IN CONTACT WITH STEEL WITH AND WITHOUT GREASE

LUBRICATION	259
1. Introduction	261
2. Tribological properties without lubrication	262
2.1 Fiber orientation on the ring specimen sliding surface	262
2.2 Tribological properties under dry conditions.....	264
3. Tribological properties under grease lubrication	270
4. Effects of the molecular mass on the tribological properties of the CF composite and steel counterpart... ..	274
4.1 Wear and creep resistance of the composite with different values of PA66 molecular mass	274
4.2 Effect of PA66 molecular mass on the wear resistance of the counterpart steel	277
5. Effects of the hardness of the counterpart steel on the tribological properties	279
5.1 Effect of the hardness of the counterpart steel on the wear and creep resistance of the composite and wear resistance of the steel	279
5.2 Hardness of fibers and wear mechanism of steel counterpart.....	282
6. Differences in the temperature dependence of the tribological properties and tribochemistry between the CF and GF composites	286
6.1 Temperature dependence of the tribological properties of the CF composite and comparison to the GF composite.....	286
6.2 Discussion on the tribofilm formation and effect of zinc carboxylate	289
6.3 Effect of the contact pressure on the tribofilm formation and temperature dependence of the tribological properties.....	292
7. Conclusions	297
CHAPTER IX: EFFECTS OF WATER ABSORPTION ON THE TRIBOLOGICAL PROPERTIES OF GF-REINFORCED PA66 IN CONTACT WITH STEEL UNDER GREASE LUBRICATION CONDITIONS	299
1. Introduction	301
2. The effect of water absorption on the mechanical properties	301
3. The effect of water absorption on the tribological properties	302
4. Conclusions	307
GENERAL CONCLUSIONS	309
REFERENCES	317
PUBLICATIONS GENERATED FROM THIS WORK	333

INTRODUCTION

In this thesis, tribological properties of unreinforced and fiber-reinforced PA66 in contact with steel under grease lubrication are studied to improve the tribological properties of polymer sliding parts including worm reducer in the automotive electric power steering. Basic tribological properties including wear and creep of each material and friction mechanism are discussed. In addition, the effects of the composition of the fiber-reinforced PA66 on the tribological properties are investigated.

Backgrounds

The requirements for lighter automobile polymer parts to achieve energy savings and to reduce carbon dioxide emissions are increasing owing to energy issues such as global warming. In addition, the use of polymer sliding parts in the automotive industry is increasing in response to the demand for higher levels of quiet accompanying the computerization and hybridization of automobiles. Recently, the requirements for the downsizing of automobiles and industrial machines and growing concern for the environment have increased the demand for reducing the size and weight of these polymer sliding parts and their capability to withstand high stress.

Among various types of resin materials, polyamide 66 (PA66) is known as an engineering plastic, and has useful properties, such as heat resistance, high strength, toughness, and high wear resistance. Therefore, PA66 is widely used for sliding parts in automobiles or industrial machines such as various types of gears, bearing retainers, and rollers. In addition, adding reinforcement fibers, such as glass fibers (GF), carbon fibers (CF), or aramid fibers (AF), is a common means to improve the tribological properties of PA66. When polymer sliding parts are used under severe conditions, oil or grease lubrication is introduced to the tribosystem to reduce the sliding heat, the friction coefficient, and wear.

The demand for the use of plastic worm gears is particularly important in the worm reducer of the automobile electric power steering (EPS) because the gears are lightweight, reduce vibration and noise, and are corrosion resistant. Fig. Intro. 1 presents the schematic of dual-pinion type EPS and worm reducer. The plastic worm gear of the reducer used in electric power steering experiences a significantly high contact pressure (over 100 MPa) under sliding conditions. Therefore, some form of grease lubrication is necessary to reduce friction between the plastic worm wheel and the steel worm shaft. The recent downsizing of automotive components, coupled with the high demand for electric power steering in large vehicles owing to their impact on fuel economy, highlights the need for robust worm reducer support. However, applying higher torque to worm reducer will lead to large deformation of the teeth of the plastic worm wheel (increase in the backlash), breakage at a much earlier stage, and increase of the sliding torque. Then, it is imperative to understand the basic tribological properties on the sliding surface and apply them to the material development and design of the sliding surface which can be used under severer conditions.

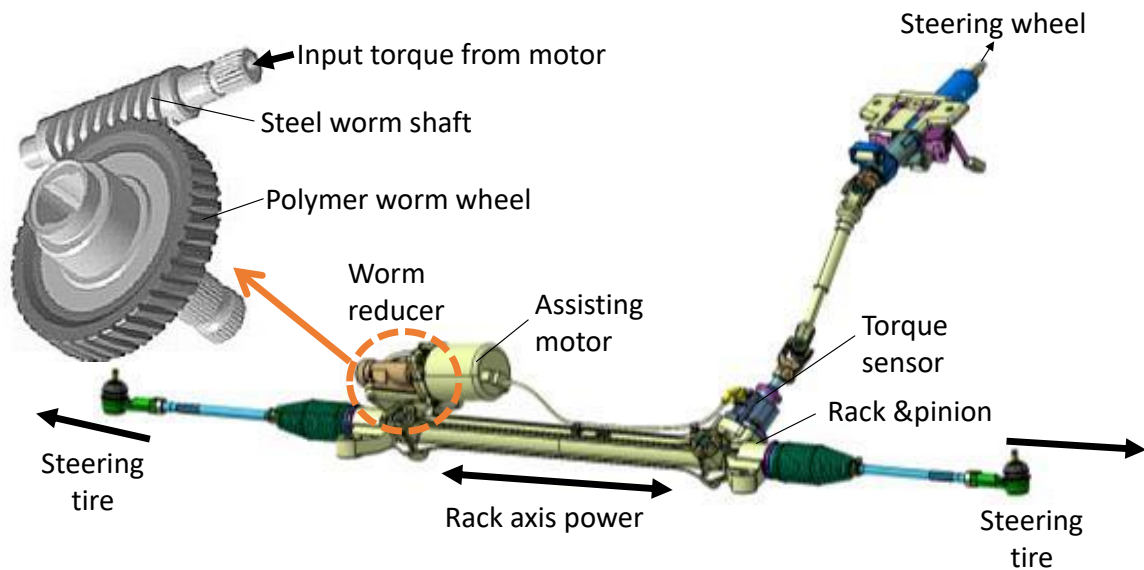


Fig. Intro. 1 Schematic of dual-pinion type EPS and worm reducer which are fabricated by JTEKT CORPORATION.

Objectives and research approaches

First, it is necessary to understand typical tribological properties during sliding of GF-reinforced PA66 and a steel counterpart under high contact pressure and grease lubricated conditions. The majority of the previous studies on the tribology of fiber-reinforced polyamide were performed in dry conditions, and there are very few reports on the tribological properties of fiber-reinforced PA66 under grease lubrication. The reason is that polymer materials have self-lubricating properties, and it is possible to use them as sliding parts without lubrication in many cases. In the present study, the sliding test which can simulate the high contact pressure contact of PA66 and steel counterpart is established, and detailed wear and creep mechanism of GF-reinforced is discussed.

It is necessary to consider not only the wear resistance of PA66 but also the wear resistance of the metallic counterpart, especially when using PA66 material reinforced with hard fibers, which may have the most aggressive effects on the metallic counterpart because the wear on both materials will lead to much earlier breakage of actual parts and to an increase of the sliding torque. However, the wear mechanism has not been clarified sufficiently. Therefore, it is necessary to understand the tribological phenomena to properly design the contact surface of the composite and to select the proper steel and grease. In the present study, we will clarify the wear mechanism of the steel counterpart, and the effect of mechanical properties of steel counterpart on the tribological properties of the contact.

Next, to use polymer sliding parts under a high temperature environment, such as inside an engine compartment of an automobile, it is necessary to understand the temperature dependence of the tribological properties. Polymer material including PA66 has temperature dependence of the mechanical and tribological properties, and several works focused on the temperature dependence of the tribological properties under dry conditions. In addition, the effects of additives on a tribochemical reaction related to grease differ at each temperature and this should be considered when we discuss the temperature dependence of the tribological properties under lubrication. Previous studies have focused on the mechanism of tribochemistry on the sliding surface of steel, ceramic, or hard coatings (such as diamond-like carbon), and on the effects of the tribological properties when using such additives. However,

regarding the sliding of polymer and steel, or the sliding between polymers, few studies have been conducted on the tribochemistry of the additives or on the effects of a tribofilm formation on the tribological properties. Therefore, we will clarify temperature dependence of the tribological properties considering the tribochemistry on the sliding surface between unreinforced or GF-reinforced PA66 and carbon steel under boundary lubrication conditions.

Friction mechanism between PA66 and steel under lubrication should also be clarified. Requirements for the friction decrease of the actual sliding parts are increasing. It is vital to understand the friction mechanism in this tribosystem and to adjust the design of the sliding surface to control the friction of the actual sliding parts, including the polymer worm wheel. Various parameters including sliding speed, normal load (contact pressure), temperature, steel hardness, and surface roughness are supposed to have an influence on the friction. In the present PhD thesis, the friction mechanism will be elucidated considering both the soft EHL theory and solid/solid contact theory under lubrication, and the difference of the friction behavior between oil and grease will be discussed.

In addition, it is required to present the guideline for the development of plastic material which can ensure the good performance of the polymer sliding parts. We will focus on the type of fibers (glass fiber, carbon fiber, and aramid fiber) and PA66 molecular mass (including the effect of reactive extrusion to increase it). Few studies have focused on the effects of these parameters on the tribological properties under grease lubrication.

In summary, in the present thesis, tribological properties of unreinforced and fiber-reinforced PA66 in contact with steel counterpart under grease lubrication will be studied to improve the tribological properties of polymer sliding parts including worm reducer in the automotive EPS. First, specific tribological properties in this tribosystem considering the wear and creep resistance of PA66 and steel, friction mechanism considering tribochemistry and various theories will be discussed. In addition, the effects of the composition of the fiber-reinforced PA66 on the tribological properties will be investigated.

Organization of the manuscript

The manuscript is organized as presented in Fig. Intro. 2.

In Chapter I, literature study will be summarized, including the development of worm reducer of automobile EPS, polymer and composite material, metallic material, lubrication oil and grease, influence of different parameters on the tribological behavior, and lubrication theories of contacts including a polymer material.

Chapter II will introduce the materials under investigation, including the material preparing process, the experimental and analytical methods, and the test conditions.

In Chapter III, basic tribological behavior of GF-reinforced PA66 in contact with carbon steel under high contact pressure and grease lubricated conditions will be investigated. Change over time of the sliding surface conditions and mechanical properties will be discussed, and the contribution of each parameter and effect of the steel hardness on the tribological properties will be elucidated. The results will serve as baselines for the study of the tribology of composite in the following chapters.

Chapter IV will investigate the influence of temperature on the tribological properties of unreinforced or GF-reinforced PA66 in contact with carbon steel under boundary lubrication with grease. This will be studied with considering the temperature dependence of the mechanical properties on the sliding surface of PA66 and the tribochemical reaction to zinc carboxylate additives in grease. XPS and ToF-SIMS analyses will be used to reveal the

formation of a carboxylate tribofilm on the steel surface and a zinc sulfide reactive film on the PA66 surface, which are related to the tribochemical reactions of the additives present in the grease used.

In Chapter **V**, the friction mechanism of the contact between unreinforced or GF-reinforced PA66 and a steel counterpart under additive-free PAO8 oil or grease lubrication will be discussed by focusing on various parameters including the normal load (contact pressure), sliding speed, temperature, and hardness of the steel counterpart. To explain the friction coefficient obtained under different test conditions, the theoretical minimum oil film thickness will be calculated using the equation of the soft elastic hydrodynamic lubrication regime, and the master curve of the relationship between Λ ratio (film thickness to roughness ratio) and the friction coefficient will be proposed. In addition, the contributions of the oil film and lubricated solid/solid contact to the friction coefficient will be discussed. Finally, the difference between PAO8 oil lubrication and grease lubrication will be elucidated.

Chapter **VI** investigates the effects of the composition of GF-reinforced PA66 on its mechanical and tribological properties under grease lubrication to aid in the development of a composite with optimal tribological properties. As important parameters of the compositions of GF composite, the types of GFs (GF surface treatment agent and GF diameter) and molecular mass of PA66 will be deeply studied.

Chapter **VII** focuses on the reactive extrusion mechanism of fiber-reinforced PA66 with added poly-carbodiimide as a way to increase the PA66 molecular mass. The reaction between PA66 and poly-carbodiimide during the extrusion and injection molding will be clarified, and effect of an addition of poly-carbodiimide on the mechanical and tribological properties will be discussed.

Chapter **VIII** focuses on the comparison of the tribological properties of carbon and glass reinforcement fibers in PA66-based composites in contact with steel with and without grease lubrication. The difference of the tribological properties between dry conditions and grease lubrication will be discussed using both CF and GF composites. In addition, the effect of the PA66 molecular mass and counterpart steel hardness on the tribological properties, and temperature dependence of the tribological properties considering the tribochemical reaction will be discussed, comparing the tribological properties of CF and GF composites.

Chapter **IX** presents the effects of water absorption on the tribological properties of GF-reinforced PA66 in contact with steel under grease lubrication conditions. PA66 is known to have the hygroscopicity, therefore it is necessary to clarify the effect of water absorption on the tribological properties.

In the general conclusions and perspectives, the conclusions of each work will be summarized, and future perspective on the present study will be stated.

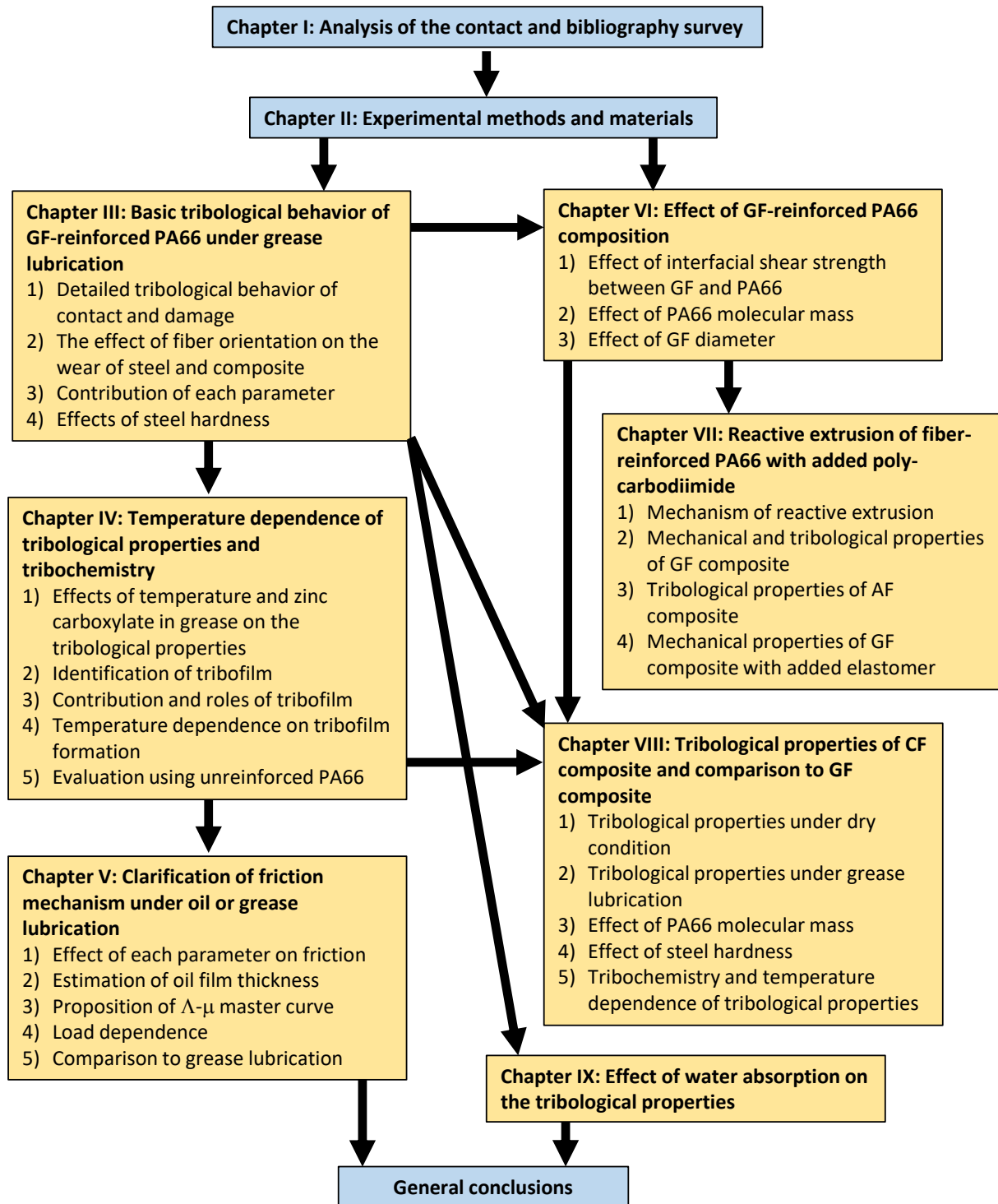


Fig. Intro. 2 Organization of the manuscript.

CHAPTER I

ANALYSIS OF THE CONTACT AND
BIBLIOGRAPHY SURVEY

CHAPTER I: ANALYSIS OF THE CONTACT AND BIBLIOGRAPHY SURVEY

1. Introduction.....	11
2. Worm reducer of automobile electric power steering (EPS)	11
2.1 General application of polymer sliding parts	11
2.2 Electric power steering systems in automobiles.....	12
2.3 Contact form of the worm reducer	13
2.4 Polymer worm wheel.....	15
2.5 Metallic worm shaft.....	17
2.6 Grease.....	18
2.7 Requirements for downsizing and high-power driving of worm reducer.....	20
3. Polymer and composite material.....	22
3.1 Polyamide (PA).....	22
3.1.1 Types of polyamides.....	23
3.1.2 Polyamide 66 (PA66)	25
3.1.3 Molecular mass of polyamides.....	25
3.1.4 Hygroscopicity of polyamides	28
3.2 Reinforcement fibers.....	29
3.2.1 Glass fibers (GFs)	30
3.2.2 Carbon fibers (CFs)	32
3.2.3 Aramid fibers (AFs).....	35
3.3 Additives	36
3.3.1 Solid lubricants	36
3.3.2 Molecular chain extender and carbodiimide compounds.....	37
3.4 Impact modifier	38
4. Metallic materials	39
5. Lubrication oil and grease	41
5.1 Characteristics of grease	41
5.2 Low friction additives	41
5.2.1 Oiliness improvers.....	41
5.2.2 Solid lubricants	42
5.2.3 Anti-wear agents	42
5.2.4 Friction modifiers	42
5.2.5 Extreme-pressure additives	42

5.3	Effect of lubrication on the tribology of polymers and composites	42
6.	Effects of different parameters on tribological behavior of polymer on steel contacts	44
6.1	Basic mechanism of friction and wear	44
6.2	Effects of temperature	45
6.3	Effects of contact pressure	46
6.4	Effects of sliding velocity	48
7.	Lubricative theories and tribology of polymer materials under oil or grease lubricated conditions	48
7.1	Elastohydrodynamic lubrication (EHL) theories	48
7.2	Lubrication regime.....	51
7.3	Estimation of the oil film formation under grease lubrication and comparison with oil lubrication	53
8.	Conclusions	58

CHAPTER I: ANALYSIS OF THE CONTACT AND BIBLIOGRAPHY SURVEY

In this chapter, the literature study is summarized to understand the research context, including the plastic sliding parts or worm reducer of electric power steering, the tribological materials, such as polymers, metallic materials, and lubricants, and tribological theories.

1. Introduction

This chapter focuses on the analysis of the contact in the worm reducer of the automobile electric power steering (EPS) and reviews the literature on the technological aspects related to this study. First, the practical applications of the polymer sliding parts are investigated. Next, the significance of the introduction of automobile EPS is stated, and the contact geometry of the polymer worm wheel and steel worm shaft inside the worm reducer, the effects of each material (polymer, steel, and grease) on the tribological properties of the worm reducer, and the significance of downsizing and the use of the EPS under severe conditions are discussed. In addition, the literature on the effects of the key parameters of polymers or composites, including the type of polyamide (PA) or reinforcement fibers, metallic material parameters, or grease parameters, particularly on the general tribological properties of the polymer or composite in contact with metallic materials is reviewed. Finally, the effects of parameters (such as temperature, sliding speed, and contact pressure) on the tribological properties are investigated. Lubrication theories, such as the soft elastohydrodynamic lubrication (EHL) theories, are presented.

2. Worm reducer of automobile electric power steering (EPS)

2.1 General application of polymer sliding parts

The requirements for lighter machine parts in automobiles or industrial machines using polymer materials to achieve energy savings and to reduce carbon dioxide emissions are increasing owing to societal challenges such as global warming. In addition, the use of polymer sliding parts in the automotive industry is increasing in response to the demand for lower levels of noise accompanying the computerization and hybridization of automobiles [1, 2, 3, 4]. Polymer tribology, as a research field, is now fully mature after approximately 50 years of the publication of numerous research articles and reports on various tribological phenomena of considerably many polymers in bulk, composite, and hybrid forms [5]. The tribological applications of polymers include gears such as spur gears [6, 7, 8, 9, 10, 11, 12, 13, 14], helical or worm gears [15, 16, 17, 18, 19], a range of bearings and bearing cages [20, 21, 22, 23, 24, 25], artificial human joint prosthesis [26, 27, 28], plain bearings [29], automobile brake pads [30], and rollers [31]. The list is increasing. For example, in the new subject of micro-electromechanical systems (MEMS), polymers (such as PMMA and PDMS) are becoming

popular as structural materials over the widely used material, Si [5]. Recently, the demand for downsizing automobiles and industrial machines and an increasing focus on environmental concerns have resulted in an increasing demand for smaller sizes and weights of parts and for the ability to apply higher stresses to plastic parts [32, 33, 34, 35]. Therefore, improvements in the mechanical properties of the resin materials are necessary.

2.2 Electric power steering systems in automobiles

Considering the automobile steering system, in the late 1960s, as passenger vehicles largely spread, hydraulic power steering (HPS), which has the characteristics of light weight and comfort, was practically applied to improve heavy steering. As motorization advanced, as well as the increase in the demand for small vehicles and female drivers, the requirement for applying power steering to light vehicles, which are difficult to equip with HPS systems, began to appear [36]. Owing to the increasing requirement for the improvement of fuel consumption because of the environmental demand, as stated in Section 2.1, the traditional HPS system has been rapidly replaced by EPS [37, 38]. In the EPS system, the output of an electric motor, which changes according to the driver's steering wheel maneuvering, is transmitted to the steering output shaft through a reducer [39]. The column-type EPS (C-EPS) was commercialized in 1988 for small vehicles because it can reduce engine power loss and eliminate the requirement to consider the hydraulic pump and pipes in the engine compartment [40], and it is the most widely used EPS in passenger vehicles because of its advantages such as low cost and small size [38]. In the traditional HPS, pump operation is required when starting the engine. Thus, engine efficiency decreases. However, in the EPS, the fuel consumption can be decreased by approximately 10% with the use of an electric motor [41]. Sadeghi et al. [42] indicated that EPS provides fuel savings as high as 0.2 to 0.3 L per 100 km compared with HPS systems. In the C-EPS, the assisting motor and worm reducer are located inside the cabin (Fig. I. 1) away from the engine compartment, to provide cost-effective power steering with good crash characteristics. For vehicles for which available package space or crash behavior creates problems with the C-EPS, single-pinion EPS systems are used. This moves the motor into the engine compartment, with an assist mechanism acting via a worm/gear to the steering pinion. For vehicles with larger masses or more direct steering ratios, or with challenging packaging constraints, dual-pinion systems can be used (Fig. I. 2) [43].

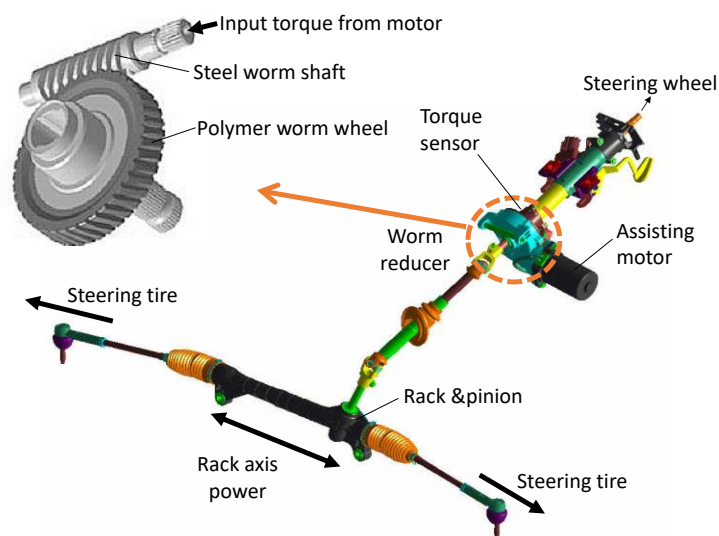


Fig. I. 1 Schematic view of a column-type EPS (C-EPS) fabricated by JTEKT CORPORATION.

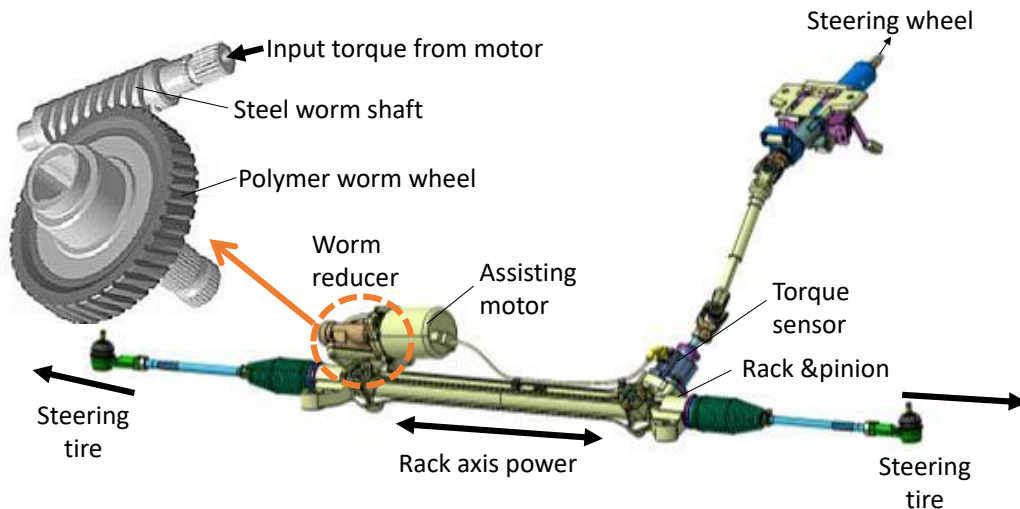


Fig. I. 2 Schematic view of dual-pinion-type EPS (DP-EPS) fabricated by JTEKT CORPORATION.

2.3 Contact form of the worm reducer

In the C-EPS, pinion-type EPS (P-EPS), and DP-EPS, a worm wheel is adopted as the reducer, and a polymer material is used for the worm wheel. This is because plastic worm wheels are favorable for weight, vibration, and noise reduction, corrosion resistance, high gear ratio, higher torque transmission efficiency than in metallic worms, and low production cost [18, 19, 37, 44, 45]. Fig. I. 3 shows a schematic view of the plastic worm wheel and metallic worm shaft in an automobile steering worm reducer. Essentially, EPS consists of an engine control unit that assists the steering control unit, torque sensor, and reduction gear module that generates compensation torque.

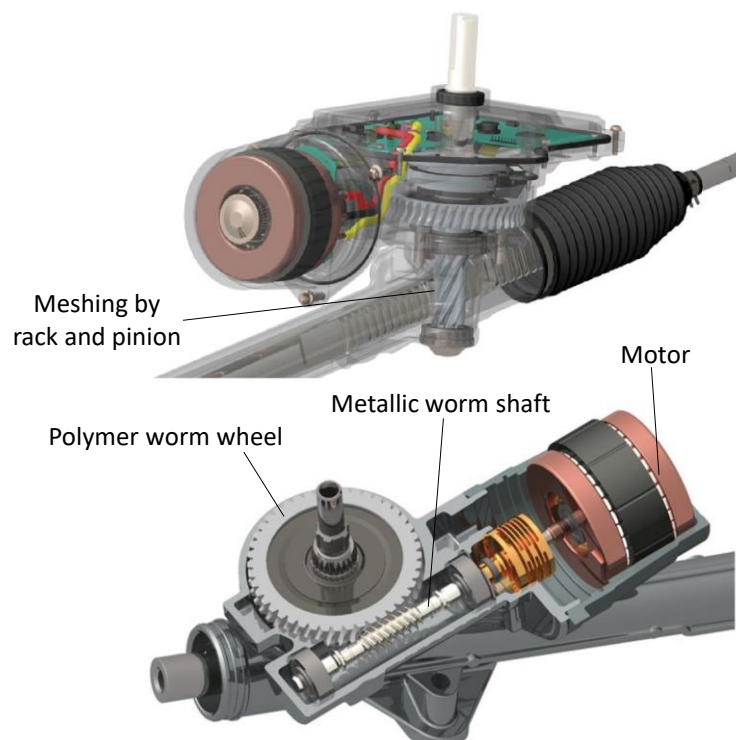


Fig. I. 3 Schematic view of the worm reducer in an automobile electric power steering composed of the plastic worm wheel and metallic worm shaft [43].

A polymer worm wheel is an important safety component that assists the steering force by supporting the load on the front axis of the automobile and is also a tribological element for which high reliability is required. The necessary characteristics of the worm wheel include suppression of the rattle noise caused by the decrease in tooth thickness of the polymer worm wheel, known as backlash (Fig. I. 4), in addition to the assurance of durability and reduction of the steering torque. Fig. I. 5 shows the contact geometry of the polymer worm wheel, which is easily affected by sliding and rolling during usage, and upon which heat generation and cooling are repeated owing to the sliding process. This combination creates a complex tribological mechanism on tooth surfaces. Wear (loss of matter) and creep (plastic deformation) affect the decrease in tooth thickness; however, separating the wear and creep from the tooth surface observation for evaluation after the durability test of the worm wheel is difficult. In addition, a high output promotes a decrease in the tooth thickness through an increase in the contact pressure on the tooth surface, which in turn decreases the durability. Consequently, the wear and creep resistances for material development and the design of the worm wheel or worm reducer must be ensured because these properties significantly affect the decrease in the tooth thickness [46].

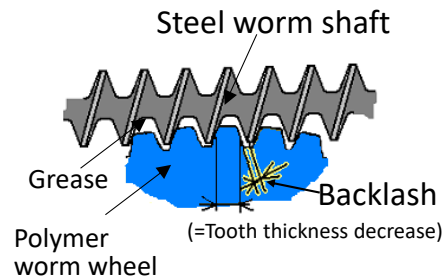


Fig. I. 4 Schematic view of meshing of steel worm shaft and polymer worm wheel.

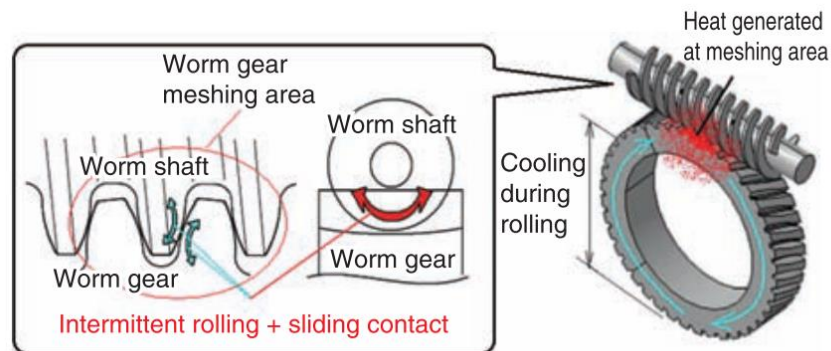


Fig. I. 5 Contact geometry of the polymer worm wheel and steel worm shaft [46].

Therefore, this study performed a sliding test of steel cylinder-polymer ring specimens, as such as test can generate a high contact pressure as observed in the actual contact of the worm reducer and evaluate the effect of pure sliding under grease lubrication (see Section 4.2 in Chapter II for details).

It is also important to decrease the rotation torque in the worm reducer to improve the steering experience. Insufficient transmission efficiency causes several steering problems, which are called “sticky” and “annoying” steering, and the only method of resolving these problems is to improve the transmission efficiency of the worm gear in the EPS system [38,

45]. Kim et al. [45] presented an efficiency prediction model of a worm gear using the friction coefficient measured in a polyamide 6 (PA6) ball on a steel disc sliding test, Hertz's law, and gear geometry. The estimated efficiency coincided well with the measured values in the actual worm gear efficiency tests under grease lubrication. Kim [38] also developed a worm gear efficiency model considering the misalignment of the metallic worm shaft of the EPS; the geometrical and tribological analyses and predicted efficiency exhibited a much better correlation with the measured values, which were affected by the output torque (normal contact pressure).

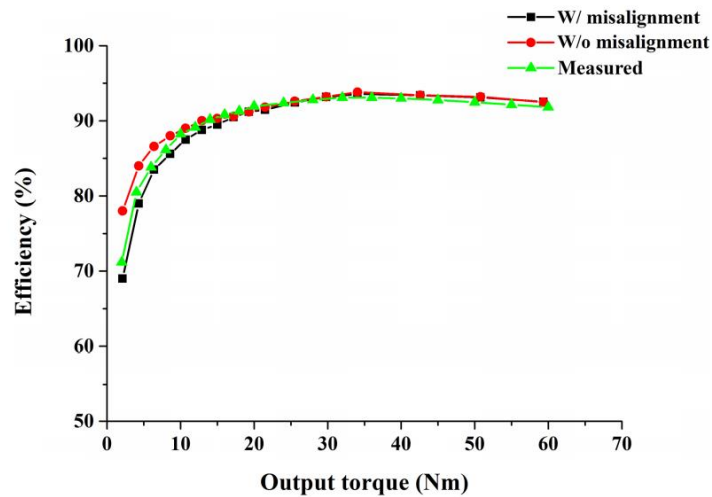


Fig. 1. 6 Measured (green) and estimated efficiency considering misalignment (black) and without misalignment (red) with different values of the output torque [38].

However, as various factors of sliding properties on the tooth surface affect the rotation torque, it is difficult to provide a simple estimation of which of these agents is the primary cause. Therefore, an integrated analysis of the factors affecting the sliding properties on the tooth surface should be performed, and the results should be applied to the design of the worm wheel or reducer and the conditions of the gear teeth [46].

2.4 Polymer worm wheel

The materials for polymer worm wheels in worm reducers include unreinforced PA6 [38, 45], unreinforced PA66 [46, 47], glass fiber (GF)- and carbon fiber (CF)-reinforced PA6 with graphite and molybdenum disulfide (MoS_2) [48], polyphenylene sulfide (PPS) [49], GF-reinforced PA66 [37, 44, 50, 51, 52], CF-reinforced PA66 [52], GF-reinforced PA12 (PA12) [41], and aramid fiber (AF)-reinforced poly-aminoamide [53]. Fig. 1. 7 shows the different types of injection-molding processes of the polymer worm wheel [41]. Generally, polymer worm wheels are fabricated through the injection molding of pellets (pin-gate system in which the melted polymer is injected from single or multiple injection points or a disc-gate system in which the melted polymer is injected at the upper position of the molding compact and spreads radially) and mechanical forming of teeth by hob-cutting. In this process, good accuracy in the dimensions of the teeth can be obtained. In contrast, the teeth can be fully formed by injection molding alone, without mechanical cutting (preliminary tooth injection). This process is a cost-saving measure because tooth formation is not necessary. However, the accuracy of the dimensions of the teeth is worse than the mechanical forming of teeth. When using the fiber-reinforced composite, the fiber orientation in the molding compact and teeth

changes depending on the gate system of the injection-molding process (Fig. I. 7), and the differences in the fiber orientation affect the mechanical properties and performance of the worm wheel (sliding torque and durability) [41].

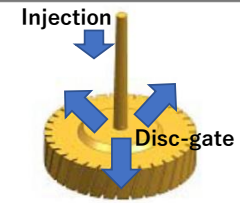
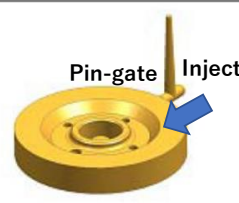
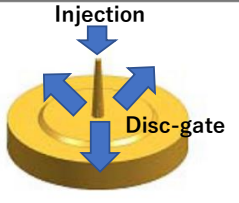
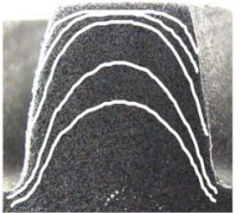
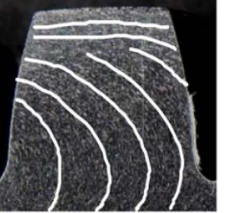
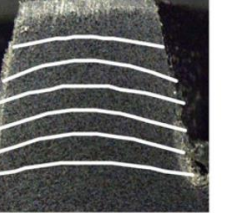
Classification	Preliminary teeth injection	Side injection	Upper injection
Shape			
Direction of glass fiber			

Fig. I. 7 Polymer worm wheel forming process and GF flow according to gate locations [41].

Kim et al. [44] designed a polymer worm wheel using computer-aided engineering (CAE) analysis and investigated the durability of an actual gear test using unreinforced PA66, GF 25 wt%-reinforced PA66, and GF 50 wt%-reinforced PA66. They compared the spur tooth and helical tooth forms (Fig. I. 8). The CAE structural analysis indicated that the helical-type worm wheel is relatively advantageous in terms of the maximum stress and strain in the application of the plastic worm wheel tooth profile and the adopted materials. Injection-molding CAE analysis indicated that a worm wheel with a 50 wt% GF reinforcement content is advantageous in terms of deformation, which has a significant effect on the operation of the worm wheel. Durability evaluation of the worm wheel backlash with respect to GF reinforcement content and compared with existing high-viscosity unreinforced PA66 worm wheels was conducted. The results indicated that the worm wheel with GF exhibited an increase in backlash after 20,000 cycles while existing high-viscosity resin tended to exhibit a dramatic increase in backlash immediately after 1,000 cycles of operation. The GF 25% worm wheel exhibited a higher backlash after 90,000 cycles. In contrast, the worm wheel with 50 wt% GF reinforcement content was relatively advantageous in terms of performance.



Fig. I. 8 Plastic worm wheels manufactured by injection molding: (a) plastic worm wheel with spur tooth form; (b) plastic worm wheel with helical tooth form [44].

The durability of the unreinforced PA66 worm wheel used as the worm reducer in an automobile EPS system under barium complex grease increased proportionally with the increase in the molecular mass of PA66 (Fig. I. 9). This is because the entanglement of the molecular chain, which is ensured by the high molecular mass of the PA66 resin, prevented the propagation of the crack caused by the creep (Fig. I. 9) [46].

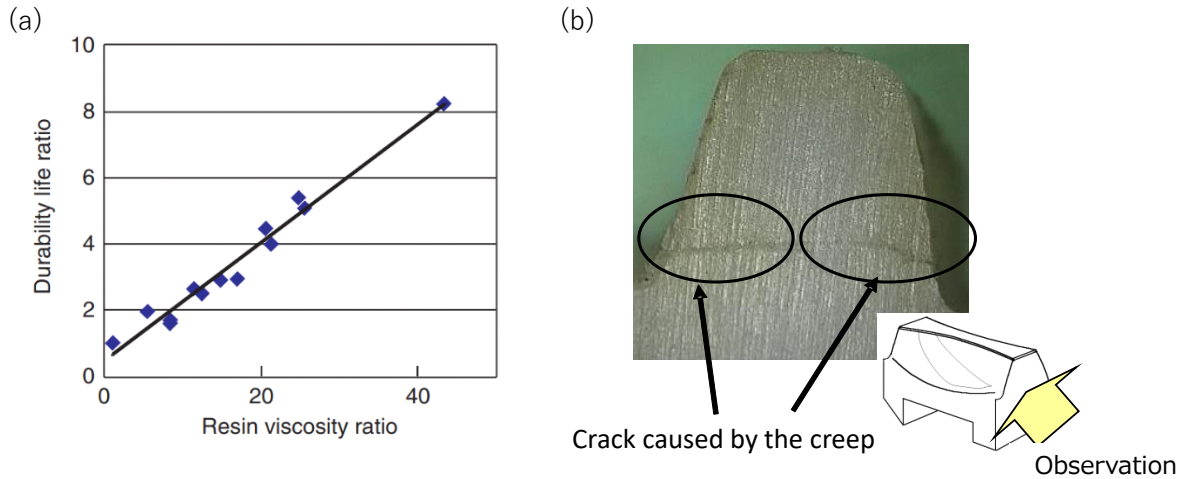


Fig. I. 9 (a) Relationship between PA66 resin viscosity ratio, which is correlated to the molecular mass, and durability life ratio of an unreinforced PA66 worm wheel in the durability test; (b) observation of a crack in the tooth of the worm wheel [46].

2.5 Metallic worm shaft

The metallic worm shaft is primarily fabricated from steel, such as S45C (carbon steel containing 0.45 wt% of carbon) of the Japanese Industrial Standard (JIS) [38, 42, 43, 45, 54]. Both the wear resistance of the polymer worm wheel and that of the metallic worm shaft must be considered, particularly when using hard-fiber-reinforced composites. This is because reinforcement fibers may have the most aggressive effects on the metallic worm shaft as the wear on both materials will result in much earlier breakage of actual parts and an increase in the sliding torque. When a metallic worm shaft is used in contact with an unreinforced polymer, the shaft should not be heat treated after the mechanical forming of the teeth or when soft steel (with Vickers hardness HV 280–300) is used. However, heat treatment such as high-frequency quenching and tempering should be used for the worm shaft after forming the teeth when the worm shaft is used meshing with the composite worm wheel, which contains hard reinforcement fibers that have destructive effects on the surface of the worm shaft. However, the heat treatment process induces a change in the dimension (distortion), deteriorating the accuracy in the meshing, and increasing the product cost by the additional heat treatment process and difficulty of tooth formation of the worm shaft.

In the literature review, studies focusing on the effects of the material or mechanical properties of the metallic worm shaft on the performance of the worm reducer were not observed; therefore, the wear mechanism has not been clarified. The proper design of the contact surface of the composite and selection of the proper steel and grease requires the tribological phenomena to be understood.

2.6 Grease

Grease lubrication is a common method of improving the reliability of the polymer worm wheel and metallic worm shaft in an EPS worm reducer. This is because the contact pressure in this tribosystem is very high, and it is necessary to decrease the friction and sliding heat [18, 41, 44, 55]. Grease lubrication is also preferred over oil lubrication because it has fewer circulating and sealing requirements [18]. As different temperatures occur at different locations of the worm reducer (engine compartment or cabin), the requirements to be satisfied by the lubricant vary accordingly. For gears in the engine compartment, a high-temperature type grease that protects the plastic against excessive thermally induced oxidation must be used [56].

Previous studies focused on the effect of grease composition on the performance of worm reducers. Bormuth et al. [55] reported the effects of various grease compositions on the efficiency and temperature of small plastic gears comprising a steel worm shaft and a PA66 worm wheel. They determined that the viscosity of the base oils and applied load had a significant effect on the friction torque. In addition, a polytetrafluoroethylene (PTFE)-type thickener results in a significant increase in efficiency compared with a lithium-soap thickener when using polyalphaolefin (PAO)-based grease. Cheng et al. [19] studied the effect of the gear design, including the gear ratio, on the stress of the gear surface, the effect of the applied load and rotation and the types of grease on the gearbox efficiency and friction coefficient, using an unreinforced PA66 or bronze worm wheel and steel worm shaft in the actual worm gear test. Two types of base oils of grease (synthetic oil and mineral oil) were compared. The polymer worm wheel had a 10% higher efficiency than the bronze worm wheel. Using the PA66 worm wheel, the gearbox efficiency increased and the friction coefficient decreased with an increase in the applied load, and synthetic oil grease exhibited a lower friction coefficient than mineral oil grease at each applied torque (Fig. I. 10). However, they did not offer an adequate discussion on the effect of different grease base oils on the friction coefficient. Conversely, Fig. I. 11 shows that the friction coefficient was almost constant as the speed increased, and a high efficiency of approximately 86% was obtained even at the lowest speed. They stated that this is because the worm wheel operated under boundary lubrication; therefore, the speed effect observed in mixed or full EHL was not confirmed. This low friction in the low-speed region is an advantage of the polymer worm wheel.

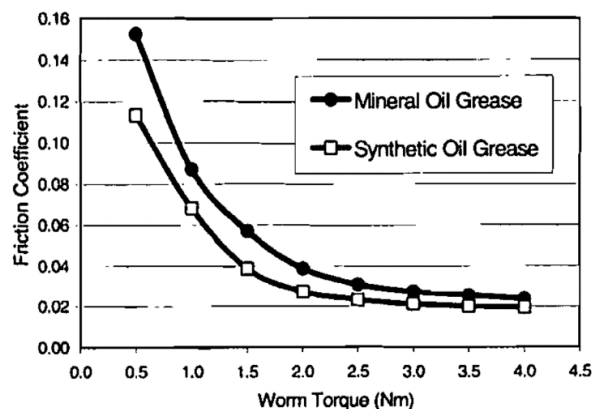


Fig. I. 10 Grease and load effects on the friction coefficient of a PA66 worm wheel (worm speed: 0.59 m/s) [19].

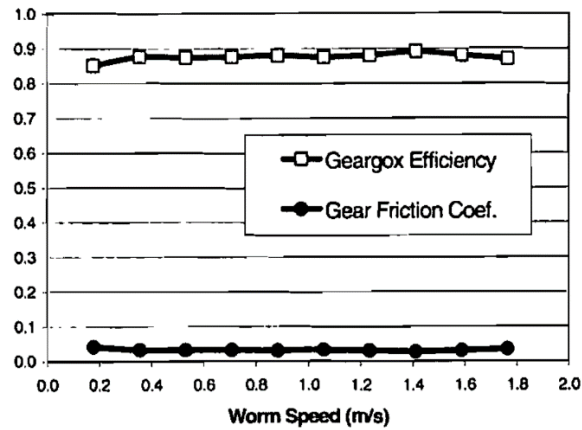


Fig. I. 11 Speed effect on the friction coefficient of the worm gear and gearbox efficiency (worm torque: 2.5 Nm) [19].

Nakata [4] reported an improvement in the performance of PA66/steel sliding components such as the worm reducer of an EPS by the establishment of grease technology that combines the prevention of starvation by improving inflow, friction reduction under boundary lubricative conditions, and the improvement of resin compatibility. The inflow into the sliding contact face was improved by using a thickener with high gelling ability, which reduced the shear viscosity in high-speed areas of over 10^2 s^{-1} . The friction coefficient under boundary lubrication conditions was reduced by more than 50% using a stearate oiliness agent, which contributed to increasing the gear efficiency (Fig. I. 12). Furthermore, the penetration of the agent into the resin was reduced by selecting an agent with metal elements. With the incorporation of these technologies into the grease for the worm reducer of the EPS, the temperature increase of the worm shaft was reduced by 20°C because of the low friction effect at the tooth meshing for the developed grease compared with the conventional grease. In addition, the life-until-breakage of the resin gear extended by 1.8 times compared with conventional grease owing to the improvement of resin compatibility and low temperature-increase effect mentioned above (Fig. I. 13).

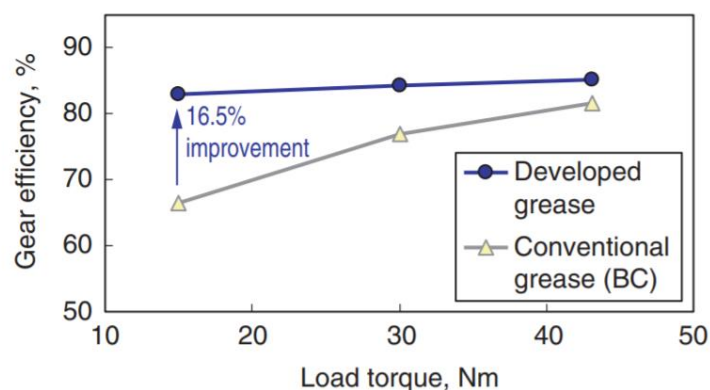


Fig. I. 12 Effects of the use of the developed grease on the improvement of the gear efficiency [4].

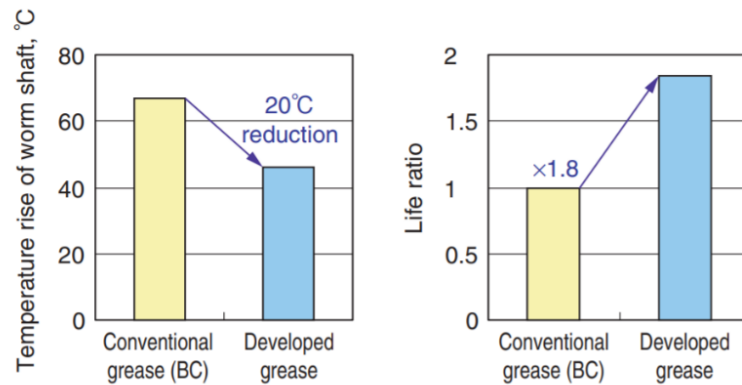


Fig. I. 13 Temperature increase of worm shaft and resin gear life up until breakage [4].

2.7 Requirements for downsizing and high-power driving of worm reducer

In recent years, the demand for the further downsizing of automotive parts and for the EPS, which is more effective in improving fuel economy than HPS, to be installed in larger vehicles has been high [46]. In conjunction with recent trends in vehicles becoming larger and tires gaining larger footprints, the motor assist torque of the EPS worm reducer has increased considerably [54]. Therefore, smaller and higher-power worm reducer (improved assist torque and performance) are required, and the development of materials for polymer worm wheels, metallic worm shafts, and greases, and the optimization of the design of the worm reducer to use under more severe conditions is required.

Watanabe et al. [54] investigated the principal factors that cause the external diameter of the polymer worm wheel for the P-EPS to increase. The fundamental reasons for the increase in the size of the worm wheels were considered, focusing on the operating conditions of the gear. They stated that the load applied to the teeth is concentrated in the addendum (the tip of the tooth) of the metallic worm shaft and the dedendum (the root of the tooth) of the polymer worm wheel. The reversing efficiency of the worm shaft deteriorated when the lead angle of the worm shaft addendum was small. An optimum design for a worm shaft and worm wheel was proposed: tooth operation occurs at the dedendum of the worm shaft and addendum of the worm wheel at low loads, and the number of operating teeth increases in conjunction with the increase in the transfer torque. The proposed design of the worm shaft and worm wheel was introduced through modification via an involute tooth profile. The worm wheel and worm shaft, which were fabricated using the proposed theory, exhibited improved durability and reversing efficiency. Therefore, a worm reducer with a polymer worm wheel with a smaller diameter than the conventional one was proposed, and its effectiveness was confirmed using an actual device (Fig. I. 14).

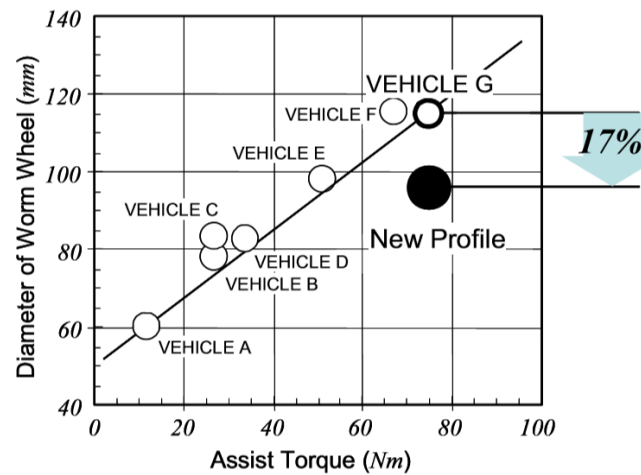


Fig. I. 14 Relationship between assist torque and the diameter of the worm wheel [54].

For large vehicles such as pickup trucks, the rack-parallel-assisted EPS (RP-EPS), which uses a ball screw, belt, and pulley as the reduction mechanism (Fig. I. 15), is currently used instead of C-EPS, P-EPS, and DP-EPS, which use a polymer worm wheel and steel worm shaft for the reduction system [57]. This is because the durability of the polymer worm wheel is not adequate for large vehicles in which rack-parallel assisted EPS is applied because of the higher output (rack axis force).

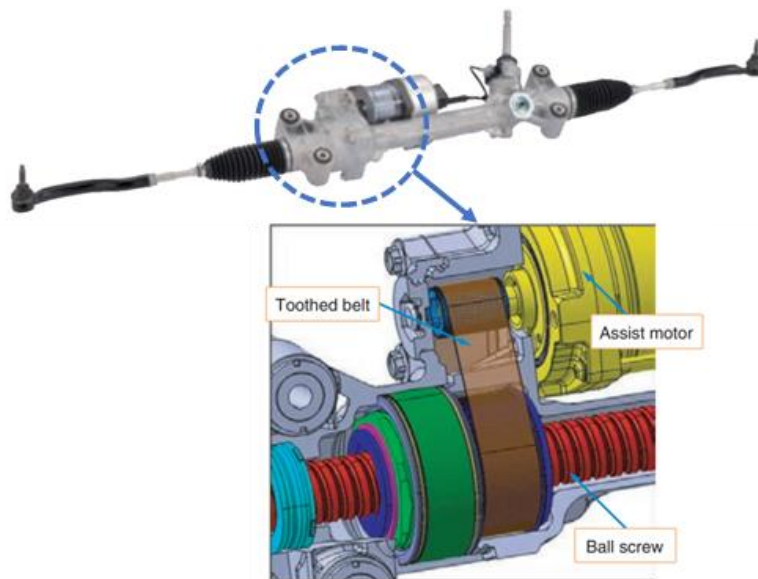


Fig. I. 15 Schematic view of RP-EPS and reducer [57].

In addition, when the polymer worm wheel is enlarged to satisfy higher outputs, the peripheral parts such as the aluminum worm reducer housing become larger, which impairs the ease of mounting the EPS to the automobile. In contrast, the RP-EPS is more expensive than the EPSs using a polymer worm wheel and steel worm shaft (e.g., DP-EPS), and the weight of the steering system is larger because the RP-EPS is equipped with a heavy ball screw. Therefore, if an inexpensive EPS that uses a polymer worm wheel can be applied in the output region where the RP-EPS is applied, the EPS product power can be improved; from this perspective, research is required on the use of the worm reducer under more severe conditions.

3. Polymer and composite material

Several types of polymers are used in many industrial applications depending on the conditions of use or their characteristics, such as mechanical properties, temperature, or environmental conditions. Fig. I. 16 shows the summary of various polymers in a pyramid depending on the temperature range, crystallinity, material cost, and difficulty of forming. Polystyrene (PS), polypropylene (PP), and polyethylene (PE) are representative examples of commodity polymers that exhibit lower mechanical properties (tensile strength in the order of 20 MPa). Commodity polymers are used in a very limited temperature range (up to 100°C), including our daily life, and the material cost is low (less than 1.13 €/kg). Engineering polymers are middle-range polymers, including PA, polybutylene terephthalate (PBT), polycarbonate (PC), and PPS. They are often called “engineering plastics” and have higher mechanical properties (tensile strength in the order of 75 MPa). They can be used at higher operating temperatures of up to 110/120°C and costs up to 11.3 €/kg. High-performance polymers have high mechanical properties, particularly under high temperatures, good wear resistance, high melting points, and very high resistance to degradation. The material costs are up to 113 €/kg. These are called “super functional polymers” or “super engineering plastics,” and include poly ether-ether ketone (PEEK) with an extremely high melting point (343°C), high strength, good mechanical properties (tensile strength up to 100 MPa), and usable temperature range up to 250°C. This group also includes polybenzimidazole (PBI), the highest heat-resistant thermoplastic with a glass transition temperature of 427°C [35].

Among the various types of polymers, we focused on PAs with various types of reinforcement fibers and additives. In this chapter, the characteristics of PAs, including PA 66, reinforcement fibers such as GFs, CFs, or AFs, and additives such as solid lubricative additives, molecular chain extenders, and impact modifiers are summarized, and the literature review focused on the tribology of the polymer or composite materials.

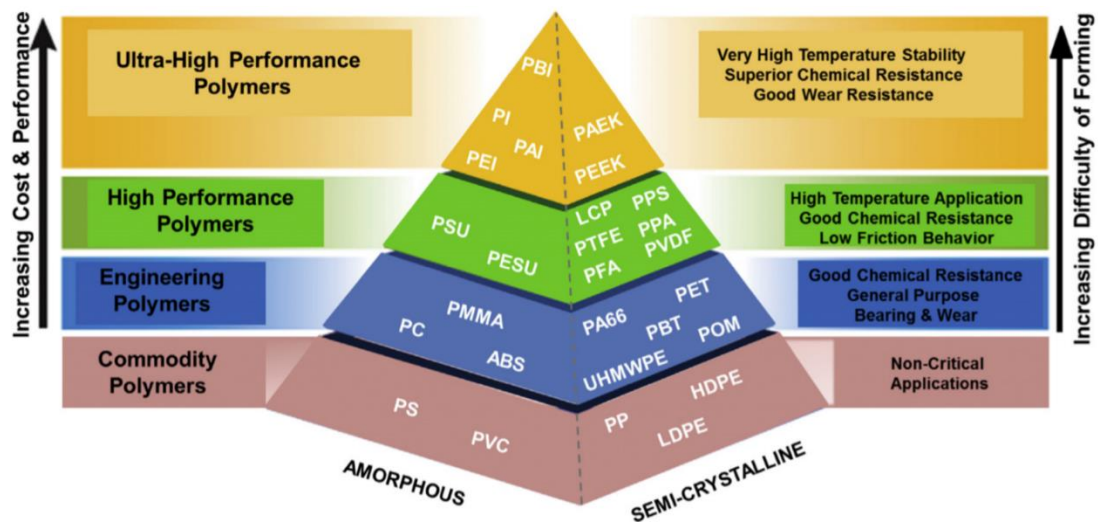


Fig. I. 16 Polymer pyramid, listing thermoplastics with an amorphous or semi-crystalline morphology with respect to cost, performance, and formability [35].

3.1 Polyamide (PA)

PAs are well-known engineering plastics. The first PA application was introduced by DuPont in 1938: PA66 for toothbrush filaments. Although fiber applications soon dominated, the use of PA as plastics increased steadily from the 1950s [58], and the share of PAs in the

global market of engineering plastics is estimated to be almost one-third [59] (Fig. I. 17). PAs were the first engineering plastics and still represent the largest and most important class of these types of materials. The combination of mechanical and thermal properties enables them to be employed for highly specified end uses and often for metal replacement applications [58].

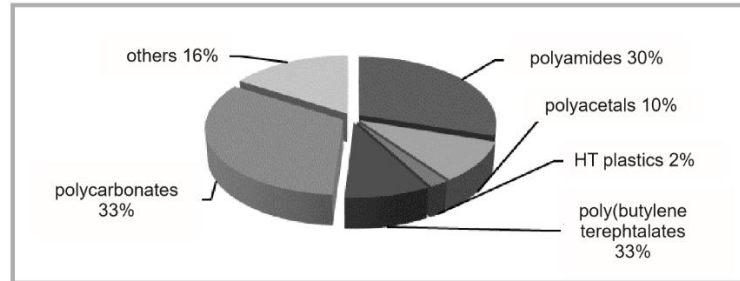


Fig. I. 17 Global market of engineering plastics summarized by type of resin [59].

3.1.1 Types of polyamides

Different types of PAs with different molecular structures are known. The methylene ($-CH_2$) to amide ($-CONH-$) ratio in PAs controls the physical and mechanical properties, and two types of PAs (addition and condensation) exist. Generally, the effects of different monomers can be summarized as follows: lengthening the aliphatic segments between the amide groups results in lower moisture absorption, strength, stiffness, and melting point (e.g., PA11 or PA12 compared with PA66). The aromatic groups increase the stiffness and strength but reduce the moisture uptake and impact strength. Some semi-aromatic PAs also have an increased melting point [58]. Examples of aliphatic PAs include PA46, PA6, PA66, PA610, PA410, PA612, and aromatic PAs such as PA6T, PA9T, and PA10T. Table I. 1 lists the mechanical properties of aliphatic addition PAs with different molecular structures ($CH_2/CONH$ ratio), and Table I. 2 lists the mechanical properties of aliphatic condensation PAs and aromatic PAs. The effects of the type of PA on the tribological properties have been reported [60, 61, 62]. Rajesh et al. [60] reported the abrasive wear resistance of ten different types of PAs using polymer pins against waterproof silicon carbide paper under various loads, and specific wear rates under abrasive wear mode exhibited a fairly good correlation with various mechanical properties such as ductility factor, stress for crack length, tensile modulus, crack growth velocity, and the time to failure under tensile stress.

Table I. 1 Mechanical properties of aliphatic addition PAs [60].

Property	Materials			
	Polyamide addition type			
	PA 6	PA 11	PA 12 (VE)	PA 12 (N)
Designation	A	B	C	D
Manufacturer	Du Pont (India) Ltd.	Elf Ato Chem, France	EMS Chemie, Switzerland	EMS Chemie, Switzerland
Trade name	Zytel	Rilsan	Grilamid L20	Grilamid L16 GM
CH ₂ /CONH ratio	5	10	11	11
Specific gravity	1.15	1.05	1.01	1.01
Average crystallite size (Å)	233	204	126	103
Cohesive energy (kJ/mol)	62.5	85	89.5	89.5
Tensile strength (MPa) ASTM D 638	55.4	40.7	47	38.2
Elongation to break (%)	378	420	446	321
Flexural modulus (MPa) ASTM D 790	59	12	37	29
Notched impact strength (kg m/m) ASTM D 256	4.92	5.90	10.82	5.90
Shore D hardness	74	66	76	79
Glass transition temperature, T_g (°C)	50	46	46	46
Melting temperature, T_m (°C)	222	179	177	178
Degradation temperature, T_d (°C)	440	440	455	450
Stress field intensity factor, K_{IC} (MPa m ^{1/2})	4.60	3.15	4.58	4.64
Fracture energy, G_C ($\times 10^4$ J/m ²)	5.37	5.89	3.90	4.43
Ductility factor (mm)	17.90	17.60	14.21	14.76
Fracture surface energy, γ ($\times 10^4$ J/m ²)	2.69	2.95	1.95	2.22
Fracture stress, σ_* (MPa)	97.4	66.7	97	98.24
Critical crack length, C_* (μ m)	5140	5135	5144	5152
Crack growth velocity, V_C (μ m/s)	527	344	913	962
Time to failure under tensile stress, t_F (s)	16.32	25.02	8.94	9.42

Table I. 2 Mechanical properties of aliphatic condensation PAs and aromatic PAs [60].

Property	Polyamide condensation type					
	PA 46	PA 66	PA 612	PA 66/610 (BM 20SBG)	Polyetheramide	Aromatic PA
Designation	E	F	G	H	I	J
Manufacturer	ERTA NV, Belgium	Du Pont (India) Ltd.	Du Pont (India) Ltd.	EMS Chemie, Switzerland	Elf Ato Chem, France	Elf Ato Chem, France
Trade name	Ertalon 46	Zytel	Zytel	Grilon BM 20SBG	PEBAX	Cristamid
CH ₂ /CONH ratio	4	5	8	12	–	–
Specific gravity	1.18	1.14	1.06	1.09	1.15	1.06
Average crystallite size (Å)	–	156	204	182	–	–
Cohesive energy (kJ/mol)	116	125	152	268	–	–
Tensile strength (MPa) ASTM D 638	89	67	43	31	14	68
Elongation to break (%)	30	433	9	100	480	11
Flexural modulus (MPa) ASTM D 790	–	64	48	31	4	51
Notched impact strength (kg m/m) ASTM D 256	8	3.93	3.93	5.90	–	1.96
Shore D hardness	84	80	81	76	53	85
Glass transition temperature, T_g (°C)	78	57	–48	47	48	–
Melting temperature, T_m (°C)	287	258	215	200	161	230
Degradation temperature, T_d (°C)	–	430	–	460	–	410
Stress field intensity factor, K_{IC} (MPa m ^{1/2})	9.31	6.10	5.24	3.56	2.07	7.78
Fracture energy, G_C ($\times 10^4$ J/m ²)	9.29	6.52	3.78	3.90	7.97	6.60
Ductility factor (mm)	10.81	15.14	14.52	16.19	21.20	13.06
Fracture surface energy, γ ($\times 10^4$ J/m ²)	4.65	3.26	1.89	1.95	3.99	3.30
Fracture stress, σ_* (MPa)	197.13	129.16	110.95	75.38	43.83	164.73
Critical crack length, C_* (μ m)	51.46	5141	5149	5146	5133	5144
Crack growth velocity, V_C (μ m/s)	801	508.3	2077.2	557.7	24.8	1706.3
Time to failure under tensile stress, t_F (s)	10.73	16.92	4.14	15.42	346.8	5.04

3.1.2 Polyamide 66 (PA66)

PA66 has a particularly high wear resistance and a balance of strength, toughness, and heat resistance properties [32, 63]. In addition, the cost of the material is much lower than that of other PAs, such as PA 46, PA 11, and any type of aromatic PA. Fig. I. 18 shows the molecular structure of the PA66. Since the 1950s, many studies have focused on the mechanical and tribological properties of unreinforced or fiber-reinforced PA66.

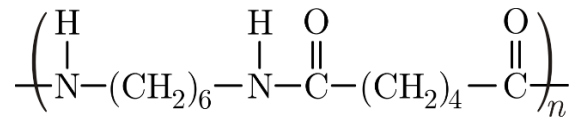


Fig. I. 18 Molecular structure of PA66.

3.1.3 Molecular mass of polyamides

The molecular mass of PAs is known to affect the tribological properties of the polymer or composites with a PA as a matrix. Schnoor et al. [64] investigated the effect of annealing PA6 under vacuum conditions at different temperatures after injection molding on the physical properties (density and thermal expansion coefficient) and wear resistance of PA6. The molecular mass of PA6 after annealing was affected by the original values of PA6 before annealing and annealing temperature, and high values of the original molecular mass and high annealing temperature did not necessarily result in a high PA6 molecular mass. In the sliding test with PA6 in contact with a 100Cr6 steel rotating ball bearing cylinder under dry conditions (contact pressure: 1 MPa), the global tendency presented in Fig. I. 19 shows that the wear rate decreased with an increase in the PA6 molecular mass, except for the sample annealed at 220°C. The reason for the improvement through the increase in the molecular mass was attributed to the stronger entanglement of the polymer molecules, higher toughness of the bulk, and higher shear viscosity. However, the wear mode of PA6 with different molecular masses was not discussed, and the effect of the annealing temperature on the wear resistance requires further discussion.

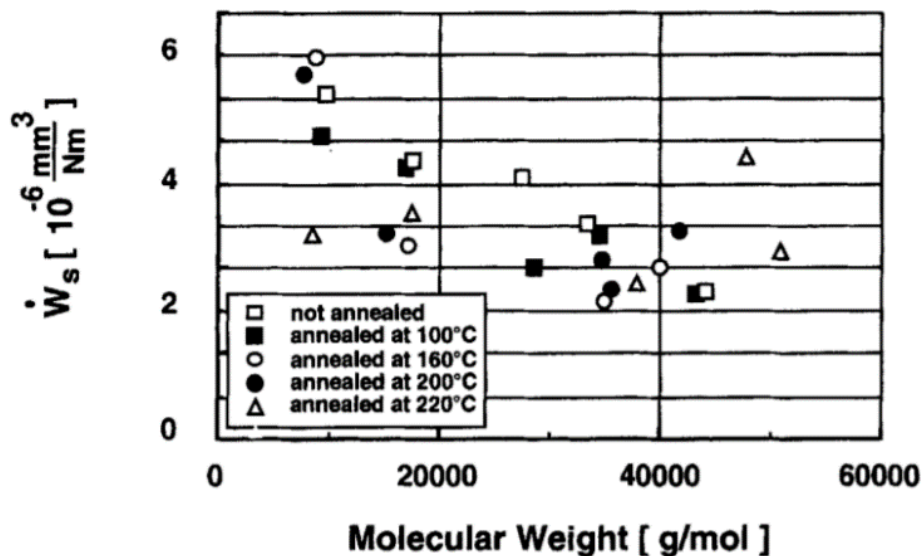


Fig. I. 19 Wear amounts of PA6 with different values of the molecular weight, which was obtained for different types of base PA6 and different temperatures of annealing [64].

The inverse effect of the molecular mass on the friction and wear of unreinforced PA66 or GF-reinforced composites in contact with carbon steel under dry conditions was also reported by Shin et al. [65]. The wear rate of the unreinforced PA66 and GF-reinforced PA66, which is governed by the adhesive wear, and the friction coefficient increased with the increase in the molecular mass of PA66 over the entire temperature range (Fig. I. 20, the results at 100°C are provided as examples). This can be explained by the increased shear strength of high-molecular-mass PA66. The melt viscosity is strongly affected by the molecular mass, and an increase in the melt viscosity increases the shear strength of PA66. The friction force related to the adhesion is proportional to the product of the actual contact area multiplied by the shear strength (detailed in Section 6.1); therefore, the shear strength increase can explain the friction and wear increase in high-molecular-mass PA66.

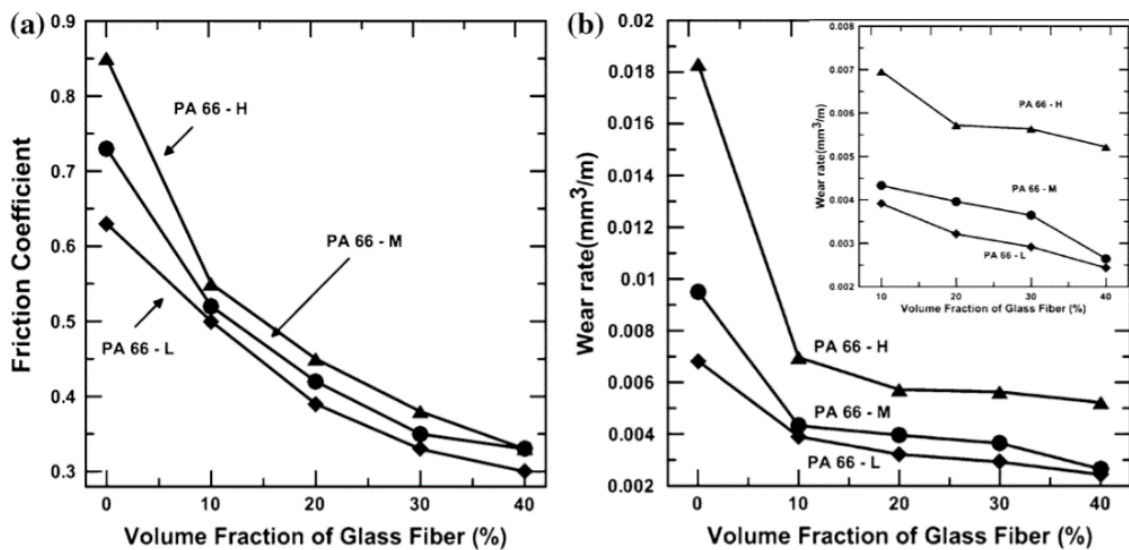


Fig. I. 20 Effect of the temperature and molecular mass of PA66 on the (a) friction coefficient and (b) wear rate of PA66 with different molecular mass and added GF amounts (H: high molecular mass, M: medium molecular mass, L: low molecular mass). Sliding tests were conducted at 100°C [65].

As observed in the work of Shin et al., many studies explained the wear mode of the PA66 or GF composites in contact with the counterpart metallic material as adhesive wear, in which a transferred tribofilm on the metallic material was observed. The adhesive wear of a polymer material results from the shear of friction junctions and involves the formation junctions, their growth, and rupture. The transfer film formation of the polymer is the most significant characteristic in the adhesive wear of polymer materials, and a thin film of soft material (polymer) is transferred onto the hard mating surface (metallic material). If the transferred polymer film is carried away from the metallic surface and is repeated, the wear rate of the polymer increases [66].

A schematic of the adhesive wear of PA66 and the formation of wear debris is shown in Fig. I. 21 [65]. Surface molecules on the PA66 are removed by the shear on the sliding surface, and the PA66 roll is formed in the process shown in Fig. I. 21 (a)–(c). In addition, when the adhesion of PA66 on the steel counterpart is severe, the shear effect results in tears in the local contact area and the formation of a transfer film of the polymer patches on the steel surface, and the patches are removed to generate wear debris in the shape of a roll when the

patches adhere to PA66 on the surface (Fig. I. 21 (d)–(f)). Considering this adhesive wear mode, the existence of GFs can reduce the adhesion between PA66 and steel (because GF is harder and less affected by temperature than PA66) and interrupt the formation of the transfer film on the steel surface. Therefore, the GF composite exhibits low friction and low wear, and the friction and wear-decreasing effect become greater with the increase in the GF amount, irrespective of the molecular mass of PA66 or temperature (Fig. I. 20).

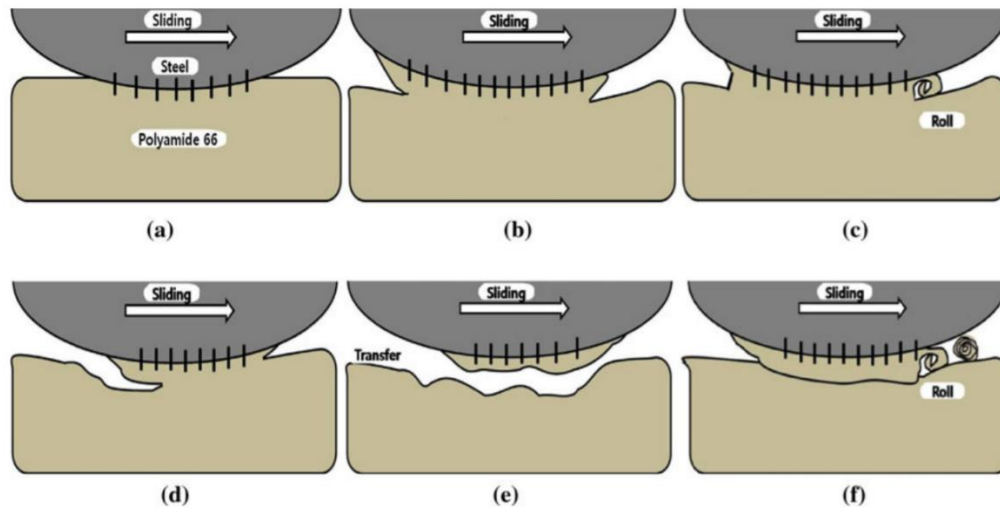


Fig. I. 21 Schematic diagrams of the adhesive wear and wear debris formation of PA66 [65].

In addition, Kurokawa et al. [67] reported that the fatigue life of a polymer gear composed of CF-reinforced PA12 under lithium-type grease lubrication could be improved by increasing the molecular mass of PA 12. Feulner et al. [68] reported that the wear resistance of unreinforced PA66 containing a cross-linking agent (triallyl isocyanurate) in contact with 100Cr6 steel under dry conditions was improved through the electric beam irradiation of the molded compact and formation of the cross-linked PA66 molecular structure at both room and high temperatures. They stated that cross-linking primarily occurs in the amorphous regions of PA66, and high crystallinity by the electric beam irradiation contributed to the improvement of the wear resistance. However, very few studies focused on the detailed mechanism of the effect of the PA molecular mass on the tribological properties under lubricated conditions.

Considering several processes to obtain fiber-reinforced composites with a high molecular mass of PAs, extruding reinforcement fibers in high molecular mass PA is a possible method. However, extruding some fillers including fibers in high molecular mass resins is difficult because the melting viscosity of the high molecular mass PA resin increases; therefore, the extruding torque becomes significantly higher and the effect of the degradation of the PA resin owing to extra heat also increases [69]. Furthermore, fabricating a continuous strand of extruded composite becomes difficult when extruding a high-viscosity resin reinforced with fibers. In addition, the solid-state post-condensation of molded compacts is another method of increasing the molecular weight of the PA composite; however, this process is time-consuming and expensive [64, 70]. Conversely, the reactive extrusion method using a molecular chain extender is a relatively simple and inexpensive method of increasing the molecular mass of PAs [71]. This technology aims to increase the molecular mass by linking molecular chains with the rapid reaction between amino or carboxyl end groups in PAs and molecular chain extenders during the extrusion process. In previous studies, various types of

additives such as caprolactam, oxazoline, epoxide, ethylene, maleic anhydride (EMA), and diisocyanate were included as the molecular chain extenders [70, 71, 72]. Ozmen et al. [71] reported that the relative viscosity of PA66 increased and the mechanical properties improved, particularly when EMA was used as the molecular chain extender.

3.1.4 Hygroscopicity of polyamides

PAs are hygroscopic because of their molecular structure, which is related to the polar amide groups around which water molecules can coordinate. Water absorption is generally concentrated in the amorphous regions of PA66, where it plasticizes the material, accompanied by the scission of the hydrogen bonding between polar amide functional groups because of the hydrophilicity of the polar amide functional groups in PA66 [58, 73]. The weakening of water-absorbed PA66 becomes more severe at high temperatures, at which the amide groups are decomposed into carboxyl, amine, and imide groups [73]. The change in the molecular structure of PA66 after water absorption reduces its strength and affects its friction and wear properties [63]. In addition, the dimensional instability related to the water absorption of PA66 has limited its application in humid environments [74]. Therefore, an understanding of the effects of the hygroscopicity of PA66 on the tribological properties is necessary with the consideration of the use of automotive components exposed to humid conditions. Kim et al. [73] demonstrated that the wear resistance of unreinforced PA66 and GF-reinforced PA66 deteriorated with water absorption under dry conditions (Fig. I. 22) because of the softening caused by the absorbed water and increased interfacial adhesion to the steel counter surface. In addition, the degraded wear characteristics of unreinforced PA66 resulting from chain scission of the amide functional group caused by water molecules were substantially improved using short-GF reinforcement. In contrast, Gasparin et al. [15] reported that the water absorption of unreinforced PA6, unreinforced PA66, GF 15–30%-reinforced PA6, and GF 15–60%-reinforced PA66 by heat treatment (immersing the PA specimens in boiling water for 2 h) did not affect the abrasion wear resistance in contact with P60 emery cloth, whereas the stiffness decreased and impact resistance increased with the increase in water absorption.

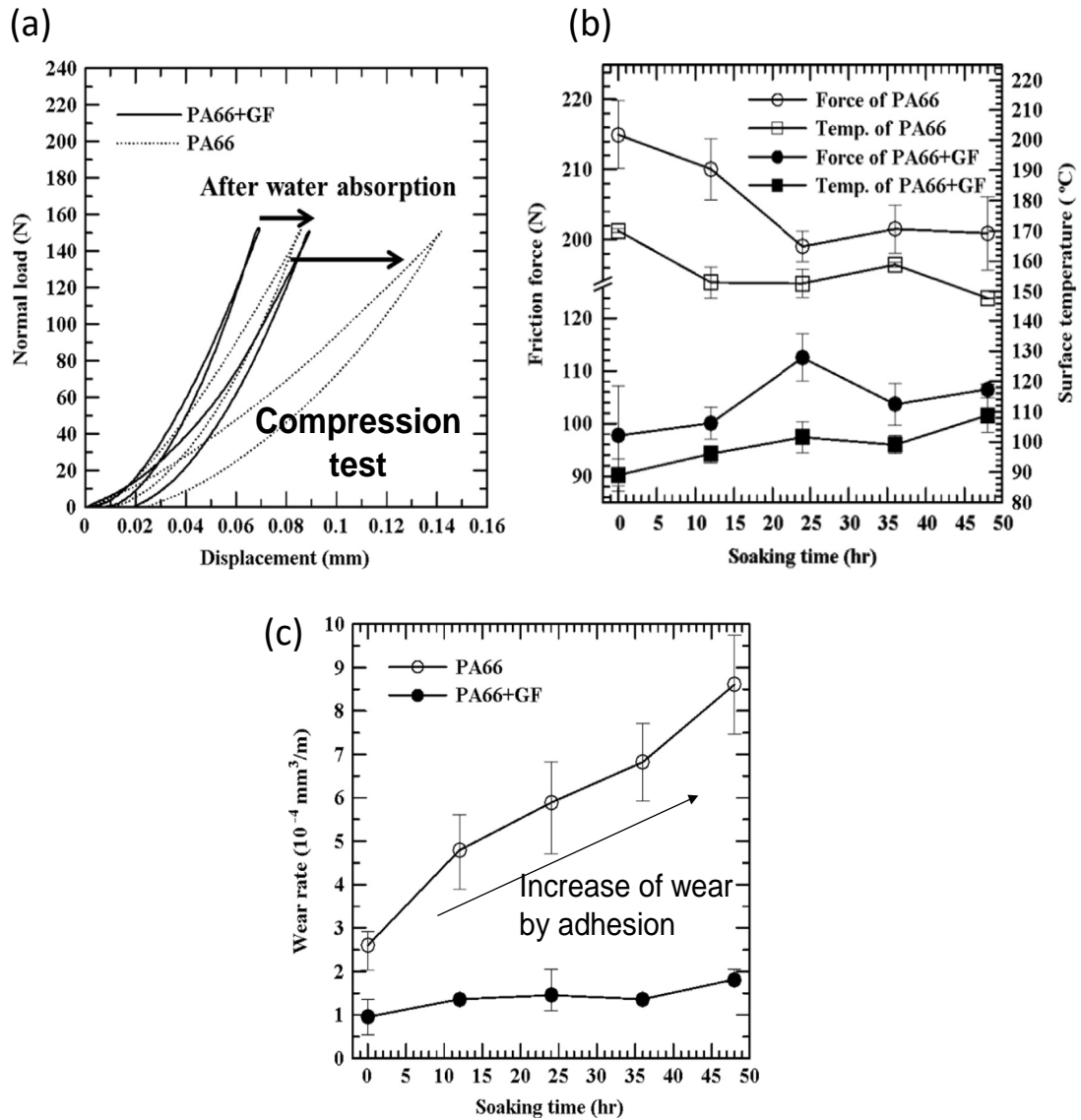


Fig. 1. 22 (a) Effect of water absorption on the compression test; (b) effect of the water absorption on the friction force and temperature; (c) effect of water absorption on the wear rate using unreinforced or GF-reinforced PA66 [73].

However, the effects of water absorption on the tribological properties under grease lubrication were not sufficiently clarified in these studies. When considering the use of actual composite components, including gears, under various types of different environments, such as different locations that are at different temperatures and humidities, it is necessary to consider the effect of water absorption on the tribological properties.

3.2 Reinforcement fibers

The mechanical and tribological characteristics of polymers are improved by adding reinforcements (short fibers), nano- and microparticles fabricated from metallic or ceramic materials, and flame retardants [75]. Adding reinforcement fibers, such as GFs, CFs, and AFs is a common method of improving the mechanical properties of PA materials [32, 63, 67, 76, 77, 78, 79, 80], thereby increasing their load-carrying capacity [77]. Polymer composites reinforced with these fibers are frequently one to four times stronger (static tensile or bending strength) and stiffer (Young's modulus) [77], whereas the elongation at break decreases. In

this section, studies focusing on the effect of the addition of reinforcement fibers on the mechanical and tribological properties of the composite are summarized.

3.2.1 Glass fibers (GFs)

GFs are inexpensive and effective in improving the mechanical properties of polymers; therefore, they are widely used for engineering plastics, including PA. Table I. 3 lists the mechanical properties of normal E-glass and special GFs (T-glass and NE-glass), which are used for the reinforcement fibers of the composite [81]. GFs are primarily synthesized from ceramics such as silicon oxide, titanium oxide, and magnesium oxide, and the blending rate determines the properties of the GFs. GFs using E-glass are used as reinforcement fibers in engineering plastics. Since the 1970s, many studies have focused on the tribological properties of GF-reinforced PAs [82, 83, 84]. The added amounts of GFs, GF diameter, interfacial shear strength between GFs and PA66, and GF orientation are some of the parameters of the GFs that affect the tribological properties.

Table I. 3 Mechanical properties of GFs [81].

Properties	Normal GF	Special GF	
	E glass	T glass	NE glass
Density, g/cm ³	2.6	2.5	2.3
Tensile strength, GPa	3.2	4.8	3.1
Tensile modulus, GPa	75	86	64
Maximum elongation rate, %	4.8	6.1	4.8
Heat expansion coefficient, $\times 10^{-6}/^{\circ}\text{C}$	5.6	2.8	3.3
Softening temperature, $^{\circ}\text{C}$	844	>1000	-
Permittivity, 1GHz	6.8	5.4	4.8
Dielectric loss tangent, 1GHz	0.0035	0.0043	0.0015

*Translated to English (Original: Japanese)

3.2.1.1 Added amounts of glass fibers

The amount of GFs affects the tribological properties of GF composites. Kim et al. [74] noted that adding GFs can decrease the friction coefficient and wear amounts of PA12 by decreasing the adhesion between PA12 and carbon steel under dry conditions; the lowest friction coefficient and better wear resistance of the PA12 composite were achieved with the addition of 30 wt% GFs. This is because the high friction coefficient of unreinforced PA12 is attributed to its adhesion to the steel surface, and the lower friction level with GF is achieved by smaller polymeric contacts on the sliding surface. Similarly, the increase in the GF amount decreases the friction and adhesive wear of the GF-reinforced PA66 composite (Fig. I. 20). In contrast, Zhou et al. [78] observed that the wear rate of PA6/PPS-CF composites in adhesive wear mode tended to increase with increasing CF content in the chromium steel ball when sliding on a composite disc.

3.2.1.2 Diameter of glass fibers

The diameter of the GFs also affects the mechanical properties of the PA/GF composites. Ramsteiner et al. [85] investigated the effect of the GF diameter on the static mechanical properties of GF-reinforced PA. In the study, the GFs were treated using the same surface agent and exhibited the same interfacial shear strength as the PA; only their diameters were varied. The diameter of the fibers (10–24 μm) does not have a strong effect on the Young's modulus of the composite, which is only affected by the amount of fibers. In contrast, the

fracture strength of the composite was significantly affected by the diameter of the GFs. The diameter of the fibers affects the stress concentration of the fibers, and an increasing fiber diameter decreases the strength of the composite. Ozawa et al. [86] reported that the static tensile strength and impact strength of GF-reinforced PA66 increased with decreasing GF diameter under the same fiber orientation conditions. They observed that the strength value predicted using a modified Kelly–Tyson model correlates well with the measured value when the strain rate of the test is considered. They demonstrated that the load that can be borne by the entire interface when the strain rate of the test is considered increases with decreasing GF diameter because of the resulting increase in the interfacial area between the GFs and PA66, and that decreasing the critical fiber length can enable the fibers to bear higher loads. Murakami et al. [50] reported that the static strength, impact strength, and fatigue properties of GF-reinforced PA66 with small-diameter GFs were superior to those of normal-diameter GF composites. Small-diameter GFs mitigate the stress concentration, which improves the durability of a composite worm wheel for an EPS system. However, very few studies reported the effects of GF diameter on the tribological properties of GF-reinforced composites under either dry or grease-lubricated conditions.

3.2.1.3 Interfacial adhesion strength between glass fiber and polymer

The interfacial shear strength between a polymer and a GF is a key parameter in terms of the properties of the GF-reinforced PA composite, as these parameters directly affect its mechanical properties. The surface of the fibers is often treated with a coupling agent or compatibilizer to increase the interfacial shear strength between the matrix resin and fibers [87]. The reaction between the reactive functional groups on the surface agent and polymer ensures good adhesion between the fibers and polymer. Aminosilane coupling agents are a representative class of surface agents used to ensure adhesion between GFs and several types of polymers [87, 88]. Polyurethane resins are also used as surface treatment agents for reinforcement fibers [89, 90]. Ethylene-acrylic ester-glycidyl methacrylate is also used to enhance the bonding between GFs and PAs [65]. The effects of the adhesion between the fibers and the matrix resin of composites on their tribological properties have been studied [91, 92, 93, 94]. Karsli et al. [91] observed that the addition of 2 wt% 1,4-phenylene-bis-oxazoline as a coupling agent increased the interfacial adhesion between GFs and PA66 and improved the adhesive wear resistance of a GF-reinforced PA66 composite in contact with a ceramic ball under dry conditions. Karsli et al. [92] also reported that thermal aging of GF- or CF-reinforced PEEK composites at 360°C improve the interfacial adhesion between the fiber and matrix surfaces as measured using dynamic mechanical analysis owing to the formation of a transcrystalline phase between the fibers and matrix resin during aging. However, few studies focused on the effects of the interfacial strength between the fibers and polymer matrices on the wear resistance of composites under grease lubrication. In particular, the effects of the two-body wear resistance of the steel counterpart caused by the presence of GFs have not been investigated. Therefore, a quantitative discussion on the effect of the interfacial shear strength of GFs and PAs on the tribological properties under grease lubrication should be conducted.

3.2.1.4 Orientation of glass fibers

The orientation of the GF also affects the tribological properties. Kim et al. [74] noted that GF-reinforced PA12 composites in a parallel orientation to the sliding direction exhibited slightly higher friction levels to the carbon steel counterpart than those in a perpendicular orientation, even if the surface area of the former was significantly larger than that of the latter, and the friction coefficient and wear decreased with the increase in the GF content (Fig. I. 23). This difference is related to the micromechanical behavior of the fibers at the sliding interface rather than the relative surface area covered by the GFs. However, the fiber orientation had a lower effect on the friction and wear of the composite than the fiber content or applied load.

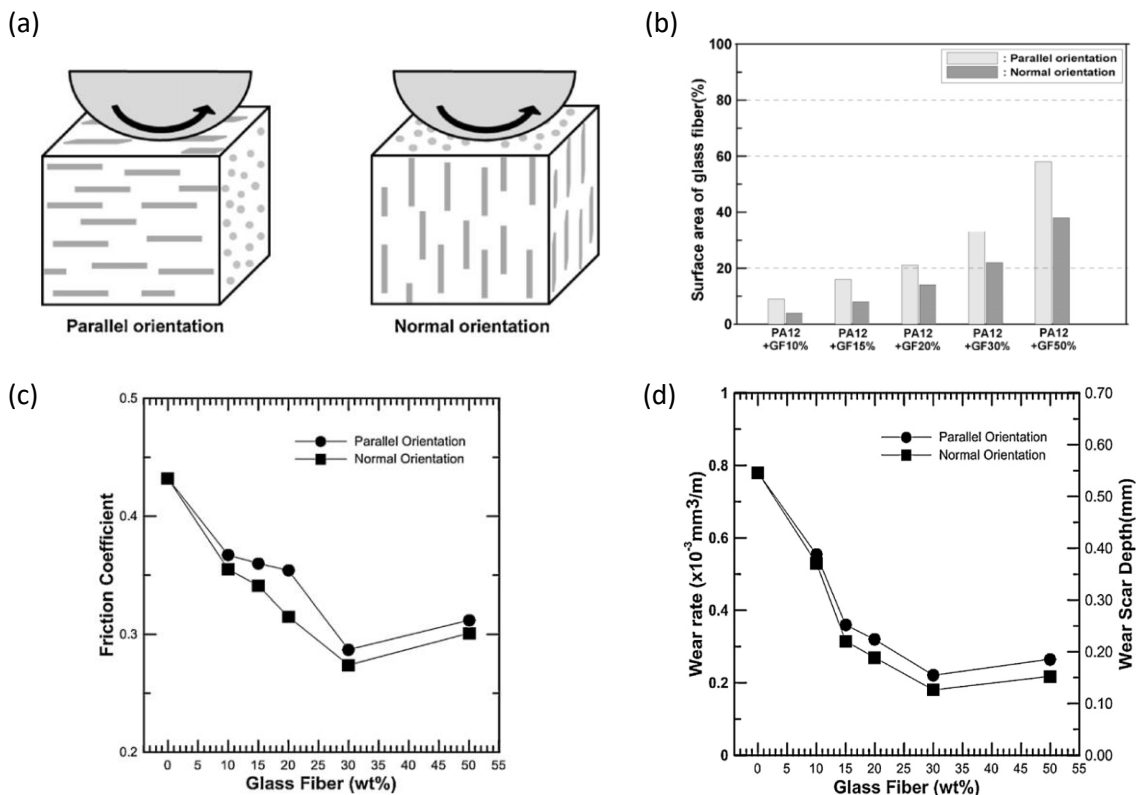


Fig. I. 23 (a) Schematic diagram of the block composite specimens with two different fiber orientations; (b) area of GFs on the sliding surface with different orientations of GFs; (c) friction coefficient as a function of GF amounts and orientation; (d) wear of the composite as a function of GF amounts and orientation [74].

3.2.2 Carbon fibers (CFs)

A CF is defined as a fiber containing at least 92 wt% of carbon, while the fiber containing at least 99% carbon is frequently called a graphite fiber. CFs are used as reinforcement fibers in engineering plastics in various industries, such as automobiles, aerospace (aircraft and space systems), military, construction, and sporting goods [95]. The cost of CFs was over 30 US\$/kg in 2010, dependent on oil price, with approximately 51% being the precursor cost, 18% utilities, 12% depreciation, 10% labor, and 9% represented by other fixed costs [96]. This is much higher than the cost of GFs (between 1.30 and 2.00 \$/kg) [97]. However, CFs have some advantages over GFs: excellent tensile properties, low density, high thermal stability, and good thermal and electrical conductivities [95]. Two different types of CFs (polyacrylonitrile (PAN)

and mesophase pitch) are well known [95]. Table I. 4 lists the mechanical properties of the CFs.

Table I. 4 Mechanical properties of CFs [98].

Characteristics	PAN CFs	Pitch CFs
Strength, GPa	1.8–7.0	1.4–3.0
Modulus, GPa	230–540	140–820
Elongation at break, %	0.4–2.4	0.2–1.3
Density, g/cm ³	1.75–1.95	2.0–2.2

CFs have also been used to improve the tribological properties of plastics for many years, and many studies on the tribological properties of CF composites have been performed [80, 99, 100]. Li et al. [101] reported the tribological properties of CF-reinforced PA6 in contact with a bearing steel (CGr15) ball under dry sliding conditions, and the CF composite exhibited better friction behavior with an increase in the CF amount because the reinforcing CFs effectively reduced the adhesion force between two sliding bodies and plow. The friction-decreasing effect can be attributed to the CF structure being similar to that of graphite, consisting of carbon atom layers (graphene sheets) arranged in a regular hexagonal pattern aligned perpendicular to the fiber axis (Fig. I. 16) [95]. The lubricating function of graphitized carbon is considered to be responsible for the decrease in the friction coefficient as its composites slide against steel. It is well documented that CF can decompose into graphite crystals, which have very good lubricating properties. The graphite debris forms a thin lubricating film on the counterface, thereby dramatically reducing the abrasion process. This results in a low friction coefficient and low wear of the composite compared with unreinforced PA [77, 102].

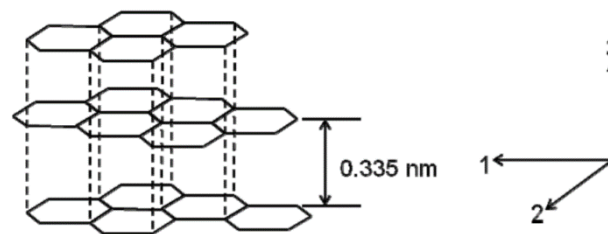


Fig. I. 24 Structure of graphitic crystals and crystal directions [95].

Tewari et al. [103] reported the wear resistance of a CF-reinforced PA66 composite under dry conditions in the abrasive wear mode (in contact with SiC abrasive paper) and compared it with the friction and wear properties in the adhesive wear mode. The wear of the CF composite increased as the CF concentration increased in the abrasive wear test, whereas the friction coefficient and wear of the composite decreased as the CF concentration increased in the adhesive wear test. The deterioration in the abrasive wear resistance was attributed to the decrease in the elongation of the composite as the CF concentration increased. In addition, the addition of PTFE to the CF-reinforced PA66 composite increased the abrasive wear of the composite, whereas the addition of PTFE improved the tribological properties in the adhesive wear mode. Therefore, the effects of the addition of CFs on the tribological properties are dependent on the wear mode. Zhou et al. [78] observed that the wear rate of PA6/polyphenylene sulfide-CFs composites in the adhesive wear mode generally increased as the CF concentration increased during sliding between a chromium steel ball and CF composite disc. Senthilvelan et al. [6] presented the differences in the failure modes of spur

gears fabricated from unreinforced, GF-reinforced, and CF-reinforced PA66; the addition of CFs to the PA66 matrix increased the thermal resistance of the composite. No appreciable tooth shape deformation or molten-material-layer formation on the fractured surfaces was observed in the CF-reinforced gears, whereas severe plastic deformation was dominant at higher applied stresses, and cracking at the root and tooth surfaces was dominant at lower stresses in the unreinforced gears. They also stated that the inferior adhesion between CF and PA66 compared with that of GF resulted in the fiber pulling out the CF from the polymer, which is attributed to the difference in typical surface energy (GF: 55–65 mJ/m², CF: 40–50 mJ/m²). Sharma et al. [93] reported that the enhancement of the interfacial adhesion between polyethersulfone (PES) and CFs by cold remote nitrogen–oxygen plasma treatment improved the mechanical and tribological properties (low friction coefficient and low wear rate) of the composite.

Studies have also focused on the aggressive effect of CF on metallic counterparts and compared it with that of GF. Theberge et al. [100] focused on the differences in the abrasive effects of CFs and GFs and observed that polymers reinforced with GFs caused at least ten times as much wear on a relatively soft counterface, such as mild steel, than polymers reinforced with CFs. Lancaster [99] reported that GF-reinforced PA66 and PTFE cause appreciably more wear and damage to steel than those reinforced with CFs. In addition, the wear rate of a counterpart bronze ball tested with a 30% GF-reinforced PA66 was 36.5 times larger than that tested with a 30% CF-reinforced polymer. Tsukamoto et al. [16] reported that the wear of an S45C steel counterpart tested with 60% CF composite was six times higher than that tested with a 10% GF composite despite large added amounts of fibers in the CF composite. In addition, no wear of steel was observed when tested with unreinforced PA6. These studies demonstrated that the aggressive effects of the CF composite on steel counterparts were mitigated compared with those of the GF composite.

Regarding the effect of the orientation of CFs, Yamamoto et al. [104] reported that CFs aligned perpendicular (transversal) to the sliding direction exhibited higher wear resistance of the CF-reinforced PEEK composite disc than those of the parallel (longitudinal) to sliding direction (Fig. I. 25) under water-lubricated conditions in contact with a Cr–Mo steel ring. They stated that the orientation of CFs in the transverse direction could be expected to prevent the polymer matrix from large deformation and severe wear as far as they could bear the normal and tangential forces without breakage and separation, compared with those in the longitudinal direction.

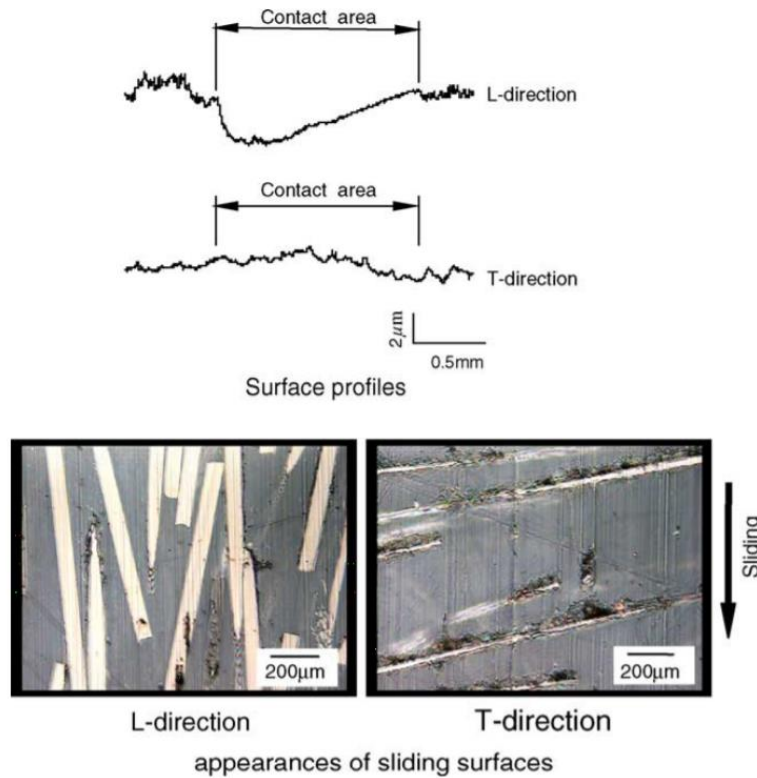


Fig. I. 25 Effect of fiber direction on wear with CF-reinforced PPS [104].

However, few studies focused on the tribological properties of CF-reinforced composites in contact with metallic materials under grease or oil lubrication. Li et al. [105] demonstrated that treating CFs with a rare earth solution improved the wear resistance of CF-reinforced polyimide (PI) in contact with GCr15 steel under oil lubrication by improving the interfacial adhesion between the CFs and the PI. Zhao et al. [106] reported the tribological properties of PI reinforced with various fillers, including CFs, GFs, and ZnS particles, in contact with GCr15 steel under oil lubrication with polyalphaolefins, and observed that the reinforcing fibers improved the wear resistance of the composites. The addition of GFs was more effective at improving the wear resistance than the addition of CFs, and a synergistic effect between the GFs and ZnS was observed. Kurokawa et al. [107] reported the performance of CF-reinforced PEEK gears under lithium grease lubrication using a pair of CF-reinforced PEEK gears and a CF-reinforced PEEK gear with a steel gear. The properties of the CFs, including the affinity between the CFs and PEEK, and the strength and modulus of the CFs, affected the wear resistance of the composite. However, few explanations have been provided for the wear mechanism of the CF-reinforced PA66 composite under grease lubrication.

3.2.3 Aramid fibers (AFs)

PAs that are used in the textile industry are aromatic PAs called aramids. AFs are a class of synthetic polymers in which the fiber-forming substance is a long-chain PA with at least 85% of the amide linkages attached directly to two aromatic rings. Poly-paraphenylene terephthalamide (PPTA, such as Kevlar fabricated by DuPont in the USA) is a para-variety of AFs and differs from its meta-variety poly-meta-phenylene isophthalamide (PMIA, such as Technora fabricated by Teijin in Japan) in its chemical structure only in the phenyl nitrogen and phenyl-carbonyl linkage positions [59]. Fig. I. 26 shows the chemical structure of AF based on PPTA and PMIA [108].

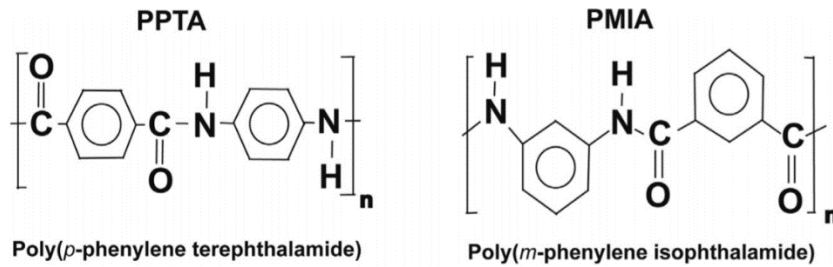


Fig. I. 26 Chemical structure of PPTA and PMIA [108].

The tribological properties of AF-reinforced composites have been actively studied in recent years owing to their high intensity, temperature, wear resistance, low shrinkage at elevated temperatures, and low creep [75, 109], and AF composites have been used for many applications in the automotive industry, such as gears, door check arms, head lamp adjustor parts, and sensor housings, including sliding parts [110]. Botan et al. [75] reported that the addition of 10 wt% of AFs to PA6 and PBT decreases wear and the temperature in contact, whereas the friction coefficient slightly increases. Bolvari et al. [110] reported the tribological properties of AF-reinforced PA66 with added PTFE, and 5–15 wt% AFs were preferred, forming a transfer film during adhesive wear. Kukureka et al. [77] investigated the tribological properties of 20% AF-reinforced PA66 under dry rolling-sliding contact against identical materials using a twin-disc wear test ring under a range of loads and slip ratios, and they observed that the addition of AFs increased the wear rate, and the friction coefficient was close to that of the unreinforced polymer. The effect of adding AFs on the decrease in the friction coefficient was smaller than that of the addition of CF or GF. Gordon et al. [79] studied the tribological properties of pairs of different amounts of AF-reinforced PA46 in unlubricated rolling-sliding non-conformal contacts, all at a slip ratio of 2%, to simulate the tribological behavior of plastic gears. The results indicated that the average friction coefficient decreased with an increase in the amount of AF, whereas wear increased, particularly at higher loads and velocities. Cracks and melting occurred on the sliding surface of unreinforced PA46, and pitting and large cracks/fractures were observed on the surface of AF-reinforced PA46 after the sliding tests. Considering the various previous studies, the merits or advantages of the addition of AFs differ depending on the type of counterparts (steel or identical polymer) and mode of sliding.

3.3 Additives

3.3.1 Solid lubricants

It is well known that solid lubricants exhibit self-lubricating behavior. PTFE, graphite, MoS₂, and ultrahigh molecular weight polyethylene (UHMWPE) are well-known solid lubricants that reduce the friction coefficient and wear rate of some composites [16, 111, 112, 113, 114, 115, 116]. Fig. I. 27 shows the microstructure of PTFE and the atomic force microscopy (AFM) image of the PTFE friction surface. It is important that solid lubricants are transferred to the counter surface and the interfacial shear stress and friction coefficient reduced [66]. The addition of PTFE reduces the friction coefficient of PA66 from 0.45 to 0.11, which is attributed to the PTFE thin-film-formation on the counterpart material. The decrease in the friction coefficient can contribute to the decrease in the sliding surface temperature and wear rate [117].

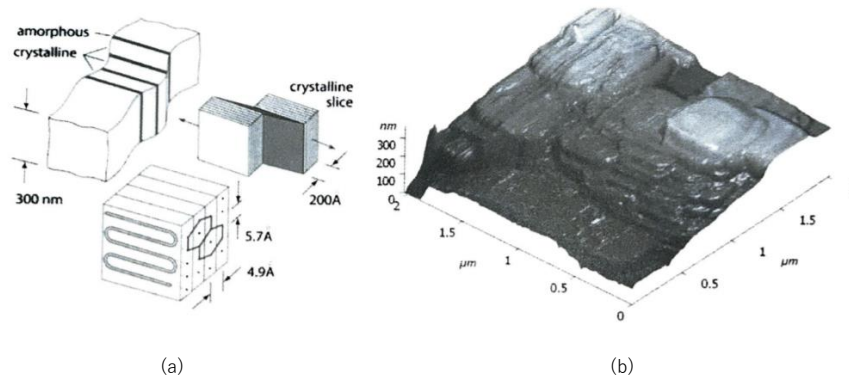


Fig. I. 27 (a) Microstructure of PTFE, (b) AFM image of PTFE friction surface [66].

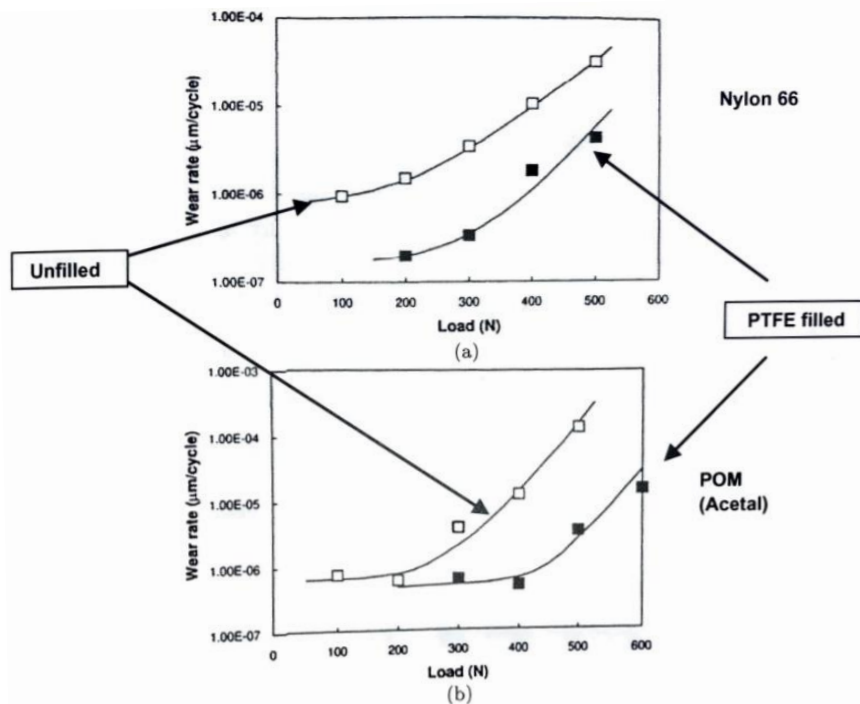


Fig. I. 28 Wear rates of (a) PA66 and (b) POM with/without PTFE fillers [117].

However, the addition effect of solid lubricants differs depending on the sliding test conditions. The addition of solid lubricants reduces the mechanical properties of the polymers. Li et al. [112] studied the effect of adding different types of solid lubricants using PA6 with 15% GF added in contact with steel under dry conditions. The combination of PTFE and UHMWPE presented the best tribological properties to reduce the friction coefficient and wear rate, whereas the addition of graphite did not improve the friction and decrease the wear of the composite.

3.3.2 Molecular chain extender and carbodiimide compounds

As presented in Section 3.1.3, reactive extrusion is a useful method of increasing the molecular mass of PA66. Carbodiimide compounds are used as new molecular chain extenders to increase the molecular mass of fiber-reinforced PA66 materials. Carbodiimide compounds contain a $-N=C=N-$ functional group and are highly reactive with chemical groups such as $-COOH$ or $-NH_2$ [118, 119]. Carbodiimide compounds are generally used as additives for plastic materials, such as polyesters and polylactic acid, to prevent hydrolysis [120, 121, 122].

3.4 Impact modifier

Plastic components are fabricated using an injection molding process with a metallic insert, and crack initiation at the interface and breakage caused by thermal shock must be considered. Injection molding with inserted metallic parts is an effective method of producing plastic–metal hybrid components [34, 123, 124]. However, the plastic parts are subjected to stress from the inserted metal parts because of the different coefficients of linear expansion for the metal and plastic materials at the area where the metal and plastic parts are in contact, particularly when the edge of the metal is sharp. Therefore, when a cyclic thermal stress is applied (heating and cooling are repeated in the long-term use of plastic parts), cracks related to the shrinkage or expansion may be initiated and propagate in the plastic parts around the inserted metal parts (Fig. I. 29). This can cause plastic parts to break [123]. Moreover, the effect of this failure mode appears to be much more severe when fiber-reinforced resin materials are used. Thus, the toughness (expressed by the elongation at breaking) and breakage energy decrease compared with those of unreinforced plastic materials [78], which facilitates the propagation of cracks. Therefore, the effects of the failure of plastic parts with inserted metal must be considered when using fiber-reinforced composite materials for metal-inserted plastic parts.

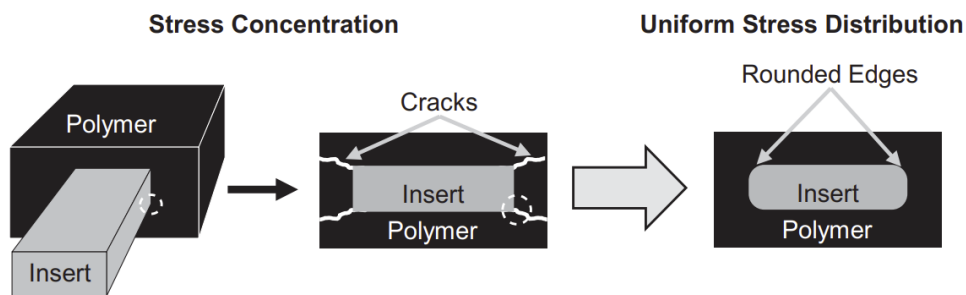


Fig. I. 29 Schematic illustration of crack initiation and the approach to reduce stress concentration with rounded edges [123].

Considering this background, the addition of an impact modifier is a common method of improving the impact strength and toughness. A representative example of an impact modifier is rubber, including acrylonitrile–butadiene rubber (NBR), ethylene–methyl acrylate copolymer (EMA), ethylene–propylene rubber (EPR), styrene–ethylene/butylene–styrene rubber (SEBS), as well as reactive elastomers such as maleic anhydride grafted SEBS (SEBS-g-GMA), and ethylene–methyl acrylate–glycidyl methacrylate random terpolymer [125]. Jahromi et al. [125] reported that the addition of glycidyl methacrylate-grafted NBR (NBR-g-GMA) increased the toughness of PA6/clay nanocomposites. They also stated that the chemical modification of NBR by GMA resulted in better dispersion of the nanoclay and ensured better mechanical properties. Mert et al. [126] also presented the addition effect of GMA as an impact modifier of PA66 with added nanoclay.

4. Metallic materials

Various types of metallic materials, which slide in contact with engineering plastic including PA or fiber-reinforced PA composite, have been reported in previous studies: 316L stainless steel [63], 440C stainless steel containing 17.5% chromium [114], 416 stainless steel [116], carbon steel containing 0.45% of carbon (such as S45C steel) [16, 65, 73, 74], chromium steel [78, 113, 127], 100Cr6 [68], AISI1045 steel [109, 128], CGr15 steel [101], Cr–Mo steel [104], 12 RMS SAE 1040 steel [100], 100Cr6 steel [64], SUJ2 bearing steel [129], 1045 HT steel [18], Ck45K-DIN steel [111], brass BS2874 (CZ121-PB4) [76], M238 (40CrMnNiMo8) [130], S355-J2 [130], bronze [82], aluminum [76], EN24 steel [76], and EN08 steel [76] in the basic sliding test, and steel (not precisely described) [54, 55], stainless steel (not precisely described) [6], stainless steel (AISI316) [9], carbon steel containing 0.45% of carbon including S45C [107], and SUM43 [38, 45] in the actual gear durability test.

Few studies discussed the effect of the type of metallic counterpart on the tribological properties of unreinforced or fiber-reinforced PA. Zabala et al. [131] presented the effect of the hardness of mold steel, which was determined by the pre-hardened process and different types of surface treatment on the friction and wear of mold steel that slid with unreinforced acrylic resin or GF-reinforced PA under dry conditions. The wear of the mold steel was significantly more severe when using GF-reinforced PA than when using unreinforced material, and the wear of the mold decreased with the increase in the mold hardness when using GF-reinforced PA (Fig. I. 30). In addition, the TiN surface treatment of the mold contributed to reducing the friction between the mold and GF-reinforced PA (Fig. I. 31), whereas the Ni-PTFE treatment decreased the friction between the mold and unreinforced material. However, the effect of the hardness or surface treatment of the mold steel on the wear resistance of the composite was not investigated.

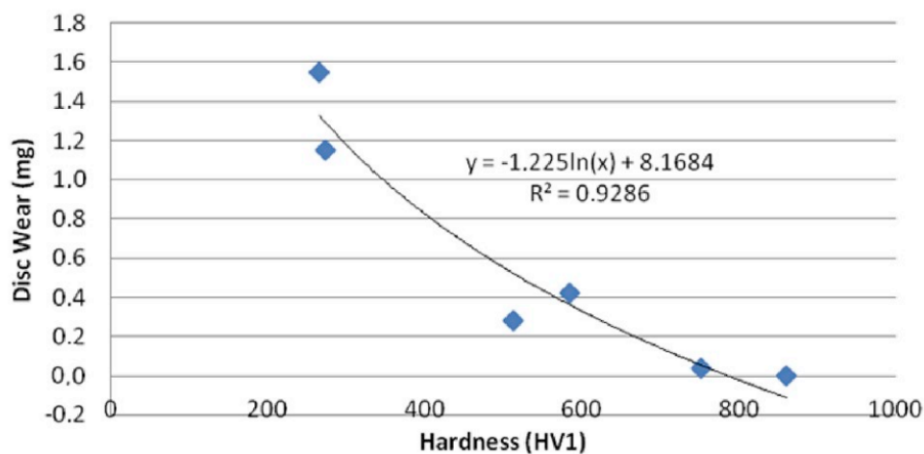


Fig. I. 30 Wear of steel with different values of the hardness of mold steel, determined using different processes of heat treatment and pre-hardened process of steel after sliding tests using GF-reinforced PA [131].

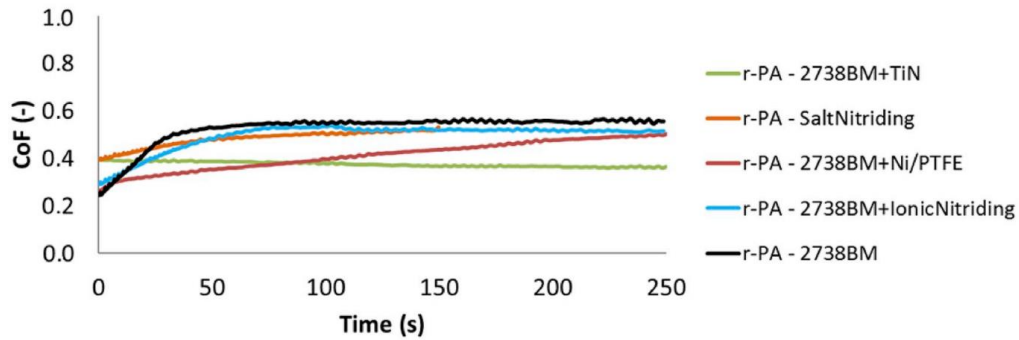


Fig. I. 31 Evolutions of the friction coefficient (CoF) in the sliding test using GF-reinforced PA and mold steel with different types of surface treatment [131].

Chen et al. [76] observed that the type of metallic counterpart (such as aluminum, brass, or steel with different surface treatments or heat treatments) had notable effects on the wear resistance of unreinforced PA66 or GF-reinforced PA66 with added PTFE and on the friction coefficient during the rolling-sliding contact (Fig. I. 32). They indicated that this difference was attributed to the capability of the metal surface to form a stable polymer transfer film and that the surface treatment of steel (such as Tufftride coating) has a significant effect on the wear rate of GF-reinforced PA66.

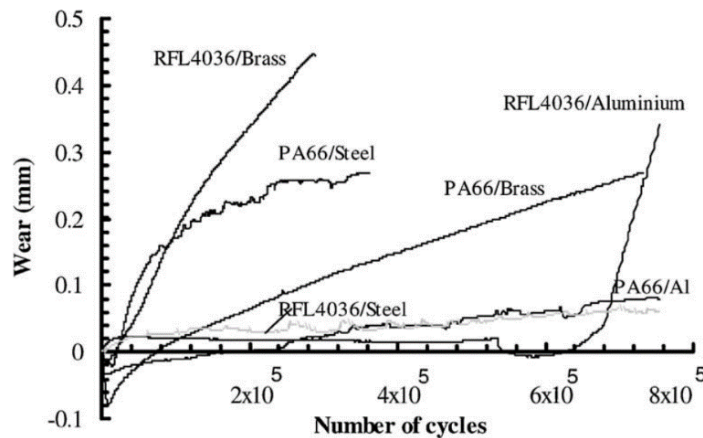


Fig. I. 32 Wear measurements of different pairs of metallic materials and PA66 materials under the same test conditions. RFL4036: GF-reinforced PA66 with added PTFE [76].

Ando et al. [130] compared the tribological properties of PA6 in contact with Cr–Mo steel (40CrMnNiMo8; M238), which has a higher yield strength (826 MPa) and hardness (227 HV) or structural steel (S355-J2), which has a lower yield strength (355 MPa) and hardness (145 HV) in the twin-disc sliding test, which had a slip ratio of 15% at room temperature under dry conditions for various normal loads and sliding velocities. M238 steel decreased the friction force, particularly for higher normal loads, whereas no difference in the sliding velocity dependence was confirmed. However, the mechanism of the difference in the tribological properties, such as the effect of the mechanical properties or hardness of steel, surface chemistry, and the difference in the transfer film thickness related to the adhesion wear, was not discussed.

Considering the abovementioned studies, all sliding tests were conducted under dry conditions, and the effects of the hardness of steel on the tribological properties of PA or composite (particularly the wear of the composite) were not discussed.

5. Lubrication oil and grease

Polymer materials are frequently used under dry conditions because their self-lubricating properties can avoid the necessity for lubrication using oil or grease with its accompanying problems of sealing and possible contamination [77, 132]. Therefore, most of the previous studies on the tribology of engineering plastics, such as PA, were conducted under dry conditions. However, oil or grease lubrication is necessary under severe sliding conditions even when using a polymer material. For example, as mentioned in Section 2.3, grease lubrication is mandatory in the use of a worm reducer of the EPS. In this chapter, the characteristics of grease are explained, and the literature on the tribology of engineering plastics, including PA66, particularly under grease lubrication, are introduced.

5.1 Characteristics of grease

Greases, one of the oldest forms of lubricating materials, act as a gel (semisolid) or solid lubricant composed of a thickening agent dispersed in a liquid lubricant or a combination of lubricants. A fiber network is formed by a soap (thickener). The lubricant oil is inside the network. The principal advantage of grease over conventional oil is its ability to remain in contact with the desired moving surfaces. Thickeners in the grease are designed to reduce migration caused by gravity, pressure, or centrifugal action. Grease is best considered as a thickened oil [133].

The liquid lubricant of the base oil in grease frequently accounts for 70–95% of the grease. Mineral oil (petroleum-derived), synthetic oil such as PAO, esters, polyglycols, and silicones (all synthesized from discrete chemical components), or natural oil (plant- and animal-derived) are examples of the base oil of grease. Thickeners constitute between 5% and 25% of the grease composition. Various thickeners were developed from 1930 to the 1980s [134]. Metallic soaps, including lithium soap [18, 129, 135], lithium complex [135, 136, 137, 138], calcium soap, and aluminum complexes are representative examples of soap-type grease thickeners. In addition, urea [4, 129, 137, 138], PTFE [55, 135], silica, expanded graphite, or clays (bentonite or hectorite) are examples of non-soap-type grease thickeners. They have different values of dropping points and therefore the maximum usable service temperature depending on the type of thickener [133].

Additives that ensure properties such as oxidative stability, wear resistance, and corrosion inhibition are added in a proportion of 0.5–10% of the grease depending on its application. In particular, additives that can reduce the friction and enhance the tribological properties are significant for the use of sliding parts, and the same type of additives as the liquid lubricating oil, such as oiliness improvers, anti-wear agents, friction modifiers, and extreme-pressure agents are largely used [133].

5.2 Low friction additives

5.2.1 Oiliness improvers

Oiliness improvers are used to decrease friction and wear by forming an oil adsorption film on the sliding surface, particularly under low normal loading conditions. Long chain fatty acids, fatty acid esters, and long-chain alcohols are known examples of oiliness improvers [133, 139, 140, 141, 142].

5.2.2 Solid lubricants

Solid lubricants are solid materials that reduce friction and mechanical interactions between surfaces in relative motion against the action of a load. MoS₂, graphite, boron nitride, and PTFE are representative examples. The effect of decreasing the friction is not related to the temperature and only to the contact pressure; therefore, solid lubricants are also useful for ambient-temperature applications such as drawing or stamping of sheet metal or bar stock [133, 134].

5.2.3 Anti-wear agents

An anti-wear agent is an additive that generally reacts with a metallic surface to form a protective film when the oil film or oxidation-protective film on the metallic surface breaks under high-load or low-speed conditions. The formed film prevents the direct contact of the sliding surface. Examples of anti-wear agents include metal dialkyldithiophosphate, including antimony and zinc, such as zinc dialkyldithiophosphate (ZnDTP), or phosphate and thiophosphate esters, such as tricresyl phosphate, di-n-octyl phosphite, and isodecyl diphenyl phosphite [133, 136, 143, 144].

5.2.4 Friction modifiers

Friction modifiers act through the tribochemical formation of a low friction surface film. Molybdenum dithiocarbamate (MoDTC) is an example, resulting in the formation of a molybdenum disulfide (MoS₂) tribofilm [136, 143, 144].

5.2.5 Extreme-pressure additives

Extreme-pressure additives are used to prevent seizures or scuffing under extreme-pressure lubrication at high temperatures. Organic sulfur, phosphorus compounds, and organic halogen compounds are known to operate as extreme-pressure additives [133, 145].

The effects of additives on the tribochemical reactions related to grease have been demonstrated to be significant. Oiliness improvers, anti-wear agents, friction modifiers, and extreme-pressure agents, which are explained above, are well-known additives for improving tribological properties. Previous studies focused on the mechanism of tribochemistry on the sliding surface of steel, ceramic, or hard coatings (such as diamond-like carbon), and the effects on the tribological properties of these additives. However, in the sliding of polymers and steel or between polymers, few studies on the tribochemistry of additives or the effect of tribofilm formation on tribological properties have been conducted.

5.3 Effect of lubrication on the tribology of polymers and composites

The number of studies that focused on the typical tribological properties under oil or grease lubrication in the basic sliding test using engineering plastics, particularly focusing on the wear mechanism of the composite or clarification of the tribochemical reaction, is significantly limited, whereas several studies have investigated the tribological properties of actual polymer parts, including gears [1, 4, 13, 44, 46, 67] or bearing [22] under lubricated conditions.

Zhang et al. [128] reported the basic tribological properties of GF- and fly-ash-reinforced monomer-casting PA6 in contact with AISI 1045 steel, which was quenched and hardened to a hardness of 40–45 HRC under dry, water-lubricated, and oil-lubricated conditions (the detailed composition of the oil was not disclosed). The friction coefficient and wear rate of the composites under oil lubrication decreased by 42.5% and 77.8%, respectively, compared with

the wear of the composite under dry conditions, whereas the wear rate of the composite under water lubrication was higher than that under dry conditions (Fig. I. 33). Water lubrication cooled the sliding surface and prevented adhesion between PA6 and steel, thereby decreasing the friction coefficient. However, the polyamide amido bonds easily absorbed water molecules, as discussed in Section 3.1.4, thereby swelling the composite and increasing the composite wear. The sliding surface of the composite under oil lubrication was covered with an oil film to reduce the abrasive wear, thereby decreasing the friction coefficient.

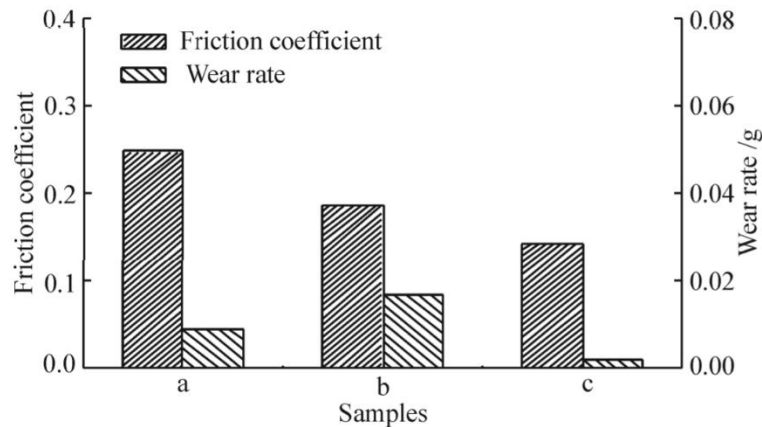


Fig. I. 33 Friction coefficient and wear of the composite under different lubricated conditions. a: dry conditions, b: water-lubricated conditions, and c: oil-lubricated conditions [128].

Wilson [135] presented the tribological properties of GF-reinforced PA46, GF-reinforced PA66, and CF-reinforced PEEK under four different types of grease lubrication in contact with a steel roller using a twin-disc test apparatus that could conduct the test under combined rolling and sliding conditions, considering the application for automotive auxiliary drives such as gears. They used different types of base oil (polyalphaolefin and synthetic hydrocarbon oil) and thickeners (lithium soap, lithium complex, and PTFE) as parameters of the grease composition. The best combination of the composite and grease was observed in terms of low friction and low wear amount of the composite; however, the detailed wear mechanism of the composite, particularly under grease lubrication was not provided. The tribological reason particular combinations exhibited better properties, or tribochemistry related to the grease, was not sufficiently discussed.

Tung et al. [18] reported the tribological behavior of unreinforced polyoxymethylene (POM) and PA6 in contact with 1045 HT steel under dry conditions or different compositions of grease (lithium-soap synthetic grease and barium soap mineral oil) lubricated conditions at various temperatures (from -15 to 150°C), in terms of the application of the polymer worm gear in the worm reducer of EPS. They indicated that grease lubrication prevented severe wear of the polymer, as observed under dry conditions. At lower temperatures, lithium-soap grease exhibited a lower friction coefficient because the polyimide thickener in a grease can develop a more rigid network that adheres to the oil, and crystallizing can be prevented. In contrast, barium soap grease exhibited better properties at higher temperatures because of the good thermal and oxidation stability of the synthetic grease. These results indicated that the composition and properties of grease affect the temperature dependence of the tribological properties of the polymer material. However, their evaluations were conducted by changing

many parameters of the grease compositions, and the tribochemistry focusing on the grease additives at different temperatures was not discussed.

Tatsumi et al. [146] presented the friction and wear behavior of PEEK in contact with steel (AISI 52100) under PAO oil boundary lubrication and compared it with that under dry conditions. PAO lubrication softened the PEEK wear track; however, it did not result in the wear of PEEK. The thickness of the PEEK transfer film on the steel counterparts affected the tribological behavior under both dry and PAO lubricated conditions, and the formation and removal of the film were dominated by the operating conditions. Tatsumi et al. [147] also investigated the tribological behavior of PEEK under PAO8 oil lubrication with an added friction modifier, and N-oleoyl had a significant effect on the improvement of the tribological properties.

Previous studies investigated the tribology of PA or other types of engineering plastics in contact with steel under grease lubrication; however, the temperature dependence on the tribological properties, or the detailed mechanism of the tribochemistry, on the sliding surface has yet to be clearly discussed.

6. Effects of different parameters on tribological behavior of polymer on steel contacts

Many factors affect the friction and wear of polymers, such as PA, and metallic materials, such as steel. In this chapter, the basic mechanism of friction and wear of polymers is discussed, and previous studies that focused on the effect of each parameter (contact pressure, sliding velocity, or temperature) on the tribological properties are summarized.

6.1 Basic mechanism of friction and wear

As presented by Bowden and Tabor [148] in 1950, on the direct (unlubricated) contact of any two materials, two mechanisms that contribute to friction should be considered. First, adhesion in the regions of actual contact is frequently remarkable. The adhesion originates from the adhesive bonds formed between the surfaces in the sliding contact [66]. Furthermore, the actual contact area is remarkably smaller than the apparent contact area (Fig. I. 34). Therefore, adhesion-related friction can be expressed as the product of the actual contact area and average shear strength. The second factor is related to the plowing, grooving, and cracking of one surface (frequently a softer polymer material) by the hard asperities on the other surface (frequently a harder metallic material) [66]. Therefore, the total friction (F) (i.e., resistance to movement along the contact surface) can be expressed by the following equation:

$$F = F_{adhesion} + F_{deformation} = A \cdot \tau + F_{deformation} \quad (I. 1)$$

where A is the total actual contact area, and τ is the shear strength of the polymer material. Practically, F is considerably similar to $F_{adhesion}$ because $F_{deformation}$ is significantly smaller than $F_{adhesion}$ [149]. Considering the relationship between the friction force, friction coefficient (μ), and normal load (W) (Fig. I. 34), the friction coefficient can be expressed by the following equation:

$$\mu = \frac{F}{W} = \frac{A\tau}{W} = \frac{\tau}{P} \quad (I. 2)$$

where P is the mean contact pressure (W/A). For polymers, τ increases linearly with an increase in the mean contact pressure.

$$\tau = \tau_0 + \mu_\infty P \quad (1.3)$$

where τ_0 is the constant intrinsic characteristic shear strength and μ_∞ is the pressure coefficient for infinite pressure. Considering equations (1.2) and (1.3), the friction coefficient can be expressed as follows:

$$\mu = \frac{\tau}{P} = \frac{\tau_0}{P} + \mu_\infty \quad (1.4)$$

Therefore, μ is a function of the pressure in the contact and can be determined by the shear strength of the material. The shear strength linearly increases with increasing contact pressure (equation (1.5)). The pressure coefficient (μ_∞) can be determined from the bulk-polymer sliding tests performed under various contact pressures because μ_∞ is the friction coefficient when the contact pressure is infinite [150, 151].

In addition, the actual contact area is generally expressed as follows.

$$A = kW^m \quad (1.5)$$

where k and m are constants. The value of A for two spheres in contact or a sphere on a plane contact is expressed by Hertz's law or Meyer's law [149].

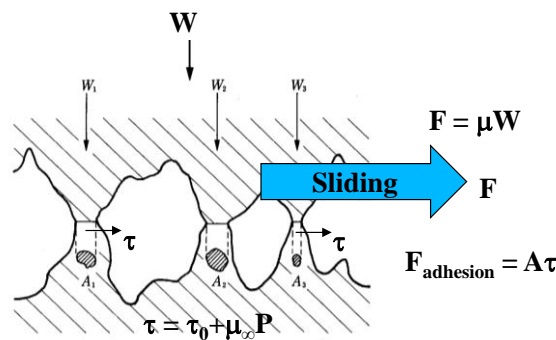


Fig. I. 34 Image of contact between two materials [66].

Therefore, the friction resulting from adhesion is affected by the actual contact area and polymer shear strength, and the increase in the temperature induces an increase in the actual contact area related to the decrease in the Young's modulus of the polymer and a decrease in the shear strength. In addition, the increase in temperature also induces deeper indentation of the steel roughness asperities in the polymer material, namely, the large deformation of the polymer material. The temperature dependence of the Young's modulus and the shear strength have an adverse effect on the friction for both adhesion and deformation (an increase in the temperature induces an increase in the friction via Young's modulus and a decrease in the friction via shear strength) [83].

6.2 Effects of temperature

Polymers as viscoelastic materials are very sensitive to sliding heat generation or temperature because temperature affects the mechanical properties of polymer materials [66]. Therefore, to use polymer sliding parts in a high-temperature environment, such as inside an engine compartment of an automobile, it is necessary to understand the

temperature dependence of the tribological properties and the effect of the temperature on the mechanical properties and tribochemistry. However, the effects of temperature on the tribological properties (friction and wear) of PAs or composite have been reported, particularly under dry conditions [65, 116, 152]. Shin et al. [65] reported that the friction coefficient and wear rate of unreinforced PA66 under dry conditions increased owing to a degradation in the mechanical properties of the resin and increased adhesion to a counterbody surface at high temperatures, considering the adhesion wear mechanism described in Section 3.1.3 (Fig. I. 35). This negative effect of the softening polymer on the increase in wear was also reported [152]. Lates et al. [116] reported that the friction coefficients of PA66, PA46, and PTFE-added PA46 under oil-lubricated conditions decreased with increasing temperature, regardless of the contact pressure and sliding speed.

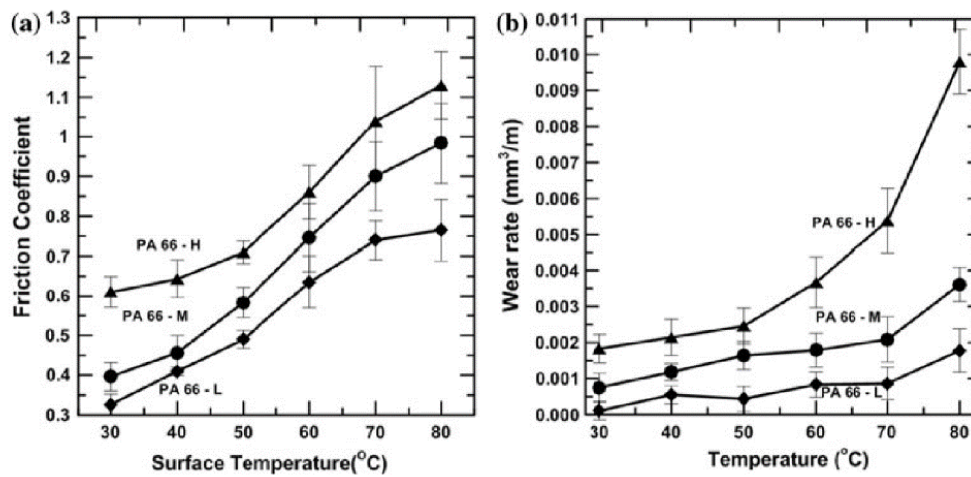


Fig. I. 35 Relationship between temperature and (a) friction coefficient, (b) wear rate of unreinforced PA66 with different molecular masses of PA66. (L): low molecular mass of PA66, (M): medium molecular mass of PA66, (H): high molecular mass of PA66 [65].

6.3 Effects of contact pressure

The contact pressure significantly affects the tribological properties of the polymer because the friction force, which is related to the adhesion, is directly affected by the normal load (see Section 6.1), particularly under dry conditions. Several studies focused on the normal load (contact pressure) dependence of the tribological properties of polymer materials. Xu et al. [109] reported the effect of load on the tribological properties of AF-reinforced PA1010 in contact with AISI1045 steel under dry conditions, and the friction coefficient decreased with an increase in the applied normal load (Fig. I. 36), including the fitting results obtained by the power approximation ($R^2: 0.996$). The effect of the applied normal load was more sensitive than that of the sliding velocity. They stated that the tendency of the friction coefficient was the same as that of the Hertzian contact law: $\mu = kW^{(n-1)}$ ($2/3 < n < 1$, k : constant value, W : applied normal load [132, 153, 154]), but the value of n was 0.40, which was less than $2/3$. This was related to the difference in the characteristics of PA and AFs (assuming a multiphase composite because of its continuous and homogeneous assumption for the material).

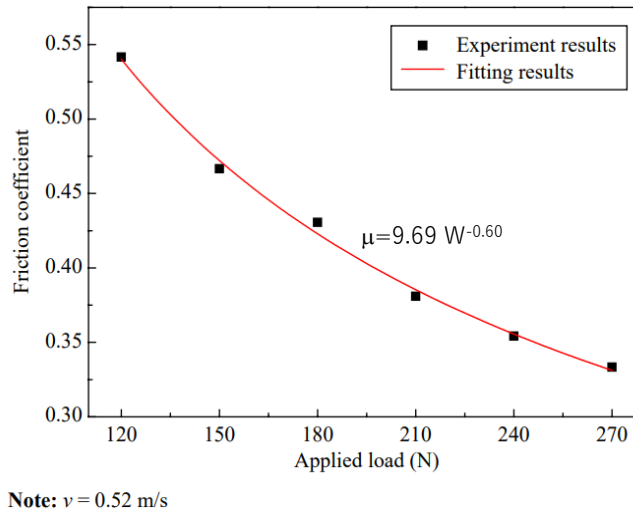


Fig. I. 36 Relationship between applied normal load and friction coefficient in the sliding of AF-reinforced PA1010 and a steel counterpart under dry conditions [109].

The same tendency that the friction coefficient decreases with an increase in the applied load was reported in [83]. Fig. I. 37 shows the evolution of the friction coefficient in the sliding of unreinforced PA6 and a steel counterpart under dry conditions for different applied loads; the figure shows that the friction coefficient decreases with an increase in the normal load. The authors explained this tendency using equations (I. 3) and (I. 4), considering the shear stress. The friction coefficient decreases with an increase in the contact pressure under lower pressures owing to the less-than-proportional increase in the actual contact area. This tendency was observed in the contact pressure range of 20–55 MPa. At a high contact pressure of over 55 MPa, the increase in the shear strength compensates for the less-than-proportional increase in the actual contact area, and the friction coefficient is independent of the apparent contact pressure.

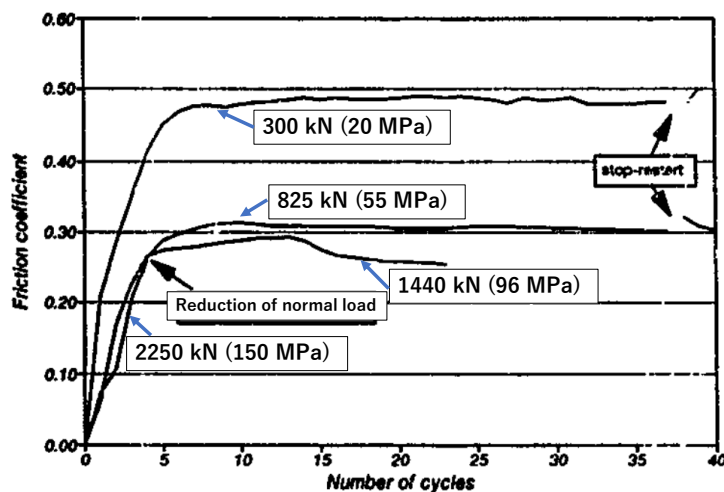


Fig. I. 37 Evolutions of the friction coefficient in the sliding of unreinforced PA6 and a steel counterpart under dry conditions for different applied loads [83].

In the actual sliding test of the PA66 worm gear and steel worm shaft under grease lubrication, the general trend for the gearbox efficiency increased, and the friction coefficient decreased with an increase in the applied load (Fig. I. 10, page 18) [19]. The friction coefficient decreased significantly between 0.5 and 2.0 Nm of applied worm torque, and the amount

tended to exhibit stable values between 2.0 and 4.0 Nm. This tendency of the friction coefficient under grease lubrication is the same as that observed in Fig. I. 37 under dry conditions. Dearn et al. [117] also stated that an increase in the applied load to a polymer spur gear increases the efficiency. Kim et al. [38] demonstrated that the friction coefficient decreased and gear efficiency increased with an increase in the applied load in an actual worm gear efficiency measurement system (SUM43 steel worm shaft and PA6 worm wheel under grease lubrication) (Fig. I. 6, page 15).

6.4 Effects of sliding velocity

Theoretically, the friction force should not depend on the sliding velocity. However, this statement is only applicable if the temperature within the contact area increases, but negligibly, particularly for polymers. Frequently, the complicated dependence of the sliding velocity on the friction is explained by the variations in the relaxation properties and physicochemical activity of macromolecules. When the test temperature approaches the glass transition temperature (T_g) of each polymer, the friction coefficient tends to depend on the sliding velocity. Conversely, no dependence of the sliding velocity tends to be observed at low temperatures [66].

Several studies focused on the effects of the sliding velocity on the tribological properties of PAs or fiber-reinforced composites. Xu et al. [109] reported that the friction coefficient of AF-reinforced PA1010 in contact with steel under dry conditions decreased with an increase in the sliding velocity. This was attributed to the change in the temperature and glass-to-viscoelastic state transitions of PA1010. At higher sliding velocities, the PA1010 was transformed from a viscoelastic state to a viscous flow state; subsequently, the viscosity of the surface material decreased and the rheological material functioned like some lubrication, and the friction coefficient decreased. Sliding velocity dependence has also been reported using GF-reinforced PA66 or PA66 with added MoS₂ in contact with steel under dry conditions [111]. Increasing the sliding velocity increased the temperature and decreased the friction coefficient of the two PA66 materials. Image analysis of the sliding surface focused on the existing condition of GFs, and the increase in the sliding velocity resulted in an increase in the proportion of elongated debonded fibers and clusters of fiber fragments. The increase in the sliding velocity resulted in a more continuous dispersion of the transferred film and its ability to remain adhered to the counterface. The homogeneity of the transfer film on the counterpart surface was improved owing to the increase in the GF fraction that covered the polymer surface, which resulted in a decrease in the friction coefficient at the expense of the increase in the composite wear.

7. Lubricative theories and tribology of polymer materials under oil or grease lubricated conditions

7.1 Elastohydrodynamic lubrication (EHL) theories

As discussed in Section 2.3, grease lubrication is introduced in the sliding of a polymer worm wheel and metallic worm shaft in the EPS reducer to ensure low friction and lower temperature in the sliding surface, which is governed by severe sliding in addition to rolling [46]. The meshing of the polymer gear under grease lubrication is reported to be the rolling contact that accompanies sliding and is used under EHL [129]. Temperature and pressure, as

well as the sliding and rolling speed, affect the EHL [155]. In full liquid lubrication, the lubrication regime is classified into four different regimes depending on the contact pressure, which affects the increase in the oil viscosity and elastic deformation. This last point is explained in many studies as follows [156, 157, 158]:

1) **Isoviscous–rigid (IR)**: When the contact pressure is low (in the range of 1 to 50 MPa, such as the contact of very similar matching shape, as observed in plain journal, circular-arc thrust bearing, industrial painting or protective coating process, or very lightly loaded cylindrical roller bearings, the contact pressure is too low to increase the viscosity of the oil or to change the contact geometry. This lubrication regime is classified as *an isoviscous–rigid* (IR) hydrodynamic lubrication.

2) **Piezoviscous–elastic (PE)**: When a very high contact pressure (0.5–4 GPa) is applied, in the rolling or sliding contact such as gears and balls or roller bearings fabricated from ceramic or steel, the consideration of the increase in the viscosity of lubricative oil and elastic deformation of the material is necessary. The oil film thickness has a significant effect on the friction, and this regime is classified as *piezoviscous–elastic* (PE) hydrodynamic lubrication, or “hard EHL.”

3) **Isoviscous–elastic (IE)**: When sliding surfaces are created from soft polymer materials (which have relatively lower Young’s moduli than metallic materials), which are observed in polymer gears, seals, human joints, tires, and bearing cages, the contact pressure (frequently in the range of 1–50 MPa) is sufficient to induce elastic deformation of the polymer material. However, these values are not sufficient to increase the viscosity of the lubricant oil, as observed in the hard EHL mode. This lubrication regime is classified as *isoviscous–elastic* (IE) hydrodynamic lubrication, or “soft EHL.”

4) **Piezoviscous–rigid (PR)**: When the sliding material is very stiff and exhibits no elastic deformation, the contact pressure is sufficiently high to increase the oil viscosity; this regime is classified as *piezoviscous–rigid* (PR) hydrodynamic lubrication. However, this regime is not often observed and is suggested for roller-end guide flanges in highly loaded cylinder tapered roller bearings.

In the contact of a polymer with a metal, the soft EHL mode is frequently applied to discuss the oil film thickness. Several equations for estimating the theoretical oil film thickness in the IE lubrication regimes have been proposed, and similar values of oil film thickness can be obtained using different formulas. Hamrock and Dowson equations [156, 159], which are cited in several studies [129, 157, 158, 160, 161, 162], are as follows:

$$H_{min} = \frac{h_{min}}{R} = 7.43 U^{0.65} W^{-0.21} (1 - 0.85 e^{-0.31k}) \quad (I. 6)$$

$$H_{central} = \frac{h_{central}}{R} = 7.32 U^{0.64} W^{-0.22} (1 - 0.72 e^{-0.28k}) \quad (I. 7)$$

where H_{min} is the minimum dimensionless film thickness, h_{min} is the minimum film thickness, $H_{central}$ is the central dimensionless film thickness, $h_{central}$ is the central film thickness, U is the dimensionless speed parameter, W is the dimensionless load parameter, and k is the ellipticity parameter, which is expressed as $k=a/b$ (a : semimajor axis of contact ellipse, b : semiminor axis of contact ellipse), ranging from 1 (for a circular configuration such as a ball-on-plate configuration) to 12 (for a configuration approaching a rectangular contact).

The dimensionless parameters U and W are defined as follows, considering the contact of the two materials (Fig. I. 38):

$$U = \frac{u\eta_0}{ER} \quad (I. 8)$$

$$W = \frac{w_l}{ER} \quad (I. 9)$$

where u is the average surface velocity.

$$u = \frac{u_1 + u_2}{2} \quad (I. 10)$$

η_0 is the viscosity of oil, w is the applied normal load, and w_l is the load per unit contact length. E and R are the effective modulus of elasticity and equivalent contact radius, respectively, as follows:

$$\frac{2}{E} = \frac{1-\nu_1^2}{E_1} + \frac{1-\nu_2^2}{E_2} \quad (I. 11)$$

$$\frac{1}{R} = \frac{1}{R_1} + \frac{1}{R_2} \quad (I. 12)$$

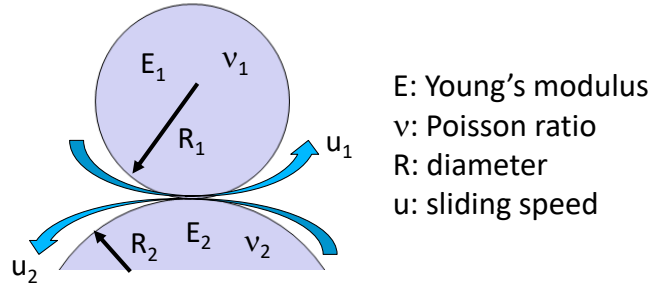


Fig. I. 38 Contact of two materials.

where E_1 and E_2 are the Young's moduli of the two materials, respectively; ν_1 and ν_2 are the Poisson ratios of the two materials; R_1 and R_2 are the contact diameters of the two materials, respectively; and u_1 and u_2 are the rotational speeds of the two materials, respectively.

To express the oil film thickness differently, Esfahanian et al. [158] presented dimensionless film-thickness equations, and this was also applied in several studies [163]. Equation (I. 6) can be expressed in terms of reduced dimensionless grouping as

$$\hat{H}_{min} = 8.70g_E^{0.67} (1 - 0.85 e^{-0.31k}) \quad (I. 13)$$

where \hat{H}_{min} indicates the different types of dimensionless minimum oil film thickness, and g_E is the dimensionless elasticity parameter expressed as follows:

$$\hat{H}_{min} = H_{min} \left(\frac{W}{U} \right)^2 \quad (I. 14)$$

$$g_E = \left(\frac{w_l^2}{\eta_0 ERu} \right)^{1/2} = \frac{W^{8/3}}{U^2} \quad (I. 15)$$

Following these equations, the central and minimum oil film thickness in the soft EHL (IE lubricated regime) at the circular point ($k=1$) is expressed as follows [157]:

$$H_{central} = 5.08g_E^{0.67} \quad (I. 16)$$

$$H_{min} = 3.28g_E^{0.67} \quad (I. 17)$$

The above equations can be reduced to

$$\frac{h_{central}}{R} = 5.08U^{0.66}W^{-0.21} \quad (I. 18)$$

$$\frac{h_{min}}{R} = 3.28U^{0.66}W^{-0.21} \quad (I. 19)$$

These equations are very similar to the equations proposed by Hamrock and Dowson ((I. 6) and (I. 7)), which can be reduced in the circular contact ($k=1$) to

$$\frac{h_{central}}{R} = 3.3U^{0.64}W^{-0.22} \quad (I. 20)$$

$$\frac{h_{min}}{R} = 2.8U^{0.65}W^{-0.21} \quad (I. 21)$$

Additionally, Takabi et al. [155] presented an equation to estimate the minimum oil film thickness differently.

$$\ddot{H}_{min} = 0.3g_E^{0.8} \quad (I. 22)$$

where \ddot{H}_{min} is the dimensionless film thickness that can be expressed differently as follows:

$$\ddot{H}_{min} = \frac{h_{min}Wl}{\eta_0Ru} \quad (I. 23)$$

Using these equations, we can estimate the minimum and central oil film thickness between two contact materials, considering the contact geometry (radius), sliding conditions (sliding speed and normal load), contact materials (Young's modulus or Poisson's ratio), and lubricant properties (viscosity and pressure–viscosity coefficient).

In addition, the estimated oil film thickness can be used to determine the likelihood and severity of asperity contact (specific film thickness: lambda ratio λ), which is the ratio of the minimum oil film thickness to the combined surface roughness of two sliding materials (Ra_1 and Ra_2). The lambda ratio was calculated as follows [160, 163, 164, 165]:

$$\lambda = \frac{h_{min}}{\sqrt{Ra_1^2 + Ra_2^2}} \quad (I. 24)$$

This explains the lubrication conditions. $\lambda < 1$ indicates boundary lubrication, $\lambda > 3$ indicates the formation of fluid film lubrication, and values in between these represent partial or mixed lubrication [161].

7.2 Lubrication regime

To estimate the oil film thickness on a sliding surface, it is necessary to determine the lubrication regime of the contact geometry under a particular load and speed to appropriately select the calculation formula for the oil film thickness. Depending on the values of the dimensionless viscosity parameters (g_V) and dimensionless elasticity parameters (g_E), we can determine which formula of the oil film estimation should be introduced among the four lubricated regimes by plotting the g_V and g_E values to the lubrication regime map. Fig. I. 39 (circular point contact) [156] and Fig. I. 40 (line contact presented by Winer and Cheng) [155] show the lubrication regime maps for each contact geometry.

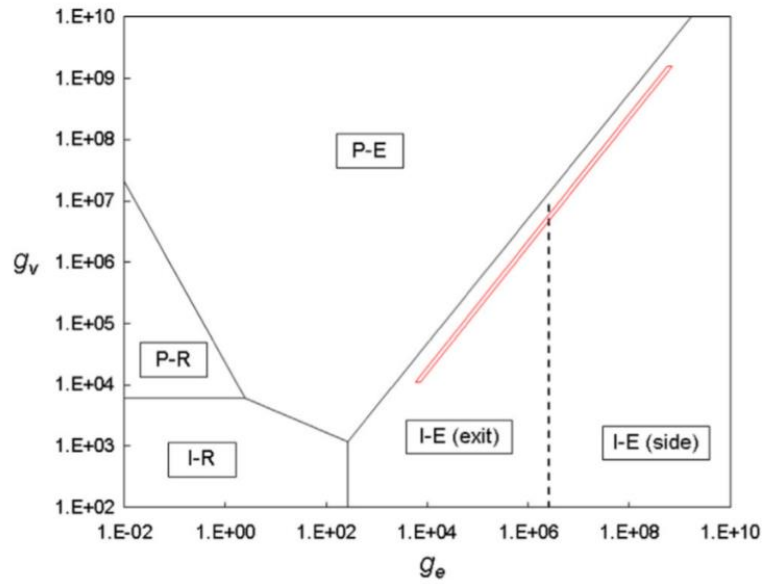


Fig. I. 39 Hydrodynamic regime map for circular point contact [156].

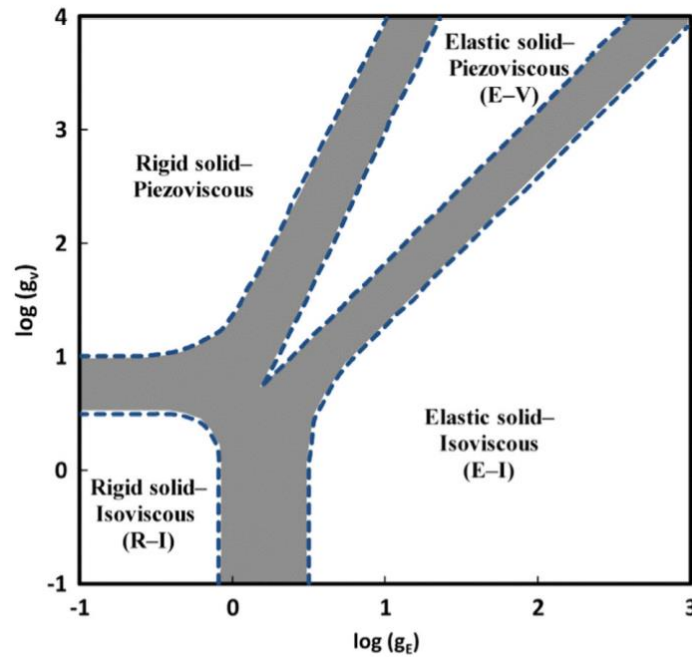


Fig. I. 40 Hydrodynamic regime map for line contact [155].

where g_E is presented in equation (I. 15), and g_V is expressed as follows:

$$g_V = \left(\frac{\alpha^2 w_l^3}{\eta_0 R^2 u} \right)^{1/2} = \left(\frac{G^2 W^3}{U} \right)^{1/2} \quad (I. 25)$$

where α is the pressure–viscosity coefficient of the lubricating oil, and G is the dimensionless material parameter expressed as follows:

$$G = \frac{E}{p_{iv,as}} = \alpha E \quad (I. 26)$$

where $p_{iv, as}$ is the asymptotic isoviscous pressure defined by Roelands. The asymptotic isoviscous pressure can be approximated using the inverse pressure–viscosity coefficient α .

7.3 Estimation of the oil film formation under grease lubrication and comparison with oil lubrication

Several studies focused on soft EHL. However, the use of engineering plastics such as PAs or composites is very limited, whereas very soft materials such as rubber, elastomer, seal material, or gel are used [160, 163]. In addition, very few studies discussed soft EHL oil film formation under grease lubrication.

Kochi et al. [129] measured both the thickness of a lubricant film based on the soft EHL theory and the traction of the oil and grease. They used an optical interferometry system in which a bearing steel ball was placed in contact with a transparent polycarbonate (PC) disc with a Young's modulus similar to that of an engineering plastic such as unreinforced PA. They also measured the oil film thickness based on hard EHL in contact with a glass disc and compared the thickness with that measured based on soft EHL. Fig. I. 41 (a) shows that the oil film thickness was thicker using PC (soft EHL) than glass (hard EHL) irrespective of the sliding speed under oil lubrication, and the pressure–viscosity coefficient did not affect the soft EHL oil film thickness. A good correlation was observed between the actual measured (plots) and theoretically calculated values (broken curves). A soft EHL film with grease was thicker than the film with its base oil (Fig. I. 41 (b)), as was the scenario for a hard EHL film. The film thickness with grease changed with different thickeners depending on its apparent viscosity at different sliding speeds, considering that the apparent viscosity of the grease decreased with an increase in the sliding speed and approached the viscosity value of the base oil (Fig. I. 42) Moreover, they demonstrated that the central oil film thickness could be theoretically predicted based on Bauer's model, which was modified based on the analysis of Dong and Qian.

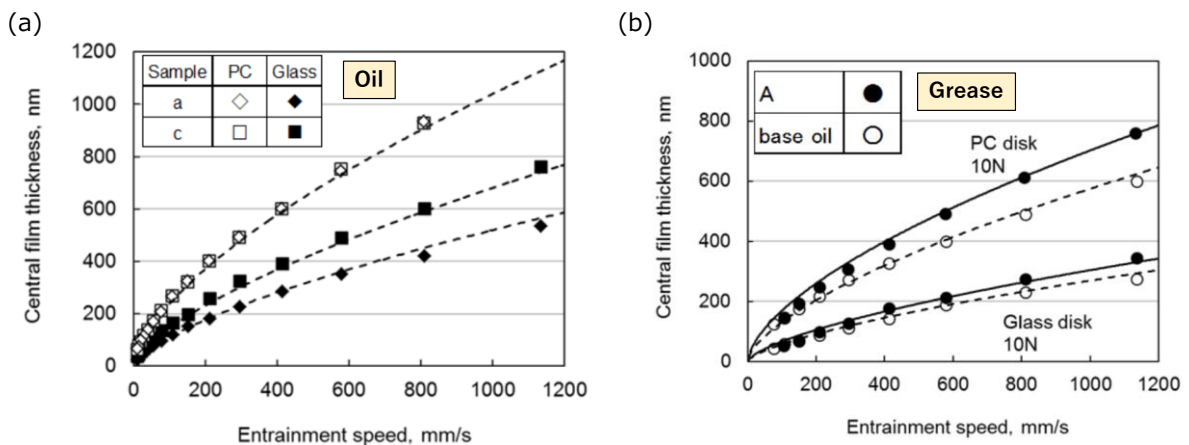


Fig. I. 41 (a) Comparison of film thickness formed with PC disc and glass disc with different values of sliding speed under oil lubrication; (b) film thickness compared between soft EHL (using PC) and hard EHL (using glass) under grease and base oil lubrication. The plots are the actual measurement values and the broken curves were calculated using EHL theories [129].

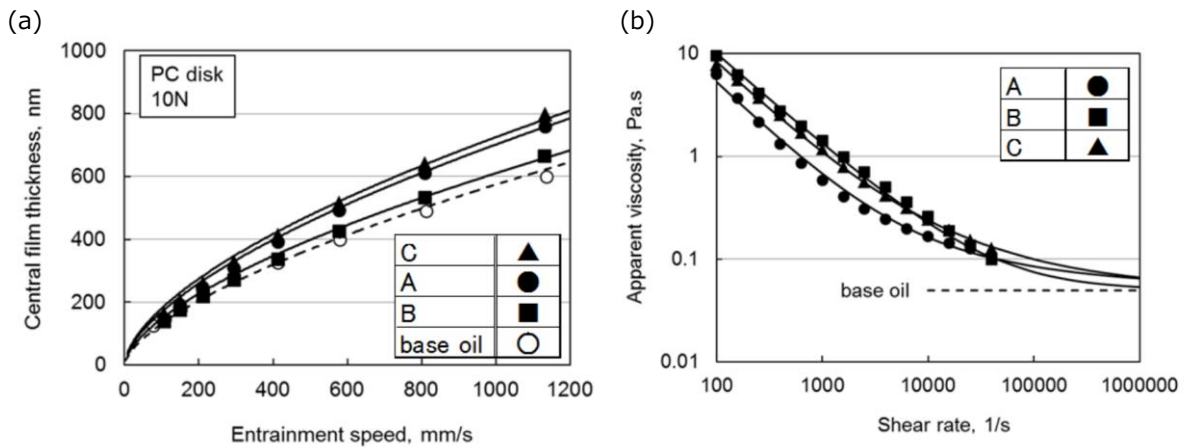


Fig. I. 42 (a) Soft EHL film thickness under grease lubrication with different types of thickeners and base oil lubrication at different sliding speeds. The plots are the actual measurement values and the broken curves were calculated using EHL theories; (b) apparent viscosity of sample grease with different types of thickeners at different sliding speeds measured using a cone-on-plate rheometer. The fitting curve was obtained using Bauer's rheology model [129].

Kanazawa et al. [137] investigated the effect of the sliding speed, temperature, viscosity of the base oil, types of thickeners, and surface roughness on the oil film thickness of grease using the interferometry method of bearing steel ball and glass disc and friction coefficient systematically and compared them with those under the base oil lubrication. Fig. I. 43 shows the measured oil film thicknesses under different conditions. In the lower sliding speed region, the film thickness was significantly larger under grease lubrication than under oil lubrication. In addition, the film thickness was determined by the type of thickener (urea type thickener was significantly thicker than lithium type). In addition, the oil viscosity of grease affected the oil film thickness of grease, whereas it significantly affected the thickness of the oil. Conversely, at a higher speed range (i.e., full-film lubrication), the film thickness was determined only by the base oil properties (primarily viscosity) at different temperatures. They stated that the transition from the thickener-dominated region (low sliding speed) to the oil-dominated region (high sliding speed) occurred at relatively constant values of the oil film thickness, and the values changed depending on the type of thickener, regardless of the temperature or sliding speed.

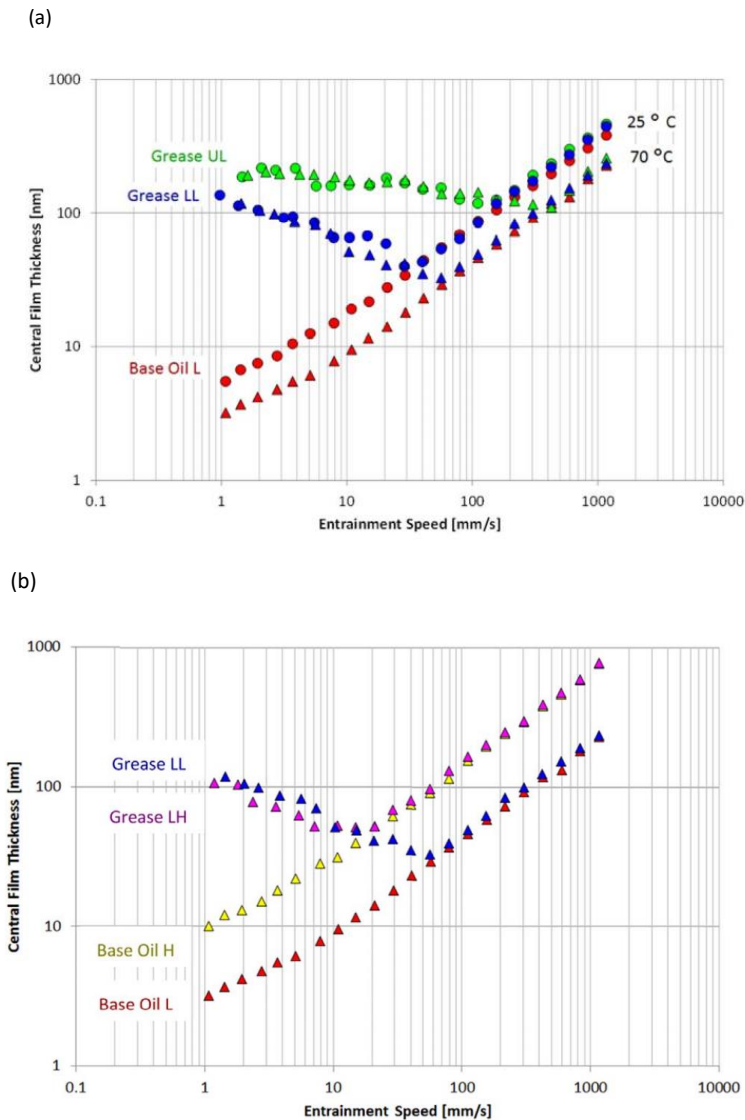


Fig. 1. 43 (a) Measured film thickness versus entrainment speed for the diurea (UL) and lithium (LL) greases and the corresponding normal viscosity base oil at 25 and 70°C; (b) measured film thickness versus entrainment speed for the lithium greases with different viscosities of base oil and the two corresponding base oils (L: low, H: high) at 70°C [137].

In addition, the effects of each parameter on the friction coefficient were systematically investigated, and each value was summarized using the lambda ratio. When considering only the film thickness of the base oil, large deviations for all grease results were observed, whereas the results under oil lubrication fit well with the friction coefficient vs. lambda curves (Fig. 1. 44). This was because of the difference in the oil film thickness of grease and base oil at lower sliding speeds; therefore, the use of the lambda ratio of only base oil cannot be expected to yield a strong correlation. In contrast, the lambda ratio depending on the actual measured oil film thickness of the grease can adequately explain the behavior of the friction coefficient.

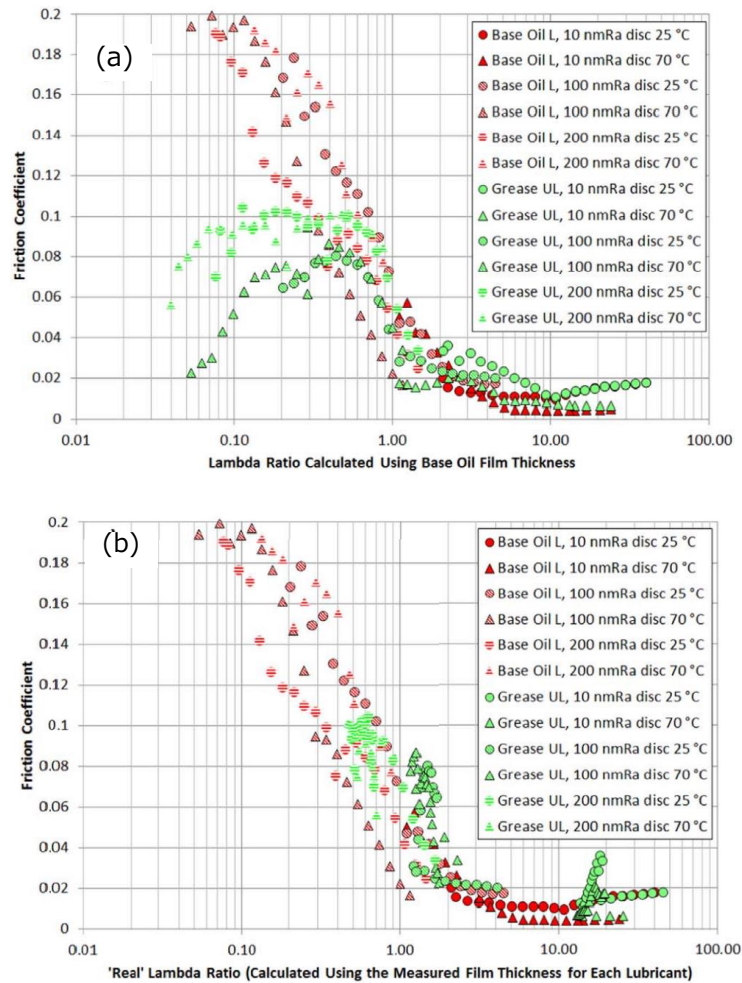


Fig. I. 44 (a) Plot of friction coefficient vs. lambda ratio calculated using base oil film thickness. Results with all surface roughness and temperature using diurea grease; (b) plot of friction coefficient vs. real lambda ratio calculated using the measured film thickness for each lubricant. Results with all surface roughness and temperature using diurea grease [137].

Laurentis et al. [166] also compared friction behavior under PAO and grease lubrication. Under grease lubrication, the friction coefficient was stable and had low values (0.005–0.03). This can be explained by fluid lubrication by the thick oil film. In contrast, under base oil lubrication, the friction coefficient exhibited a higher value at a low sliding speed and approached the same values as that under grease lubrication with an increase in the sliding speed. This was due to the transition from mixed lubrication to fluid lubrication with an increase in the sliding speed.

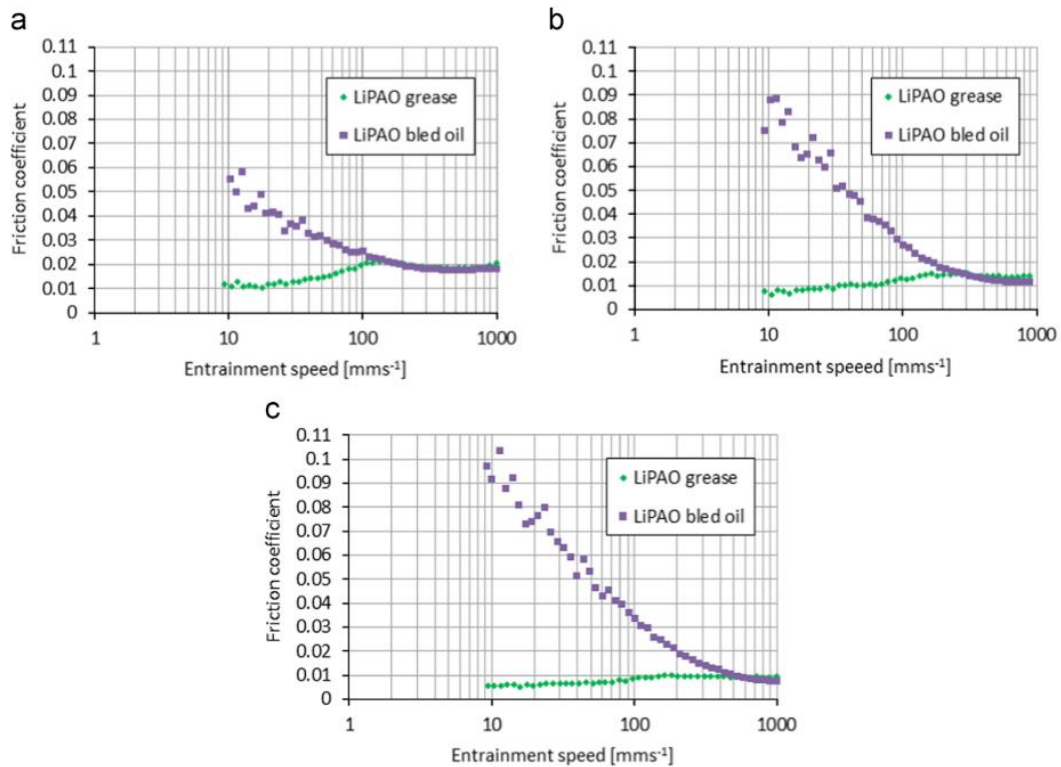


Fig. I. 45 Relationship between the entrainment speed and friction coefficient under grease lubrication and base oil lubrication at (a) 40°C, (b) 60°C, and (c) 80°C [166].

Only a few studies focused on the lubrication theory of polymer gears operating under lubricated conditions. Using transient EHL simulations, Song et al. [167] revealed that the oil film thickness of a steel–polymer gear is much higher than that of a steel–steel gear, and the oil film pressure is much lower for the former. Dearn et al. [164] conducted a theoretical oil film calculation of a polymer spur gear using EHL theories, in which the calculation formula was proposed using the dimensionless parameters g_E and g_V by Myers et al. considering the rotational speed and applied load as the parameters. They reported that the operating lubrication regime was mixed film lubrication because the oil film thickness was in the order of 0.2–0.4 μm to the surface roughness of 0.4 μm , and similar behavior to dry running polymer gears, such as the increase in the efficiency and decrease in the friction coefficient with an increase in the applied load, was observed. In addition, the effect of tooth geometry (pressure angle of the gear) on the oil film thickness was investigated, and it became full-film lubrication when high-pressure angle gears were used under high-load conditions.

8. Conclusions

Engineering plastics are widely used for sliding parts, such as worm wheels in worm reducers used in automotive EPSs. To apply the EPS to much larger vehicles or downsize the worm reducer, the development of polymer materials and the design of the worm reducer, which can ensure good durability and lower friction, are required. In this chapter, a bibliography survey was conducted considering the following aspects:

- Worm reducers of automobile EPSs
- Polymer and composite materials
- Metallic materials
- Lubrication oil and grease
- Effects of different parameters on the tribological behavior
- Lubrication theories of contacts with a polymer material

Several studies on the worm reducer performance or basic tribological properties of the polymer or composite material have been conducted, focusing on various experimental parameters. However, insufficient research has been conducted on the typical tribological properties of polymers or composites in contact with steel under grease lubrication, including the basic wear or creep occurrence mechanism, temperature dependence of the tribological properties depending on the tribofilm formation related to the grease additives, and basic friction occurrence mechanism considering the academic theories. In addition, the effect of the material parameters, including polymer or fiber types, which is significant for the development of new materials, on the tribological properties under typical sliding mode (high contact pressure, various temperature ranges, high sliding speeds, and grease lubrication) has not yet been clarified. Therefore, the tribological behavior under grease lubrication is clarified in this thesis.

CHAPTER II

EXPERIMENTAL METHODS AND
MATERIALS UNDER INVESTIGATION

CHAPTER II: EXPERIMENTAL METHODS AND MATERIALS UNDER INVESTIGATION

1. Introduction.....	63
2. Evaluated materials	63
2.1 PA66 and reinforcement fibers	63
2.1.1 Preparation for unreinforced PA66 and glass fiber-reinforced composite	64
2.1.2 Preparation for carbon fiber-reinforced PA66.....	70
2.1.3 Preparation for aramid fiber-reinforced PA66.....	70
2.1.4 Preparation for the test specimens.....	71
2.1.5 Water absorption	75
2.2 Steel material.....	76
2.3 Lubricants (grease and oil)	80
2.3.1 Urea grease	80
2.3.2 Barium complex grease	81
2.3.3 PAO8 oil.....	81
3. Analysis of the sample before tests	82
3.1 Image analysis of fiber orientation on the composite sliding surface	82
3.2 Measurements of viscosity number	83
3.3 Measurements of molecular mass	83
3.3.1 GF-reinforced PA66 composite with added poly-carbodiimide	83
3.3.2 AF-reinforced PA66 composite with added poly-carbodiimide.....	83
3.4 FT-IR measurements of PA66 with added carbodiimide compounds.....	83
3.5 Measurements of fiber length distribution inside the tensile test specimens	85
3.6 Observation of fiber orientation inside the tensile test specimens.....	85
4. Experimental set-ups and testing conditions	86
4.1 Tensile and Charpy impact tests.....	86
4.2 Sliding test at LTDS	88
4.2.1 Presentation of the tribometer and samples geometry	88
4.2.2 Tests conditions.....	90
4.2.3 Quantification of damage	93
4.3 Sliding test at JTEKT	94
4.4 Micro indentation measurement	95
4.5 Nano indentation measurement	96

5. Analysis methods after sliding tests.....	96
5.1 Optical microscopy	96
5.2 SEM and EDX.....	96
5.3 Interferometry.....	97
5.4 XPS	97
5.5 ToF-SIMS.....	97
6. Conclusions.....	98

CHAPTER II: EXPERIMENTAL METHODS AND MATERIALS UNDER INVESTIGATION

This chapter introduces the materials under investigation, including the PA66 and fiber-reinforced composite, the lubricants (grease and oil), and steel counterpart. In addition, the experimental methods including mechanical and tribological tests, and test conditions are explained. Finally, the analytical methods are introduced.

1. Introduction

This chapter introduces the materials under investigation, including the PA66 or composite with different values of molecular mass, reinforced with different types of fibers, and with addition of various types of additives. It also presents the lubricants including greases with low friction agent and anti-oxidation agent and PAO8 oil, and carbon steel counterpart with different values of hardness and structures. It introduces the measurements for the mechanical properties and sliding test conditions. Furthermore, test parameters of the sliding tests, including the normal force (and consequent contact pressure), sliding speed, and temperature, are presented in detail. Moreover, the analytical methods used before and after the tests are explained in this chapter.

2. Evaluated materials

2.1 PA66 and reinforcement fibers

Raw materials commercially available (PA66, fibers, and additives) were extruded to fabricate pellets (granules). Test specimens were then fabricated through injection molding of the pellets. Fig. II. 1 presents the flow of the preparation of PA66 or composite test specimens or plastic parts. The details of each PA66, fibers and additives are as follows.

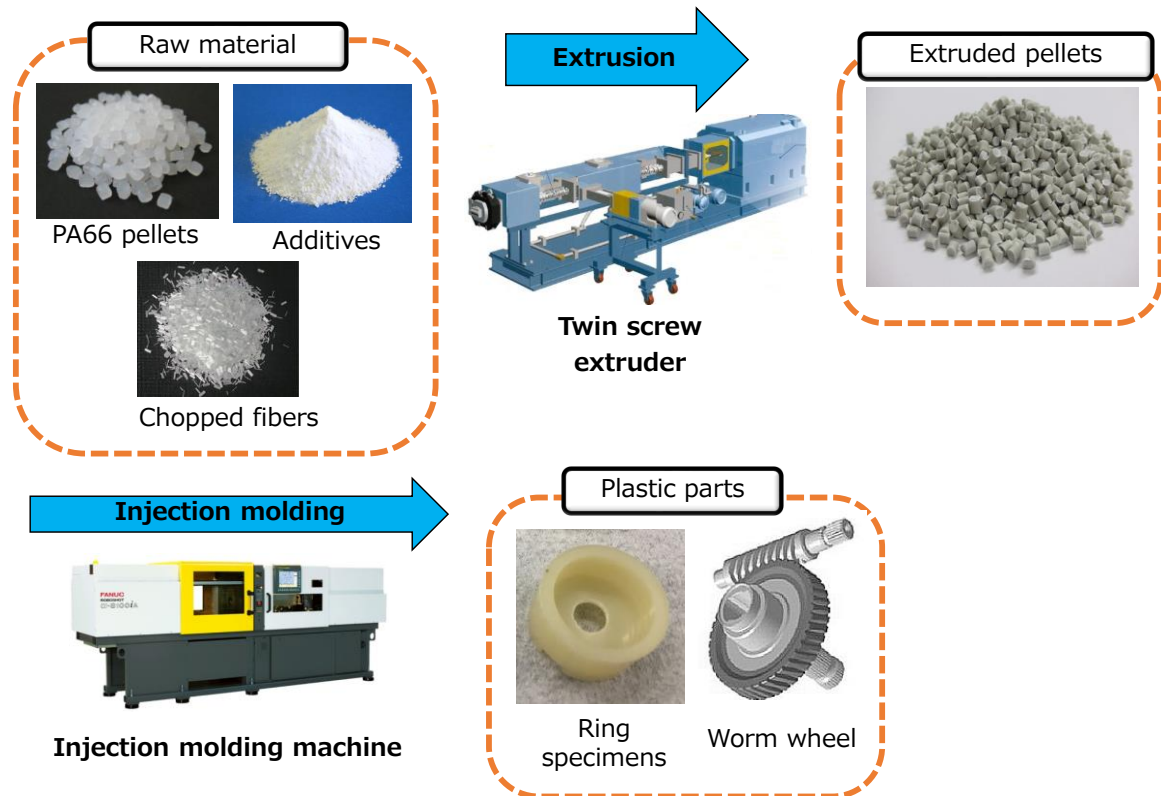


Fig. II. 1 Flow of the preparation of PA66 or composite test specimens or products.

2.1.1 Preparation for unreinforced PA66 and glass fiber-reinforced composite

Unreinforced PA66, different types of GFs, and additives were prepared for extrusion in order to prepare the GF-reinforced composite test specimens. The effects of the molecular mass of PA66, types of GFs (including GF surface treatment agent, the GF diameter, and the GFs amount), types of poly-carbodiimide compounds, and types of olefin polymers were investigated. In addition, test specimens of unreinforced PA66 were prepared directly through injection molding of pellets (granules) of commercially available PA66 with different levels of molecular mass.

2.1.1.1 Molecular mass of PA66

To investigate the effects of PA66 molecular mass, commercialized unreinforced PA66 pellets with three different molecular mass values were used as the raw PA66 material. Table II. 1 lists the viscosity numbers (VNs) of base PA66 and product code. The VNs of the raw material, which are correlated with the PA66 molecular mass, were measured via the relative viscosity method, according to the ISO307 standard (see Section 3.2 for details). Copper(I) iodide (CuI) and potassium iodide (KI) were originally extruded to each PA66 as the anti-oxidation agent of PA66 to ensure the long-term heat stability.

Table II. 1 Molecular mass of raw PA66 material.

Molecular mass level	VNs, ml/g	Number average molecular mass
Normal molecular mass	150	23,000
High molecular mass	235	40,000
Super high molecular mass	302	57,000

2.1.1.2 Glass fibers

Commercially available E-glass fiber strands were bundled and treated with a surface agent. The GF strands were then cut to a length of 3 mm. In this study, chopped GF strands were treated with one of two different GF surface treatment agents (type A and type B) to evaluate the effect of the interfacial shear strength between the GFs and PA66 on the tribological properties of the composite. GF surface treatment agent type A was specifically developed for the adhesion between PA66 and GFs, while type B was developed for the adhesion of another polymer and GFs. Chopped GF strands were provided with GFs already coated by the surface treatment agent, and all the detailed raw materials are undisclosed. However, only the surface treatment agent was extracted from the GF chopped strands by ultrasonic treatment of the strands, and gas chromatography - mass spectrometry (GC/MS) analysis of the extracts was conducted to identify the surface treatment agents. Fig. II. 2 shows the charts of the GC/MS analysis of extracted GF treatment agent type A and type B. It appears that these agents contain different types of raw material of urethane resin (m-xylene diisocyanate in type A and isophorone diisocyanate in type B).

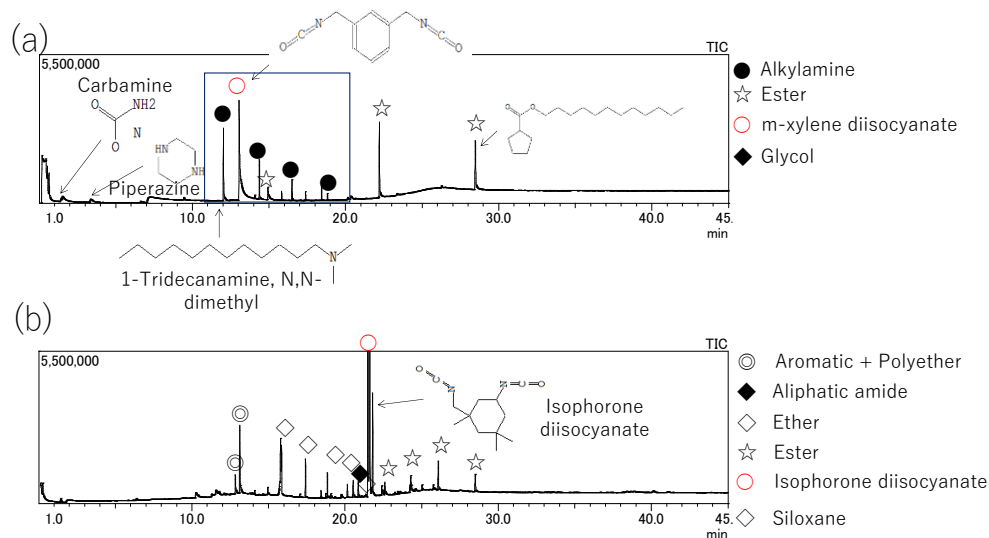


Fig. II. 2 Chart of the GC/MS analysis of GF surface treatment heated at 300°C
 (a): agent type A; (b): agent type B.

The effect of the GF diameter was also investigated. GF strands with different diameter (6.5, 9.5, 11, 13, 15, 19 μm) treated with surface treatment agent type A were prepared. Generally, the diameter of GF added to engineering plastics (including PA66) is mainly in the range of 9-15 μm [73, 74, 127, 168, 169]. In the present work, GFs with much smaller (6.5 μm) and larger diameter (19 μm) were used additionally to evaluate the effect in a wider range of GF diameter. The effect of the GF amount (15 wt% or 33 wt%, leading to changes in mechanical properties of the composite and consequently tribological properties) was also studied. Fig. II. 3 shows the appearance of used GF chopped strands observed with optical microscope.



Fig. II. 3 Appearance of used GF chopped strands observed with optical microscope.

2.1.1.3 Poly carbodiimide compounds

Two different types of carbodiimide compounds were used as the molecular chain extender to increase the molecular mass of PA66, as presented in Section 3.3.2 in Chapter I: aliphatic poly-carbodiimide and aromatic poly-carbodiimide. The main chemical structures of these carbodiimide compounds analyzed with the matrix assisted laser desorption/ionization-mass spectrometry (MALDI-MS) are presented in Fig. II. 4 and Fig. II. 5. MALDI-MS analysis was performed with using the tetrahydrofuran (THF) solvent, and using the dithranol as the matrix of the measurement. Part of the carbodiimide group in the aliphatic poly-carbodiimide compounds was changed to the urea functional group with the reaction with water, and some terminals of molecules were isocyanate group. In addition, part of the aromatic poly-carbodiimide compounds also contained the isocyanate group in addition to the diisopropylphenyl group. The number average molecular weight of poly-aromatic carbodiimide is 15,000 g/mol.

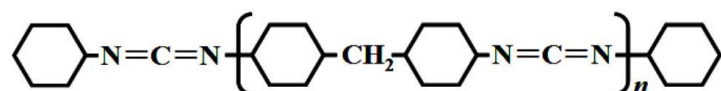


Fig. II. 4 Chemical structure of aliphatic poly-carbodiimide compounds.

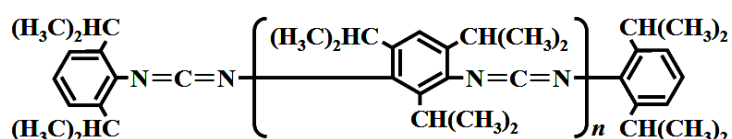


Fig. II. 5 Chemical structure of aromatic poly-carbodiimide compounds.

2.1.1.4 Olefin polymer

Several types of olefin polymers, chemically modified by a functional group such as a maleic anhydride group (-MAH) or glycidyl methacrylate group (-GMA), were also used. These olefin polymers are known to act as an impact modifier to improve the impact resistance properties [125]. Added amount of olefin polymer was 10 wt%. Olefin polymers with no chemical modification was also used to evaluate the effect of the modification. Table II. 2 lists the characteristics of used olefin polymers. These olefin polymers have the shape of pellets.

Table II. 2 Characteristics of used olefin polymers.

Types	Melting point, °C	Density, g/cm ³	Tensile strength, MPa	Tensile elongation at break, %
-MAH modification	60	0.87	>8	>1,000
-GMA modification	60	0.96	4	850
No modification	No data	0.86	No data	No data

2.1.1.5 Extrusion

Extrusion of each raw material was carried out with the compositions and feeding positions using a twin-screw extruder (TEM-26SX, Toshiba Machine Co., Ltd.). In this process, each raw material is fed into the barrel of extruder which is heated over the melting point of polymer (275-290°C when using PA66) and extruded through the kneading disc element. Then, obtained strand of extruded polymer was cooled and cut to the pellets form. Fig. II. 6 presents the schematic view of the twin screw extruder, and Fig. II. 7 shows the appearance of used twin screw extruder.

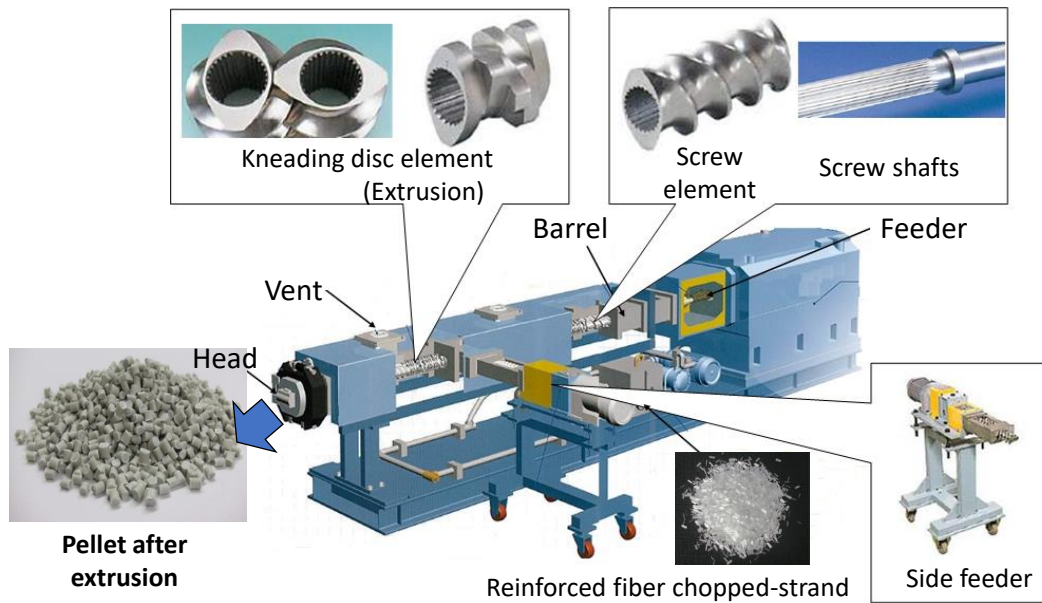


Fig. II. 6 Schematic view of the twin screw extruder (the drawing of the extruder and each part was obtained by the handout of Toshiba Machine Co., Ltd. and some explanations were added by author).



Fig. II. 7 Appearance of used twin screw extruder (JTEKT, Japan).

PA66 and olefin polymers were fed in the top feed (i.e., feeding from the root of the barrel of the twin screw extruder), while GFs were fed in the side feed (i.e., feeding from the middle of the barrel of the twin screw extruder) to prevent the damage of the fibers during the extrusion, as presented in Fig. II. 8. The effect of the feeding position of the poly carbodiimide compounds was investigated.

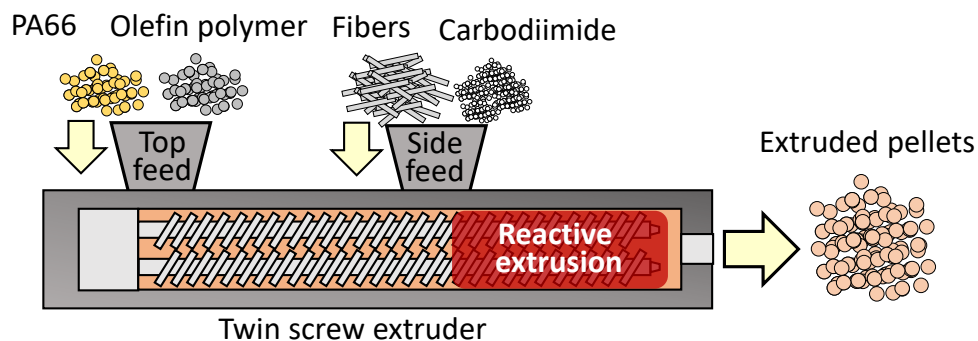


Fig. II. 8 Schematic of twin screw extrusion.

2.1.1.6 Composition of GF-reinforced PA66 and unreinforced PA66

Table II. 3 lists the compositions and mechanical/physical properties of all evaluated unreinforced and GF-reinforced PA66 materials without the addition of carbodiimide compounds or olefin polymer.

Table II. 3 Composition and mechanical/physical properties of fabricated unreinforced PA66 and GF composite materials.

No.	PA66	GF			Mechanical and physical properties		
	Level of molecular mass	Surface treatment type	Diameter, μm	Amount, wt%	Tensile Young's modulus, GPa	VN of the specimens, ml/g	Density, g/cm^3
1	Normal	A	6.5	15	5.9 ± 0.3	145	1.25
2	High	A	6.5	15	6.0 ± 0.4	193	1.25
3	Super high	A	6.5	15	5.4 ± 0.6	235	1.25
4*	Super high	A	6.5	15	6.0 ± 0.1	356	1.25
5	High	B	6.5	15	6.0 ± 0.4	not measured	1.25
6	High	A	9.5	15	5.9 ± 0.4	not measured	1.25
7	High	A	11	15	6.3 ± 0.4	not measured	1.25
8	High	A	13	15	6.5 ± 0.9	not measured	1.25
9	High	A	15	15	6.2 ± 0.6	not measured	1.25
10	High	A	19	15	5.8 ± 0.1	not measured	1.25
11	Normal	A	6.5	33	10.7 ± 0.3	not measured	1.39
12	Normal	-	-	0	3.0 ± 0.1	145	1.14
13	Super high	-	-	0	3.0 ± 0.1	302	1.14

* Sample 4 was subjected to solid-state post-condensation

Table II. 4 lists the compositions and feeding positions of all evaluated GF-reinforced PA66 materials with added carbodiimide compounds or olefin polymer. All the specimens in Table II. 4 used the normal molecular mass of PA66 and GFs with the surface treatment of Type A, the diameter of $6.5 \mu\text{m}$, and the amount of 33 wt%.

Table II. 4 Composition of fabricated GF-reinforced PA66 with added poly carbodiimide or olefin polymer.

No.	Carbodiimide compounds			Olefin polymer			Tensile Young's modulus, GPa
	Type	Amount, wt%	Feeding position	Type	Amount, wt%	Feeding position	
14	Aliphatic	2.0	Side feed	-	-	-	10.4 ± 0.8
15	Aromatic	1.0	Top feed	-	-	-	11.1 ± 0.5
16	Aromatic	2.0	Top feed	-	-	-	10.3 ± 0.9
17	Aromatic	3.0	Top feed	-	-	-	11.5 ± 0.6
18	Aromatic	1.5	Side feed	-	-	-	11.2 ± 0.4
19	Aromatic	2.0	Side feed	-	-	-	11.4 ± 0.5
20	Aromatic	2.5	Side feed	-	-	-	9.9 ± 0.3
21	Aromatic	3.0	Side feed	-	-	-	10.7 ± 0.6
22	-	-	-	-MAH modification	10	Top feed	7.1 ± 0.5
23	Aliphatic	2.0	Side feed	-MAH modification	10	Top feed	8.2 ± 0.4
24	Aliphatic	2.0	Side feed	-GMA modification	10	Top feed	8.8 ± 0.3
25	-	-	-	No modification	10	Top feed	10.3 ± 0.3
26	Aliphatic	2.0	Side feed	No modification	10	Top feed	9.3 ± 0.2

2.1.2 Preparation for carbon fiber-reinforced PA66

As raw material of CF-reinforced PA66, commercially available pellets composed of PA66 with normal or high molecular mass were prepared. Used CFs were PAN type (see Section 3.2.2 in Chapter I), and the diameter of CF was in the range of 6-8 μm . The added amount of the CFs was 10 wt%. The composition and mechanical properties of each evaluated material are listed in Table II. 5. Poly carbodiimide compounds or olefin polymer were not added to the CFs composite.

Table II. 5 Composition and properties of the CF-reinforced composite test specimens.

No.	Molecular mass of PA66	Tensile Young's modulus, GPa	VN of the specimens, ml/g	Density, g/cm^3
27	Normal	9.5 ± 0.6	150	1.18
28	High	9.5 ± 0.7	220	1.18

2.1.3 Preparation for aramid fiber-reinforced PA66

Pellets of AF-reinforced PA66 with normal or high molecular mass of PA66 with/without added carbodiimide compounds were also prepared in the same process as GF composites. Strands of AF were cut to size (fiber diameter: 12 μm , length: 3 mm) and treated with agents. Used AFs were PMIA type AFs (see Section 3.2.3 in Chapter I). Added amount of AFs was 20%. Fig. II. 9 presents the optical microscope observation image of AFs chopped strands. Table II. 6 lists the compositions and mechanical properties of AF-reinforced PA66 materials.

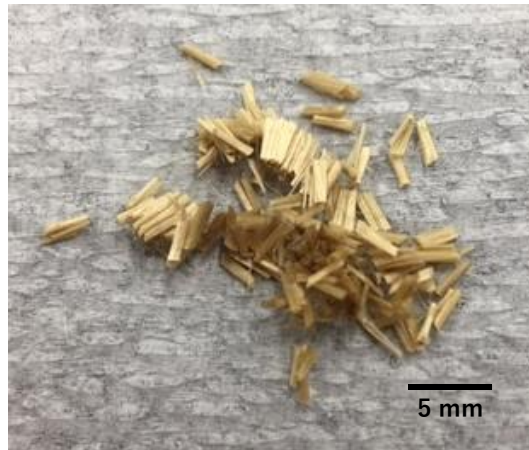


Fig. II. 9 Optical microscope observation image of AFs chopped strands.

Table II. 6 Composition and properties of the AF-reinforced composite test specimens.

No.	Molecular mass of PA66	Carbodiimide compounds			Tensile Young's modulus, GPa
		Type	Amount, wt%	Feeding position	
29	Normal	-	0	-	5.3 ± 0.3
30	High	-	0	-	5.7 ± 0.8
31	Normal	Aromatic	2.5	Side feed	4.4 ± 0.2

2.1.4 Preparation for the test specimens

2.1.4.1 Injection molding

Injection molding of obtained pellets was carried out with an injection molding machine (ROBOSHOT S-2000i 100B, FANUC CORPORATION), and tensile test specimens or Charpy impact test specimens (as presented in Section 4.1) and sliding test ring specimens (as shown in Section 4.2.1) were prepared. Fig. II. 10 shows the appearance of used injection molding machine. Fig. II. 11 shows the sliding test ring specimens just after the injection molding. Ring moldings were fabricated using disk type gate of the injection molding, and test specimens were obtained after the mechanical cutting of the sprue runner part.



Fig. II. 10 Appearance of used injection molding machine.

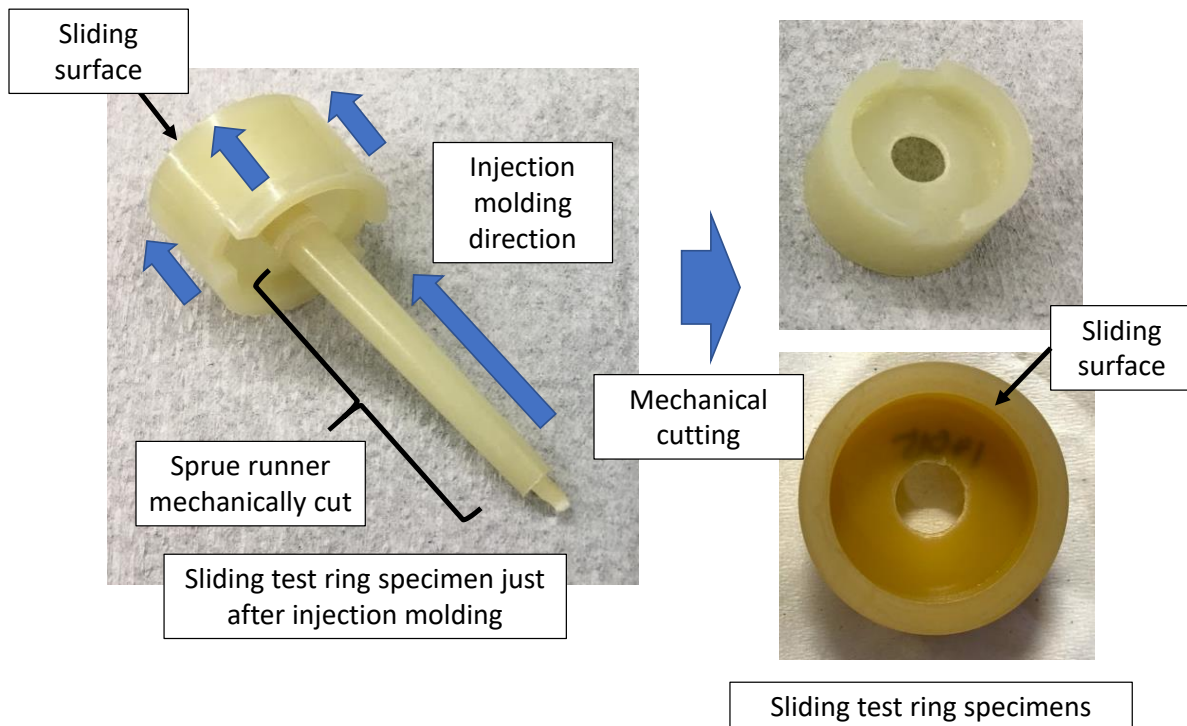


Fig. II. 11 Molded sliding test ring specimen and cutting process.

2.1.4.2 Modification of the sliding surface roughness of ring specimens

After the injection molding and removal of the sprue runner parts, composite ring specimens for sliding tests were cut in the height direction by 3 mm with a lathe. This process was conducted only for the ring specimens of fiber-reinforced composites. The objective of this process is to remove the skin layer (this skin layer has a different composition and different properties from the bulk of the samples) and then to simulate the conditions of the sliding surface of actual worm gear tooth surfaces, which are formed by mechanical hob-cutting after the injection molding process to ensure dimensional stability and to remove the skin layer in the sliding surface, as presented in Fig. II. 12. Fig. II. 13 presents the scanning electron microscope (SEM) observations of the sliding surface of actual worm gear and GF

15%-reinforced composite ring specimens before and after 3 mm cutting. Due to the flow of resin inside the metallic die during the injection molding process, the orientation of the fibers compared to the sliding surface are different in the center part of the sliding surface compared to the outer and inner parts, and this will be analyzed and discussed later in the manuscript. The effect of the cutting process on the results of sliding test was also investigated using GF 15% composite.

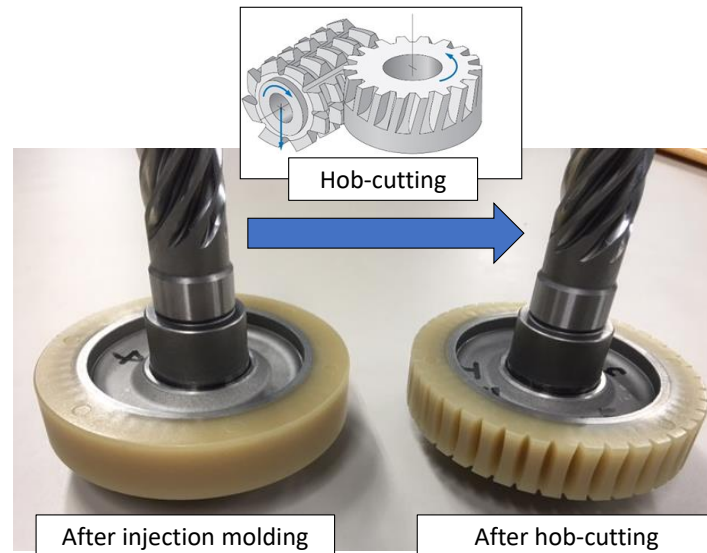


Fig. II. 12 Hob-cutting process of worm wheel after injection molding.

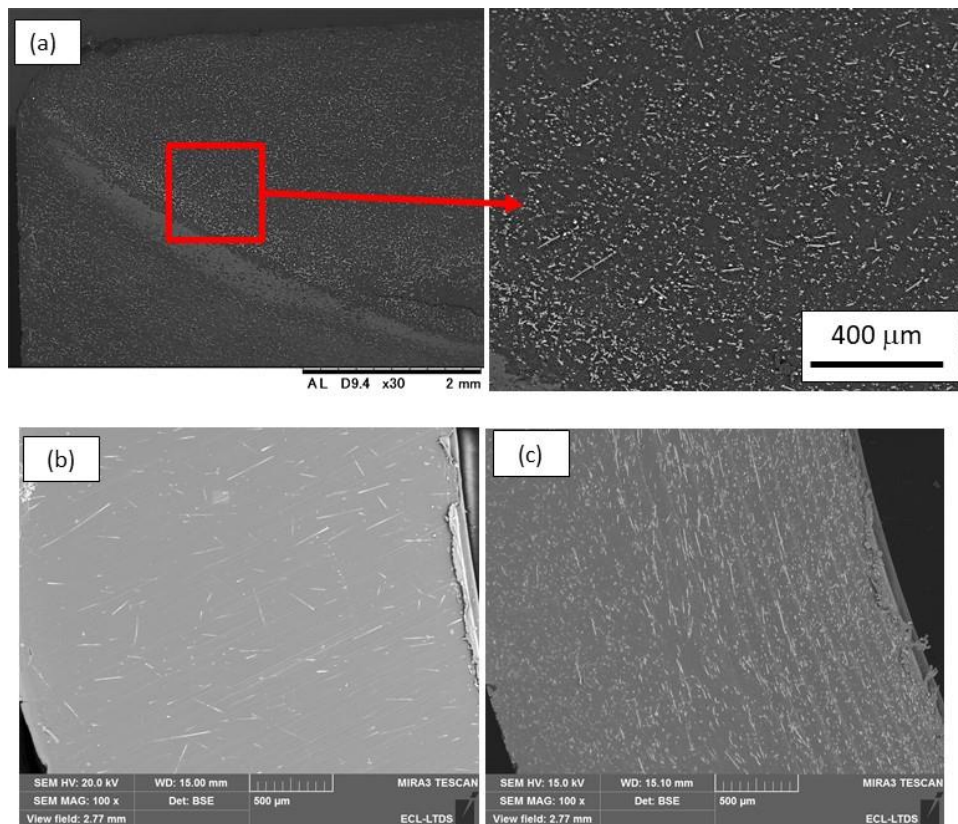


Fig. II. 13 SEM observation of the sliding surface of (a) actual worm gear; (b) GF 15% reinforced-composite ring specimens before 3 mm cutting; (c) composite ring specimens after 3 mm cutting (skin layer removed).

The sliding surface of both unreinforced PA66 and fiber-reinforced composites was polished with #600 polishing (emery) paper before each sliding test.

In addition, the effect of the sliding surface roughness of the unreinforced PA66 (sample no. 12 in Table II. 3) or GF 15% composite (sample no. 1 in Table II. 3) specimens on the friction coefficient was investigated (in Chapter V). To do so, the sliding surface of the ring test specimens was manually polished using a polishing machine and commercial polishing paper with roughness ranging from #400 to #4,000 grit. In addition, non-polished (i.e., the surface condition just after injection molding) specimens were prepared using unreinforced PA66. In the experiments in Chapter V, the sliding surface roughness (R_a) was measured using interferometry in the sliding direction of each specimen before and after the sliding tests. Fig. II. 14 shows the surface roughness measured before and after the sliding test for the unreinforced PA66 polished using #800 polishing paper. After the tilt was removed from the obtained image, the average sliding-direction surface roughness (R_a) was obtained using Vision64[®] software (Brüker).

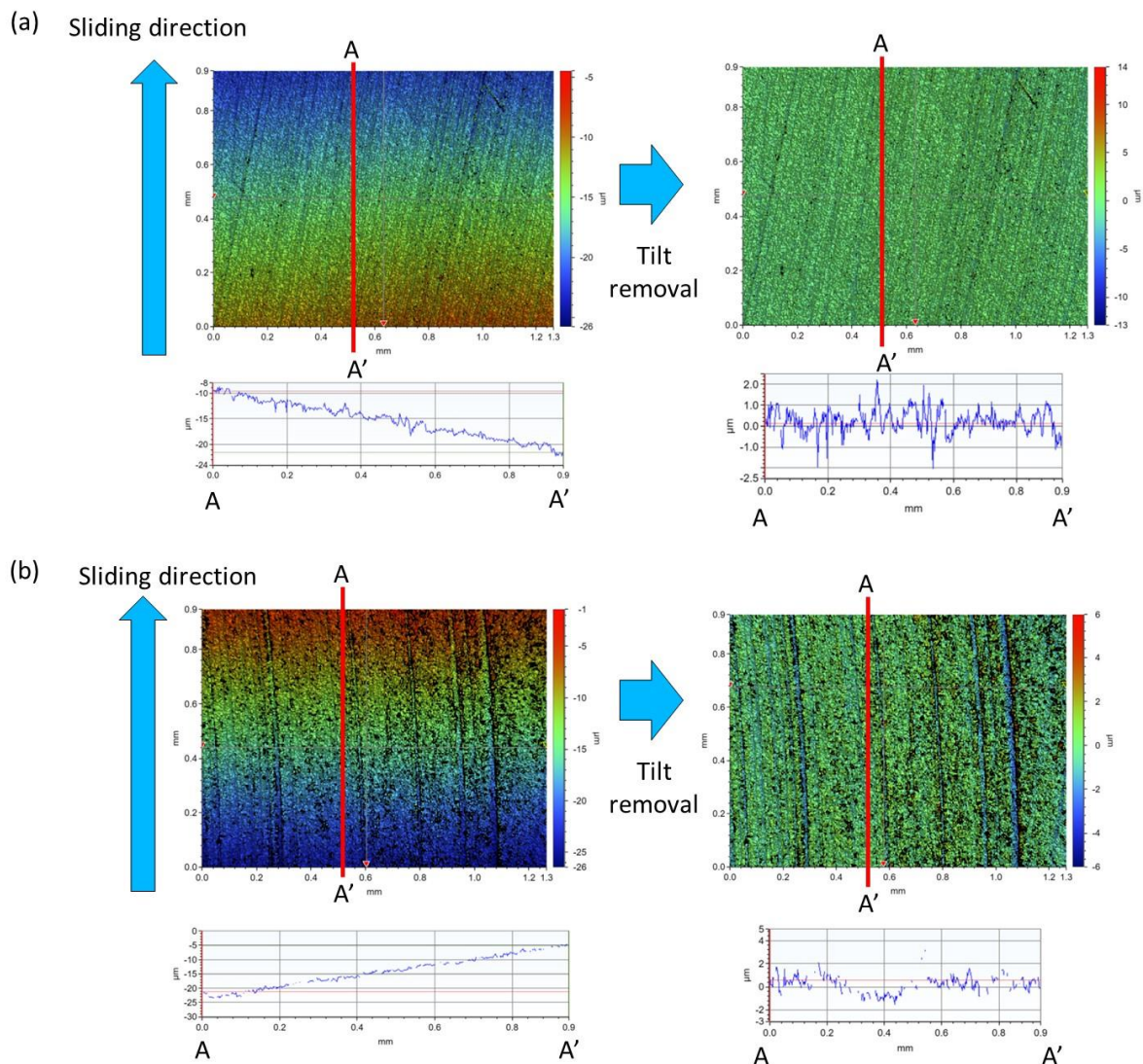


Fig. II. 14 Sliding surface roughness measured using interferometry (a) before ($R_a = 0.36 \pm 0.06 \mu\text{m}$) and (b) after ($R_a = 0.33 \pm 0.06 \mu\text{m}$) sliding test.

Table II. 7 and Table II. 8 list the numbers of the polishing paper and surface roughness R_a of the ring specimens using unreinforced PA66 and GF 15% composite, respectively.

Table II. 7 Sliding surface roughness (R_a) of ring specimens before sliding tests using unreinforced PA66.

Polishing paper	Pretest surface roughness (R_a), μm
#400	0.98 ± 0.16
#600	0.70 ± 0.05
#800	0.40 ± 0.05
No polishing (skin layer)	0.20 ± 0.05
#2,000	0.11 ± 0.01
#4,000	0.07 ± 0.00

Table II. 8 Sliding surface roughness (R_a) of ring specimens before sliding tests using GF 15% composite.

Polishing paper	Pretest surface roughness (R_a), μm
#600	0.61 ± 0.03
#800	0.47 ± 0.02
No polishing (skin layer)	0.26 ± 0.02
#2,000	0.20 ± 0.07
#4,000	0.06 ± 0.00

2.1.4.3 Solid-state post condensation

One sample was subjected to solid-state post-condensation to increase the molecular mass of the test specimen; the post-condensation was conducted at 220°C for 10 h and under vacuum conditions to avoid the oxidation of PA66.

2.1.5 Water absorption

In order to evaluate the effect of hygroscopicity of PA66 on the tribological properties, water absorption to the composite specimens (sample no. 2 in Table II. 3) was conducted using stable temperature and humidity chamber. Table II. 9 lists the conditions. The water absorption rate of the specimens before and after the sliding tests was measured through Karl Fischer titration using the Aqualyte CN (Hiranuma Co.) as catholyte and Aqualyte RS-A (Hiranuma Co.) as anode liquid, or measurement of the sample weight before/after the water absorption.

Table II. 9 Water absorption conditions.

Temperature	50°C
Humidity	95%RH
Test duration	256 hr

2.2 Steel material

Steel cylinders used for the sliding tests described in Section 4.2.1 were fabricated using S45C steel, which contains 0.45% carbon, following JIS G 4051. Young's modulus of S45C material is 205 GPa [170-172]. First, the cylinders were prepared using non heat treated steel to simulate a steel worm shaft wherein the formed teeth were not heat treated. These cylinders are hereinafter referred to as "softer" steel cylinders when the steel hardness effect is discussed. Sliding surface was polished using a centerless grinding process. Fig. II. 15 presents the drawing of the steel cylinder. Fig. II. 16 presents the steel cylinder roughness measured using interferometry before the sliding tests. After the cylindrical shape of the obtained image was removed, the average sliding-direction surface roughness (R_a) was obtained. Surface roughness of the cylinder in the sliding direction is $0.12 \pm 0.03 \mu\text{m}$ which was measured using interferometer.

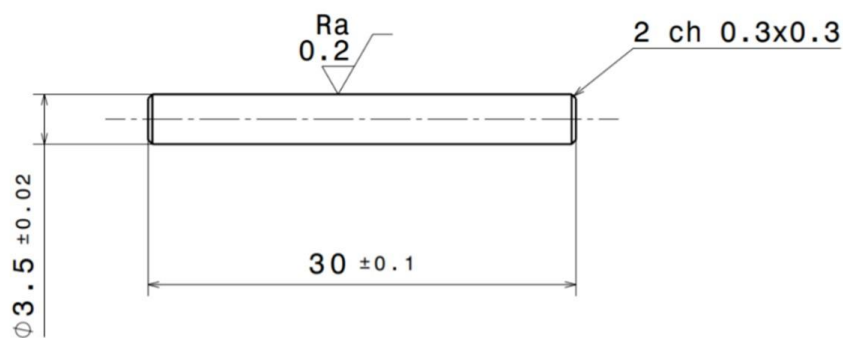


Fig. II. 15 Drawing of the steel cylinder.

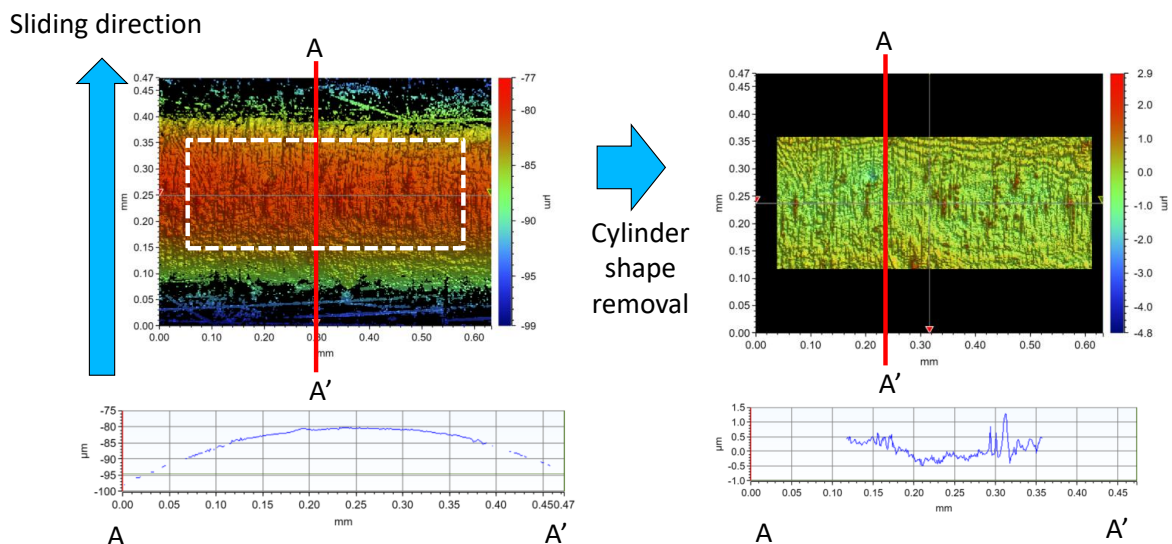


Fig. II. 16 Interferometry images of the steel cylinder surface before and after the removal of cylindrical shape.

In addition to the raw carbon steel, cylinders with different values of hardness and microstructures were prepared by applying different heat treatment processes (quench hardening and tempering) to S45C cylinders, as presented in Fig. II. 17. These cylinders are hereinafter referred to as "harder" steel cylinders when the steel hardness effect is discussed. This simulates the steel worm shaft in which heat treatment after the formation of teeth was

introduced. First, the same types of S45C cylinders with a diameter of 3.6 mm were prepared and heat treatments under different conditions were applied. Afterward, each sample was machined to a diameter of 3.5 mm using the same process to obtain the same roughness and to remove the surface black film due to heat treatment.

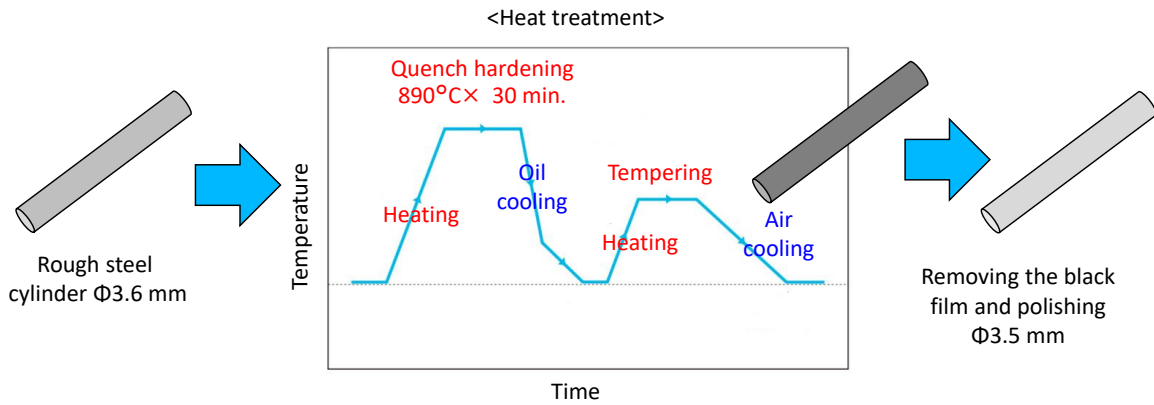


Fig. II. 17 Heat treatment process of steel cylinder.

Furthermore, C45 steel cylinders (containing 0.45% of carbon but fabricated using a different type of raw steel) with lower surface hardness without heat treatment, and SUJ2 steel cylinders (bearing steel which contains 0.95-1.10 % of carbon, 0.15-0.35% of silicon, and <0.5% of manganese, following JIS G4805) with higher surface hardness with heat treatment, were prepared. Table II. 10 presents the material, heat treatment conditions, the hardness of the cylinders measured through micro indentation in the way described in Section 4.4, and the Vickers hardness on the sliding surface of the cylinders.

Table II. 10 Heat treatment conditions for steel cylinders. Values of the hardness are the average values for five measurements.

Material	Quench hardening	Tempering	Hardness measured by micro indentation, GPa	Vickers hardness
C45	-	-	3.9 ± 0.1	208
S45C	-	-	4.5 ± 0.1	311
S45C	890°C × 30 min. Oil cooling	412°C×60 min. Air cooling	5.4 ± 0.2	416
S45C		300°C×60 min. Air cooling	7.2 ± 0.1	515
S45C		120°C×60 min. Air cooling	9.9 ± 0.2	659
SUJ2	835°C × 10 min. Oil cooling	180°C×60 min. Air cooling	Not measured	789

Optical microscope observation images (using Epiphot200 by Nikon) of the S45C steel structure with different hardness and that of SUJ2, which were obtained after Nital etching of a cross-section, are presented in Fig. II. 18. The structure of S45C steel with hardness of 4.5 GPa that has not been heat treated can be composed of ferrite and pearlite. On the other hand, in the sample that was tempered at a low temperature after quenching, a structure originated by martensite is observed, and it can become sorbite as the tempering temperature increased. In addition, optical microscope observation (using VHX-1000 by Keyence) images of the C45 and S45C without heat treatment, which were obtained after Nital etching of a cross-section, are presented in Fig. II. 19. Grain size in C45 seems much larger than that of S45C.

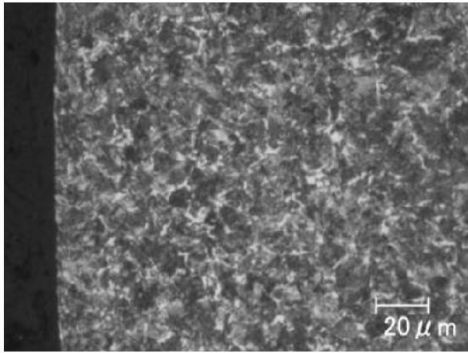
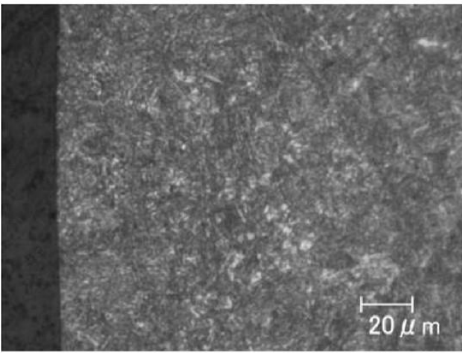
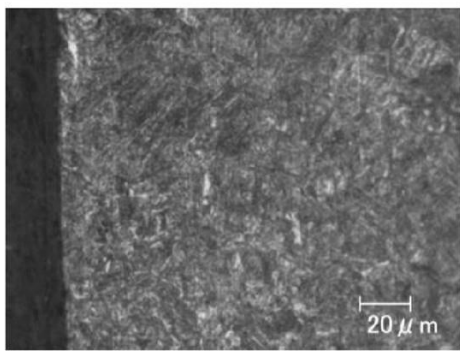
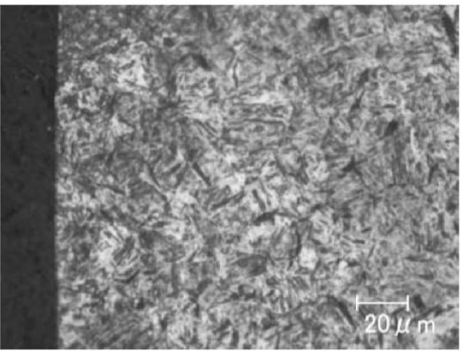
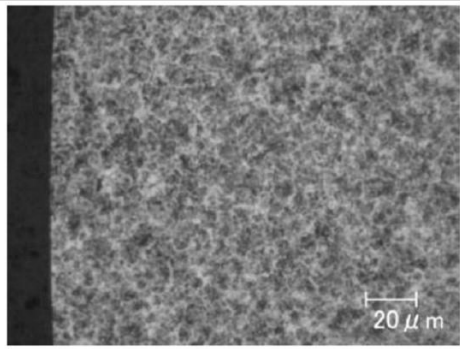
Steel type, hardness	S45C, 4.5 GPa	S45C, 5.4 GPa
Structure		
Steel type, hardness	S45C, 7.2 GPa	S45C, 9.9 GPa
Structure		
Steel type	SUJ2	
Structure		

Fig. II. 18 Optical microscope observation images of cross-sectioned steel structures (S45C with different hardness and SUJ2).

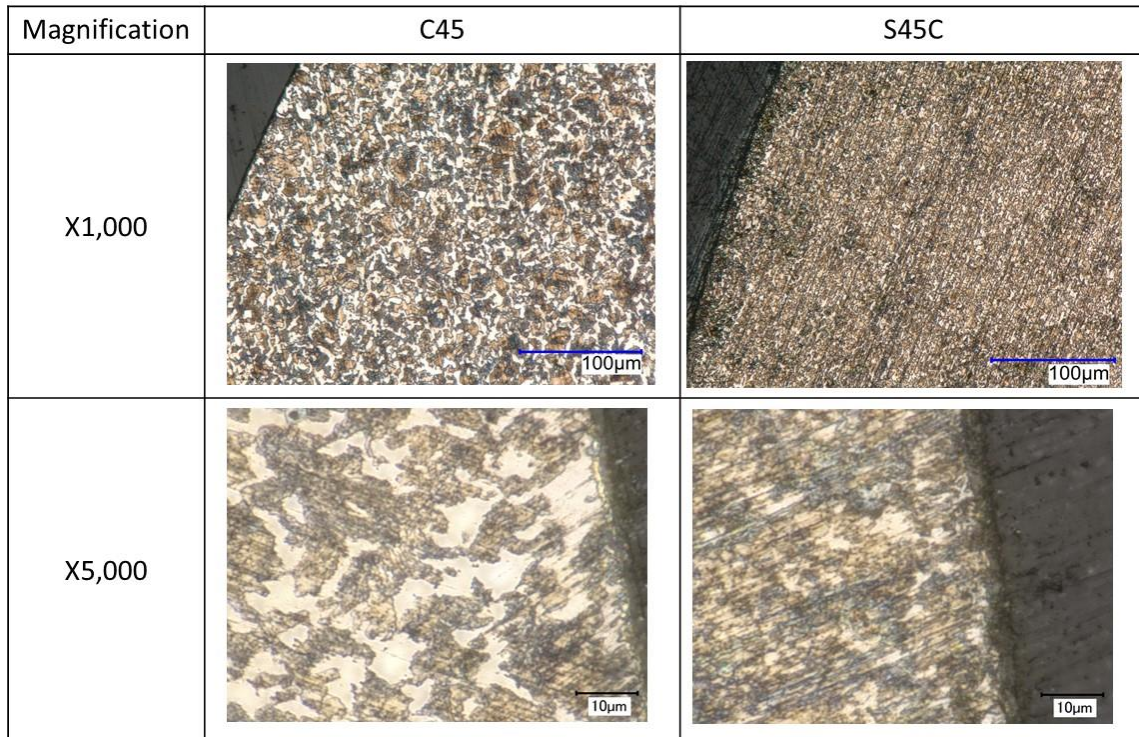


Fig. II. 19 Optical microscope observation images of cross-sectioned steel structures (comparison of C45 and S45C).

Fig. II. 20 shows the interferometry images of the steel cylinder surface before and after the removal of cylindrical shape, using the cylinder after heat treatment with the hardness of 9.89 GPa. This cylinder was also used in Chapter V, and surface roughness R_a in the sliding direction is $0.08 \pm 0.01 \mu\text{m}$.

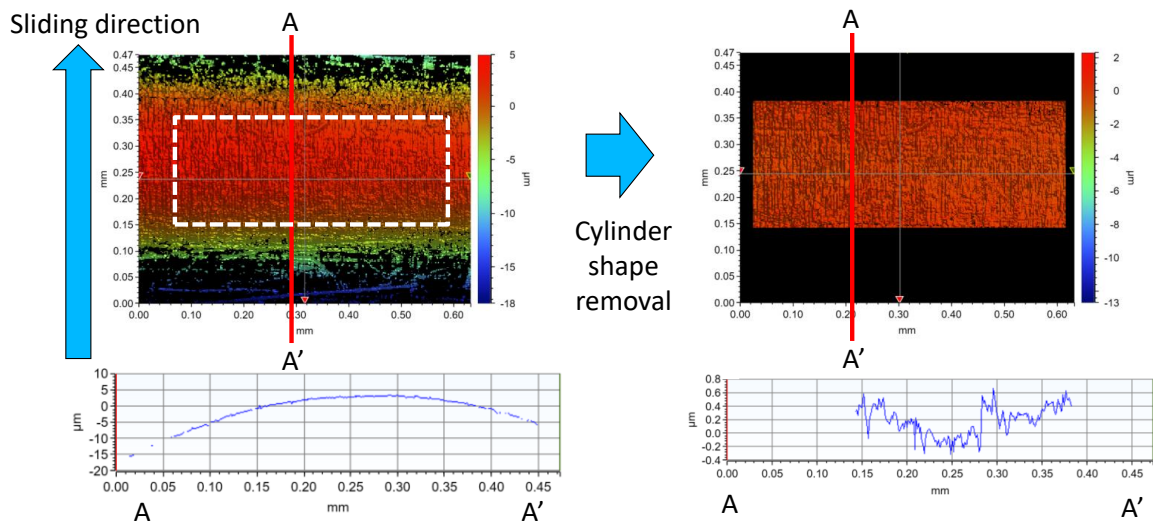


Fig. II. 20 Interferometry images of the steel cylinder surface before and after the removal of cylindrical shape (using the cylinder after heat treatment, hardness: 9.89 GPa).

2.3 Lubricants (grease and oil)

Several types of lubricants (grease and oil) were used in the sliding test to simulate the sliding system of actual worm reducer and to clarify the friction mechanism.

2.3.1 Urea grease

The urea grease is composed of poly- α -olefin 8 (PAO8) as the base oil, diurea as a thickener, zinc carboxylate as a low friction agent, and an anti-oxidation agent containing sulfur compounds. The kinematic viscosity and pressure-viscosity coefficient of used PAO8 base oil as a function of temperature are as shown in Fig. II. 21. Diurea thickener was synthesized by the reaction of diisocyanate and several types of monoamine, and it was mixed to the base oil at specific rates. Zinc carboxylate is a mixture of different types of zinc carboxylates, including stearate, palmitate, and oleate. The added amount of zinc carboxylate was in the range of 5-8 wt%, and the added amount of sulfur type anti-oxidation agent was in the range of 0.5-3 wt% to the total composition of grease. Detailed chemical structure of the sulfur type anti-oxidation agent was not disclosed by the grease company; however, several compounds including 2-Mercaptobenzothiazole, dithiocarbamate, and 2-Mercaptobenzimidazole are summarized as a representative example of the sulfur type anti-oxidation agent, as presented in Fig. II. 22.

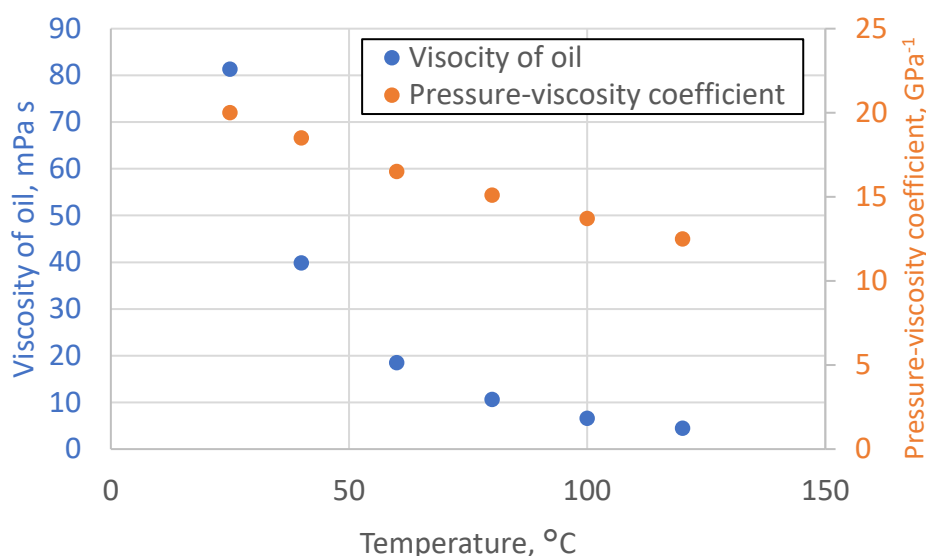


Fig. II. 21 Viscosity and pressure-viscosity coefficient of PAO8 base oil as a function of temperature.



Fig. II. 22 Chemical structures of the sulfur type anti-oxidation agent.

The effects of the addition of each additive to grease were discussed based on an evaluation of the different types of grease applied. Table II. 11 lists the composition of each tested grease. The consistency (cone penetration) of the evaluated greases is 300.

Table II. 11 Composition of tested grease.

Grease number	Base oil	Thickener	Low friction agent	Anti-oxidation agent
No. 1	PAO8	Diurea	Zinc carboxylate	Sulfur type agent
No. 2	PAO8	Diurea	-	Sulfur type agent
No. 3	PAO8	Diurea	Zinc carboxylate	-

2.3.2 Barium complex grease

The barium complex grease used in Chapter VII and Chapter IX is composed of poly- α -olefin 6 (PAO6) as the base oil, barium complex as a thickener. The kinematic viscosity of PAO6 is 31 mm²/s at 40°C and 6 mm²/s at 100°C [173]. Other specific information on the grease composition is not disclosed.

2.3.3 PAO8 oil

PAO8 oil (Durasyn® 168, INEOS) was used as the lubricating oil in the sliding tests because it does not contain any specific additives such as friction modifiers or extreme pressure additives for improving the tribological properties in Chapter V. This oil is not completely identical to the PAO8 oil as a base oil in the urea grease (presented in Section 2.3.1). Fig. II. 23 presents the viscosity of the PAO8 oil plotted as a function of temperature, as measured using a corn-rotor rheometer (AR2000, TA Instruments). The measurement shear rate was 100 s⁻¹, the cone angle was 4°, and the measurement gap was 111 μ m.

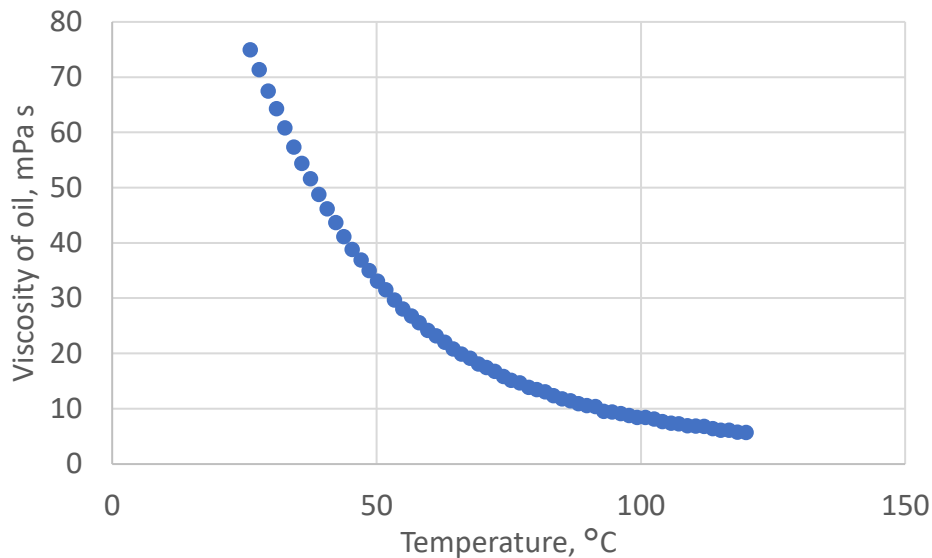


Fig. II. 23 Temperature dependence of the oil viscosity measured using the rheometer.

3. Analysis of the sample before tests

3.1 Image analysis of fiber orientation on the composite sliding surface

In order to understand the aggressive effects of the fibers on the steel counterpart during the tribological tests, the fiber orientation at the sliding surface of the composite ring was evaluated quantitatively using image analysis technic. First, the sliding surface of the ring specimen was polished using #4,000 polishing paper, and three SEM images of the inner/center/outer positions were obtained at a magnification of $\times 300$ in backscattered electron (BSE) mode, as shown in Fig. II. 24 (composite sample no. 1 in Table II. 3 is used as an example).

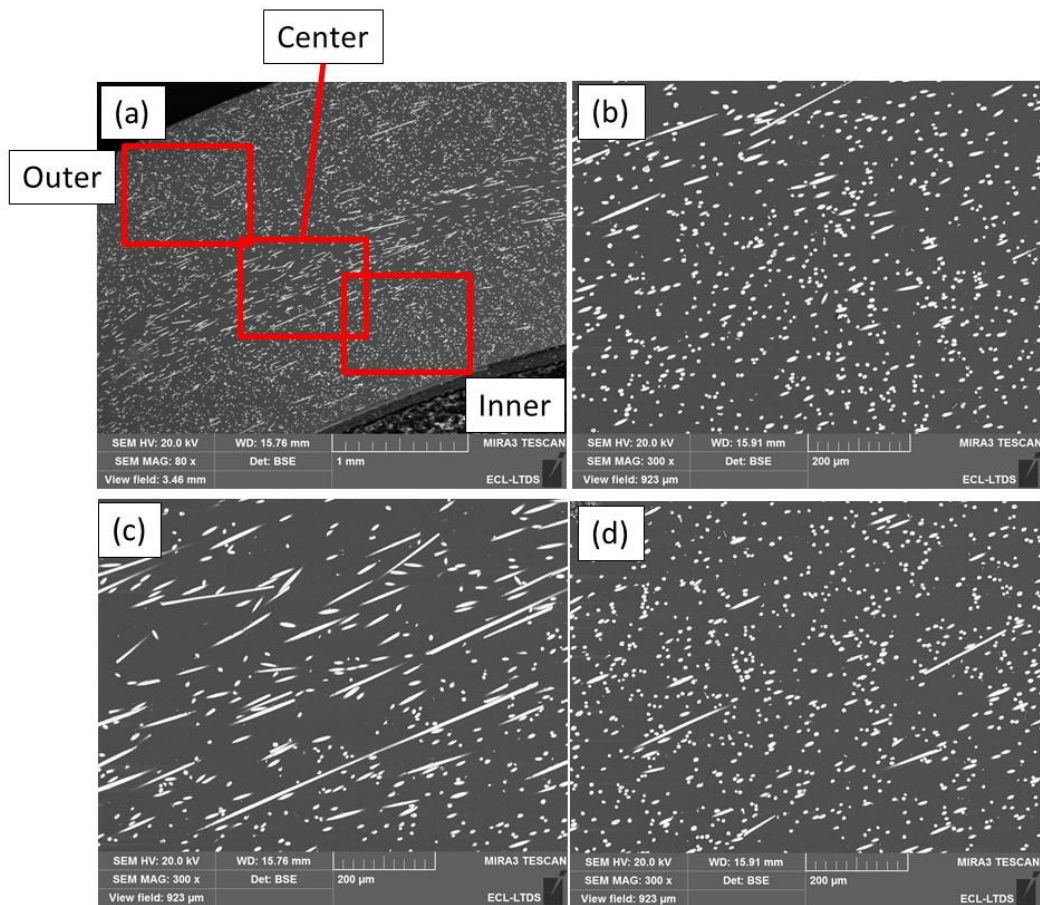


Fig. II. 24 SEM BSE images of the sliding surface of composite sample no. 1 at different locations of the ring sliding test specimen: (a) global view; (b) inner position; (c) center position; (d) outer position.

Next, the PA66 and fibers areas were separated by binarization using the software imageJ by Wayne Rasband (Fig. II. 25), and the total area of the fibers and total perimeter of the fibers (which is a measure of the total contact area between the fibers and PA66) were calculated. Only particles with area of $10 \mu\text{m}^2$ or more were extracted to exclude the particles coming from the polishing paper and noise from the image analysis. The circularity of each particle was calculated using the following equation:

$$C = \frac{4\pi S}{L^2} \quad (\text{II. 1})$$

where C is the circularity of the particle, S is the surface area of the particle, and L is the perimeter of the particle. Circularity is an indicator of the orientation of the fibers at the sliding surface. Circularity values close to 1 correspond to a circular shape, which in turn indicates that the fibers are oriented perpendicular to the sliding surface. In contrast, lower circularity values correspond to elliptical or fibrous shapes, which indicate that the fibers are oriented parallel to the sliding direction.

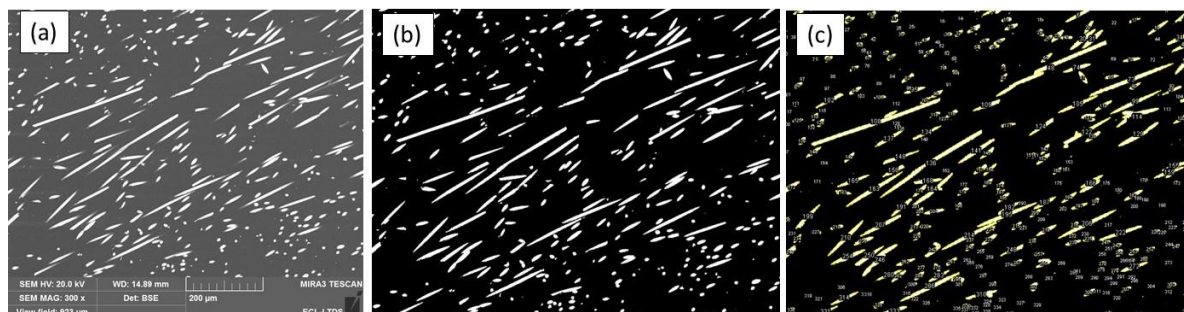


Fig. II. 25 Image analysis process: (a) obtained SEM image; (b) binarized image; (c) image showing particle analysis.

3.2 Measurements of viscosity number

The VN of the test specimens (after injection molding) without poly carbodiimide compounds was measured via the relative viscosity method, according to the ISO307 standard, with a formic acid solvent at 25°C. VN is correlated with the PA66 molecular mass.

3.3 Measurements of molecular mass

3.3.1 GF-reinforced PA66 composite with added poly-carbodiimide

The number average molecular masses of the pellets and molded test specimens were measured using the relative viscosity method with a formic acid solvent at 25°C, according to standard ISO307. Obtained viscosity number was converted to the number average molecular mass by using the pre-prepared calibration curve, which was obtained with the gel permeation chromatography (GPC) method of reference PA66 material using the HFIP (hexafluoro-2-propanol) solvent to flow the dissolved PA66 in the column of GPC.

3.3.2 AF-reinforced PA66 composite with added poly-carbodiimide

The molecular masses of the AF-reinforced PA66 were measured through the GPC method using THF solvent. PA66 was turned into a derivative by trifluoroacetic acid anhydride (TFA) before the GPC measurement to be dissolved by THF solvent [174].

3.4 FT-IR measurements of PA66 with added carbodiimide compounds

The extent of carbodiimide reaction in each process was measured by Fourier transform infrared spectroscopy (FT-IR), as shown in Fig. II. 26. First, the surface of the pellets or molded test specimens was sliced to a thickness of 50–100 μm using a microtome. Then, the thickness of the samples was made uniform using a hand press machine, and the thicknesses of the sliced samples were measured with a micrometer. Then, using an FT-IR transmission method with a KBr tablet, the absorbance (peak strength), A , of the peak corresponding to the carbodiimide group ($-\text{N}=\text{C}=\text{N}-$) was measured at approximately 2160 cm^{-1} . The amount of carbodiimide in each sample, C , was then calculated using the Lambert–Beer law:

$$A = \epsilon Lc \quad (\text{II. 2})$$

where ϵ is the molar absorption index, and L is the thickness of the sample. Thus, the molar adsorption index, ϵ , for each carbodiimide compound was calculated based on the slope of the calibration curve created by measuring the peak strength, A , of carbodiimide samples with different concentrations. Fig. II. 27 presents the example of FT-IR chart of the GF-reinforced PA66 with added aromatic poly-carbodiimide in this measurement method. In addition to the peaks related to the polyamide, typical peak of carbodiimide group in $2,160\text{ cm}^{-1}$ was detected.

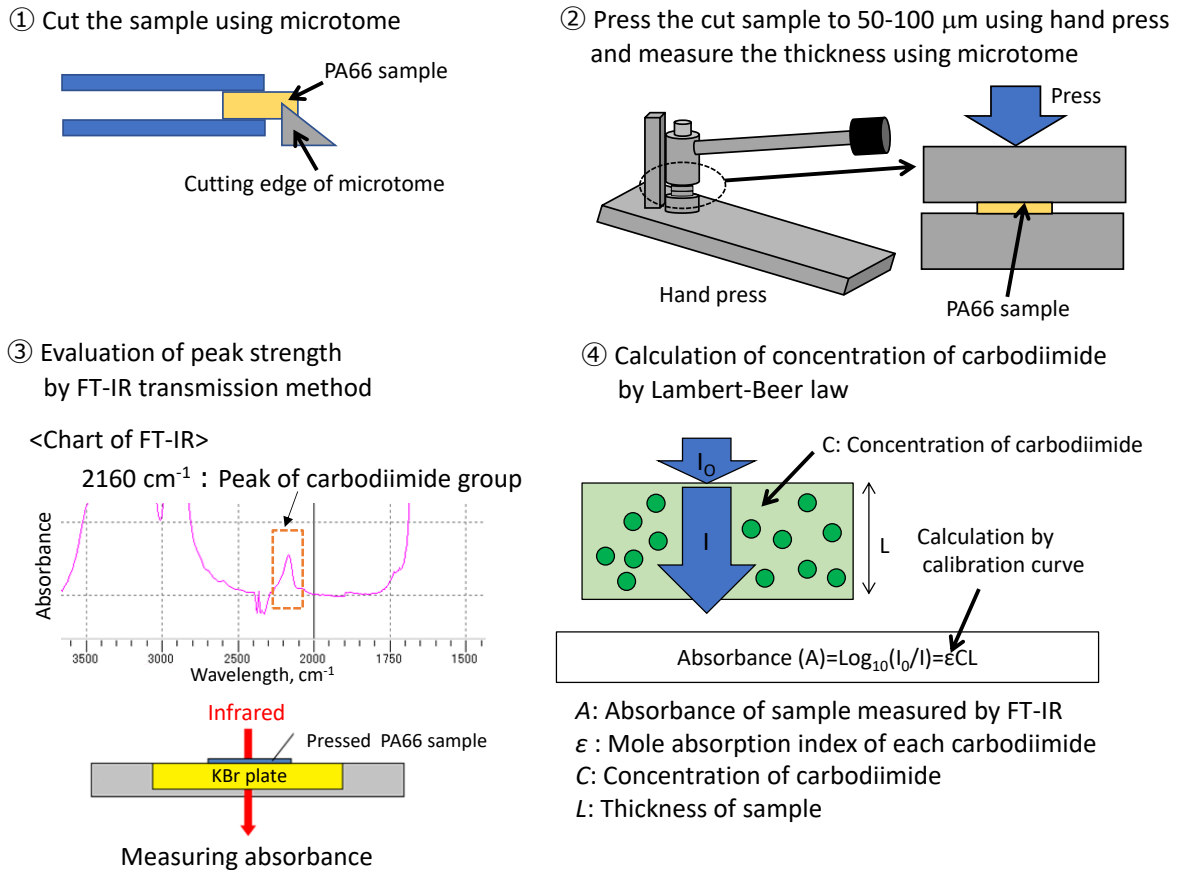


Fig. II. 26 Method for measurement of the extent of carbodiimide reaction.

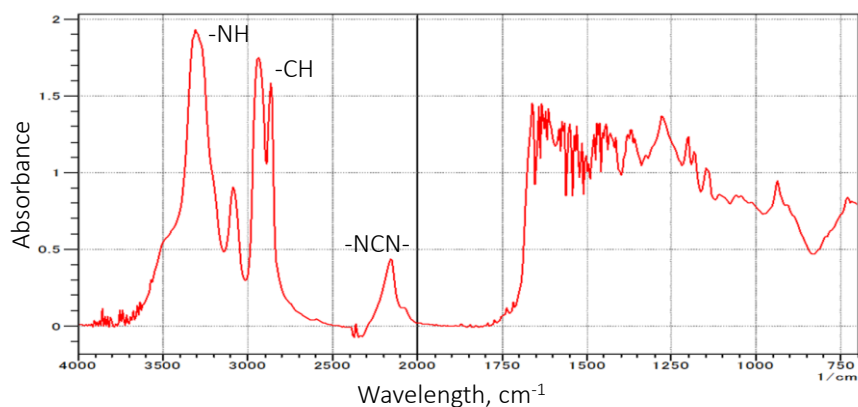


Fig. II. 27 FT-IR chart of PA66 with added aromatic poly-carbodiimide.

3.5 Measurements of fiber length distribution inside the tensile test specimens

The fiber length distribution of the GFs in the tensile test specimens was measured to estimate the interfacial shear strength of the GFs and PA66 matrix (in Chapter VI). First, 30 mg of the molding of the composite was cut from the center position of the specimens. This fragment was then combusted using a TG-DTA (thermogravimeter-differential thermal analyzer) at 650°C for 2 h, and the residual GFs were retrieved. Finally, the length distribution of the GFs with a length of 0.07 mm or greater was measured automatically using an optical microscope and image analysis.

3.6 Observation of fiber orientation inside the tensile test specimens

The fiber orientation inside the tensile test specimens was observed also to estimate the interfacial shear strength of the GFs and PA66 matrix (in Chapter VI) using the following process. First, the cut test specimen was embedded in epoxy resin and cured. Then, specimens with 4 mm thickness of the skin layer (0.3 mm depth from the top surface of the specimen) and core layer (2 mm depth from the top surface of the specimen) surfaces were obtained by polishing, as presented in Fig. II. 28. Subsequently, each surface was observed using SEM in BSE mode to obtain images of the GF orientation. The average orientation angle relative to the base axis (direction of the tensile test) was estimated by image analysis of the binarized images using the software package image J. Image analysis was conducted using six SEM images with different fields of view; as in the fiber length measurement, only fibers with a length of over 0.07 mm were analyzed.

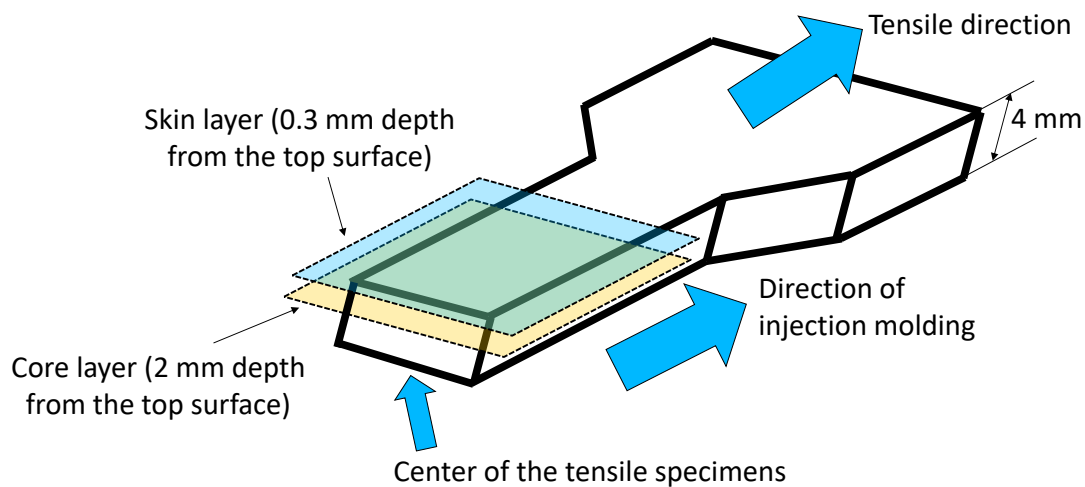


Fig. II. 28 Image of the tensile test specimens for the observation of fiber orientation observation.

4. Experimental set-ups and testing conditions

4.1 Tensile and Charpy impact tests

In order to measure the basic static mechanical properties, the tensile mechanical properties of specimens were measured following standard ISO527 using Autograph AGS-20kNG (SHIMADZU CORPORATION, Japan). Fig. II. 29 shows the schematic of tensile test specimens. Initial distance between chucks was 115 mm. Two stickers with markers were attached to the tensile test specimens, and the distance between markers was measured using camera. Young's modulus of the specimens was measured by the initial slope of stress-strain curve (in the region of the strain: 0.05-0.25%). Table II. 12 lists the tensile test conditions.

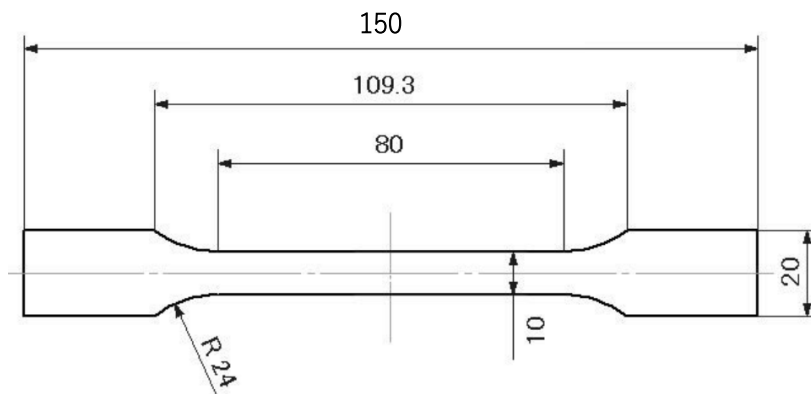


Fig. II. 29 Schematic of tensile test specimen.

Table II. 12 Test conditions for the tensile tests.

Tensile test specimens shape		150 mm × 10 mm × 4 mm
Test conditions	Tensile speed	0% - 1% of the strain: 1 mm /s Above 1% of the strain: 5 mm/s
	Temperature	25°C or 120°C
Measured data		- Tensile strength - Young's modulus -Tensile elongation at break -Tensile breakage energy *

*Tensile breakage energy is the integral value of stress-strain curve of the tensile tests (Fig. II. 30), and it indicates the toughness of the material.

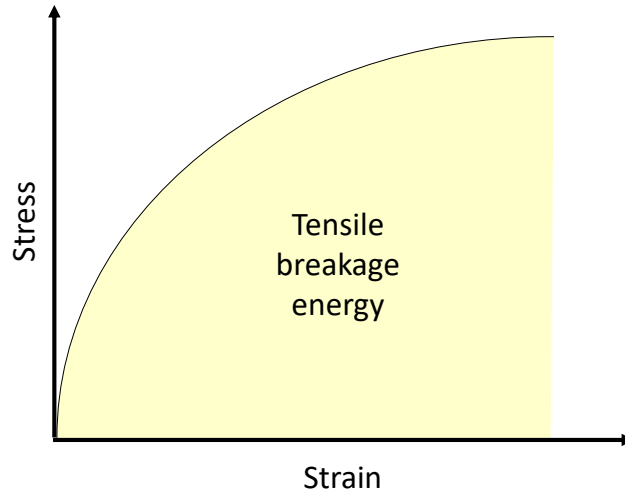


Fig. II. 30 Example of the tensile breakage energy in the stress-strain curve of the tensile test.

Notched Charpy impact test was performed following standard ISO 179 for the composite material with added olefin polymer. Fig. II. 31 shows the schematic of Charpy impact test specimen. Table II. 13 lists the test conditions.

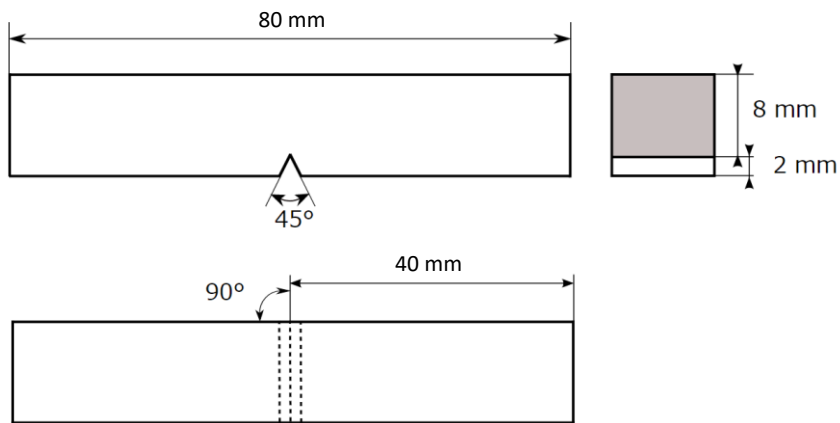


Fig. II. 31 Schematic of Charpy impact test specimen.

Table II. 13 Test conditions for the Charpy impact tests.

Impact test specimens shape		80 mm × 10 mm × 4 mm
Test conditions	Speed	3.8 m/s
	Temperature	25°C
Measured data		Charpy impact strength

4.2 Sliding test at LTDS

4.2.1 Presentation of the tribometer and samples geometry

The tribological properties were evaluated via sliding tests with grease/oil lubrication or in dry conditions, using a rotating PA66 or composite ring in contact with four fixed steel cylinders, using a tribometer developed in Laboratoire de Tribologie et Dynamique des Systèmes (LTDS), based on a spindle Electrobroche SD 5084, Precise, France. Fig. II. 32 presents the schematic view of the test specimens used for the sliding test as well as the tribometer setup. Fig. II. 33 shows the appearance of used tribometer.

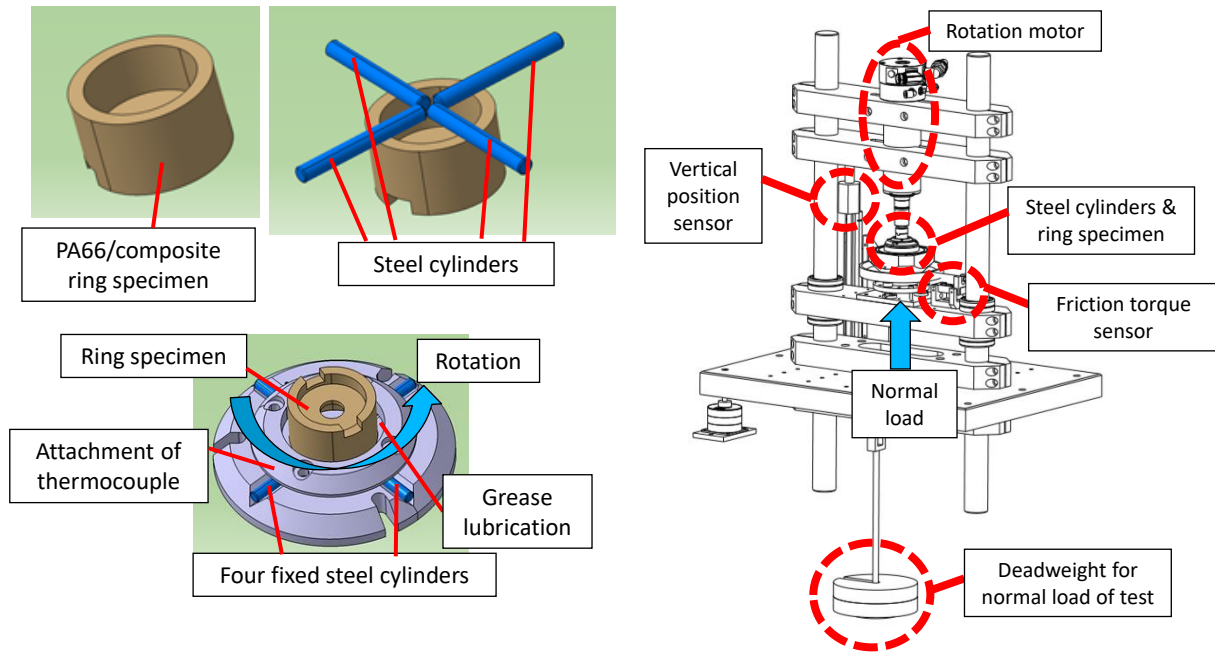


Fig. II. 32 Schematics of the test specimens and the sliding test setup (tribometer in LTDS).

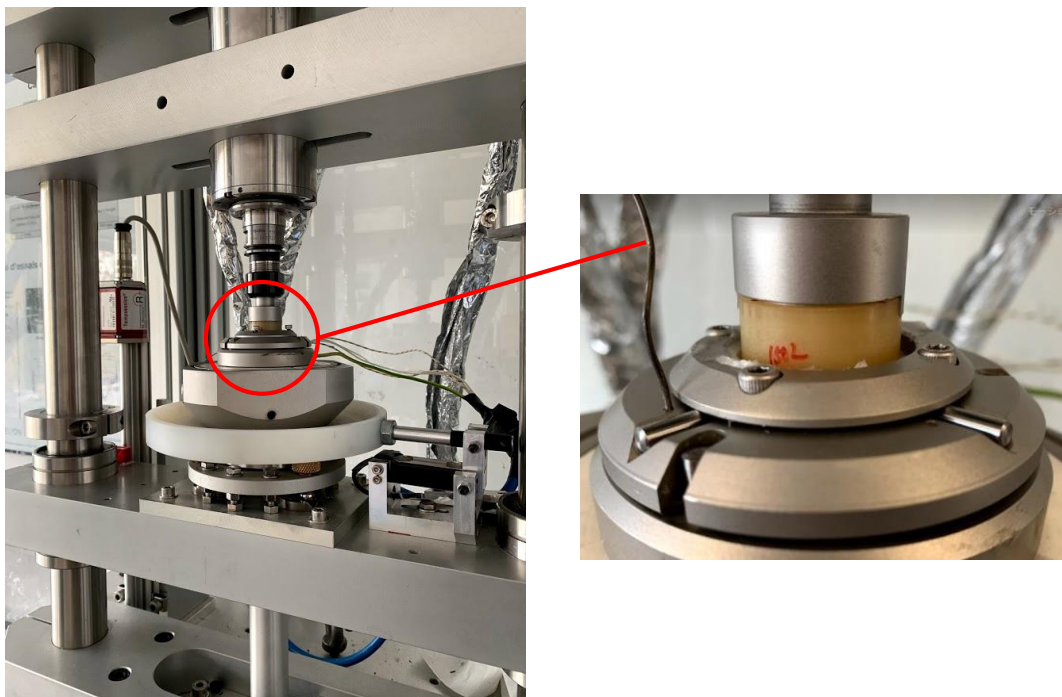


Fig. II. 33 Appearance of used tribometer in LTDS.

Table II. 14 lists the geometries of steel cylinder and ring sliding test specimen. Fig. II. 34 shows the drawing of the ring sliding test specimen.

Table II. 14 Geometries of steel cylinder and ring sliding test specimen.

Steel cylinders (×4)	Diameter	3.5 mm
	Length	30 mm
PA66 ring (JIS K 7218)	Outer diameter	25.6 mm
	Inner diameter	20 mm
	Height	15 mm (for unreinforced PA66) 12 mm (for fiber-reinforced PA66)

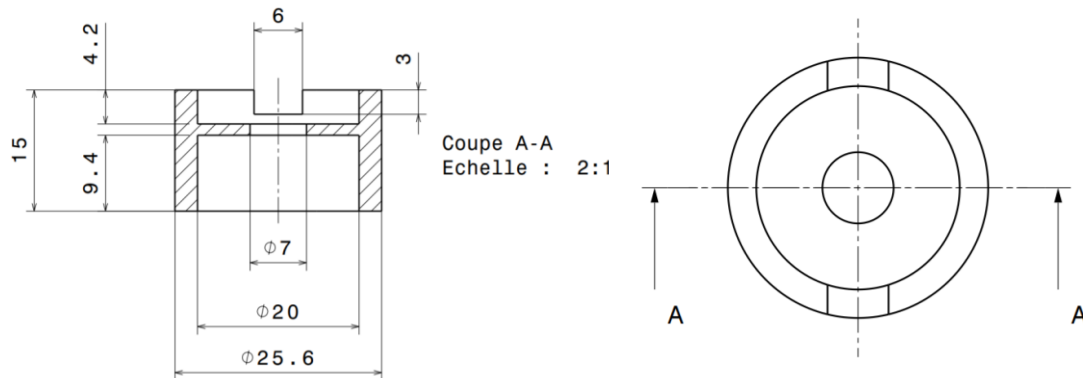


Fig. II. 34 Drawing of the ring sliding test specimen.

In this tribometer, the contact is formed by four elementary linear contacts between the four steel cylinders and the polymer or composite ring. With this test setup, it is possible to perform sliding tests under high contact pressure and sliding conditions, similar to those encountered by commercial worm gears. When the tests were performed under grease lubrication, 0.85 g of grease was prepared in the sample holder for each test. When the tests were performed under oil lubrication, the oil was poured and filled in the steel cylinders sample holder. Each ring test specimen was cleaned using heptane solvent in ultrasonic bath before the sliding test to remove the wear debris of polishing process explained in Section 2.1.4.2. A normal load was applied using dead weights, and the tribometer is designed so that 25% of this normal load is applied to each of the four elementary linear contact zones.

During the tests, the temperature of the steel cylinder holder was measured using a thermocouple. For the sliding tests conducted at higher temperature than room temperature, two cartridge heaters were inserted into the sample holder of the steel cylinders, and the sample holder and steel cylinders were heated.

The friction torque (T) was measured with a force sensor, and the friction coefficient (μ) was calculated using the normal load (N) and the mean rotation radius (r , 11.4 mm).

$$\mu = \frac{T}{rN} \quad (\text{II. 3})$$

Friction torque was measured every 0.01 s, and the average value and maximum value of the friction coefficient calculated in 1 s increments. One cycle in this sliding test represents one rotation of 360° of the ring specimens.

4.2.2 Tests conditions

Effects of various parameters on the tribological properties were investigated as following.

4.2.2.1 Normal load (and consequent contact pressure)

The basic and constant normal load of between 220 and 350 N (corresponding to 55-87.5 N for each of the four line contacts) was applied in the sliding tests under grease lubrication. Under this normal load, we can compare the difference of the wear and creep resistance of different materials at short test duration as the accelerated tests in contrast to the long-term actual gear durability tests. On the other hand, this value in the normal load is too high and severe under dry conditions because the friction coefficient and friction force are very high. Therefore, the normal load was reduced to 120 N when sliding tests were conducted under dry conditions (in Chapter VIII).

In addition, for some tests, the normal load was changed over the sliding cycles at the same rotational speed (790 rpm) according to the profile presented in Fig. II. 35 by changing the deadweight; namely, the normal load was increased and decreased three times to investigate the normal load (i.e., contact pressure) dependence of the friction coefficient at the same rotational speed (in Chapter V). It became possible to investigate the normal load (contact pressure) dependence of the friction coefficient under the same rotation speed.

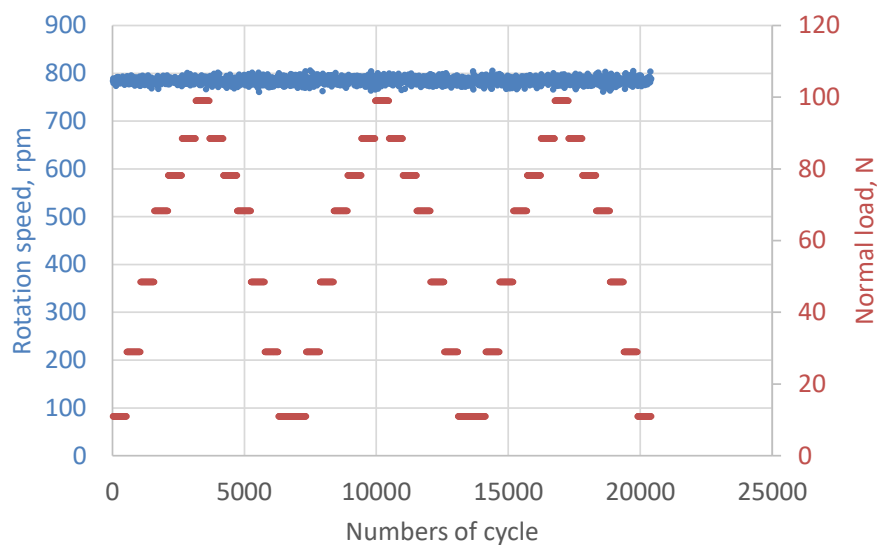


Fig. II. 35 Profiles of the sliding tests for normal load dependence under the same rotation speed.

4.2.2.2 Rotation speed

The basic and constant rotation speed of 790 rpm (corresponding to a mean sliding speed of 1 m/s at the mean rotation radius of 11.4 mm) was introduced in each sliding test except for Chapter V. This speed is the same level as that in actual gear durability test.

In addition, for some tests, the rotation speed was changed during a test according to the profile shown in Fig. II. 36 for the constant normal load (50 N). It became possible to investigate the sliding speed dependence of the friction coefficient for the same normal load.

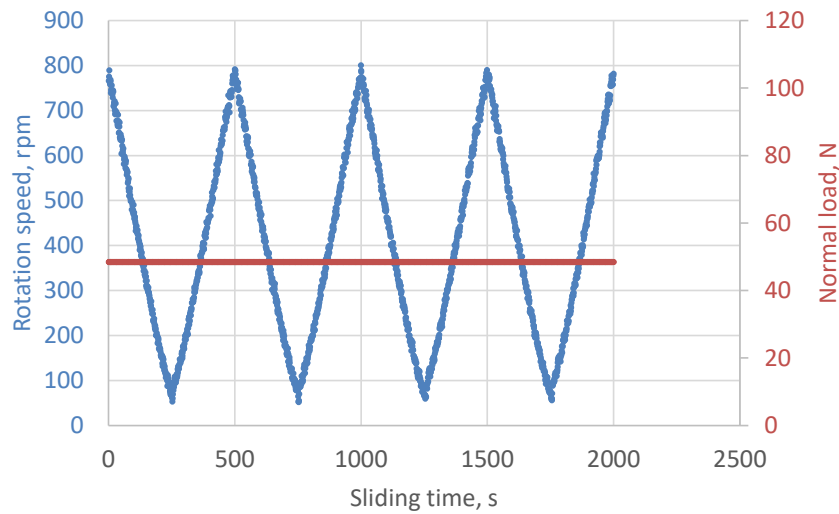


Fig. II. 36 Profiles of the sliding tests for rotation speed dependence under the same normal load.

4.2.2.3 Stopping periods in intermittent sliding contact

Intermittent sliding, in which rotation (during 10 s) and stopping periods (1, 20, and 200 s) are alternated, was introduced to reduce excessive sliding heat generation, when the wear and creep resistance of the material were evaluated. Fig. II. 37 shows the profile images of the intermittent sliding contact with a stopping phase of 1 s and 200 s. The objective of the introduction of the intermittent sliding contact is also to accelerate the wear of the material through the introduction of restart from stopping phase in high static friction coefficient. In the sliding tests for a stopping time of 200 s between each 10 s period of sliding, it allows us to control and maintain a given temperature for each test.

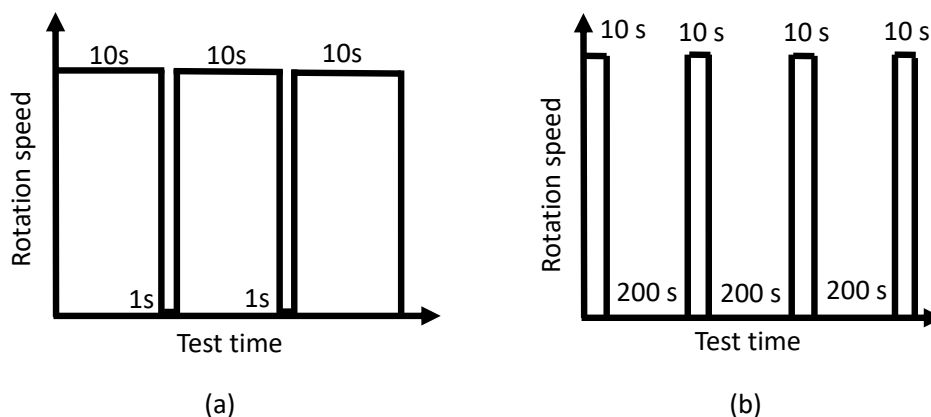


Fig. II. 37 Profile image of intermittent sliding contact: (a) 10 s sliding and 1 s stopping; (b) 10 s sliding and 200 s stopping.

In the sliding tests to evaluate the friction coefficient under lower normal load (10-100 N), the intermittent phase was not introduced, and tests were conducted with continuous sliding (in Chapter V).

4.2.2.4 Temperature

The basic difference of the tribological properties was investigated at room temperature. In addition, the effects of the temperature on the tribological properties were investigated at 80, 100, and 120°C (in Chapters IV, V, and VIII).

4.2.2.5 Summary

Table II. 15 lists the sliding test conditions to investigate the wear and creep resistance of the PA66 or composite (in Chapters III, IV, VI, and VIII). Contact pressure was estimated depending on the Hertzian theory using the tensile Young's modulus of unreinforced PA66 and GF 15% composite at room temperature.

Table II. 15 Test conditions for the sliding tests to evaluate the wear and creep resistance of the PA66 or composite.

Rotation speed	790 rpm			
Mean sliding speed	1 m/s (Mean radius of the contact area: 11.4 mm)			
Normal load	120 N	220 N	350 N	220 - 350 N
Hertzian contact pressure for unreinforced PA66 at RT	80 MPa	Not tested	136 MPa	108-136 MPa
Hertzian contact pressure for GF 15% composite at RT	111 MPa	150 MPa	189 MPa	150-189 MPa
Total test duration	11 - 74 min: intermittent process (10 s sliding and 1 s stopping)	240 min: intermittent process (10 s sliding and 20 s stopping)	16 - 117 min: intermittent process (10 s sliding and 1 s stopping)	24 - 2,826 min: intermittent process (10 s sliding and 200 s stopping)
Total sliding cycles	7,600 - 51 700	61,800	10,900 - 82,200	1,000 - 104,100
Total sliding duration	10 - 67 min.	80 min.	14 - 106 min.	1 - 135 min.
Environment temperature	25°C	25°C	25°C	25 - 120°C
Lubrication	Dry	Grease	Grease	Grease

In addition, Table II. 16 lists the sliding test conditions to investigate the friction coefficient under various test conditions (in Chapter V).

Table II. 16 Test conditions for the sliding tests to evaluate the friction coefficient PA66 or composite.

Rotation speed	up to 1,567 rpm
Mean sliding speed	up to 2 m/s (Mean contact-area radius: 11.4 mm)
Normal load	10 - 100 N
Hertzian contact pressure for unreinforced PA66 at RT	23 - 64 MPa
Hertzian contact pressure for GF 15% composite at RT	30 - 90 MPa
Total test duration	1,560 – 2,000 s
Total sliding cycles	7,800 – 20,400 cycles
Environment temperature	25 - 120°C
Lubrication	PAO8 oil (stated in Section 2.3.3) / Urea grease (stated in Section 2.3.1)

4.2.3 Quantification of damage

The weight and height of each PA66 or composite ring specimen were measured using the balance and micrometer before and after each sliding test to estimate the wear and creep separately. To remove the effect of hygroscopicity of PA66 as explained in Section 3.1.4 in Chapter I, the ring specimens were heated at 80°C for at least 12 h using oven before and after the sliding tests and absorbed water was evaporated. The total height loss (h_{total} , the difference in the height of the ring specimen before and after the sliding test) was the summation result of creep and wear. The wear height loss (h_{wear}) was calculated from the wear mass of the ring specimen (M_{wear}), the density of the PA66 or composite (d), and the sliding surface area (s , approximately 200 mm²) using the following equation (assuming a uniform wear over the contact surface of the ring):

$$h_{wear} = \frac{M_{wear}}{ds} \quad (\text{II. 4})$$

The creep height loss (h_{creep}) was estimated subtracting h_{wear} from h_{total} .

$$h_{creep} = h_{total} - h_{wear} \quad (\text{II. 5})$$

Furthermore, the vertical displacement of the steel cylinders sample holder was directly measured during the sliding tests using the vertical position sensor. However, this value was not exactly the same as the height loss of the composite ring measured before/after sliding tests because the composite ring specimens expanded because of the heat generated by sliding during the tests and then contracted because of cooling after each test.

4.3 Sliding test at JTEKT

Part of the sliding tests (in Chapters VII and IX) were conducted using the tribometer in JTEKT Corporation, Japan, which was made by Yonekura Corporation, Japan. The basic contact geometry is the same as the other one, as presented in Fig. II. 38. Fig. II. 39 presents the appearance of used tribometer in JTEKT. Table II. 17 lists the sliding test conditions.

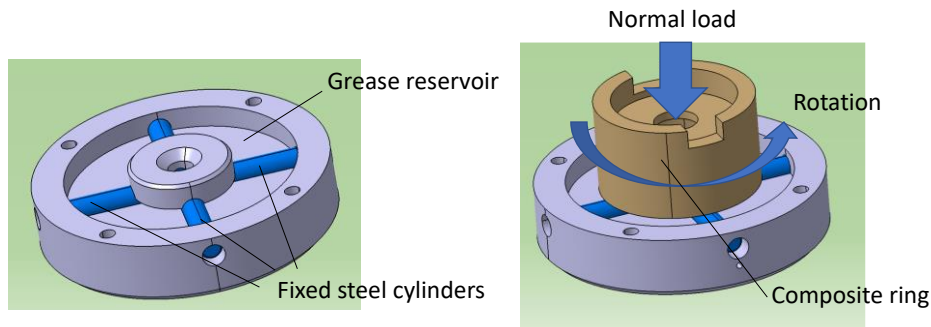


Fig. II. 38 Schematic view of the steel cylinders-composite ring sliding tests conducted in JTEKT.



Fig. II. 39 Appearance of used tribometer in JTEKT.

Table II. 17 Test conditions for the sliding tests at JTEKT.

Rotation speed	790 rpm
Mean sliding speed	1 m/s (Mean contact-area radius: 11.4 mm)
Normal load	220 N
Total test duration	240 min. intermittent process (10 s sliding and 20 s stopping)
Environment temperature	25°C
Lubrication	Barium complex grease (stated in Section 2.3.2)

4.4 Micro indentation measurement

The Young's modulus and hardness of the sliding surface of the GF-reinforced PA66 composite and unreinforced PA66 were measured based on the micro indentation at different temperatures. The micro indentation device used, developed by Alemnis [175], can operate at up to 600°C in a SEM. The heating procedure and temperature matching between the tip and sample used to conduct precise temperature tests at different temperatures are described in [176]. Experimental tests were conducted using a Berkovich tip made of tungsten carbide. The hardness and Young's modulus were both calculated using the Oliver–Pharr method [177]. Table II. 18 presents the measurement conditions. More particularly, the loading and unloading procedures were applied using a constant strain rate, which is important for time-dependent materials such as PA66 [178]. In addition, a high strain rate value of 0.2 s^{-1} was chosen to avoid a nose formation in the unloading curve, preventing the unloading stiffness calculation [179]. Finally, the thermal drift was checked by applying a holding time at a constant load of 2 mN during 60 s.

Table II. 18 Micro indentation test conditions.

Tested material	GF 15% composite	Unreinforced PA66
Type of indenter	Berkovich (WC)	Berkovich (WC)
Maximum normal load	500 mN	250 mN
Indentation test procedure	Loading strain rate \dot{P}/P : 0.2 s^{-1} Holding time at 500 mN: 10 s Unloading strain rate \dot{P}/P : 0.2 s^{-1} Holding time at 2 mN (checking thermal drift): 60 s	Loading strain rate \dot{P}/P : 0.2 s^{-1} Holding time at 250 mN: 10 s Unloading strain rate \dot{P}/P : 0.2 s^{-1} Holding time at 2 mN (checking thermal drift): 60 s
Temperature	25°C, 80°C, 120°C	25°C, 80°C, 120°C

In addition, the Young's modulus of the composite sliding surface after tests with different cycle numbers and hardness of the sliding surface of the steel cylinder were measured through other type of the micro indentation at RT. Table II. 19 lists the measurement conditions.

Table II. 19 Micro indentation test conditions.

Tested material	GF 15% composite	Steel cylinder
Type of indenter	Vickers	Vickers
Maximum normal load	1,500 mN	300 mN
Indentation test procedure	Load: 0→1,500 mN for 10 s Creep: 1,500 mN for 5 s Unload: 1,500 mN⇒40 mN for 4 s	Load: 0→300 mN for 10 s Creep: 300 mN for 5 s Unload: 300 mN⇒40 mN for 4 s

4.5 Nano indentation measurement

To discuss the relationship between the hardness of the steel counterpart and that of the reinforcement fibers on the tribological properties, the hardness of a single fiber was measured using the following process. First, cut strands of fiber were embedded in an epoxy resin in the perpendicular and horizontal directions, as presented in Fig. II. 40, and the epoxy resin was cured. Then, the surface of the epoxy resin was polished, and the hardness of the fibers was measured using nanoindentation. The measurements were performed with a Berkovich indenter and normal loads of 4,000 μN for the GFs and 4,000 to 13,000 μN for the CFs.

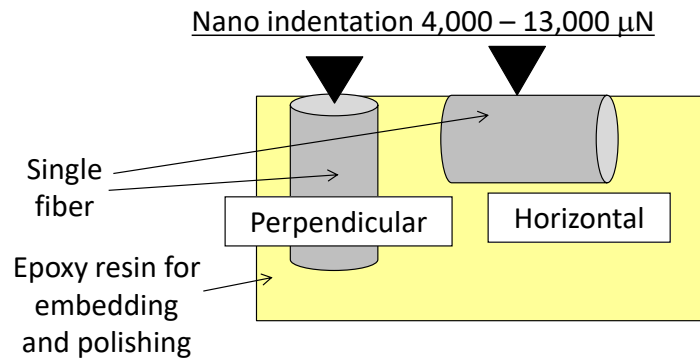


Fig. II. 40 Schematic of the nanoindentation hardness measurements of fibers.

5. Analysis methods after sliding tests

After the sliding tests, the sliding surfaces of the PA66 or composite rings and steel cylinders were examined with various methods, including optical microscopy, SEM with X-ray dispersive spectrometry (EDX), optical interferometry, X-ray photoelectron spectroscopy (XPS), and time-of-flight secondary ion mass spectrometry (ToF-SIMS).

5.1 Optical microscopy

An optical microscope (Keyence, VHX-6000) was used to observe the wear scar of the PA66 or composite rings and steel cylinders. It was also used to estimate the surface area of the sliding surface of the composite ring after sliding tests because the surface area changes after sliding tests through creep of the specimen.

5.2 SEM and EDX

The sliding surfaces of the PA66 or composite ring and steel cylinders after the tests were observed through SEM using a MIRA3 (TESCAN, Ltd.). An X-ray dispersive spectrometry (EDX) analysis was conducted using a X-Max (Oxford Instruments plc) to detect the chemical elements of a tribofilm under the boundary lubrication of the sliding surface of the steel cylinders and a ring. The test specimens of the PA66 or composite ring do not conduct electricity, therefore the ring specimens were metallic-coated (both sliding surface and opposite side) using gold coater to obtain clear SEM images by avoiding the charge-up.

5.3 Interferometry

Interferometer (GT-K1, Bruker, Ltd.) was used to observe the wear scar of the steel cylinders and evaluate the wear amount of the cylinders after each test. The removal of the cylindrical shape was conducted for the observation of the steel cylinders with curvature.

5.4 XPS

X-ray photoelectron spectroscopy (XPS) was conducted using a ULVAC-PHI Versa Probe II apparatus to detect the chemical states of the elements composing the tribofilm on the steel and PA66. The X-ray source is Al K α operating at 1,486.6 eV, and the size of the X-ray spot is 200 μm . A neutralizing electron gun was applied. The energy scale was calibrated using the C1s binding energy located at 284.8 eV. First, a wide range survey of 1,200 eV was conducted to identify all chemical elements with a pass energy of 187 eV. Next, a narrow range survey of each chemical element was conducted at a pass energy of 23 eV to identify the different chemical states, and a quantitative analysis was applied based on the curve fitting of each peak using Multipak software. Before the XPS analysis, analyzed samples (taken after the sliding tests) were carefully washed using an ultrasonic bath in a heptane solvent (98%, Chimie-plus) for 20 min and ultrapure heptane (>99%, Chimie-plus) for 20 min to remove the attached grease and conduct the surface observations and analysis. Fig. II. 41 shows the appearance of used XPS.

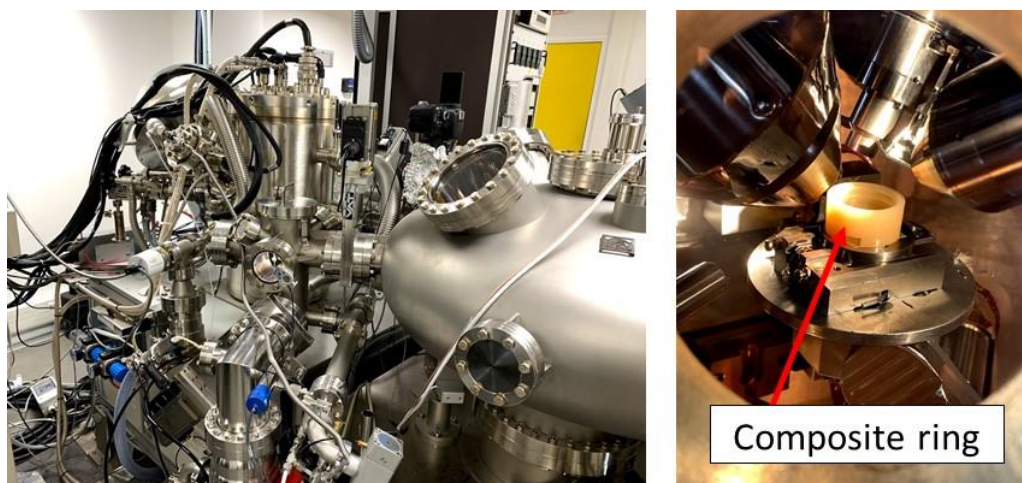


Fig. II. 41 Appearance of used XPS.

5.5 ToF-SIMS

Time-of-Flight Secondary Ion Mass Spectrometry (ToF-SIMS) of the steel cylinders and PA66 ring after the tests was performed using a TOF-SIMS 5 (ION-TOF Co.) to detect the composition of the sliding surface. An area of $100 \times 100 \mu\text{m}^2$ was used for the spectroscopic analysis, and an area of $500 \times 500 \mu\text{m}^2$ was used for the chemical mapping. The depth of the analysis was lower than 10 \AA (first monolayers). For the liquid metal ion gun (LMIG), Bi₃ was used as the source of the primary ions. Qualitative depth profiles on the steel cylinder surface were also investigated by repeating the low energy Cs⁺ ion sputtering (500 eV) and conducting ToF-SIMS measurements. Observed specimens were carefully washed through the same process as for XPS analysis. Fig. II. 42 presents the appearance of used ToF-SIMS at Science & Surface (<https://www.science-et-surface.fr/>).



Fig. II. 42 Appearance of used ToF-SIMS.

6. Conclusions

In this chapter, experimental materials, test methods, and analysis methods are presented. Using these materials and test methods, the basic tribological properties in this system, including the wear and creep resistance of the composite and steel counterpart, temperature dependence of the tribological properties, and the friction occurrence mechanism are clarified at first. In addition, based on the clarified basic tribological behavior, the effects of the composition of the composite including PA66 molecular mass and types of the fibers are investigated, and the tribological behavior of actual worm wheel is also discussed.

CHAPTER III

BASIC TRIBOLOGICAL BEHAVIOR OF GF-REINFORCED PA66 IN CONTACT WITH CARBON STEEL UNDER HIGH CONTACT PRESSURE AND GREASE LUBRICATION

CHAPTER III: BASIC TRIBOLOGICAL BEHAVIOR OF GF-REINFORCED PA66 IN CONTACT WITH CARBON STEEL UNDER HIGH CONTACT PRESSURE AND GREASE LUBRICATION

1. Introduction.....	101
2. Detailed tribological behavior of the contact and damage of the GF-reinforced composite and unreinforced PA66	101
2.1 Sliding test results and observation of samples after test	101
2.2 Change over time of the sliding surface and reason of height decrease (contribution of wear and creep)	106
2.3 Effect of fiber orientation and change in the surface mechanical properties	111
2.4 The difference of the tribological properties in unreinforced PA66 and GF-reinforced PA66 composite	116
3. The effect of fiber orientation on the wear behavior of steel counterpart and composite.....	118
3.1 Wear behavior of counterpart steel and effect of the fiber orientation in the composite ring	118
3.2 Effect of the fiber exposure on the sliding surface.....	120
4. Contribution of each parameter to the increase of friction and damage.....	123
5. Effects of the hardness of the steel counterpart	128
6. Conclusions.....	130

CHAPTER III: BASIC TRIBOLOGICAL BEHAVIOR OF GF-REINFORCED PA66 IN CONTACT WITH CARBON STEEL UNDER HIGH CONTACT PRESSURE AND GREASE LUBRICATION

This chapter introduces the basic tribological behavior of GF-reinforced PA66 in contact with carbon steel under high contact pressure and grease lubricated conditions. The investigated basic behavior will serve as a basic knowledge for the study of the effects of other parameters or material compositions in next chapters.

1. Introduction

This chapter focuses on the typical tribological properties during sliding of GF-reinforced PA66 and a steel counterpart under high contact pressure in grease lubricated conditions (i.e., the wear resistance of GF-reinforced PA66 and steel, and the friction properties of the contact). First, the detailed tribological behavior and change over time of the tribological properties were investigated, and the contribution of each parameter such as the damage in the sliding surface, the contamination by wear debris in the grease, and the increase of surface temperature on the tribological properties were elucidated. The wear resistance of the steel counterpart was also discussed, considering the fiber orientation on the composite sliding surface. Furthermore, the effects of the mechanical properties of the steel counterpart on the tribological behavior were evaluated. In this chapter, GF 15% composite with normal molecular mass (sample no. 1 in Table II. 3) and grease containing zinc carboxylate and sulfur type anti-oxidation agent (sample no. 1 in Table II. 11) were used. The comparison to unreinforced PA66 was also conducted using the sample no. 12 in Table II. 3.

2. Detailed tribological behavior of the contact and damage of the GF-reinforced composite and unreinforced PA66

2.1 Sliding test results and observation of samples after test

Fig. III. 1 shows the evolutions of the vertical displacement, the temperature, and the average friction coefficient (μ) during 61,500 cycles for a normal load of 350 N and a stopping time of 1 s (after every 10 s of sliding), with the steel cylinders (hardness: 4.5 GPa), using GF composite. The temperature of the sliding surface was increased from 25°C to 102°C. The displacement did not increase in the initial stage of the test (indicating that neither wear nor creep occurred) and the average friction coefficient was 0.035–0.045. After the initial stage (around 21,000 cycles), both the maximum friction coefficient (maximum value of 100 measurements every 0.01 s in 1 s) and average friction coefficient (average value of 100 measurements every 0.01 s in 1 s) started to increase, as presented in Fig. III. 2 (before the increase of the vertical displacement), and then sudden increase in the vertical displacement

of 0.1 mm was observed (inflection point of the vertical displacement). At the sudden increase point, the slope of the temperature increased, which is related to the increase in the friction coefficient and consequently in heat dissipated in the contact. Afterward, a steady state displacement was observed, and then the displacement began to increase proportionally to the number of cycles. The sliding tests were performed under the same conditions using the same materials seven times, and the first sudden increase in the vertical displacement ranged between 19,000 cycles and 23,000 cycles.

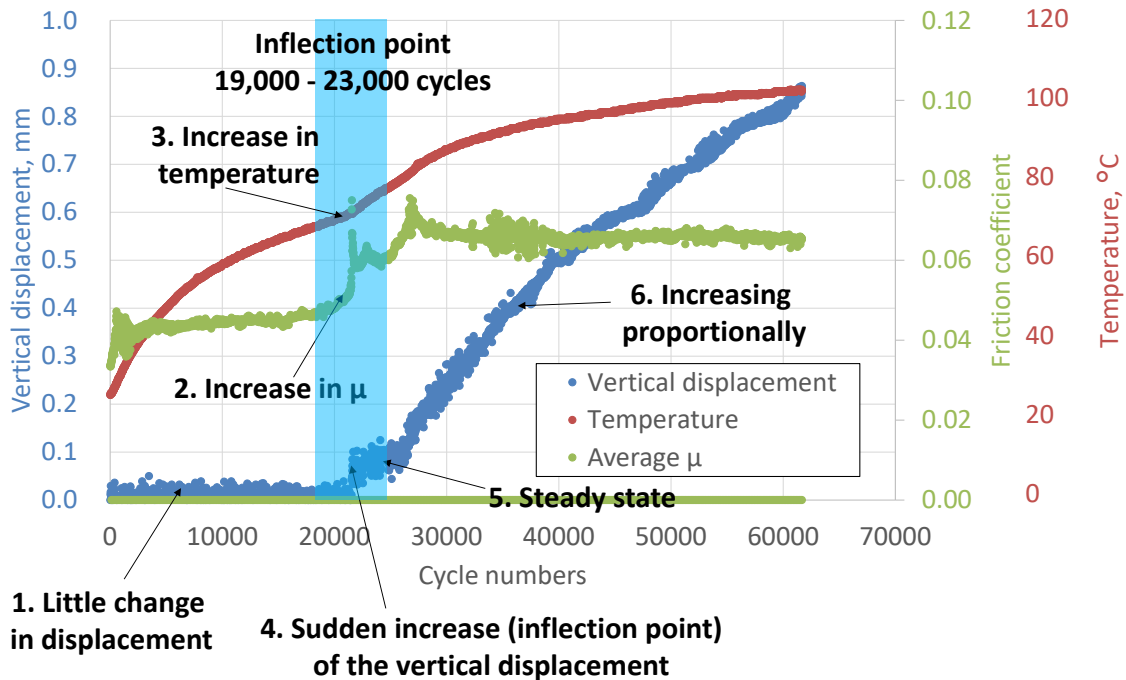


Fig. III. 1 Evolutions of the vertical displacement, the average friction coefficient, and the temperature over 61,500 cycles.

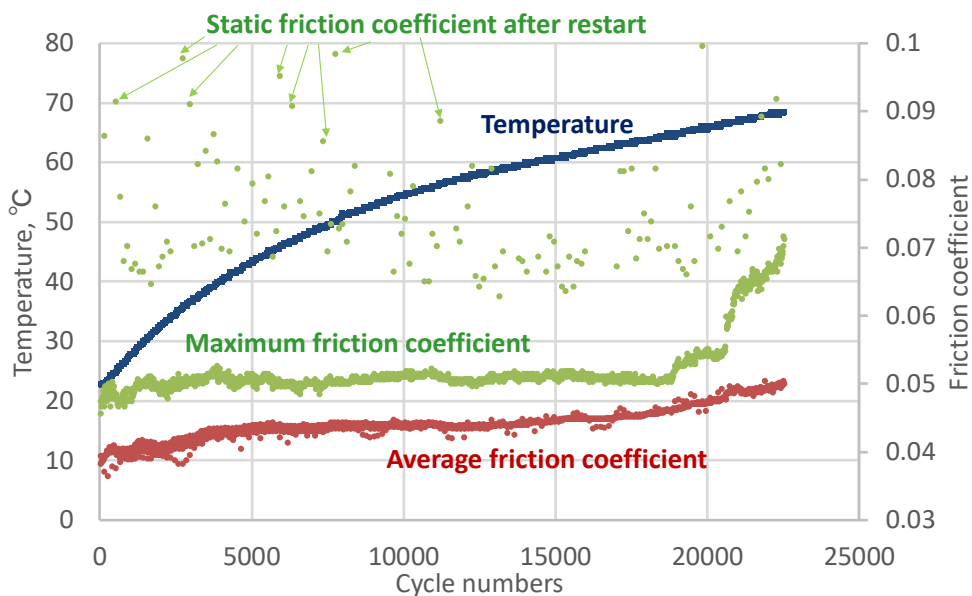


Fig. III. 2 Evolutions of the temperature and the friction coefficient before the sudden increase of the vertical displacement.

Example of the evolution of the friction coefficient for 2 s from the restart of the sliding after stopping phase is shown in Fig. III. 3. The static friction coefficient increased to approximately 0.07–0.08, and then decreased.

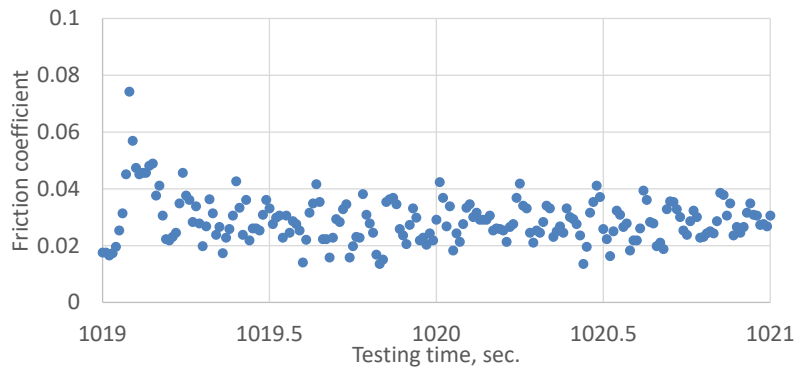


Fig. III. 3 Evolution of the friction coefficient after a restart.

Fig. III. 4 presents each test specimen and grease before and after the sliding test of 61,500 cycles, as observed by optical microscope. The entire sliding surface of the composite ring was damaged, and the sliding surface was expanded in both inner and outer directions; this indicated that both wear and creep occurred during sliding, and 0.575 mm (70.4%) was wear and 0.242 mm (29.6%) was creep, which were estimated by the calculation explained in Section 4.2 in Chapter II. The sliding surface of the steel cylinders was worn severely (exhibiting scratches in the sliding direction), indicating that 2-body abrasive wear occurred. The total wear volume of the four steel cylinders after 61,500 cycles was 0.158 mm³ and was much less than the wear volume of the composite ring after 61,500 cycles, which was 112 mm³.

	Composite ring	Steel cylinder	Grease
Before sliding test			
After Sliding test	 Wear amount of composite: 0.14 g Wear volume: 112 mm ³ Height decrease: 0.82 mm	 Wear volume: 0.158 mm ³ (Total of four cylinders)	

Fig. III. 4 Test specimens and grease before/after the test (observed by optical microscope).

Fig. III. 5 presents SEM observations of the composite sliding surface after 61,500 cycles, which were performed under the BSE mode, where the white area is the GFs and the gray area is the PA66. It was revealed that the severe damage (peeling) on the entire surface occurred and GFs partially peel off due to a not good enough adhesion to PA66 matrix. In addition, the color of the grease changed from a light color to black, as shown in Fig. III. 4.

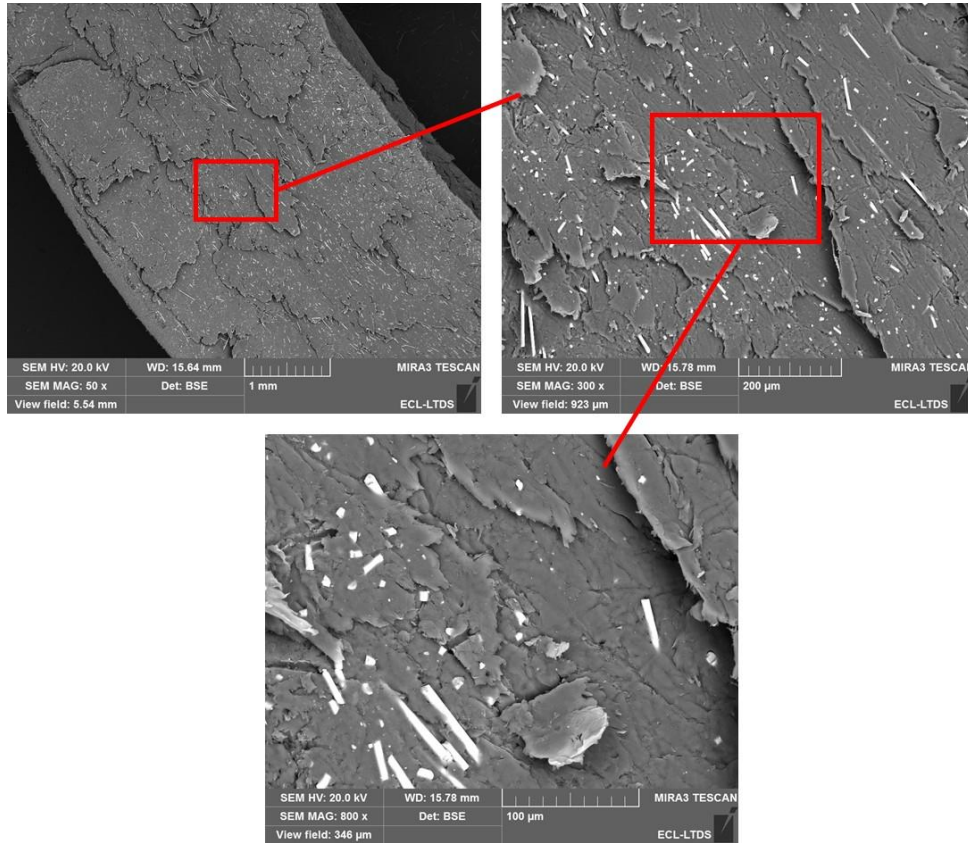


Fig. III. 5 SEM observations of composite sliding surface after 61,500 cycles.

Fig. III. 6 shows the wear debris inside the grease after a sliding test. The image was obtained by centrifugation of the grease to separate the base oil and then heating the residue to evaporate any organic agents (such as thickeners). The presence of fibers can be observed in the wear debris. In addition, the elements related to GFs (Si, Al) and carbon steel (Fe) were detected by SEM-EDX analysis of the wear debris in the grease as shown in Fig. III. 7.

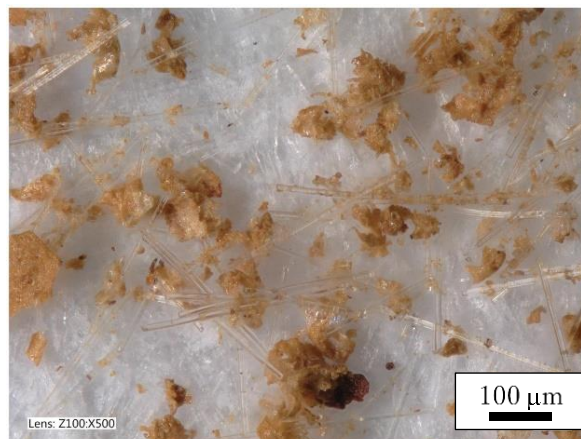


Fig. III. 6 Optical microscope image of wear debris in grease.

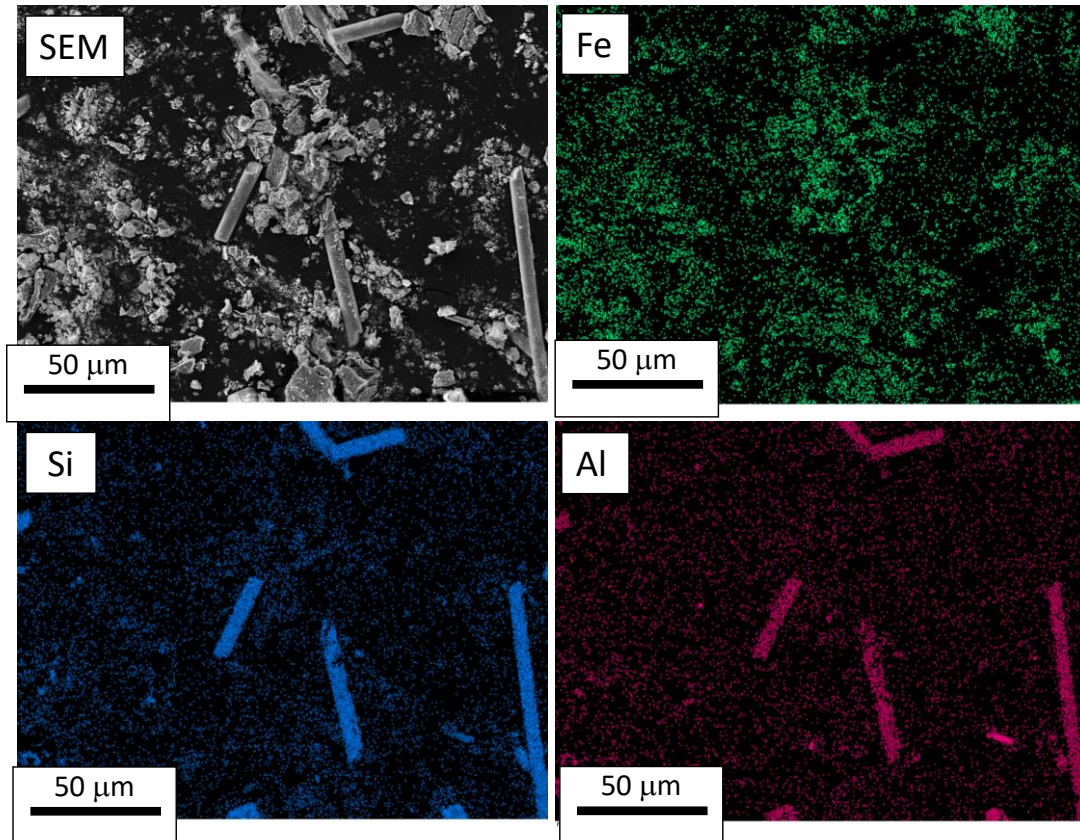


Fig. III. 7 SEM-EDX analysis of wear debris in grease.

Besides, the temperature shown in Fig. III. 1 was measured using thermocouple attached in the steel cylinder sample holder. To discuss the difference in the temperature between the sample holder and steel cylinder itself, the cylinder with a hole of 1.1 mm diameter was mechanically fabricated additionally, and the temperature inside the steel cylinder during the sliding test was investigated, as shown in Fig. III. 8. Fig. III. 9 presents the evolutions of the vertical displacement and the difference in the temperature of the sample holder and steel cylinder using the soft steel cylinder with the hardness of 3.9 GPa under the same test conditions presented in this section (the effect of the hardness on the tribological properties will be explained in Section 5 in this chapter). The temperature measured inside the steel cylinder was 15-30°C higher than that of the sample holder. Fig. III. 10 shows the comparison of the sample holder temperature and steel cylinder temperature, and linear approximation. Therefore, the temperature of the steel cylinder under these test conditions can be estimated.

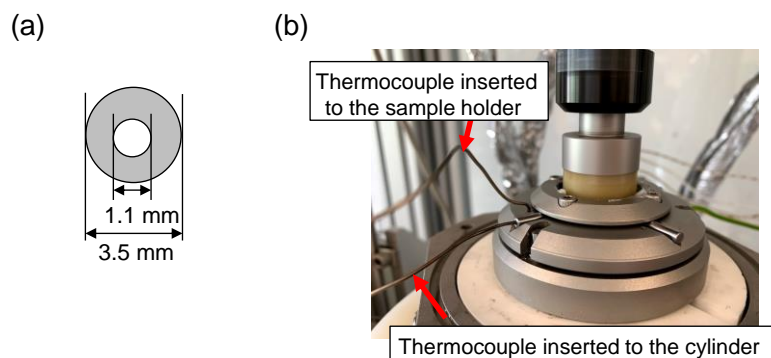


Fig. III. 8 (a) Cross section of the steel cylinder with hole; (b) testing apparatus.

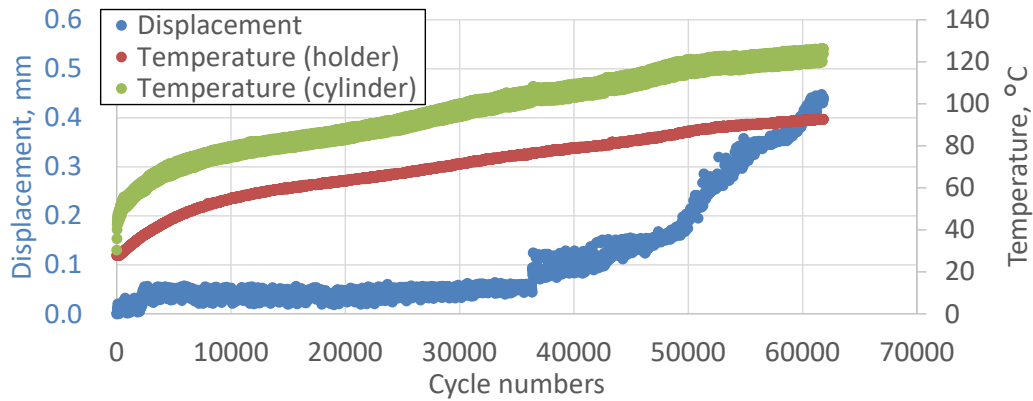


Fig. III. 9 Evolutions of the vertical displacement and the difference in the temperature of the sample holder and steel cylinder using the steel cylinder with the hardness of 3.9 GPa.

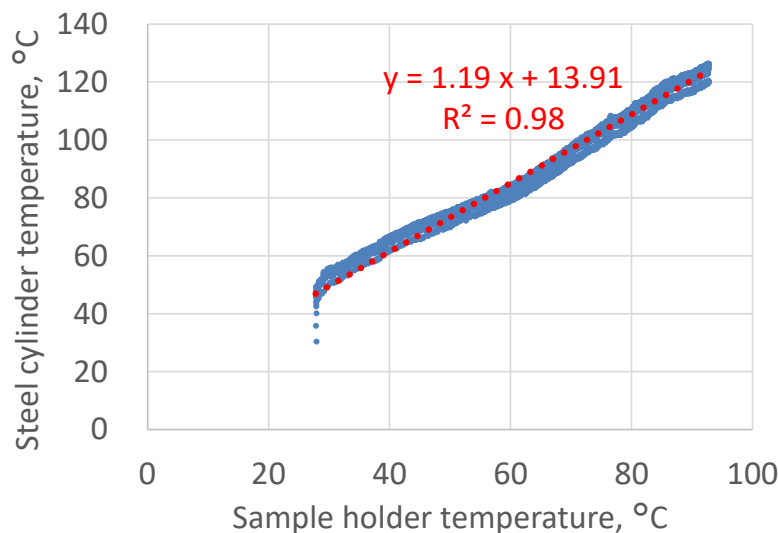


Fig. III. 10 Comparison of the sample holder temperature and steel cylinder temperature.

2.2 Change over time of the sliding surface and reason of height decrease (contribution of wear and creep)

To clarify the reasons for the first sudden increase in the vertical displacement and to estimate the ratio of wear and creep in each stage, eight individual tests with different cycle numbers were performed.

Fig. III. 11 shows the absolute value of the wear and the creep represented by the total height loss, and the calculated ratio of wear and creep for each cycle. There was good correlation between the creep, and the surface area after the sliding tests (measured with the optical microscope), which is supposed to be directly related to the creep of the composite ring, as presented in Fig. III. 12. In the initial stage of the sliding test (in other words, before the first sudden increase in the vertical displacement), the height decrease was mainly due to creep (plastic deformation); however, the effects of wear started to increase after the first sudden increase, and in the last stage of the sliding test, the main factor contributing to height loss was wear.

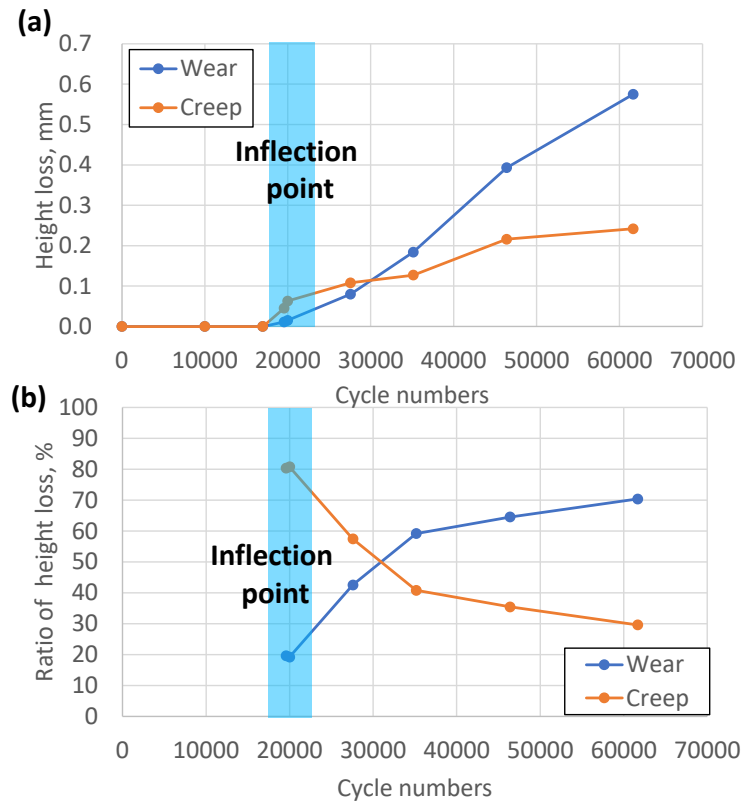


Fig. III. 11 (a) Height loss representing wear and creep at different cycles and (b) height loss ratio due to wear and creep.

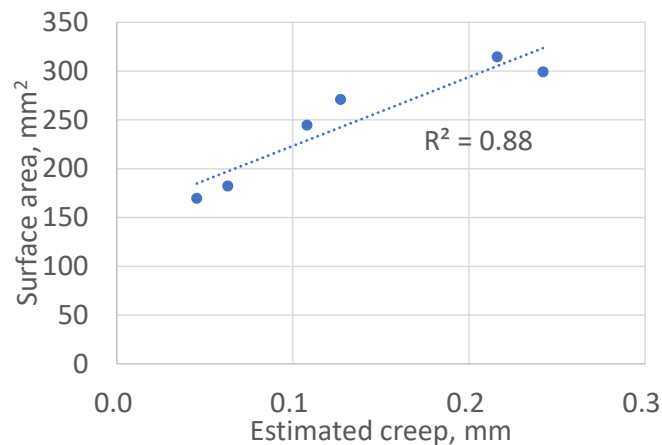


Fig. III. 12 Relationship between estimated creep and the surface area after a sliding test.

The process involving wear and creep during the sliding tests was clarified by detailed observations as follows. Fig. III. 13 and Fig. III. 14 show optical microscope observations of the sliding surface of the composite ring after different numbers of cycles. At 10,000 and 17,000 cycles, partial peeling of the sliding surface has already occurred, especially in the center region, despite before the sudden increase of the vertical displacement. At 22,531 cycles (just before the sudden increase of the vertical displacement for this test), the peeling of the center area of the sliding surface was advanced. In the sample tested for 19,995 cycles (just after the sudden increase for this test), peeling of the center area of the sliding surface was observed. From then on (after 27,571 cycles), peeling spread across the entire sliding surface.

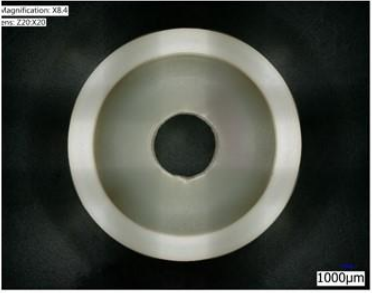
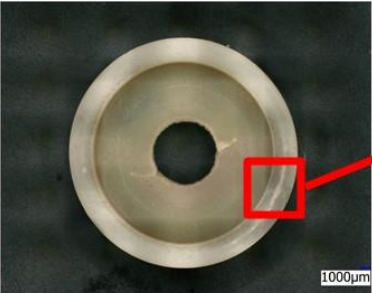

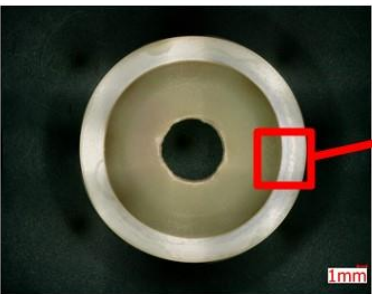

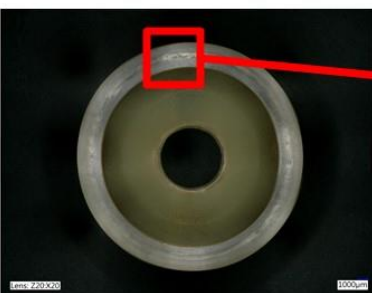

Cycles	All surface	Peeled area
0		-
10,000		
17,000		
22,531 (Just before the inflection point)		

Fig. III. 13 Optical microscope observations of the sliding surface of composite rings for various test durations (0-22,531 cycles: before the sudden increase).

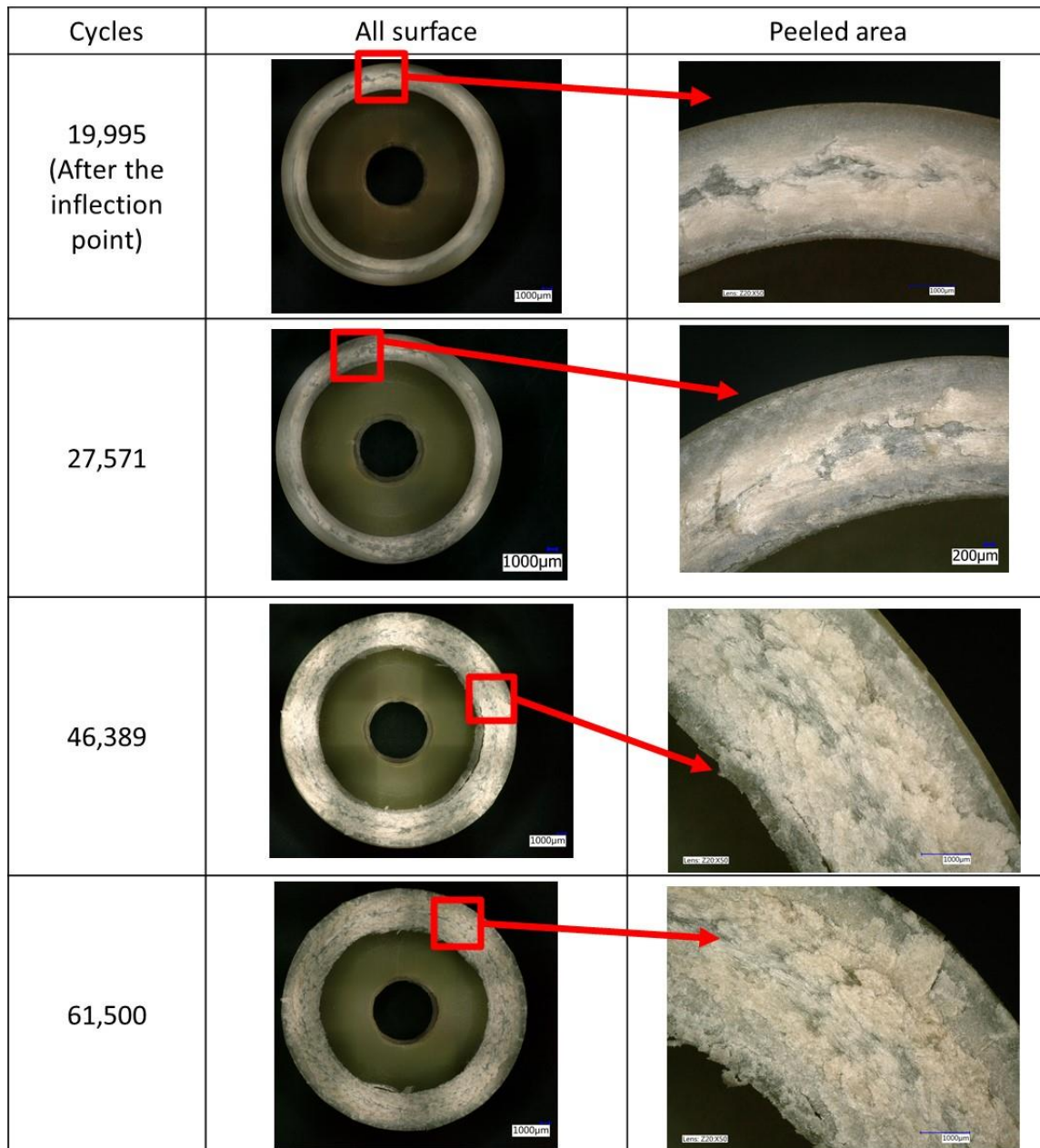


Fig. III. 14 Optical microscope observations of the sliding surface of composite rings for various test durations (19,995-61,500 cycles: after the sudden increase).

In addition, Fig. III. 15 presents the SEM observations of the sliding surface of the composite ring after different numbers of cycles. After 10,000 cycles, small holes in the PA66 are observed. However, GFs adhered to PA66 correctly and severe damage is not observed. At 17,000 cycles, additional damage is observed; holes where the GFs had fallen off the sliding surface were observed, and scratches of the sliding surface related to the missing GFs are observed. At 22,531 cycles (just before the sudden increase of the vertical displacement in this test), even in an area where severe peeling was not present (observed with the optical microscope), peeling off of GFs, damage to GFs, and wear debris from the steel are confirmed. In addition, some scratches are observed in the sliding direction. The wear of the steel cylinders will be studied deeply in Section 3.1.

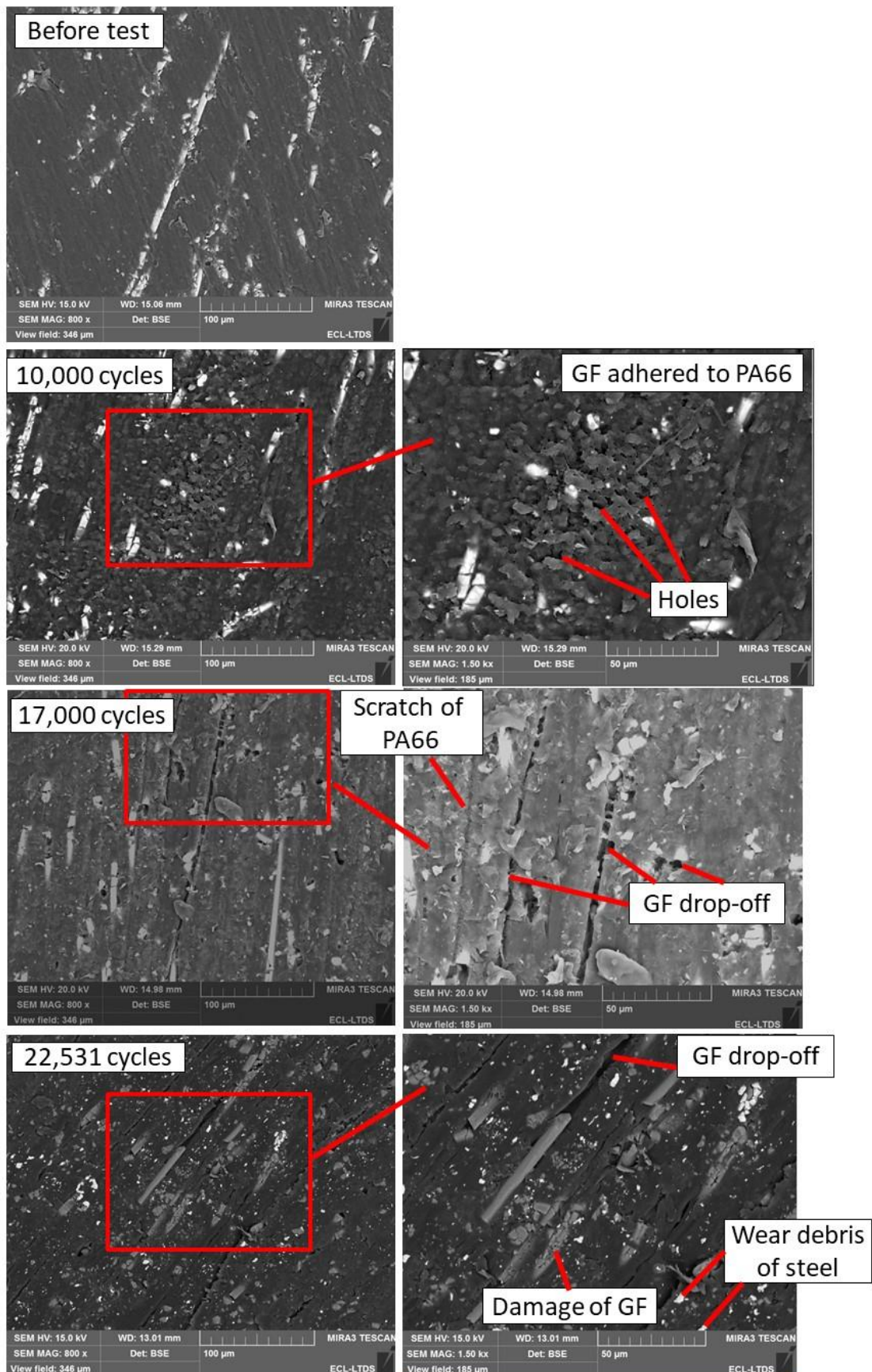


Fig. III. 15 SEM observations of the sliding surface of the composite after different numbers of cycles.

2.3 Effect of fiber orientation and change in the surface mechanical properties

The reason why the peeling of the composite was promoted especially in the center area was explained through the fiber orientation at the sliding surface of the composite ring. The differences in fiber orientation in the composite ring were evaluated quantitatively with an image analysis of the sliding surface of a composite ring in the process presented in Section 3.1 in Chapter II. Fig. III. 16 presents SEM BSE images of the sliding surface of composite in each area. Table III. 1 lists the calculated total area and total perimeter of GFs in each area. Both values are similar in each area, therefore it is confirmed that the differences of the wear in the composite in each area are not attributed to the total area or perimeter of GFs.

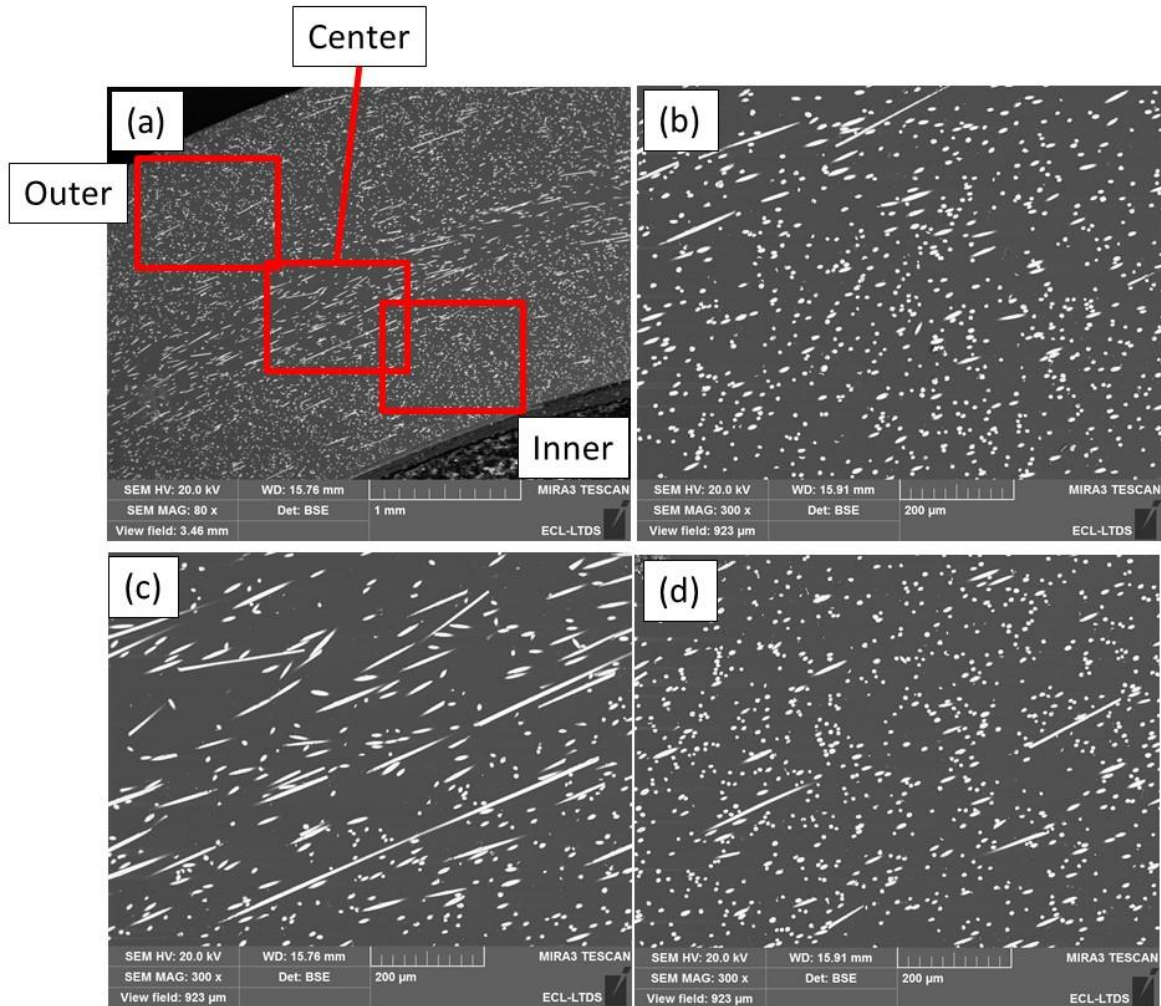


Fig. III. 16 SEM BSE images of the sliding surface before test of composite in each area: (a) global view; (b) inner position; (c) center position; (d) outer position.

Table III. 1 Calculated total area and total perimeter of GFs in each area (average values of different three positions).

Area	Area of GFs in sliding surface	Total perimeter of GFs
Inner area	$8.4 \pm 0.1\%$	25.3 ± 1.0 mm
Center area	$8.8 \pm 0.8\%$	23.3 ± 2.3 mm
Outer area	$8.0 \pm 0.2\%$	24.8 ± 1.3 mm

Fig. III. 17 presents the relationship between the circularity of the GF (explained in Section 3.1 in Chapter II) and cumulative area of GFs, and Table III. 2 lists the average value of C_{50} in each area (C_{50} is the value of the circularity when the cumulative area of GFs is 50%).

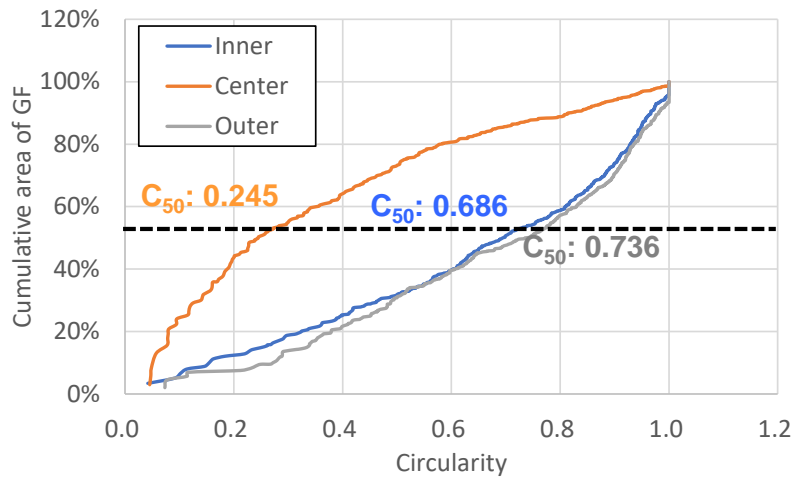


Fig. III. 17 Example of the relationship between the circularity of GFs and cumulative area of GFs.

Table III. 2 Values of C_{50} (the circularity when the cumulative area of GFs is 50%, the average value of different three positions).

Area	Values of C_{50}
Inner area	0.63 ± 0.09
Center area	0.25 ± 0.04
Outer area	0.73 ± 0.07

The results indicate that the circularity in the center area is much lower than in the inner/outer areas, meaning that the majority of GFs in the center area are aligned in parallel with the sliding direction. Therefore, the GFs can be easily peeled off because of the sliding shear stress; therefore, peeling of the composite material easily occurred. On the other hand, the circularity in the inner/outer areas is much higher than in the center area; therefore, the GFs are perpendicular to the contact surface in these areas, and the wear of the composite ring is reduced because GFs are hard to be peeled off by sliding shear stress.

In addition, the reason why the differences in GFs orientation occurred can be explained as follows: inside the metal die during the injection molding process, the solidification speed is much higher in the inner and outer areas of the composite ring because these parts are in contact with the surface of the metal die which is colder than the center part of the ring; therefore, the GFs are oriented to the direction of resin flow. On the other hand, in the center area of the composite ring, the solidification speed is much lower because this area is not in contact with the metal die; therefore the GFs flow before solidification occurs in the metal die.

To discuss the damage of the composite sliding surface quantitatively, the mechanical properties of the sliding surface measured by micro indentation were discussed. Using this method, the size of the indentation after a measurement was approximately 100 μm . Therefore, the mechanical properties of not only the fibers (diameter: 6.5 μm) and the PA66 itself, but also the composite itself, can be discussed. First, Fig. III. 18 shows the hardness and

Young's modulus of the sliding surface of GF 15% composite measured through micro indentation in each area before test. Average values in center area tend to be higher than in inner or outer area; however, significant differences are not observed considering the variations of results. These results were different from those which can be expected through the fiber orientation, in which fiber aligns in horizontal direction in center area as presented in Table III. 2, and may be related to the small difference of fiber area in each area as presented in Table III. 1. Besides, the Young's modulus through the micro indentation (measured in the compression direction) was 17.6-30.7% lower than that measured through the tensile test (5.9 ± 0.3 GPa).

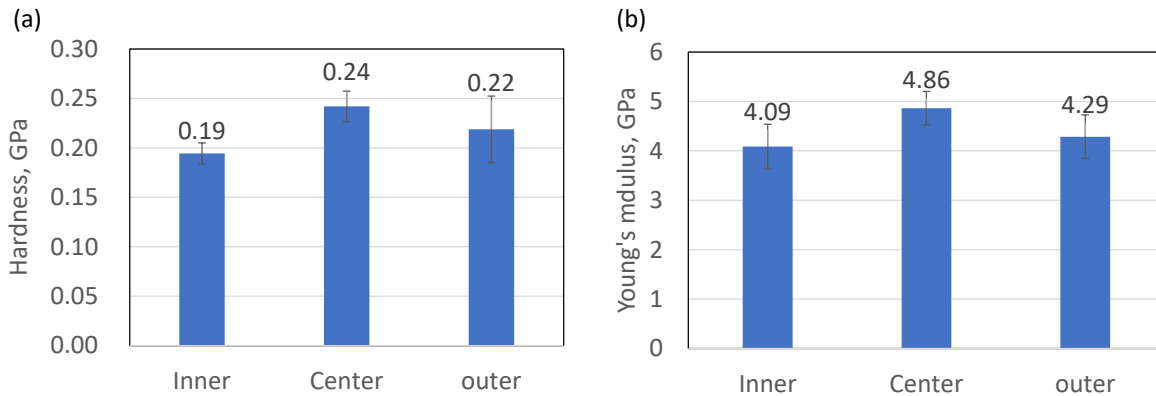


Fig. III. 18 (a) Hardness and (b) Young's modulus of the sliding surface of GF 15% composite measured through micro indentation in each area.

Next, in the samples after 10,000, 17,000 (before the sudden increase), and 19,900 cycles (just after the sudden increase in this test), the surface mechanical properties on the peeled and less-peeled area were investigated. Fig. III. 19 and Fig. III. 20 present the optical microscope observations of the sliding surface after 10,000 and 17,000 cycles respectively and results of the hardness and Young's modulus in each area. Measured values are the average values of 5 to 10 different points. On both peeled and less peeled area, the decreasing tendency in the hardness and Young's modulus was observed. However, the values were lower on the peeled area than less-peeled area. Fig. III. 21 represents the SEM images of the sliding surface after 17,000 cycles. In the less-peeled area which showed relatively higher mechanical properties, the adhesion between PA66 and GF can be ensured, and damage was not observed. In contrast, the damage including peeling of PA66 or GF and scratch of PA66 as observed in Fig. III. 15 was observed. Therefore, the difference in the damage on the surface can be related to the difference in the decrease in the mechanical properties.

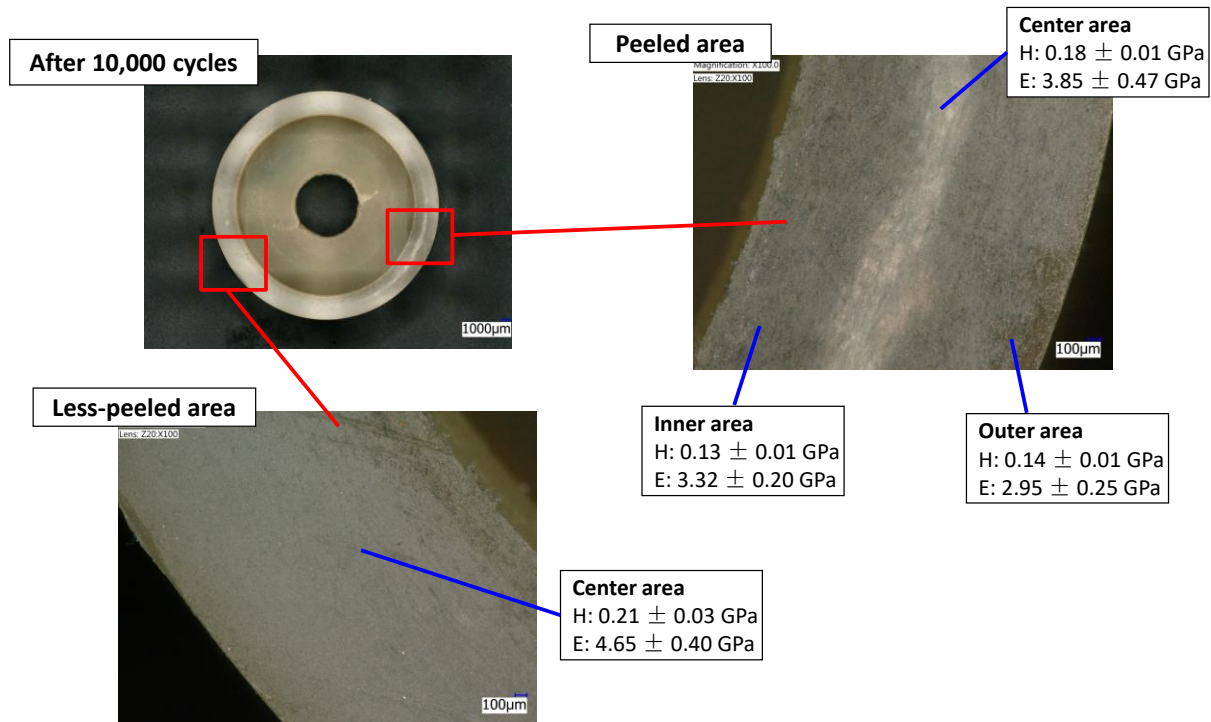


Fig. III. 19 Optical microscope observation of the sliding surface after 10,000 cycles and results of the hardness and Young's modulus in each area (H: hardness, E: Young's modulus).

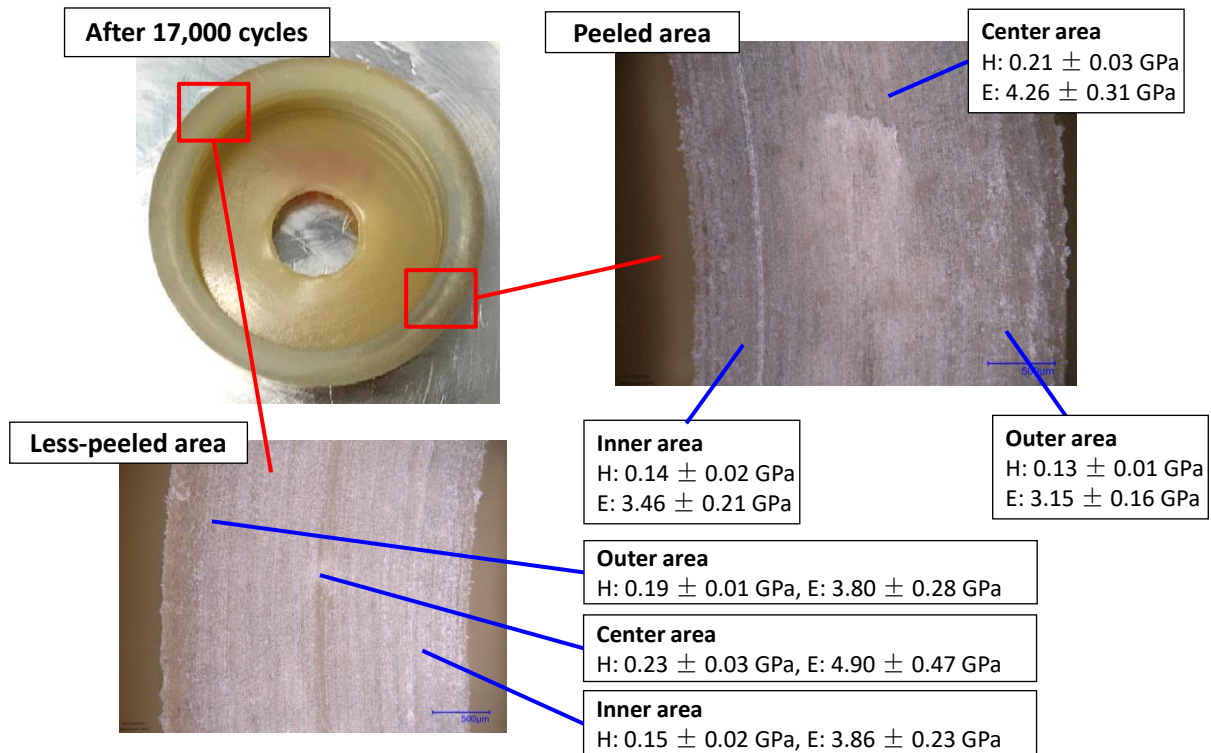


Fig. III. 20 Optical microscope observations of the sliding surface after 17,000 cycles and results of the hardness and Young's modulus in each area (H: hardness, E: Young's modulus).

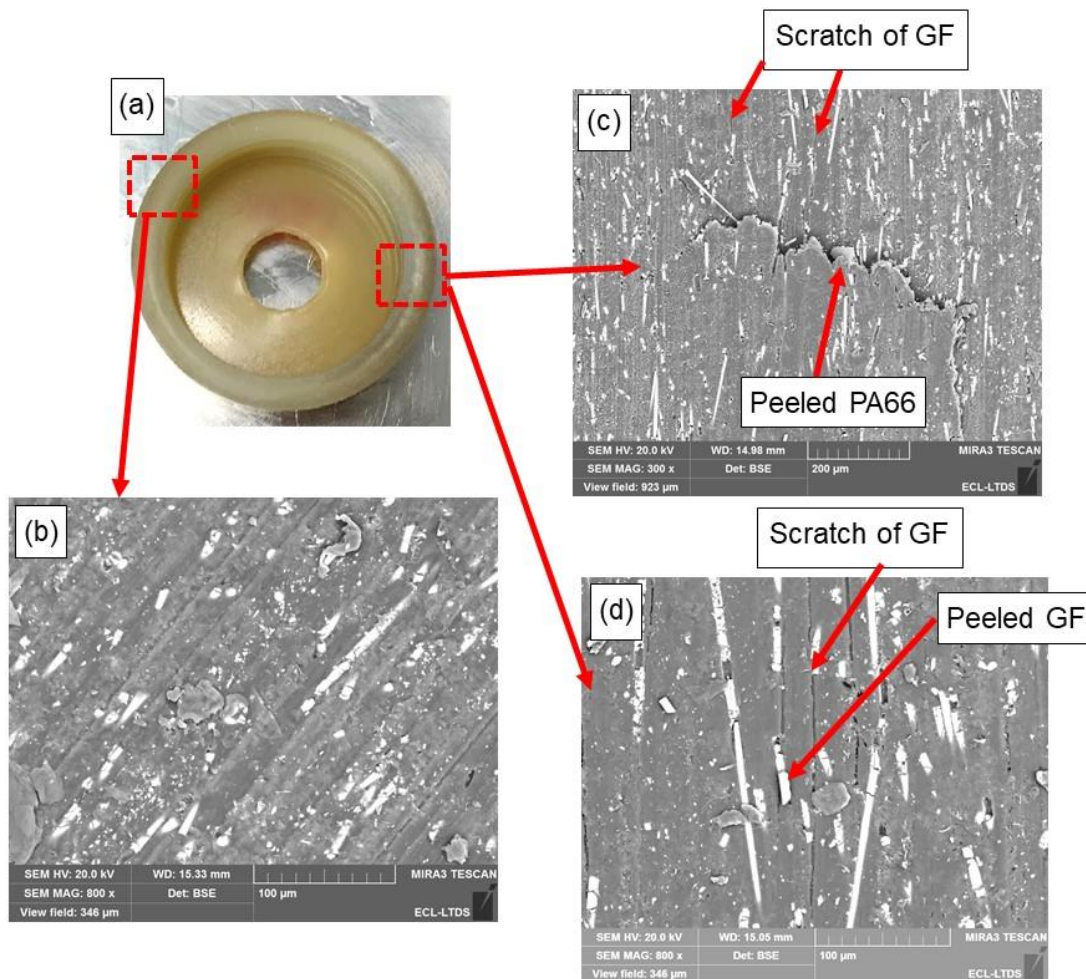


Fig. III. 21 (a) Optical microscope observation and SEM observations of (b) less-peeled area; (c) and (d) peeled area of the composite ring after 17,000 cycles.

Furthermore, Fig. III. 22 shows the optical microscope observations of the sliding surface after 19,900 cycles (just after the sudden increase in the vertical displacement) and results of the hardness and Young's modulus in each area. On the severely peeled area, the values of the hardness and Young's modulus significantly decreased compared to 10,000 or 17,000 cycles, whereas severe decrease in the mechanical properties were not observed on less-peeled area even after 19,900 cycles. In summary, Fig. III. 23 presents the obtained hardness and Young's modulus in a center area on less-peeled and a peeled area for different numbers of cycles. The damage to the sliding surface was related to the mechanical properties in a quantitative manner. Considering these mechanical properties and the observations made using a microscope and SEM, the friction coefficient is considered to have increased owing to the damage incurred by the sliding surface, and initial creep was induced by the decrease in the mechanical properties of the composite due to the damage (peeling off of GFs and scratching of PA66). Afterward, the GFs dropped off continuously from the sliding surface and further wear was promoted as the sliding cycles increased in number.

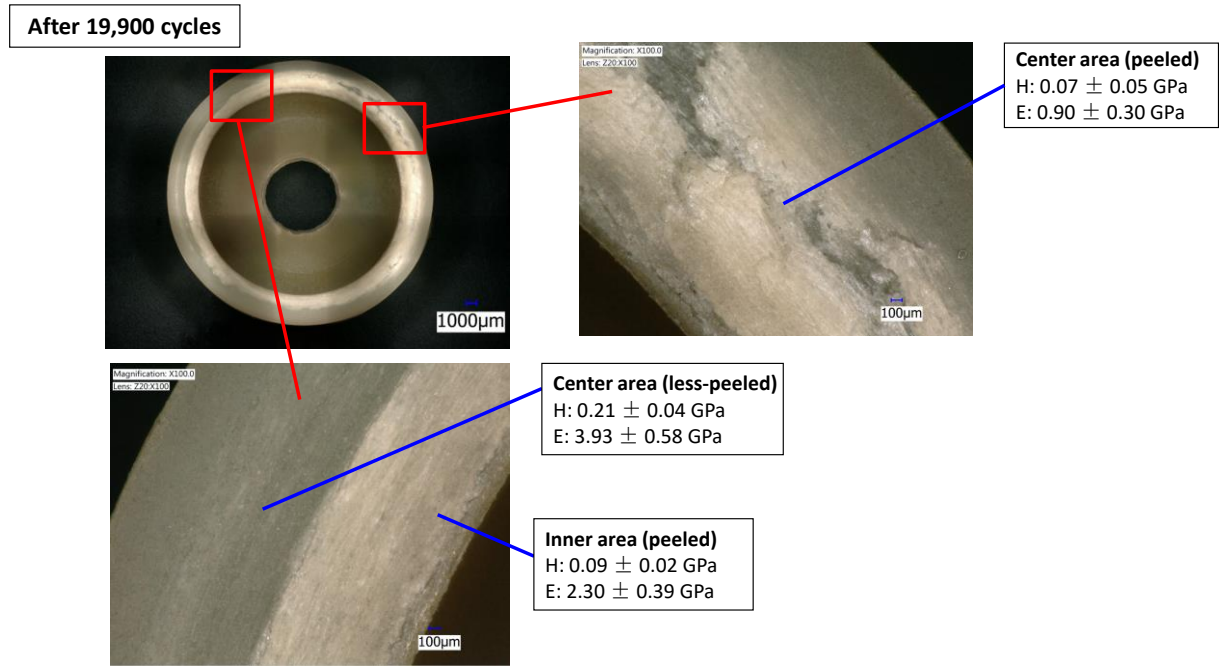


Fig. III. 22 Optical microscope observations of the sliding surface after 19,950 cycles and results of the hardness and Young's modulus in each area (H: hardness, E: Young's modulus).

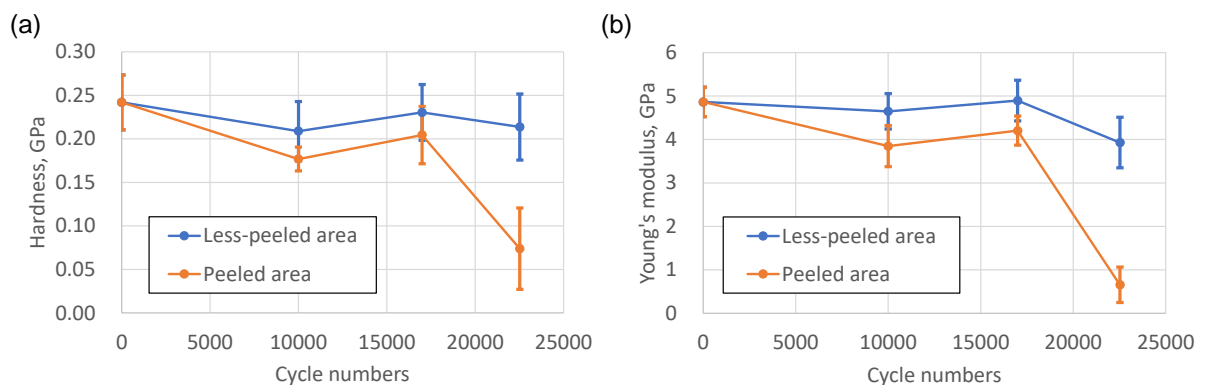


Fig. III. 23 Young's modulus of the sliding surface of the composite ring at different cycles (measured by micro indentation, average values of five measurements).

2.4 The difference of the tribological properties in unreinforced PA66 and GF-reinforced PA66 composite

In addition, the differences of the tribological properties between GF 15% reinforced composite and unreinforced PA66 were investigated. Fig. III. 24 presents the evolution of the friction coefficient, temperature, and vertical displacement under the same test conditions as the previous ones. The Hertzian contact pressure at room temperature was 189 MPa for the GF 15% composite, and 136 MPa for the unreinforced PA66, considering the lower Young's modulus of the unreinforced PA66 than GF composite. Sliding tests were conducted at least twice for each material.

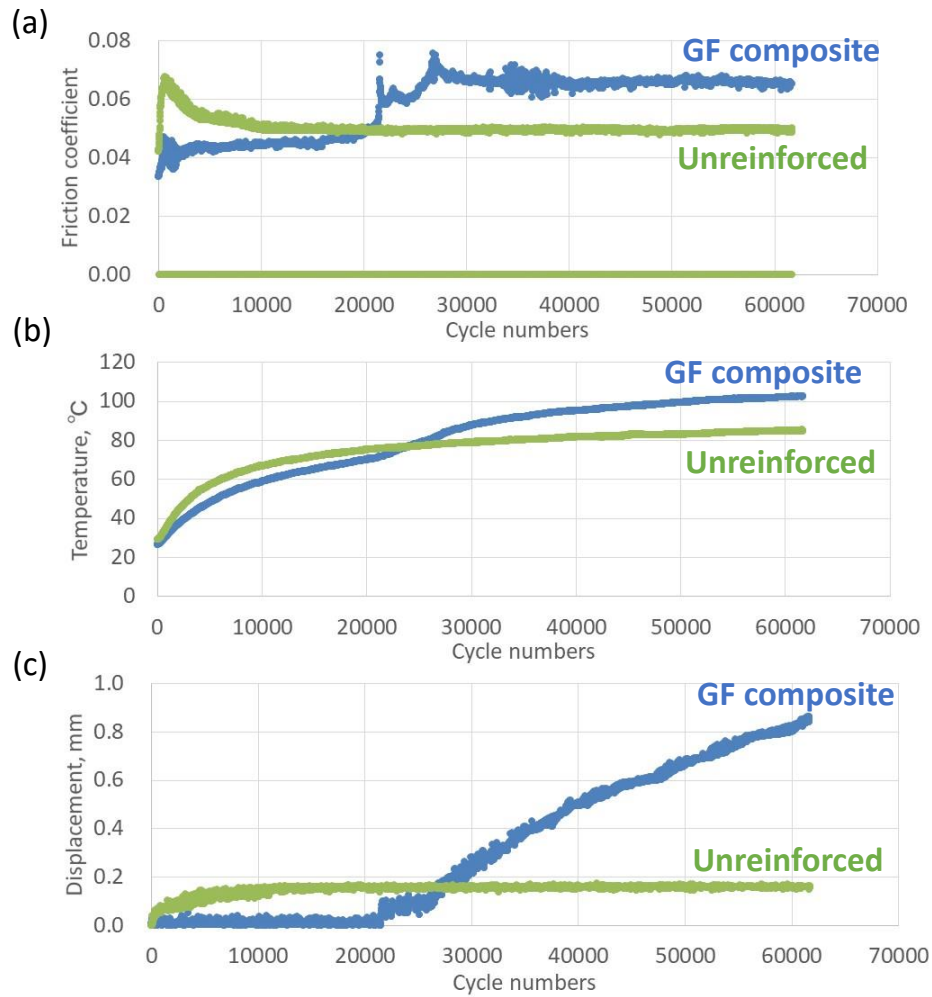


Fig. III. 24 Evolutions of (a) the friction coefficient; (b) the temperature; (c) the vertical displacement of the unreinforced PA66 and GF-reinforced composite.

During the initial 20,000 cycles, the friction coefficient, the temperature, and the vertical displacement of the unreinforced PA66 exhibit higher values than those of the GF-reinforced composite, even under higher contact pressure in the GF-reinforced composite. However, sudden increase in the friction coefficient and the vertical displacement are observed in the GF composites after 20,000 cycles, and the displacement of the GF composite increases although that of the unreinforced PA66 shows stable values until 61,700 cycles. The temperature in the unreinforced PA66 shows lower values than that of the GF composite after 25,000 cycles, as the sliding heat generation was reduced by lower friction coefficient.

Fig. III. 25 presents the optical microscope observations of the sliding surface of the ring specimens and the wear/creep/total height loss of the ring specimens after each number of cycles. The wear height loss of the unreinforced PA66 was relatively small, and 75% of the total height loss was due to creep. No severe wear on the sliding surface was observed. In contrast, the wear had a larger effect than the creep and all the sliding surface was severely damaged in the GF composites. Considering these results, the initial creep (until 20,000 cycles) of the unreinforced PA66 with lower Young's modulus can be reduced by the GFs reinforcements; however, the adverse effect of wear typically occurs in the GF composite with the increase in the sliding cycle numbers. In addition, the effect of the wear is significantly lower in the unreinforced PA66 under grease lubricated conditions, and creep which is

induced by the wear (the damage of the sliding surface and the decrease in the surface mechanical properties) can be reduced. Thus, in the material development of the GF composite, the improvement in the wear resistance is supposed to be significant. In addition, significant lower steel wear was observed using unreinforced PA66 than that using GF composite.

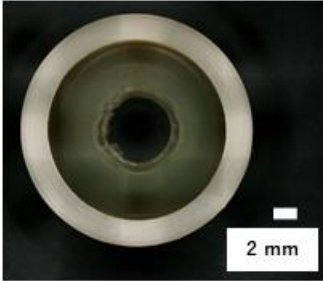
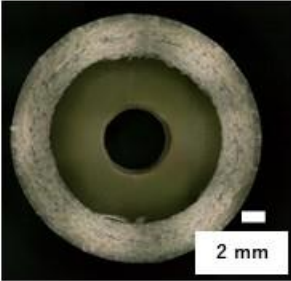
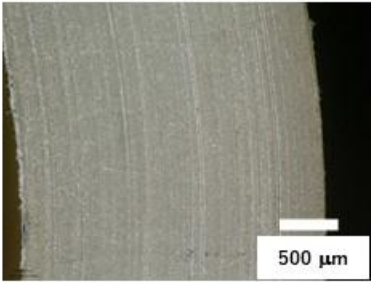

	Unreinforced PA66 after 61,704 cycles	GF 15% composite after 61,665 cycles
Entire sliding surface		
Magnified image		
Wear height loss	0.023 mm	0.575 mm
Creep height loss	0.062 mm	0.242 mm
Total height loss	0.085 mm	0.817 mm

Fig. III. 25 Optical microscope observations of the sliding surface of the ring specimens and the wear/creep/total height loss of the ring specimens.

3. The effect of fiber orientation on the wear behavior of steel counterpart and composite

3.1 Wear behavior of counterpart steel and effect of the fiber orientation in the composite ring

The wear behavior of the counterpart steel cylinder was investigated. Fig. III. 26 shows the wear volume of the steel cylinder for different cycles under the test conditions discussed in Section 2.1. Wear was measured by interferometry and corresponds to the total wear volume of the four cylinders. The wear volume increased proportionally with the number of cycles, contrarily to what is observed in the wear of the composite.

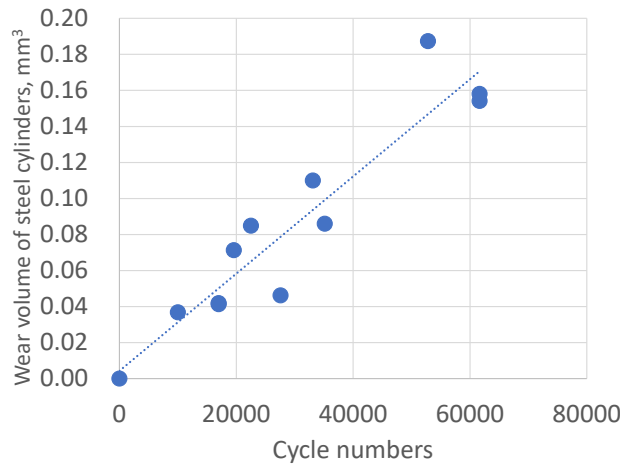


Fig. III. 26 Wear volume of steel cylinder for different numbers of sliding cycles.

Fig. III. 27 presents an optical microscope observation of a steel cylinder after 22,531 cycles (just before the first sudden increase of the displacement), interferometric images of the cylinder before and after removal of the cylindrical shape for a better visualization of the wear, and a central 2D profile measured through interferometry. The left area corresponds to the inner diameter side of the composite ring, and the right area corresponds to the outer diameter side of the composite ring. Severe wear of the steel cylinder, which appears to be 2-body abrasive wear, occurred even before the sudden increase of the vertical displacement. This is related to the relative hardness of the steel and of the GFs.

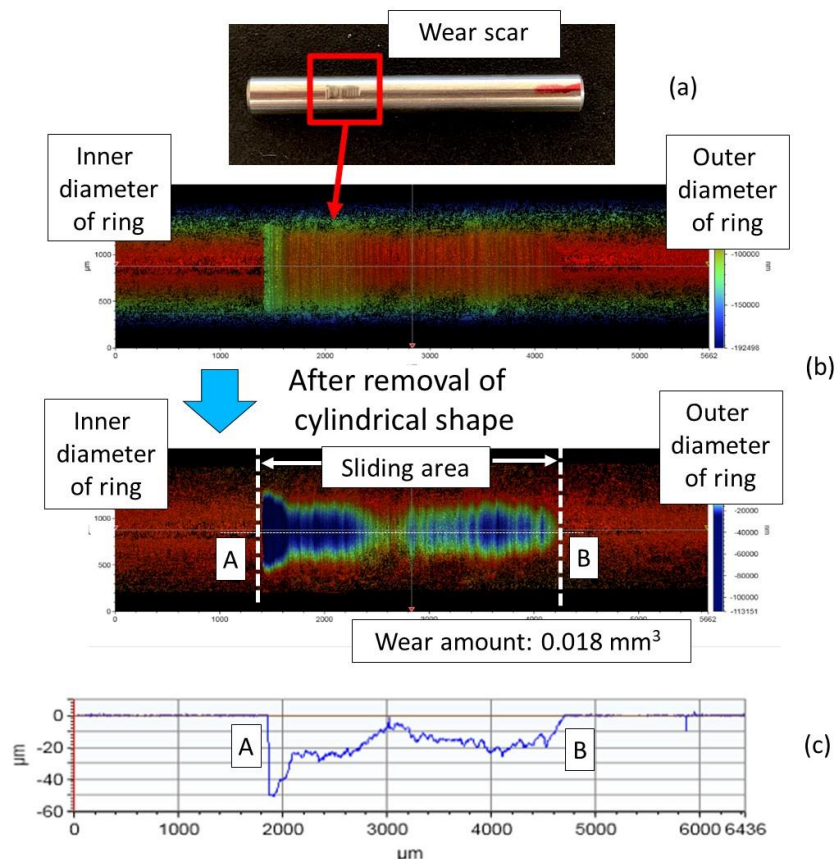


Fig. III. 27 Observation of steel cylinder after 22,531 cycles by (a) optical microscope and (b) 3D images of interferometry; (c) central 2D profile measured through interferometry.

The hardness of GF was measured using the process explained in Section 4.5 in Chapter II. Fig. III. 28 shows the load displacement curve for the measurements and the obtained hardness of the GF in each direction. The hardness of GF was approximately 5.7 GPa and this value is much higher than the hardness of steel without heat treatment (4.5 GPa). No difference in hardness was observed between the horizontal and perpendicular directions. Therefore, the higher hardness of GF than steel is supposed to have induced the wear of the steel counterpart.

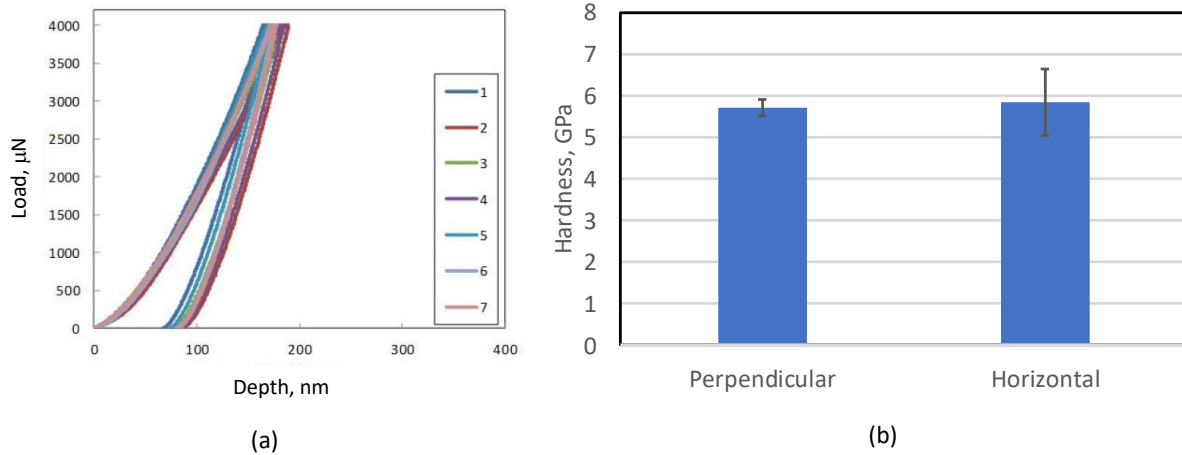


Fig. III. 28 (a) Load-displacement curves obtained using nano indentation measurements and (b) measured hardness of GF in each direction (average values in seven measurements).

Furthermore, the wear of the steel cylinder in the center area was much lower compared to the surface sides, as observed in Fig. III. 27. This exhibits an inverse tendency to the wear of the composite ring, as discussed in Section 2.2. The differences in wear for each area of the steel can also be discussed through the differences in fiber orientation in the composite ring as listed in Table III. 2. Lower circularity is measured in the center area than in the inner/outer areas, meaning that the majority of GFs in the center area are aligned in parallel with the sliding direction. Therefore, the number of edges of GFs which have much higher aggressive effects on the steel is lower, and wear in this area of the steel cylinder was much lower. On the other hand, the circularity of the inner/outer areas is much higher than in the center area; therefore, the GFs are perpendicular to the contact surface. As a consequence, the wear on the steel cylinder is promoted because the number of edges of GFs is much higher compared to the center area, as observed in Fig. III. 16.

3.2 Effect of the fiber exposure on the sliding surface

In Sections 2 and 3.1, the composite ring specimens were cut by 3 mm and polished to simulate the sliding surfaces of actual gear tooth surface which are formed by mechanical hob-cutting, as presented in Section 2.1.4.1 in Chapter II. On the other hand, if the gear teeth are formed through only the injection molding (without mechanical hob-cutting), the fiber orientation on the sliding surface is supposed to change. In order to simulate this sliding surface condition, GF composite ring specimens without mechanical cutting (conditions just after the injection molding) were prepared and the effect on the tribological properties of the composite and wear resistance of the steel were investigated. Fig. III. 29 shows SEM observations, binarization images through image analysis, and estimated area of GFs on the sliding surface with/without mechanical cutting before the sliding tests.

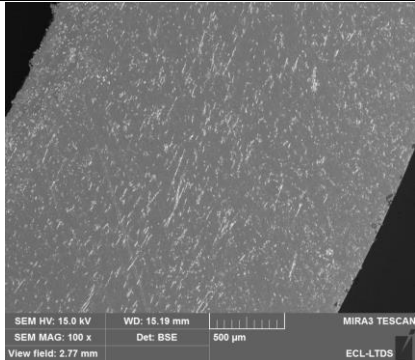
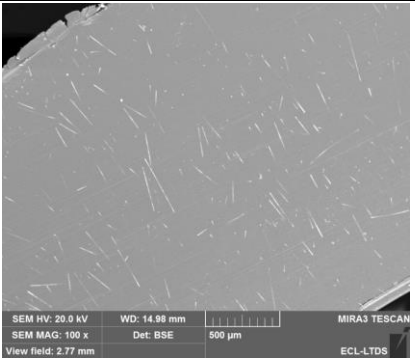
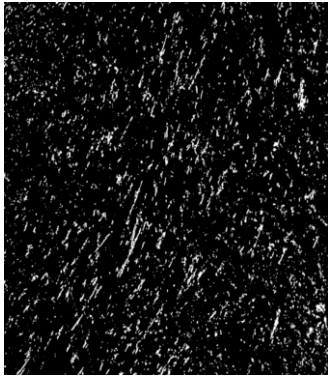
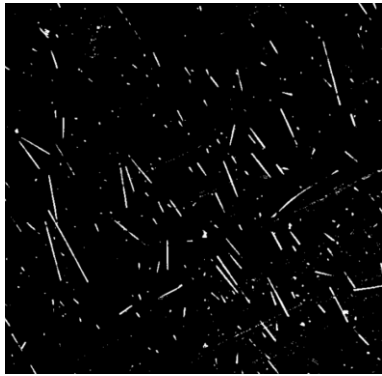
	With mechanical cutting	Without mechanical cutting
SEM observations		
Binarization images by image analysis		
Area of GFs on the sliding surface	7.2%	2.5%

Fig. III. 29 SEM observations, binarization images by image analysis, and estimated area of GFs on the sliding surface with/without mechanical cutting in sliding direction.

The proportion of exposed GFs on the sliding surface after mechanical cutting is three times higher than that without mechanical cutting. This is because the skin layer of PA66 was formed on the sliding surface of the ring specimens during the injection molding process, leading to lower amount of GFs. Fig. III. 30 presents the evolutions of the friction coefficient, the temperature, and the vertical displacement with/without mechanical cutting in the same sliding test conditions as Section 2.

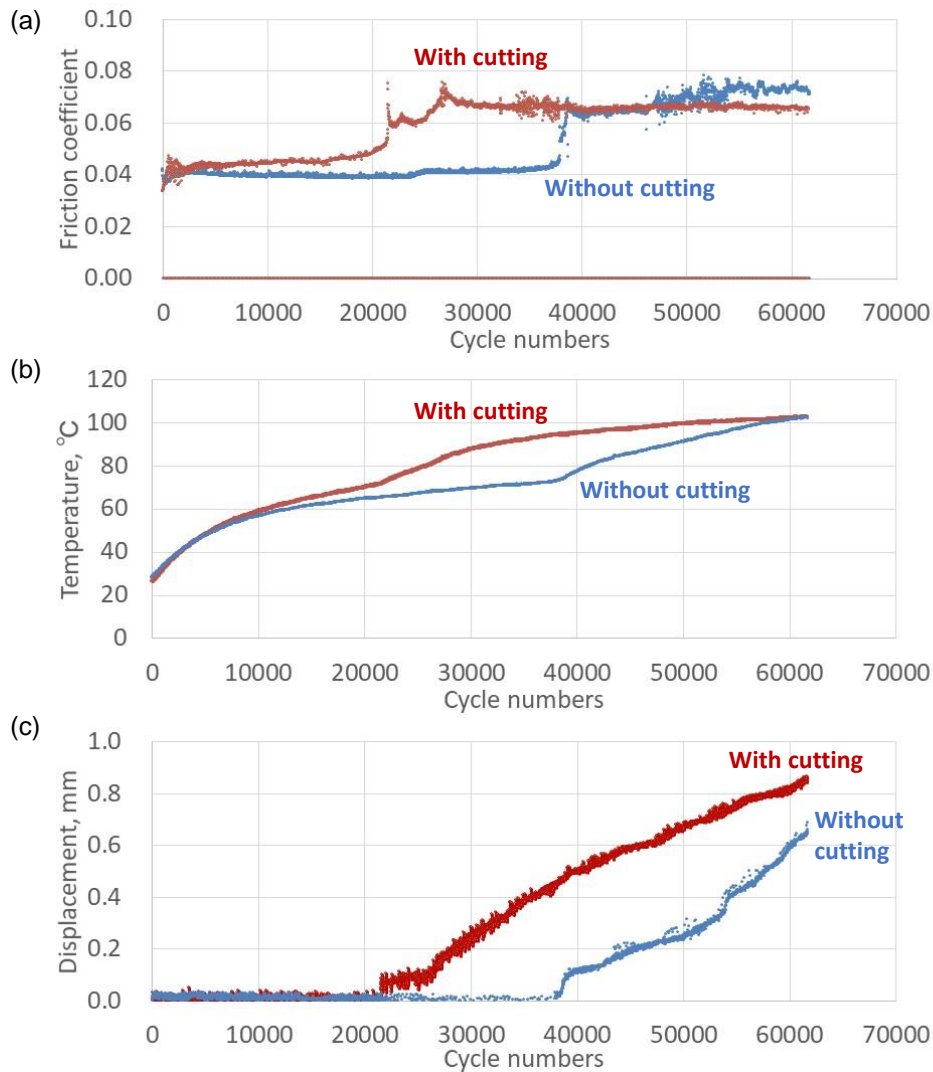


Fig. III. 30 Evolutions of (a) the friction coefficient; (b) the temperature; (c) the vertical displacement with/without mechanical cutting.

Cycle number at the sudden increases in the friction coefficient and vertical displacement becomes approximately 1.8 times higher in the case without mechanical cutting. In addition, low friction coefficient is supposed to reduce the sliding heat generation. Thus, better tribological properties were observed in the case without mechanical cutting. This is because the numbers of GFs and interface between GFs and PA66 which are the origin of the composite can be decreased. In addition, Fig. III. 31 shows optical microscope observation images, interferometric images, 2D profiles, and wear amounts of the steel cylinders after the sliding tests for 61,500 cycles with/without mechanical cutting. Wear of the steel cylinder was significantly lower in the case without cutting because of the low GFs area and interface between GFs and PA66 on the sliding surface. Therefore, the behavior of the GF composite without cutting is intermediate between the behavior of the GF composite with mechanical cutting and that of the unreinforced PA66, as the amount of GFs in the surface without mechanical cutting is lower than the one in the surface with mechanical cutting. Thus, the direct formation of the gear teeth through the injection molding can also contribute to reduce

the aggressive effect of GFs to the steel counterpart (namely steel worm shaft in the actual worm reducer).

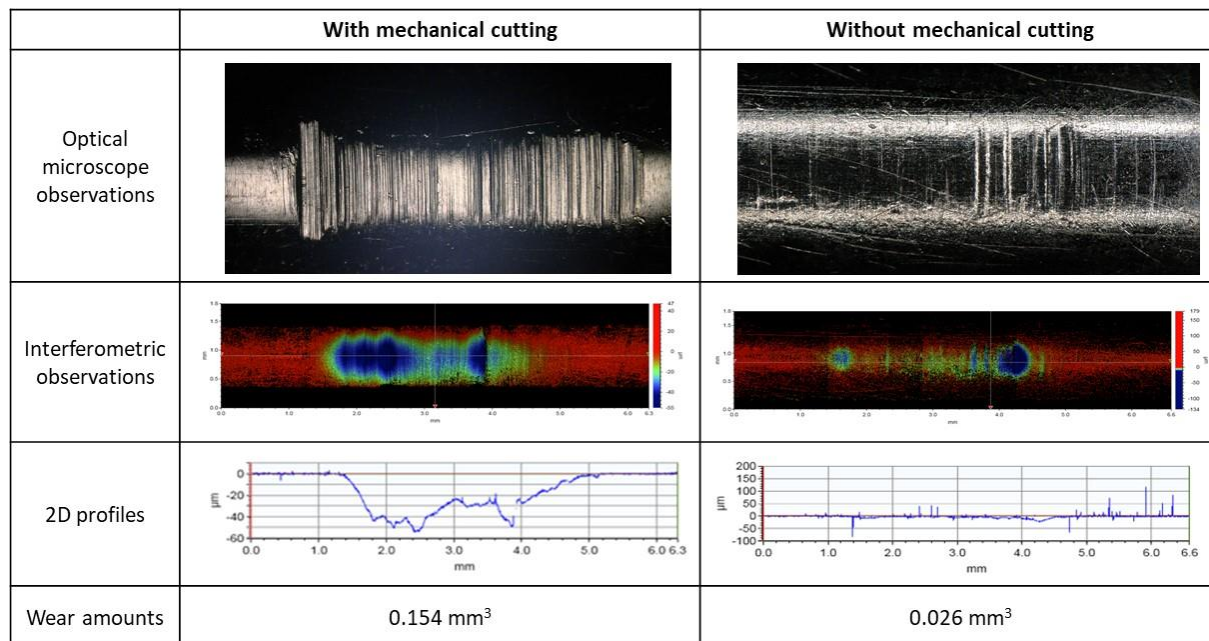


Fig. III. 31 Optical microscope observed images, interferometric images, 2D profiles, and wear amounts of the steel cylinders after the sliding tests for 61,500 cycles with/without mechanical cutting.

4. Contribution of each parameter to the increase of friction and damage

The individual contributions of four parameters: the evolution of the sliding surface, the contamination of grease by wear debris, the wear of the steel cylinder, and the increasing sliding surface temperature were investigated by performing sliding tests under different conditions. Steel cylinders without heat treatment (hardness: 4.5 GPa) were used, and the same normal load and sliding speed as discussed in Section 2 were applied in all tests to clarify the contribution of each parameter separately.

First, the effect of the sliding surface damage was investigated. Pre-damaged composite rings after 17,000 cycles, 20,000 cycles, and 30,000 cycles were prepared, and sliding tests were performed using these pre-damaged rings under the same test conditions, using new steel cylinders and grease. Fig. III. 32 presents the sliding surfaces before the sliding tests and the results of the sliding tests. The average friction coefficient becomes much higher with increased pre-damaged cycles. The temperature depends on the value of the friction coefficient, and a higher friction coefficient induces a greater increase of the temperature. In addition, the sudden increase of the vertical displacement occurs much earlier with increased pre-damaged cycles. Considering these results, it is worth mentioning that the initial surface condition of the composite ring has a significantly strong effect on the increase in friction and therefore on the ultimate damage.

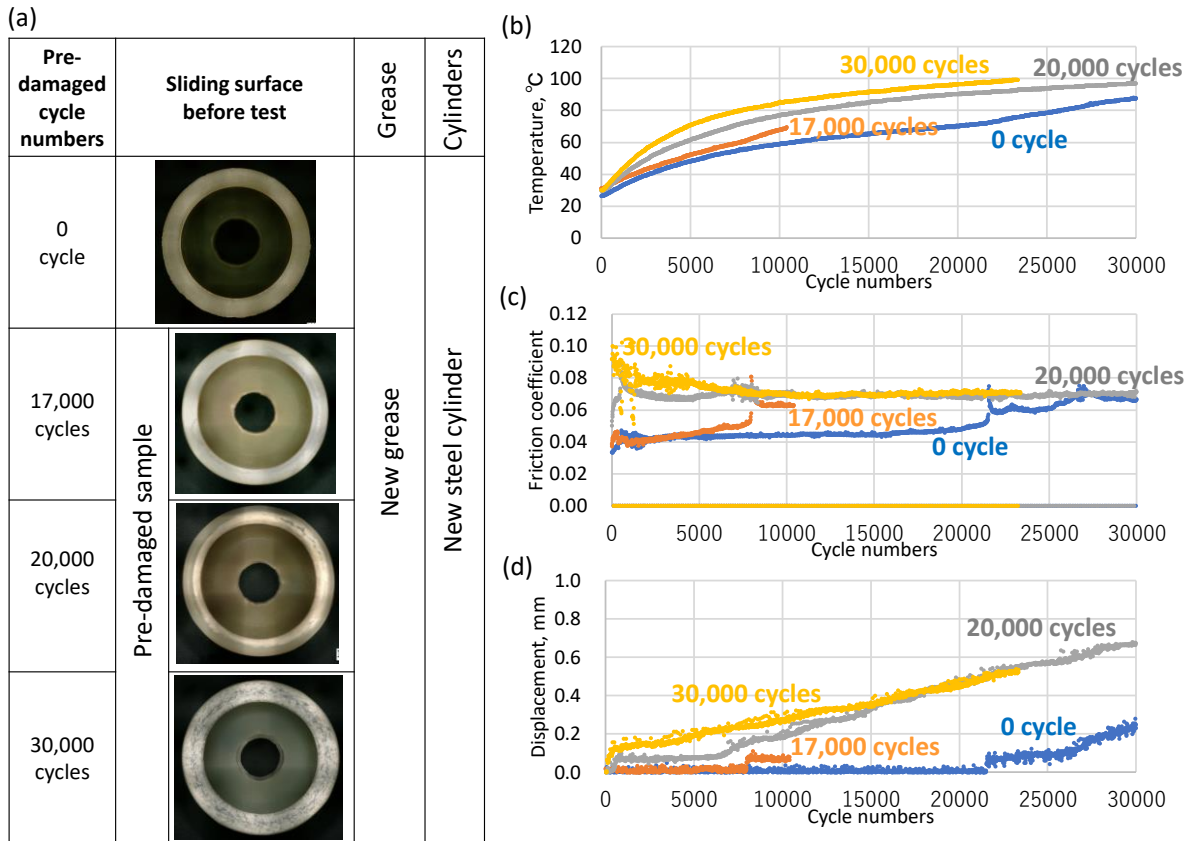


Fig. III. 32 (a) Sliding surface of pre-damaged composite rings before sliding tests; (b) evolutions of temperature; (c) evolutions of friction coefficient; (d) evolutions of displacement.

The effect of the contamination of grease by wear debris on the friction and damage was investigated. After a sliding test of 61,500 cycles under the standard test conditions, grease was collected. This grease contains wear debris consisting of steel and GFs, as explained in Section 2.1 (Fig. III. 6). A new sliding test was then performed using the same amounts of this contaminated grease to compare the results when using new grease. Fig. III. 33 presents the sample holder of a steel cylinder with the tested grease and the results of sliding tests. The sliding time evolution of the friction coefficient, temperature, and displacement were the same in both greases. In addition, the wear amount and morphology of the counterpart steel was also at the same level (with using new grease: 0.156 mm^3 , using the contaminated grease: 0.151 mm^3 in the total wear amount of four cylinders measured by interferometry) as presented in Fig. III. 34.

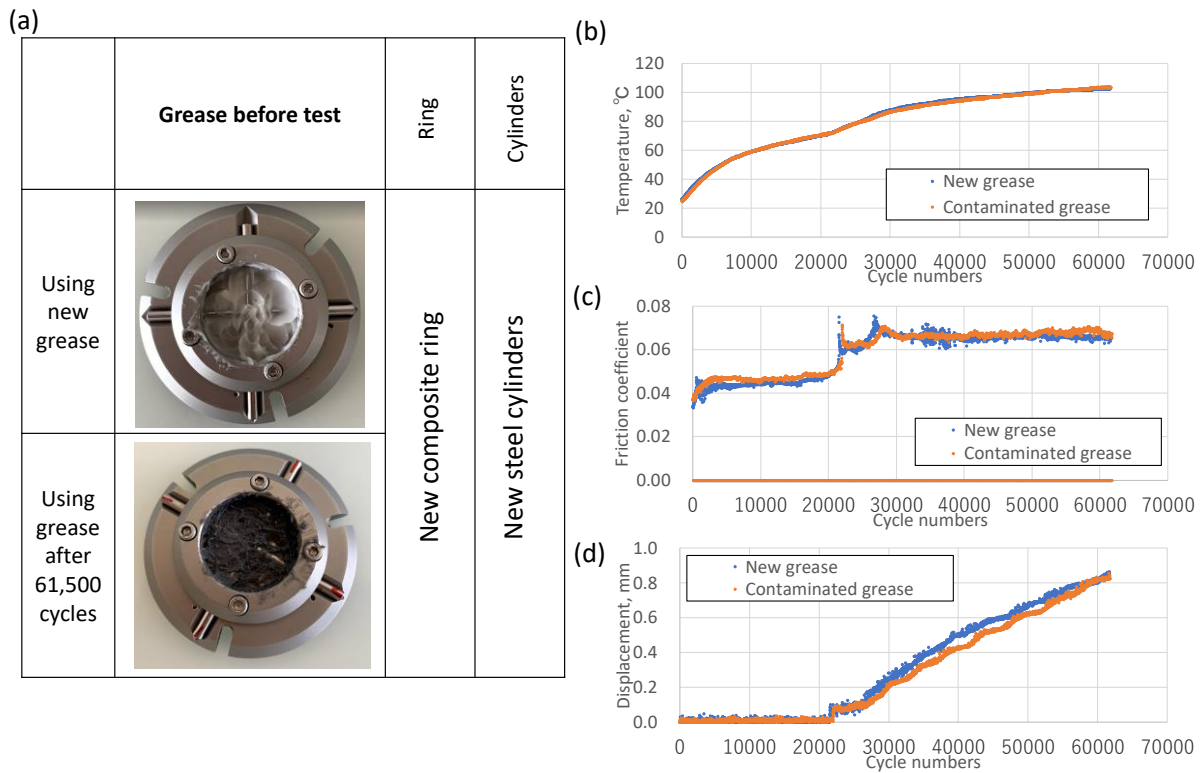


Fig. III. 33 (a) Grease in sample holder before sliding tests; (b) evolutions of temperature; (c) evolutions of friction coefficient; (d) evolutions of displacement.

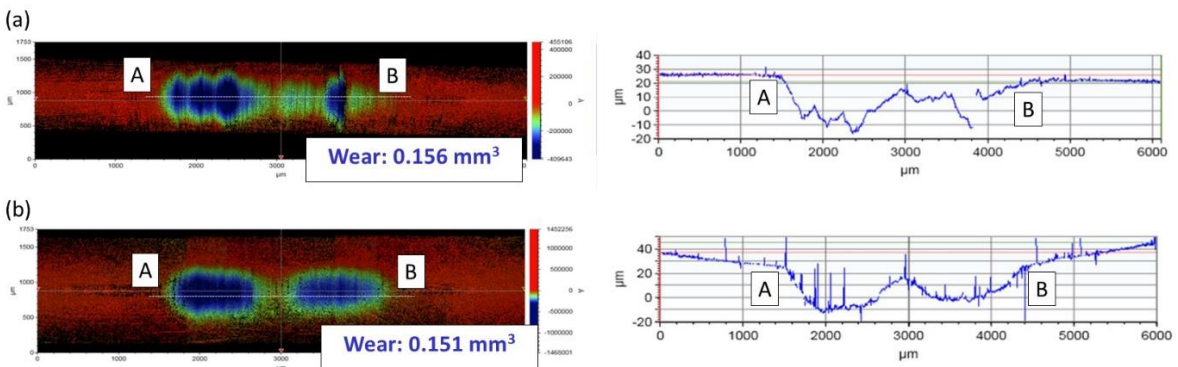


Fig. III. 34 Observations and central 2D profiles of counterpart steel after sliding test by interferometric measurement (a) using new grease; (b) using contaminated grease.

Given these results, there is no effect of the initial presence of wear debris in grease on the friction and wear of composite and steel. In addition, the wear mode of the steel is not 3-body abrasion; rather it is 2-body abrasion, because the wear debris of dropped off GFs and steel which were present in the contaminated grease had no negative effects on the tribological properties of the contact, and wear of the steel is affected by the GFs embedded in the PA66 when considering the wear scar of steel presented in Fig. III. 6. Furthermore, the wear mode of the composite was also not 3-body abrasion, and the wear resistance of the composite is dominated by the modification of its sliding surface, as mentioned above.

The effect of the worn steel cylinder was also investigated. Pre-damaged steel cylinders after a 17,000 cycle sliding test were prepared, and a new sliding test was performed using these pre-damaged cylinders with new composite rings and grease. Fig. III. 35 presents the

steel cylinders before and after the sliding tests. The friction coefficient tends to decrease when using the pre-damaged steel cylinders compared to the results with new cylinders, and the temperature decreased. In addition, when using the pre-damaged steel cylinders, the sudden increase of the vertical displacement occurs much later than when using new cylinders. The reason why using the pre-damaged steel cylinders improved the tribological properties of the contact appears to be a decrease of the contact pressure when using the worn cylinders. Therefore, the friction coefficient and temperature decreased, and wear resistance was improved.

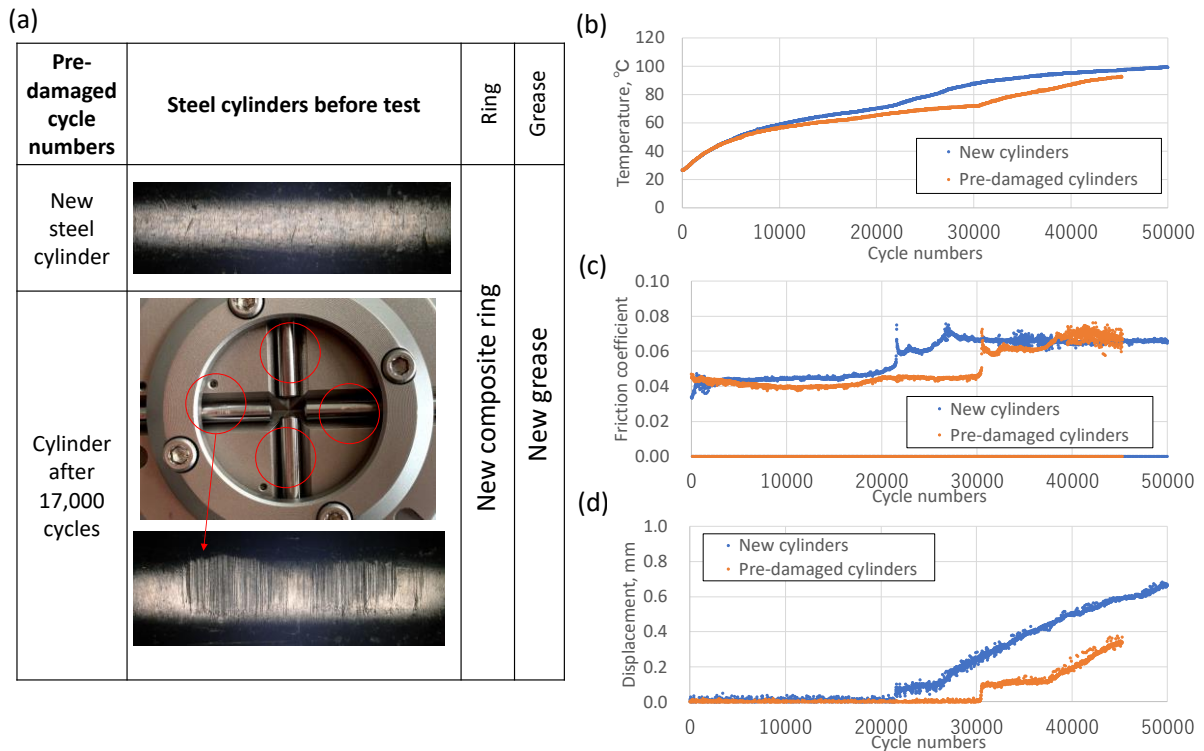


Fig. III. 35 (a) Sliding surface of a pre-damaged steel cylinder before sliding tests; (b) evolutions of temperature; (c) evolutions of friction coefficient; (d) evolutions of displacement.

Additionally, the effect of the increase of temperature was investigated by performing sliding tests in which the test was stopped after 17,000 cycles and restarted once the temperature fell to room temperature. Fig. III. 36 presents the test conditions. Test no. 1 used the normal test conditions without stopping after 17,000 cycles. In test no. 2, the sliding test was intentionally stopped after 17,000 cycles (before the sudden increase of the vertical displacement) and the temperature decreased to room temperature (the normal load was removed to avoid creep during the cooling period), and the sliding test was restarted without changing the grease or steel cylinders. In test no. 3, the sliding test was stopped at the same number of cycles and the temperature was allowed to decrease under the same conditions, but the grease was replaced with new grease before restarting the sliding test. In test no. 4, steel cylinders were replaced with new ones; however, the grease was not changed before the restart of the sliding test after 17,000 cycles. Furthermore, in test no. 5, the grease and cylinders were both replaced after 17,000 cycles and the sliding test was restarted. Fig. III. 36 (b), (c), and (d) present these test results.

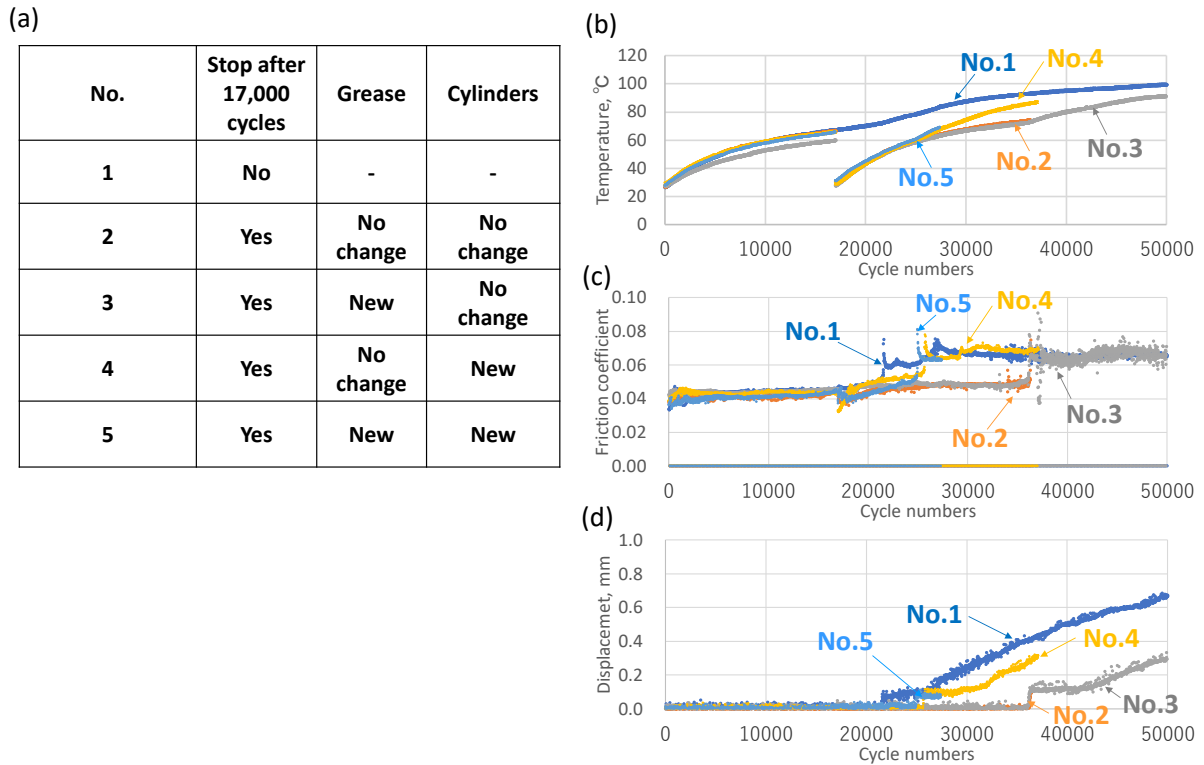


Fig. III. 36 (a) Test conditions; (b) evolutions of temperature; (c) evolutions of friction coefficient; (d) evolutions of displacement.

Comparing the results of tests no. 1 and no. 2, the sudden increase of the friction coefficient and vertical displacement occurs much later when the test is stopped after 17,000 cycles than when the test is not stopped. This is attributed to the recovery of the surface mechanical properties of the composite ring from the decrease of the temperature; the tribological properties were improved compared to the continuous sliding condition. Thus, it can be stated that the increase in temperature deteriorates the tribological properties. Comparing the results of tests no. 2 and no. 3, very similar results were obtained, even if the grease was replaced after the stop at 17,000 cycles in test no. 3, further verifying that there are no adverse effects due to contamination of the grease by wear debris, as mentioned previously. Comparing the results of tests no. 2 and no. 4, the sudden increase of the friction coefficient and vertical displacement occurs much earlier in test no. 4 than in no. 2. This result is attributed to the increase in contact pressure that results after replacing the worn cylinders with new ones in test no. 4, as mentioned previously. In addition, comparing tests no. 4 and no. 5, the timing of the sudden increases is the same. This is also attributed to the fact that contamination of the grease has no effect on the tribological properties, because the wear mode is not 3-body abrasion but is rather 2-body abrasion.

Consequently, the wear of the composite and particularly the linear increase in the vertical displacement are mainly dependent on the number of contact cycles and the contact pressure, and is less dependent on the contamination of the grease by wear debris or wear of the steel cylinder. Therefore, we can conclude that the wear of the composite could be induced by contact fatigue, generating the maximum von-Mises stress below the contact surface, which can induce the peeling observed.

5. Effects of the hardness of the steel counterpart

As discussed in Section 2.5 in Chapter I, the hardness of counterpart steel influences the production process of actual worm reducer. The effects of the hardness of the counterpart steel cylinder on the tribological properties were investigated. Tests were performed with cylinders having different values of hardness (from 3.9 GPa to 9.9 GPa, measured by micro indentation). Total sliding cycles were 33,000 cycles. Fig. III. 37 presents the estimated wear, creep, and total height loss of the GF composite ring for different values of steel cylinder hardness. Fig. III. 38 shows the wear volume of the counterpart steel cylinders for different values of hardness (total of the wear of four cylinders).

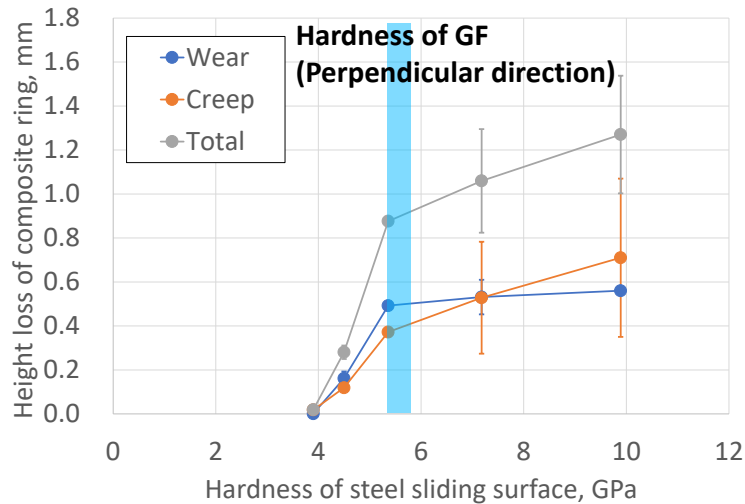


Fig. III. 37 Wear, creep, and total height loss of composite ring for different hardness values of steel cylinders, as measured by micro indentation (average values of two measurements).

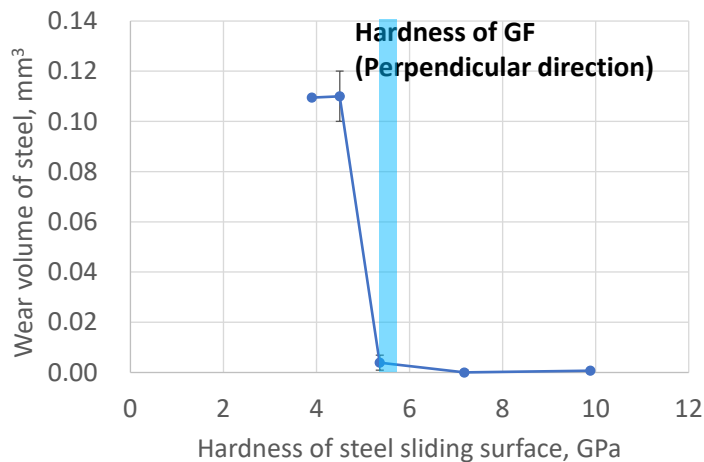


Fig. III. 38 Wear volume of counterpart steel cylinder for different hardness values. Hardness is measured by micro indentation (average values of two measurements).

Fig. III. 39 presents the results for each sliding test.

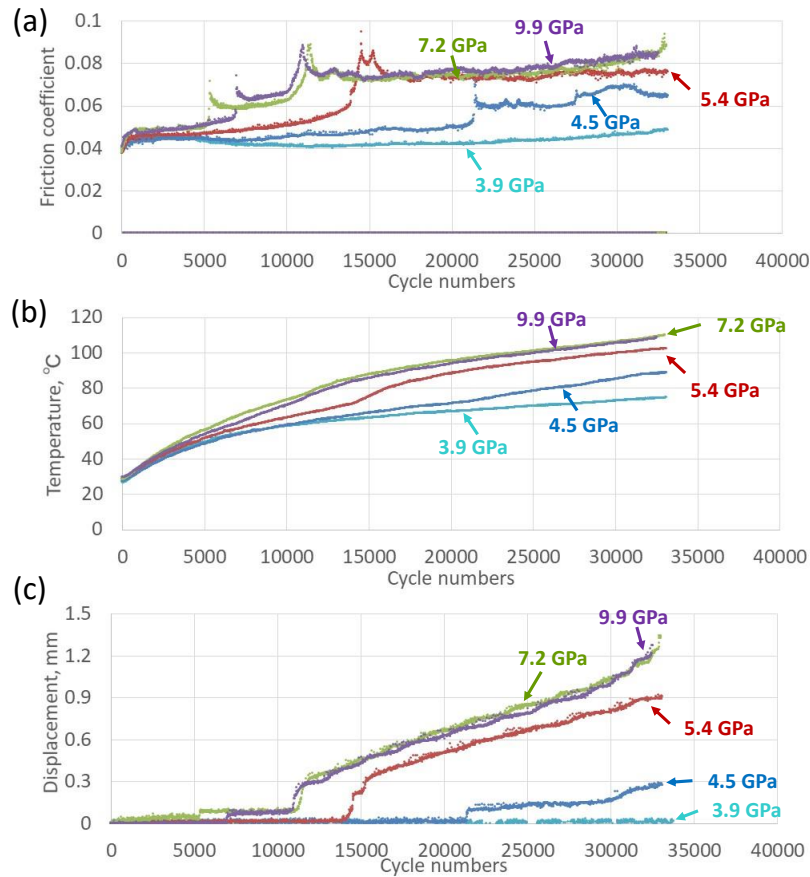


Fig. III. 39 Test results for different values of hardness of steel cylinders; (a) evolutions of friction coefficient; (b) evolutions of temperature; (c) evolutions of displacement.

Fig. III. 40 presents microscope observation images of the sliding surface of the composite ring after the tests.

Hardness of steel	3.9 GPa	4.5 GPa	5.4 GPa
Composite ring sliding surface			
Hardness of steel	7.2 GPa	9.9 GPa	
Composite ring sliding surface			

Fig. III. 40 Microscope observations of sliding surface of composite rings after tests using counterpart steel cylinders with different values of hardness.

It is observed that wear and creep of the composite increase with increasing hardness of the counterpart steel cylinders from 3.9 GPa to 5.4 GPa. On the other hand, wear is at the same level and the slope of the increase in creep decreases for hardness values ranging from 5.4 GPa to 9.9 GPa. Moreover, the sudden increase in the friction coefficient and the vertical displacement occurs much earlier when using harder steel cylinders (from 3.9 GPa to 7.2 GPa), and sliding surface temperature is also increased. The evolution of the temperature, the friction coefficient, and the vertical displacement is the same between 7.2 GPa and 9.9 GPa. On the other hand, the wear of the counterpart steel cylinders sharply decreases with increasing hardness of the steel cylinders from 3.9 GPa to 5.4 GPa, and very little wear of steel is observed for hardness values ranging from 5.4 GPa to 9.9 GPa. No change in the color of the grease was observed in this range.

These results are explained by the difference between the hardness of the GF and the counterpart steel cylinders. The hardness of GF was approximately 5.7 GPa regardless of the GFs direction as presented in Fig. III. 28, and the value was close to the hardness of steel with a hardness of 5.4 GPa. Considering these results, it can be stated that when the hardness of the counterpart steel is significantly lower than the hardness of the GF, the wear of the composite and the damage to GFs are reduced, while the aggressive effects of GF on the softer counterpart steel increase. In addition, the wear and creep of the composite decrease owing to the effects of the decreased local contact pressure between GF and steel, which are related to the lower hardness of the steel. Furthermore, the large amount of wear on the counterpart steel induces a further decrease of the contact pressure, and wear and creep of the composite are also reduced. By contrast, wear and creep of the composite increased with increasing hardness of the counterpart steel because the aggressive effects of GFs on the steel decreased, and the aggressive effects of the steel on the composite increased, as presented in Fig. III. 37 and Fig. III. 38. The contact pressure remains at a higher level because the wear on the steel cylinders decreased. In addition, the higher contact pressure between GF and steel related to much higher hardness of the steel increases the wear and creep of the composite.

6. Conclusions

The tribological mechanisms of GF-reinforced PA66 sliding in contact with a steel counterpart under high contact pressure in grease-lubricated conditions were clarified. The following points have been highlighted.

1) Detailed tribological behavior of the contact and damage of the GF composite and unreinforced PA66

An initial sudden increase of the vertical displacement during sliding tests was observed and it was related to the creep of the composite ring. After this sudden increase, the wear of the composite increased linearly with increasing number of cycles. The mechanical properties of the sliding surface change over time according to the damage inflicted on the sliding surface of the composite, and the damage to the sliding surface induces the increase of creep and friction coefficient. The wear of the unreinforced PA66 was not observed, whereas initial creep was larger than that of the GF composite.

2) Wear behavior of counterpart steel and the effect of the fiber orientation of the composite

An important effect regarding the fiber orientation on the sliding surface of the composite was observed on the wear resistance of the counterpart steel and composite. The aggressive effects observed on the counterpart steel were much greater when fibers were oriented in the perpendicular direction. By contrast, the wear of the composite increased when the fibers were aligned parallel to the sliding direction.

3) Contribution of some sliding conditions on the increase of friction and damage

The damage to the sliding surface of the composite ring has an important effect. The contamination of the grease has no effect on the friction coefficient and damage. Friction and damage of the composite were reduced when worn steel was used, which is attributed to a decrease of the contact pressure. Damage on the composite ring decreased with decreasing temperature, which is attributed to the recovery of the mechanical properties of the composite once it cools.

4) Effects of the hardness of the counterpart steel

The relative hardness between the steel and fibers is important in understanding the wear induced in the steel and composite. The wear resistance of the composite is improved when the hardness of the counterpart steel is lower, because aggressive effects on a composite that has harder fibers are reduced when the steel is softer, while the wear on a steel cylinder reduces the contact pressure.

Chapter III focused on the basic tribological properties of the GF composite or unreinforced PA66 in contact with carbon steel under grease lubrication tested at room temperature accompanying sliding heat generation. However, the mechanical and physical properties of PA66 or grease with additives are highly influenced by the temperature, and it is vital to understand the temperature dependence of the tribological properties to apply the results into actual parts. In the next chapter, the effect of the temperature on the tribological properties of the GF composite or unreinforced PA66 in contact with carbon steel under grease lubrication will be discussed, and the effect of the zinc carboxylate as an additive in grease will be elucidated.

CHAPTER IV

EFFECTS OF TEMPERATURE AND
ADDITION OF ZINC CARBOXYLATE TO
GREASE ON THE TRIBOLOGICAL
PROPERTIES OF PA66 IN CONTACT
WITH CARBON STEEL

CHAPTER IV: EFFECTS OF TEMPERATURE AND ADDITION OF ZINC CARBOXYLATE TO GREASE ON THE TRIBOLOGICAL PROPERTIES OF PA66 IN CONTACT WITH CARBON STEEL

1. Introduction.....	135
2. Effects of adding zinc carboxylate to grease under test conditions with sliding heat generation using GF-reinforced PA66	136
3. Temperature dependence of the tribological properties and effects of adding zinc carboxylate to grease.....	138
3.1 Temperature dependence of the tribological properties under 1 s stopping condition using GF-reinforced PA66.....	138
3.2 Temperature dependence of the tribological properties under test conditions at stable temperature using GF-reinforced PA66.....	139
3.3 Relationship between the mechanical properties and tribological properties, and effect of the tribochemistry	143
3.4 The temperature dependence and effect of the zinc carboxylate on the wear resistance of steel counterpart	145
3.5 The effect of the intermittent duration of sliding on the tribological properties...	146
4. Identification of the tribofilm on the surface of steel and composite at 80°C.....	148
4.1 Tribofilm analysis on the steel cylinder	148
4.1.1 SEM observation and EDX analysis	148
4.1.2 XPS analysis	151
4.1.3 ToF-SIMS analysis	153
4.2 Tribofilm analysis on the GF-reinforced PA66 composite.....	156
4.2.1 SEM observation and EDX analysis	156
4.2.2 XPS analysis	158
4.2.3 ToF-SIMS analysis	160
4.3 Tribochemical reaction on the sliding surface	160
5. Contribution and roles of tribofilm on the tribological properties	161
6. Temperature dependence on tribofilm formation	164
7. Effects of adding zinc carboxylate to grease on the tribological properties of unreinforced PA66	165
8. Conclusions.....	169

CHAPTER IV: EFFECTS OF TEMPERATURE AND ADDITION OF ZINC CARBOXYLATE TO GREASE ON THE TRIBOLOGICAL PROPERTIES OF PA66 IN CONTACT WITH CARBON STEEL

In this chapter, the influence of temperature on the tribological properties of unreinforced or GF-reinforced PA66 in contact with carbon steel under boundary lubrication with grease was studied. We consider the temperature dependence of the mechanical properties on the sliding surface of PA66 and the tribochemical reaction with zinc carboxylate additives in grease.

1. Introduction

In order to use the plastic sliding parts under high-temperature environment such as inside the automobile engine compartment, it is significant to understand the temperature dependence of the tribological properties. However, bibliography survey revealed that the temperature dependence of the tribological properties, or the detailed mechanism of the tribochemistry, on the sliding surface have yet to be clearly discussed on the tribology of PAs or other types of engineering plastic in contact with steel under grease lubrication. In addition, several types of additives are added to grease to improve the tribological properties; however, regarding the sliding of polymer or composite and steel, or the sliding between polymers, few studies have been conducted on the tribochemistry of the additives or on the effects of a tribofilm formation on the tribological properties.

Considering these backgrounds and basic tribological behaviors which were elucidated in Chapter III, the effects of the temperature and adding zinc carboxylate to grease on the tribological properties of unreinforced or GF-reinforced PA66 in contact with carbon steel under boundary lubrication which exhibited the direct contact and explicit wear scar of steel and GF composite or PA66 were investigated in this chapter. Zinc carboxylate is an oiliness improver and is considered to work more effectively as a low friction agent under lower contact pressure conditions in the sliding of PA66 and steel than in the sliding between steel sheets [4, 133]. In addition, zinc carboxylate has a good affinity with PA66 [4]. First, the effects on the tribological properties of GF-reinforced PA66 in contact with steel when adding zinc carboxylate to grease at different temperatures were investigated. Next, the composition of a tribofilm on steel and PA66 surfaces was identified through a chemical analysis including XPS and ToF-SIMS, and the effects of the tribofilm formation on the tribological properties were discussed herein.

In this chapter, the GF 15% composite with normal molecular mass (sample no. 1 in Table II. 3) and unreinforced PA66 (sample no. 12 in Table II. 3) were used. Table IV. 1 lists the composition of tested greases in this chapter. Grease containing zinc carboxylate and sulfur type anti-oxidation agent (grease no. 1 in Table IV. 1) was mainly used, and adding effect of each additive was discussed separately using greases no. 2 and 3. The steel cylinders with the hardness of 4.5 GPa were used in the experiments in this chapter.

Table IV. 1 Composition of tested greases.

Grease number	Base oil	Thickener	Low friction agent	Anti-oxidation agent
No. 1	PAO8	Diurea	Zinc carboxylate	Sulfur type agent
No. 2	PAO8	Diurea	-	Sulfur type agent
No. 3	PAO8	Diurea	Zinc carboxylate	-

2. Effects of adding zinc carboxylate to grease under test conditions with sliding heat generation using GF-reinforced PA66

First, the effects of adding zinc carboxylate to grease were investigated at room temperature with sliding heat generation using GF-reinforced PA66 (the same test conditions as used in Chapter III). Fig. IV. 1 shows the evolutions of the friction coefficient, the temperature, and the vertical displacement under the test conditions for a stopping time of 1 s (after every 10 s of sliding) using a GF-reinforced PA66 composite and grease with or without zinc carboxylate (grease no. 1 and grease no. 2) for a normal load of 350 N.

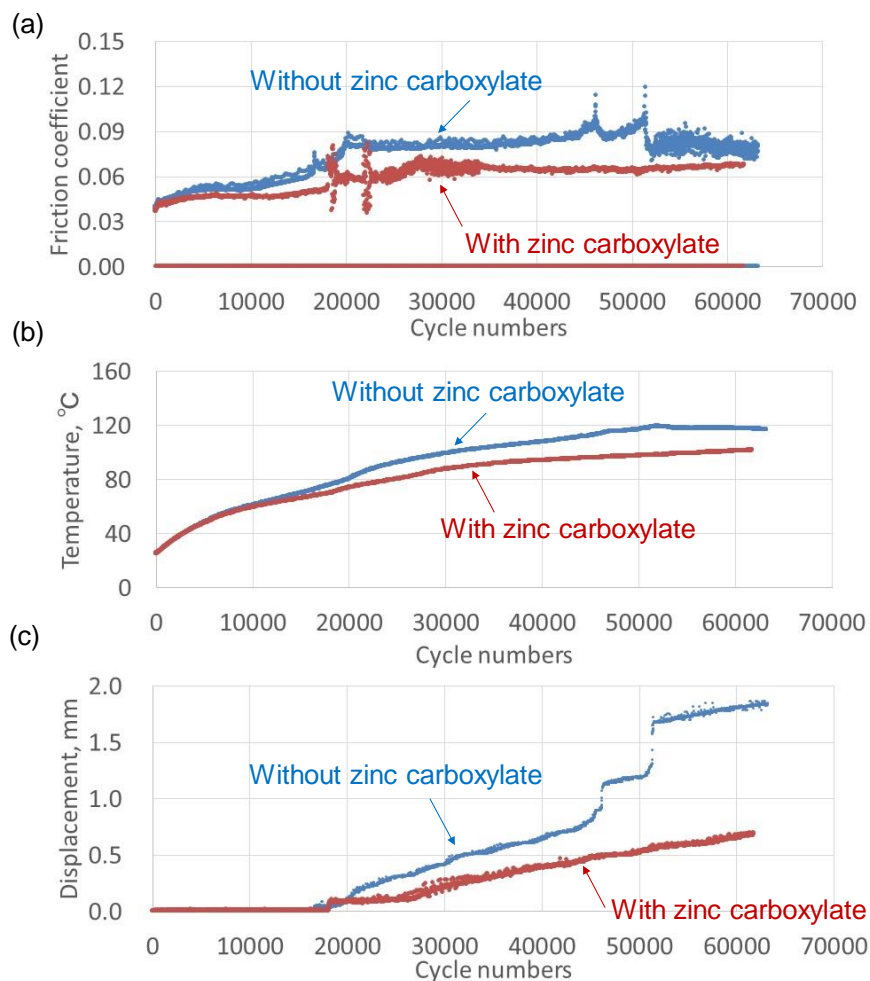


Fig. IV. 1 Evolutions of (a) friction coefficient, (b) temperature, and (c) vertical displacement during the sliding test with GF-reinforced PA66 and grease with or without zinc carboxylate for a stopping time of 1 s.

In the first 10,000 cycles (when the temperature is below 60°C), there is no effect of adding zinc carboxylate on the evolution of the friction coefficient and the temperature. However, the friction coefficient during the tests without zinc carboxylate increased after the temperature reached above 60°C (the first 10,000 cycles), and a difference in the rate of increase in temperature can be observed. The average friction coefficient during the sliding with zinc carboxylate is 0.059 ± 0.009 , which is 18.1% lower than the value without zinc carboxylate (0.072 ± 0.014). In addition, the rate of increase in the displacement is higher in the tests without zinc carboxylate, and a rapid increase in the displacement is observed at 45,000 and 52,000 cycles.

Fig. IV. 2 shows the height loss of the creep and wear of the composite ring after 61,500 cycles, which was estimated using the procedure described in Section 4.2.3 in Chapter II. These results indicate that adding zinc carboxylate to grease decreases the creep of the composite because preventing the increase in temperature on the sliding surface related to a relatively lower friction coefficient prevents a degradation of mechanical properties and an increase in shear stress on the sliding surface. This confirms the friction reduction properties of this type of additive.

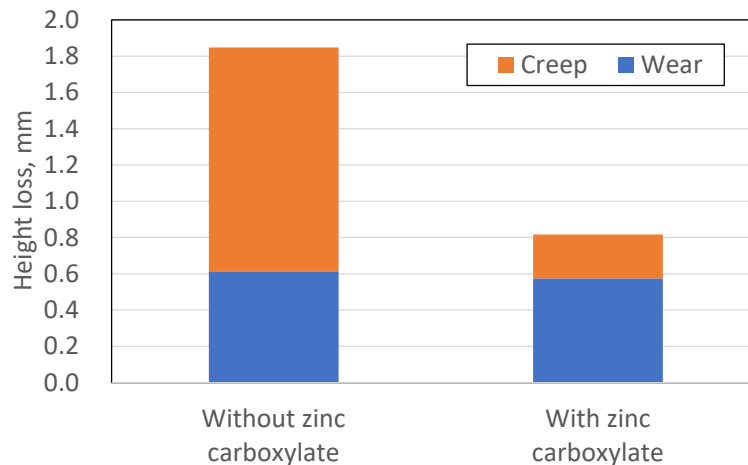


Fig. IV. 2 Height loss of the creep and wear of the composite ring after 61,500 cycles.

Fig. IV. 3 shows the observations of the sliding surface before and after the sliding tests with an optical microscope. As observed in Chapter III, the entire sliding surface of the composite ring undergoes peeling, and an exposure of the GFs can be observed after the sliding tests. In addition, the sliding surface is expanded in both the inner and outer directions. The total area of the sliding surface is wider for the composite ring tested without zinc carboxylate, which is related to the large creep of the composite. This creep is caused by the decrease in the surface mechanical properties related to the damage by sliding, such as the scratching of PA66 or peeling off of fibers. In addition, no explicit difference in the wear of steel counterpart (total of four steel cylinders) after sliding tests was observed. Wear of steel counterpart was 0.135 mm^3 using grease without zinc carboxylate and 0.154 mm^3 using grease with zinc carboxylate. Therefore, as observed in the GF composite wear, zinc carboxylate in grease does not induce a significant difference in steel counterpart wear under these test conditions.

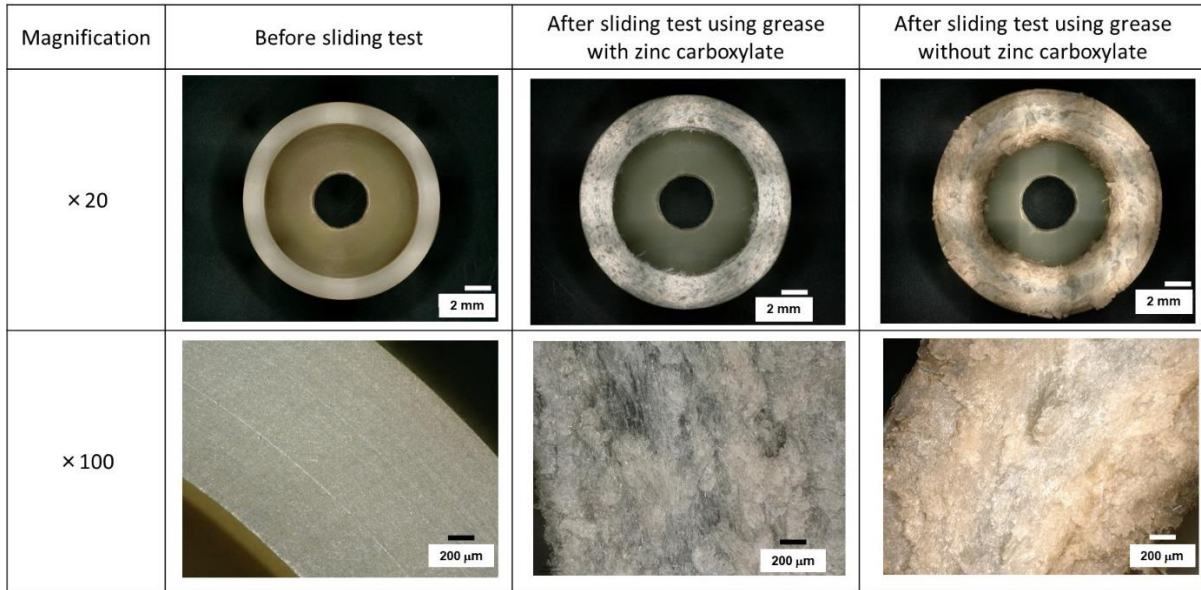


Fig. IV. 3 Optical microscope observations of the sliding surface of the composite ring before and after the sliding tests.

3. Temperature dependence of the tribological properties and effects of adding zinc carboxylate to grease

Next, temperature dependence of the tribological properties and effects of adding zinc carboxylate to grease were investigated in detail under various test conditions.

3.1 Temperature dependence of the tribological properties under 1 s stopping condition using GF-reinforced PA66

Sliding test at 120°C was conducted using GF composite and grease with zinc carboxylate (grease no. 1 in Table IV. 1) under the same test conditions as conducted in Section 2, and the results were compared to the results obtained at room temperature. Fig. IV. 4 presents the evolutions of the friction coefficient, the temperature, and the vertical displacement during the sliding test at each temperature. Whereas the friction coefficient exhibits lower values at 120°C than at room temperature, the evolutions of the vertical displacement look the same.

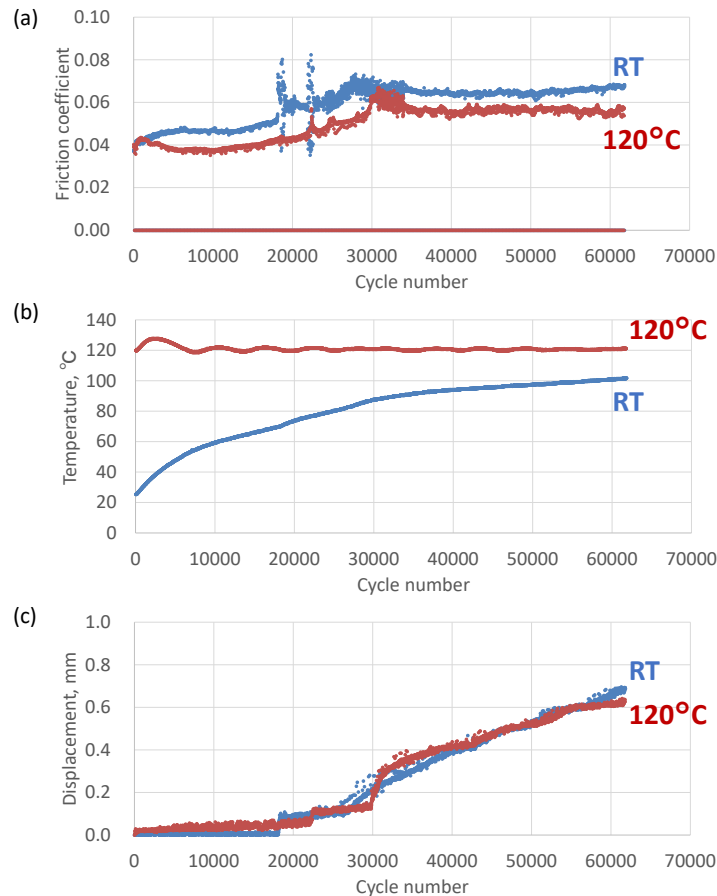


Fig. IV. 4 Evolutions of (a) friction coefficient, (b) temperature, and (c) vertical displacement during the sliding test with GF-reinforced PA66 and grease with zinc carboxylate conducted at room temperature (RT) or 120°C.

However, under this test condition, the effects of the temperature on the tribological properties cannot be discussed alone because an increase in the temperature through sliding heat generation occurs particularly when test is conducted at room temperature. In order to evaluate the difference in the tribological properties at different temperatures much more clearly, sliding tests with a stopping time of 200 s between each 10 s period of sliding which allows us to control and maintain a given temperature for each test at different temperatures were conducted, using grease with or without zinc carboxylate.

3.2 Temperature dependence of the tribological properties under test conditions at stable temperature using GF-reinforced PA66

Fig. IV. 5 shows the evolutions of the friction coefficient, the vertical displacement, and the temperature at room temperature under grease lubrication with or without zinc carboxylate with a stopping time of 200 s between each 10 s period for a normal load of 350 N. No differences in the friction coefficient and displacement can be observed, and the increase in the friction coefficient and the vertical displacement is observed after 10,000 cycles in both greases. This increase is related to the damage on the composite surface (peeling off of fibers and scratching of PA66) which induces the increase in the friction coefficient and sudden creep (plastic deformation), as presented in Chapter III. In addition, there is a slight temperature increase from ambient temperature to 33°C, even if there is a very large stopping time.

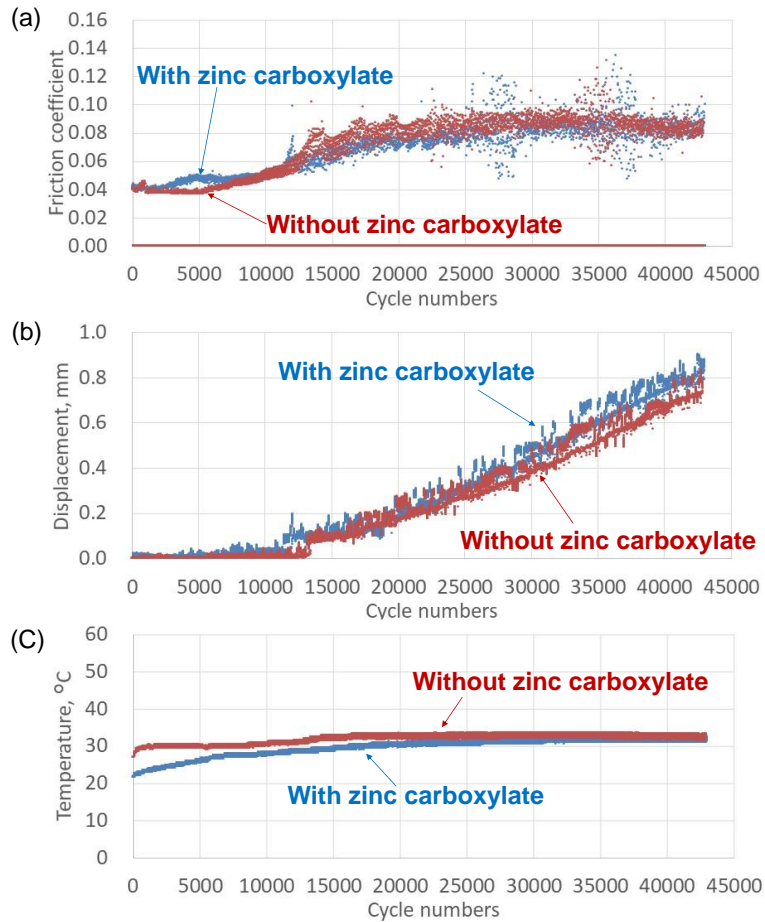


Fig. IV. 5 Evolutions of (a) friction coefficient and (b) vertical displacement at room temperature using grease with or without zinc carboxylate.

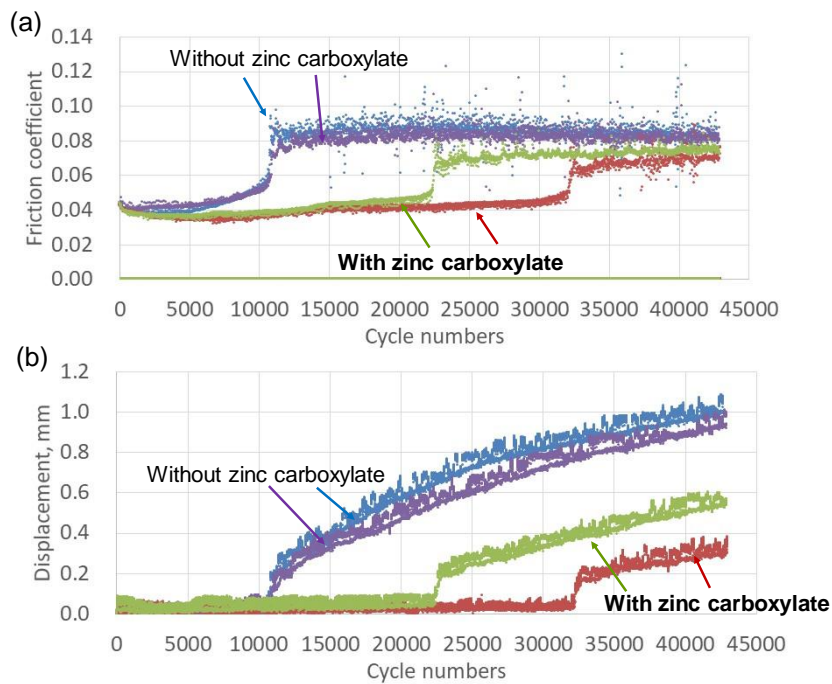


Fig. IV. 6 Evolutions of (a) friction coefficient and (b) vertical displacement at 80°C using grease with or without zinc carboxylate.

Fig. IV. 6 shows the evolutions of the friction coefficient and the displacement at 80°C under the same test conditions. Significant differences in both the friction coefficient and displacement can be observed for tests with or without zinc carboxylate in grease. Using grease with zinc carboxylate, the friction coefficient decreases during the initial stage of the sliding, and sudden increases in the friction coefficient and displacement are observed at larger numbers of cycles ($27,500 \pm 5,000$ cycles) than without zinc carboxylate (11,000 cycles). The average value of the friction coefficient during the initial 5,000 cycles when using grease without zinc carboxylate is 0.045, and is 0.037 with zinc carboxylate (a decrease of 22%). After 43,000 cycles, the displacement is 0.472 ± 0.092 mm for tests with zinc carboxylate, compared to 0.989 ± 0.004 mm for tests without zinc carboxylate.

Fig. IV. 7 shows the evolutions of the friction coefficient and the displacement at 120°C under the same test conditions. The effect of the decrease in the friction coefficient is observed during both the initial phase of the sliding and after the increase in friction. However, no beneficial effect on the displacement is observed. We can even conclude that, at 120°C, displacement is higher when zinc carboxylate is added to grease. Given these results, it was confirmed that the effects of the addition of zinc carboxylate on grease differ at each temperature.

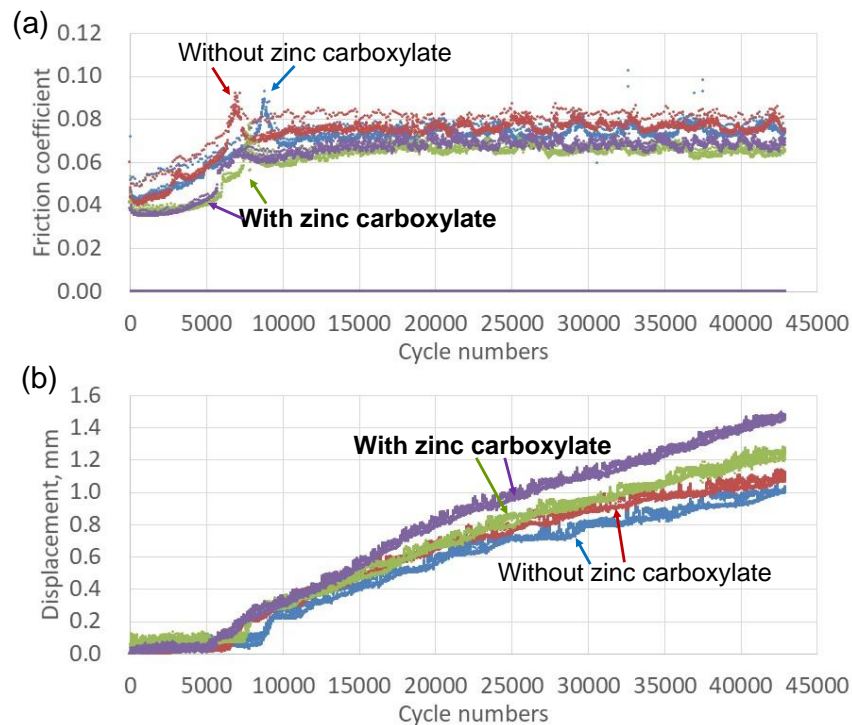


Fig. IV. 7 Evolutions of (a) friction coefficient and (b) vertical displacement at 120°C using grease with or without zinc carboxylate.

In summary, Fig. IV. 8 shows the height loss of the GF-reinforced PA66 composite (which is a summation of the wear and creep) after 42,000 cycles at each temperature. When using grease without zinc carboxylate, the wear and creep increase with an increase in temperature from room temperature to 80°C. The wear then increases from 80°C to 120°C, and the creep presents almost the same value at 80°C and 120°C. In contrast, when using grease with zinc carboxylate, no increase in wear or creep at 80°C is observed compared to those at room temperature, and they increase between 80°C and 100°C. In addition, no significant difference

of wear and creep between 100°C and 120°C is observed.

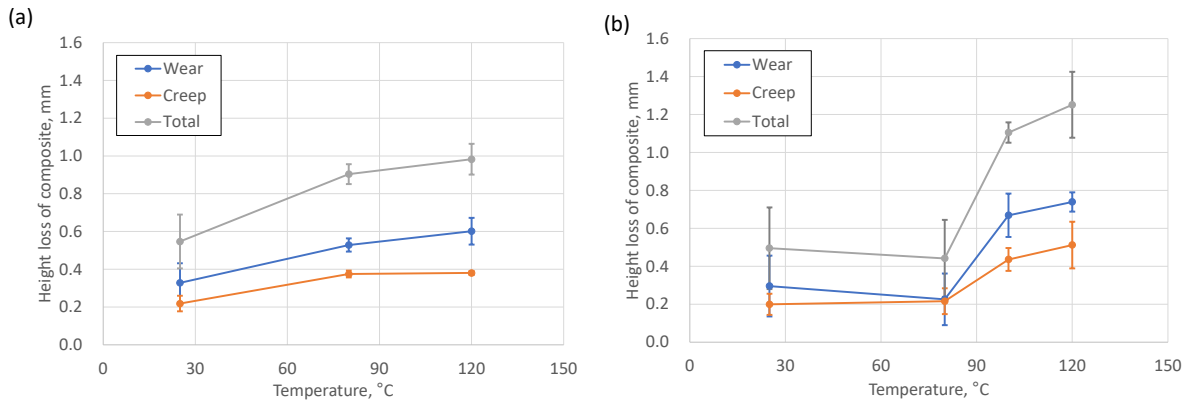


Fig. IV. 8 Total height loss, wear height loss, and creep height loss of composite ring after 42,000 cycles during tests for a stopping time of 200 s (a) without and (b) with zinc carboxylate in grease. Sliding tests were conducted for two times at each temperature.

Fig. IV. 9 shows the sliding surface after the sliding tests. Worn surfaces of the composite ring are similar for the tests with or without zinc carboxylate, at both room temperature and 120°C. At 80°C, the width of the worn ring is smaller during the tests with zinc carboxylate added to the grease compared to tests without zinc carboxylate, confirming the beneficial effect of zinc carboxylate at this temperature level.

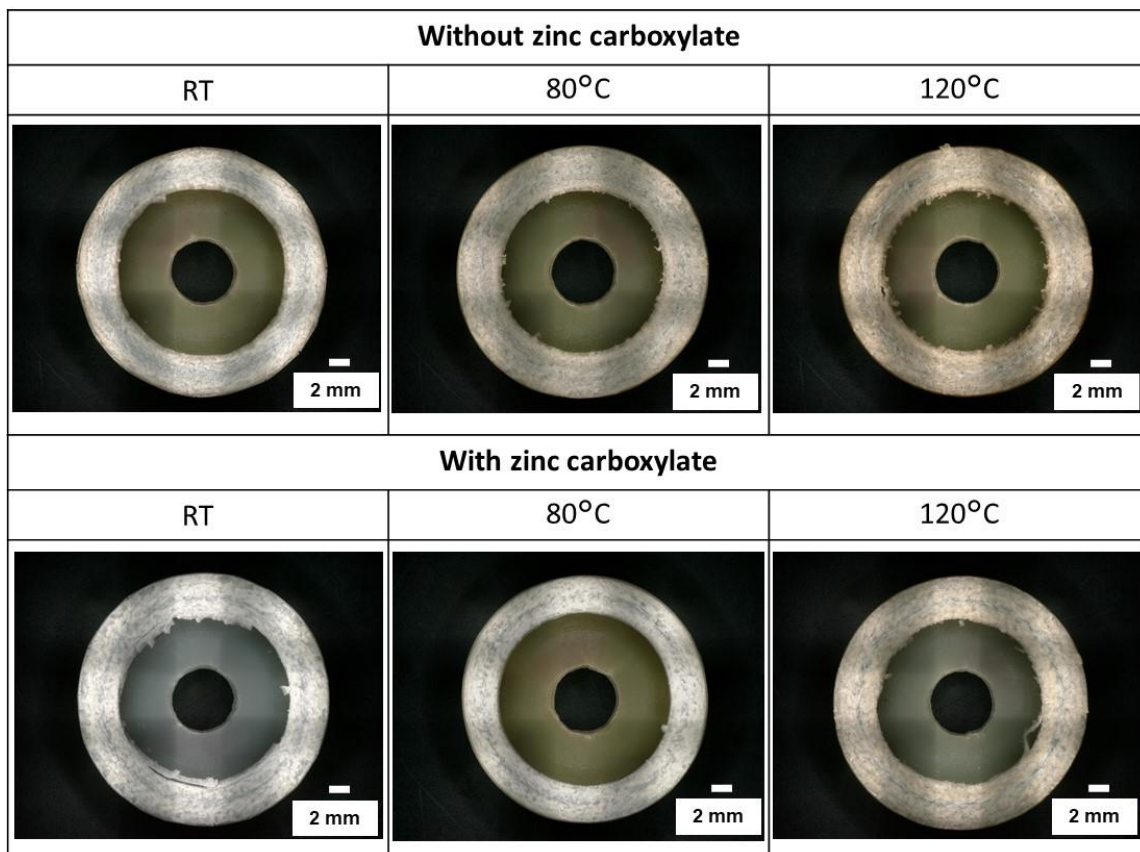


Fig. IV. 9 Optical microscope observations on the sliding surface of the composite ring after sliding tests at RT, 80°C and 120°C, with or without zinc carboxylate added to the grease.

3.3 Relationship between the mechanical properties and tribological properties, and effect of the tribochemistry

To discuss the relationship between the mechanical properties and tribological properties, surface mechanical properties at each temperature was measured through micro indentation process as explained in Section 4.4 of Chapter II. Fig. IV. 10 shows a load-displacement curve of the measurement on the surface of the GF composite ring and unreinforced PA66 ring before the sliding test, measured as a function of temperature. Fig. IV. 11 shows the evolutions with temperature of the Young's modulus, hardness of the micro-indentation test (maximum normal load of 500 mN for GF composite and 250 mN for unreinforced PA66 maintained during a 10 s period). As expected, when the temperature is increased, the hardness and Young's modulus both decrease. In addition, the values of the hardness and Young's modulus of the GF composite are higher than those of the unreinforced PA66.

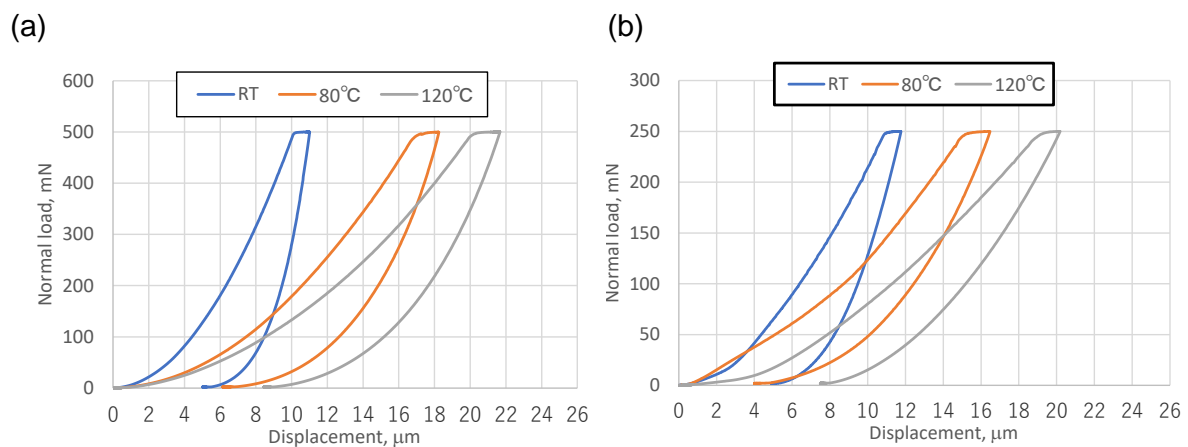


Fig. IV. 10 Load–displacement curve of micro indentation measurement at different temperatures. (a) GF-reinforced PA66 composite; (b) unreinforced PA66.

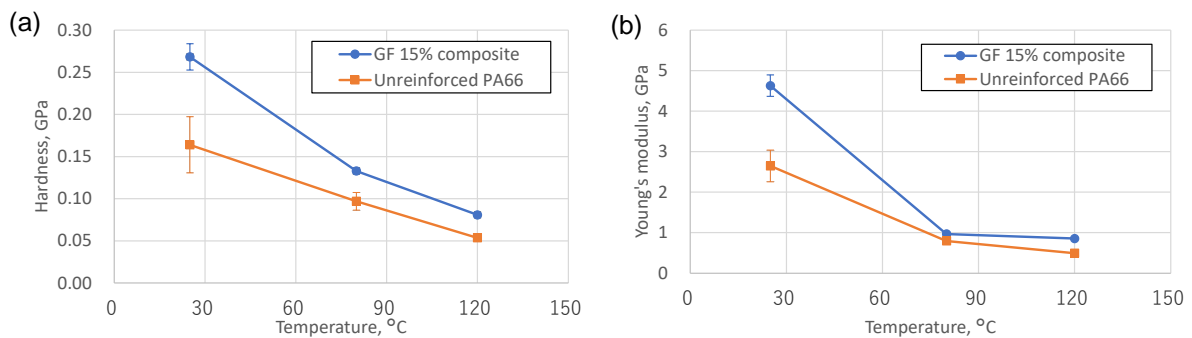


Fig. IV. 11 (a) Hardness and (b) Young's modulus on the sliding surface of the GF-reinforced PA66 composite and unreinforced PA66 at different temperatures. Measurement was conducted three times at each temperature.

Fig. IV. 12 shows that, without zinc carboxylate, good correlations occur between the hardness and wear height loss, and between the Young's modulus and creep height loss. Therefore, the wear and creep of the composite under test conditions using grease without zinc carboxylate can be explained based on the evolution of the elasto-visco-plastic mechanical properties of the composite as a function of temperature. However, no typical correlations were observed in the results with zinc carboxylate, leading to the conclusion that

the addition of the zinc carboxylate to grease has an impact on the tribological properties (through tribochemistry).

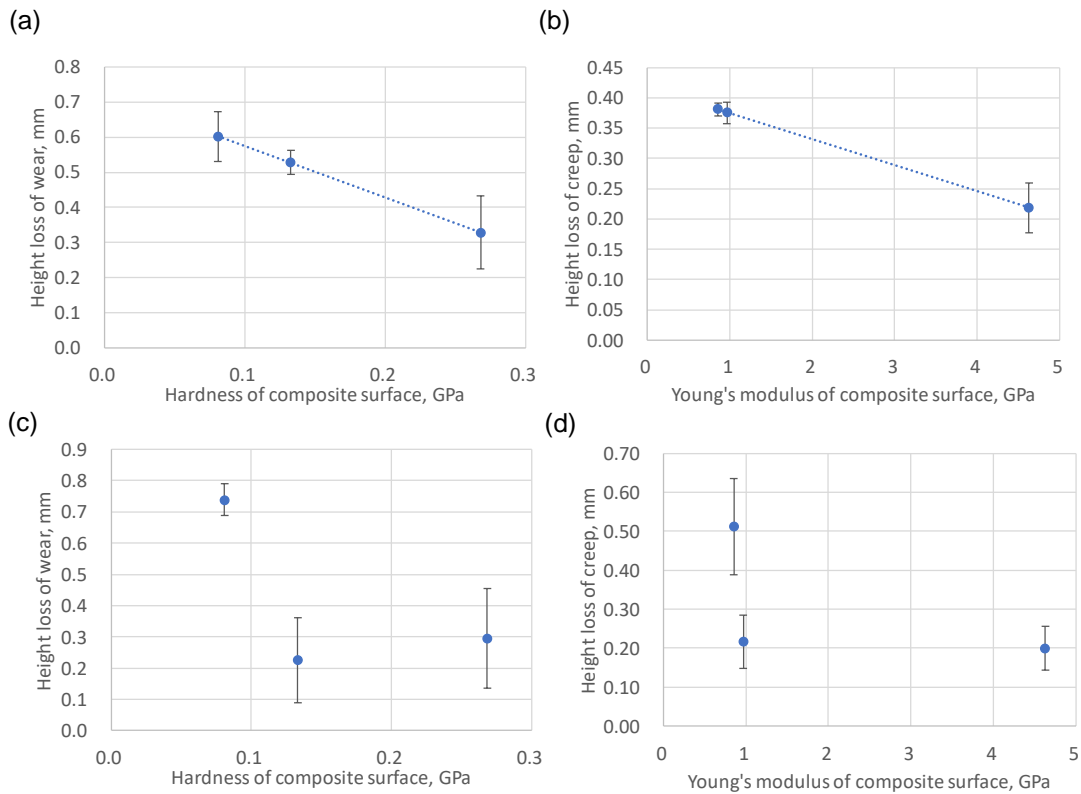


Fig. IV. 12 Relationships between (a) the hardness of the composite and the wear height loss of the composite ring; (b) the Young's modulus of the composite and the creep height loss of the composite ring; ((a) and (b) without zinc carboxylate in grease); (c) the hardness of the composite and wear height loss of the composite ring; and (d) the Young's modulus of the composite and the creep height loss of the composite ring ((c) and (d) with zinc carboxylate in grease).

In addition, Fig. IV. 13 shows the contributions of the increase in temperature and the addition of zinc carboxylate to grease on the increase in the wear and creep height losses of the composite. Negative values represent improvements in the tribological properties (i.e., the decrease in wear and creep), and positive values represent the deterioration in the tribological properties (i.e., the increase in wear and creep), when considering that the base value is the result at room temperature using grease without zinc carboxylate. The results indicate that the addition of zinc carboxylate to grease has a weak impact on the wear and creep resistance at room temperature. The positive effect of the addition of zinc carboxylate on the improvement of the wear and creep resistance is greater than the negative effects of the increase in temperature at 80°C. However, improvements in the wear and creep resistance by the addition of zinc carboxylate were not observed at 120°C.

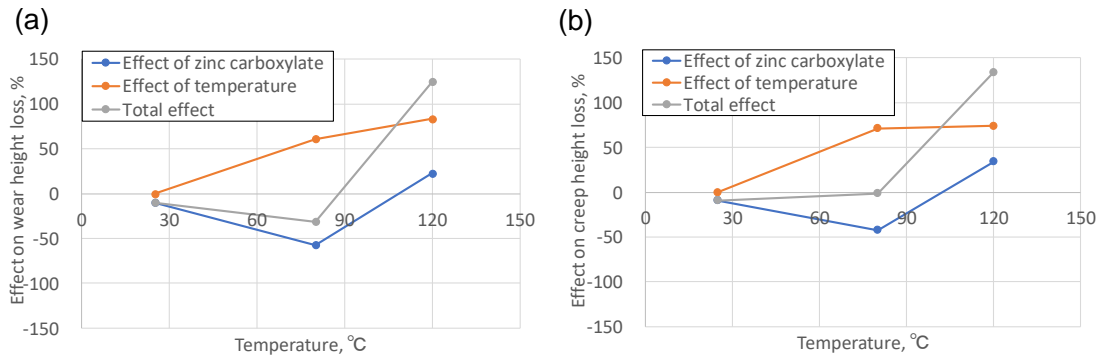


Fig. IV. 13 Contribution of the increase in temperature and the addition of zinc carboxylate to grease toward the (a) wear and (b) creep height losses. The base value indicates the results at room temperature using grease without zinc carboxylate.

3.4 The temperature dependence and effect of the zinc carboxylate on the wear resistance of steel counterpart

The effect of the temperature and addition of zinc carboxylate to grease on the wear resistance of steel counterpart was also investigated. Fig. IV. 14 shows the wear volume of the steel counterpart (total wear amount of four cylinders) at each temperature using grease with or without zinc carboxylate, and Fig. IV. 15 shows the optical microscope observations of the steel cylinder after sliding tests at different temperatures. The wear of the steel cylinders, which is considered to be 2-body abrasive wear observed in the sliding direction related to the presence of GFs, increases globally with an increase in the temperature. By contrast, the effect of the decrease in the wear amounts of the steel cylinders is observed by the addition of zinc carboxylate at 80°C.

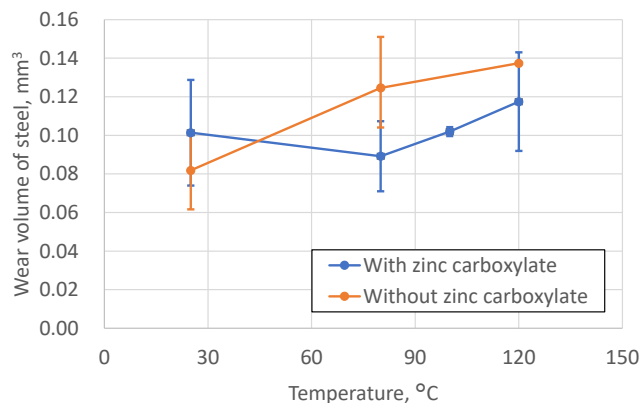


Fig. IV. 14 Wear volume of steel cylinders at each temperature using grease with or without zinc carboxylate (average value of two measurements).

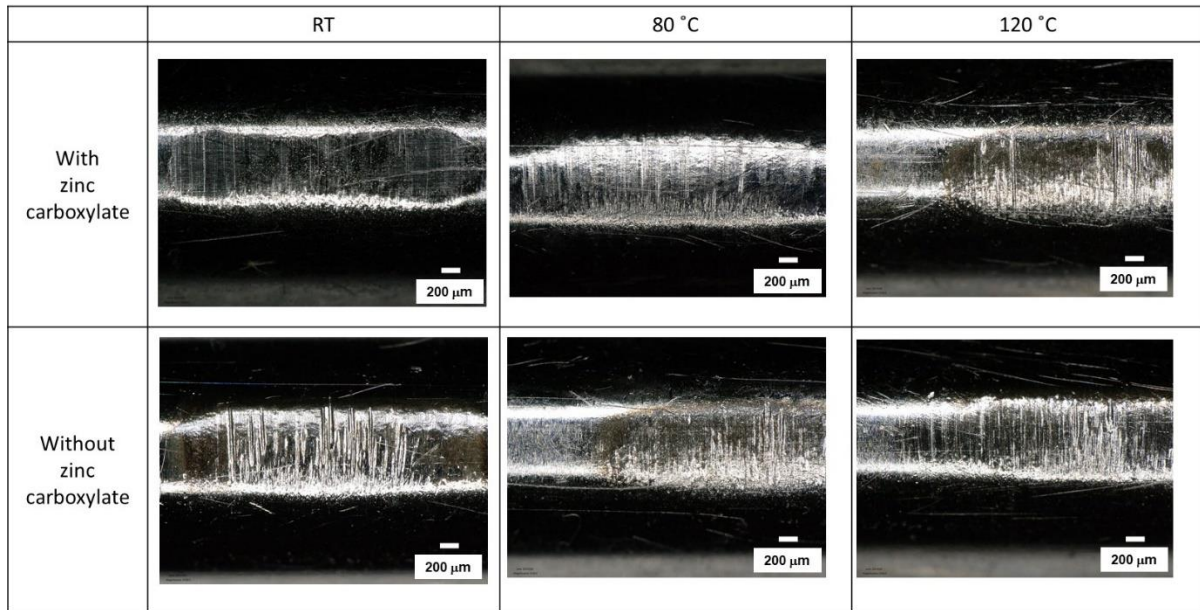


Fig. IV. 15 Optical microscope observations of steel surface after sliding tests at different temperatures.

3.5 The effect of the intermittent duration of sliding on the tribological properties

Besides, the comparison of the evolutions of the friction coefficient and the vertical displacement with different intermittent duration is presented in Fig. IV. 16 (the same evolutions as shown in Fig. IV. 4 and Fig. IV. 7), using GF-reinforced PA66 and grease with zinc carboxylate conducted at 120°C with 1 s stopping or 200 s stopping between each 10 s sliding period.

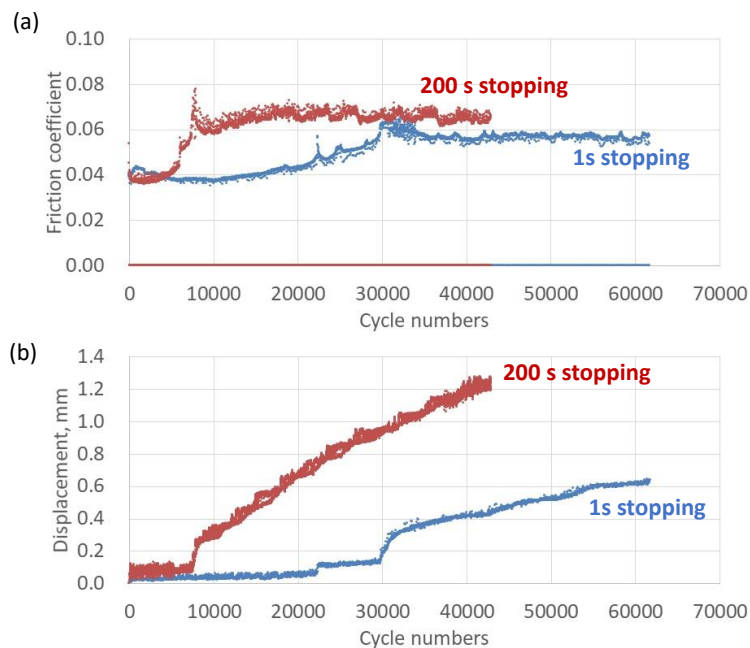


Fig. IV. 16 Evolutions of (a) friction coefficient, (b) vertical displacement during the sliding test with GF-reinforced PA66 and grease with zinc carboxylate conducted with 1 s stopping or 200 s stopping at 120°C.

It was confirmed that the long-term stopping duration induced the increase in the friction coefficient and deterioration in the wear and creep resistance, whereas the contact pressure or contact numbers were the same in these two conditions. In addition, the wear volume of the steel cylinders in 200 s stopping after 42,000 cycles was 0.092 mm^3 , and that in 1 s stopping after 61,500 cycles was 0.461 mm^3 . This is the inverse tendency to the wear resistance of GF composite. These results can be explained as follows. In the test of 200 s stopping, the total test duration under normal load was longer (19.4 hr) than that in 1 s stopping test (1.47 hr). Therefore, the effect of creep at 120°C should become much severer. In addition, the long-term stopping phase increased the effect of adhesion to the steel counterpart during the stopping phase, and the static friction coefficient in the initial stage in 200 s stopping test is higher (0.101) than that in 1 s stopping test (0.071), as Fig. IV. 17 presents the maximum friction coefficient in each 1 s and extracted static friction coefficient. In addition, the large creep decreased the contact pressure through the increase in the sliding surface area of the composite ring specimens, then the aggressive effects of GFs to the steel counterpart are supposed to be decreased.

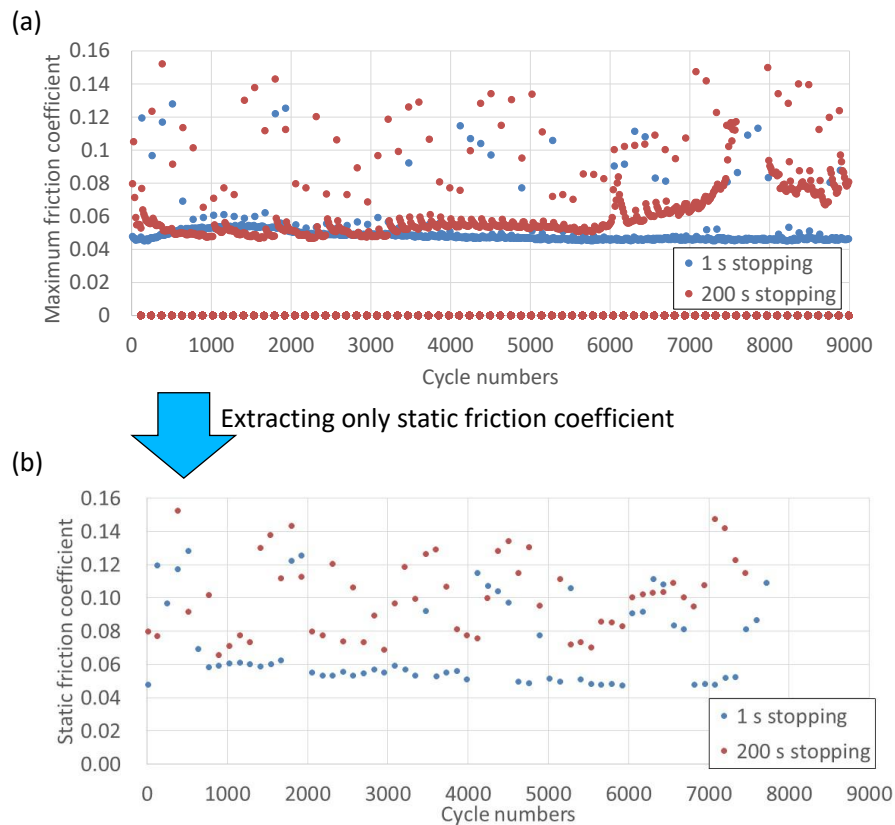


Fig. IV. 17 Evolutions of (a) the maximum friction coefficient and (b) extracted static friction coefficient in 1 s and 200 s stopping.

In summary, the results presented in this section confirm that the addition of zinc carboxylate plays a role in the tribological properties of the contact under investigation, and that this effect depends on the temperature. Because we can expect this effect to be related to tribochemical reactions, it may be interesting to analyze the surface chemistry of the wear scars at 80°C (where the beneficial effect is the most important), which is the objective of the next section.

4. Identification of the tribofilm on the surface of steel and composite at 80°C

To clarify the improvements on the tribological properties through the addition of zinc carboxylate to grease at 80°C, sliding surfaces of steel cylinders and a GF-reinforced PA66 composite ring after 13,000 cycles of the sliding test for a stopping time of 200 s (before the sudden increase in the vertical displacement) were analyzed.

4.1 Tribofilm analysis on the steel cylinder

4.1.1 SEM observation and EDX analysis

Fig. IV. 18 shows SEM images of the sliding surface of a steel cylinder. Numerous dark heterogeneous patches from the submicron level to 20 μm in size can be seen on the sliding surface after the test. The results of the EDX point analysis of the dark patches presented in Fig. IV. 19 indicate that the proportion of Fe decreases in the patch area compared to the no patch area, and that these patches are composed of the chemical elements of C and O, and small amounts of elements related to the additives of grease (Zn, S). These patches were not removed after an additional washing in an ultrasonic bath using heptane solvent for 20 min. after the first EDX analysis for 20 min., and they remained completely at the same location, as presented in Fig. IV. 20. Therefore, these patches were strongly adhered to the sliding surface of the steel cylinders.

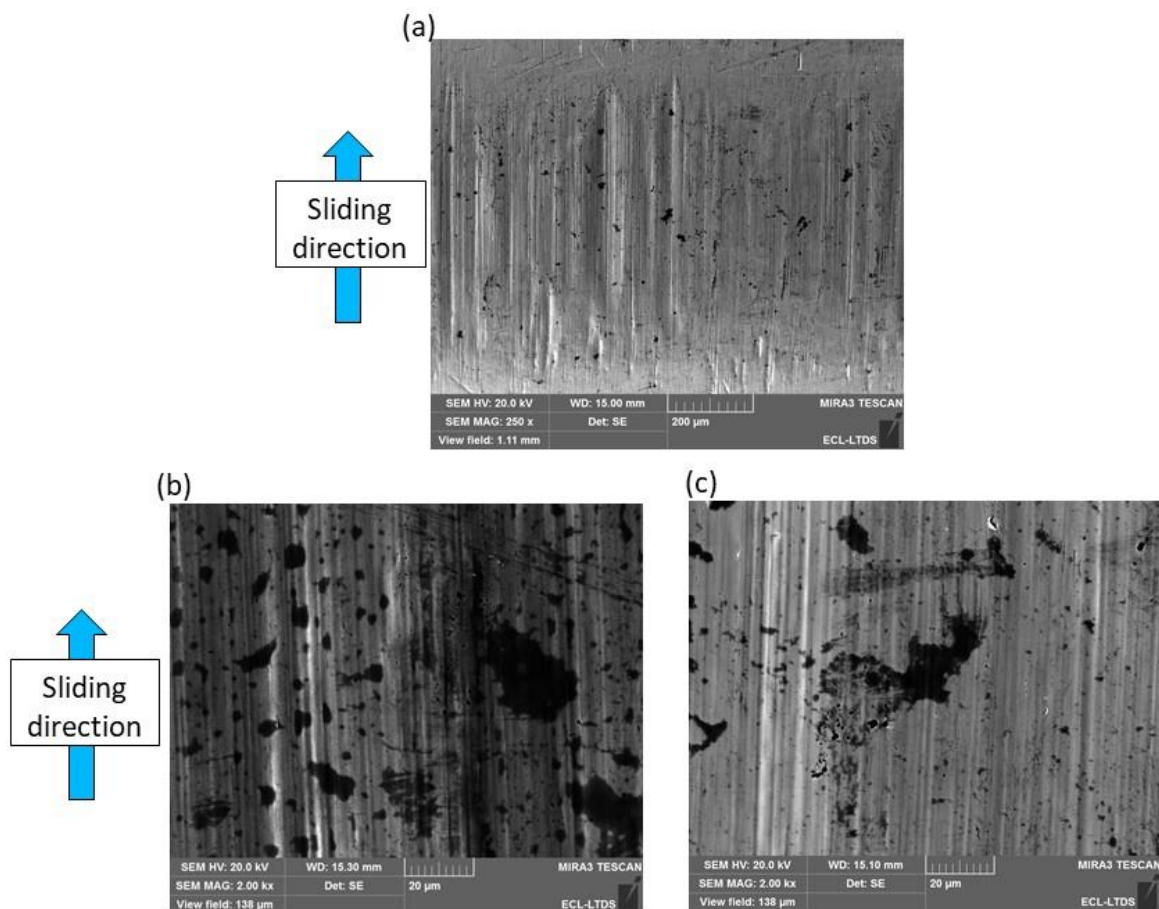


Fig. IV. 18 SEM images on the sliding surface of a steel cylinder after 13,000 cycles: (a) at a magnification of $\times 300$; (b) and (c) at a magnification of $\times 2,000$.

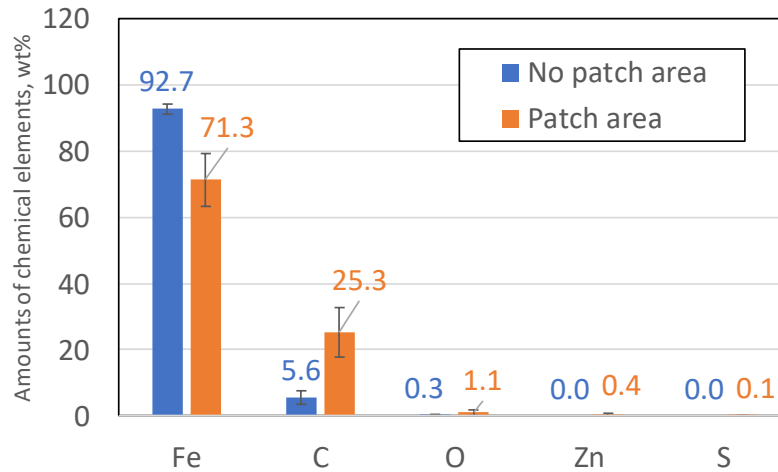


Fig. IV. 19 Amounts of each chemical element measured using a point analysis of EDX (average value of five measurements).

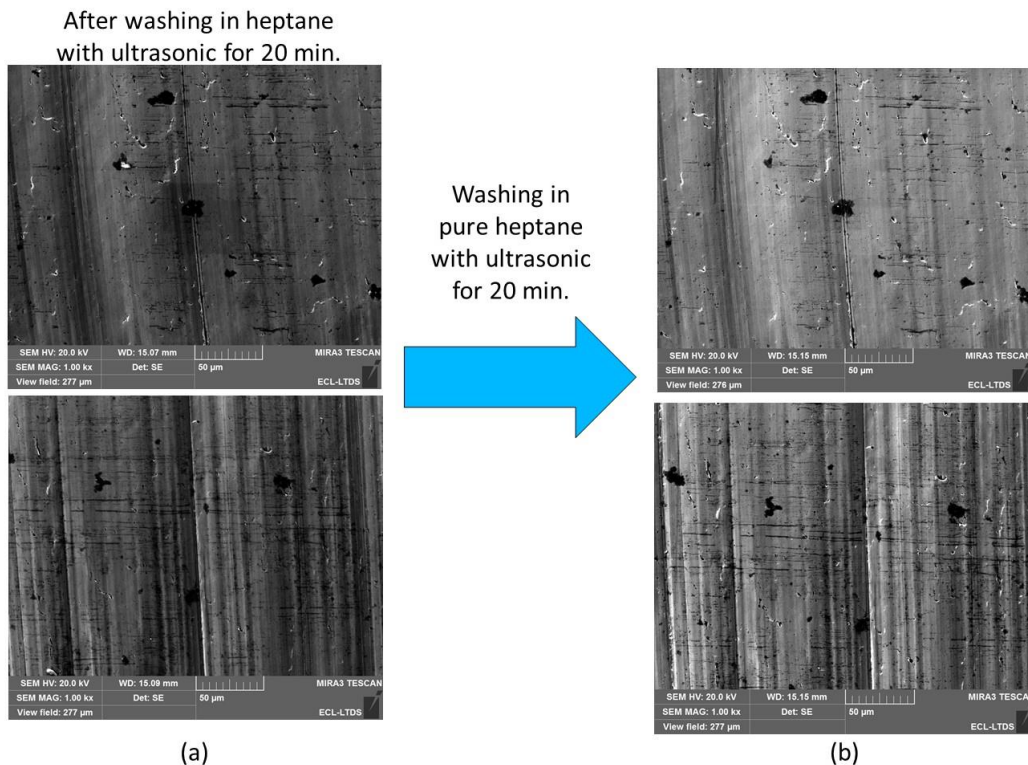


Fig. IV. 20 SEM images on the sliding surface of a steel cylinder after 13,000 cycles: (a) after washing in heptane with ultrasonic for 20 min.; (b) observations in the same place as (a) after additional washing in pure heptane for 20 min.

Fig. IV. 21 shows the SEM images of a new steel cylinder (without sliding tests). Sliding surface is not uniform and some polished marks which may be attributed to the polishing process of the cylinder and some gray spots can be observed; however, dark patches as observed in Fig. IV. 18 are not present.

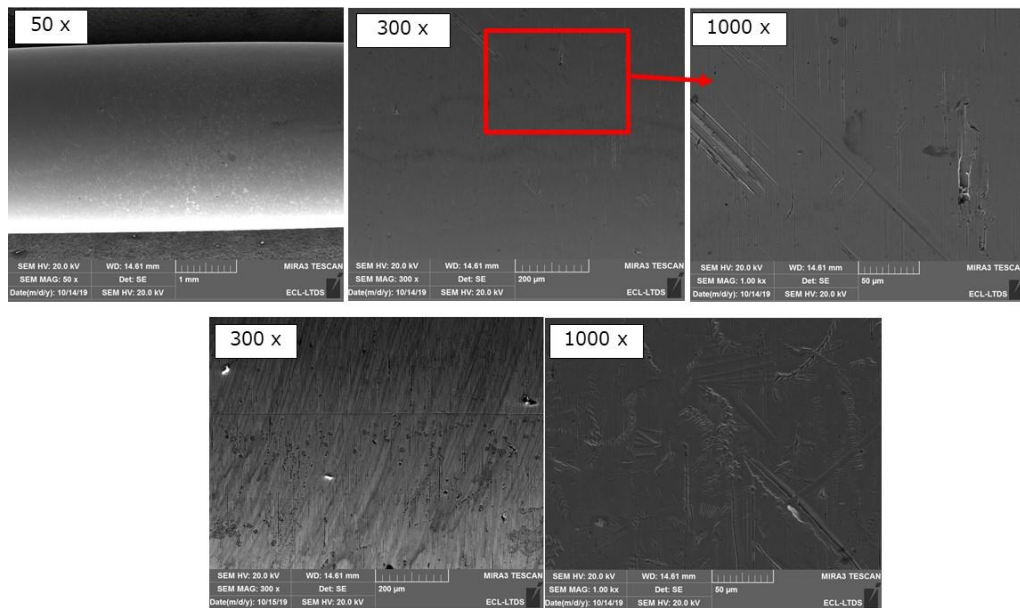


Fig. IV. 21 SEM images of new steel cylinder (without sliding tests).

In contrast, Fig. IV. 22 presents a SEM observation of a cylinder heated with grease at 80°C for 6 h in contact with a composite ring at a normal load of 350 N (the same temperature, normal load, and duration as the sliding tests over 13,000 cycles, but without sliding), and Fig. IV. 23 presents a SEM observation of a cylinder heated with grease at 80°C for 6 h without a normal load (not contacted with a composite ring) after the same washing process. Patches containing the same types of chemical elements (C, O) are also observed on the surface of both cylinders without sliding. Therefore, these patches after sliding for 13,000 cycles would be an adsorbed film related to heating with grease or mixture of an adsorbed film and a tribofilm formed during the sliding tests as a consequence of the tribochemical reactions between the additives in the grease and the material surfaces under contact pressure, shear, and temperature. To identify the detailed chemical compositions of these patches and confirm whether these patches are the tribofilm or not, we conducted additional chemical analyses.

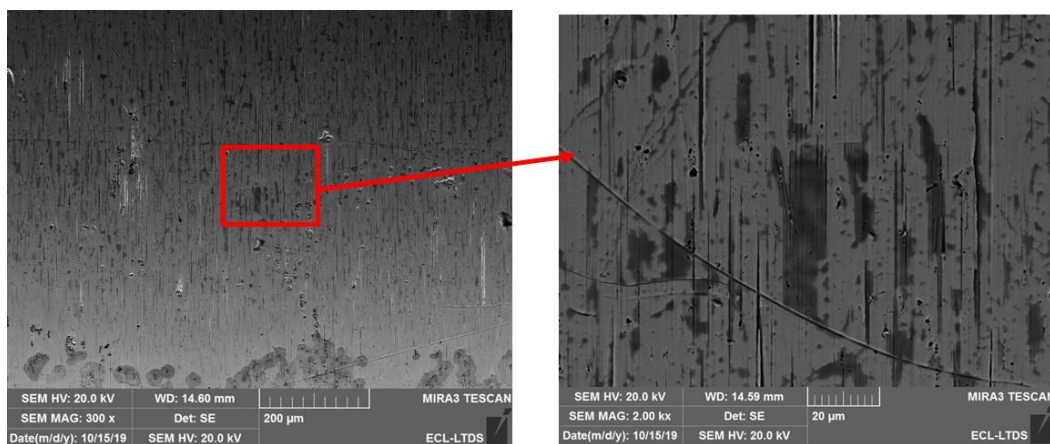


Fig. IV. 22 SEM images of cylinder heated with grease at 80°C for 6 h in contact with a composite ring without sliding.

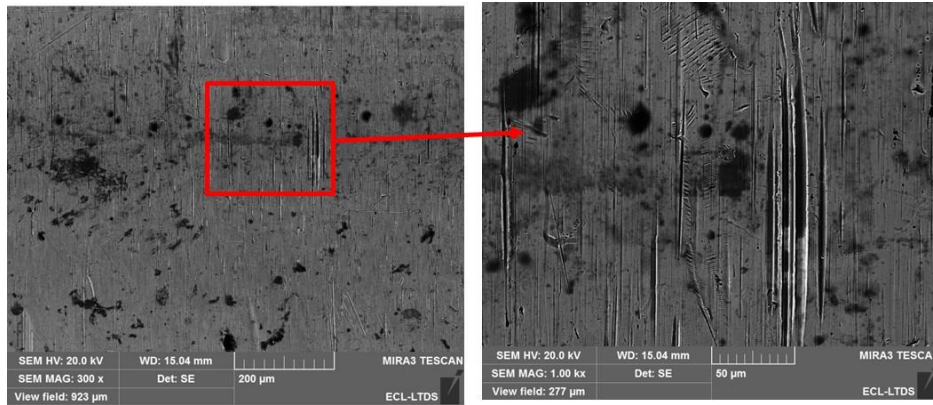


Fig. IV. 23 SEM images of cylinder heated with grease at 80°C for 6 h without normal load and sliding.

4.1.2 XPS analysis

XPS analysis was conducted to identify the composition of the surface film on the steel samples, including the surface of the new steel cylinder, the cylinder after 13,000 cycles of the sliding test with no wear area (with grease contact for 6 h at 80°C), and the cylinder in wear area, as presented in Fig. IV. 24.

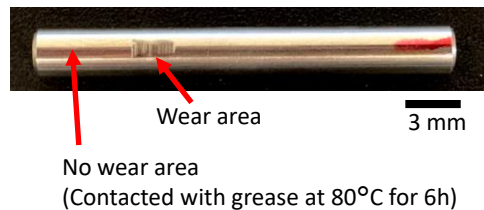


Fig. IV. 24 XPS analysis areas of the steel cylinder (observed using a microscope).

Fig. IV. 25 shows the results of XPS analysis of steel cylinder in wide scanning analysis, and amounts of each chemical state estimated based on the curve fitting of the XPS analysis results. Blue lines are the results of new cylinder (before the sliding test), green lines are the results of the no sliding area which was in contact with grease at 80°C and red lines are the results of the wear area after sliding tests. C, O, and Fe are mainly detected. Zn (related to zinc carboxylate in grease) and N (related to urea thickener of grease) are detected typically after the contact even without sliding, and the detected values decrease after sliding. Fig. IV. 26 presents the charts of XPS analysis in narrow range analysis for carbon, zinc, sulfur, and oxygen, and amounts of each chemical state estimated based on the curve fitting of the XPS analysis results. First, the formation of the carboxylate film was discussed. The increase in the amount of O-C=O bond after the contact with grease without sliding is observed compared to the new cylinder, and it is relatively lower in the wear area. However, the atomic ratio of C-C bond to O-C=O bond on the steel surface after heating without/with sliding is not equal and in the range of 6.14 to 20.58 (theoretically, 15 in palmitate and 17 in stearate considering the chemical structure of zinc palmitate or zinc stearate, which are representative examples of carboxylate). In addition, the atomic ratio of O-C=O bond to Zn_{2p3} is in the range of 8.66 to 12.0 (theoretically 2 in both palmitate and stearate). Therefore, these results cannot characterize the formation of the carboxylate film including stearate or palmitate on the steel surface. This is because hydrocarbon which is composed of C, H, and O is not possible to distinguish explicitly the adventitious carbon originating from the contamination in

atmosphere and the hydrocarbon on the tribofilm. In addition, very small peaks of Zn_{2p3} and S_{2p} can be detected on both no sliding area and wear area. On the surface of wear area, the amounts of Zn_{2p3} and S_{2p} are the same (0.27). This means small amount of ZnS compounds are supposed to be formed on the steel surface.

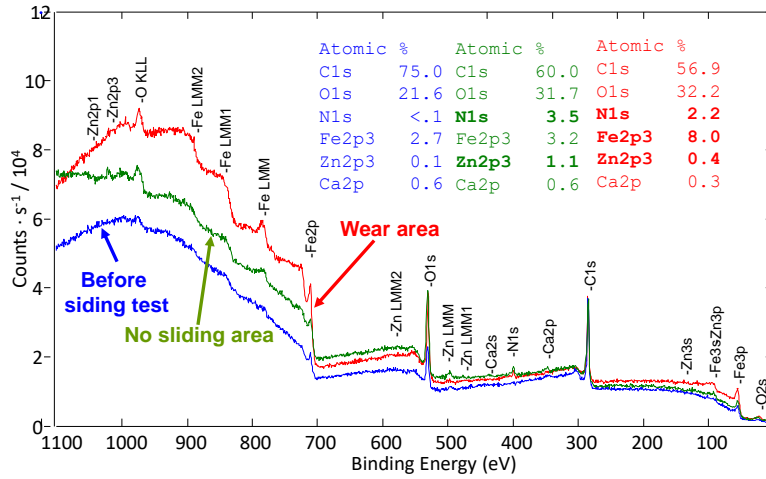


Fig. IV. 25 Results of XPS analysis of steel cylinder in wide scanning analysis.

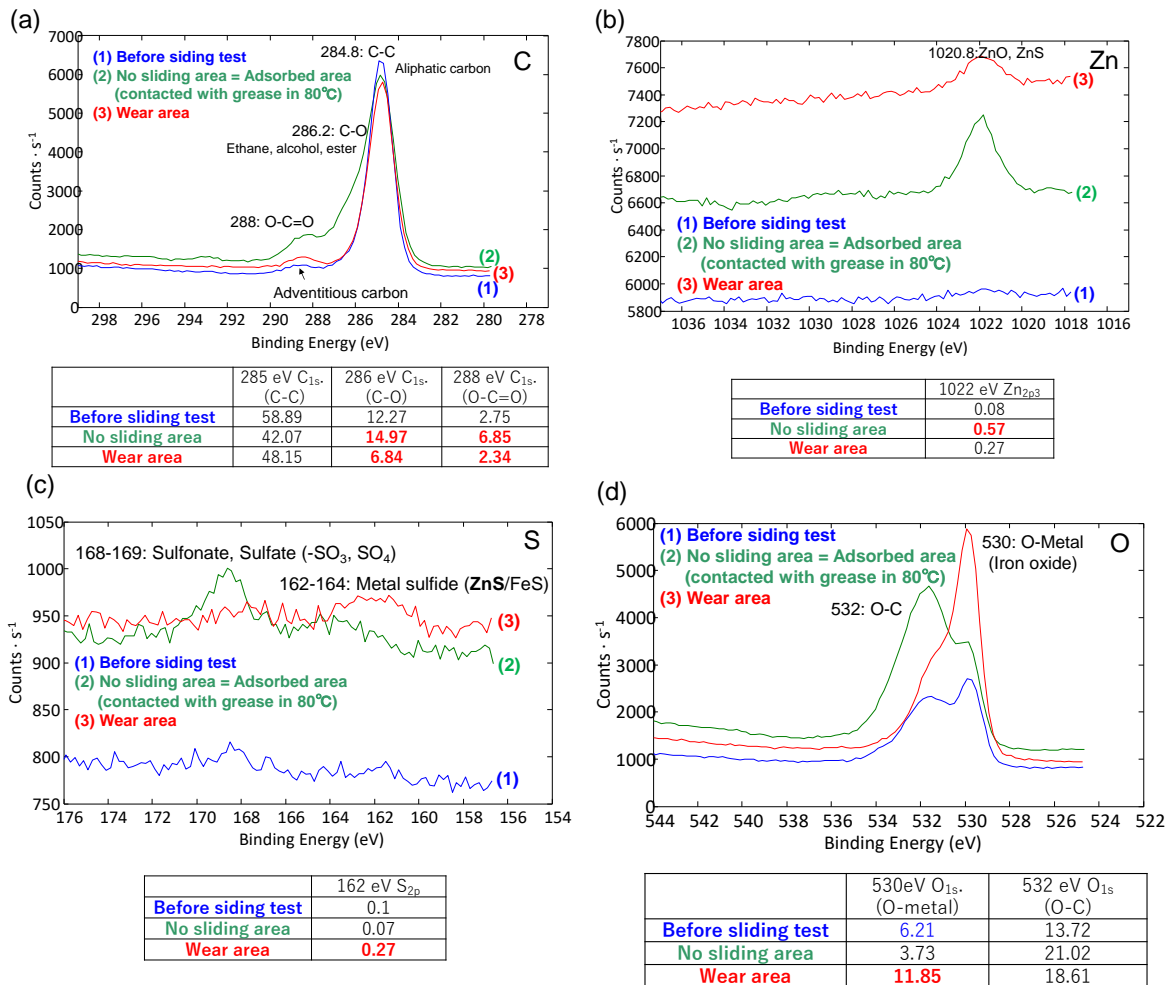


Fig. IV. 26 Charts of XPS analysis and amounts of each chemical state estimated based on the curve fitting of the XPS analysis results: (a) C; (b) Zn; (c) S; (d) O.

In summary, the XPS analysis results did not identify the composition of the patches (film) on the surface of the steel cylinder, although small amount of ZnS was observed. Therefore, ToF-SIMS analysis which is supposed to be advantageous to detect the hydrocarbon film was conducted to identify the composition.

4.1.3 ToF-SIMS analysis

ToF-SIMS analysis was conducted on the surface of the new steel cylinder, the cylinder after 13,000 cycles of the sliding test with no wear area (with grease contact for 6 h at 80°C), and the cylinder in wear area, as already presented in Fig. IV. 24.

Fig. IV. 27 shows the relative intensities of the detected carboxylates ions in each analyzed area, which were obtained based on the normalization of the intensity of FeO_2^- . Fig. IV. 28 shows the chemical mapping of stearic and palmitic ions on the steel cylinder after the sliding test in the no wear and wear areas (the decrease in the concentration of ions at the top and bottom of all images is due to the curvature of the steel cylinder). Six different types of carboxylates were detected from all analyzed surfaces, with palmitic and stearic ions having the highest concentrations. Intensities related to palmitic and stearic ions particularly increase in the no wear area as compared to the surface of the new cylinder (without a sliding test). It is then considered that different types of carboxylates coming from zinc carboxylates additive added to the grease were adsorbed into the steel surface by heating at 80°C. Furthermore, the intensities of the carboxylates ions on the wear surface are greater than on the no wear area. This indicates that the formation of the tribofilm was accelerated by the energy induced by the sliding (i.e., the pressure, shear, and heat), in addition to the simply adsorbed film. Chemical mapping images indicate that the intensities of the stearic or palmitic ions are higher in all areas of the sliding surface than on the surface without sliding. In addition, the same types of carboxylates are detected even on the surface of the new cylinder after the same washing process using an ultrasonic and organic solvent. Some of these carboxylates are thought to be derived from the oil used during the machining process of the steel cylinders, or rust-preventive oil used during the preservation of the steel cylinders.

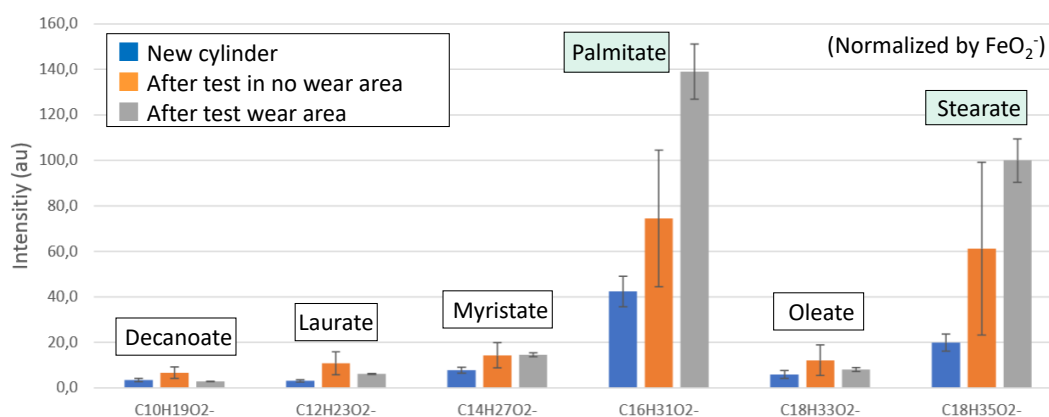


Fig. IV. 27 Relative intensities of carboxylates in each analyzed area on the steel surface measured using ToF-SIMS (average value of three different analyses).

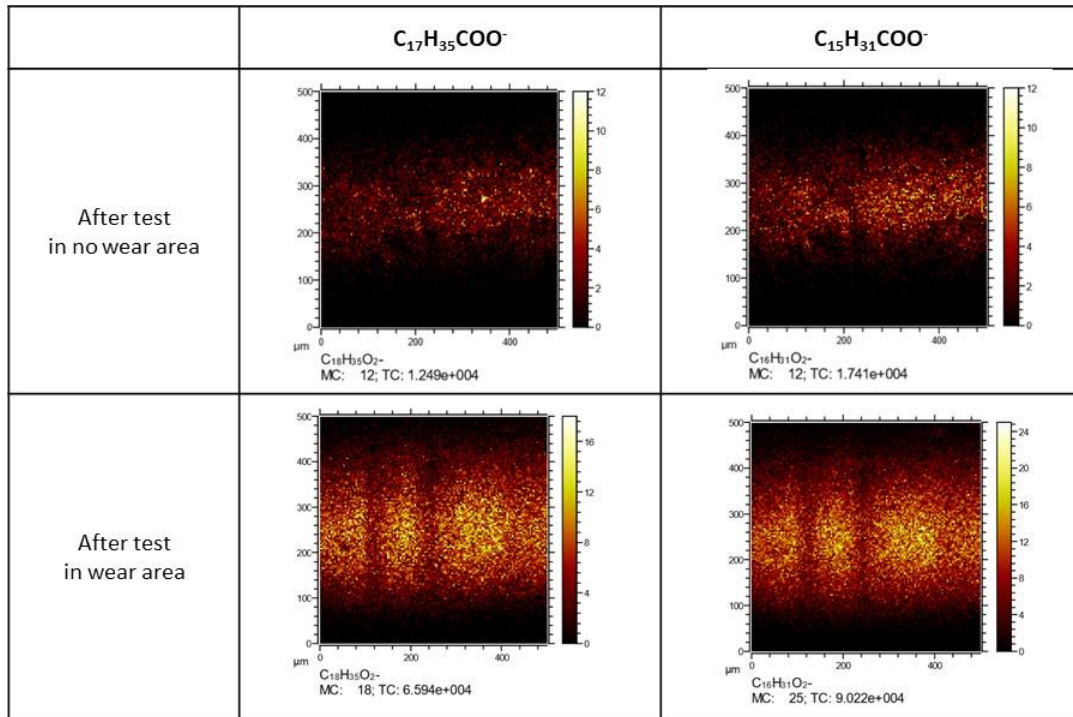


Fig. IV. 28 Chemical mapping of stearic and palmitic ions on the steel cylinders analyzed using ToF-SIMS.

Furthermore, a depth profile analysis was conducted to investigate the presence of the film from the outermost surface to the core of the substrate. Fig. IV. 29 shows the depth profile of the steel cylinder after 13,000 cycles of the sliding test in the no wear area (in contact with the grease at 80°C for 6 h) and the wear area. The intensities are normalized by the iron bulk signal at the end of the profiles. In both areas, an iron oxide layer is observed on the steel surface, and the depth profile is similar. However, much larger amounts of carboxylates (stearic or palmitic ions) are present on the surface of the wear area compared to the no wear area. Both carboxylates and iron oxide (Fe_2O_4^-) decrease gradually with an increase in the sputter time. Therefore, it is believed that a non-uniform carboxylates-based tribofilm is present on the iron oxide layer.

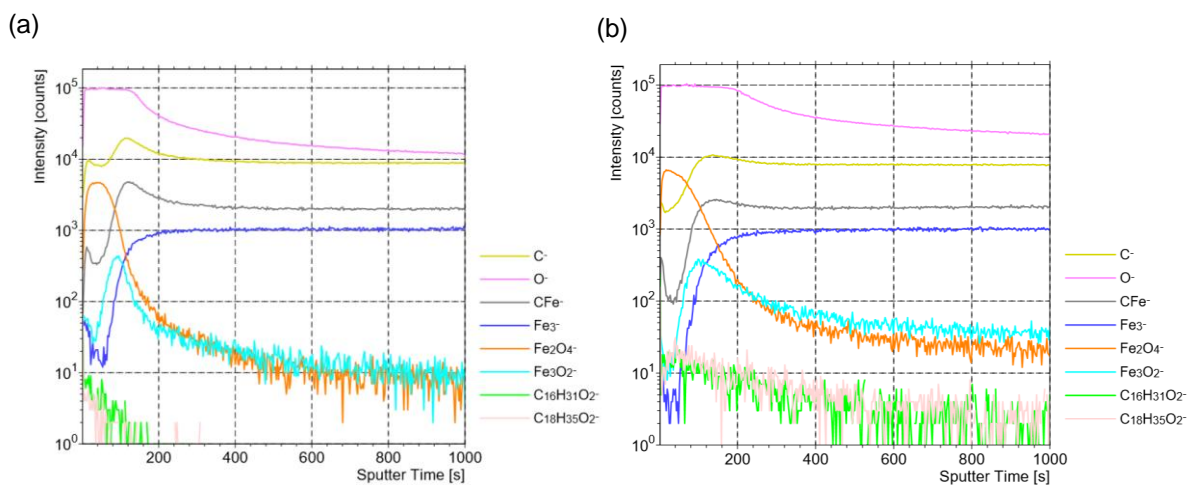


Fig. IV. 29 Depth profile of ToF-SIMS analysis on the steel cylinder: (a) no wear and (b) wear areas.

Fig. IV. 30 shows 3D images of the repartition of stearic and palmitic ions (observed area of $80\ \mu\text{m} \times 80\ \mu\text{m}$, where the depth of scale of the 3D images is unknown, but is extremely small compared to $80\ \mu\text{m}$) and 2D images of stearic ions observed from the top surface in both the no wear and wear areas. In the wear area, stearic and palmitic ions are heterogeneously distributed, and also exist in the form of spots (indicating a high local concentration of carboxylates) on the sliding surface. The lateral size of these spots is approximately $5\text{--}20\ \mu\text{m}$, i.e., the same size as the dark patches observed using SEM. The depth of these spots cannot be precisely measured, but we may expect that it is more at the nano-scale than at the micro-scale (considering the measurement depth of ToF-SIMS). Therefore, these spots are considered to be formed from softened carboxylates that form the iron carboxylates on the steel surface [140].

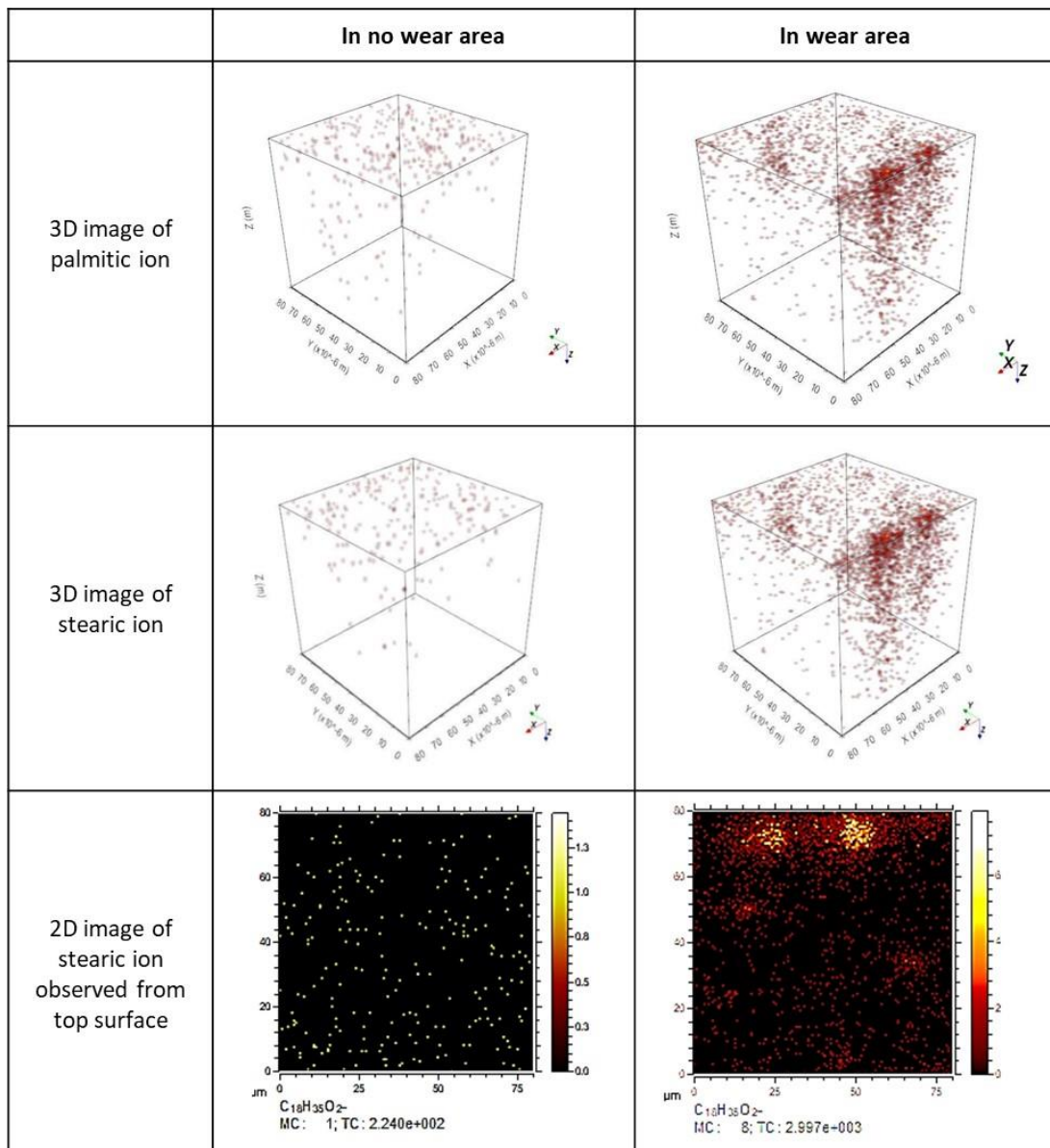


Fig. IV. 30 3D images of stearic and palmitic ions (observed area of $80\ \mu\text{m} \times 80\ \mu\text{m}$) and 2D images of stearic ions observed from the top surface in the no wear area and the wear area analyzed using ToF-SIMS.

Fig. IV. 31 shows the relative intensity of Zn^{+} (originating from zinc carboxylate in the grease) on the surface of each steel cylinder normalized based on the signal of Fe^{+} and analyzed using ToF-SIMS. The number of zinc ions is higher on the cylinder surface after 13,000 cycles of the sliding test in the no wear area than in the new cylinder without sliding. However, the number of zinc ions in the cylinder in the wear area is lower than that in the no wear area. In addition, Fig. IV. 32 shows the chemical mapping images of Zn^{+} , SO_3^{-} , CSN^{-} , and CNO^{-} (the last three ions are considered to have originated from the sulfur-type anti-oxidation agent or diurea thickener in the grease, and no compound related to the base oil was observed) on the surface of the steel cylinder analyzed using ToF-SIMS. The intensities of these peaks on the surface of the no wear area are higher than those in the wear area. This tendency differs from the analysis results of the carboxylates (palmitate or stearate).

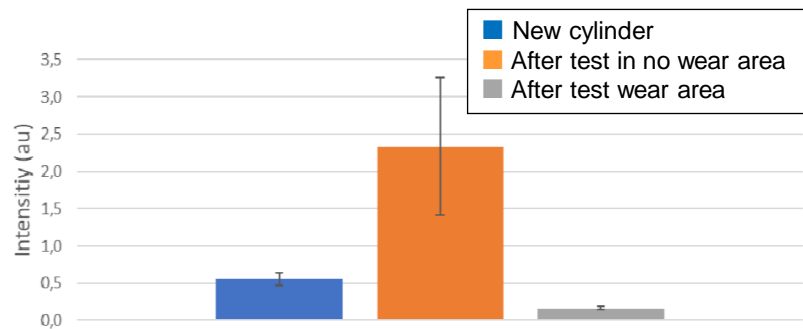


Fig. IV. 31 Relative intensity of Zn^{+} on the surface of each steel cylinder normalized by the Fe^{+} signal through a ToF-SIMS analysis (average value of three different analyses).

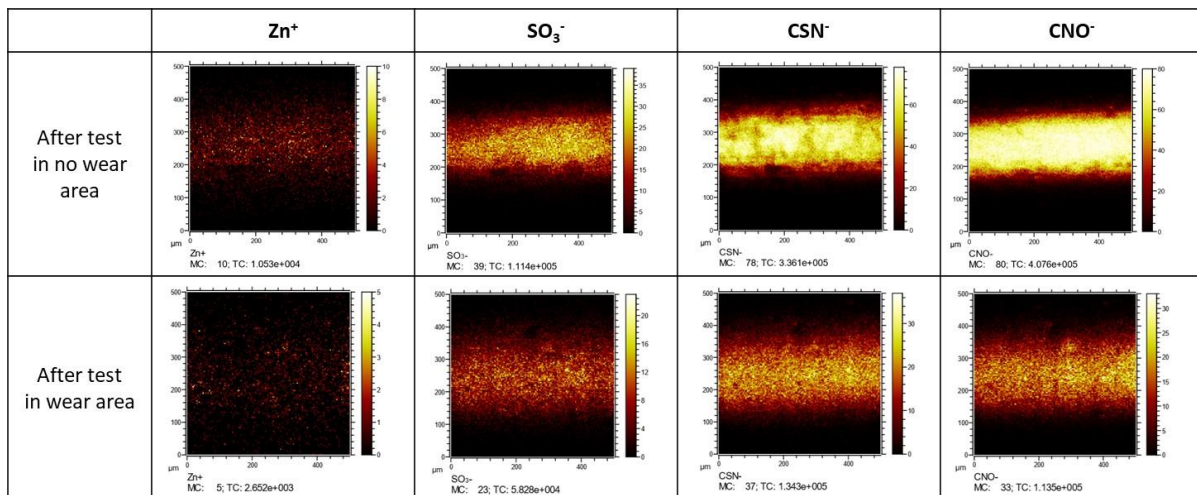


Fig. IV. 32 Chemical mapping of Zn^{+} , SO_3^{-} , CSN^{-} , and CNO^{-} based on a ToF-SIMS analysis on the surface of the steel cylinder in the no wear area or the wear area.

4.2 Tribofilm analysis on the GF-reinforced PA66 composite

4.2.1 SEM observation and EDX analysis

The chemical composition on the surface of the GF-reinforced PA66 ring was analyzed to clarify the chemical reaction on the composite. Fig. IV. 33 shows the evolutions of the amounts of Zn and S on the sliding surface of the composite after different numbers of cycles of the sliding tests at 80°C as measured using EDX, presenting the evolutions of the vertical displacement and the friction coefficient of the sliding test described in Section 3. Although

Zn and S were not detected from the surface of the composite ring after 1,000 cycles, the amounts of Zn and S increase after 5,000 cycles until the sudden increase of the vertical displacement, and decrease at 42,000 cycles. Fig. IV. 34 shows the SEM and EDX images of Si (related to the GF), and Zn and S after 13,000 cycles of the sliding test at 80°C. There is a tendency for Zn and S to exist at the same location of the composite ring.

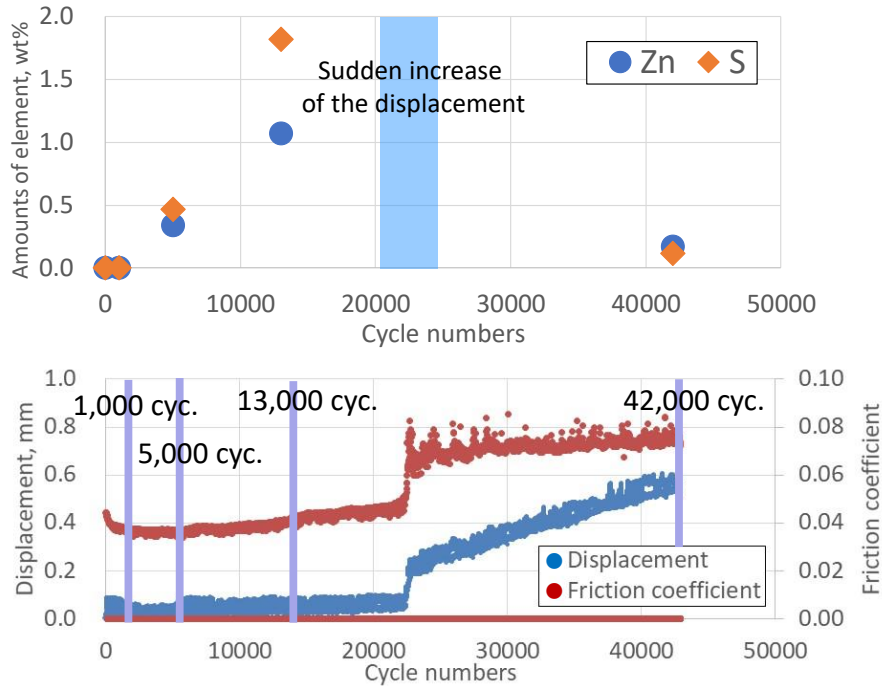


Fig. IV. 33 Evolutions of the amounts of Zn and S on the sliding surface of the composite after different numbers of cycles of the sliding test at 80°C as measured using EDX.

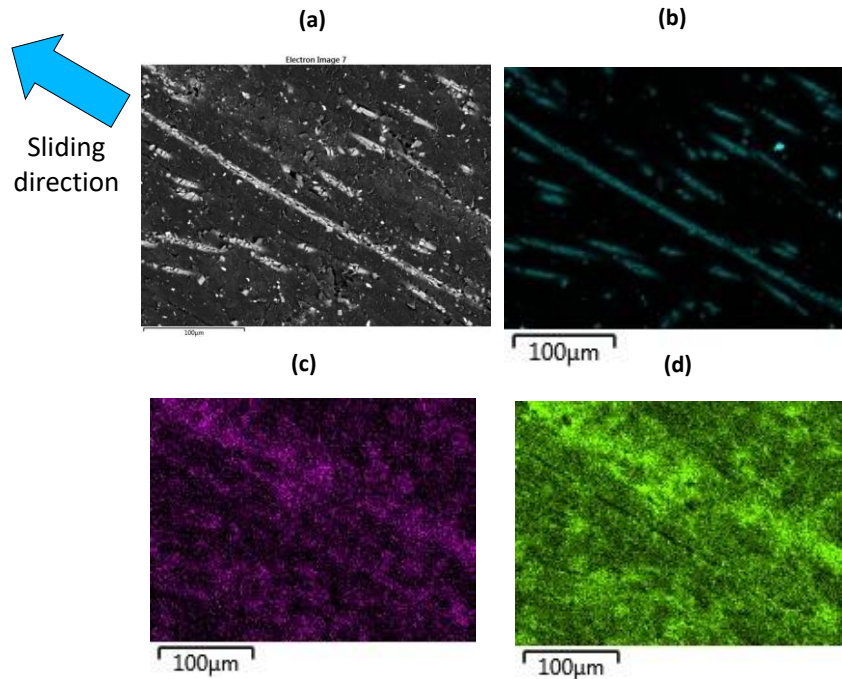


Fig. IV. 34 SEM and EDX images of composite surface after 13,000 cycles of the sliding test at 80°C; (a) SEM image and EDX images of (b) Si, (c) Zn, and (d) S.

4.2.2 XPS analysis

To identify the chemical states of Zn and S, an XPS analysis of the sliding surface of GF-reinforced PA66 composite after 13,000 cycles of the sliding test at 80°C was carried out. Four different areas of the sliding surface (the inner area, two different center areas, and the outer area) were analyzed, along with the surface of the new composite ring as a baseline.

Fig. IV. 35 presents the obtained chart of XPS analysis in wide range analysis, and Fig. IV. 36 presents the narrow range analysis of S and Zn. These results show that the peaks of S_{2p} and Zn_{2p3} are detected only on the surface after the tests in the four analyzed areas. The position of the S_{2p} peak indicates the presence of a sulfide and agrees well with the binding energies measured in ZnS [180, 181]. The measured binding energy for Zn of 1021.6 eV can correspond to both ZnO or ZnS [180, 181]; however, because no metallic oxide contribution is found in the O_{1s} region, it is probable that the signal in Zn_{2p} is related to ZnS almost entirely. In addition, the fitting data of these peaks listed in Table IV. 2 indicate that the atomic ratio of S_{2p} and Zn_{2p3} is approximately the same in all areas, and is near 1. Therefore, the formation of a reactive ZnS tribofilm by the reaction of zinc carboxylate and a sulfur-type anti-oxidation agent induced by sliding was identified. On the other hand, Table IV. 3 lists the amounts of each chemical state related to C estimated based on the curve fitting of the XPS analysis results. The proportion of O-C=O bond was lower in the sliding area than new surface, and it is not possible to characterize the formation of a hydrocarbon film on the composite surface.

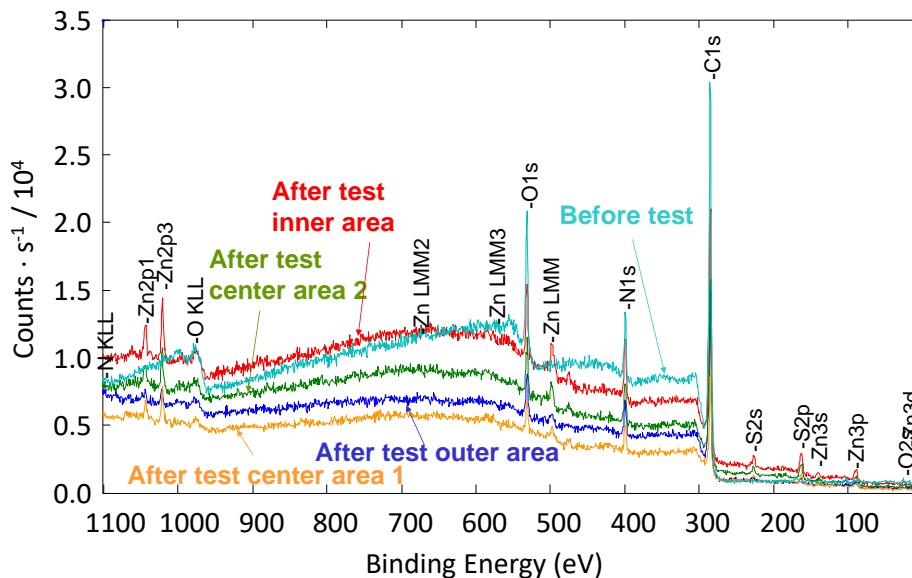


Fig. IV. 35 Results of XPS wide scanning analysis of composite surface before/after the sliding tests for 13,000 cycles at 80°C using the grease containing zinc carboxylate and sulfur-type anti-oxidation agent.

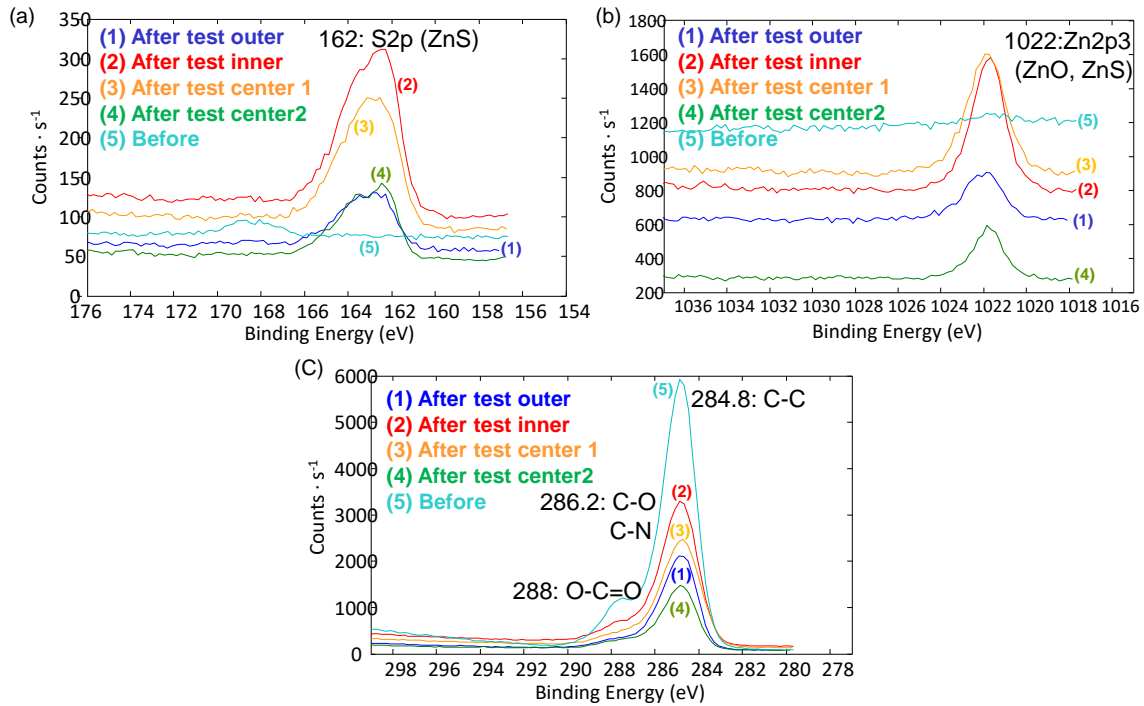


Fig. IV. 36 Results of narrow scanning XPS analysis of composite surface before/after the sliding tests for 13,000 cycles at 80°C using the grease containing zinc carboxylate and sulfur-type anti-oxidation agent; (a) S_{2p} ; (b) Zn_{2p3} ; (c) C.

Table IV. 2 Amounts of each chemical state estimated based on the curve fitting of the XPS analysis results (S_{2p} and Zn_{2p3}).

	162 eV S_{2p}	1022 eV Zn_{2p3}	Ratio of S_{2p}/Zn_{2p3}
After test of outer area	0.9 at%	1.0 at%	0.9
After test of center area 1	1.7 at%	1.9 at%	0.9
After test of center area 2	1.7 at%	1.3 at%	1.3
After test of inner area	1.7 at%	1.5 at%	1.1
Before test	0.0 at%	0.1 at%	-

Table IV. 3 Amounts of each chemical state estimated based on the curve fitting of the XPS analysis results (C).

	285 eV C_{1s} . (C-C)	286 eV C_{1s} . (C-O)	288 eV C_{1s} . (O-C=O)
After test of outer area	57.5 at%	13.6 at%	5.8 at%
After test of center area 1	57.3 at%	10.7 at%	5.9 at%
After test of center area 2	57.9 at%	11.6 at%	6.4 at%
After test of inner area	55.8 at%	11.0 at%	6.7 at%
Before test	58.9 at%	9.9 at%	8.9 at%

4.2.3 ToF-SIMS analysis

In addition, to investigate the presence or not of a carboxylates film on the surface of the GF-reinforced PA66 composite ring, a ToF-SIMS analysis of the composite surface was also conducted. However, no peaks of carboxylates (palmitic or stearic ions) were detected from the surface of the new composite ring (without a sliding test), the composite ring in which a 350 N normal load was applied for 6 h in the presence of grease at 80°C, or the composite ring after 13,000 cycles of the sliding test at 80°C, contrary to the results obtained for the surface of the steel cylinder after the same number of cycles. This result indicates that carboxylates preferentially adhere to the surface of the steel and do not adhere to the surface of GF-reinforced PA66.

4.3 Tribochemical reaction on the sliding surface

To investigate the location of the ZnS tribofilm on the surface of the composite, an EDX point analysis was conducted on the PA66 and GF surfaces using the same composite ring after 13,000 cycles of the sliding test at 80°C. Fig. IV. 37 shows the amounts of each chemical element on the surfaces of the PA66 and GF (composed of Si, Ca, Al, Mg and O). The average values of the measurement at five different locations are shown. The results indicate that a ZnS tribofilm is only present on the surface of the PA66, and no ZnS tribofilm was identified on the surface of the GF, the reason for which is related to the difference in the contact pressure in each area. The hardness of the GF (5.7 GPa measured based on the nano indentation) is much higher than the hardness of the PA66 (0.16 GPa measured based on the micro indentation). It is the same for the Young's modulus. Therefore, the partial contact pressure between the GF and steel is very large compared to the one between PA66 and steel; and, if formed, the ZnS tribofilm on the GF is considered to be easily peeled off by the sliding.

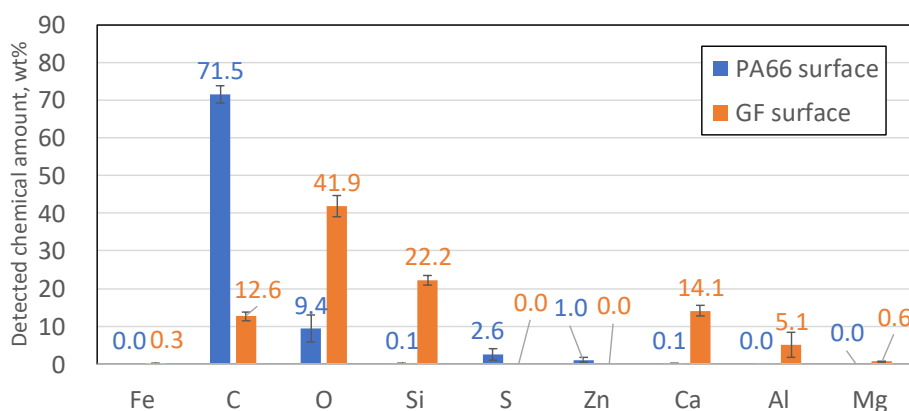


Fig. IV. 37 Amounts of chemical elements on the surface of PA66 and GF measured using EDX after 13,000 cycles of the sliding test at 80°C using grease which contains zinc carboxylate and sulfur-type anti-oxidation agent (average value of five different measurement areas).

Fig. IV. 38 shows sketches of the tribochemical reaction on the sliding surface of the composite and steel. For the sake of simplicity, the roughness of either counterbody (which is much larger than the sizes of the molecules) is not shown in these images. The carboxylates of zinc carboxylates additives bind to the iron of the steel surface to form what is called in the literature a “soap” layer (iron carboxylates [140, 182]), and zinc goes to the polymer part of the composite and reacts with sulfur present in the anti-oxidation agent to form ZnS.

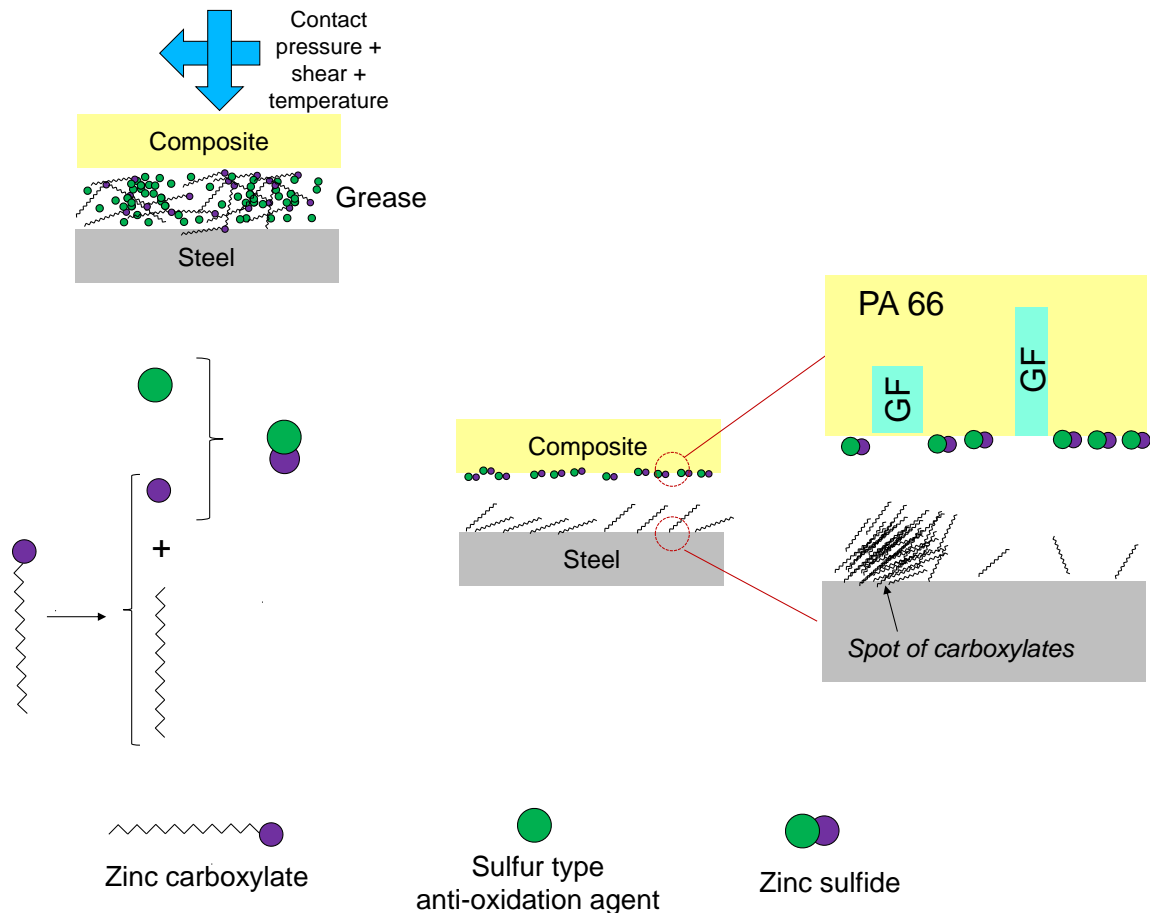


Fig. IV. 38 Tribochemical reaction on the sliding surface. The lateral and depth scales are not respected in these images.

5. Contribution and roles of tribofilm on the tribological properties

To clarify the effects of the carboxylate tribofilm on the steel surface and the effects of the ZnS tribofilm on the PA66 surface on the improvement of the tribological properties, additional sliding tests were conducted at 80°C using grease containing zinc carboxylate but not a sulfur-type anti-oxidation agent (grease no. 3 in Table IV. 1), applying a stopping time of 200 s (allowing us to maintain a constant temperature), using GF-reinforced composite. Fig. IV. 39 shows the evolutions of the friction coefficient and the vertical displacement, comparing the results of grease no. 1 and grease no. 2, as previously shown in Fig. IV. 6. Using grease no. 3, the sudden increases in the friction coefficient and in the vertical displacement appear much later than when using grease no. 2 (without zinc carboxylate but with a sulfur-type anti-oxidation agent). By comparing the results with grease no. 3 and grease no. 1, we can conclude that, with zinc carboxylate present in the grease, the addition of a sulfur-type anti-oxidation agent allow a low-friction coefficient to be maintained for a greater number of cycles, leading to lower wear; however, this has no impact on the friction coefficient values before or after the sudden increase, indicating that the effects of the addition of zinc carboxylate on the improvement of the tribological properties is greater than the effect of the addition of a sulfur-type anti-oxidation agent. Consequently, we can conclude that a reduction in the friction

induced by the creation of carboxylates patches on the steel cylinder is the main effect of the presence of additives in the grease, and on the tribological behavior of the contact.

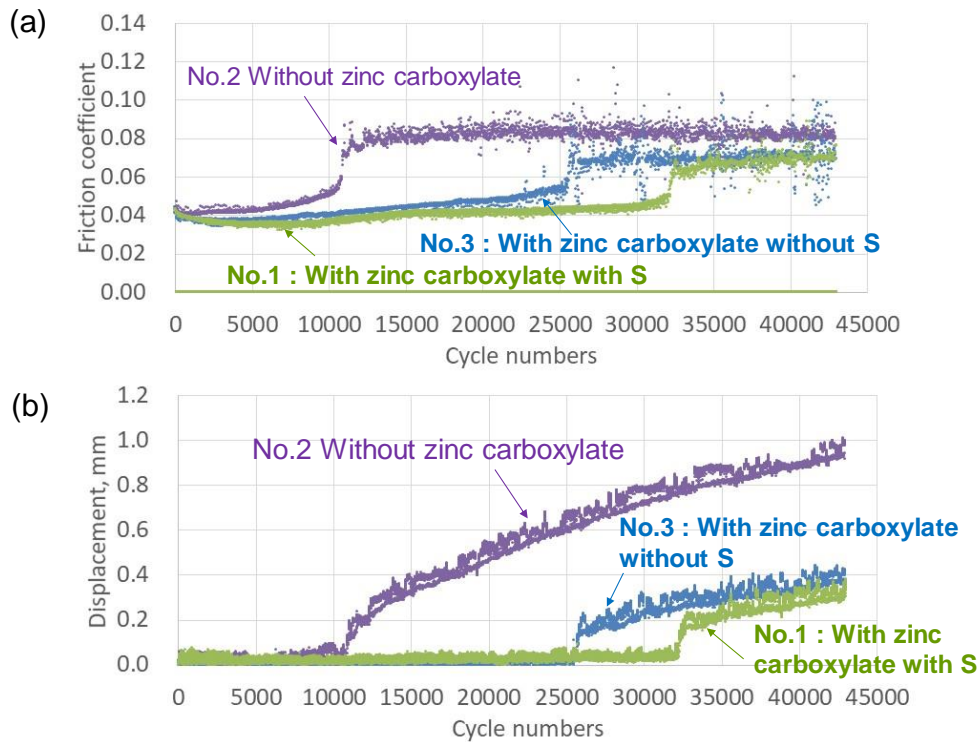


Fig. IV. 39 Evolutions of (a) friction coefficient and (b) displacement during the sliding test at 80°C using grease no. 1, 2, or 3 and GF-reinforced composite.

Fig. IV. 40 shows a narrow scan analysis of the XPS in the composite surface after 13,000 cycles of a sliding test at 80°C when using grease no. 1 (containing both zinc carboxylate and a sulfur-type anti-oxidation agent) and grease no. 3 (containing zinc carboxylate but not a sulfur-type anti-oxidation agent). Table IV. 4 lists the amounts of each chemical state obtained by the peak fitting of the results of the XPS analysis. The detected amounts of not only S_{2p} but also Zn_{2p3} were low even when the surface was obtained by a sliding test using grease containing zinc carboxylate. Therefore, the estimated amount of the ZnS tribofilm is significantly low on the composite surface after the test without a sulfur-type anti-oxidation agent. It is indeed necessary to have a source of sulfur to form an adherent ZnS film on the surface of the composite, and there is no adhesion of Zn alone when S is not present, confirming the tribochemistry origin of the presence of Zn and S on the surface of the composite. These results confirm that the contribution of a carboxylates tribofilm on the steel is much greater than the effect of the formation of the ZnS tribofilm on the PA66 surface in terms of the improvement of the tribological properties.

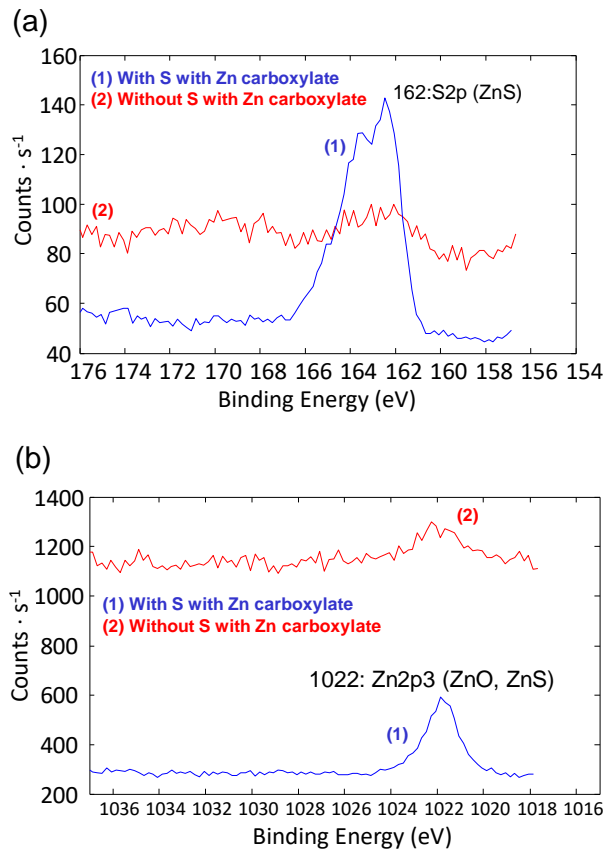


Fig. IV. 40 Results of XPS analysis of the composite surface after 13,000 cycles of a sliding test at 80°C using grease no. 1 or no. 3: narrow range scanning of (a) S and (b) Zn.

Table IV. 4 Amounts of each chemical state estimated by the curve fitting of the XPS analysis results after 13,000 cycles of a sliding test at 80°C using grease no. 1 or no. 3.

	162 eV S _{2p}	1022 eV Zn _{2p3}
With sulfur-type anti-oxidation agent with zinc carboxylate	1.5 at%	1.4 at%
Without sulfur-type anti-oxidation agent with zinc carboxylate	0.1 at%	0.1 at%

The reason for the improvement of the tribological properties through the addition of zinc carboxylate is discussed herein, along with the decreasing effect of the friction coefficient described in Section 3. Fig. IV. 41 shows the maximum friction coefficient for each 1 s (the friction coefficient is measured every 0.01 s and the maximum value during each 1 s was extracted) of the sliding test for a stopping time of 200 s at 80°C when using grease no. 1 or grease no. 2, and GF-reinforced composite. The maximum friction coefficient upon a restart after the 200 s stopping phase is the static coefficient, the value of which is higher than the maximum value of the friction coefficient during the sliding phase over the remaining 199 s. The results indicate that the average values of the static coefficient during the initial 10,000 cycles with or without the addition of zinc carboxylate (grease no. 1 and grease no. 2) are 0.093 and 0.138, respectively. Therefore, the addition of zinc carboxylate decreases the adhesion between the composite and steel during the stopping phase, and the damage of the

contact surface after the restart can be decreased. Consequently, the wear and creep of the composite and the wear of the steel counterpart are reduced.

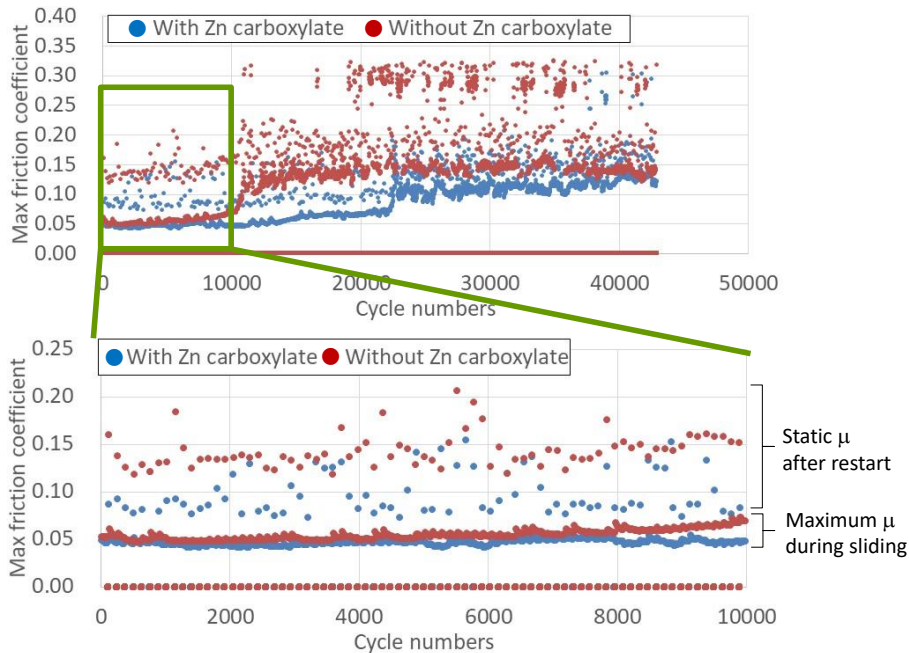


Fig. IV. 41 Evolutions of maximum friction coefficient during the sliding tests for a stopping time of 200 s at 80°C when using grease no. 1 or grease no. 2 and GF-reinforced composite.

6. Temperature dependence on tribofilm formation

To better understand the effect of temperature on the tribological properties, as presented in Section 3, the amounts of Zn and S on the sliding surface of the GF-reinforced PA66 composite after the sliding tests were measured based on EDX using grease no. 1 (containing both zinc carboxylate and sulfur-type anti-oxidation agent). Fig. IV. 42 shows the SEM and EDX images of Zn and S on the sliding surface after the test for a stopping time of 200 s for different temperatures and cycle numbers. The detected amounts of Zn and S after 13,000 cycles of the test at room temperature are significantly lower, and these results can explain why the addition of zinc carboxylate did not improve the tribological properties at room temperature: We can consider the thermal activation needed for tribochemistry as not being reached during the tests at room temperature. The detected amounts of Zn and S after 5,000 cycles of the sliding test at 120°C are higher than those at 80°C for the same numbers of cycles. The presence of Zn and S tribofilms can explain the decrease in the friction coefficient at 120°C through the addition of zinc carboxylate and a sulfur-type anti-oxidation agent into the grease. However, an improvement in the wear and creep by the addition of zinc carboxylate was not observed, as presented in Section 3, because the effect of the degradation in the mechanical properties (the hardness of the sliding surface of the composite, as described in Section 3) at 120°C is considered to be greater than the positive effect of the tribofilm formation. In addition, the transition temperatures of carboxylate on the steel surface (iron carboxylate soap), such as laurate, myristate, palmitate, or stearate are 110°C–140°C (much higher than the melting point of each fatty acid itself) [140, 182]. Therefore, adhesion between the molecules in the boundary film is diminished and a breakdown of the

soap film on the steel is considered to occur by the sliding heat during the test at 100-120°C, leading to the increase in the wear and creep of the composite as presented in Fig. IV. 8 .

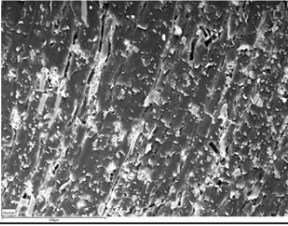
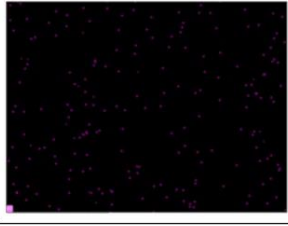

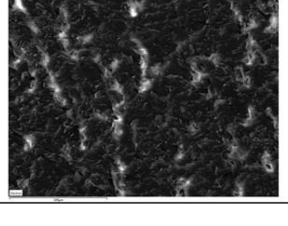
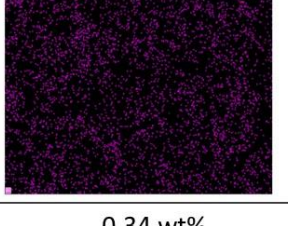
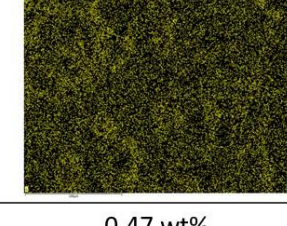
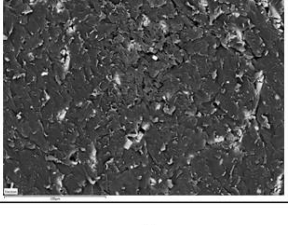
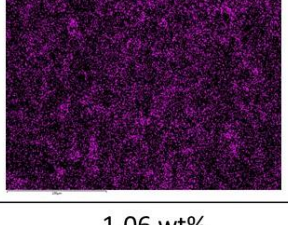
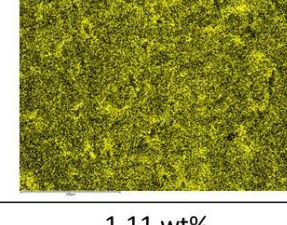
	SEM	Zn	S
RT 13,000 cycles			
	-	0.10 wt%	0.01 wt%
80°C 5,000 cycles			
	-	0.34 wt%	0.47 wt%
120°C 5,000 cycles			
	-	1.06 wt%	1.11 wt%

Fig. IV. 42 SEM and EDX images of Zn and S for different values of temperature and numbers of cycles of the sliding tests for a stopping time of 200 s using grease no.1 and GF-reinforced PA66 composite.

7. Effects of adding zinc carboxylate to grease on the tribological properties of unreinforced PA66

The effects of adding zinc carboxylate to grease on the tribological properties of unreinforced PA66 were investigated during the sliding test under a stopping time of 1 s (inducing a temperature increase from the heat generated by sliding). Fig. IV. 43 shows the evolutions of the friction coefficient, the temperature, and the vertical displacement using grease with or without zinc carboxylate (grease no. 1 and grease no. 2). The average friction coefficient during the sliding is 0.050 ± 0.003 with zinc carboxylate and 0.054 ± 0.004 without zinc carboxylate, and a slight effect of the decrease in the friction coefficient is observed. However, the effect of the addition of zinc carboxylate to grease on the decrease in the friction coefficient is much lower than the effect observed in GF-reinforced PA66. In addition, a slight effect from the decrease in temperature was observed by the decrease in the friction coefficient. A gradual increase in creep during the initial phase of the sliding test is observed. However, the proportional increase in the vertical displacement related to the wear, as observed in the GF-reinforced PA66, is not confirmed. Furthermore, a slight effect from the addition of zinc carboxylate on the decrease in the displacement is observed. The height loss

after 61,500 cycles of unreinforced PA66 is smaller than the height loss of GF-reinforced PA66. Regardless of the addition of zinc carboxylate to the grease, a wear height loss was not observed, and most of the height loss (80%–95%) was creep.

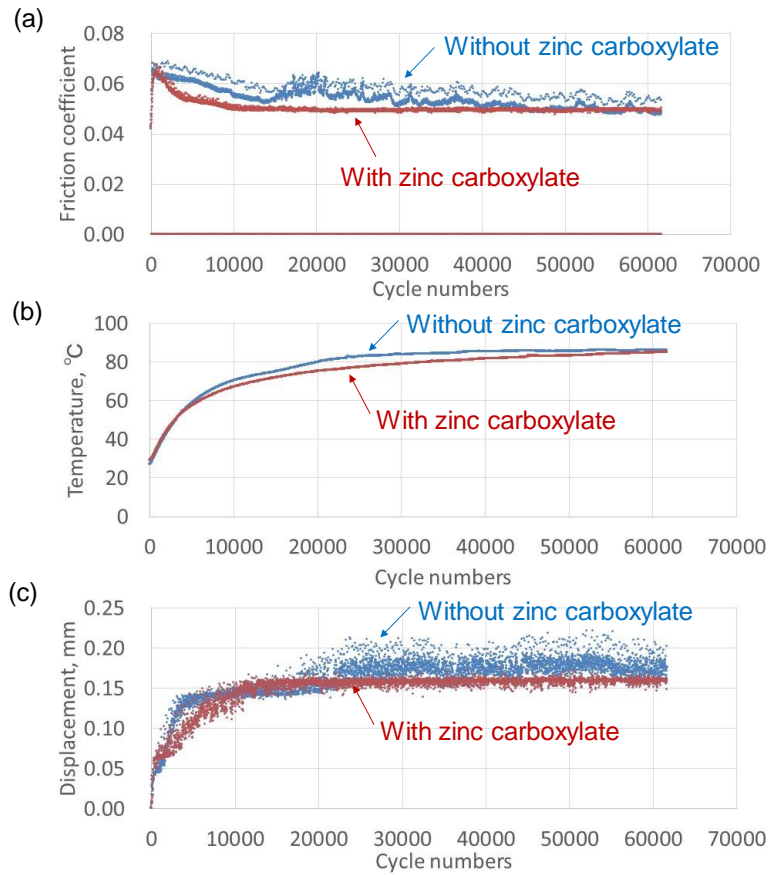


Fig. IV. 43 Evolutions of (a) friction coefficient, (b) temperature, and (c) vertical displacement in the sliding tests with a 1 s stopping phase of unreinforced PA66 with or without zinc carboxylate in grease.

Fig. IV. 44 shows the optical microscope observations of the sliding surface of the unreinforced PA66. A sliding scar was observed in samples with and without zinc carboxylate added to the grease. However, severe wear or a peeling of the surface observed in GF-reinforced PA66 was not observed.

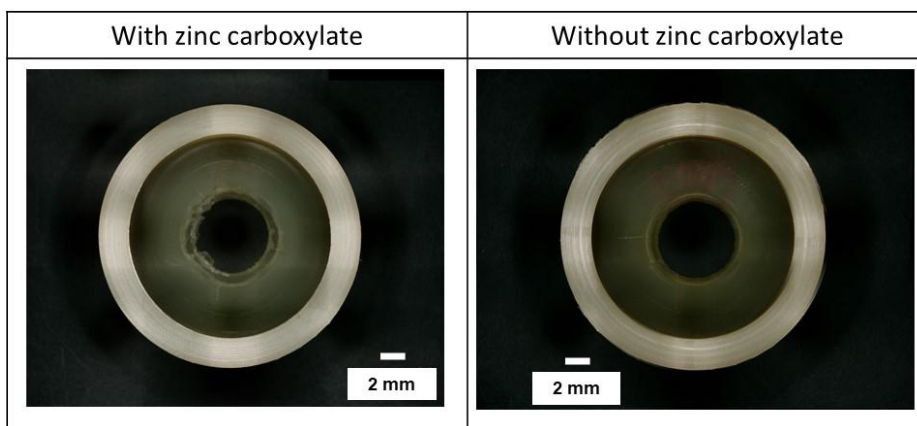


Fig. IV. 44 Optical microscope observations of the sliding surface of unreinforced PA66.

To compare the tribofilm formation between unreinforced PA66 and GF-reinforced PA66, sliding tests under the same conditions as presented in Section 3 (at 80°C, 200 s stopping, for 13,000 cycles) were conducted using grease with or without zinc carboxylate (grease no. 1 and grease no. 2). Fig. IV. 45 shows the evolutions of the friction coefficient and the vertical displacement. A decrease of 11.7% in the average friction coefficient is observed, which is less than the effect in GF-reinforced PA66. In addition, a slight effect of the decrease in displacement is observed.

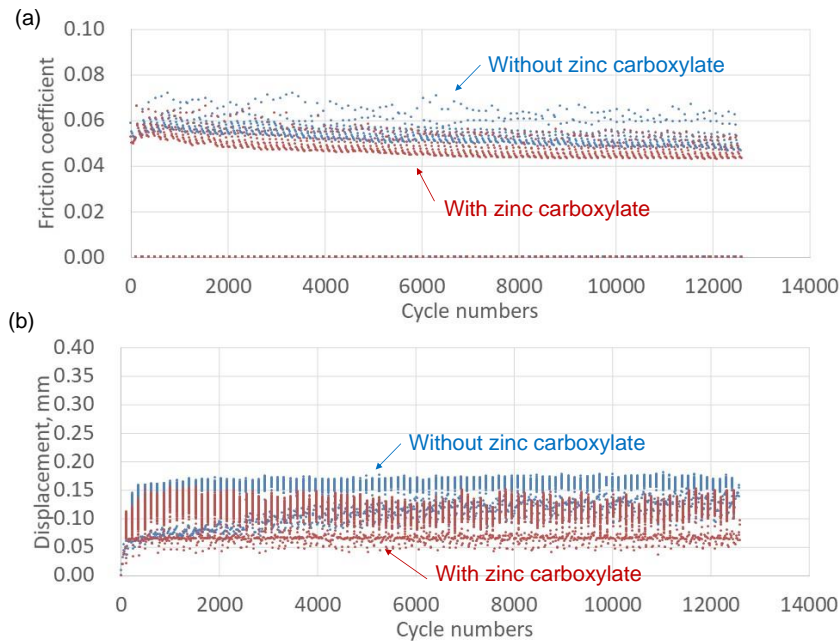


Fig. IV. 45 Evolutions of (a) friction coefficient and (b) vertical displacement during the sliding test at 80°C, with a 200 s stopping phase of the unreinforced PA66 with or without zinc carboxylate in grease.

Fig. IV. 46 shows the SEM observations of the steel cylinder after the sliding test when using the grease containing zinc carboxylate. As with the test using GF-reinforced PA66, dark patches can be seen on the sliding surface. However, the total area of the patches is less than that of the cylinder after the test with a GF-reinforced PA66, as shown in Fig. IV. 18.

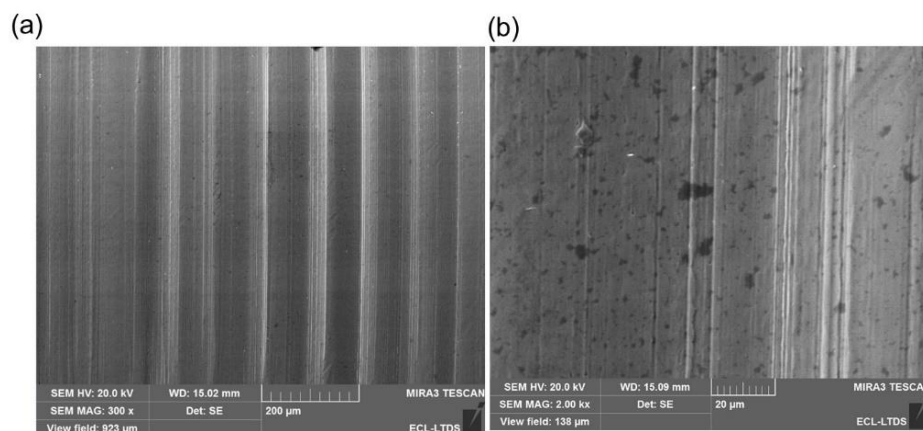


Fig. IV. 46 SEM observations of the steel cylinder after 13,000 cycles of the sliding test with unreinforced PA66 with grease containing zinc carboxylate (grease no. 1) (a) at a magnification of $\times 300$; (b) at a magnification of $\times 2,000$.

Fig. IV. 47 shows the detected amounts of the chemical elements measured by the point analysis of the patches with EDX, as compared with the amounts on the new steel cylinder, and on the cylinder tested with GF-reinforced PA66 under the same test conditions, as presented in Section 4.1. The proportion of C and O increases and that of Fe decreases compared to the new steel cylinder. However, the detected amounts are smaller than in the results for the test with GF-reinforced PA66, and Zn and S are not detected at all. Considering the results of the ToF-SIMS analysis presented in Section 4.1, a tribofilm of carboxylates composed of hydrocarbon and oxygen was considered to have formed. This difference in the detected amounts of chemical elements and the area of the patches is attributed to the difference in the contact pressure between the PA66 and steel. The Young's modulus of the GF composite is higher than that of the unreinforced PA66 owing to the addition of stiff GF. Therefore, the higher contact pressure in the sliding test between the GF composite and steel promotes the formation of a tribofilm on the steel surface, and the effect of the decrease in the friction coefficient becomes greater.

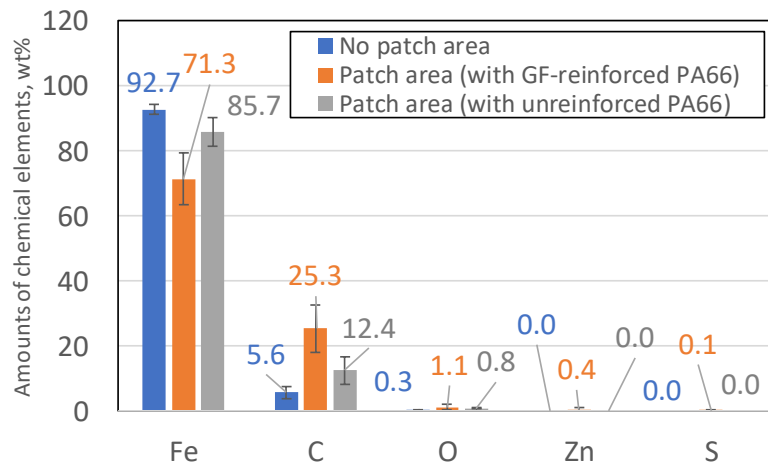


Fig. IV. 47 Detected amounts of chemical elements of the steel cylinder after 13,000 cycles of the sliding test with unreinforced PA66 with grease containing zinc carboxylate (grease no. 1) measured using EDX (average value of three different analyses).

In addition, Fig. IV. 48 shows an SEM image of the sliding surface of unreinforced PA66 after 13,000 cycles of the sliding test under the same conditions. Fig. IV. 49 shows the detected chemical elements measured using EDX as compared with the results of the new unreinforced PA66 ring (without sliding test). The results indicate that Zn and S are detected along with Fe related to the wear debris of the steel counterpart, and ZnS tribofilm is considered to have formed on the surface of the unreinforced PA66, similar to what happened for the GF-reinforced PA66.

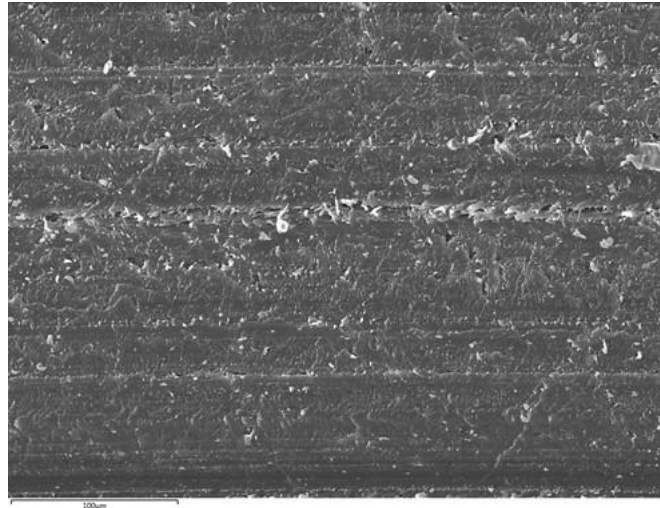


Fig. IV. 48 SEM observation of the sliding surface of unreinforced PA66 ring after 13,000 cycles of the sliding test at 80°C with 200 s stopping phase with zinc carboxylate added to the grease (grease no. 1).

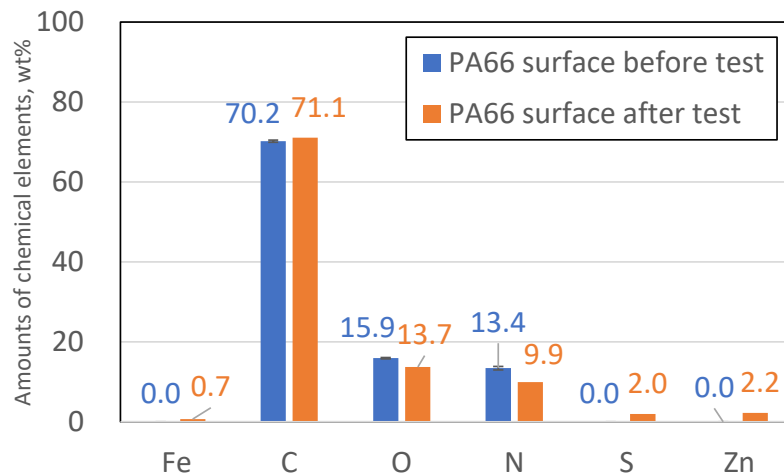


Fig. IV. 49 Amounts of chemical elements on the surface of PA66 before/after 13,000 cycles of the sliding test at 80°C with 200 s stopping phase with zinc carboxylate added grease (grease no. 1) as measured using EDX (average value of three different analyses).

8. Conclusions

The effects of temperature and the addition of zinc carboxylate to grease on the tribological properties of PA66 in contact with carbon steel were clarified. The tribological properties can be described by considering the temperature dependence of both the mechanical properties of PA66 and the tribochemistry. The following points have been highlighted.

1) Wear and creep resistance of GF-reinforced PA66 using grease without the addition of zinc carboxylate

Wear and creep resistance of GF-reinforced PA66 deteriorated with an increase in temperature using grease without the addition of zinc carboxylate. This can be explained by

the temperature dependence of the mechanical properties on the sliding surface of the composite (hardness and Young's modulus) as measured based on the micro indentation procedure.

2) Effects of the addition of zinc carboxylate on the tribological properties

The effects of the addition of zinc carboxylate were investigated at each temperature. The effects of the improvement of the tribological properties were not observed at room temperature. Significant effects of the addition of zinc carboxylate in the grease, such as a decrease in the friction coefficient, a decrease in the wear and creep of the composite, and a decrease in the wear of the steel counterpart, were observed at 80°C. The decrease in the friction coefficient was observed at 120°C. However, the effect of the decrease in the wear and creep was not confirmed at high temperature.

3) Analysis of tribofilm formation

A ToF-SIMS analysis of the steel surface after the sliding test at 80°C revealed the formation of a heterogeneous tribofilm composed of carboxylates. An XPS analysis of the GF-reinforced PA66 composite surface showed the presence of a ZnS reactive tribofilm related to the tribochemical reaction between zinc carboxylate and sulfur-type anti-oxidation agent on the polymer surface only.

4) Contribution of each tribofilm formation

The contribution of the formation of the carboxylates tribofilm on the steel surface in the improvement of the tribological properties is greater than that of the formation of a ZnS tribofilm on the PA66 surface.

Chapters III and IV focused particularly on the wear and creep resistance of unreinforced PA66 or GF composites and wear resistance of steel counterparts under boundary lubricated conditions using grease under fixed high contact pressure and sliding speed. On the other hand, when considering the operating environment of the actual sliding parts, it is important to understand not only the wear or creep resistance but also the friction properties under a much wider range of load, sliding speed, and temperature conditions. In particular, the mechanical properties of the polymer material and lubricants can be highly influenced by temperature; therefore, understanding the influence of temperature on friction is important. In the next chapter, the friction mechanism will be clarified under various conditions based on the soft EHL and solid-contact theories.

CHAPTER V

FRICTION MECHANISM OF
UNREINFORCED AND GF-
REINFORCED PA66 IN CONTACT
WITH STEEL UNDER PAO8 OIL OR
GREASE LUBRICATION

CHAPTER V: FRICTION MECHANISM OF UNREINFORCED AND GF-REINFORCED PA66 IN CONTACT WITH STEEL UNDER PAO8 OIL OR GREASE LUBRICATION

1. Introduction.....	173
2. Friction mechanism under PAO8 oil lubrication	175
2.1 Effect of ring surface roughness, sliding speed, and temperature on friction coefficient	175
2.2 Oil film thickness estimated based on lubrication regime	178
2.3 Development of Λ -friction coefficient master curve.....	182
2.4 Effect of normal load (contact pressure) on friction coefficient.....	183
2.5 Effect of steel counterpart hardness on friction coefficient	185
2.6 Effect of GF reinforcement on friction coefficient	187
3. Friction mechanism under grease lubrication	192
3.1 Difference of the friction mechanism between PAO8 oil lubrication and grease without zinc carboxylate lubrication	192
3.2 Effect of addition of zinc carboxylate to grease under various test conditions.....	196
4. Conclusions.....	204

CHAPTER V: FRICTION MECHANISM OF UNREINFORCED AND GF-REINFORCED PA66 IN CONTACT WITH STEEL UNDER PAO8 OIL OR GREASE LUBRICATION

In this chapter, the friction mechanism of the contact between PA66 and steel under oil or grease lubrication was discussed by focusing on various sliding and material parameters. To explain the friction behavior, the theories of soft EHL, solid/solid contact, and tribochemistry were introduced.

1. Introduction

In the previous chapters, the tribological mechanism of the unreinforced or GF-reinforced PA66 in contact with carbon steel under grease lubrication, and the effects of temperature and tribochemistry related to the low friction additives (e.g., zinc carboxylate) in grease on the tribological properties were discussed. Previous chapters, however, focused particularly on the wear or creep resistance of unreinforced or GF-reinforced PA66 and steel counterparts under boundary lubricated conditions using grease under fixed high contact pressure and sliding speed conditions to simulate the contact and sliding of a motor-assisted worm reducer in an EPS. Therefore, the experimental conditions were set so that the tests could be accelerated to evaluate each property. On the other hand, when considering the operating environment of the actual sliding parts including the worm reducer, it is vital to understand the friction properties under a much wider range of load, sliding speed, and temperature conditions. In particular, the mechanical properties of the polymer-based material and the lubricants can be highly influenced by temperature; therefore, understanding the influence of temperature on friction is important.

In addition, as presented in Section 2.4 in Chapter I, for polymer worm wheels, it is also important to consider tooth formation because it can influence the sliding surface roughness and friction. Polymer worm wheels are usually fabricated by injection molding of disk and then mechanically forming the teeth by hob cutting, which results in high accuracy of tooth dimensions. However, when worm wheels are fabricated using a GF composite, the fibers are exposed on the sliding surface, which severely damages the steel counterpart and can initiate crack formation and propagation. In contrast, the teeth can be fully formed by injection molding without requiring any mechanical cutting, which not only reduces the cost (because the teeth do not have to be mechanically formed) but also improves the wear resistance of the GF composites or the GF-induced damage because the GF exposure can be reduced by the formation of a skin layer on the sliding surface, as presented in Section 3.2 in Chapter III. However, the tooth dimensions can be less accurate than the dimensions of mechanically formed teeth. Additionally, running-in is introduced after injection molding to ensure good matching between the polymer worm wheel and the steel worm shaft. Considering these tooth formation processes, the roughness of the sliding surface is determined by the hob

cutting or running-in conditions or by the surface roughness of the metal die used for injection molding, particularly when the teeth are directly formed using injection molding, and the roughness is supposed to influence the friction. Therefore, it is vital to understand the relationship between the sliding surface roughness and friction properties and to adjust the design of the sliding surface to control the friction of the actual sliding parts, including the polymer worm wheel.

Furthermore, the hardness of the steel counterpart can be an important parameter for understanding the friction mechanism. As discussed in Section 5 in Chapter III, high-hardness steel counterparts induced less wear resistance in the GF-reinforced PA66 composite and more wear resistance in steel, which can be explained by comparing the hardness of the GFs and the steel counterpart. Considering an actual worm reducer, as discussed in Section 2.5 in Chapter I, when softer steel (not heat treated after tooth formation) is used for the steel worm shaft, the steel wear resistance is supposed to deteriorate despite the good wear resistance of the counterpart GF composites. Conversely, when the steel worm shaft is heat treated after tooth formation, the wear resistances of the GF composite and steel counterpart can decrease and increase, respectively. In addition, insufficient dimensional stability related to heat-induced distortion results in inadequate worm reducer performance (i.e., increase of the sliding torque or short-term durability). Therefore, it is important to understand the effect of steel hardness on the friction between steel and the PA66 or the GF composites under lubrication.

Therefore, this chapter focuses on clarifying the friction mechanism between steel and the PA66 or the GF composite under oil or grease lubrication. Polymer sliding parts in contact with steel, including the worm wheel in EPS worm reducer, are used under both oil or grease lubrication. In particular, it is difficult to fundamentally understand the grease lubrication friction mechanism because it is necessary to consider the speed-dependent apparent viscosity of the grease (a non-Newtonian fluid that affects the oil film thickness [129]), the thixotropic properties of the grease, and any possible tribochemical reactions and tribofilm formations, all of which are related to the additives (used to improve the tribological properties) in addition to the lubrication theory of pure oil. Therefore, at first, the effect of each parameter on the friction between the PA66 or GF composite and carbon steel under additive-free PAO8 oil lubrication was investigated, and the effects of various parameters including the normal load (contact pressure), sliding speed, temperature, roughness, and hardness of the steel counterpart on the friction were investigated. Then, the difference of the friction behavior between oil and grease lubrication, and effect of the addition of zinc carboxylate to grease as focused in Chapter IV were additionally investigated. The results were discussed based on the theories of soft EHL, solid/solid contact, and tribochemistry.

In this chapter, unreinforced PA66 (sample no. 12 in Table II. 3) and the GF 15% composite with normal molecular mass (sample no. 1 in Table II. 3) were used. Roughness of ring specimens sliding surface before sliding tests was changed in the way as explained in Section 2.1.4.2 in Chapter II. The details of used PAO8 oil were presented in Section 2.3.3 in Chapter II. In addition, two different types of PAO8-based urea grease without or with zinc carboxylate were used as presented in Section 2.3.1 in Chapter II. The steel cylinders with the hardness of 4.5 GPa (referred to as “softer steel”) and those with the hardness of 9.9 GPa (referred to as “harder steel”) as explained in Section 2.2 in Chapter II were used in the experiments of this chapter.

2. Friction mechanism under PAO8 oil lubrication

2.1 Effect of ring surface roughness, sliding speed, and temperature on friction coefficient

To understand the basic friction mechanism of this tribosystem, the effects of the ring surface roughness and sliding speed on the friction coefficient were investigated at room temperature under PAO8 oil lubrication. During the sliding tests, the rotation speed was changed during a test according to the profile shown in Fig. II. 36 for a constant normal load (50 N). To eliminate the effect of the steel cylinder wear and the consequent change in the contact geometry, harder steel cylinders were used. In addition, to understand the basic friction mechanism, unreinforced PA66 ring specimens were used. Fig. V. 1 presents the friction coefficient evolutions obtained for different surface roughness at different rotation speeds at room temperature. The initial sliding-direction surface roughness (R_a) of the unreinforced PA66 ranged from 0.03 to 0.98 μm depending on the polishing process. The global tendency was that the friction coefficient was higher at low rotation speeds and lower at high ones, gradually increasing with decreasing rotation speed and vice versa. The friction coefficient was higher when the initial surface roughness was higher. No remarkable differences were observed between the evolutions obtained for $R_a = 0.03$ and 0.07 μm or for $R_a = 0.40$ and 0.98 μm . Furthermore, these evolutions as a function of surface roughness did not change until the end of the sliding tests. For $R_a = 0.98$ and 0.40 μm , the friction coefficient decreased gradually during sliding at the same rotation speed. In contrast, the friction coefficient was identical to or higher than the initial ones obtained during sliding at the same rotation speed in the range $R_a = 0.03$ –0.20 μm .

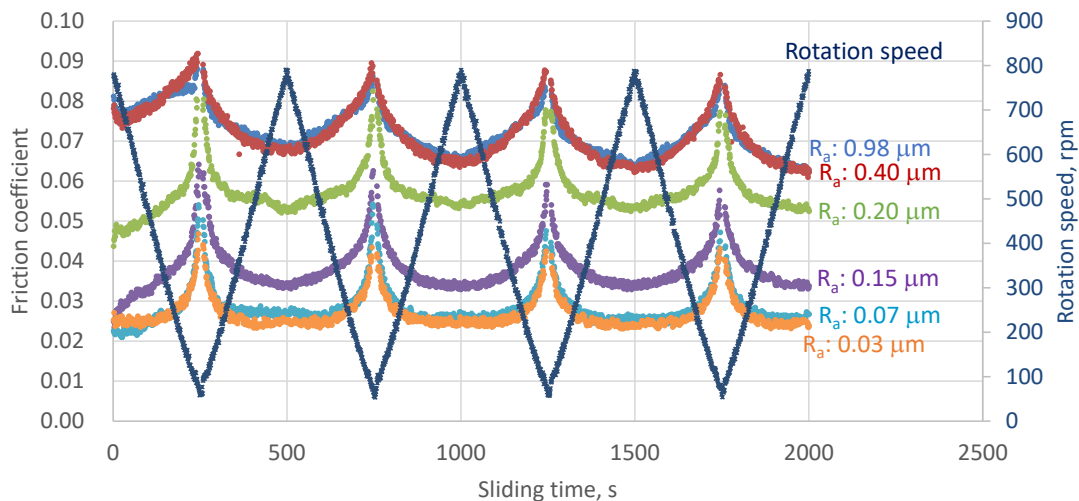


Fig. V. 1 Friction coefficient evolutions obtained for different surface roughness of unreinforced PA66 ring specimens measured at different rotation speed at room temperature.

To investigate the wider effect of the rotation speed on the friction coefficient, a sliding test was conducted using unreinforced PA66, wherein the maximum rotation speed was 1,567 rpm (i.e., double the maximum speed presented in Fig. V. 1) with $R_a = 0.06$ μm . Fig. V. 2 shows the evolution of the friction coefficient obtained at different rotation speed. Despite the increased rotation speed, no remarkable change in the minimum friction coefficient was observed, whereas the friction coefficient increased when the rotation speed was low.

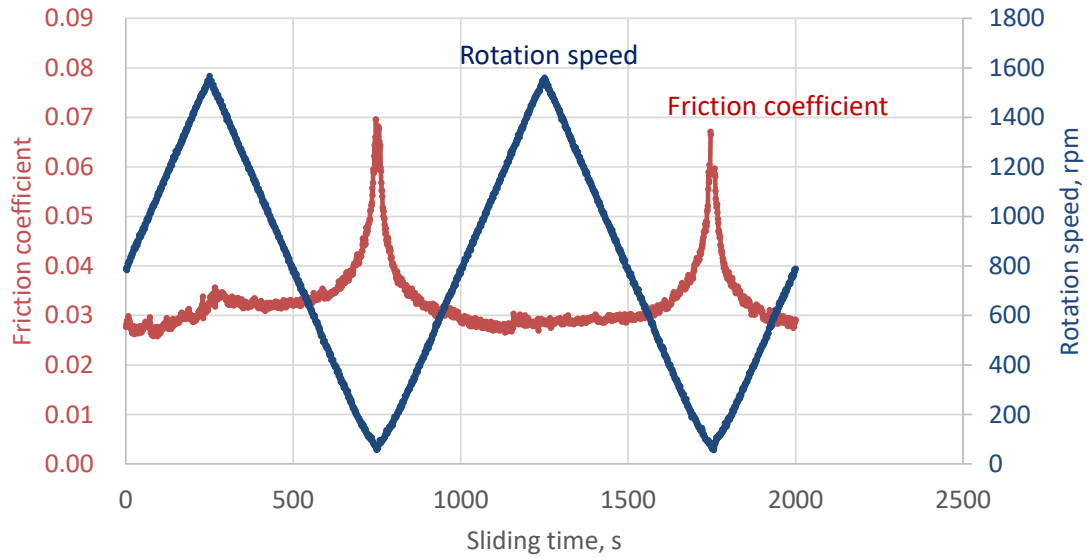


Fig. V. 2 Evolution of friction coefficient measured at different rotation speed up to 1,567 rpm.

Furthermore, the temperature dependence of the friction coefficient was investigated using samples showing surface roughness $R_a = 0.07 \mu\text{m}$ (i.e., polished with #4,000 paper). Fig. V. 3 presents the evolutions of the friction coefficient at different temperatures (room temperature RT, 80 and 120°C) and rotation speeds. The initial friction coefficients similarly presented in the range 0.025–0.03 and increased with decreasing sliding speed, as observed in Fig. V. 1. At room temperature, the low friction coefficients (0.025) stabilized between 200 and 790 rpm during sliding and increased or decreased gradually with decreasing or increasing rotation speed at 80 or 120°C, respectively. In addition, the global tendency of the friction coefficients gradually increased at the same rotation speed during sliding at 80 or 120°C and were higher when the temperature was higher, particularly in the latter part of the sliding tests.

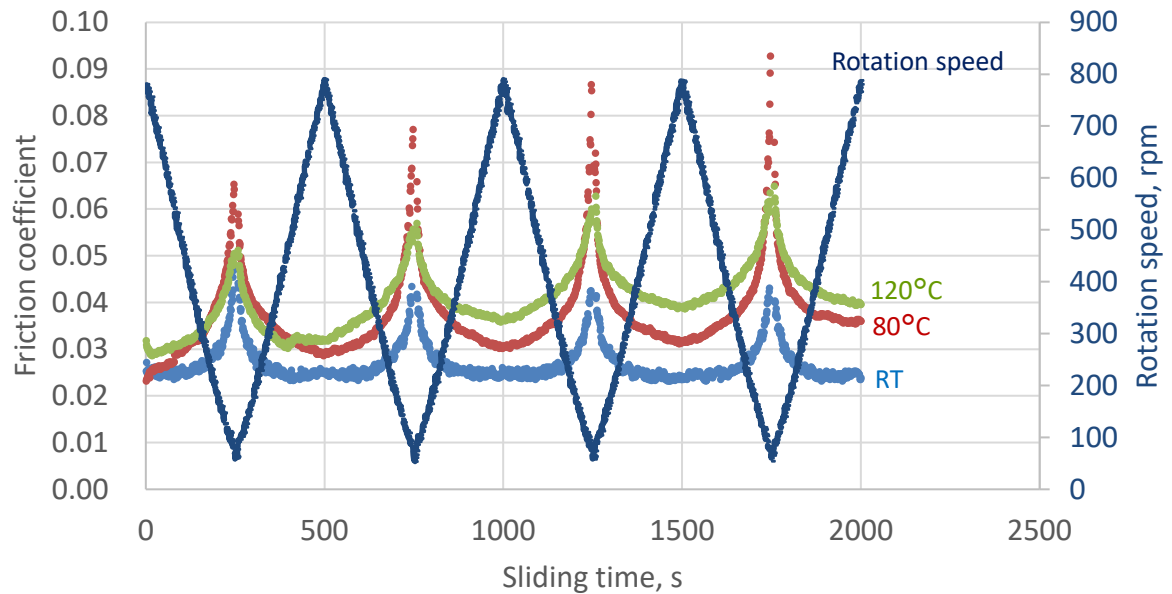


Fig. V. 3 Friction coefficient evolutions of unreinforced PA66 specimens measured at different temperature and rotation speed.

Fig. V. 4 presents the relationship between the friction coefficient and the sliding speed measured under each test condition. Clearly, the friction coefficient was influenced by each parameter (e.g., roughness and temperature), resulting in different values of friction coefficient for a given rotation speed.

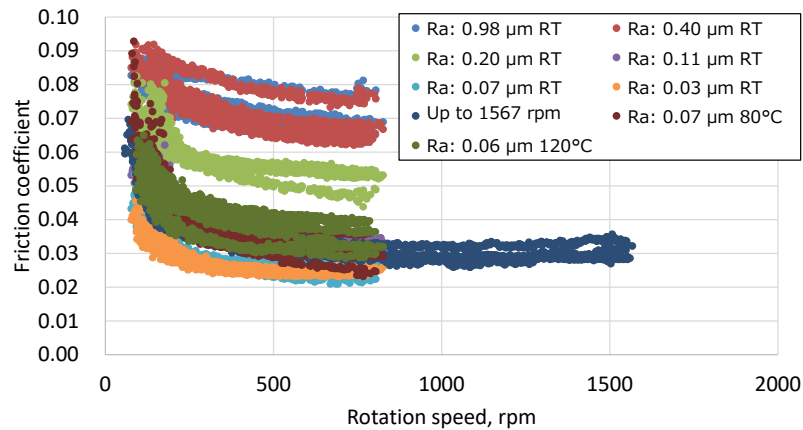


Fig. V. 4 Relationship between sliding speed and friction coefficient measured under each test condition.

Fig. V. 5 presents the optical microscope images of the unreinforced PA66 ring specimen (i.e., the specimen with an initial R_a of 0.03 μm in Fig. V. 1) sliding surface before and after the sliding test. Several sliding marks, which are supposed to be steel cylinder asperity-related two-body abrasive wear, are clearly observed in the sliding direction. Table V. 1 lists the sliding-direction sliding surface roughness (R_a) of the ring specimens measured using interferometry before and after the sliding tests. R_a decreased after the sliding tests when the initial R_a was above 0.40 μm , which can be attributed to polishing when the rough PA66 surface slid with a cylinder showing a lower R_a (= 0.08 μm for the cylinder). In contrast, R_a increased when the initial R_a was low, particularly during the sliding test conducted at room temperature. In addition, the harder steel cylinder did not show any explicit wear.

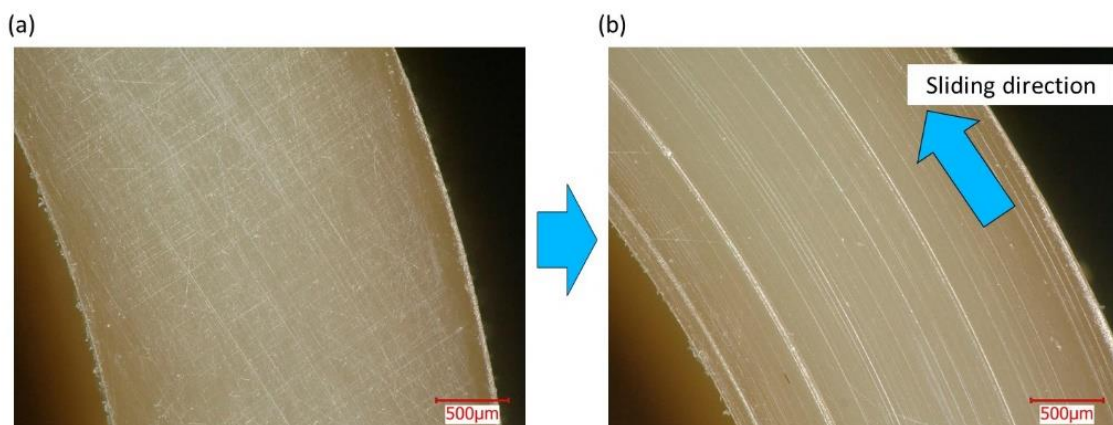


Fig. V. 5 Optical microscope images taken (a) before and (b) after sliding test.

Table V. 1 Sliding surface roughness (R_a) of ring specimens before and after sliding tests.

Polishing paper	Temperature, °C	Pre-test surface roughness (R_a), μm	Post-test surface roughness (R_a), μm
#400	RT	0.98 ± 0.16	0.46 ± 0.05
#800	RT	0.40 ± 0.05	0.35 ± 0.10
No polishing (skin layer)	RT	0.20 ± 0.05	0.20 ± 0.03
#2,000	RT	0.11 ± 0.01	0.23 ± 0.06
#4,000	RT	0.07 ± 0.00	0.13 ± 0.01
#4,000	RT	0.03 ± 0.00	0.06 ± 0.01
#4,000 *	RT	0.07 ± 0.00	0.13 ± 0.01
#4,000	80	0.07 ± 0.01	0.07 ± 0.01
#4,000	120	0.06 ± 0.02	0.07 ± 0.01

*Surface roughness measured at higher rotation speeds, as explained in Fig. V. 2.

To analyze these results by systematically considering the sliding conditions and changes in the sliding surface roughness, we focused on the oil film formation and the lambda ratio on the sliding surface. The process of estimating the oil film thickness is described in the next section.

2.2 Oil film thickness estimated based on lubrication regime

The actual oil film thickness is usually measured using optical interferometry with a steel ball and a transparent glass disk to simulate the rolling–sliding contact of a bearing [129]. To date, few studies have focused on lubrication theories of polymer materials including engineering plastics. However, in the present study, the theoretical oil film thickness was estimated based on EHL for a flat-cylinder pure-sliding contact to discuss the plausible friction mechanism.

To estimate the oil film thickness on a sliding surface, it is necessary to determine the lubrication regime of the contact geometry under a given applied load and sliding speed to select the appropriate formula for calculating the oil film thickness, as presented in Section 7.1 in Chapter I. Depending on the values of the dimensionless elasticity and viscosity parameters (g_E and g_V , respectively), we can determine the governing lubrication regime of a line contact and the appropriate formula for estimating the oil film thickness by plotting the obtained g_E and g_V in a lubrication regime map, as explained in Section 7.2 in Chapter I and Fig. I. 40. g_E and g_V can be estimated using the equations (I. 15) and (I. 25). Pressure–viscosity coefficient α of the PAO8 oil is 20 GPa^{-1} at room temperature. Furthermore, load per unit w_l is obtained from the following equation, considering the four-point contact between the ring

specimen and the steel cylinders and the contact length (i.e., the width of the ring specimens $l = 2.8$ mm, as presented in Fig. V. 6).

$$w_l = \frac{w}{4l} \quad (\text{V. 1})$$

where w is the normal load applied during the sliding tests.

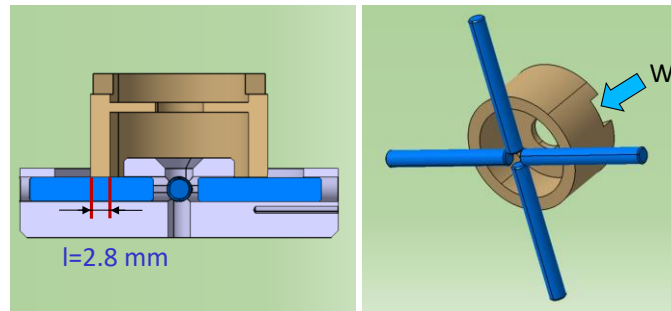


Fig. V. 6 Contact geometry of sliding test performed with ring specimen and four steel cylinders.

E , R , and u , which are necessary to estimate g_E and g_V , as explained in equations (I. 11), (I. 12), and (I. 10), were estimated considering the contact between the two parts as presented in Fig. I. 38. E_1 and E_2 are the Young's moduli of the steel cylinder and PA66 ring specimens, respectively; ν_1 and ν_2 are the Poisson ratios of the cylinder and ring, respectively; R_1 and R_2 are the contact diameters of the cylinder and ring specimens, respectively (i.e., R_2 is infinite); and u_1 and u_2 are the sliding speeds of the cylinder and ring specimens (i.e., $u_1 = 0$), respectively.

In addition, it is necessary to consider the temperature dependence of the oil viscosity and the PA66 mechanical properties to determine the lubrication regime and estimate the theoretical oil film thickness at each temperature. Lubrication oil is a Newtonian fluid; therefore, the viscosity is constant for different rotation speeds at the same temperature. The viscosity of the PAO8 oil measured using a rheometer at each temperature is shown in Fig. II. 23. As listed in Table V. 2, the oil viscosity decreased with increasing temperature, and the measured viscosities decreased by 82.1% and 92.4% at 80 and 120°C, respectively, compared to the corresponding viscosities measured at room temperature. The Young's moduli of the unreinforced PA66 measured using microindentation at each temperature were presented in Fig. IV. 11. The Young's modulus decreased with increasing temperature. From the oil viscosity and Young's modulus obtained for the unreinforced PA66, g_E and g_V were estimated under each test condition (e.g., different rotation speeds, normal loads, and temperatures) and were superimposed on the presented lubrication regime map (Fig. I. 40), as shown in Fig. V. 7.

Table V. 2 Oil viscosity at different temperature.

Temperature, °C	Viscosity, mPa s
RT	74.9
80	13.5
120	5.7

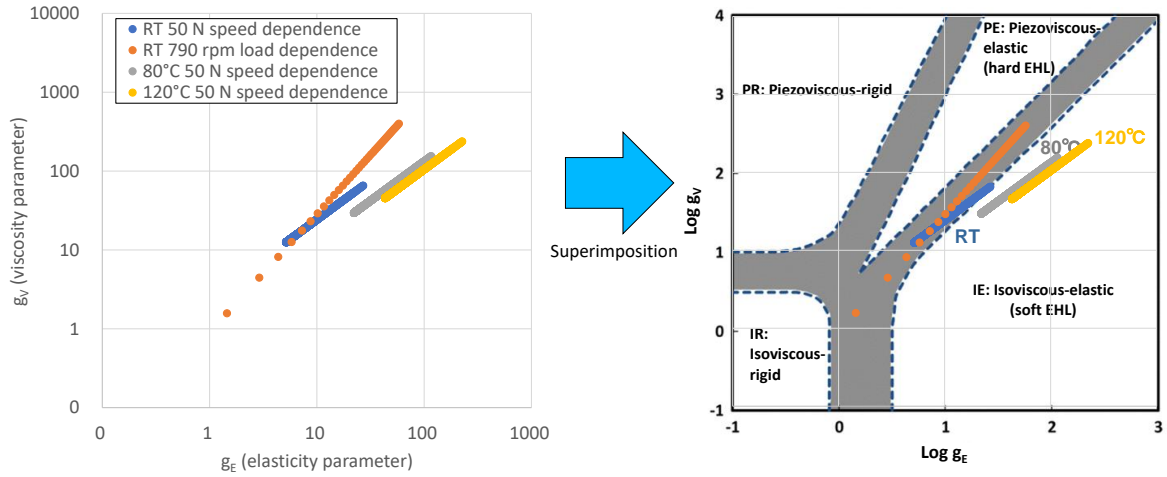


Fig. V. 7 Lubrication regime map showing g_E and g_V estimated under each sliding condition. Colors in both plots correspond to the same data points.

At room temperature, each data point was categorized at the threshold of either the isoviscous–elastic (IE) lubrication regime (dominated by soft EHL) or the piezoviscous–elastic (PE) lubrication regime (dominated by hard EHL). Usually, sliding-polymer materials (e.g., elastomers or plastics used in windscreen wipers, seals, or bearing polymer cages) are categorized in the IE lubrication regime [147, 157, 160] wherein although the elastic deformation must be considered, the contact pressure is too low to increase the oil viscosity. However, it is assumed that the lubrication regime in the current study more likely approached PE because the small diameter steel cylinders induced high contact pressure and because the Young’s modulus of the PA66 was one order of magnitude higher than that of the elastomer. In contrast, the lubrication regime approached IE with increasing temperature because the PA66 softened with decreasing Young’s modulus and became much more plastic-like with increasing temperature.

Several equations for estimating the theoretical oil film thickness in the IE and PE lubrication regimes have been proposed, and the present study uses the more common Hamrock and Dowson equations [156, 159], as presented in Section 7.1 in Chapter I. The following equations were used to estimate the theoretical minimum oil film thickness in each lubrication regime:

In the IE lubrication regime (as presented in equation (I. 6)),

$$H_{min} = \frac{h_{min}}{R} = 7.43 U^{0.65} W^{-0.21} (1 - 0.85 e^{-0.31k}) \quad (V. 2)$$

In the PE lubrication regime,

$$H_{min} = \frac{h_{min}}{R} = 3.63 U^{0.68} G^{0.49} W^{-0.073} (1 - e^{-0.68k}) \quad (V. 3)$$

where H_{min} is the minimum dimensionless film thickness, h_{min} is the minimum film thickness, U is the dimensionless speed parameter, W is the dimensionless load parameter, G is the material parameter, and k is the ellipticity parameter ranging from 1 (for a circular configuration such as a ball-on-plate configuration) to 12 (for a configuration approaching a rectangular contact). The dimensionless parameters U , W , and G are defined as equations (I. 8), (I. 9), and (I. 26).

Although few studies have actually measured the oil film thickness of line contacts fabricated using engineering plastics including PA66, the oil film thickness, measured at the point contact between a transparent PC disk (instead of a transparent glass disk used to measure the oil film thickness by interferometry) and a steel ball in the rolling–sliding contact presented by Kochi et al. [129], and the corresponding oil film thickness estimated based on the Hamrock and Dowson soft EHL theories, were well correlated. Therefore, the theoretical oil film thickness estimated based on EHL for a line contact fabricated using PA66 should be reliable.

By substituting each obtained parameter into the equations for the IE and PE lubrication regimes, the theoretical minimum oil film thicknesses were estimated based on a function of rotation speed under a normal load of 50 N at room temperature, as shown in Fig. V. 8. The minimum oil film thickness increased with increasing the rotation speed, and the differences between the oil film thicknesses estimated based on the equations for the IE and PE regimes were negligible at all the rotation speeds. Therefore, under these sliding conditions, there was no difference between the estimated oil film thicknesses, even without considering the increased oil viscosity, because the lubrication regime was categorized at just the threshold of the IE and PE regimes.

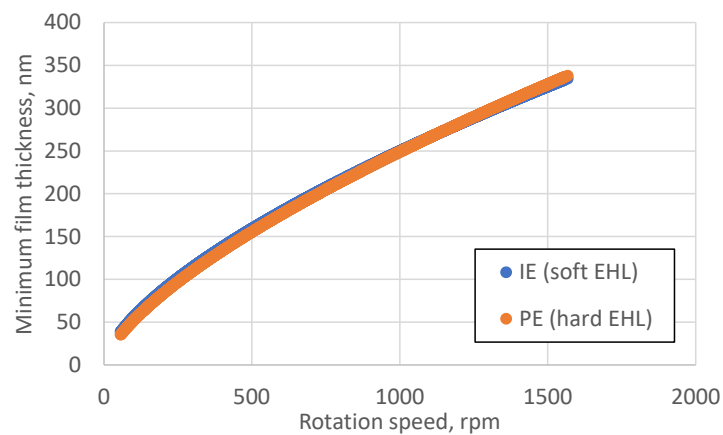


Fig. V. 8 Theoretical minimum oil film thickness estimated based on equation for IE (soft EHL) or PE (hard EHL) lubrication regime.

Fig. V. 9 presents the evolution of the theoretical minimum oil film thicknesses estimated using the equation for the IE (i.e., soft EHL) lubrication regime at each temperature with the rotation speed and the normal load. The oil thickness decreased with increasing temperature. Although the viscosity decreased by 82.1 and 92.4% at 80 and 120°C compared to the viscosity at room temperature, respectively, the theoretical minimum oil film thickness remained at 55.4 and 39.0% at 80 and 120°C compared to the thickness at room temperature, respectively, under the sliding conditions where the normal load was 50 N and the rotation speed was 790 rpm. This tendency cannot be observed in the sliding of metallic materials because the Young’s modulus decreases at high temperature, thereby preventing the oil film thickness from decreasing.

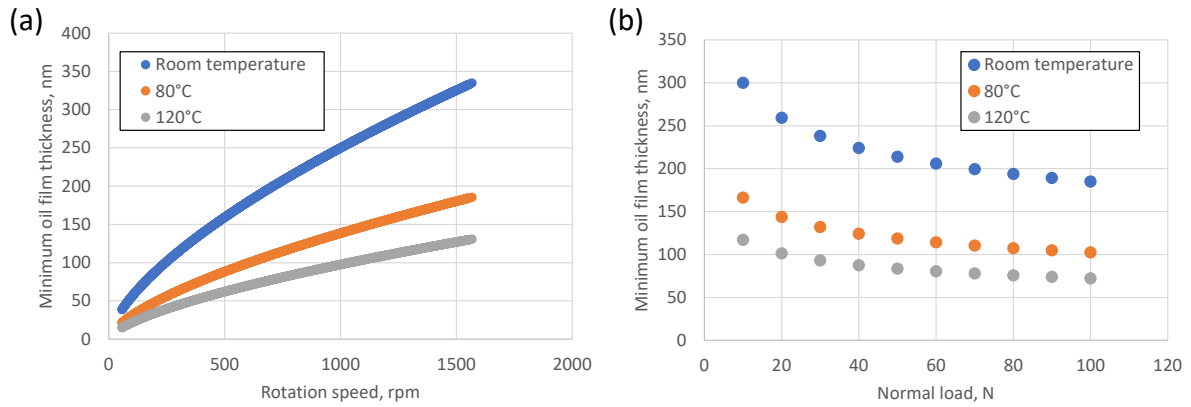


Fig. V. 9 Evolutions of estimated theoretical minimum oil film thickness with (a) the rotation speed and (b) normal load dependences.

2.3 Development of Λ -friction coefficient master curve

As explained in Section 7.1 in Chapter I, the estimated oil film thicknesses can be used to determine the likelihood and severity of asperity contacts by calculating the lambda ratio (Λ), the ratio of the minimum oil film thickness to the combined surface roughness of two sliding materials (R_{a1} and R_{a2}). Λ can be calculated as follows:

$$\Lambda = \frac{h_{min}}{\sqrt{Ra_1^2 + Ra_2^2}} \quad (V. 4)$$

In addition, because the sliding surface roughness changed during the sliding test (as discussed in Section 2.1), we introduced the postulation that roughness R_a changed (increased or decreased) linearly during sliding to calculate Λ at each sliding time. Fig. V. 10 shows the relationship between the measured friction coefficient and Λ calculated under different test conditions (e.g., various initial surface roughness, rotation speed, and temperatures; that is, the same friction data as those shown in Fig. V. 4). The obtained master curve shows that the friction coefficient could be approximated by Λ regardless of the test conditions or surface roughness for the same normal load when unreinforced PA66 and harder steel were used under oil lubrication. In the low- Λ regime (between 0 and 1.5), the friction coefficient decreased with increasing Λ , which is typical in the boundary and mixed lubrication regimes wherein the contact is affected by the solid direct points of contact. Conversely, in the high- Λ regime (above 1.5), the low friction coefficient was very similar (in the range 0.025–0.035) because the proportion of the contact separated by the oil film increased (i.e., fluid lubrication), and the direct contact effect should be mitigated. This tendency is consistent with the Stribeck curve.

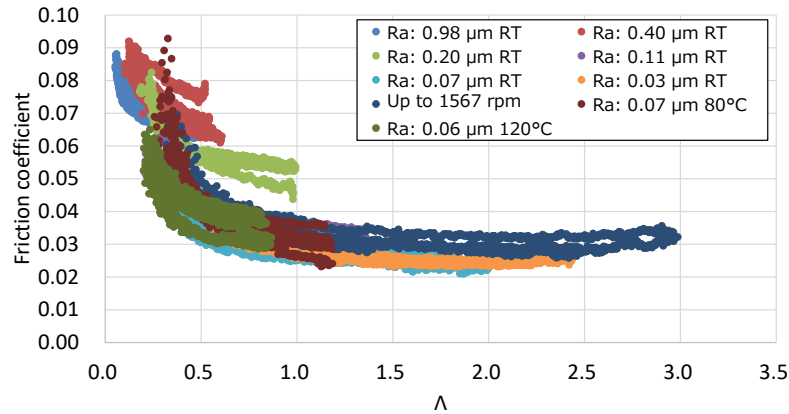


Fig. V. 10 Λ - μ master curve.

2.4 Effect of normal load (contact pressure) on friction coefficient

In addition, the effect of the normal load (and thus contact pressure) on the friction coefficient was investigated, and the obtained results were analyzed using the proposed theories. Sliding tests were conducted under the profiles presented in Fig. II. 35 at a rotation speed of 790 rpm at room temperature. Fig. V. 11 presents the evolutions of the friction coefficient obtained for different normal loads and sliding surface roughness of the unreinforced PA66 ring specimens with the harder steel. As previously observed, a higher surface roughness led to a higher friction coefficient for any normal load. When the initial surface roughness was low (0.03 μm), the friction coefficient remained low and stabilized in the range 0.02–0.03. Conversely, when the initial surface roughness was high (e.g., 0.23 or 0.68 μm), the friction coefficient decreased with increasing normal load. In addition, with the initial $R_a = 0.23$ or 0.68 μm , the difference between the friction coefficients was smaller in the last stage of the sliding test than in the initial stage.

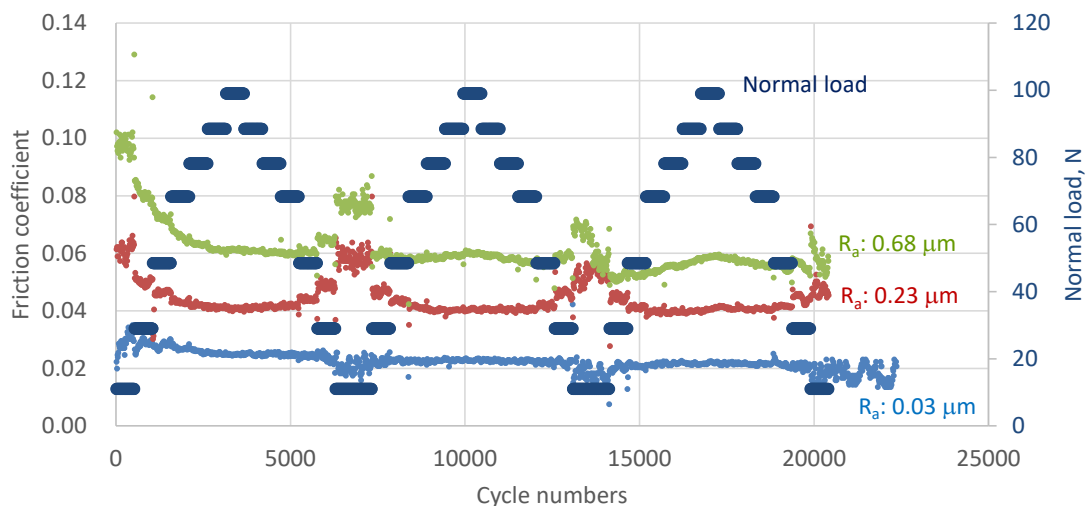


Fig. V. 11 Friction coefficient evolutions obtained for unreinforced PA66 ring specimens under different normal loads and sliding surface roughness.

To further discuss these results, the theoretical oil film thickness was calculated for different normal loads, as presented in Fig. V. 9 (b), to obtain the relation between Λ and the friction coefficient by postulating that the surface roughness (R_a) changed linearly during the

sliding test. Then, the obtained relation was superimposed on the previously obtained Λ -friction coefficient master curve, as shown in Fig. V. 12 (the master curve from Fig. V. 10 is shown in gray). The results obtained when $R_a = 0.03 \mu\text{m}$ were consistent with the Λ -friction coefficient master curve, meaning that these contacts are under fluid or mixed lubrication. Therefore, the constant friction coefficient for each normal load can be explained by the few contact points between the PA66 and the steel. The results obtained when $R_a = 0.23$ or $0.68 \mu\text{m}$, on the other hand, did not coincide with the Λ -friction coefficient master curve. These results showed that the friction coefficient decreased with increasing normal load, which is opposite to the Stribeck curve observed in the mixed lubrication regime.

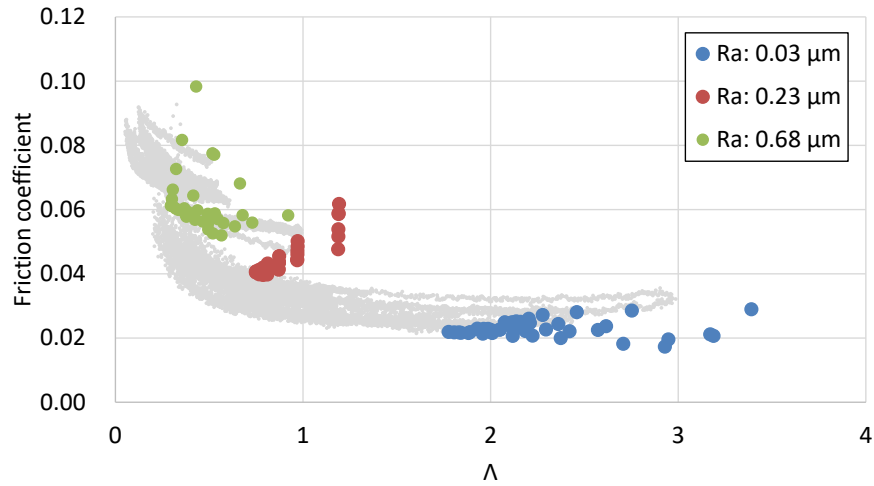


Fig. V. 12 Relationship between Λ and friction coefficient superimposed on Λ - μ master curve (gray) shown in Fig. V. 10.

To explain the normal load dependence of the friction coefficient, the Bowden and Tabor laws which were explained in Section 6.1 in Chapter I, were applied to these results. In this theory, the friction coefficient was modeled as in the following equation.

$$\mu = \frac{\tau}{P} = \frac{\tau_0}{P} + \mu_\infty \quad (\text{V. 5})$$

where τ is the shear strength of the polymer material, P is the mean contact pressure, τ_0 is the constant intrinsic characteristic shear strength, and μ_∞ is the pressure coefficient for an infinite pressure.

Fig. V. 13 shows the relationships between the normal load and inverse contact pressure and the friction coefficient for unreinforced PA66 ring specimens showing different surface roughness and under different normal loads. Each contact pressure was estimated based on the Hertzian theory. When $R_a = 0.03 \mu\text{m}$, the friction coefficient was approximately identical for each contact pressure, and the slope (τ_0) in the linear approximation equation (i.e., the relation between the inverse of P and the friction coefficient) was negative, meaning that the normal load dependence of the friction coefficient cannot be explained by the Bowden and Tabor law (i.e., the direct solid contact based theory). Therefore, the lubrication theory based explanation (i.e., the Λ - μ curve) is reasonable (Fig. V. 10). In contrast, when the initial R_a was higher, the slope (τ_0) in the linear approximation equation was positive, which is supposed to depend on the polymer mechanical properties and in fact, high correlation coefficients ($R^2 > 0.9$) were observed, meaning that the normal load dependence of the friction coefficient

can be explained using the Bowden and Tabor law. Therefore, it is reasonable that these results cannot be discussed through lubrication theory.

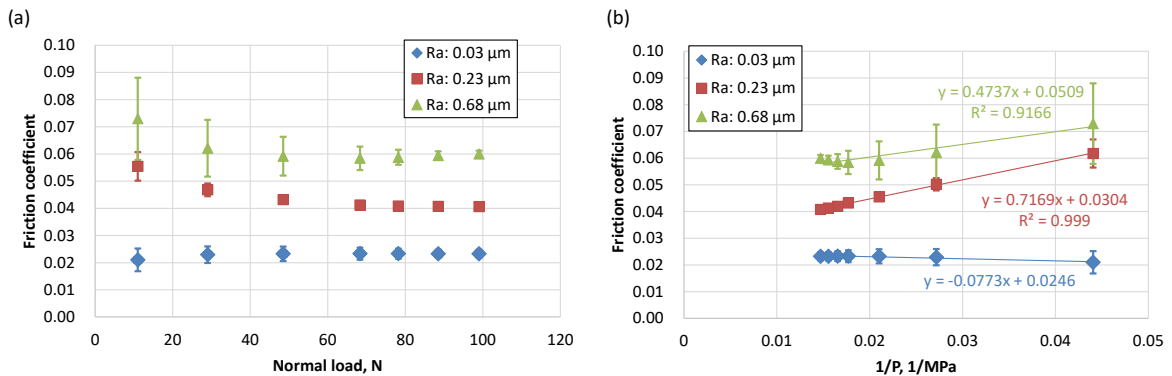


Fig. V. 13 Relationships between (a) normal load and friction coefficient and (b) inverse contact pressure and friction coefficient for different normal loads and surface roughness of unreinforced PA66 ring specimens.

2.5 Effect of steel counterpart hardness on friction coefficient

As mentioned in Section 1, it is necessary to investigate the effect of the steel counterpart hardness on the friction coefficient because the counterpart hardness is determined by the heat treatment conditions; therefore, they should be selected appropriately. First, the effect of the steel hardness on the rotation speed dependence of the friction coefficient was investigated, as presented in Fig. V. 14, using the unreinforced PA66 ring specimens showing roughness $R_a = 0.06 \mu\text{m}$ under a normal load of 50 N. No typical differences were observed between the friction coefficient evolutions in tests with the softer and harder steels. In addition, the steel counterpart did not show any visible wear, even on the surface of the softer steel. Considering these results, severe direct contact, which induces the wear of the steel counterpart, was not supposed to occur. Therefore, the influence of the oil film formation was remarkable, and the steel hardness negligibly affected the friction coefficient.

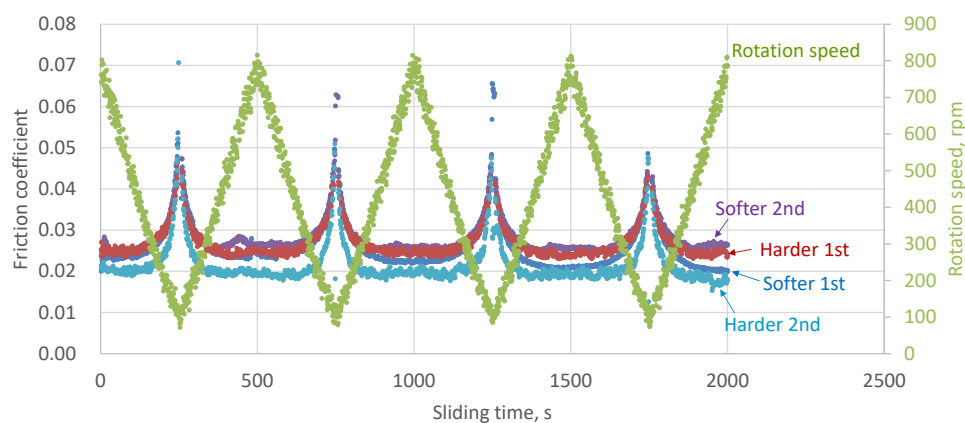


Fig. V. 14 Friction coefficient evolutions obtained for different rotation speeds and counterpart steel hardness measured using unreinforced PA66. Initial surface $R_a = 0.06 \mu\text{m}$ (two tests were conducted for each steel hardness).

Next, the rotation speed dependence of the friction coefficient was similarly investigated using unreinforced PA66 showing a much rougher ($R_a = 0.20 \mu\text{m}$) sliding surface. Fig. V. 15 shows the friction coefficient evolutions. Unlike the results obtained using the harder steel or at $R_a = 0.05 \mu\text{m}$, the friction coefficient suddenly and reproducibly increased after the surfaces had slid for 400 s. In addition, the softer steel cylinder was partially worn after sliding for 750 s, as shown in Fig. V. 16. The steel wore even when using the unreinforced PA66, which did not contain any reinforcement fibers (such as GFs that may show abrasion on the steel counterpart). Furthermore, the steel wear was influenced by the roughness (i.e., surface asperities) of the PA66. Worn steel can be an evidence of the direct contact between the PA66 and steel, and steel wear is supposed to suddenly increase the friction coefficient. In addition, although the steel surface was partly worn, the friction coefficient of the softer steel exhibited the same tendency as that of the harder steel by suddenly increasing after the surfaces had slid for 400 s.

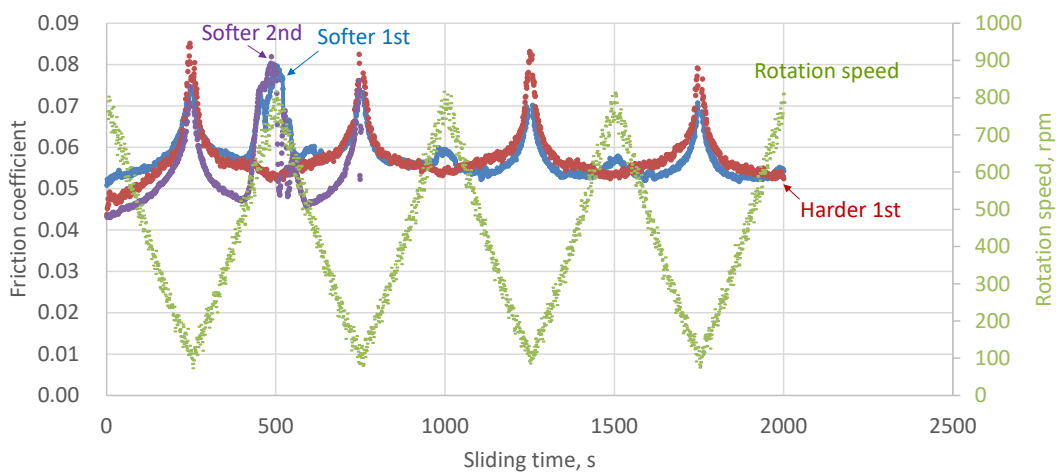


Fig. V. 15 Friction coefficient evolutions obtained for different rotation speeds and counterpart steel hardness measured using unreinforced PA66. Initial surface $R_a = 0.20 \mu\text{m}$.

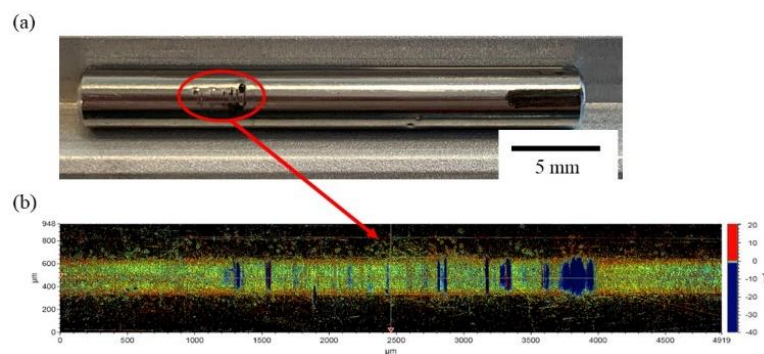


Fig. V. 16 (a) Optical microscope image and (b) interferometric measurement (after cylinder shape was removed) after softer steel cylinder had slid for 750 s.

2.6 Effect of GF reinforcement on friction coefficient

In the actual application of PA66 sliding parts, reinforcement fibers including GFs can improve the mechanical properties. Therefore, it is vital to consider the GF composite friction mechanism and compare it to that of the unreinforced PA66. To discuss the lubrication theory for the GF composite as for the unreinforced PA66, the lubrication regime and theoretical oil film were investigated by considering the different mechanical properties (e.g., the Young's modulus of the sliding surface measured by micro indentation) of the GF composite, as presented in Fig. IV. 11. The GF composite shows a higher Young's modulus than the unreinforced PA66. Fig. V. 17 shows g_E and g_V obtained under each sliding test condition and superimposed on the lubrication regime map presented in Fig. I. 40. Analogous to the unreinforced PA66, each data point was categorized at the boundary between the IE (soft EHL) and PE (hard EHL) regimes at room temperature and slightly approached the hard EHL regime because the fiber reinforcement had increased the Young's modulus compared to that of the unreinforced PA66. Meanwhile, each data point obtained at 80 and 120°C was still categorized in the soft EHL regime.

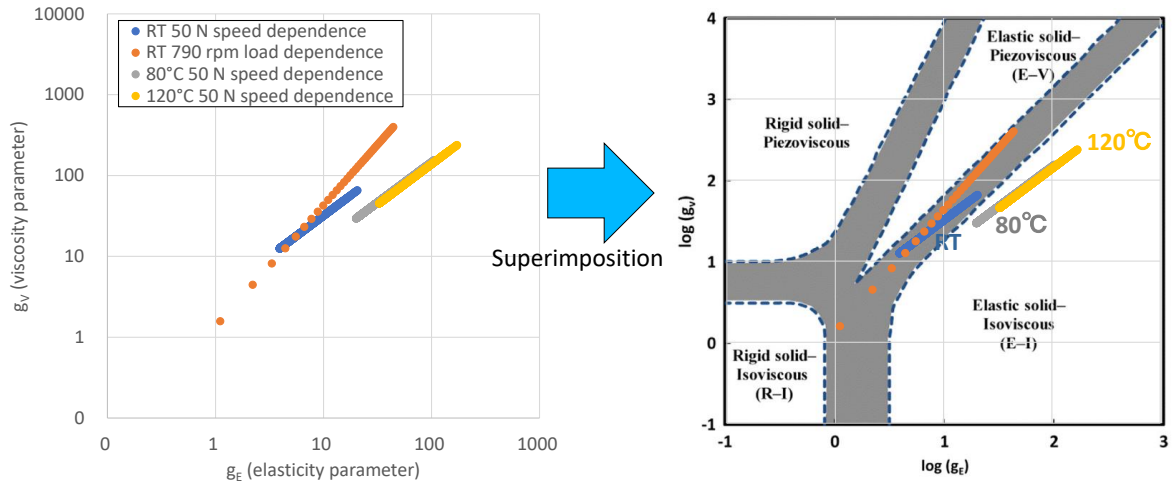


Fig. V. 17 g_E and g_V obtained under each sliding test condition for GF composite and superimposed on lubrication regime map presented in Fig. I. 40. Colors in both plots correspond to the same data points.

Then, the theoretical oil film thickness was calculated using the equation for the IE lubrication regime (equation (V. 2)). Fig. V. 18 compares the theoretical minimum oil film thicknesses obtained for the unreinforced PA66 and the GF composite at room temperature and under a normal load of 50 N at various rotation speeds, and the temperature dependence of the oil film thickness obtained for only the GF composite. At room temperature, the theoretical oil film thickness obtained using the GF composite was 21.5% lower than that obtained using the unreinforced PA66 at 790 rpm because the fiber reinforcement had increased the Young's modulus. As observed for the unreinforced PA66, the oil film thickness decreased with increasing temperature or decreasing rotation speed. Then, the effect of each parameter on the GF composite friction coefficient was investigated using the obtained oil film thickness.

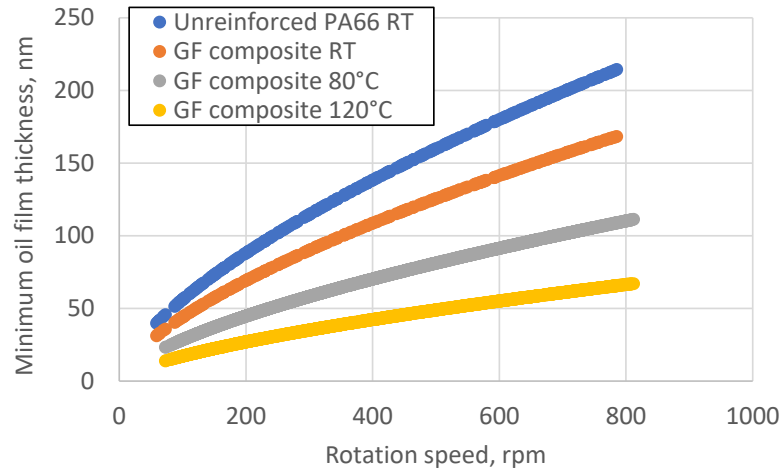


Fig. V. 18 Evolutions of theoretical minimum oil film thickness vs. rotation speed at room temperature for both unreinforced PA66 and GF composite and at various temperatures only for GF composite (for normal load of 50 N).

Fig. V. 19 presents the rotation speed, sliding surface roughness, and temperature dependences of the friction coefficients obtained using the GF composite and the harder steel, and Table V. 3 lists the sliding surface roughness obtained before and after each sliding test. The initial sliding surface roughness of the GF composite was higher than that of the unreinforced PA66 polished under the same conditions, which is supposed to be owing to the GFs exposed on the sliding surface. The GF composite hardness (5.9 GPa) was lower than that of the harder steel (9.9 GPa), and the steel cylinder did not show any visible wear after each sliding test. The global tendency was that the friction coefficient increased with increasing composite sliding surface roughness, decreasing rotation speed, and increasing temperature. The GF composite friction coefficient obtained at each temperature and rotation speed was similar to that obtained using the unreinforced PA66 and polished using the same polishing paper (#4,000). Furthermore, the GF composite and unreinforced PA66 both showed similar initial friction coefficient even if the theoretical minimum oil film thickness obtained using the GF composite was thinner than that obtained using the unreinforced PA66. Although the friction coefficient under dry conditions usually decreases when reinforcement fibers including GFs are added [65], the friction coefficient did not explicitly decrease when the fiber composites are used under oil lubrication. Furthermore, as observed for the unreinforced PA66, R_a increased for the smooth samples after the sliding tests, whereas polishing during sliding decreased R_a when the initial R_a was above $0.47 \mu\text{m}$.

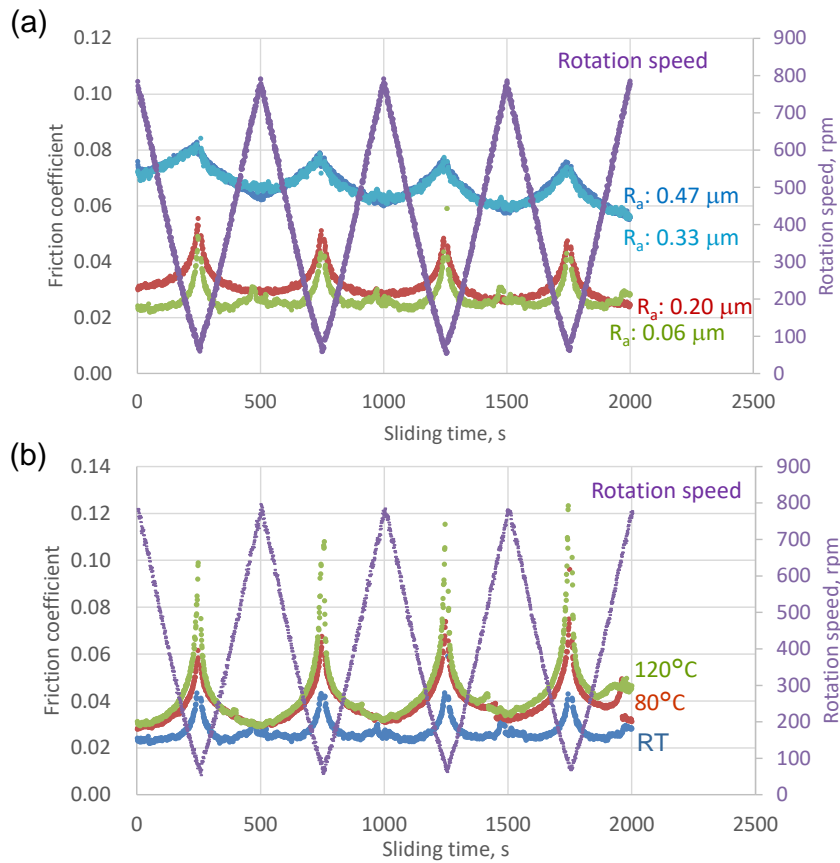


Fig. V. 19 (a) Rotation speed and sliding surface roughness dependencies obtained at room temperature and (b) rotation speed and temperature dependencies of friction coefficient obtained using smooth GF composite and harder steel.

Table V. 3 Sliding surface roughness (R_a) measured before and after each sliding test.

Polishing paper	Temperature, °C	Pre-test R_a , μm	Post-test R_a , μm
#4,000	RT	0.06 ± 0.00	0.07 ± 0.01
#2,000	RT	0.20 ± 0.07	0.24 ± 0.08
#800	RT	0.33 ± 0.02	0.27 ± 0.08
#800	RT	0.47 ± 0.02	0.42 ± 0.08
#4,000	80	0.07 ± 0.01	0.08 ± 0.01
#4,000	120	0.08 ± 0.01	0.08 ± 0.02

Considering the composite sliding surface roughness obtained before and after the sliding tests (as listed in Table V. 3), the effect of the calculated Λ on the friction coefficient is discussed by postulating that the surface roughness changed linearly during the sliding tests. Fig. V. 20 presents the relationship between Λ and the friction coefficient obtained using the GF composite. For comparison, the relationship is superimposed on the master curve obtained using the unreinforced PA66 (Fig. V. 10). As observed for the unreinforced PA66, the friction coefficient decreased with increasing Λ (for low Λ). In addition, the GF composite friction coefficients were lower than the unreinforced PA66 ones for the same Λ ; namely, the GF

composite could show lower friction coefficients than the unreinforced PA66 for smaller Λ . This can be explained by the relatively low direct contact area between the GF composite and the steel, which is related to the exposed GF. The friction coefficient obtained using the GF composite, however, did not become lower than that of the unreinforced PA66 polished using the same polishing paper. The sliding surface roughness of the GF composite was much higher than that of the unreinforced PA66, and the theoretical minimum oil film thickness obtained using the GF composite became thinner owing to the higher Young's modulus compared to that of the unreinforced PA66. Therefore, the effect of the lower contact area, which decreased the friction coefficient, was supposed to be canceled by the oil film formation weaker than that of the unreinforced PA66.

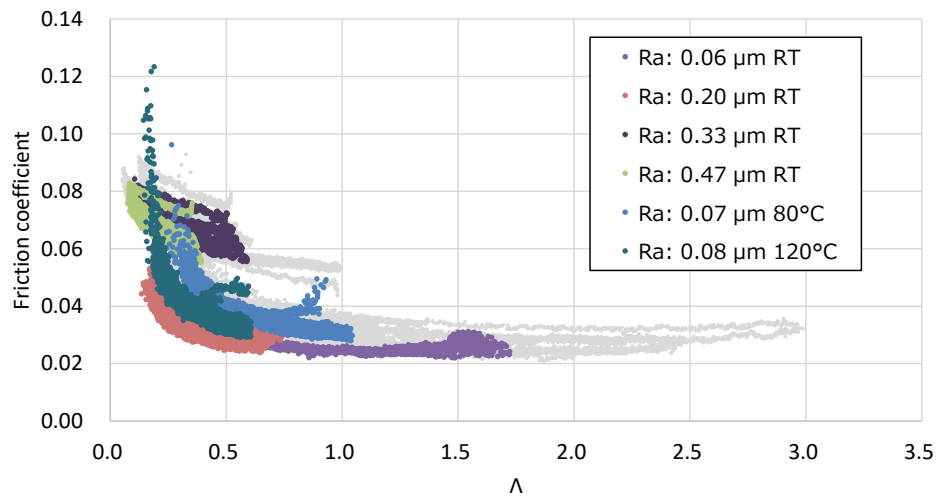


Fig. V. 20 Relationship between calculated Λ and friction coefficient obtained using GF composite compared to same relationship obtained using master Λ - μ curve (gray) for unreinforced PA66.

Furthermore, the effect of the steel cylinder hardness on the friction coefficient obtained using the GF composite was investigated. GF induces abrasion on steel counterparts, particularly when the counterpart is softer than the GF. In this section, the effect of the steel hardness on the friction coefficient obtained for a lower normal load (i.e., contact pressure) was investigated. Fig. V. 21 presents the friction coefficient evolutions obtained using either the GF composite or the unreinforced PA66 and either the softer or harder steel at different rotation speeds. For each specimen, the sliding surface was polished using #800 polishing paper before the sliding tests. As observed for the unreinforced PA66 (Fig. V. 15, where the R_a of the ring specimens is much lower), the friction coefficient suddenly increased with increasing rotation speed only when the softer steel was used. In addition to the suddenly increased friction coefficient, neither the absolute values nor the rotation speed dependence of the friction coefficients obtained using the unreinforced PA66 and the GF composite were explicitly different. Fig. V. 22 presents the interferometric measurements and Table V. 4 lists the roughness and wear volume of the softer steel cylinder (after the cylindrical shape was removed) after the sliding tests performed using the unreinforced PA66 and the GF composite. The steel counterpart showed a wear scar on the steel cylinder surface tested in contact with both the unreinforced PA66 and the GF composite. The roughness of the sliding surface and wear volume of the cylinder tested with GF composite were higher than those tested with

unreinforced PA66, confirming that the GF composite containing hard fibers showed more severe abrasion on the steel counterpart than the unreinforced PA66 did.

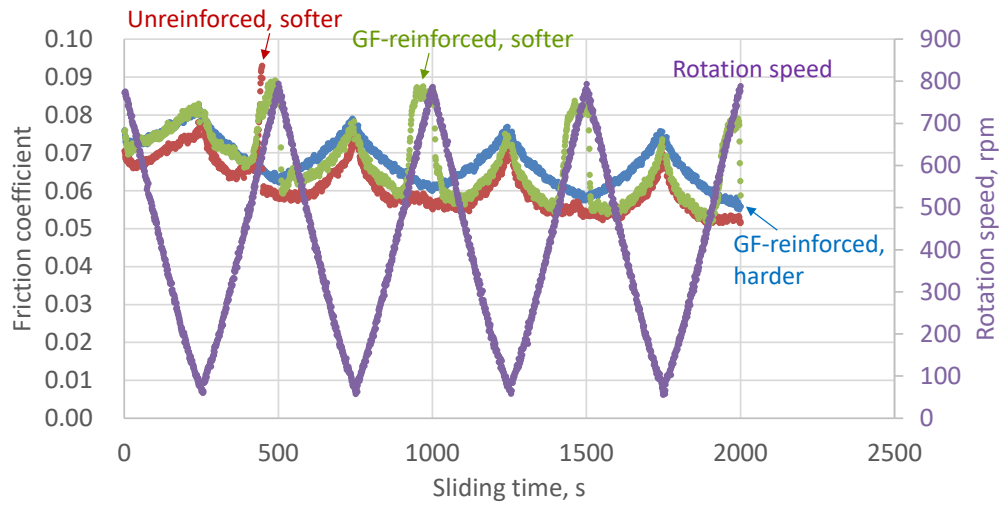


Fig. V. 21 Friction coefficient evolutions obtained at different rotation speed for either GF composite or unreinforced PA66 and either softer or harder steel.

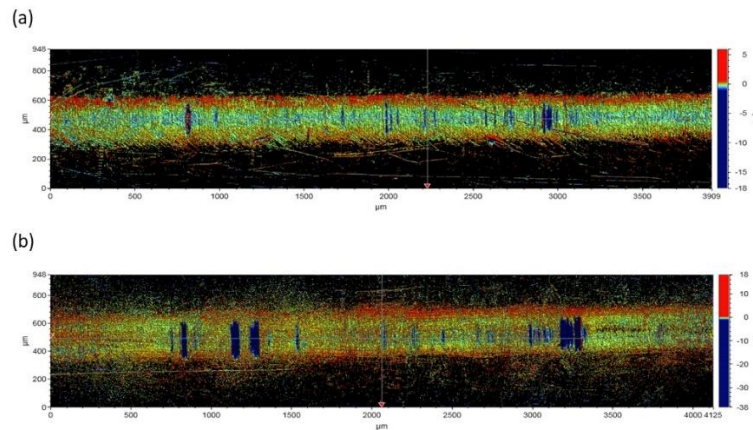


Fig. V. 22 Interferometric measurements of steel cylinder (after cylindrical shape was removed) after sliding tests in contact with (a) unreinforced PA66 and (b) GF composite.

Table V. 4 Roughness and wear volume of softer steel cylinder measured after sliding tests.

Ring specimen	S_a (μm)	R_a (μm)	Wear volume* (mm^3)
Unreinforced PA66	0.29 ± 0.070	0.09 ± 0.04	5.3×10^{-4}
GF-reinforced PA66	0.38 ± 0.046	0.17 ± 0.03	11.0×10^{-4}

* Total of four steel cylinders

3. Friction mechanism under grease lubrication

3.1 Difference of the friction mechanism between PAO8 oil lubrication and grease without zinc carboxylate lubrication

As explained in Section 7.3 in Chapter I, several works [129, 137, 166] focused on the difference in the friction mechanism between oil lubrication and grease lubrication, considering the differences in the sliding speed dependence of the oil film thickness and friction coefficient which are caused by the sliding speed dependence of apparent viscosity of grease and influence of grease soap (thickener). It is necessary to understand this difference also in the sliding of PA66 and carbon steel. First, to simply compare the oil lubrication and grease lubrication, PAO8-based urea grease without zinc carboxylate was prepared, and the effects of each parameter (rotation speed, normal load, temperature, and sliding surface roughness) on the difference in the friction behavior were investigated using unreinforced PA66 and harder steel, comparing with the friction behavior under PAO8 oil lubrication presented in Section 2. Fig. V. 23 shows the rotation speed dependence of the friction coefficient using unreinforced PA66 ($R_a = 0.06\text{-}0.07 \mu\text{m}$ which was obtained by polishing using #4,000 polishing paper) under PAO8 oil lubrication and grease without zinc carboxylate lubrication at room temperature.

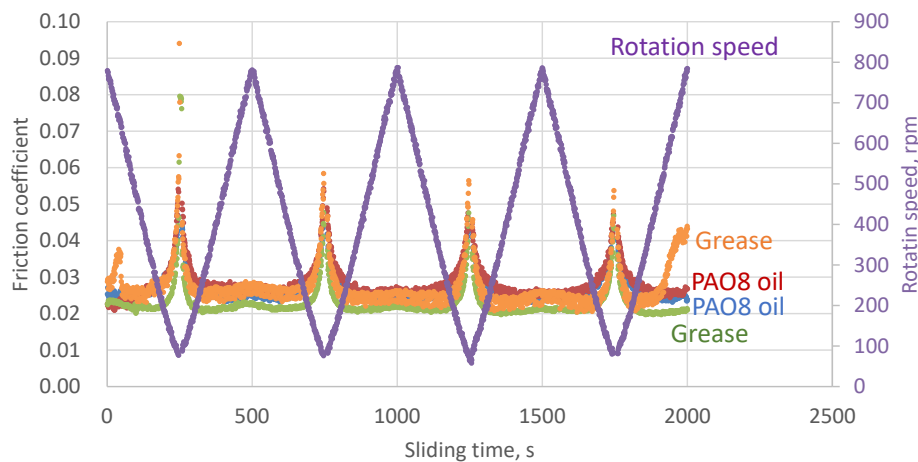


Fig. V. 23 Rotation speed dependence of the friction coefficient using unreinforced PA66 ($R_a = 0.07 \mu\text{m}$) under PAO8 oil and grease without zinc carboxylate lubrication at room temperature. Sliding tests were conducted two times in each lubricant.

As explained in Section 2.3, under PAO8 lubrication and this test condition, friction behavior was mainly dominated by fluid lubrication as presented in proposed Λ - μ master curve. Comparing the friction behavior under PAO8 oil lubrication with that under grease lubrication, no significant differences were observed; friction coefficient using both lubricants shows identical values and increases with decreasing rotation speed. In addition, no great increase in the temperature during sliding was observed because normal load was low and the effect of sliding heat generation was negligible.

Next, the effect of the normal load (contact pressure) was investigated using the same combination of the PA66 ring specimens, steel cylinders, and lubricants at room temperature. Fig. V. 24 presents the evolutions of the friction coefficient for different values of a normal load.

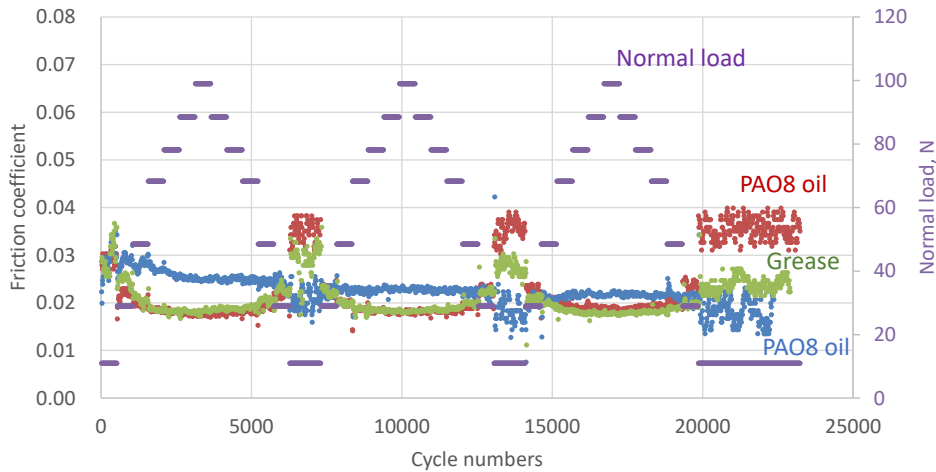


Fig. V. 24 Normal load dependence of the friction coefficient using unreinforced PA66 (R_a : $0.07 \mu\text{m}$) under PAO8 oil and grease without zinc carboxylate lubrication.

As explained in Section 2.4, under PAO8 lubrication, load dependence of the friction coefficient under this condition was mainly dominated by fluid lubrication, considering the proposed Λ - μ master curve. No significant difference in the friction coefficient was also observed between PAO8 oil lubrication and grease lubrication.

In addition, the effect of the temperature on the friction coefficient was investigated using the same combination of the PA66 ring specimens, steel cylinders, and lubricants. Fig. V. 25 presents the rotation speed dependence of the friction coefficient under oil lubrication at 80°C and grease lubrication at room temperature and 80°C . As observed in the friction behavior under PAO8 oil lubrication as explained in Section 2.1, friction coefficient becomes higher at 80°C than at room temperature also under grease lubrication because of the decrease in Λ and transition of the lubrication regime (approximation from fluid lubrication to mixed lubrication). Grease lubrication shows slightly lower friction coefficient in the initial stage of the sliding than PAO8 oil lubrication at 80°C ; however, no significant differences in the friction coefficient were observed in the later stage of the sliding.

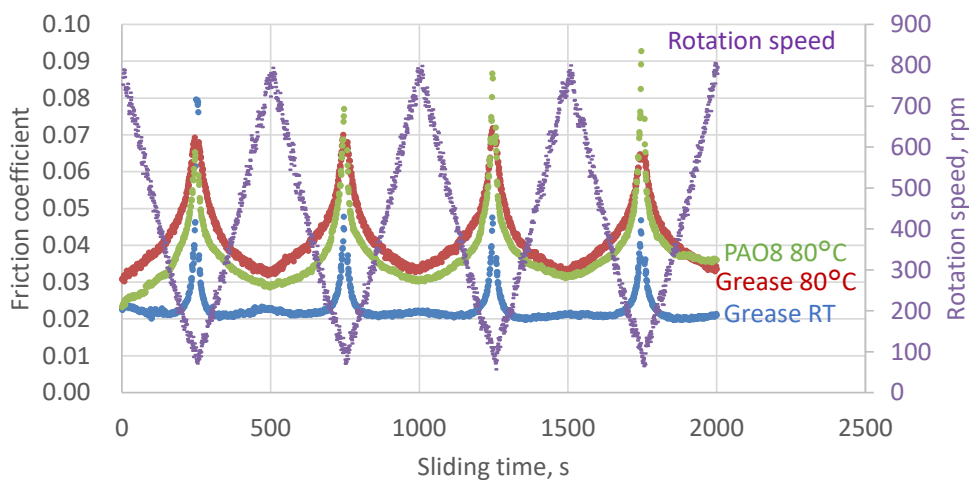
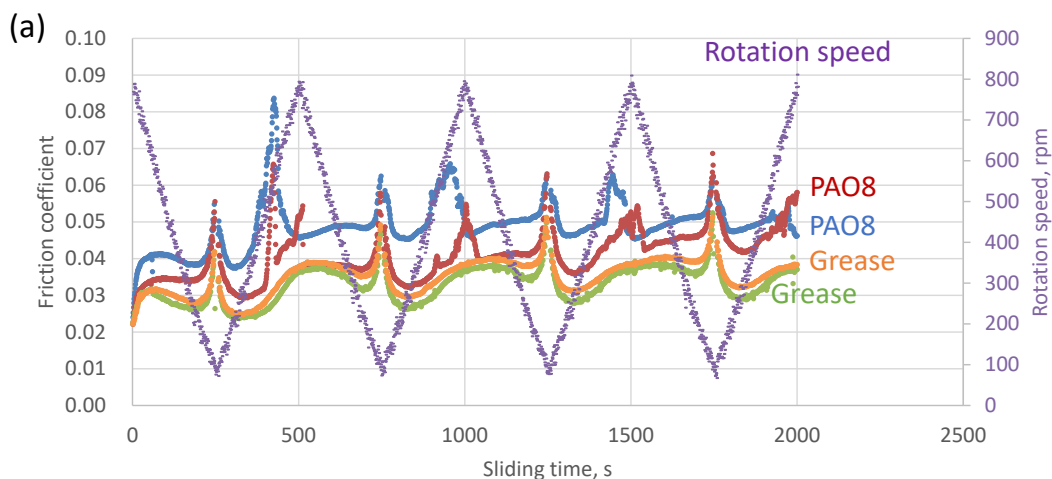


Fig. V. 25 Evolutions of the friction coefficient under oil lubrication at 80°C and under grease lubrication at room temperature and 80°C .

In summary, regardless of different values of rotation speed, normal load, and temperature, using unreinforced PA66 ring specimens with smooth sliding surface ($R_a = 0.06\text{--}0.07\ \mu\text{m}$ which was obtained by polishing using #4,000 polishing paper), no explicit differences in the friction coefficient and friction evolution were observed between PAO8 oil and grease lubrication. To explain these behaviors, we can propose the two following assumptions. (1) Apparent viscosity of grease in the range of tested sliding speed and viscosity of PAO8 oil are identical. Therefore, oil film thickness under each condition is identical. Then, no explicit differences in Λ under each test condition and in the friction coefficient were observed. (2) Even if the apparent viscosity of grease is higher than the PAO8 oil viscosity, this difference is negligible to influence the friction behavior under mild test conditions.

To elucidate the friction behavior much more deeply, additional sliding tests were conducted under much severer conditions. Fig. V. 26 presents the sliding speed dependence of the friction coefficient and temperature for a normal load of 220 N tested at room temperature using the same combination of PA66 ring specimens, steel cylinders, and lubricants. Observed temperature is not a temperature on the sliding surface but that of the steel cylinder sample holder which is supposed to be much lower than the sliding surface temperature. Unlike friction behavior for a normal load of 50 N presented in Fig. V. 23, PAO8 oil lubrication shows higher friction coefficient than grease lubrication. Tendency that the friction coefficient increases with increasing the rotation speed is observed under both PAO8 oil and grease lubrication. In addition, the increase in the temperature which can be related to the sliding heat generation is observed, and PAO8 lubrication shows higher temperature than grease lubrication. The theoretical oil film thickness, as presented in Fig. V. 9, presents that the oil film thickness decreases with the increase in the normal load (contact pressure). In addition, the higher normal load induces the sliding heat generation, and it also leads to the decrease in the oil viscosity and decrease in the oil film thickness. Therefore, the friction coefficient became higher for 220 N under both PAO8 oil and grease lubrication than for 50 N by the transition of the lubrication regime (decrease in Λ).



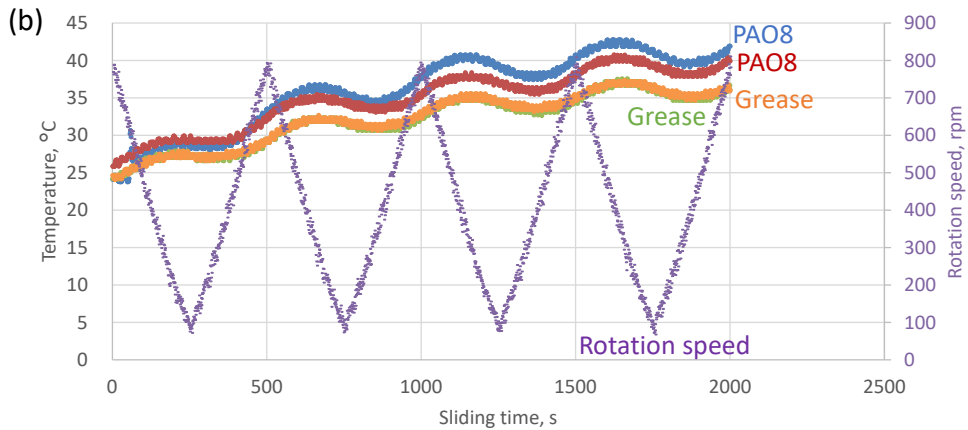


Fig. V. 26 Evolutions of (a) the friction coefficient and (b) the temperature under PAO8 oil and grease lubrication for a normal load of 220 N.

Furthermore, sliding speed dependence of the friction coefficient was also investigated using unreinforced PA66 with higher sliding surface roughness ($R_a = 0.20 \mu\text{m}$ where sliding surface is skin layer without polishing) for a normal load of 50 N at room temperature. Under PAO8 oil lubrication, friction coefficient is mainly dominated by the mixed lubrication in this sliding surface roughness, as explained in Section 2.3. Unlike the friction behavior with $R_a = 0.07 \mu\text{m}$ as presented in Fig. V. 23, grease shows slightly lower friction coefficient than PAO8 oil, whereas increase in the friction coefficient is observed when sliding speed decreases in both surface roughness. In addition, as also observed under PAO8 oil lubrication, the friction coefficient under grease lubrication with $R_a = 0.20 \mu\text{m}$ is higher than that with $R_a = 0.06\text{-}0.07 \mu\text{m}$. This also can be explained by the transition of lubrication regime (decrease in Λ).

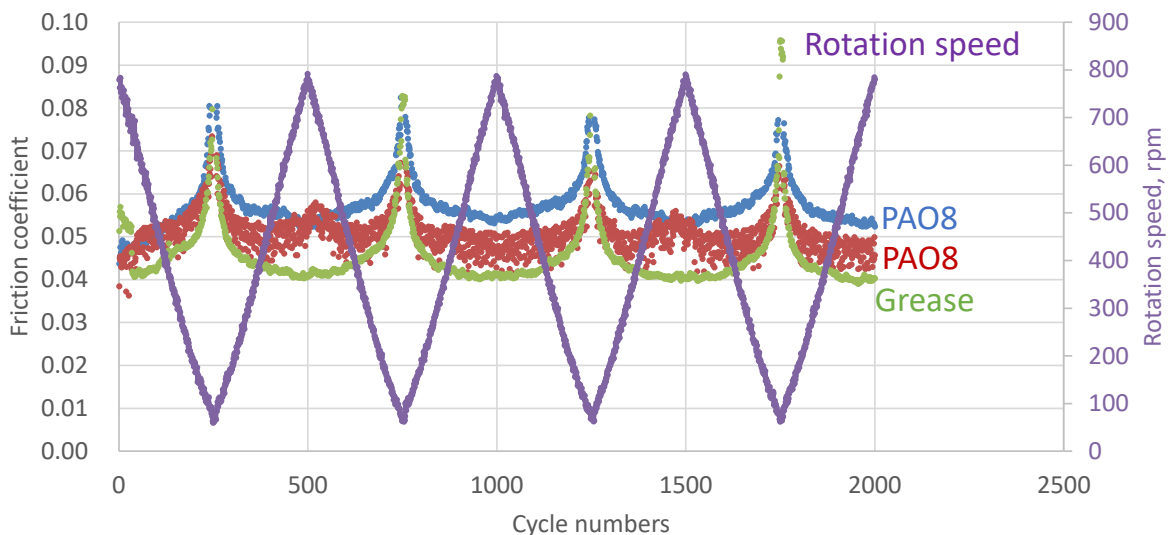


Fig. V. 27 Rotation speed dependence of the friction coefficient using unreinforced PA66 which was not polished (skin layer) under PAO8 oil and grease without zinc carboxylate lubrication.

In summary, following conclusions can be highlighted when comparing PAO8 oil lubrication and grease lubrication in this sliding configuration. In the case where oil film is formed easily (closer to the fluid lubrication regime with higher Λ), such as under lower

normal load or with lower sliding surface roughness, effect of solid contact can be reduced even under PAO8 oil lubrication with lower viscosity than grease. And low friction coefficient, which is identical to that under grease lubrication, can be obtained. Under fluid lubrication, theoretically, higher viscosity of grease is expected to exhibit higher friction coefficient, considering Stribeck curve. No increase in the friction coefficient, however, was observed under the test conditions of the present study. On the other hand, in the case of high normal load or high sliding surface roughness, where oil film formation becomes more difficult (the effect of mixed and boundary lubrication becomes larger with lower Λ), grease with higher viscosity can reduce the solid contact compared to PAO8 oil lubrication, and thus lower friction coefficient can be obtained. Therefore, the difference in the friction behavior between PAO8 oil lubrication and grease lubrication depends on the severity of the contact.

3.2 Effect of addition of zinc carboxylate to grease under various test conditions

In chapter IV, the effects of the addition of zinc carboxylate to grease on especially wear and creep resistance of GF-reinforced or unreinforced PA66 were investigated under severe boundary lubrication conditions for a normal load of 350 N at each temperature. In this section, the effect of zinc carboxylate addition to grease is discussed under much lower normal load conditions. First, the rotation speed dependence of the friction coefficient using unreinforced PA66 with smooth sliding surface ($R_a = 0.06-0.07 \mu\text{m}$ which was obtained by polishing using #4,000 polishing paper) and harder steel under grease without or with zinc carboxylate was investigated at room temperature. Fig. V. 28 presents the evolutions of the friction coefficient under grease without (presented in Fig. V. 23) or with zinc carboxylate lubrication.

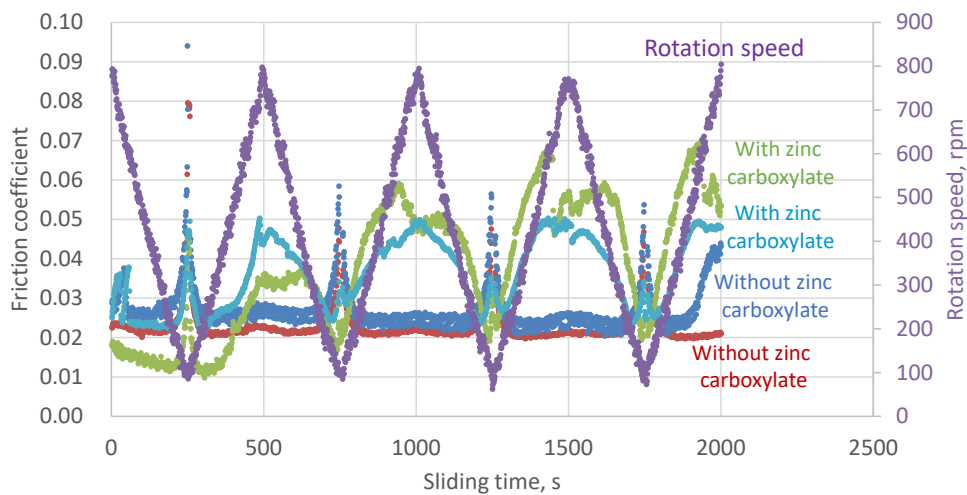


Fig. V. 28 Rotation speed dependence of the friction coefficient using unreinforced PA66 ($R_a = 0.06-0.07 \mu\text{m}$) under grease without or with zinc carboxylate lubrication at room temperature. Sliding tests were conducted two times with each grease.

The explicit difference in the friction behavior is observed. Only when zinc carboxylate was added to grease, the friction behavior is not stable; friction coefficient increases when the rotation speed increases, and decreases when the rotation speed decreases, in addition to the increase in the friction coefficient when rotation speed is under 300 rpm. This increase in the friction coefficient cannot be explained by the Stribeck curve or EHL theory. In addition, the same tendency was observed under the same sliding test conditions with higher sliding

surface roughness of unreinforced PA66 ring specimens ($R_a = 0.20 \mu\text{m}$ where the sliding surface was skin layer without polishing), as presented in Fig. V. 29. In addition to the higher friction coefficient which is related to high surface roughness, the increase in the friction coefficient when increasing the rotation speed and the decrease in the friction coefficient when decreasing the rotation speed are observed only when grease with zinc carboxylate is used.

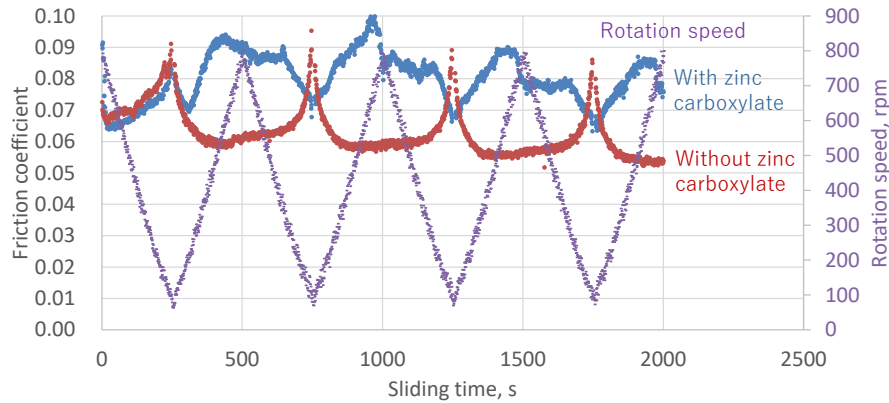


Fig. V. 29 Rotation speed dependence of the friction coefficient using unreinforced PA66 ($R_a = 0.07 \mu\text{m}$) under grease without or with zinc carboxylate lubrication. Sliding test was conducted two times with each grease.

This unstable behavior was also observed in the normal load dependence of the friction coefficient using the same combination of PA66 ($R_a = 0.07 \mu\text{m}$), harder steel, and lubricants, as presented in Fig. V. 30. In the initial stage of the sliding tests, no definite difference in the friction behavior is observed; however, friction coefficient starts to increase after 8,000 cycles and then suddenly decreases. To consider this unstable behavior of the friction coefficient when zinc carboxylate is added to grease, the sliding surfaces of the steel cylinder and unreinforced PA66 ring were observed and analyzed using SEM-EDX.

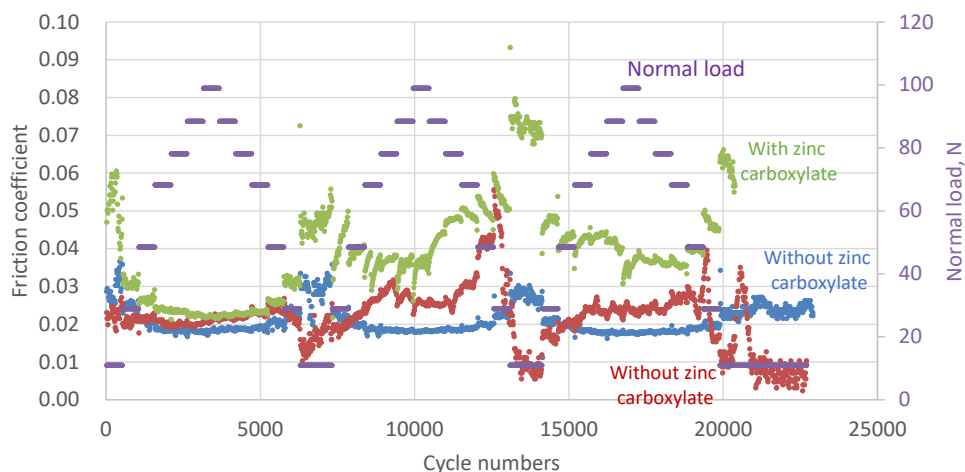


Fig. V. 30 Normal load dependence of the friction coefficient using unreinforced PA66 ($R_a = 0.07 \mu\text{m}$) under grease without or with zinc carboxylate lubrication.

To investigate the reason why there is a difference in the friction behavior, sliding surfaces after sliding tests were observed. Fig. V. 31 shows the SEM observations of the sliding surface

of the steel cylinders after the sliding tests under grease without zinc carboxylate lubrication (presented in Fig. V. 28). Before the SEM observations, analyzed samples were carefully washed using an ultrasonic bath in a heptane solvent for 20 min to remove the attached grease. No explicit formation of a film on the sliding surface was observed at lower magnification, whereas scratches in the sliding direction were observed in the wear scar at higher magnification. On the other hand, Fig. V. 32 presents the SEM observations of the sliding surface of the steel cylinders after the sliding test under grease with zinc carboxylate lubrication (presented in Fig. V. 28). Unlike steel cylinder tested under grease without zinc carboxylate lubrication, film formation can be observed on the sliding area at lower magnification. In addition, at higher magnification, several dark patches were observed. EDX analysis revealed that these dark patches contain higher amount of C which is supposed to be originated from the grease composition (thickener or zinc carboxylate) and very small amount of Zn which is related to zinc carboxylate, in addition to Fe, Si, and Mn which are originated from S45C carbon steel. Outside dark patches, only the elements related to S45C steel (Fe, Mn, Si, and C) were detected. In addition, the sliding surfaces on the counterpart PA66 ring specimens were observed and analyzed using SEM-EDX in both ring specimens, as presented in Fig. V. 33. Scratch in the sliding direction which can be caused by the asperity of steel counterpart is observed, as on the sliding surface under PAO8 oil lubrication, as presented in Fig. V. 5. EDX analysis reveals that only C and O originated from PA66 are detected, aside from Au related to gold coating (for SEM observation of electric insulating PA66). Zn (originated from zinc carboxylate) and S (originated from sulfur type anti-oxidation agent) are not observed, regardless of the zinc carboxylate addition to grease. This result coincides with that observed in Section 6 in Chapter IV under much severe contact conditions which explained no positive effect of zinc carboxylate addition to grease on the tribological properties at room temperature.

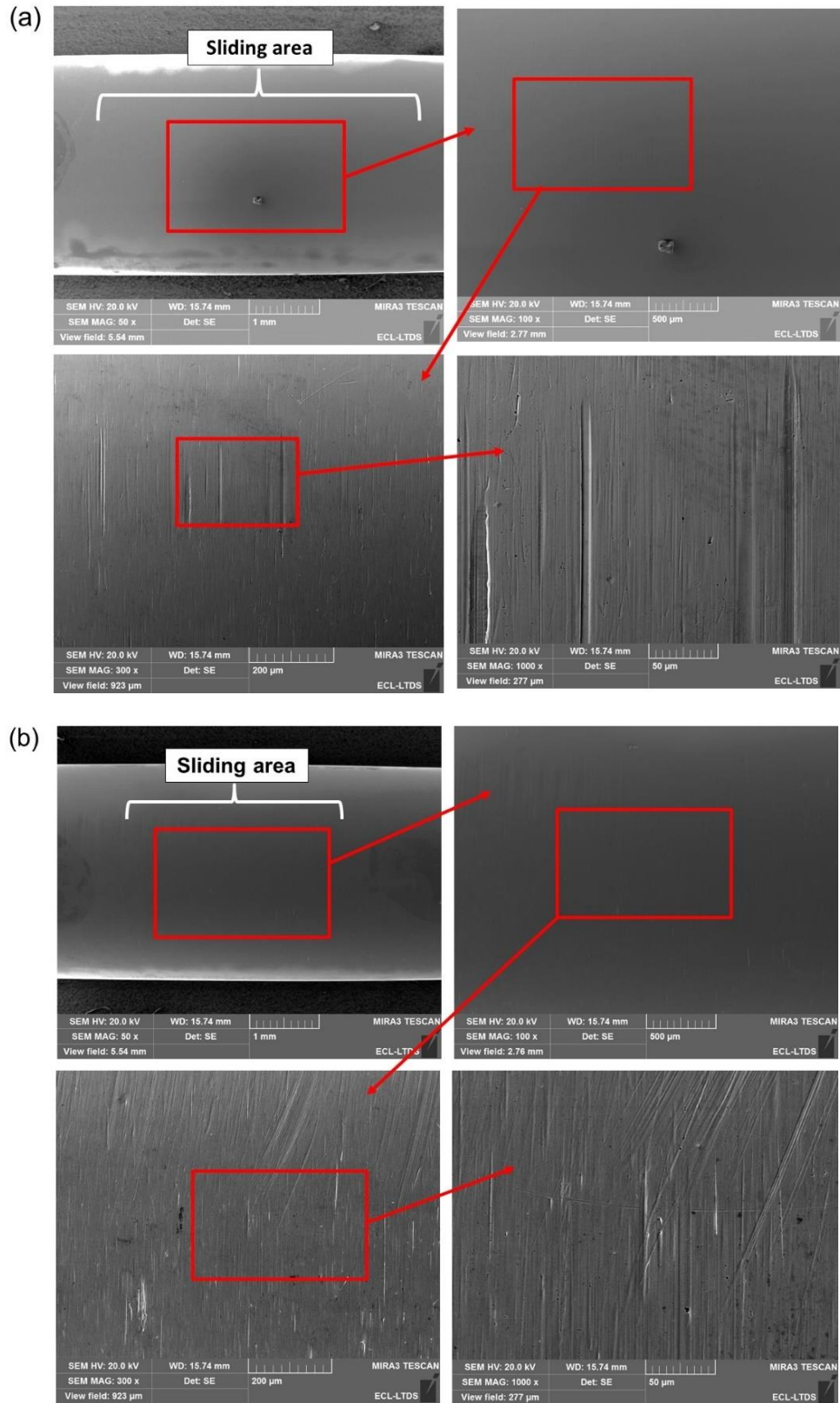


Fig. V. 31 SEM observations of the sliding surface of the steel cylinders after the sliding test under grease without zinc carboxylate lubrication (presented in Fig. V. 28). Two cylinders (a) and (b) were observed.

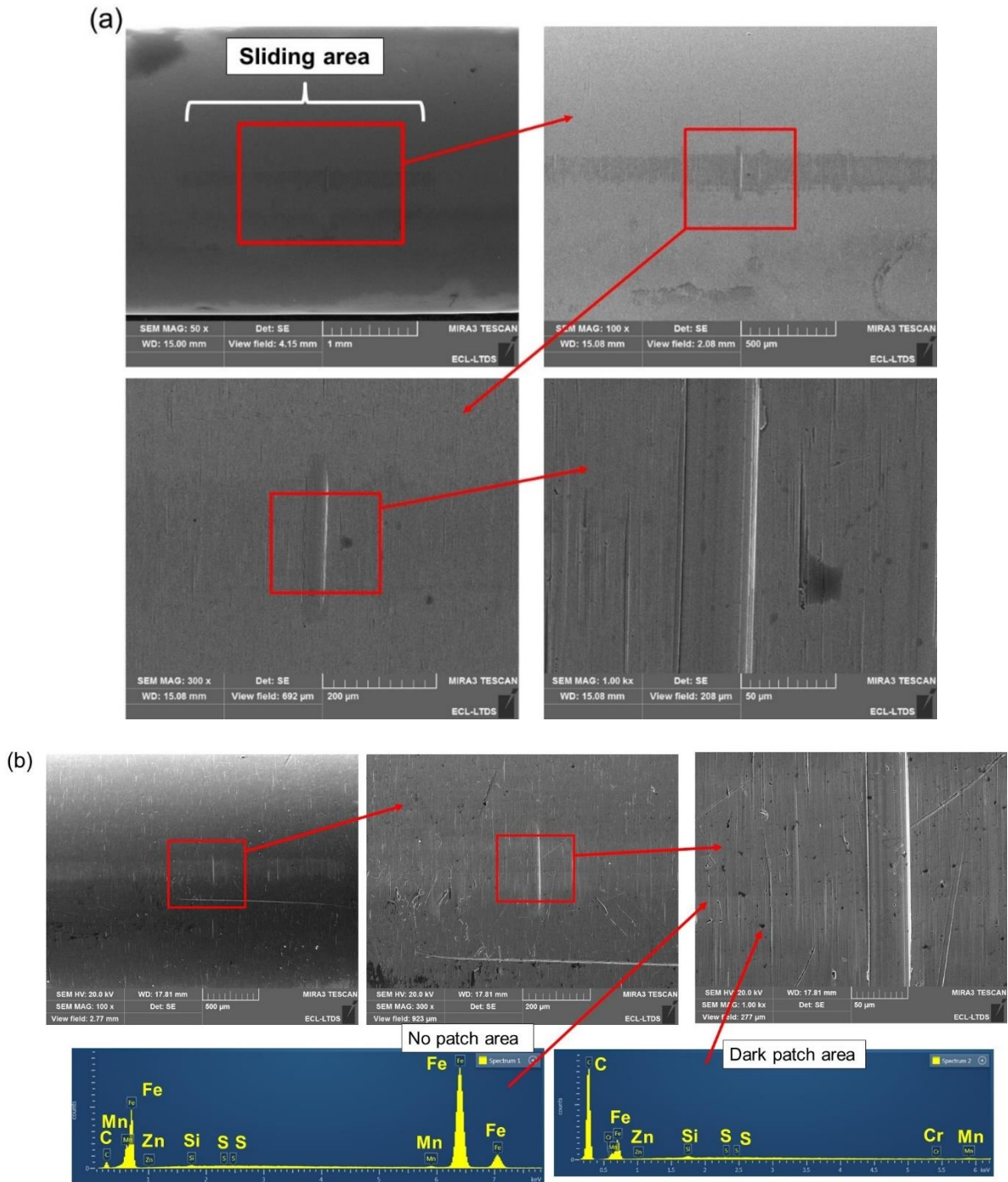


Fig. V. 32 SEM observations of the sliding surface of the steel cylinders after the sliding test under grease with zinc carboxylate lubrication (presented in Fig. V. 28). Two cylinders (a) and (b) were observed. Point EDX analysis was conducted in the image (b).

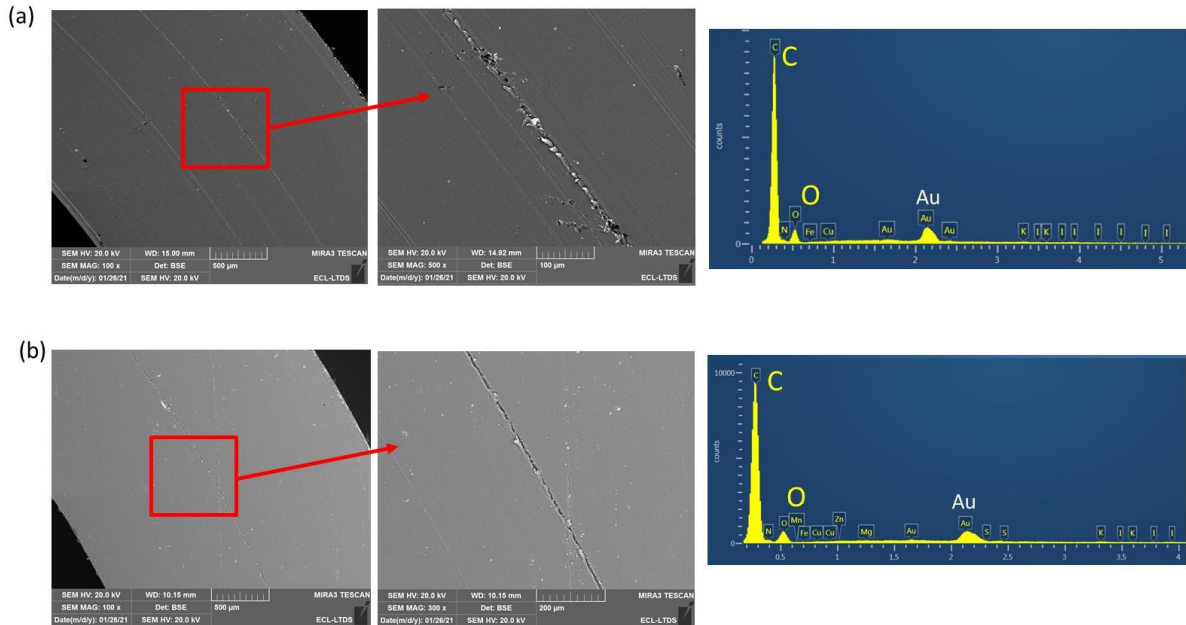


Fig. V. 33 SEM observations and EDX analysis of the sliding surface of the unreinforced PA66 ring specimens after the sliding test under grease (a) without and (b) with zinc carboxylate lubrication (presented in Fig. V. 28).

These results can be explained by following hypothesis. Because sliding surface temperature (around 30°C) can be lower than the softening temperature of zinc carboxylate, zinc carboxylate is present in the solid state during sliding. Therefore, zinc carboxylate cannot contribute to induce the tribochemical reaction to form the tribofilm on the steel and PA66 which can improve the tribological properties, as presented in Fig. IV. 38. Instead, zinc carboxylate formed different solid film on the steel sliding surface and prevented oil film formation. This influence became significant when rotation speed was high because rotation induced the increase in the sliding surface temperature and decrease in the PAO8 oil viscosity and in the oil film thickness. Consequently, the friction coefficient increased with increasing the rotation speed. To verify this hypothesis on the friction behavior, sliding test was conducted at 80°C where softening of the zinc carboxylate can be promoted and where tribochemical reaction which improved the tribological properties under severer conditions was observed, as presented in Chapter IV. Fig. V. 34 shows the friction coefficient evolutions with different values of the rotation speed at 80°C using the unreinforced PA66 ring specimens ($R_a = 0.07 \mu\text{m}$) and harder steel under PAO8 oil and grease without or with zinc carboxylate lubrication. Unlike the friction behavior at room temperature as observed in Fig. V. 28, friction coefficient shows no increase when the rotation speed increases under grease with zinc carboxylate lubrication. In addition, the friction coefficient is lower under grease with zinc carboxylate lubrication at each rotation speed than that under grease without zinc carboxylate lubrication. Therefore, the effect of the zinc carboxylate addition is completely different between room temperature and 80°C.

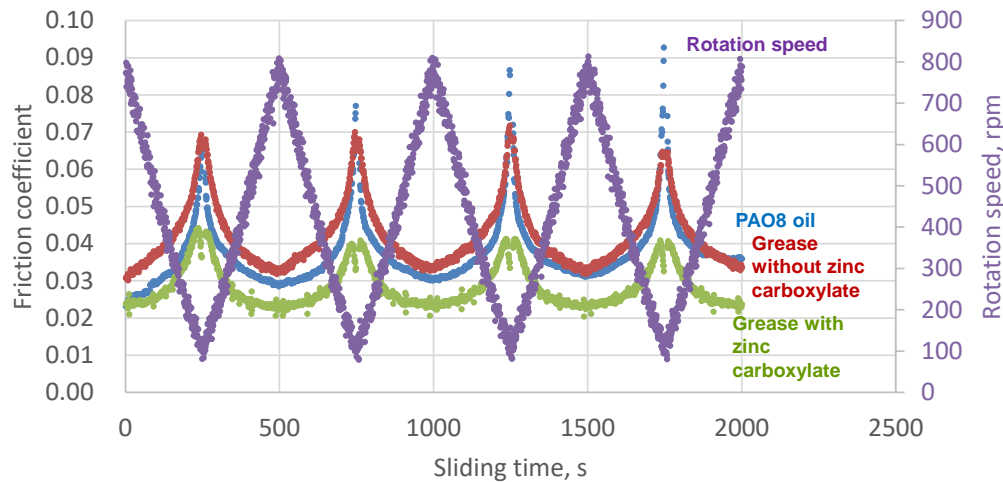


Fig. V. 34 Rotation speed dependence of the friction coefficient using unreinforced PA66 ($R_a = 0.07 \mu\text{m}$) and harder steel at 80°C under PAO8 oil and grease with or without zinc carboxylate lubrication.

Fig. V. 35 presents the SEM-EDX observations on the steel cylinder surface after sliding test at 80°C under grease with zinc carboxylate lubrication. Several dark patches can be observed on the sliding surface. The proportion of the patches seems to be higher than that observed in Fig. V. 32 (tested at room temperature). Point EDX analysis revealed that range of 19-24 wt% of C was detected in dark patch area, and this is higher than in no-patch area (range of 4-4.5 wt%). In addition, small amounts of Zn (range of 0.3-0.8 wt%) were detected. This tendency coincides with EDX analysis on the steel cylinder surface after the sliding test at 80°C for a normal load of 350 N under the same grease lubrication, as presented in Fig. IV. 19. As ToF-SIMS analysis presented in Section 4.1.3 in Chapter IV, the formation of the carboxylate tribofilm including palmitate and stearate on the steel tested at 80°C was observed. Therefore, on the sliding surface, at 80°C , softened zinc carboxylate is supposed to form the tribofilm, and this film can contribute to decrease the friction on the contact surface, as well as film does not inhibit the oil film formation. In addition, Fig. V. 36 shows the SEM-EDX observation of the sliding surface of counterpart PA66 ring after the sliding test at 80°C . Unlike at room temperature, small amounts of Zn and S are detected on the PA66 sliding surface, in addition to C, O, and N which are originated from PA66. This can be, as discussed in Section 4.2.2 in Chapter IV, ZnS compounds tribofilm which was formed through tribochemical reaction of zinc carboxylate and sulfur type anti-oxidation agent in grease during sliding, and ZnS also seems to contribute to decrease the friction coefficient. However, the amounts of Zn and S are much lower (<0.2 wt%) than that observed in Fig. IV. 33 on the PA66 ring tested at 80°C for a normal load of 350 N. This is because the normal load in Fig. V. 34 (50 N) is lower than that in Fig. IV. 33 (350 N). In addition, because the sliding surface roughness of PA66 is lower than the previous one, direct contact area between PA66 and steel becomes smaller. It brings more oil film formation, and the effect of tribochemical reaction on the direct contact surface can be reduced.

In summary, the addition of zinc carboxylate to grease provided adverse effect on the friction coefficient at room temperature because zinc carboxylate does not soften and prevents the good oil film formation. By contrast, the zinc carboxylate leads to lower friction coefficient by the tribochemical reaction without prevention of oil film formation at 80°C .

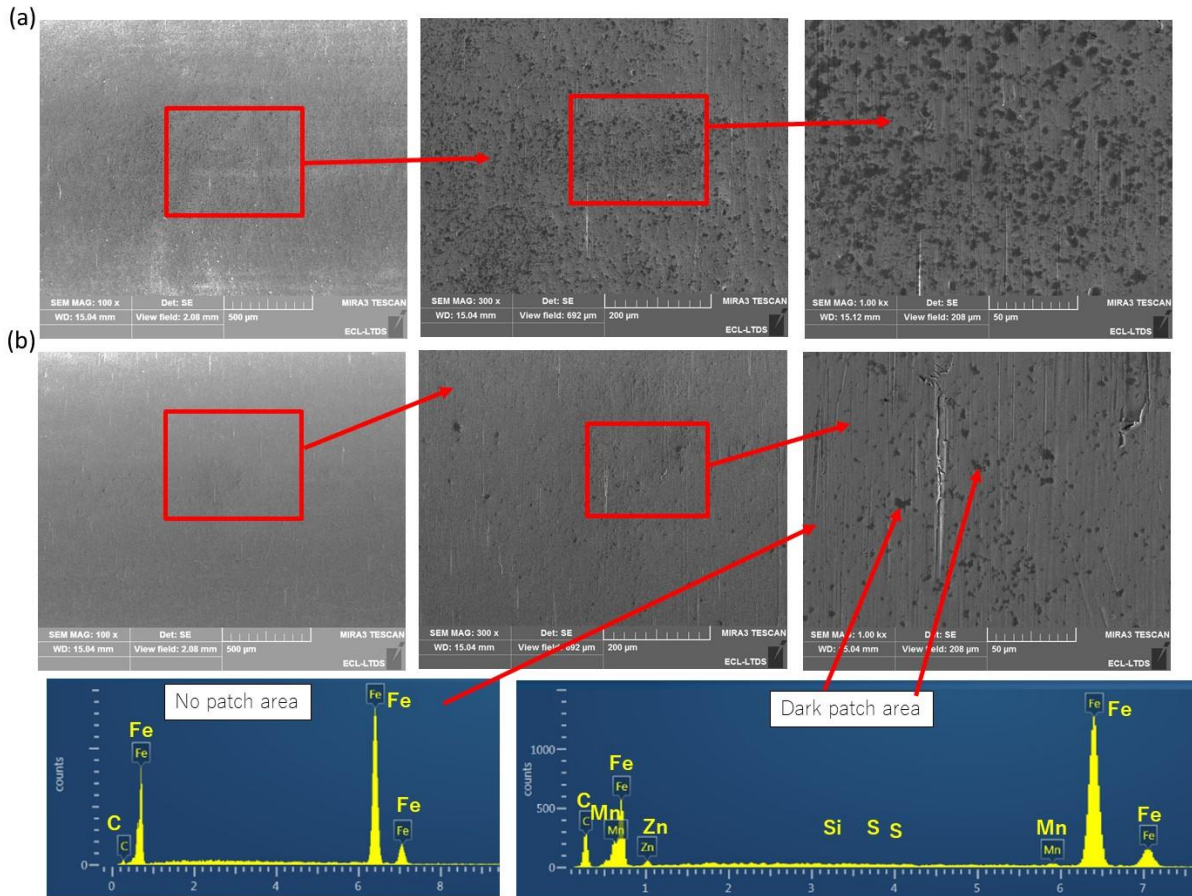


Fig. V. 35 SEM observations and EDX analysis of the sliding surface of the steel cylinders after the sliding test at 80°C under grease with zinc carboxylate lubrication (presented in Fig. V. 34). Two cylinders (a) and (b) were observed.

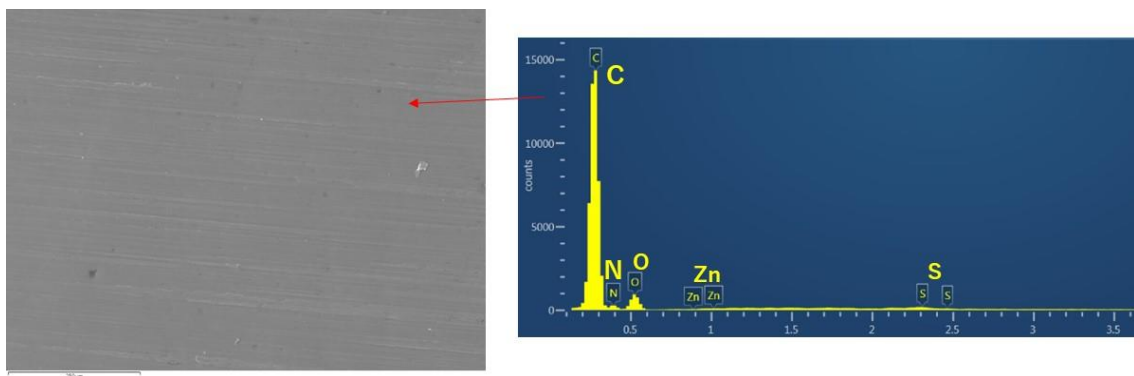


Fig. V. 36 SEM observations and EDX analysis of the sliding surface of the PA66 ring after the sliding test at 80°C under grease with zinc carboxylate lubrication (presented in Fig. V. 34).

4. Conclusions

The friction mechanisms of unreinforced and GF-reinforced PA66 in contact with carbon steel under PAO8 oil lubrication and PAO8-based urea grease lubrication were elucidated. The following points should be highlighted.

1) Friction mechanism under PAO8 oil lubrication

(1) Effect of ring surface roughness, sliding speed, and temperature on friction coefficient

The friction coefficient increased with increasing initial surface roughness of PA66 ring specimens sliding surface, decreasing sliding speed, and increasing temperature. The sliding surface roughness decreased after the sliding tests when the initial sliding surface roughness was high.

(2) Friction coefficient obtained using estimated oil film thickness and Λ

The theoretical minimum oil film thickness was estimated considering various sliding conditions and the temperature dependence of the oil viscosity and Young's modulus of unreinforced PA66, using the equation for soft EHL presented by Hamrock and Dowson. In addition, the Λ - μ master curve (wherein the friction coefficient decreased with increasing Λ) was presented considering the change in the sliding surface roughness during the sliding test under different test conditions.

(3) Effect of normal load on friction coefficient

The normal load dependence of the friction coefficient can be explained by the proposed Λ - μ curve when the initial surface roughness is low. The Bowden and Tabor law, on the other hand, explained the normal load dependence well, and the results did not coincide with the proposed Λ - μ curve when the initial surface roughness was higher because the effect of the direct contact between the PA66 and steel became more remarkable than the influence of the oil film formation.

(4) Effect of steel hardness on friction coefficient

The use of softer steel suddenly increased the friction coefficient only when the initial PA66 roughness was high, which is related to the direct contact between the PA66 and steel counterpart and the degree of steel wear.

(5) Effect of GF reinforcement on friction coefficient

The effects of the sliding speed, initial sliding surface roughness, and temperature on the friction coefficient were investigated for the GF composite, and they showed the same tendencies as observed for the unreinforced PA66. The minimum oil film thickness was calculated considering the higher Young's modulus of the GF composite. The Λ - μ master curve was obtained for the GF composite and compared to that obtained for the unreinforced PA66, thereby confirming that a lower friction coefficient can be obtained using the GF composite compared to the unreinforced PA66 for the same Λ .

2) Friction mechanism under grease lubrication

(1) The difference of the friction mechanism between PAO8 oil lubrication and grease without zinc carboxylate lubrication

In the case where oil film is formed easily, such as under low normal load or with low sliding surface roughness, effect of solid contact can be reduced even under PAO8 oil lubrication with lower viscosity than grease. And low friction coefficient, which is identical as that under grease lubrication, can be obtained. On the other hand, in the case of high normal load or high sliding surface roughness, where oil film formation becomes more difficult, grease with higher viscosity can reduce the solid contact compared to PAO8 oil lubrication, and thus lower friction coefficient can be obtained. Therefore, the difference in the friction behavior between PAO8 oil lubrication and grease lubrication depends on the severity of the contact.

(2) The effect of addition of zinc carboxylate to grease under various test conditions

The addition of zinc carboxylate increased the friction coefficient at room temperature particularly when rotation speed is high because zinc carboxylate does not soften and prevents the good oil film formation. By contrast, the zinc carboxylate leads to lower friction coefficient by the tribochemical reaction without prevention of oil film formation at 80°C.

In Chapters III, IV and V, tribological properties (wear and creep of unreinforced or GF-reinforced PA66, wear of steel, and friction) were elucidated mainly under grease lubrication. All of this leads to a better understanding of the behavior of this contact and the effects of the test parameters. On top of that, it is required to elucidate the effect of the PA66 composite composition on the tribological properties to develop PA66 composite to meet the requirements for the downsizing and using under severe conditions. Therefore, in the subsequent chapters, the effects of composite composition, including the type of reinforcement fibers or PA66 molecular mass, on the tribological properties will be clarified.

CHAPTER VI

EFFECTS OF GF PROPERTIES AND
POLYMER MOLECULAR MASS ON
THE MECHANICAL AND
TRIBOLOGICAL PROPERTIES OF A
PA66-BASED COMPOSITE

**CHAPTER VI: EFFECTS OF GF PROPERTIES AND POLYMER MOLECULAR MASS
ON THE MECHANICAL AND TRIBOLOGICAL PROPERTIES OF A
PA66-BASED COMPOSITE**

1. Introduction.....	209
2. Effects of the interfacial shear strength between the GFs and PA66 on the mechanical and tribological properties.....	210
2.1 Effect of the interfacial shear strength on the mechanical properties	210
2.2 Effect of the interfacial shear strength on the tribological properties	211
2.3 Effect of the GF orientation on the sliding surface with different GF surface treatment agents.....	216
2.4 Estimation of the interfacial shear strength based on Kelly-Tyson model	217
3. Effects of the PA66 molecular mass on the mechanical and tribological properties ..	221
3.1 Effect of the PA66 molecular mass on the wear and creep resistance of GF composite	221
3.2 Effect of the PA66 molecular mass on the wear resistance of steel counterpart ..	225
3.3 Effect of the PA66 molecular mass on the fiber orientation on the sliding surface of GF composite ring specimen	225
3.4 Mechanism of the improvement in the tribological properties of GF composite with the increase in the PA66 molecular mass	226
4. Effects of GF diameter on the mechanical and tribological properties	230
4.1 Effect of GF diameter on the tensile mechanical properties	230
4.2 Effect of GF diameter on the wear and creep resistance of the composite	230
4.3 Effect of GF diameter on the wear resistance of steel counterpart	234
5. Conclusions.....	241

CHAPTER VI: EFFECTS OF GF PROPERTIES AND POLYMER MOLECULAR MASS ON THE MECHANICAL AND TRIBOLOGICAL PROPERTIES OF A PA66-BASED COMPOSITE

In this chapter, the effects of the composition of GF-reinforced PA66 on its mechanical and tribological properties under grease lubrication were investigated to aid in the development of a composite with optimal tribological properties. As important parameters of the compositions of GF composite, the types of GFs (GF surface treatment agent and GF diameter) and molecular mass of PA66 were deeply studied.

1. Introduction

In Chapter III, the tribological properties of a GF-reinforced PA66 composite in contact with carbon steel under high contact-pressure, grease lubricated sliding conditions were investigated. Sliding induced characteristic damage to the surface of the composite and degradation of its mechanical properties, which in turn leads to an increase in the friction, and creep and wear of the composite. In addition, the GFs have an aggressive effect on the steel counterpart via a two-body abrasive wear mode. Furthermore, the effect of the properties of the steel counterpart on the wear resistance of both the composite and the steel counterpart itself was studied. Subsequently, in Chapter IV, the temperature dependence of the tribological properties of the GF-reinforced PA66 in contact with carbon steel were studied. The mechanical properties of the PA66 composite surface and tribofilm formation related to the grease additives at each temperature well explained the temperature dependence of the tribological properties. In addition, in Chapter V, the friction mechanism under oil and grease lubrication under various test conditions was investigated, and it was explained based on the soft-EHL theory and solid/solid contact theory under lubricated conditions. However, these studies were conducted using a single type of GF-reinforced PA66 composite, and the effects of the composition of the composite which are significant for the material development were not investigated.

Therefore, the development of guidelines for the formulation of GF-reinforced PA66 composites with good wear and creep resistance and low aggressive effects on their steel counterpart is necessary. In this chapter, the effects of the composition of GF-reinforced PA66 on its mechanical and tribological properties were investigated to aid in the development of a composite with optimal tribological properties. As the parameters on the composition of the GF composite, this chapter focuses on the effects of the molecular mass of PA66, the diameter of the GFs, and the interfacial strength between the GFs and PA66, which is determined by the GF surface treatment agent, on the tribological properties of GF-reinforced PA66 in contact with steel under grease lubrication. Composite specimens were designed specifically to clarify the effects of each of these material parameters separately, and the effects of these parameters on the wear and creep resistance of the composite, the wear resistance of the

steel counterpart, and the friction coefficient were elucidated and explained in terms of the mechanical properties and the condition of the sliding surface.

Table VI. 1 lists the composition and mechanical/physical properties of evaluated GF composites, coinciding with the sample list presented in Table II. 3, and details in each composite were explained in Chapter II. Solid-state post condensation at 220°C was conducted for sample no. 4 to increase the molecular mass of PA66. Grease no. 1 containing zinc carboxylate and sulfur type anti-oxidation agent in Table II. 11 and steel cylinder with the hardness of 4.5 GPa were used in the experiments of this chapter. All of the sliding tests in this chapter were conducted for a normal load of 350 N under the sliding speed of 1 m/s at room temperature, with 10 s sliding and 1 s stopping phase, as conducted in Chapter III.

Table VI. 1 Composition and mechanical/physical properties of evaluated GF composites.

No.	PA66	GF			Mechanical and physical properties		
	Level of molecular mass	Surface treatment	Diameter, μm	Amount, wt%	Tensile Young's modulus, GPa	VN of the specimens, ml/g	Density, g/cm^3
1	Normal	Type A	6.5	15	5.9 ± 0.3	145	1.25
2	High	Type A	6.5	15	6.0 ± 0.4	193	1.25
3	Super high	Type A	6.5	15	5.4 ± 0.6	235	1.25
4	Super high*	Type A	6.5	15	6.0 ± 0.1	356	1.25
5	High	Type B	6.5	15	6.0 ± 0.4	-	1.25
6	High	Type A	9.5	15	5.9 ± 0.4	-	1.25
7	High	Type A	11	15	6.3 ± 0.4	-	1.25
8	High	Type A	13	15	6.5 ± 0.9	-	1.25
9	High	Type A	15	15	6.2 ± 0.6	-	1.25
10	High	Type A	19	15	5.8 ± 0.1	-	1.25

* Solid-state post condensation after injection molding of the specimens

2. Effects of the interfacial shear strength between the GFs and PA66 on the mechanical and tribological properties

2.1 Effect of the interfacial shear strength on the mechanical properties

First, the effect of the interfacial shear strength between GF and PA66 on the mechanical properties was studied, using the GF composites with fixed GF diameter (6.5 μm) and molecular mass of PA66 (VN: 235 ml/g) to investigate only the effect of the GF surface treatment agent. Table VI. 2 compares the effect of the two different GF surface treatment agents (i.e., composite samples no. 2 and 5, the difference of the surface treatment agent was explained in Section 2.1.1.2 of Chapter II) on their tensile mechanical properties (tensile strength, Young's modulus, tensile elongation at break, and tensile breakage energy). The

tensile strength, tensile elongation at break, and tensile breakage energy of the composite in which the GFs were treated with the type A surface treatment agent were higher than those of the type B sample by 8.1%, 43.3%, and 78.7%, respectively. In contrast, no difference was observed among the Young's moduli of the composites. These results indicate that the choice of GF surface treatment agent only affected properties related to the breakage of the composite. This tendency is also reported in [183]. The Young's modulus was calculated from the initial slope of the stress–strain curve; thus, it was not affected by the GF surface treatment agent, but was instead determined exclusively by the GF content of the composite.

Table VI. 2 Effects of the GF surface treatment agent on the mechanical properties of composites that differed only in the GF surface treatment agent used. The values are averages of five measurements, representing the standard deviation.

	Type A	Type B
Tensile strength	154.0 ± 0.4 MPa	142 ± 2.9 MPa
Young's modulus	6.0 ± 0.4 GPa	6.0 ± 0.4 GPa
Tensile elongation at break	5.1 ± 0.1%	3.5 ± 0.2%
Tensile breakage energy	10.9 ± 0.2 J	6.1 ± 0.6 J

2.2 Effect of the interfacial shear strength on the tribological properties

Next, the effect on the tribological properties were investigated. Fig. VI. 1 shows the evolutions of the friction coefficient, temperature, and vertical displacement during the sliding tests of samples no. 2 and 5. Using the type B sample, which exhibited poorer mechanical properties, sudden increases in the friction coefficient were observed after 4,100/6,100 cycles, 14,200/21,000 cycles, and 48,700/61,600 cycles in the first and second repetitions of the sliding test, respectively. Little increase in the vertical displacement was observed after the first increase in the friction coefficient at 4,100/6,100 cycles; however, the displacement increased significantly following the friction coefficient increase at 14,200/21,000 cycles. The displacement then increased gradually until another large increase in the displacement was observed after the final friction coefficient increase at 48,700/61,600 cycles. In contrast, the friction coefficient and temperature of the type A sample were lower than those of the type B sample, particularly after 6,000 cycles, and no sudden increases in the friction coefficient or displacement were observed until 66,400 and 80,000 cycles in the first sliding test and 80,000 cycles in the second, respectively. Based on these results, the tribological properties of the composite in which the GFs were treated with type B were worse than those of the type A sample; this tendency agreed with the results of the tensile mechanical property tests.

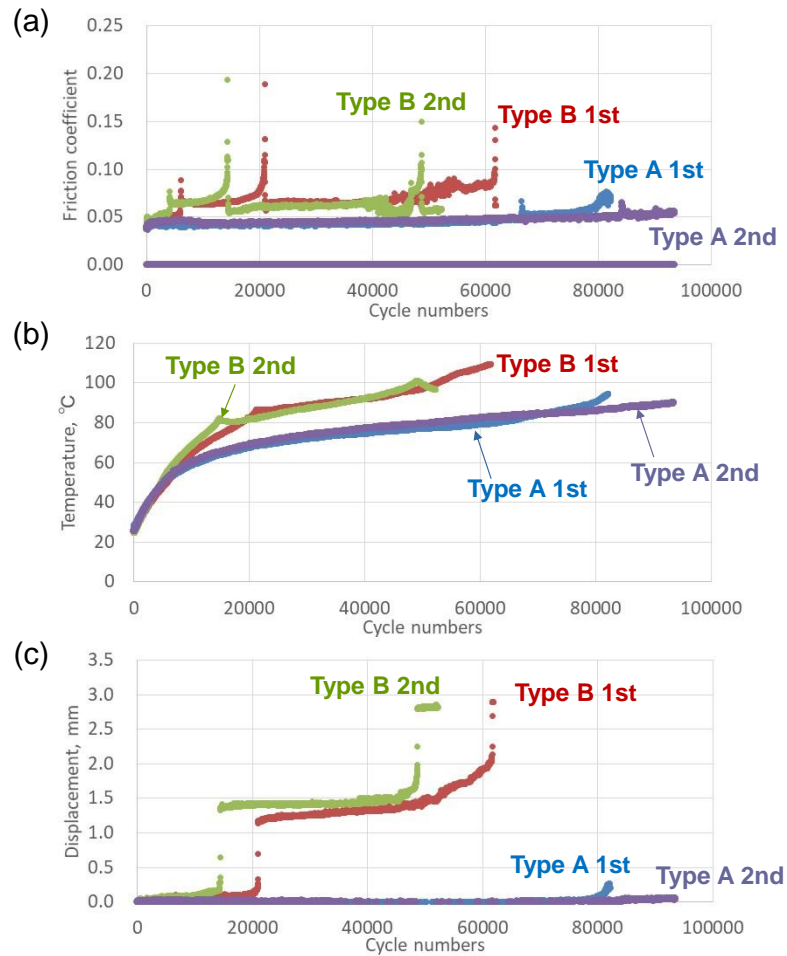


Fig. VI. 1 Evolutions of (a) the friction coefficient, (b) temperature, (c) and vertical displacement of composite samples that differed only in the GF surface treatment agent used.

To clarify the mechanism by which the different GF surface treatment agents induced different tribological properties, the sliding tests were intentionally stopped at 6,500 cycles (just before the first sudden increase in the friction coefficient of the type B sample) and at 22,300 cycles (between the first and second increases in the friction coefficient of the type B sample), and the sliding surfaces of the two samples were analyzed and compared. Fig. VI. 2 presents the wear and creep height loss of the samples at 6,500 and 22,300 cycles. Little wear was observed for either of the samples at either of the measurement points; most of the height decrease was due to creep. These results confirmed that the significant increase in the displacement observed in Fig. VI. 1 was mainly due to creep via plastic deformation of the composite. This increase in the vertical displacement which is considered to be the creep (plastic deformation which accompanies little weight loss of wear) was also observed in Chapter III, and this creep was caused by the decrease in the surface mechanical properties related to the damage through cyclic loading of the sliding, such as the scratching of PA66 or peeled off of fibers. The creep height loss values for the type B sample were much greater than those of the type A sample at both cycle numbers, whereas the wear height loss values were relatively similar for both samples.

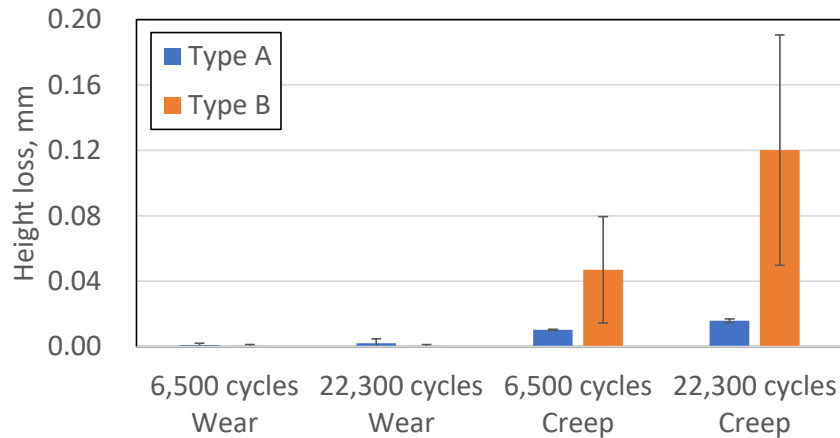


Fig. VI. 2 Wear and creep height losses at different cycle numbers in composites that differed only in the GF surface treatment agents used.

Fig. VI. 3 shows SEM images of the center position of both composite surfaces after 6,500 cycles and 22,300 cycles. At both measurement points, greater amounts of interfacial GF peeling, peeled GFs, and holes originating from GFs, which were also observed in Chapter III, were observed for the type B composite than for the type A composite. Additionally, particularly after 22,300 cycles, no severe GF breakage was observed on the type B composite; the GFs remained intact with long fiber length, but gaps between the GFs and PA66 were present due to poor adhesion of the fibers to the PA66. In contrast, the GFs used in the type A composite were shortened and damaged; however, good adhesion between the GFs and PA66 was maintained. These observations indicate that the interfacial adhesion of the GFs treated with type A to PA66 was stronger than that of those treated with type B, and that peeling of the type B GFs from the PA66 by the shear force during sliding occurred more readily than breakage of the GFs themselves due to the weak GF/PA66 adhesion. Therefore, the mechanical properties of the type B composite surface were easily degraded, leading to scratching of the PA66. Additionally, based on the wear and creep mechanisms of the composite in this tribosystem, which were elucidated in Chapter III, we concluded that propagation of the scratches and creep-related height loss occurred earlier due to the low toughness of the type B composite.

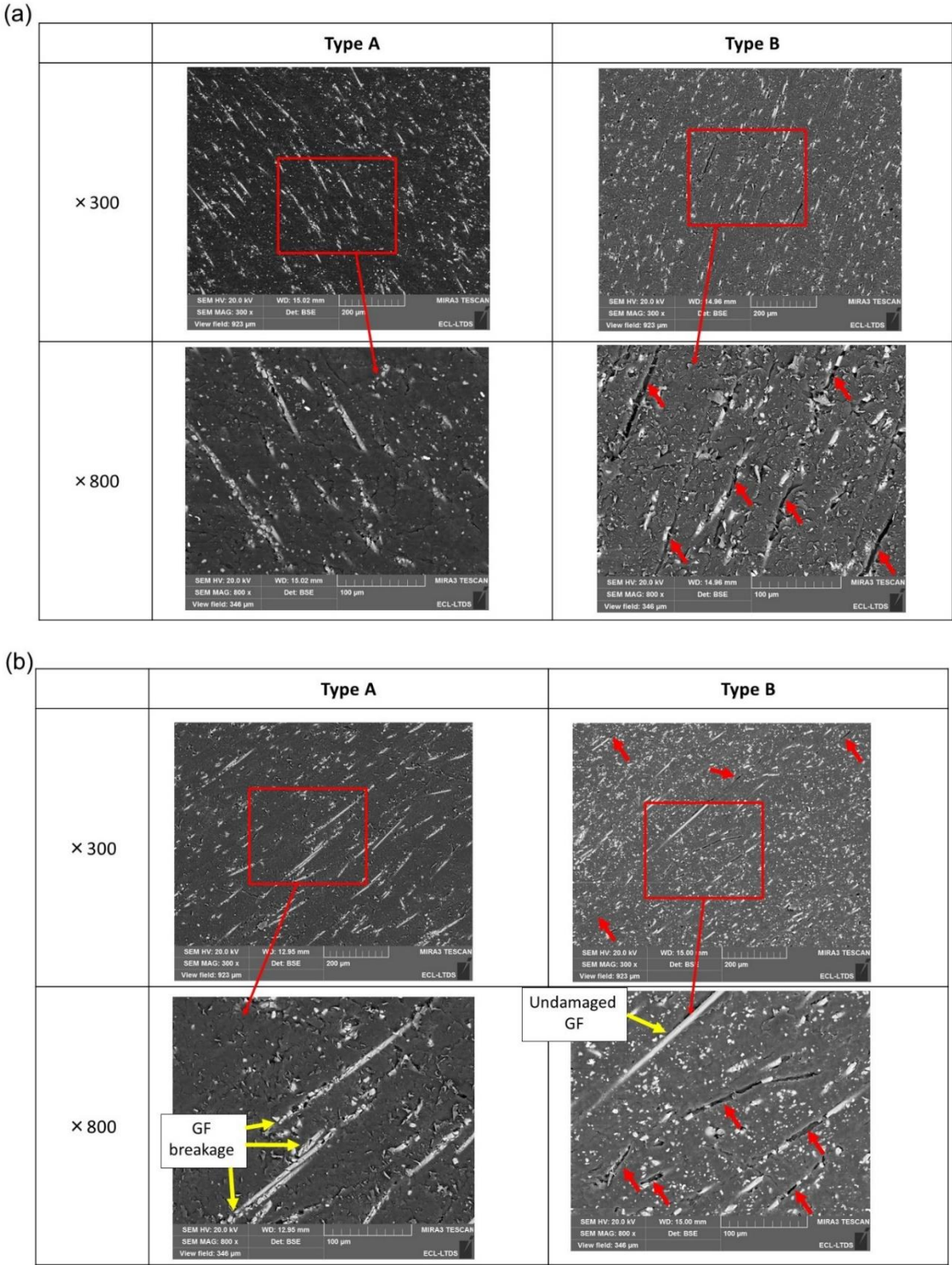


Fig. VI. 3 SEM images of the sliding surfaces of the composites fabricated using different surface treatment agents (a) after 6,500 cycles and (b) after 22,300 cycles. Red arrows indicate holes originating from the detachment of GFs from the composite.

The effect of the adhesion between the PA66 and GFs on the wear of the steel counterparts was also investigated. Fig. VI. 4 presents the wear volumes of the steel counterparts (total wear of the four steel cylinders, measured through interferometry) after the sliding tests with composites fabricated using different GF surface treatment agents, and Fig. VI. 5 presents the interferometry images themselves and central 2D profiles perpendicular

to sliding direction. At both 6,500 cycles and 22,300 cycles, the wear volume of the steel counterparts used with the type B composite was larger, while the wear morphology of the steel was the same for both composites. These results indicate that the adhesion between the PA66 and GFs influences the aggressive effects of the GFs on the steel counterparts. In Chapter III, the wear volume of the steel counterparts increases when the GFs are oriented perpendicularly to the sliding surface compared to when they are oriented in the parallel direction. This is because the edges of the GF, which have a strong aggressive effect on the steel counterparts, are exposed more easily in this orientation. In addition, the wear mode of the steel counterparts is two-body abrasion rather than three-body abrasion, and the aggressive effects of GFs that remain adhered to the sliding surface are greater than those of GFs that have completely detached from the composite surface and are present as a contaminant in the grease. Therefore, the type B composite, with its lower interfacial shear strength between PA66 and the GFs, exhibited earlier interfacial peeling and gap formation between the PA66 and the GFs, and exposure of the GF edges occurred in earlier cycles, leading to the high wear volume of the steel counterparts.

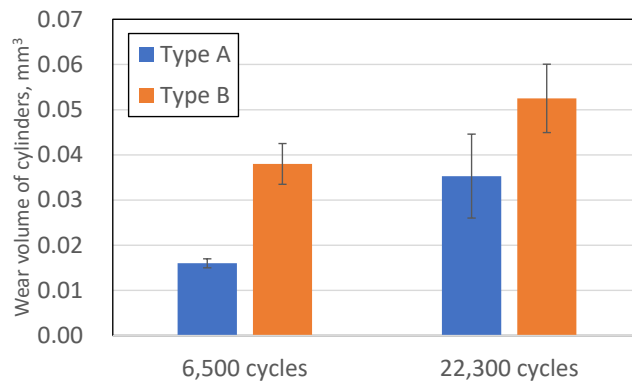


Fig. VI. 4 Wear volume of the steel counterparts at different cycle numbers using composites that differed only in the GF surface treatment agent used.

Type of agent	Cycle numbers	Observations of wear scar	Central 2D profiles
Type A	6,500 cycles		
	22,300 cycles		
Type B	6,500 cycles		
	22,300 cycles		

Fig. VI. 5 Observations of the steel counterparts and central 2D profiles using interferometry (perpendicular to sliding direction).

2.3 Effect of the GF orientation on the sliding surface with different GF surface treatment agents

In order to discuss their aggressive effect on the steel counterparts, the orientation of the GFs on the composite surface was estimated using the surface image analysis method presented in Section 3.1 in Chapter II. Fig. VI. 6 shows the total areas and perimeters of the GFs in the composites fabricated using the two GF surface treatment agents. The total area of the GFs treated with the type A surface agent was slightly larger than that of the GFs treated with type B, while no clear trend in the total perimeter of the GFs was observed. These results do not explain the different wear on the steel counterparts, because the wear in the tests using the type A composite, which had a larger total GF area on the sliding surface, was smaller than that in the tests using the type B composite.

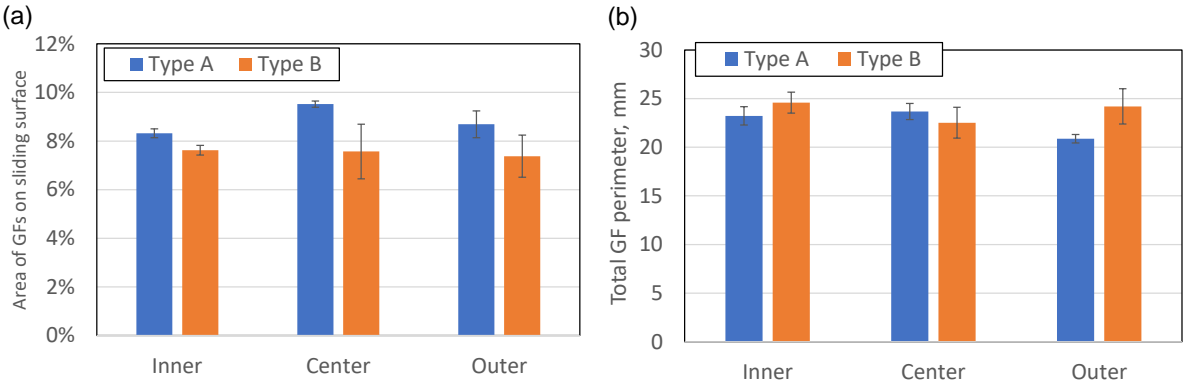


Fig. VI. 6 (a) Calculated total area and (b) total perimeter of the GFs on composites that differed only in the surface treatment agent used. Three measurements were conducted at each position.

Fig. VI. 7 shows the relationship between the circularity of the GFs and the cumulative frequency of the GF area, as well as the average value of C_{50} at different positions (C_{50} is the circularity value at which the cumulative GF area frequency is 50%). The results indicate that the circularity at the center position was much lower than that at the inner/outer positions for both composites, indicating that the majority of the GFs at the center position were aligned parallel to the sliding direction. However, the relative orientations of the GFs at the inner, center, and outer positions was the same regardless of the type of surface agent used.

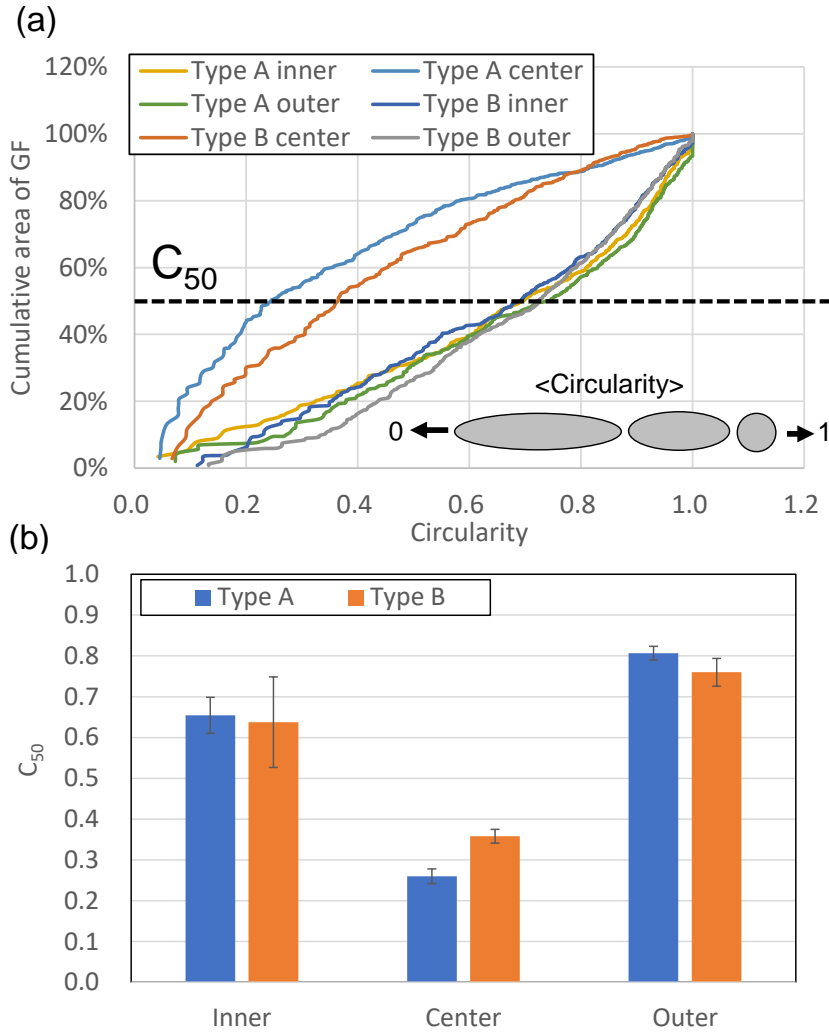


Fig. VI. 7 (a) Relationship between the circularity of the GFs and the cumulative frequency of the GF area. (b) Value of C_{50} at the different positions of composite rings that differed only in the GF surface treatment agent used. Three measurements were conducted at each position.

2.4 Estimation of the interfacial shear strength based on Kelly-Tyson model

In order to discuss the interfacial shear strength between the PA66 and GFs in the two composites quantitatively, a version of the Kelly–Tyson model was introduced [184] that was modified to consider the orientation of the reinforcement fibers [168, 185]. This model is frequently used to understand the mechanism of adhesion between resins and fibers, and takes into consideration the strength of the composite, fiber orientation, and fiber length distribution of the tensile specimens. The modified Kelly–Tyson model is presented below:

$$\sigma_t = f_0 \left\{ \sum_{l_i < l_c} \left(\frac{\sigma_f V_i l_i}{2l_c} \right) + \sum_{l_j > l_c} \left[\sigma_f V_j \left(1 - \frac{l_c}{2l_j} \right) \right] \right\} + \sigma_m (1 - V_f) \quad (\text{VI. 1})$$

where σ_t is the tensile strength of the composite, f_0 is the fiber orientation efficiency factor, σ_f is the strength of the fibers (3.2 GPa for E glass), σ_m is the tensile strength of the matrix resin (82 MPa for unreinforced PA66), l_c is the critical fiber length, l_i is a fiber length below the critical fiber length, l_j is a fiber length above the critical fiber length, V_i and V_j are the fiber

volume fractions of l_i and l_j , respectively (each l_i , l_j , V_i , and V_j can be estimated by the actual measurement of the fiber length distribution and calculation of the critical fiber length which can explain the tensile strength of the composite), and V_f is the volume fraction of the fibers (here 7.3%). The fiber orientation can be measured through SEM image analysis, and the fiber orientation efficiency factor f_0 can be determined using the following equation:

$$f_0 = \sum_n a_n \cos^4 \theta_n \quad (\text{VI. 2})$$

where a_n is the proportion of fibers that form an angle θ_n with respect to the flow direction of injection molding as presented in Fig. VI. 8. The critical fiber length l_c is defined as the minimum fiber length necessary for the fiber stress to reach the maximum strength of the fiber σ_f at the fiber ends [168].

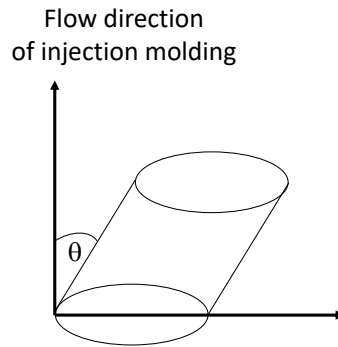


Fig. VI. 8 Fiber orientation angle θ_n .

The interfacial shear strength τ can be calculated using the following equation:

$$l_c = \frac{\sigma_f d}{2\tau} \quad (\text{VI. 3})$$

where d is the fiber diameter (6.5 μm). Therefore, the interfacial shear strength τ can be estimated using the values of the fiber orientation efficiency factor f_0 and critical fiber length l_c using equations (VI. 1), (VI. 2), and (VI. 3).

The fiber length distribution of the GFs in the tensile test specimens was measured through the following process. First, 30 mg of the molding of the composite was cut from the center position of the specimens (Fig. VI. 9). This fragment was then combusted using a thermogravimeter-differential thermal analyzer (TG-DTA) at 650°C for 2 h, and the residual GFs were retrieved. Finally, the length distribution of the GFs (total number: 425–912) with a length of 0.07 mm or greater was measured automatically using an optical microscope and image analysis software. Fig. VI. 10 presents the relationship between the length and cumulative frequency of the length of the GFs from the composites prepared using the two surface treatment agents. No significant differences in their fiber length distributions were observed, and the number average fiber lengths of the type A and type B composites were 0.199 mm (± 0.005 mm) and 0.210 mm (± 0.001 mm), respectively. The similar fiber length distributions were attributed to the fact that these two GF-based composites were fabricated using PA66 with the same molecular mass, the same amount of GFs, and the same GF diameter through the same extrusion and injection molding process. These results indicated that the surface treatment agent did not affect the fiber length distribution.

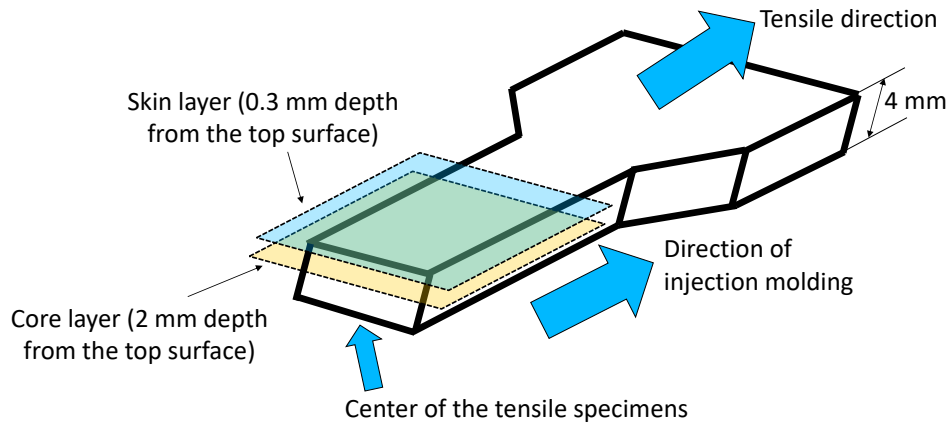


Fig. VI. 9 Image of the tensile test specimens.

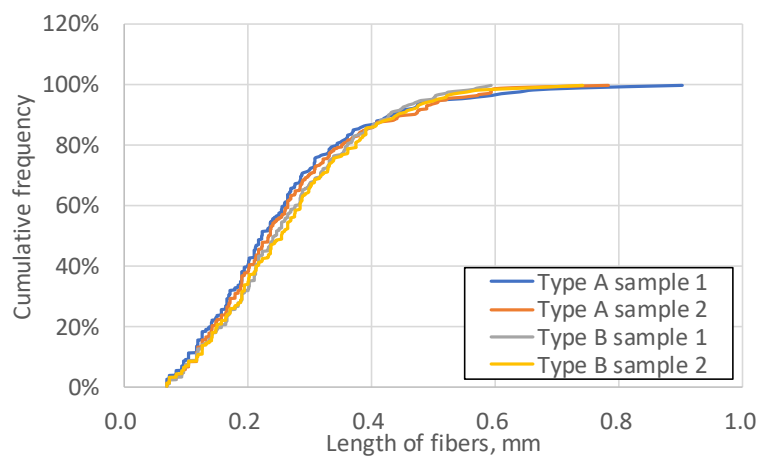


Fig. VI. 10 Relationship between the GF length and the cumulative frequency of GFs for composites that differed only in the surface treatment agent used.

The fiber orientation efficiency factor f_0 was then estimated using the following process. First, the test specimen was embedded in epoxy resin and cured. Then, specimens with 4 mm thickness of the skin layer (0.3 mm depth from the top surface of the specimen) and core layer (2 mm depth from the top surface of the specimen) surfaces were obtained by polishing, as presented in Fig. VI. 9. Subsequently, each surface was observed using SEM in BSE mode to obtain images of the GF orientation, which are presented in Fig. VI. 11. The average orientation angle θ relative to the base axis (direction of the tensile test) was estimated by image analysis of the binarized images using the software package image J. Image analysis was conducted using six SEM images with different fields of view; as in the fiber length measurement, only fibers with a length of over 0.07 mm were analyzed. The transverse direction is the direction of the injection molding and of the tensile test. Fig. VI. 12 shows the relationship between the orientation angle θ and the cumulative frequency of the GF orientation. As in the fiber length distribution, no significant difference in GF orientation was observed between the samples prepared using the different surface treatment agents on either the core or skin surface. The average orientation angles θ for the type A composite were 17.6° (core surface) and 14.3° (skin surface), while those of the type B composite were 13.6° (core surface) and 16.5° (skin surface).

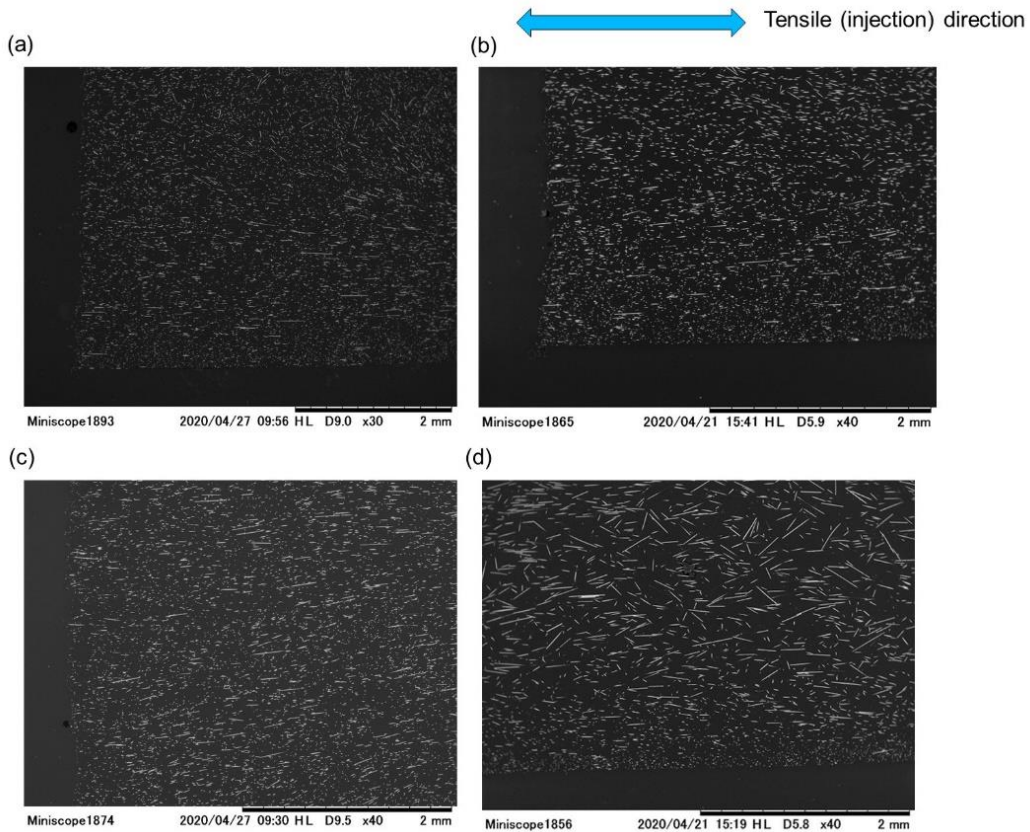


Fig. VI. 11 SEM BSE observations of the tensile specimens: (a) type A composite core layer; (b) type A composite skin layer; (c) type B composite core layer; (d) type B composite skin layer.

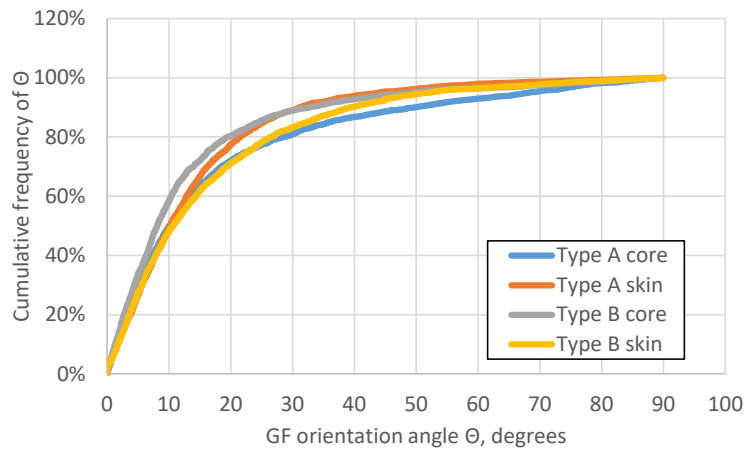


Fig. VI. 12 Relationship between the GF orientation angle and the cumulative frequency of the GF orientation on the surfaces of composites that differed only in the GF surface treatment agent used.

Table VI. 3 lists the estimated fiber angle relative to the injection (tensile) direction (θ_n , average values for the core layer and skin layer), the fiber orientation efficiency factor f_0 estimated from equation (VI. 2), and the critical fiber length l_c estimated from equation (VI. 1) for the composites prepared using the two surface treatment agents. The critical fiber length l_c for the type A composite was lower than that of the type B composite, which indicates that

when the type A agent is used, many more fibers contribute to building up the axial fiber stress to the maximum strength of the fiber σ_f at the fiber ends than when the type B agent is used.

Based on the obtained values, the interfacial shear strength τ was estimated using equation (VI. 3); these values are also listed in Table VI. 3. The τ values of the type A and type B composites were 33.6 ± 0.8 MPa and 25.7 ± 0.5 MPa, respectively, i.e., the interfacial shear of the type A composite was 7.9 MPa (30.6%) higher than that of the type B composite. These values are similar to those previously reported for PA/GF composites (39–40 MPa [85], 24.0 MPa [86], and 33.5–48.4 MPa [168]). Therefore, the interfacial shear strengths of the tensile test specimens exhibited the expected tendency based on the results of the sliding test and the SEM images of the sliding surfaces.

Table VI. 3 Estimated values of θ_n , f_0 , l_c , and τ for composites that differed only in the GF surface treatment agent used.

	θ_n	f_0	l_c	τ
Type A	16.0° (0.278 rad)	0.855	0.305 mm	33.6 ± 0.8 MPa
Type B	15.0° (0.262 rad)	0.870	0.410 mm	25.7 ± 0.5 MPa

In summary, each interfacial shear strength between the PA66 matrix and the GFs with different types of GF surface treatment agent was estimated quantitatively based on the modified Kelly-Tyson model. High interfacial shear strength led to good wear resistance of both GF composite and steel counterpart by the prevention of the peeling of GFs and exposure of GF edges.

3. Effects of the PA66 molecular mass on the mechanical and tribological properties

3.1 Effect of the PA66 molecular mass on the wear and creep resistance of GF composite

The effects of the molecular mass of PA66 on the mechanical and tribological properties of the GF-reinforced PA66 composites were evaluated using composite samples that were prepared using PA66 matrix with four different molecular mass values (samples no. 1, 2, 3, and 4, see Table VI. 1). These samples contained the same type and content of GFs (surface treatment agent: type A, GF diameter: 6.5 μ m, GF amount: 15 wt%). Fig. VI. 13 shows the wear and creep height losses of these composites after various numbers of sliding test cycles. The results indicated that the wear or creep at a given cycle number decreased with increasing molecular mass of the PA66 composite.

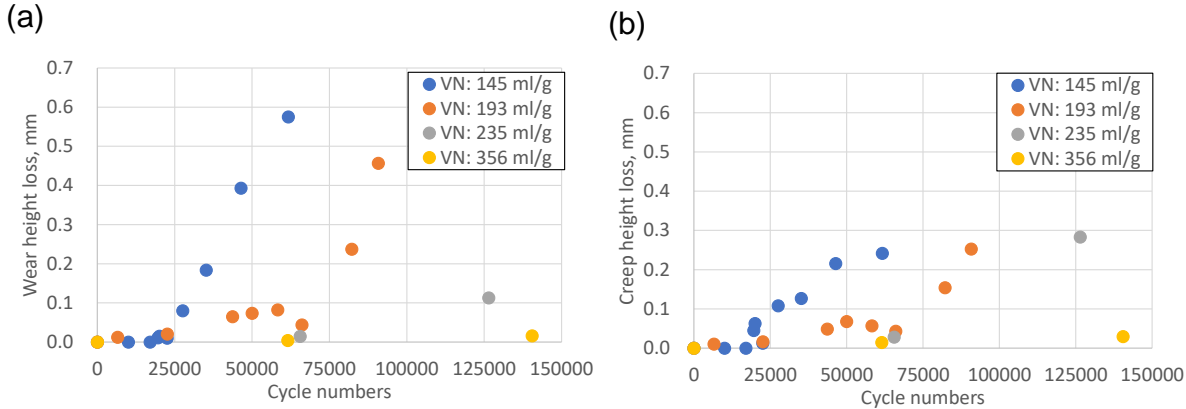


Fig. VI. 13 (a) Wear height loss and (b) creep height loss as a function of the cycle numbers in sliding tests of GF-reinforced composites that differed only in their PA66 molecular mass (VN).

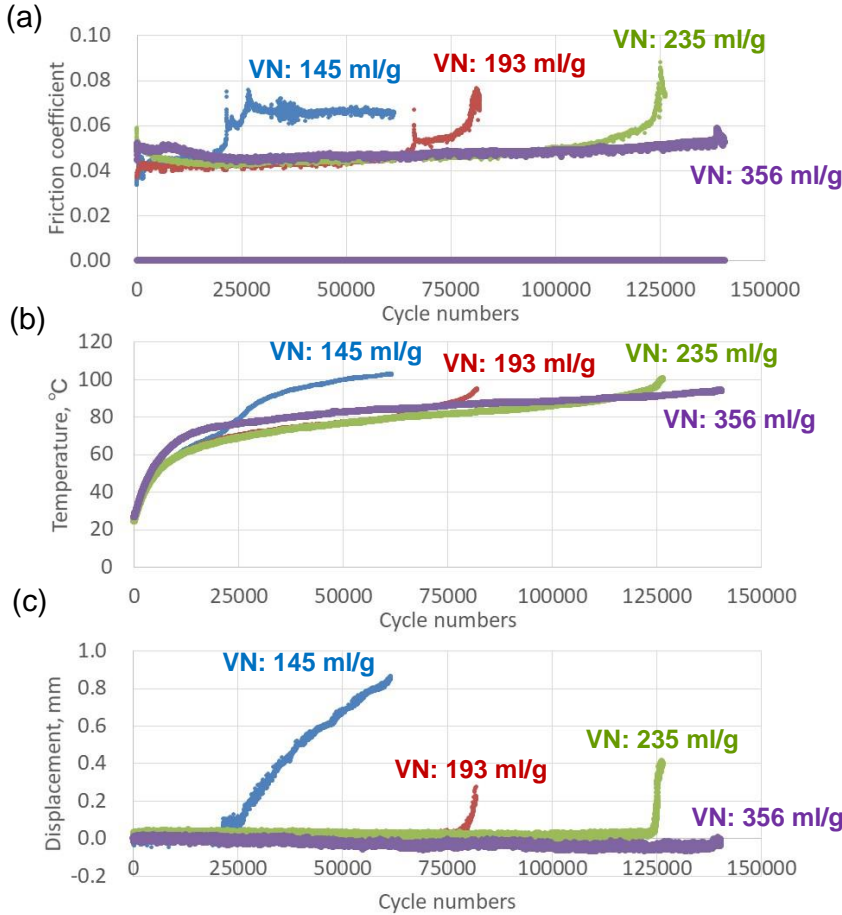


Fig. VI. 14 Evolutions of (a) the friction coefficient, (b) the temperature, (c) and the vertical displacement with cycle number in the sliding tests of composites that differed only in their PA66 molecular mass (VN).

Fig. VI. 14 presents the evolutions of the friction coefficient, temperature, and vertical displacement with the cycle number. The sudden increases in the friction coefficient, temperature, and vertical displacement were observed at later cycle numbers for the composites with greater PA66 molecular mass values; for example, a sudden increase in the

vertical displacement occurred at 22,000 cycles for the composite with a VN of 145 ml/g, 80,000 cycles for the 193 ml/g composite, and 125,000 cycles for the 235 ml/g composite, whereas no increase in the vertical displacement was observed until 140,000 cycles for the composite with a VN of 356 ml/g.

Fig. VI. 15 shows optical microscope and SEM images of the sliding surfaces of the 145 ml/g and 193 ml/g composites after 22,500 cycles. Peeling was observed at the center region of the 145 ml/g composite. Additionally, scratching of the PA66 and several holes related to detached GFs were observed via SEM, even in regions of the surface where peeling was not observed in the optical microscope images. In contrast, no severe peeling or damage was observed on any part of the sliding surface of the 193 ml/g composite.

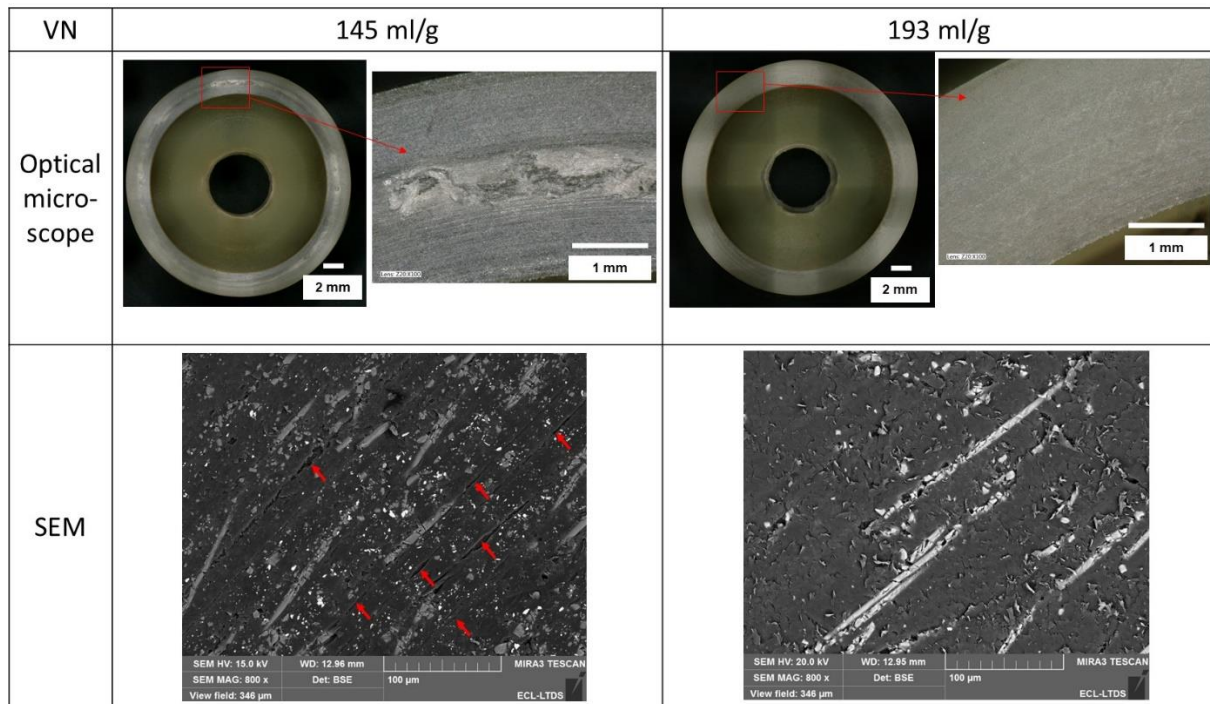
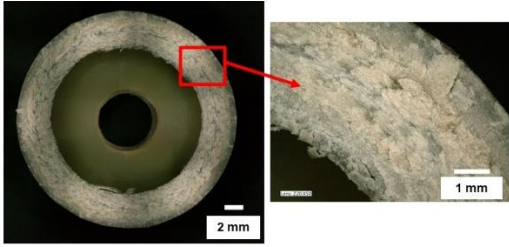
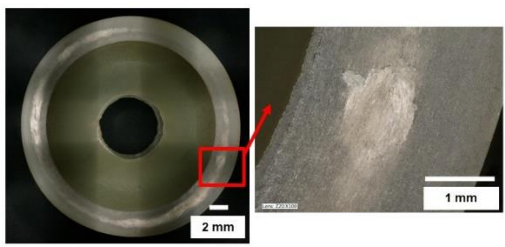
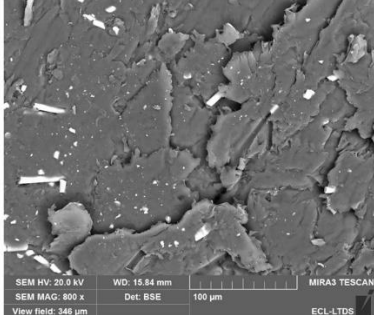
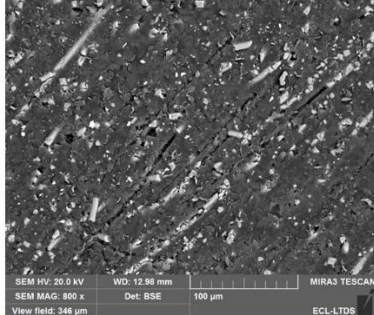


Fig. VI. 15 Optical microscope and SEM observations of the sliding surface of the composite ring before and after the sliding tests after 22,500 cycles.

To study the wear phenomena of the composite samples with high VN values (>145 ml/g), longer tests were conducted. Fig. VI. 16 presents the optical microscope and SEM images of the sliding surfaces of the 145 ml/g composite after 61,500 cycles and those of the 193 ml/g and 235 ml/g composites after 65,500 cycles, along with the wear and creep height loss after each test. In contrast to the limited wear observed after 22,500 cycles, the entire sliding surface of the 145 ml/g sample was worn after 61,500 cycles, and severe peeling of the PA66 resin was observed via SEM. The wear height loss was greater than the creep height loss. In the case of the 193 ml/g sample, peeling of the center region and hole formation on the composite surface were observed after 65,500 cycles. In contrast, no severe peeling was observed on any part of the sliding surface of the 235 ml/g composite after 65,500 cycles, although weak sliding marks were present. The wear height losses of the 193 ml/g and 235 ml/g samples were significantly lower than that of the 145 ml/g sample. The creep height losses of these high molecular mass samples were greater than their wear height losses; however, their creep values were much lower than that of the 145 ml/g sample. Consequently,

increasing the molecular mass of PA66 was concluded to decrease the damage to the sliding surface, leading to improved wear and creep resistance in the composites.

VN	145 ml/g (61,500 cycles)	193 ml/g (65,500 cycles)
Optical microscope		
SEM	 SEM HV: 20.0 kV SEM MAG: 800 x View field: 348 µm WD: 15.84 mm Det: BSE 100 µm MIRA3 TESCAN ECL-LTDS	 SEM HV: 20.0 kV SEM MAG: 800 x View field: 348 µm WD: 12.88 mm Det: BSE 100 µm MIRA3 TESCAN ECL-LTDS
Wear height	0.575 mm	0.001 mm
Creep height	0.242 mm	0.043 mm

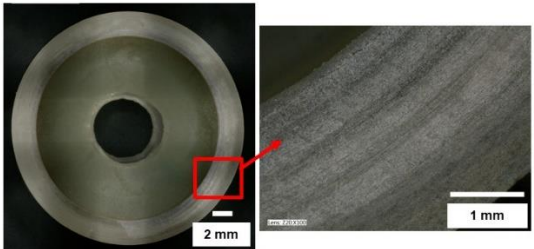
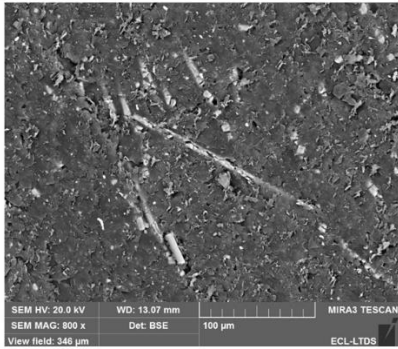
VN	235 ml/g (65,500 cycles)
Optical microscope	
SEM	 SEM HV: 20.0 kV SEM MAG: 800 x View field: 348 µm WD: 13.07 mm Det: BSE 100 µm MIRA3 TESCAN ECL-LTDS
Wear height	0.015 mm
Creep height	0.028 mm

Fig. VI. 16 Optical microscope and SEM images of the sliding surfaces of composites that differed only in their PA66 molecular mass (VN) after 61,500–65,500 cycles.

3.2 Effect of the PA66 molecular mass on the wear resistance of steel counterpart

The effect of the molecular mass of the PA66 on the wear resistance of the steel counterparts was also investigated. Fig. VI. 17 shows the wear volume of the steel counterparts (total wear volume of the four steel cylinders, measured using interferometry) after different numbers of cycles with the composite samples with different molecular masses of PA66. The wear volume of the steel counterparts increased proportionally with increasing cycle numbers. Similarly to the wear resistance of the composite, the wear of the steel counterparts also decreased with increasing PA66 molecular mass for any given cycle number. This indicates that not only the wear and creep resistance of the composite, but also the wear resistance of the steel counterparts, are improved by increasing the molecular mass of the PA66 in the composite. In Chapter III, the wear mode of the steel counterparts was reported to be two-body abrasion caused by the GFs on the surface of the composite. Therefore, the mechanism by which the use of higher molecular mass PA66 in the composite decreases its aggressive effect on the steel counterpart via this wear mode is discussed later in this section in terms of the GF orientation on the sliding surface and mechanical properties of the composite.

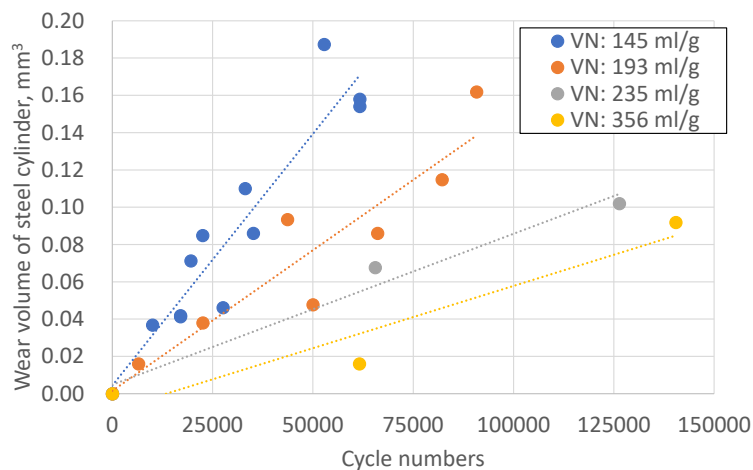


Fig. VI. 17 Wear volume of the steel cylinders after different cycle numbers of the sliding test using composites that differed only in their PA66 molecular mass (VN).

3.3 Effect of the PA66 molecular mass on the fiber orientation on the sliding surface of GF composite ring specimen

The effect of the molecular mass on the tribological properties was discussed from the viewpoint of the fiber orientation on the sliding surface. Fig. VI. 18 shows the results of image analysis (calculated total GF areas, total GF perimeters, relationship between the GF circularity and cumulative area, and average value of C_{50}) at different positions of the composite rings with different values of PA66 molecular mass. No significant differences among the GF areas or total perimeters were observed at the different positions, nor was a significant difference in the circularity (GF orientation) observed between composites with different molecular masses for a given position on the composite ring. These results demonstrate that the effect of the PA66 molecular mass on the wear or creep resistance of the composite and the wear resistance of the steel counterpart cannot be explained in terms of the orientation of the GFs relative to the sliding surface.

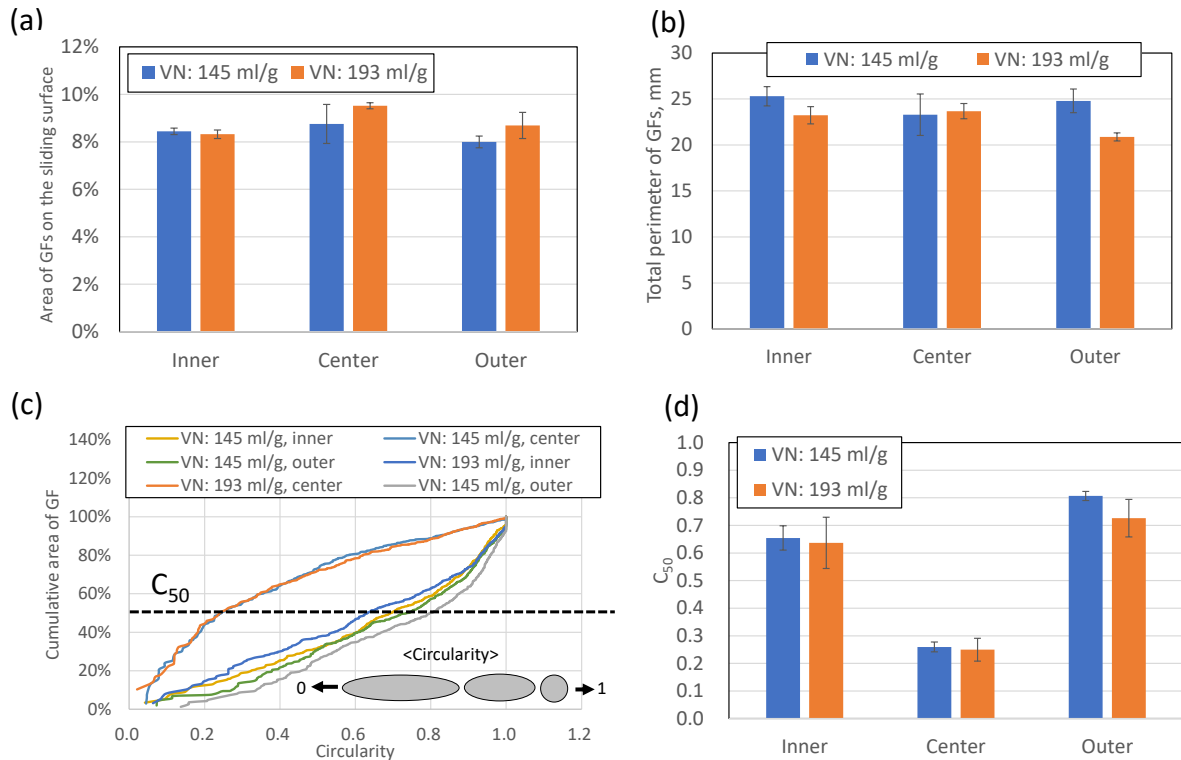


Fig. VI. 18 (a) Total GF area; (b) total GF perimeter; (c) relationship between the circularity of the GFs and the cumulative frequency of GF area; (d) value of C_{50} at different positions of composite rings that differed only in their PA66 molecular mass (VN). Three measurements were conducted at each position.

3.4 Mechanism of the improvement in the tribological properties of GF composite with the increase in the PA66 molecular mass

To discuss the reason why the increase in the molecular mass of the PA66 can reduce the wear of the steel counterpart, the effect of the mechanical properties of the PA66 or GF composite was investigated. Fig. VI. 19 shows the Young's modulus and the hardness at the surfaces of the composite rings fabricated using PA66 with two different molecular mass values, which were measured using micro-indentation. Test conditions are presented in Table II. 19. No differences between the Young's moduli or hardness values of the samples were observed, which indicated that the PA66 molecular mass did not affect the elasticity or plasticity of the composite.

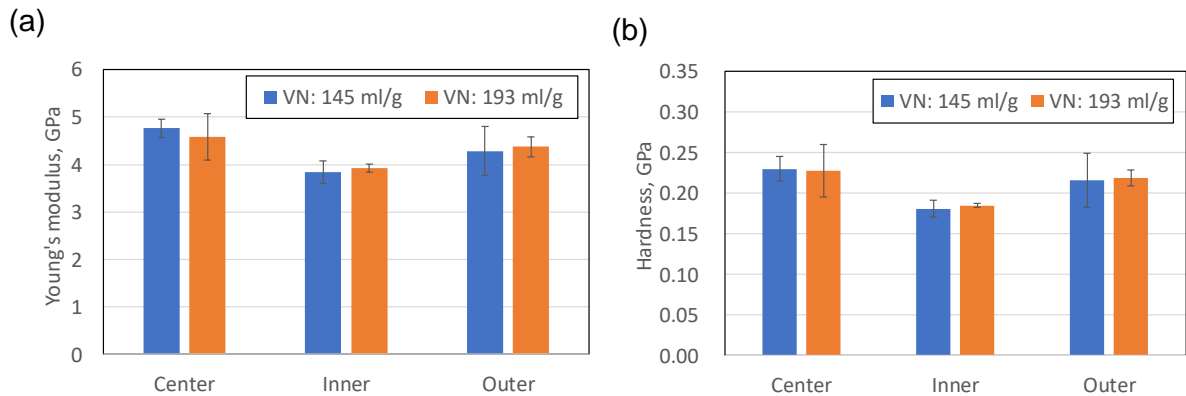


Fig. VI. 19 (a) Young's modulus and (b) hardness of the sliding surfaces of composite rings that differed only in their PA66 molecular mass (VN). Three measurements were conducted at each position.

Based on these results, we then focused on the toughness of the PA66 as a possible origin of the effect of its molecular mass on the wear resistance of the steel counterpart and composite. Evaluation of the toughness of the composite using the composite rings (sliding test specimens) was difficult. Therefore, the toughness of the composites was evaluated using tensile test samples from the tensile elongation at break or tensile breakage energy. Fig. VI. 20 presents the stress–strain curves obtained in the tensile tests using unreinforced PA66 samples with different molecular mass values (raw PA66 of composite sample with VN: 150 ml/g and VN: 302 ml/g).

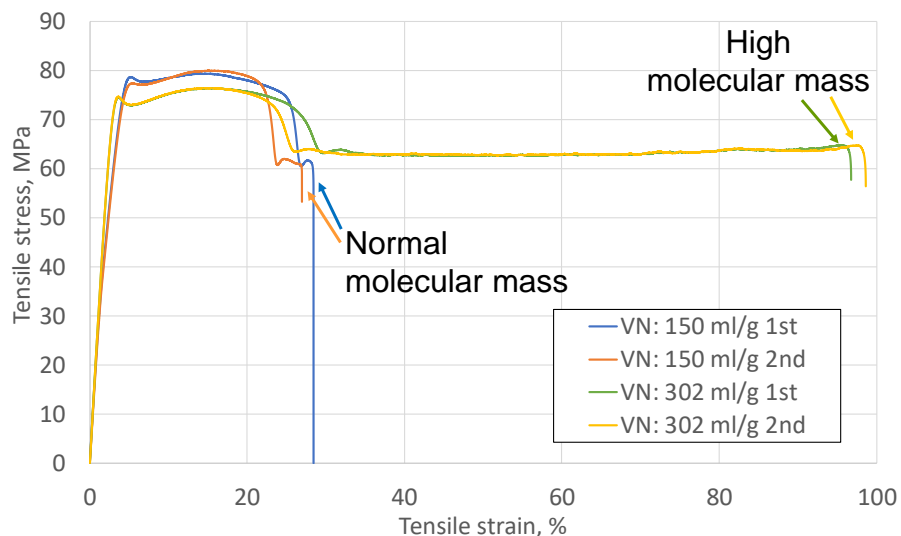


Fig. VI. 20 Stress–strain curves from the tensile tests of unreinforced PA66 samples with different molecular mass values.

Although their Young's moduli in the initial stage of the test and their yield strength values were very similar, the elongation at break of the high molecular mass PA66 sample was 3.5 times higher than that of the normal molecular mass sample. This result indicates that increasing the molecular mass of PA66 does not improve its strength and stiffness, but does greatly improve its toughness. Additionally, the effect of the molecular mass of PA66 on the tensile mechanical properties of the GF-reinforced PA66 composites were investigated. Fig. VI. 21 shows the stress–strain curves obtained in tensile tests using GF-reinforced PA66

composite samples with different PA66 molecular masses (samples no. 1, 2, 3, and 4). Fig. VI. 22 shows the relationship between the PA66 molecular mass of the GF-reinforced PA66 samples and their tensile mechanical properties. Similarly to the case of the unreinforced PA66, the molecular mass of PA66 had only a weak influence on the tensile strength and Young's modulus (confirming the micro-indentation results); however, the toughness (tensile elongation at break and tensile breakage energy) increased with the molecular mass.

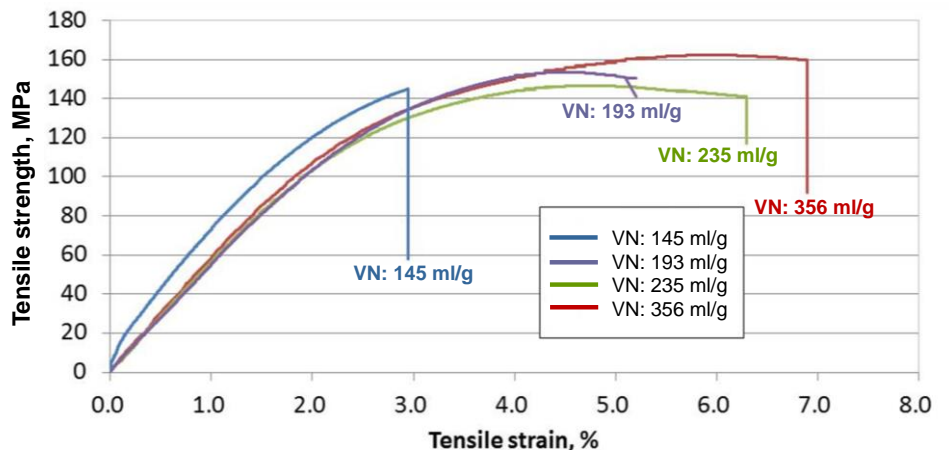


Fig. VI. 21 Stress–strain curves from the tensile tests of GF-reinforced composites that differed only in their PA66 molecular mass (VN).

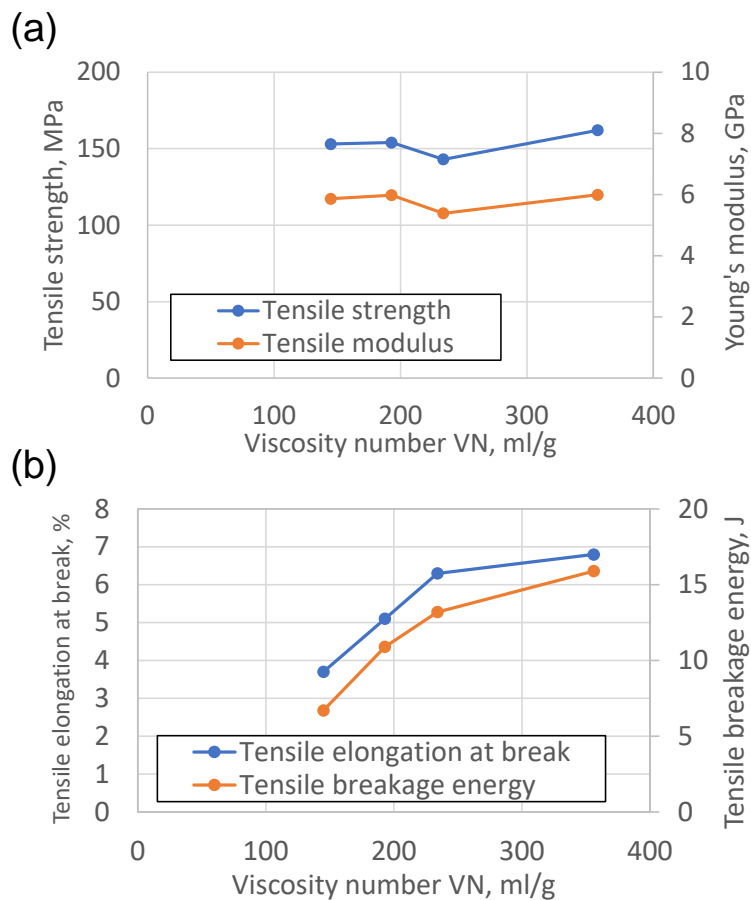


Fig. VI. 22 Relationship between the VN of the composite and the (a) tensile strength and Young's modulus and the (b) tensile elongation at break and tensile breakage energy.

Given these results, a mechanism to explain the effect of the molecular mass of PA66 on the wear of the steel counterpart and the composite is proposed. The interfacial shear strength between PA66 and GF should be the same in the composites with different PA66 molecular masses (i.e., samples no. 1, 3, 4, and 4) because the same GF surface treatment agent was used in their preparation, and the differences among their tensile strengths were small. In contrast, the elongation of the PA66 resin due to its shear strength increases with its molecular mass, and thus, the resin can more easily follow the deformation of the fibers due to the local shear induced by sliding. Consequently, fewer interfacial gaps between PA66 and the GFs are generated during sliding. This reduces the exposure of GF edges, which have a highly aggressive effect on the steel counterpart, which in turn reduces the two-body abrasive wear of the steel counterpart. Additionally, the propagation of the scratching of PA66, which originates from gaps between PA66 and GF, is reduced due to the high toughness of the high molecular mass polymer. Fig. VI. 23 illustrates the different wear modes during sliding contact for composites with different values of PA66 molecular mass. As shown, the damage to the sliding surface is decreased, as presented in Fig. VI. 15 and Fig. VI. 16, and the wear and creep of the composite are reduced.

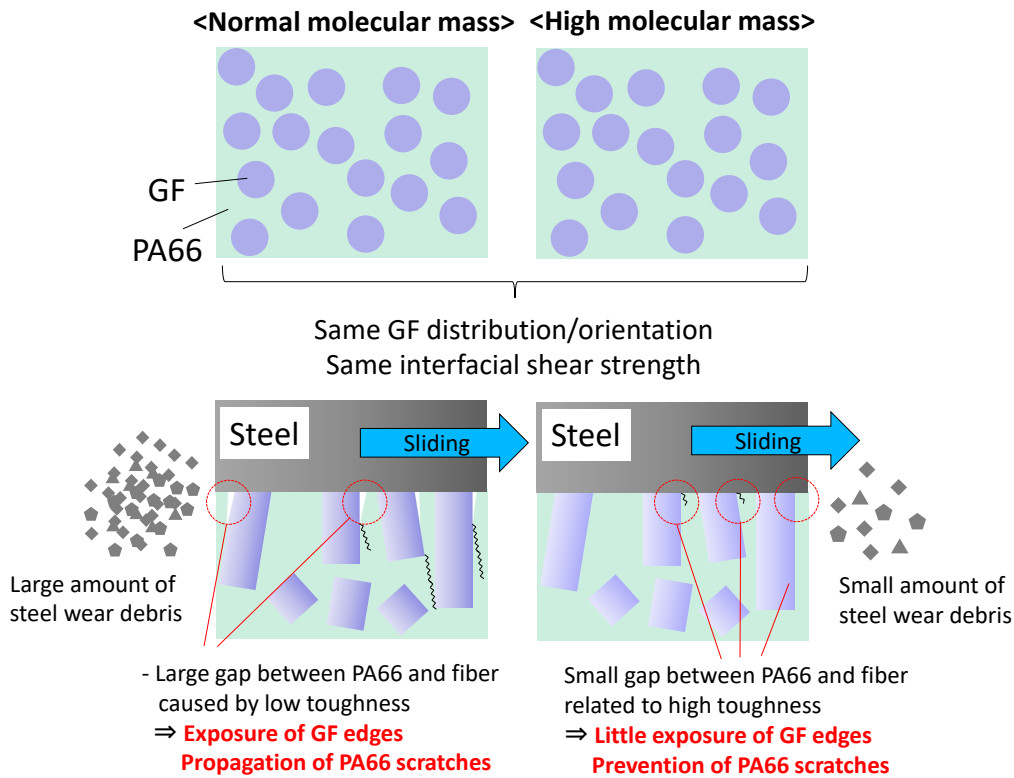


Fig. VI. 23 Schematic of the different wear modes of composites with different values of PA66 molecular mass.

In terms of practical application, these results suggest that a composite worm gear in contact with a steel worm shaft could be fabricated using a GF-reinforced PA66 composite with a high PA66 molecular mass. This would obviate the need for expensive heat treatment of the steel to increase its hardness and wear resistance, as the higher molecular mass composite would reduce the wear of both the soft steel and the composite. The use of soft steel would also permit easy machining of the teeth via mechanical cutting.

4. Effects of GF diameter on the mechanical and tribological properties

4.1 Effect of GF diameter on the tensile mechanical properties

In order to investigate the effects of the GF diameter, composite samples containing GFs of different diameters were prepared (samples no. 2, 6-10). In these samples, the molecular mass of the raw PA66, the GF surface treatment agent (type A), and the GF content (15 wt%) were the same. First, the effect of the GF diameter on the tensile mechanical properties was investigated. Fig. VI. 24 shows the tensile mechanical properties of these composites. The tensile strength increased with decreasing GF diameter; the tensile strength of the composite containing 6.5 μm diameter GFs was 38.1 MPa (32.9%) higher than that of the composite with 19 μm GFs. The tensile elongation at break and tensile breakage energy also increased with decreasing GF diameter. The tensile elongation at break and tensile breakage energy of the composite with 6.5 μm GFs were 1.90 and 2.72 times higher than those of the composite with 19 μm GFs, respectively. In contrast, the Young's moduli of the composites were not affected by the GF diameter. Thus, the GF diameter affected only the mechanical properties related to irreversible deformation (plasticity and breakage) of the composite. The increased interfacial area between the GFs and PA66 in the smaller diameter GFs allows them to bear higher stresses without breaking; these results are in agreement with those presented in previous studies [85, 86, 107], as explained in Chapter I.

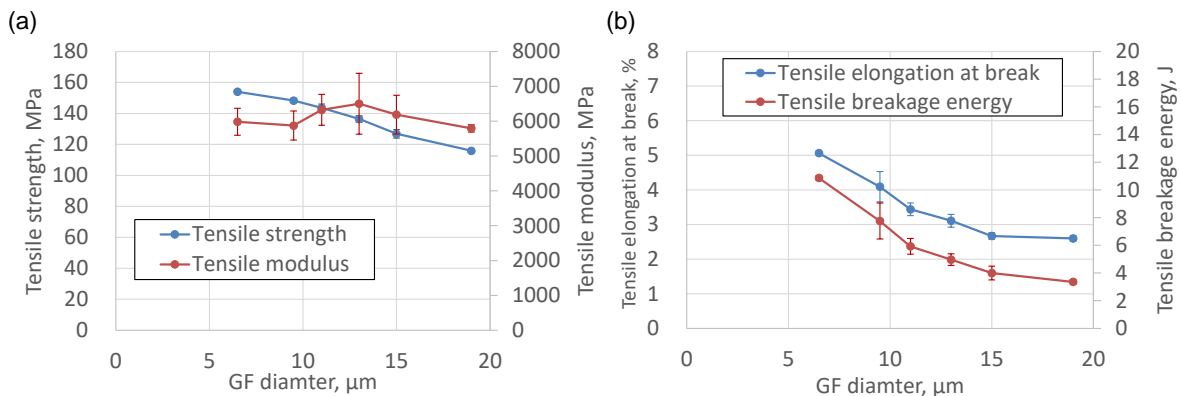


Fig. VI. 24 Tensile mechanical properties of GF-reinforced PA66 composites that differed only in GF diameter: (a) tensile strength and Young's modulus; (b) tensile elongation at break and tensile breakage energy. Each value is the average value of five measurements.

4.2 Effect of GF diameter on the wear and creep resistance of the composite

Next, the effects of the GF diameter on the tribological properties were investigated. Fig. VI. 25 shows the evolutions of the friction coefficient, temperature, and vertical displacement of the composite samples with different GF diameters during the sliding tests; the tests were stopped at 50,000 cycles. The friction coefficient increased with increasing GF diameter. The friction coefficient of the composite with 6.5 μm GFs remained low throughout the 50,000 cycles, and no sudden increase in its value was observed. The composites with GF diameters of 9.5, 13, and 19 μm did exhibit sudden friction coefficient increases; these sudden increases occurred at earlier cycle numbers with increasing GF diameter. The rate of temperature increase corresponded to the friction coefficient for each GF diameter, and the temperature increased with increasing GF diameter. No sudden increase in the displacement was observed

during the 50,000 cycles for the composite with a GF diameter of 6.5 μm . In contrast, sudden increases in displacement were observed for the 9.5, 13, and 19 μm GF samples at the same cycle numbers as the sudden increases in the friction coefficient.

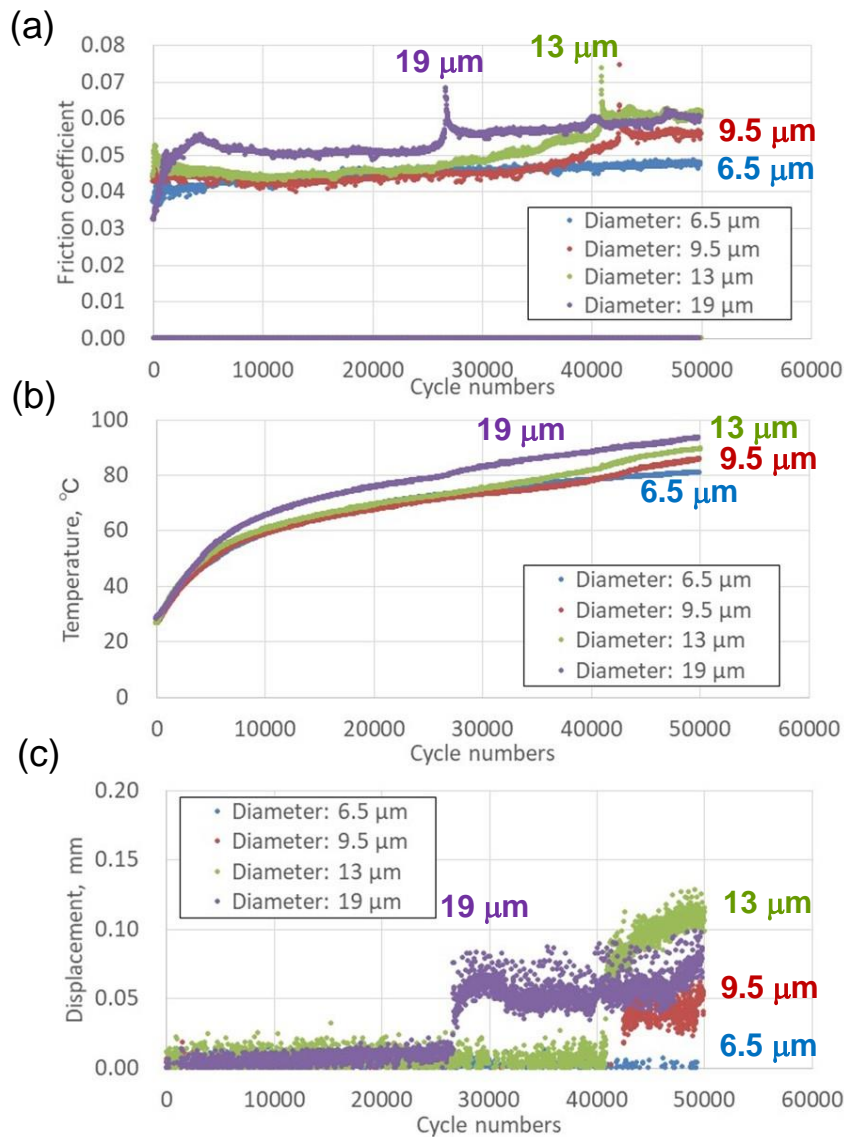


Fig. VI. 25 Evolutions of (a) the friction coefficient, (b) the temperature, and (c) the vertical displacement of composites that differed only in GF diameter during 50,000 cycles test.

Fig. VI. 26 shows optical microscope images of the sliding surfaces after 50,000 cycles. No severe peeling was observed on the sliding surface of the composite with a GF diameter of 6.5 μm . In contrast, evident peeling occurred at the center region of the composite rings with GF diameters of 9.5, 13, and 19 μm . This difference was attributed to the decreased strength and toughness of the samples with larger GF diameters, which could accelerate the damage on the sliding surface. The plastic deformation (sudden increase in the displacement) and peeling on the sliding surface were believed to occur via the mechanism of sliding surface damage reported in Chapter III.

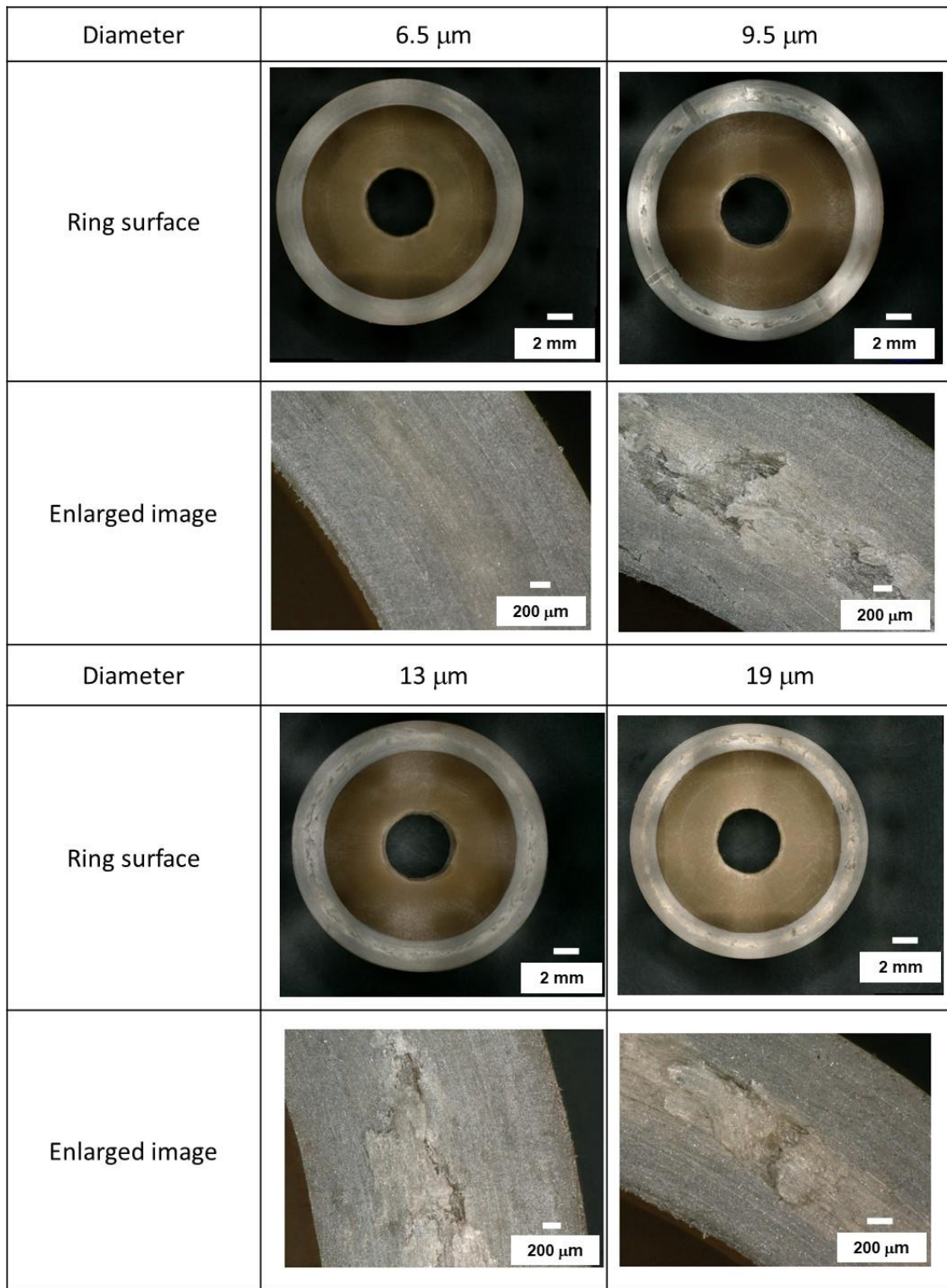


Fig. VI. 26 Optical microscope images of the sliding surfaces of the composites with different GF diameters after 50,000 cycles.

Fig. VI. 27 shows the evolutions of the friction coefficient, temperature, and vertical displacement of the composite samples containing GFs of different diameters during longer sliding tests. Similarly to what happens in the 50,000 cycle tests, the friction coefficient and temperature were generally lower for samples with smaller GF diameters. Additionally, the sudden increases in the friction coefficient and vertical displacement occurred earlier for

samples with larger GF diameters. The same pattern was observed for the increase in the displacement. For the composite with a GF diameter of 6.5 μm , the displacement increased suddenly at 66,000 cycles and then remained nearly constant until 80,000 cycles, after which it increased rapidly. In comparison, the rates of increase in the displacement were smaller for the composites with GF diameters of 9.5 μm or 13 μm . Fig. VI. 28 presents the relationship between the GF diameter and the cycle number at which the first sudden increase in the friction coefficient occurred; these data were fitted using a power approximation. The same tendency was observed as in the 50,000 cycle test; i.e., the cycle number at which the first sudden increase in the friction coefficient occurred increased with decreasing GF diameter. Additionally, for the composite with 19 μm GFs, the rate of the increase in the displacement was much lower than that of the 9.5 μm and 13 μm GF samples. The absolute value of the displacement was also lower, despite the fact that the first sudden increase in the friction coefficient and displacement occurred at a lower cycle number. Hence, the order of the absolute values of the displacements of the samples with different GF diameters varied at different cycle numbers.

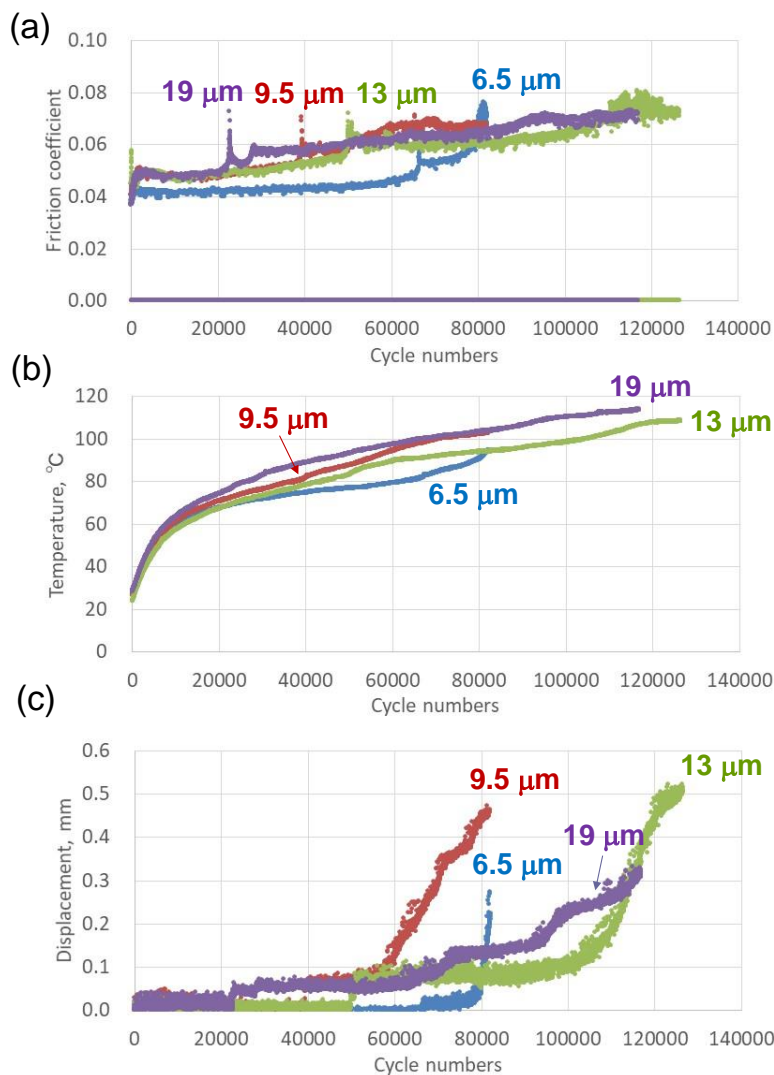


Fig. VI. 27 Evolutions of (a) the friction coefficient, (b) the temperature, (c) and the vertical displacement of composites that differed only in GF diameter in the longer sliding test.

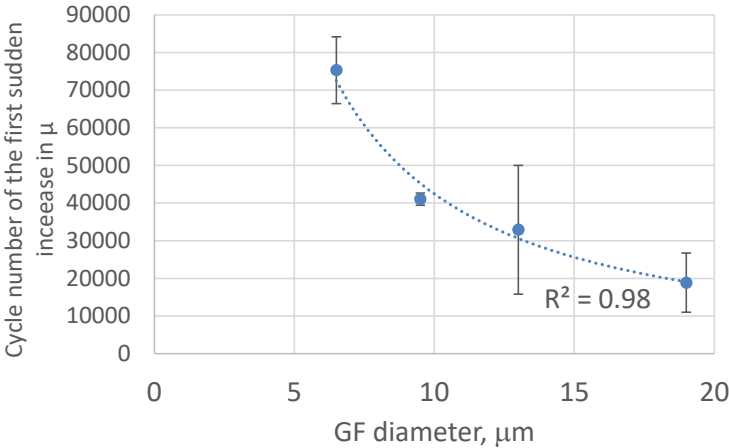


Fig. VI. 28 Relationship between the GF diameter and the cycle number at which the first sudden increase in the friction coefficient occurred. Each value is the average value of three values.

4.3 Effect of GF diameter on the wear resistance of steel counterpart

The effects of GF diameter on the wear resistance of steel counterpart were also investigated, and the changes in the order of the displacement values were related to the difference in contact pressure due to the wear of the steel cylinders. Fig. VI. 29 presents the wear volume of the steel counterparts tested using composites with different GF diameters after different cycle numbers. Linear fitting of this data indicated that the wear of the steel cylinders increased proportionally with the cycle number; the fitting equations had high correlation coefficient values. The results also show that the wear of the steel counterpart increased with the diameter of the GFs. The wear volume on the steel using the 19 μm diameter GF composite was 3–6 times larger than that observed using the 6.5 μm diameter GF composite. Therefore, as the wear on the steel cylinders increases, the contact pressure becomes lower, which should reduce the rate of increase in the displacement (i.e., wear and creep of the composite). Summarizing the above, the use of small diameter GFs is not usually effective to reduce the wear and creep of the composite over the entire sliding duration.

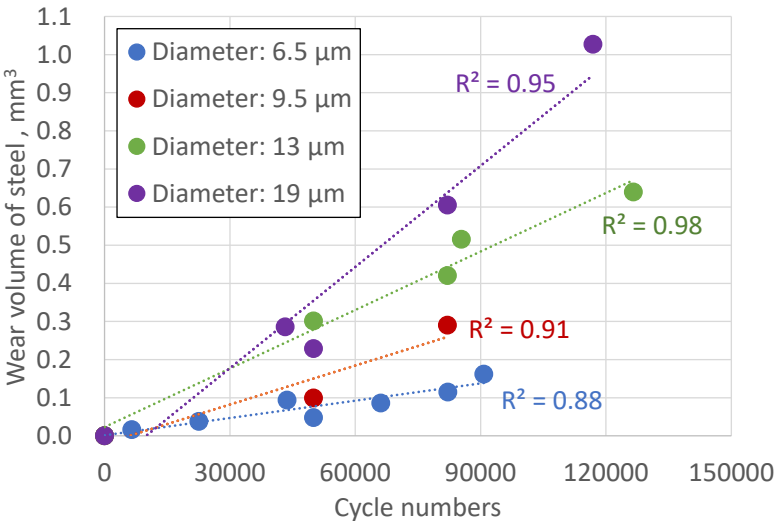
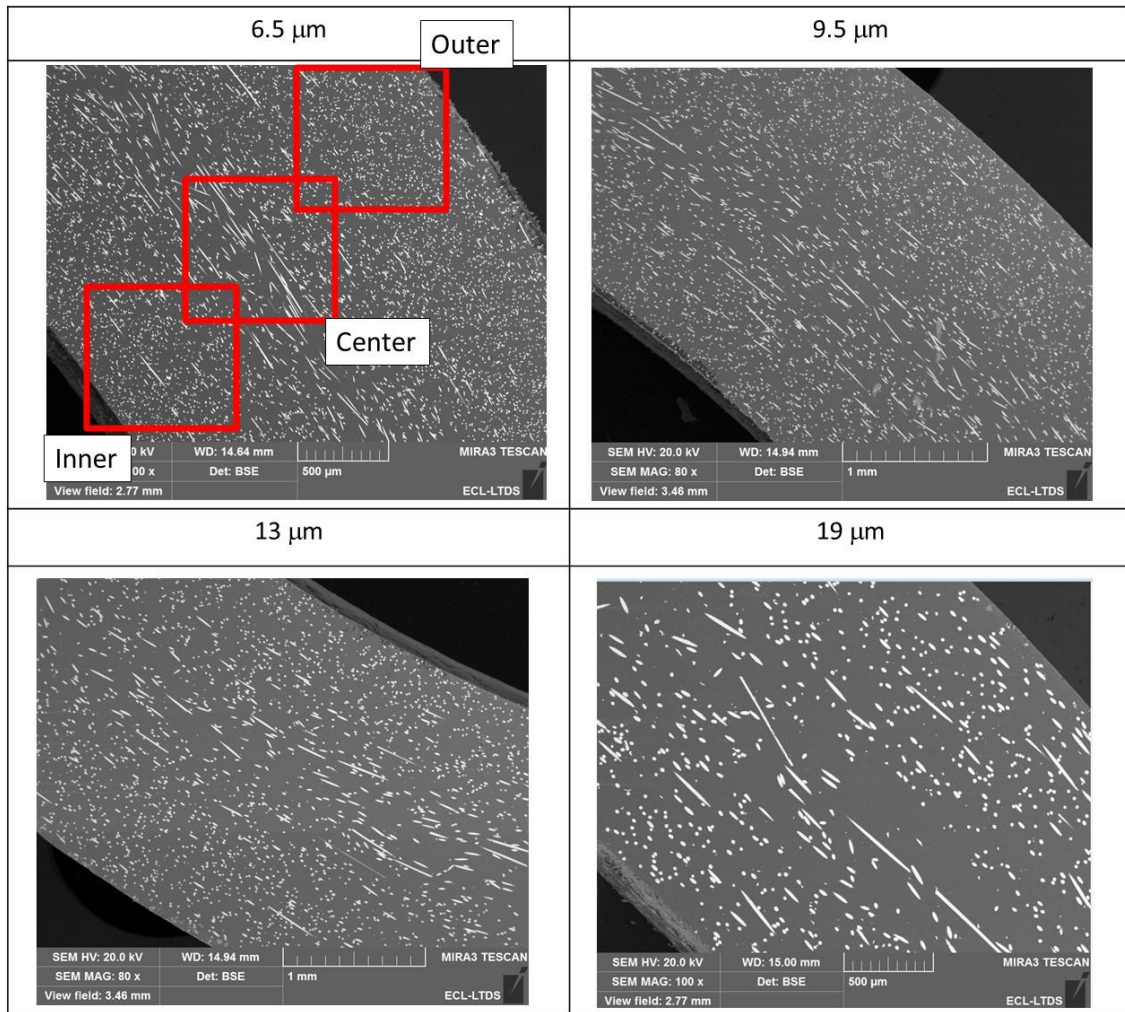


Fig. VI. 29 Wear volume of the steel cylinders at different cycle numbers for composites that differed only in GF diameter.

In order to clarify the mechanism by which GFs with a larger diameter accelerated the wear of the steel cylinders, the orientation of the GFs on the sliding surfaces of the composite ring before the sliding tests was investigated using image analysis. Fig. VI. 30 shows the surface SEM BSE images of the composite rings with different GF diameters after being polished with #4000 abrasive paper at different magnifications (image analysis was conducted using the image with magnification at x300).

(a)



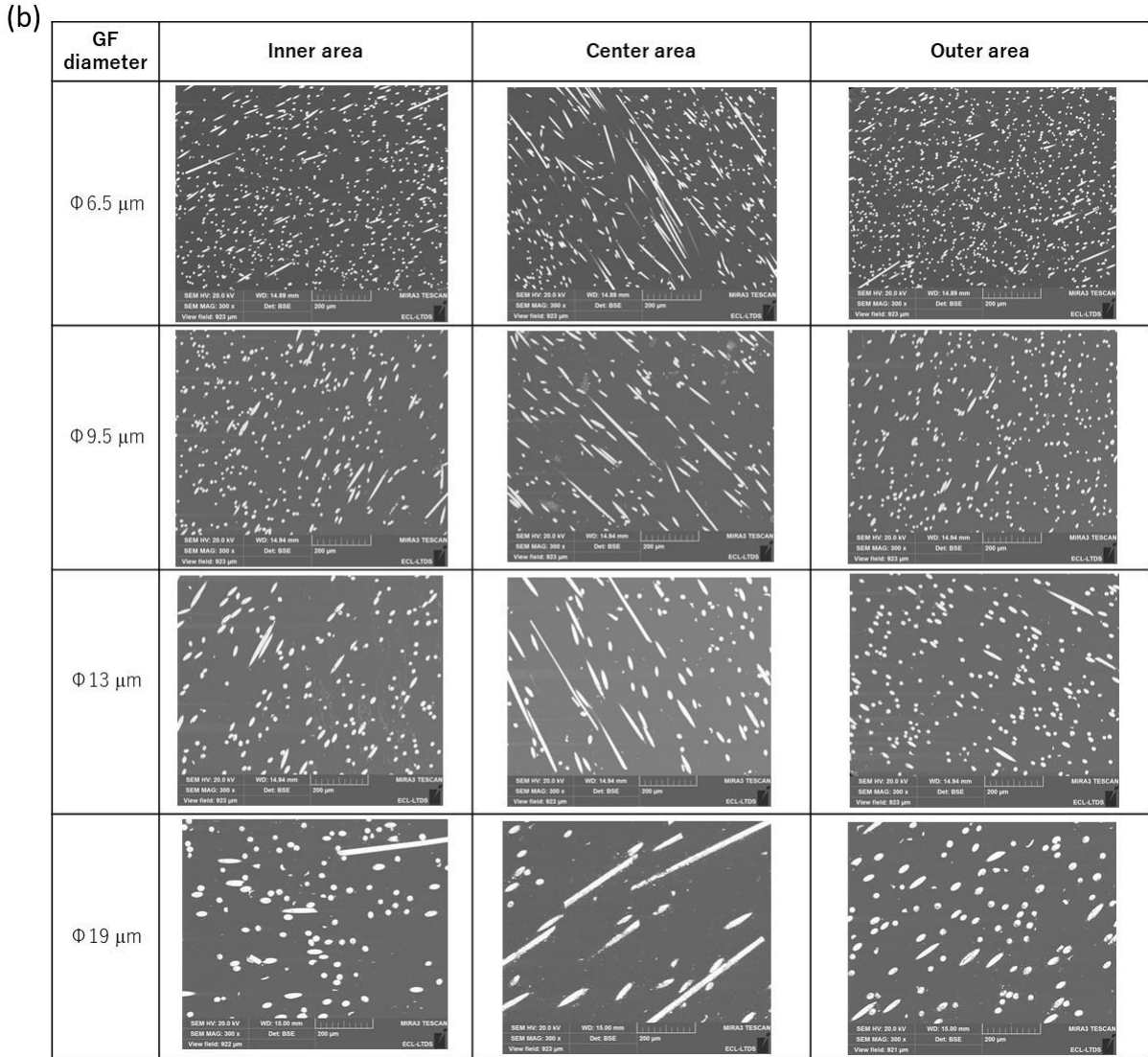


Fig. VI. 30 SEM BSE images of the surfaces of the composite rings with different GF diameters before the sliding tests: (a) magnification at x80; (b) magnification at x300.

Image analysis was conducted at three different locations at each of the three positions (inner, center, and outer, as presented in Fig. VI. 30b) of the sliding surface of the composite rings (36 images in total). Fig. VI. 31 shows the relationship between the circularity of the GFs and the cumulative frequency of the GF area, and C_{50} values of the composites with different GF diameters at each position. The global tendency on the GF orientation is the same, and C_{50} values at the center positions were lower than those at the inner or outer positions, regardless of the GF diameter. This indicates that the GFs in the center region of the sliding surface were oriented more perpendicularly than those in the inner or outer regions. This is the same trend as observed in other materials. Additionally, the C_{50} values at the outer position tended to be higher than those at the inner position regardless of the GF diameter. This was attributed to the resin flow inside the metal die, which is determined by the injection molding conditions and the structure of the metal die. We will see now how the C_{50} values at each position can explain the differences in the wear of the steel cylinders at different positions.

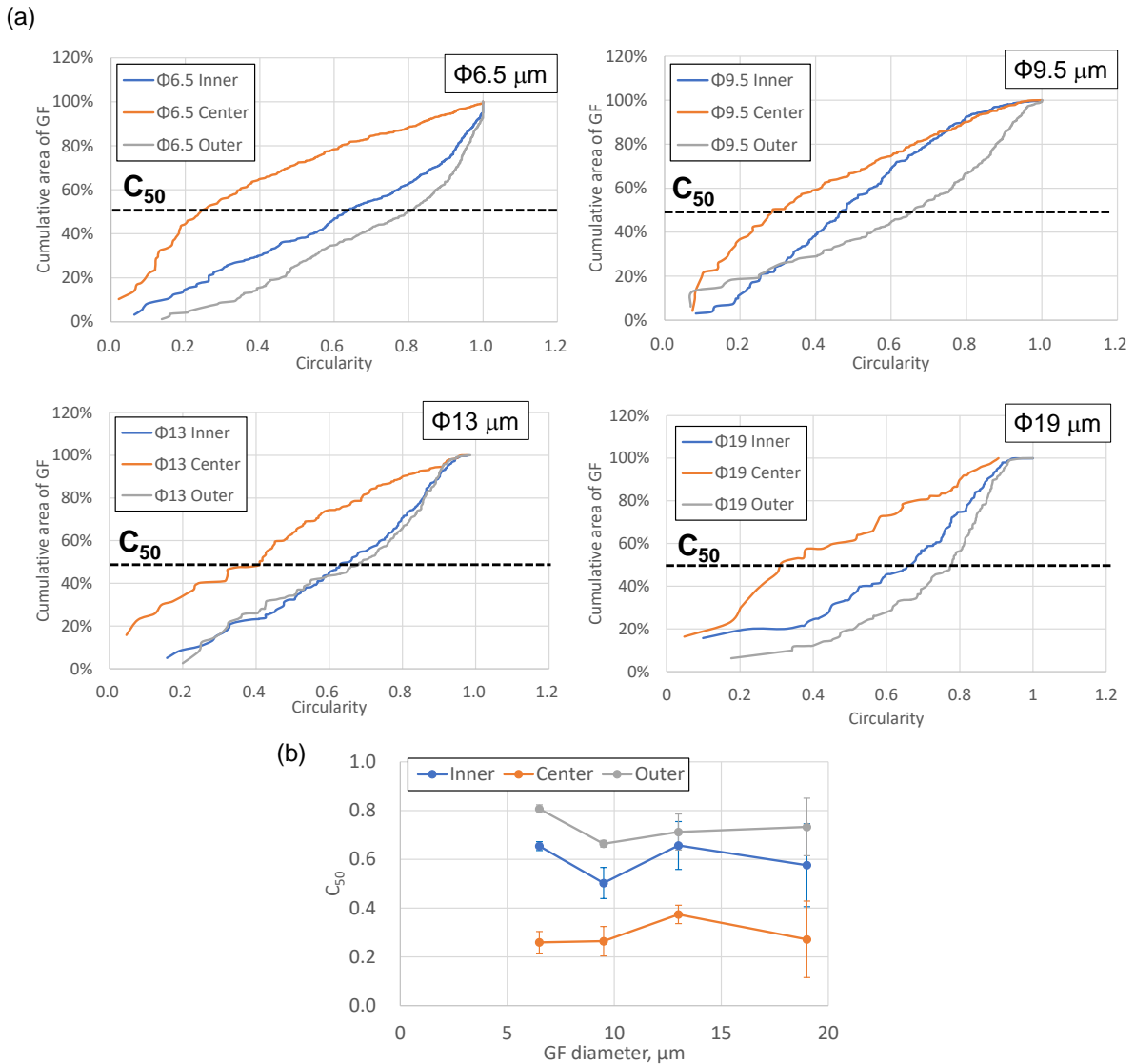


Fig. VI. 31 (a) Relationship between the circularity of the GFs and the cumulative frequency of the GF area using GF composites with different GF diameters. (b) C_{50} values at different positions of the surface of the composites with different GF diameters. Three measurements were conducted at each position.

Fig. VI. 32 shows interferometry measurements of the steel cylinders after 50,000 cycles after the removal of cylindrical shape, and central 2D profile. The wear volumes of the steel cylinders at positions corresponding to the inner, center, and outer positions of the composite ring were estimated, and are presented in Fig. VI. 33a. Fig. VI. 33b presents the relationship between the C_{50} values on the sliding surface of the composite and the wear of the steel cylinders at each position. The C_{50} values correlated well with the wear of the steel cylinders after the sliding tests with the composites with different GF diameters, which indicated that the wear volume at each position of the steel cylinders could be explained by the fiber orientation on the surface of its GF composite ring counterpart. However, the overall trend of the GF orientation was the same regardless of the GF diameter; thus, the effect of the diameter of the GFs on the wear of the steel cannot be explained by the fiber orientation.

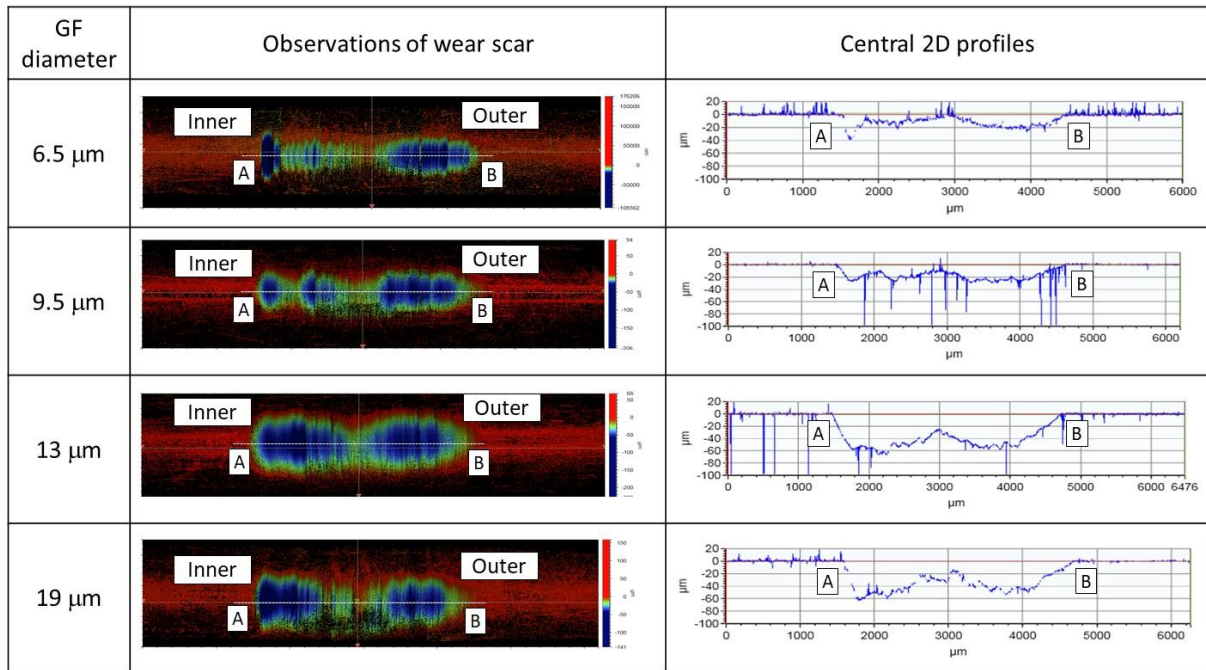


Fig. VI. 32 Observations of the steel counterparts and central 2D profiles using interferometry.

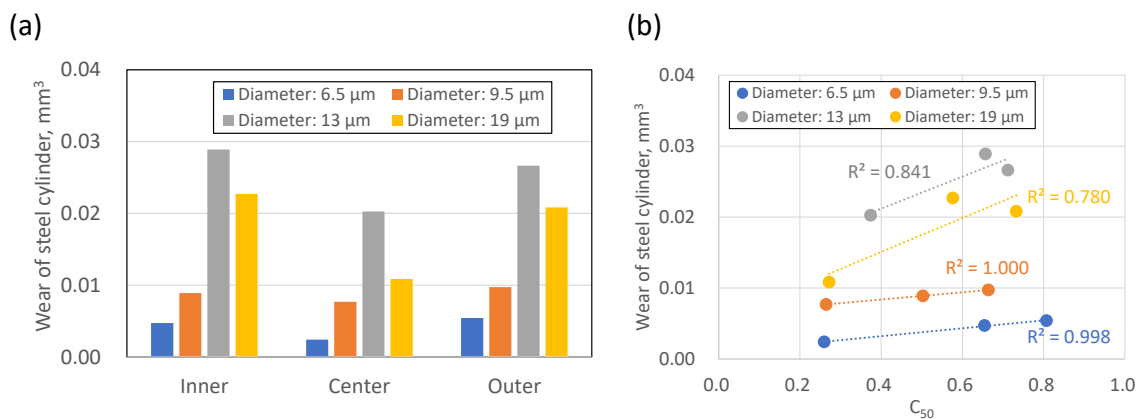


Fig. VI. 33 (a) Wear of the steel cylinders at positions corresponding to the inner, center, and outer positions of the composite ring after 50,000 cycles. (b) Relationship between the C_{50} values on the sliding surface of the composite and the wear of the steel cylinders at each position after 50,000 cycles.

In addition, Fig. VI. 34 shows the total GF area and total GF perimeter, which are correlated to the total contact area between the GF and PA66 on the sliding surface, for the composites with different GF diameter values. No difference in the total GF area was observed between the different positions on the composite surface. In contrast, the total GF perimeter decreased with increasing GF diameter. The total GF perimeter of the 6.5 μm diameter GFs was 2.00–2.48 times larger than that of the 19 μm diameter ones. This result can explain the difference in the wear of the steel counterpart by composites with different GF diameters. The interfacial shear strength between PA66 and the GFs was the same regardless of the GF diameter because the same PA66 and GF surface treatment agent was used for all the samples [107]. Therefore, the total energy of the adhesion between the PA66 and GFs increased with increasing total GF perimeter (i.e., the contact area between the PA66 and GFs). With greater

adhesion energy, more sliding cycles are required to induce interfacial peeling between the GFs and PA66, and the exposure of the GF edges due to the shear energy of sliding is reduced. Furthermore, the fracture strength of individual small diameter GFs is lower than that of large diameter fibers; thus, small GFs on the sliding surface of the composite are more easily damaged by the shear stress of sliding. GF debris was present in the grease at the end of test; however, this debris had little aggressive effect on the steel due to the two-body abrasion mode of the steel counterpart. In contrast, the larger GFs were less easily damaged or removed by the shear stress of sliding. Therefore, the effect of the two-body abrasion was more severe. Based on these two phenomena, we concluded that the steel wear can be reduced by decreasing the GF diameter.

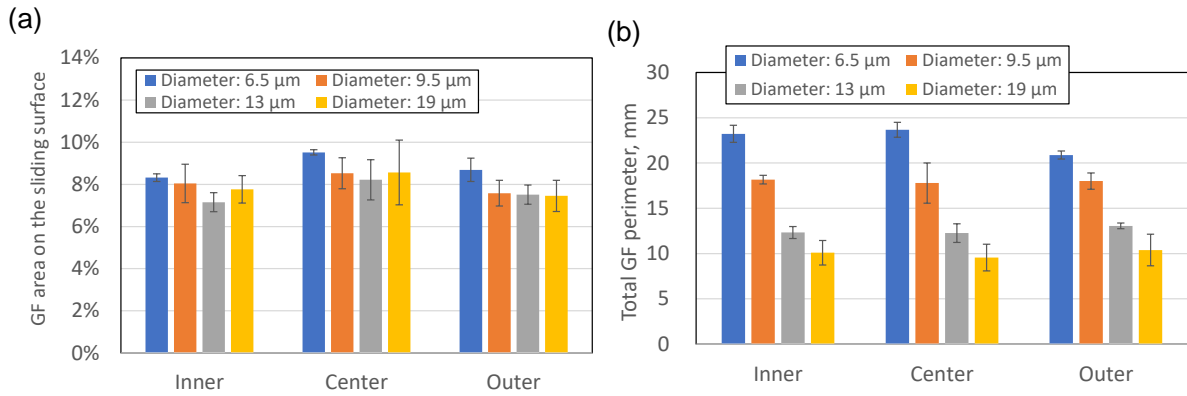


Fig. VI. 34 (a) Total GF area and (b) total GF perimeter on the sliding surfaces of composites that differed only in GF diameter. Three measurements were conducted at each position.

The wear debris from the steel counterpart was also analyzed. As shown in Fig. VI. 35, the sliding surfaces of the composites with GF diameters of 6.5 μm and 19 μm were observed using SEM after 50,000 cycles. EDX analysis was conducted to observe the distribution of the attached Fe, which is related to the wear debris of the steel counterpart. Afterwards, binarization of Fe particles in the image and particle analysis were conducted using the software package image J. Only particles with surface areas of 5 μm^2 or more were considered due of the noisiness of EDX images. Fig. VI. 36 shows the relationship between the size of the Fe particles and the cumulative frequency of the Fe particle area. The average size of the Fe wear debris for the composite with a GF diameter of 19 μm was much larger than that of the composite with 6.5 μm fibers. The area of the Fe wear debris at 50% cumulative frequency of Fe particle area for the 19 μm diameter composite was 34.2 μm^2 ; this value was 3.45 times higher than that of the 6.5 μm diameter composite (9.9 μm^2). This was attributed to the size of the GFs on the sliding surface of the composite, which had a significant effect on the two-body abrasion of the steel.

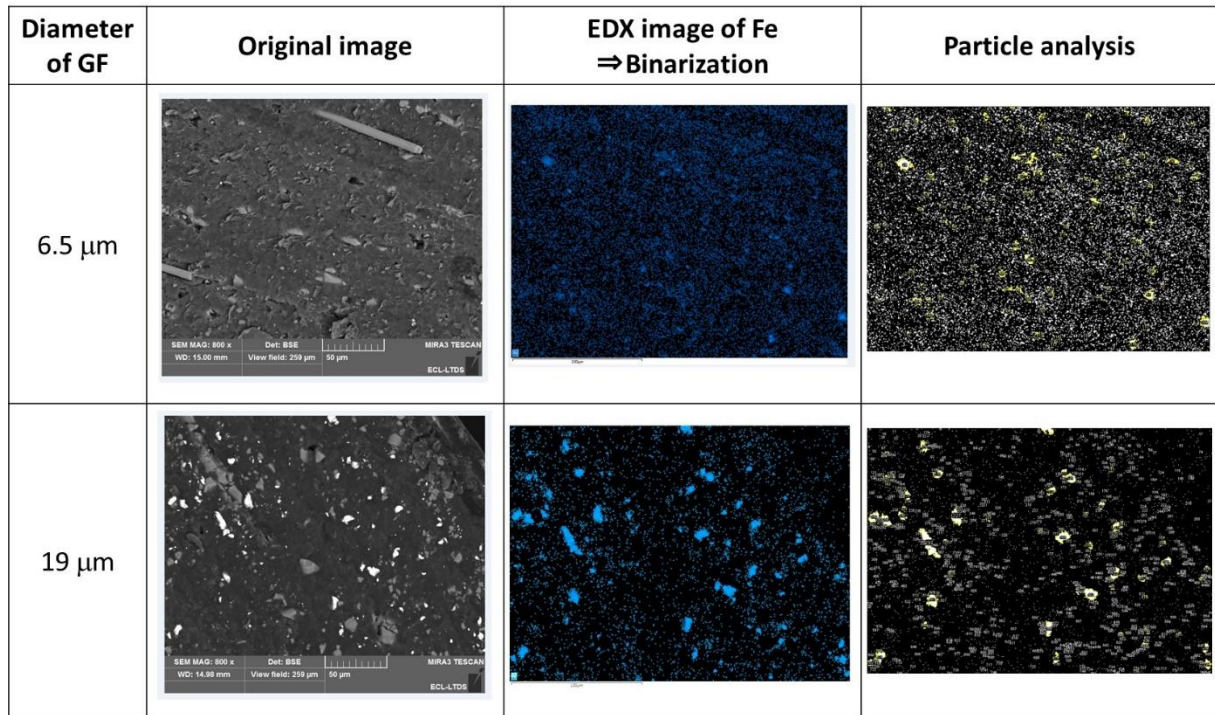


Fig. VI. 35 SEM observations of the sliding surfaces of composites with different GF diameters after 50,000 cycles sliding test and image analysis of Fe wear debris.

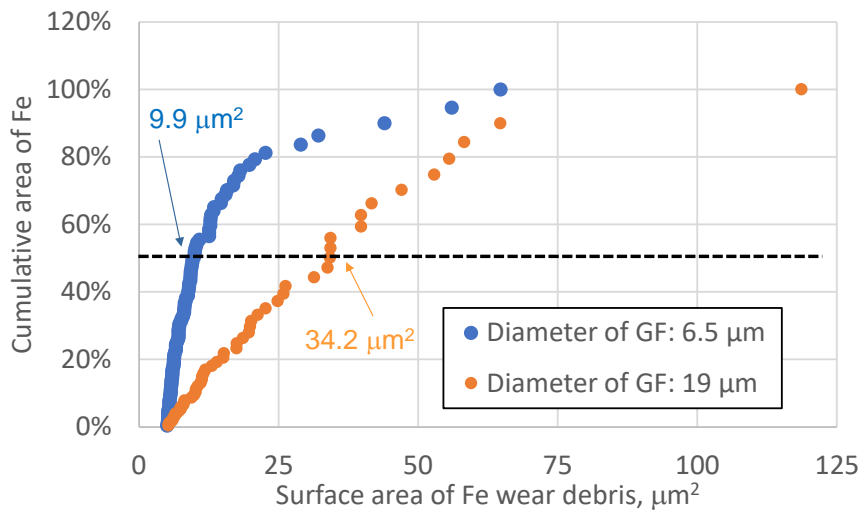


Fig. VI. 36 Relationship between the surface area of Fe wear debris and the cumulative frequency of Fe area.

Fig. VI. 37 schematically illustrates the effect of the GF diameter on the tribological properties of the GF-reinforced PA66 composite and steel system discussed above.

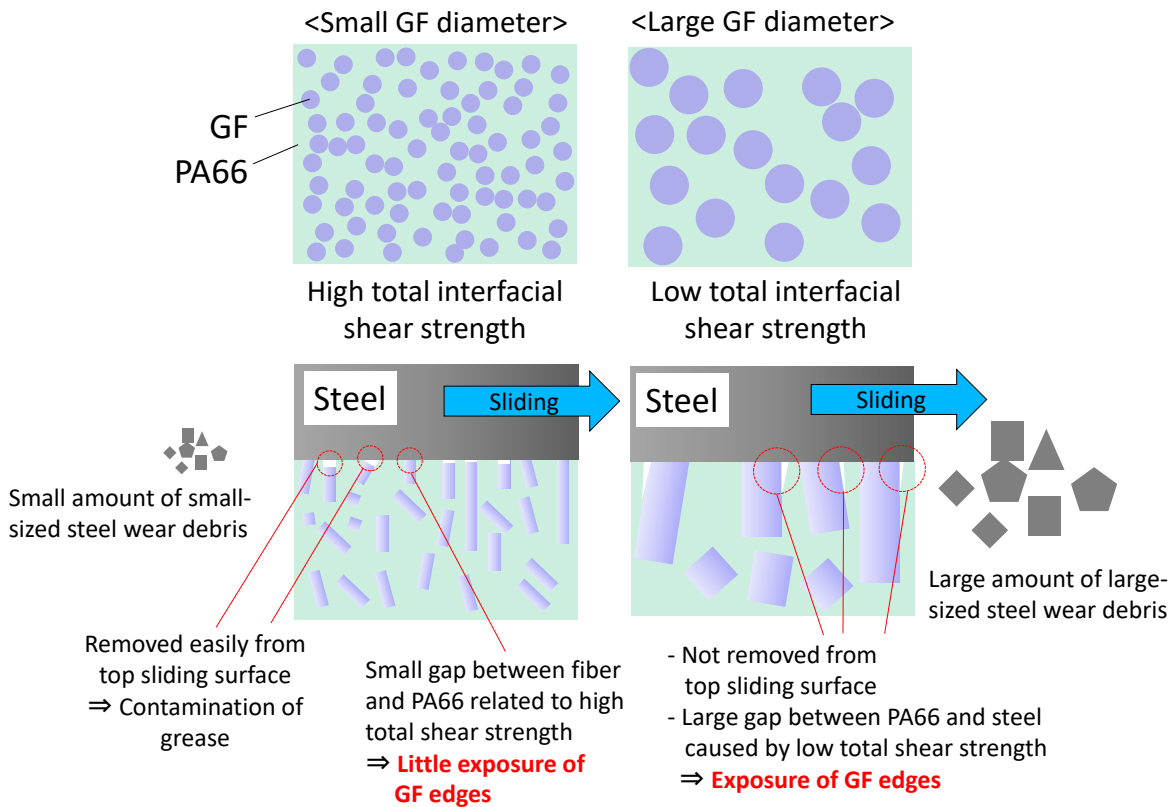


Fig. VI. 37 Schematic of the effects of the GF diameter on the tribological properties.

5. Conclusions

The tribological properties of different GF-reinforced PA66 composites in contact with carbon steel were studied under grease lubricated conditions. The effects of the composition of the composite on the tribological properties were investigated with the aim of developing a composite with optimized tribological properties. The main findings have been highlighted below.

1) Effects of the interfacial shear strength between PA66 and GF

High interfacial shear strength between the PA66 matrix and the GFs reduced the friction coefficient and wear of the composite. Good adhesion between PA66 and GF prevented the degradation of the mechanical properties of the composite surface during sliding, which is related to the peeling of glass fibers and the initiation and propagation of the scratches. The wear resistance of the steel counterpart was also enhanced by increasing the interfacial shear strength, as high interfacial strength prevents the exposure of GF edges, which have a strongly aggressive effect on the steel counterpart. The difference in the interfacial shear strength resulting from the use of different glass fiber surface treatment agents was discussed quantitatively using a modified Kelly–Tyson model that accounts for the length and orientation of the fibers.

2) Effects of the molecular mass of PA66

The wear resistances of both the GF-reinforced PA66 composite and the steel counterpart were improved by increasing the molecular mass of the PA66. The high elongation of the high molecular mass PA66 reduced the interfacial peeling between GF and PA66 due to the shear stress induced by sliding and prevented the exposure of the GF edges, which have a strongly aggressive effect on the steel counterpart via a two-body abrasive wear mode. Additionally, the high toughness of the high molecular mass PA66 reduced the propagation of scratches on PA66, which originated at the interface between PA66 and the GFs, and enhanced the wear and creep resistance of the composite.

3) Effects of GF diameter on the mechanical and tribological properties

The wear of the steel counterparts reduced with decreasing GF diameter. Image analysis revealed that the total interfacial area between GF and PA66 increased when small diameter GFs were used. This indicates that surfaces with high interfacial adhesion energy can bear higher sliding energies without interfacial peeling between GF and PA66. The wear and creep resistances of the composite also improved when smaller diameter GFs were used because the strength and toughness of the composite were enhanced by the increase in the interfacial adhesion area.

This chapter focused particularly on the effect of the composition of the GF composite on the mechanical and tribological properties. Increase in the PA66 molecular mass, particularly, improved wear resistance of both the GF composite and steel counterpart. Several methods to increase the PA66 molecular mass can be presented, and addition of a molecular chain extender which has reactivity with PA is one possible way. In the next chapter, the reactive extrusion process will be studied using the poly-carbodiimide compounds as a molecular chain extender, and the effect of the addition of the poly-carbodiimide compounds on the mechanical and tribological properties of the composite will be discussed.

CHAPTER VII

REACTIVE EXTRUSION MECHANISM, MECHANICAL AND TRIBOLOGICAL BEHAVIOR OF FIBER-REINFORCED PA66 WITH ADDED CARBODIIMIDE

CHAPTER VII: REACTIVE EXTRUSION MECHANISM, MECHANICAL AND TRIBOLOGICAL BEHAVIOR OF FIBER-REINFORCED PA66 WITH ADDED CARBODIIMIDE

1. Introduction.....	245
2. Effects of the structure surrounding the carbodiimide group on the reaction velocity and mechanism	247
3. Effects of the carbodiimide feeding position in the twin screw extruder and the amount of added carbodiimide	248
4. Wear resistance of GF composite with added carbodiimide	250
5. Wear resistance of AF composite with added carbodiimide	252
6. Toughness of PA66-GF-carbodiimide with added olefin polymer.....	254
7. Conclusions.....	256

CHAPTER VII: REACTIVE EXTRUSION MECHANISM, MECHANICAL AND TRIBOLOGICAL BEHAVIOR OF FIBER-REINFORCED PA66 WITH ADDED CARBODIIMIDE

Reactive extrusion is a method to obtain fiber-reinforced composites with high molecular mass. In this chapter, the reactive extrusion mechanism of GF or AF-reinforced PA66 with added carbodiimide was clarified, and the mechanical and tribological properties of the materials were evaluated.

1. Introduction

In chapter VI, the effect of the composition of GF composite on the mechanical properties and tribological properties were investigated, and increase in the PA66 molecular mass contributed to the improvement of wear resistance of both the GF composite and steel counterpart through the prevention of debonding of fibers and PA66. As presented in Section 3.3.2 in Chapter I, reactive extrusion using molecular chain extender is a way to obtain efficiently GF-reinforced composite with high molecular mass. In this chapter, we focused on the reactive extrusion using poly-carbodiimide as a new type of molecular chain extender. The effects of each parameter in the extrusion reaction process, e.g., the feeding position of poly-carbodiimide compounds in the twin screw extruder, the amounts of added carbodiimide compounds, and the structure surrounding the poly-carbodiimide group, were investigated. In addition, the mechanical properties (including tensile properties and impact strength) and wear resistance of the carbodiimide-added fiber-reinforced PA66 material in contact with carbon steel under grease lubrication were also analyzed.

Table VII. 1 lists the composition and mechanical/physical properties of evaluated GF 33% composites, and Table VII. 2 lists those of AF 20% composites. The details in each composite were explained in Section 2.1 in Chapter II. When olefin polymer was added, added amounts were 10 wt%, and fed in top feed. In the sliding tests, single type of barium complex grease which was presented in Section 2.3.2 in Chapter II and bearing steel cylinders with the Vickers hardness of HV 789 as explained in Section 2.2 in Chapter II were used. In addition, the sliding tests in this chapter were conducted using the tribometer in JTEKT Corporation as explained in Section 4.3 in Chapter II, which has the same contact geometry as that used in previous chapters.

Table VII. 1 Composition of fabricated GF 33% composite with added poly-carbodiimide or olefin polymer.

	Carbodiimide			Olefin polymer type	Young's modulus, GPa
	Type	Amounts, wt%	Feeding position		
1	-	-	-	-	10.7 ± 0.3
2	Aliphatic	2.0	Side feed	-	10.4 ± 0.8
3	Aromatic	1.0	Top feed	-	11.1 ± 0.5
4	Aromatic	2.0	Top feed	-	10.3 ± 0.9
5	Aromatic	3.0	Top feed	-	11.5 ± 0.6
6	Aromatic	1.5	Side feed	-	11.2 ± 0.4
7	Aromatic	2.0	Side feed	-	11.4 ± 0.5
8	Aromatic	2.5	Side feed	-	9.9 ± 0.3
9	Aromatic	3.0	Side feed	-	10.7 ± 0.6
10	-	-	-	-MAH modification	7.1 ± 0.5
11	Aliphatic	2.0	Side feed	-MAH modification	8.2 ± 0.4
12	Aliphatic	2.0	Side feed	-GMA modification	8.8 ± 0.3
13	-	-	-	No modification	10.3 ± 0.3
14	Aliphatic	2.0	Side feed	No modification	9.3 ± 0.2

Table VII. 2 Composition and properties of the AF 20% composite.

	Molecular mass of raw PA66 (before extrusion)	Carbodiimide compounds			Tensile Young's modulus, GPa
		Type	Amounts, wt%	Feeding position	
15	Normal	-	-	-	5.3 ± 0.3
16	High	-	-	-	5.7 ± 0.8
17	Normal	Aromatic	2.5	Side feed	4.4 ± 0.2

2. Effects of the structure surrounding the carbodiimide group on the reaction velocity and mechanism

First, the effects of the chemical structure of the poly-carbodiimide compounds on the reaction were investigated. Fig. VII. 1 shows the variation in the number average molecular mass for each process (samples no. 1, 7, 8). A higher molecular mass was obtained for both the pellets and molded samples compared to the raw PA66 material by adding carbodiimide compounds. When the aliphatic poly-carbodiimide compounds were used, very high molecular mass of the extruded pellets was obtained; however, the molecular mass decreased after the injection molding process. In addition, the amount of carbodiimide remaining in the pellets was less than 0.05%, compared to the initially added 2%; here, the remaining carbodiimide is not defined as the amount of functional group itself, but as the converted amount as carbodiimide compounds, which was measured as explained in Section 3.4 in Chapter II. This demonstrates that the reaction velocity of the carbodiimide compounds was very high. Therefore, the added carbodiimide compounds were almost exhausted through reactions during the extrusion of pellets, and the effects of decomposition reactions became significant during injection molding. On the other hand, when aromatic poly-carbodiimide compounds were used, the reaction velocity was much lower compared to that for the aliphatic carbodiimide. It was then possible to obtain remaining 0.6–0.9% unreacted carbodiimide, compared to the initially added 2–2.5%. This was because the reaction between the carbodiimide groups and the functional groups in the PA was delayed because the poly-aromatic carbodiimide compounds contain isopropyl groups, which created steric hindrance near the carbodiimide group; the reaction was also hindered by resonance stabilization related to the double bonds in the molecular structure. Therefore, the remaining unreacted carbodiimide reacted during the injection molding process in preference to the decomposition reaction; thus, the molecular mass of the molded samples was ultimately increased.

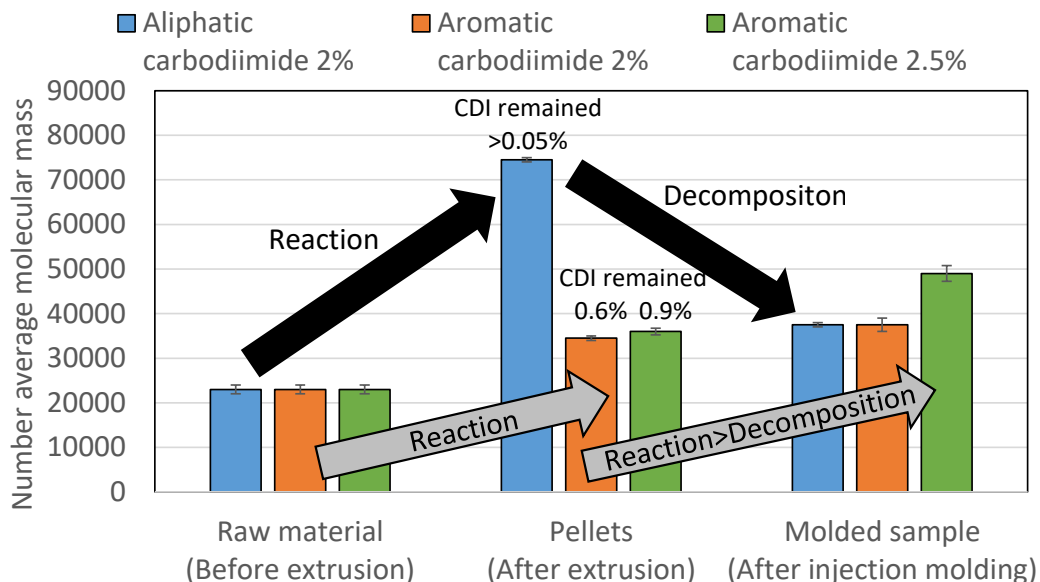


Fig. VII. 1 Variation of the molecular mass for each process (CDI: carbodiimide compound).

3. Effects of the carbodiimide feeding position in the twin screw extruder and the amount of added carbodiimide

The effect of the carbodiimide addition on the tensile mechanical properties was investigated. Fig. VII. 2 shows the tensile breakage energy for samples with varying amounts of aromatic poly-carbodiimide added (samples no. 1, 3–9) with different feeding positions.

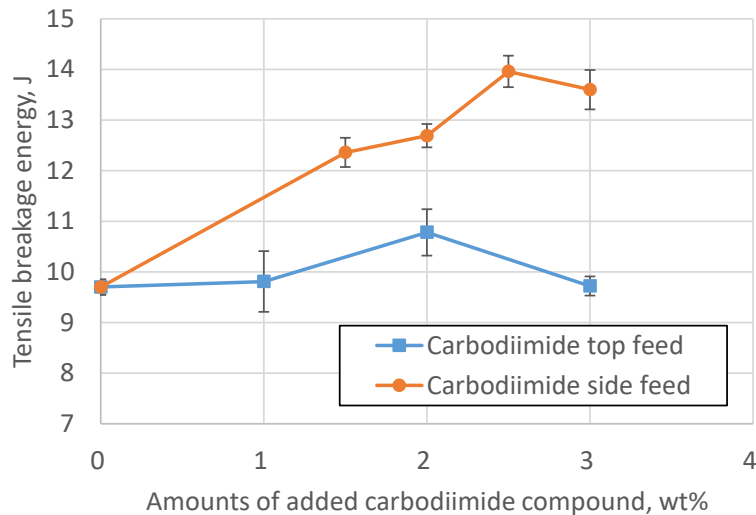


Fig. VII. 2 Relationship between the amount of added aromatic carbodiimide compound and the tensile breakage energy.

When aromatic carbodiimide compounds were fed from the side feeder, the tensile breakage energy was greater for each amount of added carbodiimide compared to top feeding. In addition, for side-feeding of the carbodiimide compounds, the maximum tensile breakage energy was obtained when 2.5 wt% carbodiimide was added. This can be explained by the following reasons. (1) There was a correlation between the molecular mass of molded samples and the tensile elongation at break, as shown in Fig. VII. 3. (2) When 2.5 wt% carbodiimide was added, the molecular mass of the molded samples was highest. (3) The effect of the amount of added carbodiimide on the tensile strength was weak compared to the tensile elongation at break, as shown in Fig. VII. 3 and Fig. VII. 4, and thus the contribution of the tensile elongation at break was more significant than the effect of the tensile breakage energy. Fig. VII. 5 shows the relationship between the amounts of remaining carbodiimide in the pellet and the tensile breakage energy. Regardless of the feeding position and amount of carbodiimide compound, the tensile breakage energy increased with increasing remaining carbodiimide in the pellet. With top feeding of the carbodiimide compounds, the reaction time inside the twin screw extruder was long, and the effect of exhausting the carbodiimide became significant. In contrast, with side feeding of the carbodiimide compounds, the reaction time inside the twin screw extruder was short. It is thus possible that unreacted carbodiimide remained in the pellets, and in the subsequent injection molding process, much higher molecular mass of the molded samples were obtained through additional reaction.

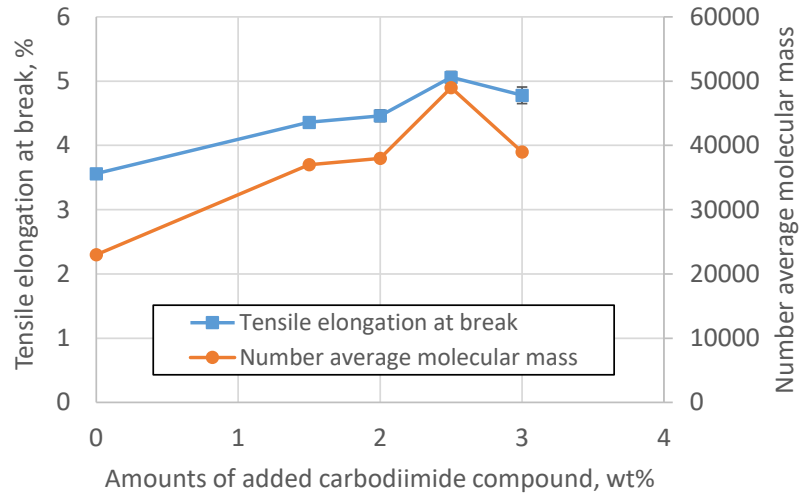


Fig. VII. 3 Evolutions of tensile elongation at break and number average molecular mass with the amount of added carbodiimide compound.

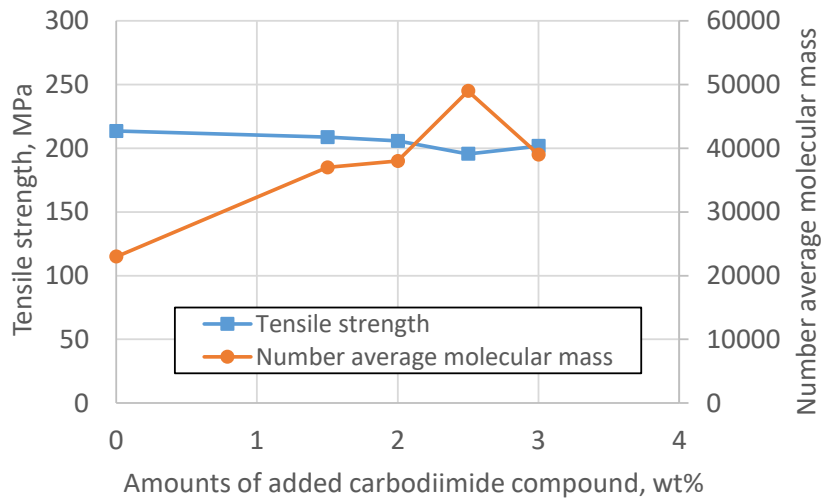


Fig. VII. 4 Evolutions of tensile strength and number average molecular mass with the amount of added carbodiimide compound.

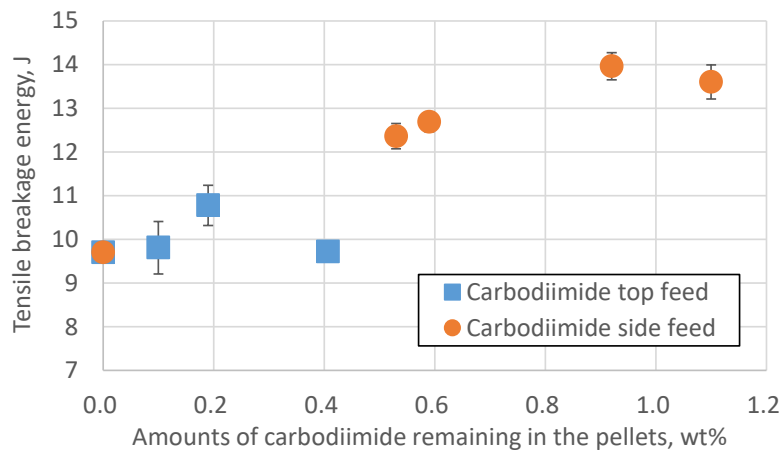


Fig. VII. 5 Evolutions of the tensile breakage energy with the amount of carbodiimide remaining in the pellets.

4. Wear resistance of GF composite with added carbodiimide

Tribological properties of the GF composite with added carbodiimide were investigated for a normal load of 220 N with an intermittent contact which includes 10 s sliding and 20 s stopping phase at room temperature. Fig. VII. 6 shows the height loss after the sliding tests and the molecular mass for various GF-reinforced PA66 materials. A low height loss value indicates good wear resistance. The wear of the composite is significantly decreased with the addition of carbodiimide compounds, corresponding to an increase in the PA66 molecular mass. This is the same tendency as observed in Section 3 in Chapter VI, and high toughness of PA66 with high PA66 molecular mass was supposed to contribute to prevent the generation of the gap between PA66 and GFs, and consequently the wear of the composite decreases.

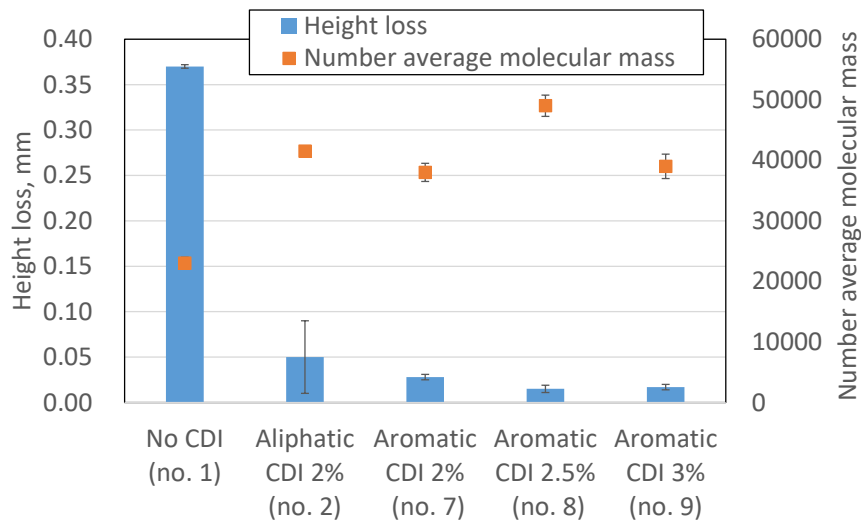


Fig. VII. 6 Height loss after the sliding test and number average molecular mass for different samples.

Fig. VII. 7 shows an optical microscope image of the sliding surface of the specimen without added carbodiimide (sample no. 1) after the sliding test. Peeling of the composite sliding surface related to high contact pressure wear was observed on the whole sliding surface.

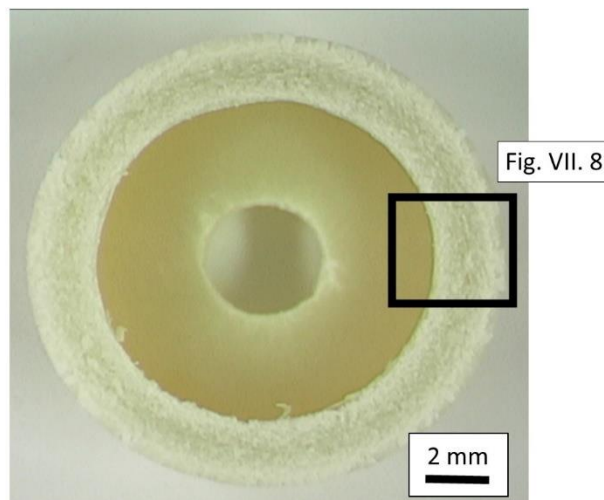


Fig. VII. 7 Optical microscope image of the sliding surface of the material without added carbodiimide (sample no. 1).

Fig. VII. 8 shows an SEM image of the surface of the same sample. Peeling of the resin, exposure and dropping off of the fibers, and agglomeration of broken fibers can be observed.

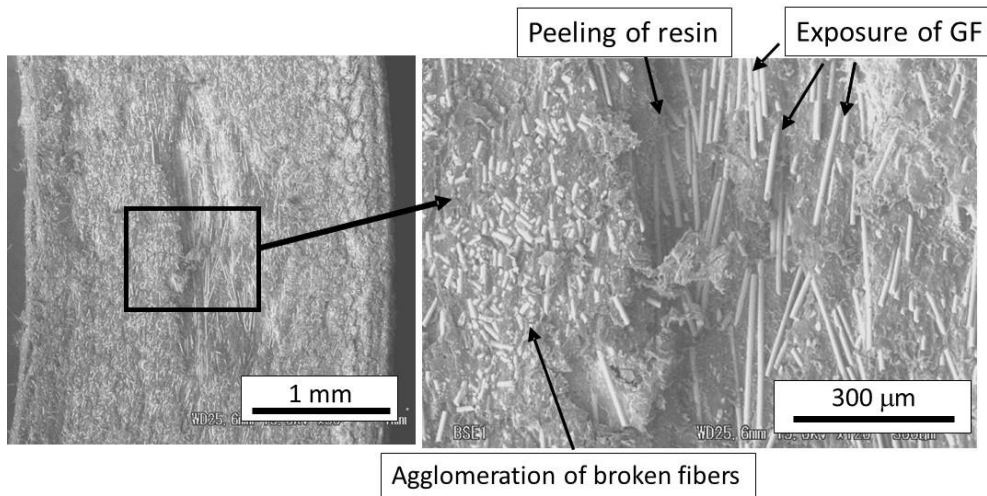


Fig. VII. 8 SEM images of the sliding surface of the material without added carbodiimide (sample no. 1).

In contrast, Fig. VII. 9 shows the sliding surface of a material with added carbodiimide compounds (sample no. 8). Peeling of the sliding surface was limited to a small area, compared to the material without added carbodiimide.

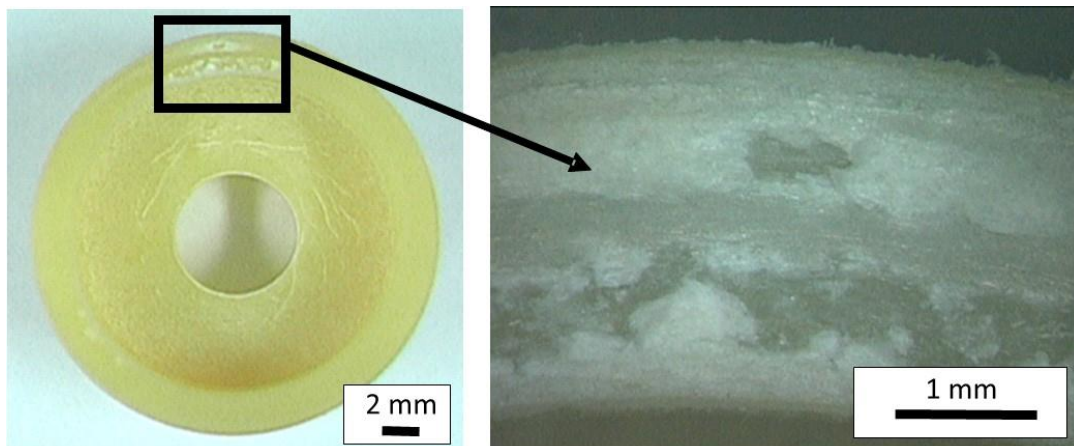


Fig. VII. 9 Optical microscope image of the sliding surface of the material with added carbodiimide (sample no. 8).

Thus, it was confirmed that addition of carbodiimide compounds to GF-reinforced PA66 composites can increase the molecular mass, and it can contribute to decrease the wear of composites. This is related to the fact that the toughness of composite was increased as presented in the results of tensile test, and the initiation and the propagation of the cracks by sliding were prevented, with the same mechanism as explained in Section 3 in Chapter VI.

5. Wear resistance of AF composite with added carbodiimide

In addition to the GF composite, the effects of the addition of the poly-carbodiimide compounds on the tribological properties were investigated using AF-reinforced composite. For the AF-reinforced material, a composite material was prepared in which AF was extruded with high molecular mass raw PA66 (sample no. 16; viscosity number of the raw resin: 235 ml/g). In addition, the wear resistance of this material was then investigated in comparison to the materials with or without carbodiimide added with normal molecular mass raw PA66 (samples no. 15 and 17; viscosity number of the raw resin: 150 ml/g). Consequently, the effect of the molecular mass of raw PA66 and poly-carbodiimide addition on the wear resistance of the AF-reinforced composite was investigated. Fig. VII. 10 shows the height loss after the sliding test and the molecular mass of specimens of the AF-reinforced PA66 composite material.

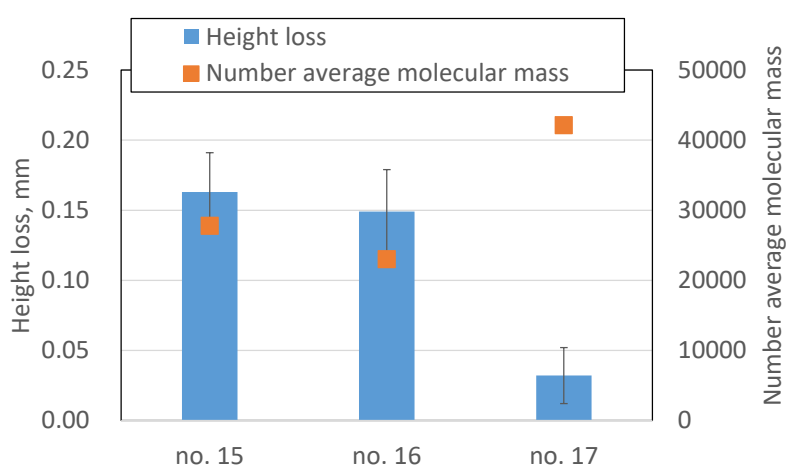


Fig. VII. 10 Height loss after sliding tests and the number average molecular mass for each sample.

The results show that the wear was decreased largely by the addition of carbodiimide compounds and the increase in molecular mass. Therefore, the increase in the PA66 molecular mass can also contribute to improve the wear resistance of AF-reinforced PA66. Extruding AF with high molecular mass PA66 (sample no. 16), the molecular mass of the molded specimen was much lower than that of the material with carbodiimide added, and was approximately equal to that of the material extruded with normal molecular mass PA66. Thus, the effect of decomposition during extrusion was much more significant. We suppose that this is because AF are soft organic fibers, which are difficult to be damaged through the shear force of extrusion, compared to GF and CF. Therefore, the viscosity of the melted resin, temperature, and torque during extrusion were increased, and the effect of decomposition during extrusion became much more severe. By contrast, for the carbodiimide-added material (sample no. 17), 0.9 wt% carbodiimide could remain unreacted in the pellets compared to the original added amounts (2.5 wt%), which was measured in the way as explained in Section 3.4 in Chapter II, the same as in the GF-reinforced composite material (see Fig. VII. 1). Thus, AF was extruded with low molecular mass PA66, i.e., under conditions of low resin viscosity, and reacted further during the injection molding process. Therefore, a high molecular mass of molded samples and high wear resistance were obtained.

Fig. VII. 11 shows optical microscope images of the sliding surfaces after sliding tests. For the material without added carbodiimide (sample no. 15), exposure of fibers was observed on all sliding surfaces, and peeling of the sliding surface was also observed. In contrast, for the material with added carbodiimide (sample no. 17), the resin peeling was partially limited, and the exposure of fibers was controlled. This difference of wear mode is attributed to the difference of the strength of the molecular chain entanglement, and the initiation and propagation of the cracks were reduced in the high molecular mass specimens which were obtained by carbodiimide addition. In addition, considering their chemical structures, carbodiimide is assumed to be reactive not only with PA, but also with AF, which are fully aromatic PA fibers. Therefore, adding carbodiimide compounds likely contributes to improving the adhesion strength between the PA66 resin and AF in addition to its effect of increasing the molecular mass. Thus, in high contact pressure sliding conditions, the dropping off of fibers was likely reduced by the high molecular mass related to the addition of carbodiimide compounds. In addition, high wear resistance was obtained.

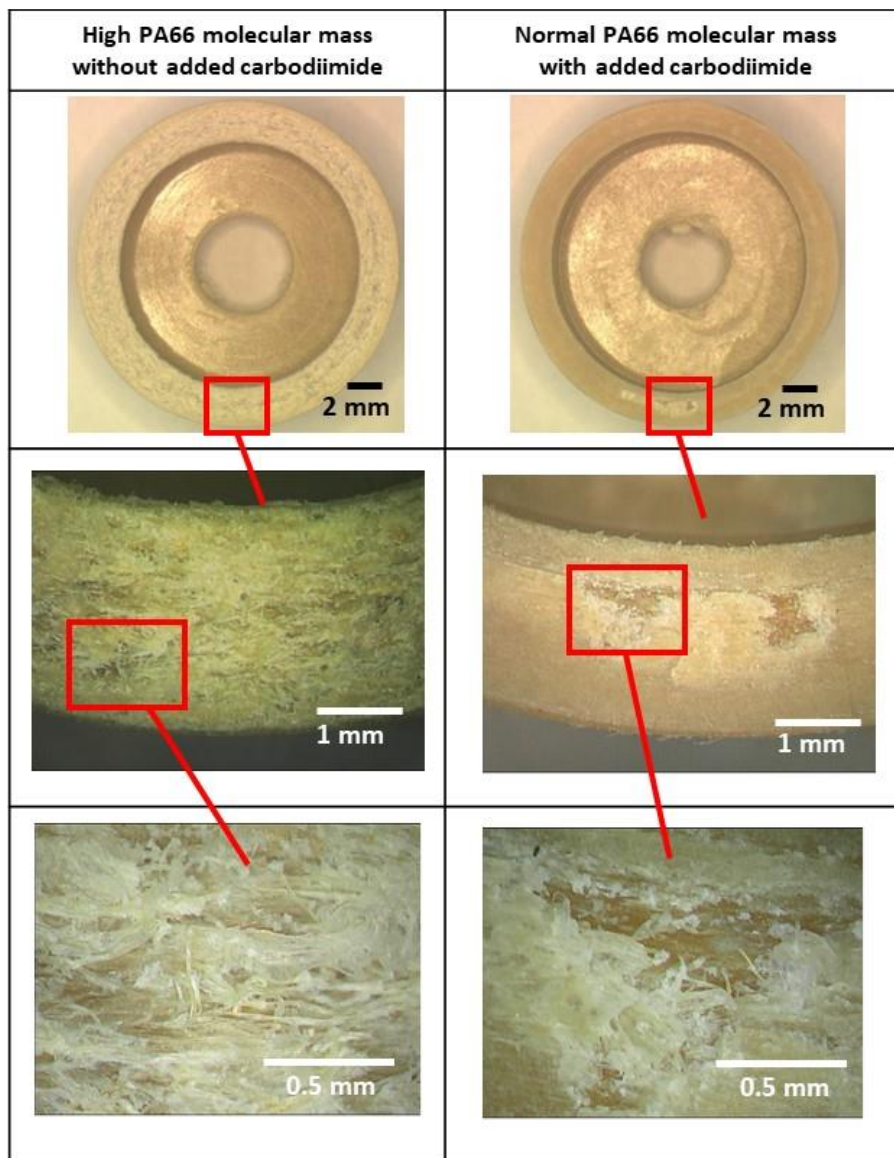


Fig. VII. 11 Optical microscope observations of the sliding surface of AF-reinforced PA66 materials.

6. Toughness of PA66-GF-carbodiimide with added olefin polymer

The effects of adding olefin polymer to the PA66-GF-carbodiimide material on the mechanical properties were investigated to reflect a case in which a much higher impact strength and toughness may be required. Fig. VII. 12 shows the Charpy impact strength, which acts as a barometer of the impact resistance properties of a material. Furthermore, Fig. VII. 13 shows the tensile breakage energy, which indicates the toughness of a material.

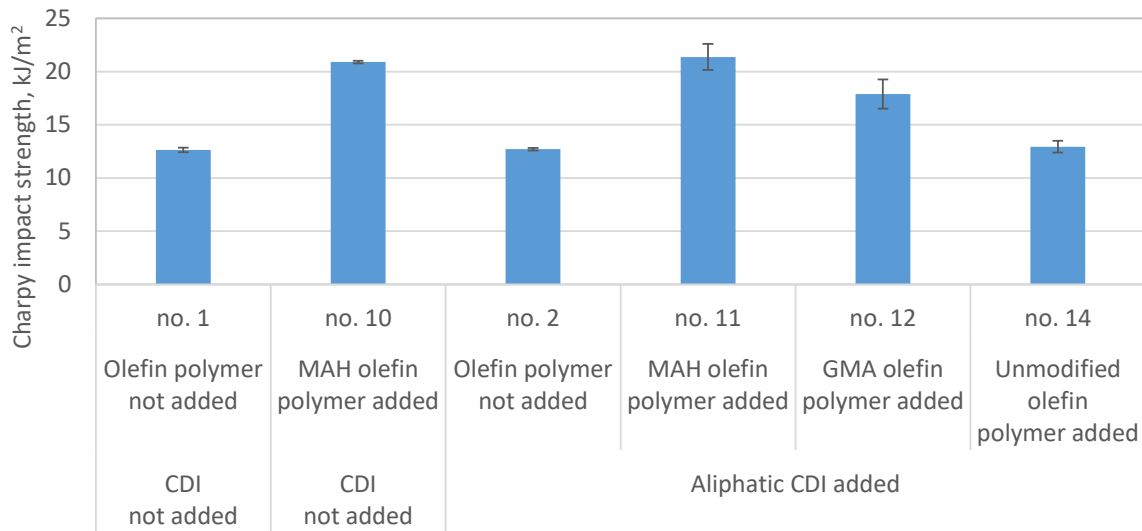


Fig. VII. 12 Charpy impact strength for various materials.

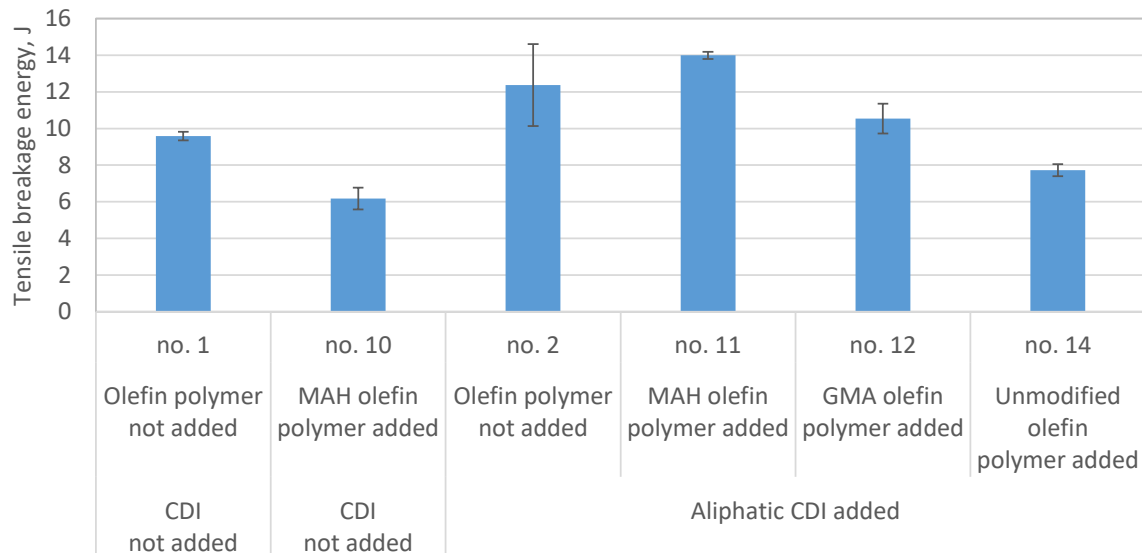


Fig. VII. 13 Tensile breakage energy for various materials.

When the MAH-modified olefin polymer was added, an improvement in the Charpy impact strength was observed. However, the tensile breakage energy decreased (see samples no. 1 and 10). This was because the tensile strength and tensile elongation at break decreased with the addition of the soft olefin polymer. In addition, when carbodiimide was added without adding the olefin polymer, the tensile breakage energy was increased, as described in Section 3. However, improvement in the Charpy impact strength was not observed (see samples no.

1 and 2). On the other hand, when adding both the MAH-modified olefin polymer and aliphatic poly-carbodiimide compounds, a synergistic improvement effect on the tensile breakage energy, which was not predicted by the results of the addition of each individually, was obtained in addition to the improvement in the Charpy impact strength (see samples no. 1, 2, 10, and 11). Furthermore, this synergistic effect was observed only when MAH-modified olefin polymer was added. When GMA-modified olefin polymer (sample no. 12) was added, these effects became less pronounced. Furthermore, no improvement in the tensile breakage energy or Charpy impact strength were observed when the unmodified olefin polymer was added (sample no. 14).

In addition, the distribution of the olefin polymer in the molded samples was investigated to consider the reactive properties of each component in the material with no added carbodiimide; the results are shown in Fig. VII. 14. When unmodified poly-olefin polymer was added (no. 13), the olefin polymer existed as 5–10 μm coarse-sized grains. In contrast, when the MAH-modified olefin polymer was added (no. 10), the olefin polymer existed as sub-micron-sized grains. These results demonstrate that the MAH-modified functional group had a high affinity for PA66, and the olefin polymer was in contact with a much larger surface area of PA66. Hence, the olefin polymer can exist in finely dispersed conditions and exert a strong effect on improving the impact resistance properties. Meanwhile, the unmodified olefin polymer was in contact with a smaller surface area of PA66 because the unmodified polymer did not contain a functional group with strong affinity. Consequently, the distribution size became coarse, and a weak effect on improving the impact resistance was obtained.

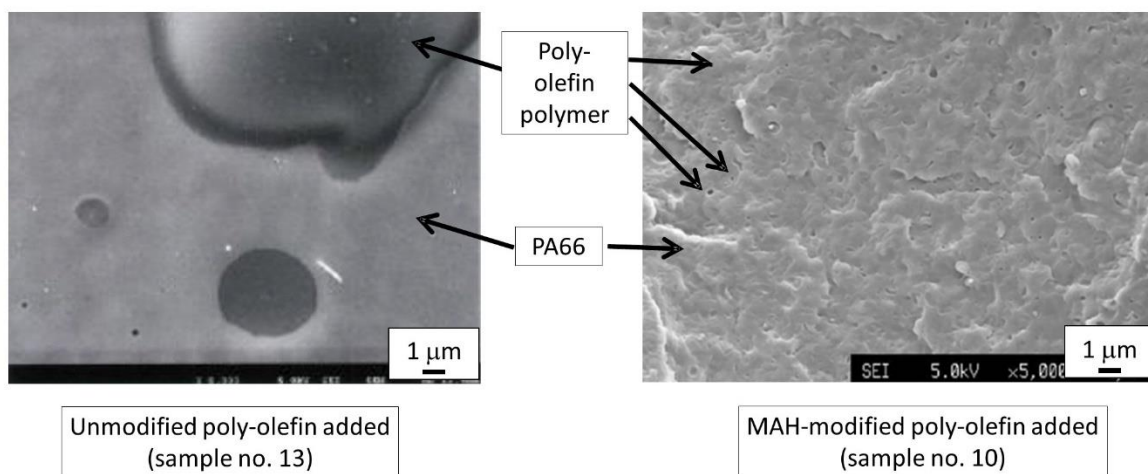


Fig. VII. 14 SEM images of the poly-olefin distribution.

The reactivity of the MAH-modified olefin polymer and carbodiimide compounds were verified using FT-IR analyses. Fig. VII. 15 shows the change in the FT-IR detected peak before and after heating the material at 260°C, temperature at which the olefin polymer was swelled by toluene and the powder of the carbodiimide compounds was penetrated. The results show that the strengths of the -COOH (carboxyl) peak at 1,710 cm^{-1} and the -CO-O-CO- (carboxylic acid anhydride) peak at 1,790 cm^{-1} , which are related to the structure of the MAH-modified olefin polymer, decreased with heating, as did the strength of the -NCN- (carbodiimide) peak at 2,120 cm^{-1} . The -NH-CO-NH- (urea) peak at 1,640 cm^{-1} and -NCO (isocyanate) peak at 2,260 cm^{-1} were newly detected. This was because the carboxyl functional group in the MAH reacted with the carbodiimide group and new chemical bond structures were obtained.

Hence, the PA66, carbodiimide, and MAH-modified olefin polymer reacted with each other, and the bonding at each interface was supposed to be strengthened. Consequently, it appears that synergistic effects for improving the toughness can be obtained, beyond those obtained by the addition of each ingredient individually.

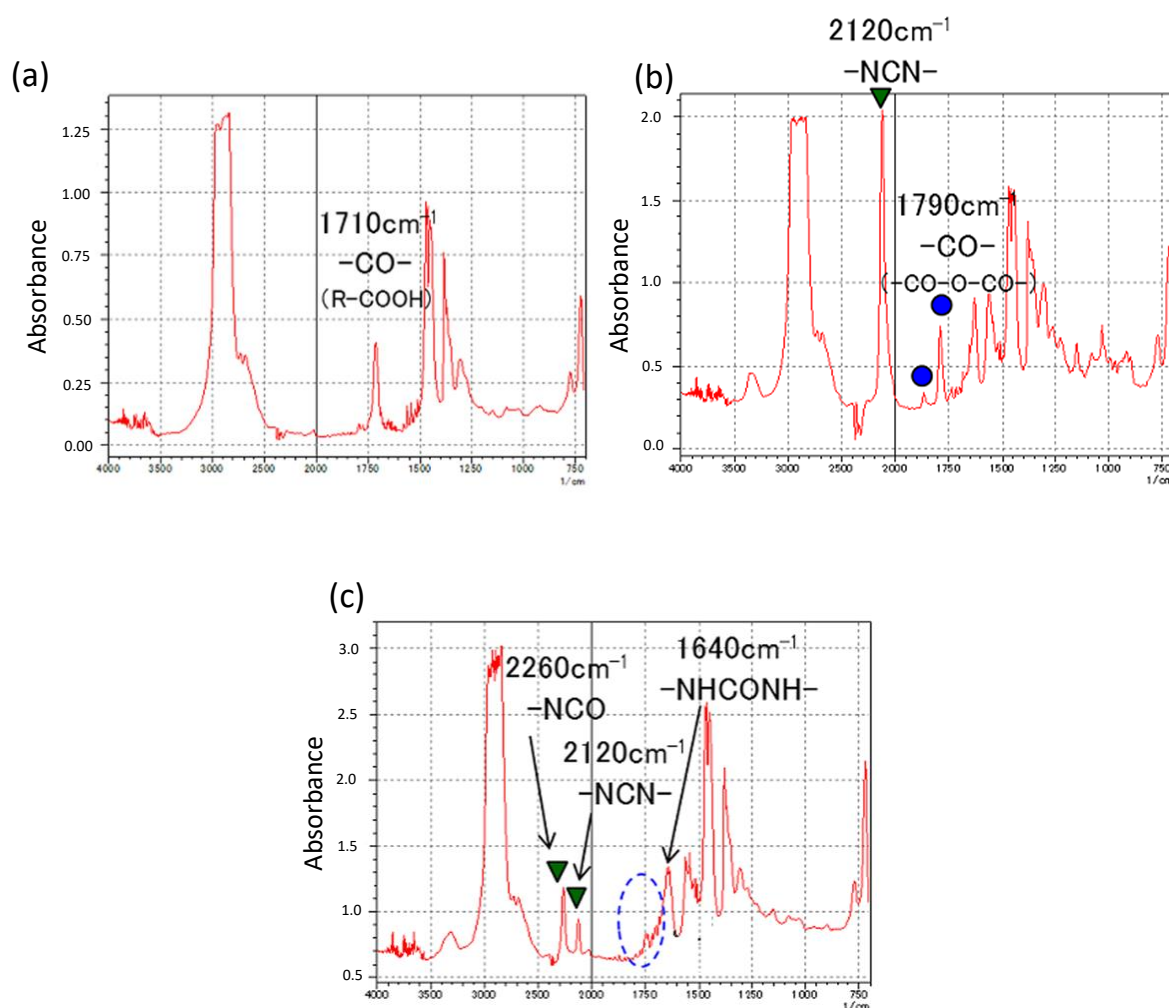


Fig. VII. 15 FT-IR spectra obtained before and after heating: (a) only poly-olefin polymer; (b) poly-olefin polymer with carbodiimide before heating; (c) poly-olefin polymer with carbodiimide after heating.

7. Conclusions

The reaction mechanism for a fiber-reinforced PA66 with added carbodiimide during extrusion was clarified, and the mechanical properties and tribological behavior were investigated. The following points have been highlighted.

1) Reactive extrusion mechanism and effect on the mechanical properties

Addition of carbodiimide compounds to GF-reinforced PA66 increases the molecular mass of the PA66 and improves the toughness. Using aromatic carbodiimide contributes to controlling the reaction velocity, allowing the carbodiimide to remain partially unreacted in the extruded pellets. In addition, a much higher toughness was obtained with side-feeding of

the carbodiimide compounds in the twin screw extruder, and therefore the toughness generally increased with increasing unreacted carbodiimide in the pellets.

2) Wear resistance of fiber-reinforced composite with added carbodiimide compound

The wear resistance of GF- or AF-reinforced PA66 materials under high contact pressure and grease-lubricated conditions is improved significantly by the addition of carbodiimide compounds and the increase in molecular mass.

3) Effect of the addition of carbodiimide compound and olefin polymer on the toughness of GF composite

Synergistic effects on the improvement in toughness were confirmed by adding both carbodiimide and a MAH-modified olefin polymer. The reason for these synergistic effects is suggested to be the reactions between PA66, carbodiimide, and the olefin polymer, which increased the interfacial strength between each component.

In Chapters VI and VII, the effect of the increase in the PA66 molecular mass on the improvement of the wear resistance of the GF composite and AF composite was confirmed. In addition to these materials, CF composites are well-known to be materials used for polymer sliding parts. In the next chapter, the tribological properties of the CF-reinforced PA66 under dry and grease lubricated conditions will be investigated, and it will be compared to those of the GF composite.

CHAPTER VIII

COMPARISON OF THE TRIBOLOGICAL PROPERTIES OF CARBON/GLASS FIBER-REINFORCED PA66-BASED COMPOSITES IN CONTACT WITH STEEL WITH AND WITHOUT GREASE LUBRICATION

**CHAPTER VIII: COMPARISON OF THE TRIBOLOGICAL PROPERTIES OF
CARBON/GLASS FIBER-REINFORCED PA66-BASED COMPOSITES
IN CONTACT WITH STEEL WITH AND WITHOUT GREASE
LUBRICATION**

1. Introduction.....	261
2. Tribological properties without lubrication.....	262
2.1 Fiber orientation on the ring specimen sliding surface.....	262
2.2 Tribological properties under dry conditions.....	264
3. Tribological properties under grease lubrication.....	270
4. Effects of the molecular mass on the tribological properties of the CF composite and steel counterpart.....	274
4.1 Wear and creep resistance of the composite with different values of PA66 molecular mass.....	274
4.2 Effect of PA66 molecular mass on the wear resistance of the counterpart steel ..	277
5. Effects of the hardness of the counterpart steel on the tribological properties.....	279
5.1 Effect of the hardness of the counterpart steel on the wear and creep resistance of the composite and wear resistance of the steel ..	279
5.2 Hardness of fibers and wear mechanism of steel counterpart.....	282
6. Differences in the temperature dependence of the tribological properties and tribochemistry between the CF and GF composites	286
6.1 Temperature dependence of the tribological properties of the CF composite and comparison to the GF composite	286
6.2 Discussion on the tribofilm formation and effect of zinc carboxylate	289
6.3 Effect of the contact pressure on the tribofilm formation and temperature dependence of the tribological properties.....	292
7. Conclusions.....	297

CHAPTER VIII: COMPARISON OF THE TRIBOLOGICAL PROPERTIES OF CARBON/GLASS FIBER-REINFORCED PA66-BASED COMPOSITES IN CONTACT WITH STEEL WITH AND WITHOUT GREASE LUBRICATION

In this chapter, the tribological mechanism of CF-reinforced PA66 composites in contact with a steel was investigated under both dry and grease lubricated conditions. The effects of the molecular mass of the PA66, the hardness of the counterpart steel, and the temperature on the tribological properties were studied under grease lubrication and compared to unreinforced and GF-reinforced PA66.

1. Introduction

In the previous chapters, the tribological properties of a GF-reinforced PA66 composite in contact with carbon steel under high contact pressure and grease lubricated conditions were mainly investigated, including the wear and creep occurrence mechanism, the effect of the temperature and tribochemistry, and the GF composite composition effect. In addition to GFs, CFs can be used as reinforcement fibers in engineering plastics and are widely used in various industries, as stated in Section 3.2.2 in Chapter I. Few studies have focused on the tribological properties of a CF-reinforced composite in contact with a metallic material particularly under grease or oil lubrication. This chapter focused on clarifying the tribological mechanism of CF-reinforced PA66 composites in contact with a steel counterpart, including the differences in the tribological properties of the CF composite under dry and grease lubrication. The effects of the molecular mass of PA66, hardness of the counterpart steel, and temperature on the tribological properties (wear and creep resistance of the composite and counterpart steel wear resistance) were studied under grease lubrication conditions, and the properties of unreinforced, CF-reinforced, and GF-reinforced PA66 were compared.

Table VIII. 1 lists the composition and mechanical/physical properties of evaluated polymer materials, and details for each material were explained in Chapter II. Table VIII. 2 lists the compositions of the greases used for sliding tests under grease lubrication. All the sliding tests (analyzed in Sections 2 to 5) were conducted using grease no. 1 (the detailed composition of the grease can be found in Section 2.3.1 in Chapter II). In addition, to elucidate the tribochemical reaction mechanism, a grease without zinc carboxylate (no. 2) was also evaluated, and it will be explained in Section 6. The effect of the steel cylinder hardness was also investigated in the range of the hardness measured through micro indentation (from 4.5 to 7.2 GPa), as explained in Section 2.2 in Chapter II.

Table VIII. 1 Compositions and mechanical/physical properties of evaluated GF composites.

No.	Level of PA66 molecular mass	Fiber type	Fiber fraction		Mechanical and physical properties		
			wt%	vol%	VN, ml/g	Density, g/cm ³	Tensile Young's modulus, GPa
1	Normal	CF	10	6.8	150	1.18	9.5 ± 0.6
2	High	CF	10	6.8	220	1.18	9.5 ± 0.7
3	Normal	GF	15	7.4	145	1.25	5.9 ± 0.3
4	High	GF	15	7.4	193	1.25	6.0 ± 0.4
5	Normal	GF	33	18.3	145	1.39	10.7 ± 0.3
6	Normal	-	-	-	145	1.14	3.0 ± 0.1

Table VIII. 2 Compositions of the evaluated greases.

No.	Base oil	Thickener	Low friction agent	Anti-oxidation agent
1	PAO8	Diurea	Zinc carboxylate	Sulfur type agent
2	PAO8	Diurea	-	Sulfur type agent

2. Tribological properties without lubrication

First, the tribological properties under dry conditions were investigated using the same contact geometry, as described in the previous chapters, to understand the differences in the tribological behavior of the unreinforced PA66 and fiber-reinforced composites with and without grease lubrication.

2.1 Fiber orientation on the ring specimen sliding surface

Before conducting the sliding tests, fiber orientation of the CF composite on the sliding surface was observed and compared to that of GF composite. The sliding surface of the new ring specimen (i.e., before sliding tests) using CF 10% composite (sample no. 1) was polished using #4,000 polishing paper, and three SEM images of the inner/center/outer positions were obtained at a magnification of ×300 in backscattered electron (BSE) mode. Fig. VIII. 1 shows the observations. Then, the image analysis was conducted in the way as presented in Section 3.1 in Chapter II, and compared to the analysis of GF 15% composite (no. 3) which was presented in Section 2.3 in Chapter III. The weight fraction of fibers was different between samples no. 1 and no. 3; however, the volume fraction of the fibers was similar (6.8% and 7.4%, respectively) because of the density difference of the GFs and CFs, as listed in Table VIII. 1. Fig. VIII. 2 shows a comparison of the calculated total area of the fibers on the surfaces of the CF 10% composite and GF 15% composite through image analysis. The average values of the GF 15% composite were generally higher than those of the CF 10% composite; however, no significant difference was observed after considering the standard deviation of the values. Fig. VIII. 3 shows the relationship between the circularity of the CFs and the cumulative frequency of the fiber area on the CF 10% composite surface, and the average value of C_{50} at different positions (C_{50} is the circularity value at which the cumulative CF area frequency is 50%). The results indicate that the circularity at the center position was much lower than that at the inner/outer positions. Namely, considerably more fibers at the center position were aligned

parallel to the sliding direction than those at the inner and outer positions, and more fibers at the inner and outer positions were aligned perpendicularly to the sliding direction. This same trend was observed in the GF composite, as presented in Section 2.3 in Chapter III.

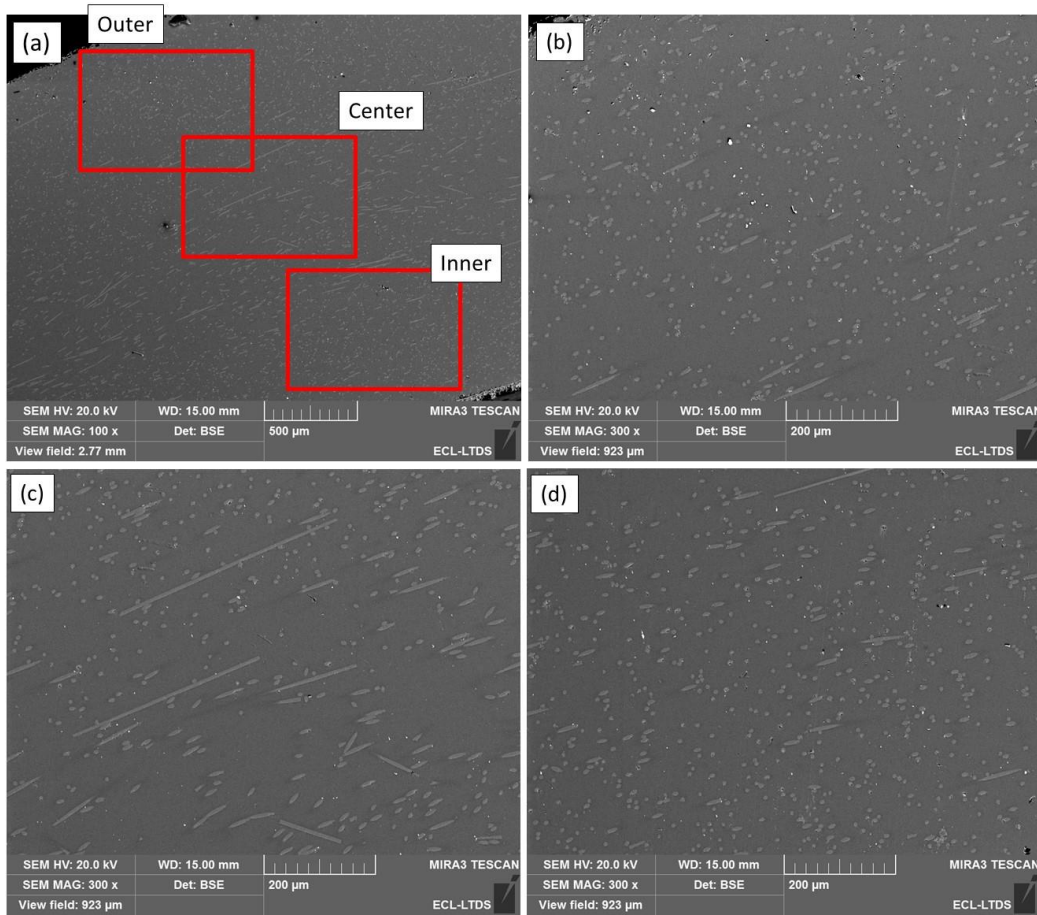


Fig. VIII. 1 SEM BSE images of the sliding surface of CF composite at different locations of the ring sliding test specimen: (a) global view; (b) inner position; (c) center position; (d) outer position.

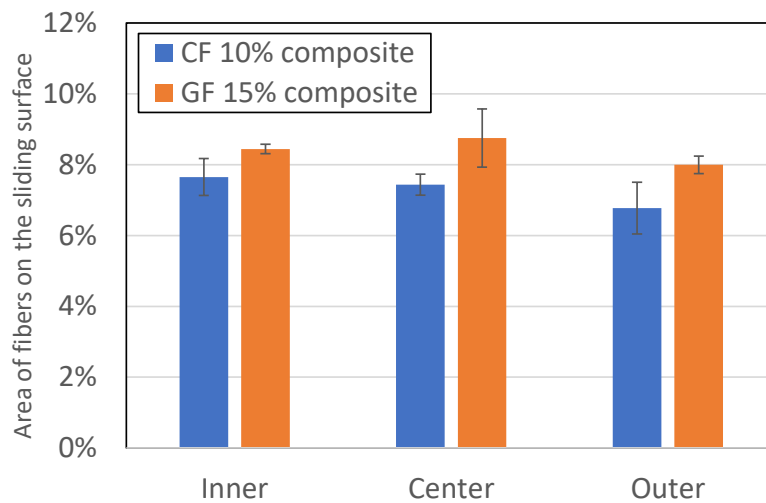


Fig. VIII. 2 Calculated total area of the fibers on the CF 10% composite (no. 1) and GF 15% composite (no. 3). Three measurements were conducted at each position.

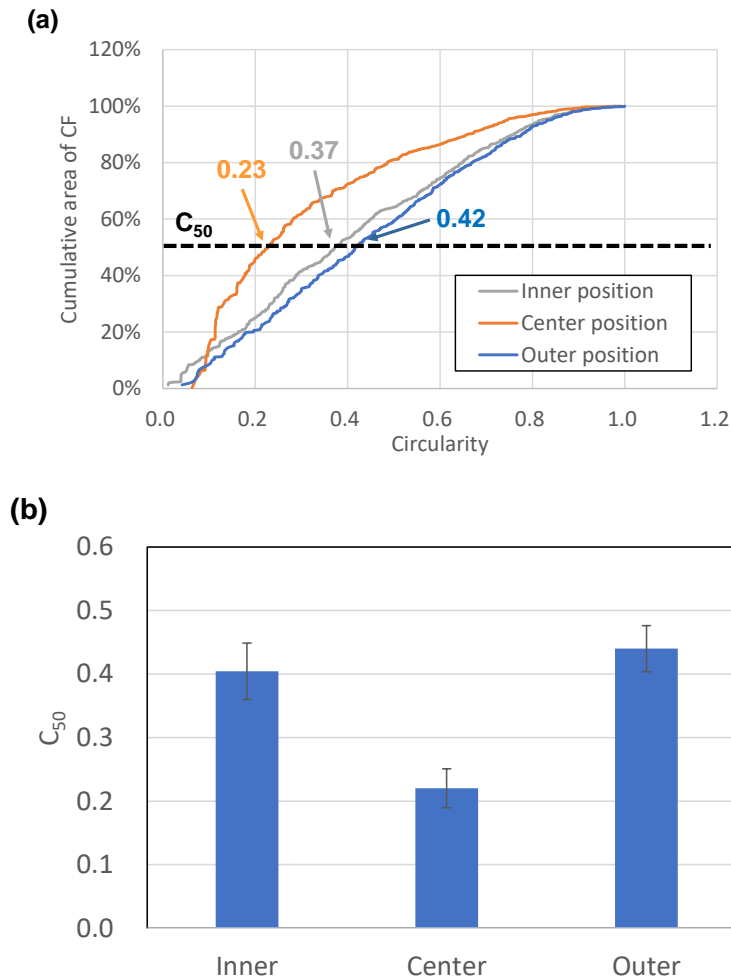


Fig. VIII. 3 (a) Examples of the relationship between the circularity of the CFs and the cumulative area of CF; (b) value of C_{50} at the different positions on the CF composite ring. Three measurements were conducted at each position.

2.2 Tribological properties under dry conditions

Tribological properties of the CF composite was investigated under dry conditions and compared to those of the GF composite and unreinforced PA66. Fig. VIII. 4 presents the evolutions of the friction coefficient, temperature, and vertical displacement of the PA66 composite with 10 wt% CF (sample no. 1), the PA66 composite with 15 wt% GF (no. 3), and the unreinforced PA66 (no. 6) under a normal load of 120 N and dry conditions using the steel cylinders with a hardness of 4.5 GPa; an intermittent process was used, i.e., sliding for 10 s followed by stopping for 1 s (this led to an increase in the contact temperature due to sliding heat generation, from room temperature to more than 100°C). Furthermore, because the Young's moduli differed between the materials, the initial Hertzian contact pressure was different: 140 MPa for the tests with the CF 10% composite, 112 MPa for the GF 15% composite, and 80 MPa for the unreinforced PA66 at room temperature. The sliding tests were conducted at least twice for each material under the same normal load. Fig. VIII. 5 and Fig. VIII. 6 present the optical microscope observations of the surface of the ring specimens and wear debris after the sliding tests, along with the weight, creep, and total height loss estimated using the method presented in Section 4.2.3 in Chapter II.

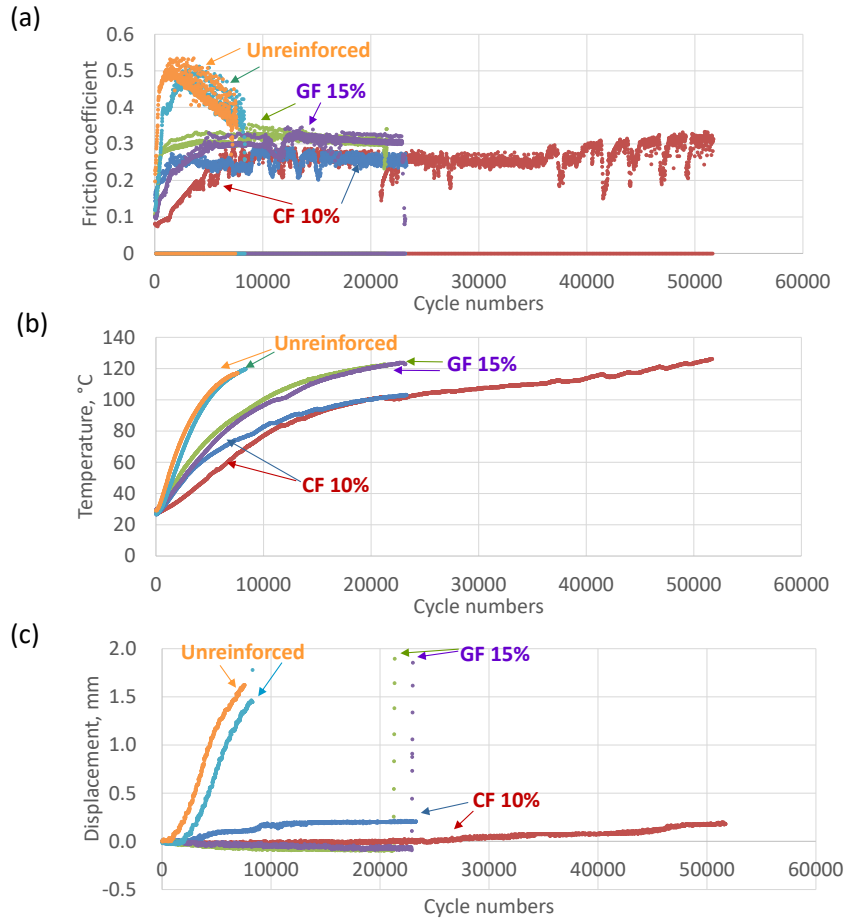


Fig. VIII. 4 Evolutions of the (a) friction coefficient, (b) temperature, and (c) vertical displacement during the sliding tests under dry conditions and a normal load of 120 N with sliding for 10 s followed by stopping for 1 s.

The friction coefficient in this test using the CF composite was lower than that of the GF composite. The average friction coefficient using the CF composite (up to 20,000 cycles) was 0.230 ± 0.055 , and that of the GF composite was 0.306 ± 0.025 (33.0% higher). In addition, the average friction coefficients using the CF and GF composites from 15,000 to 20,000 cycles (after each value became stable) were 0.256 ± 0.022 and 0.305 ± 0.010 , respectively. This indicates that the stabilized friction coefficient using the GF-reinforced composite was 19.4% higher than that of the CF-reinforced composite. High friction coefficient induces sliding heat generation and, thus, high temperature; the CF-reinforced composite exhibits a lower friction coefficient and temperature than the GF composite. A sudden large increase in the vertical displacement was observed in the GF composite at 21,000-23,000 cycles, and it was more closely related to the plastic deformation (creep) of the composite caused by the high friction coefficient, high temperature, and shear stress than the wear of the composite, considering that the composite ring lost very little weight and almost no wear debris was observed after 21,000-23,000 cycles. In contrast, a gradual increase in the vertical displacement caused by the wear was observed in the CF composite, while the sudden increase in the displacement (as observed in the GF composite) did not occur. Unlike the GF composite, 88% of the height loss was caused by wear, and only 12% was caused by creep, after 51,968 cycles. Wear debris was observed, which had an indefinite shape (including fibers). These results indicate that the CF composite did not have superior wear resistance compared to the GF composite under

these test conditions, despite its lower friction coefficient; however, the lower friction coefficient reduced the amount of heat generated and prevented the plastic deformation of the CF composite. In contrast, the friction coefficient and temperature of the unreinforced PA66 became higher than those of the GF and CF composites, and the rate of increase in the vertical displacement was also high. The difference in the temperature cannot be related to the difference in the thermal conductivity of evaluated materials because the difference in the thermal conductivity is negligible; 0.32 W/mK for the unreinforced PA66, 0.36 W/mK for the GF composite, and 0.34 W/mK for the CF composite. CF is known to exhibit high (10 W/mK) thermal conductivity [186]; however, short CFs have difficulty forming a thermal conductive pass inside the molding compact. Therefore, the difference in temperature evolution is not related to the difference in thermal conductivity but it is related to the difference in the friction coefficient. The generation of fibrous wear debris was observed, and the sudden increase in the displacement related to the creep (plastic deformation) was observed after 8,300 cycles. This indicates that the addition of the reinforcement fibers reduced the friction and improved the tribological properties, and the diminishing effect of the friction coefficient in the CF composite was much larger than that in the GF composite under the dry test conditions in this contact geometry (leading to less creep).

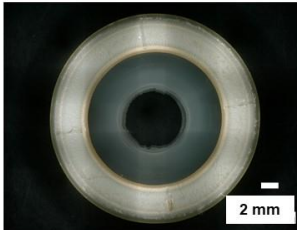
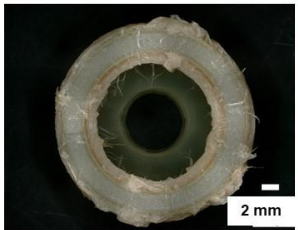
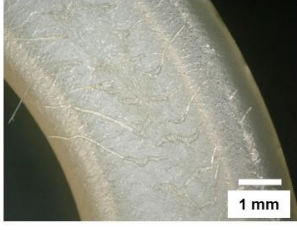

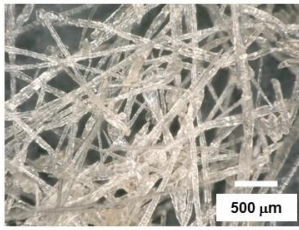
	Unreinforced PA66 7,575 cycles (before sudden increase in the displacement)	Unreinforced PA66 8,332 cycles (after sudden increase in the displacement)
Entire ring surfaces		
Magnified ring images		
Wear debris		
Wear height loss	0.934 mm	0.987 mm
Creep height loss	0.716 mm	1.575 mm
Total height loss	1.650 mm	2.562 mm

Fig. VIII. 5 Optical microscope observations of the ring specimens and wear debris, and the wear/creep/total height loss of the unreinforced PA66 after 7,575 and 8,332 cycles of the sliding tests under dry conditions and a normal load of 120 N.


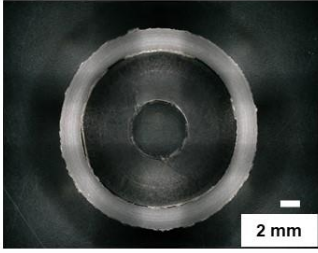
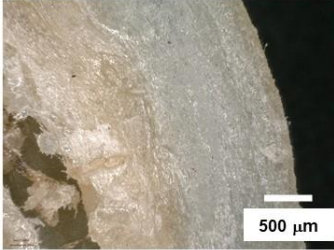
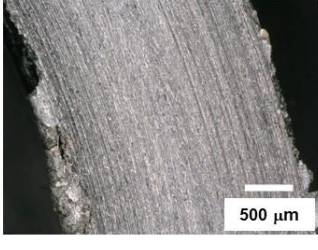
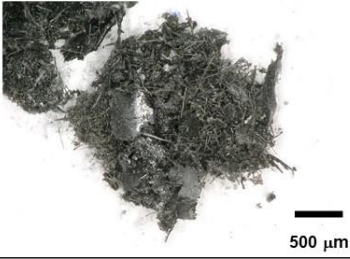
	GF 15% composite 21,528 cycles	CF 10% composite 51,968 cycles
Entire ring surfaces		
Magnified ring images		
Wear debris	Almost no wear debris	
Wear height loss	0.050 mm	0.255 mm
Creep height loss	3.178 mm	0.023 mm
Total height loss	3.228 mm	0.278 mm

Fig. VIII. 6 Optical microscope observations of the ring specimens and wear debris, and the wear/creep/total height loss of the GF 15% composite after 21,528 cycles, and CF 10% composite after 51,968 cycles of the sliding tests under dry conditions and a normal load of 120 N.

Fig. VIII. 7 presents the optical microscope observations of the steel cylinders after testing for 7,575 cycles with the unreinforced PA66, 21,528 cycles with the GF 15% composite, and 23,249 cycles with the CF 10% composite under the same test conditions, and wear amount of steel cylinder. The steel cylinders were washed using an ultrasonic bath with a heptane solvent before the observations. The sliding surface was brown after testing with the GF composite, and black wear debris was attached to the edge of the sliding surface after testing with the CF composite; in contrast, explicit wear scars and the attachment of wear debris were not observed after testing with the unreinforced PA66. The wear volume of the steel cylinder tested with the CF composite was higher than that of the cylinder tested with the GF composite.

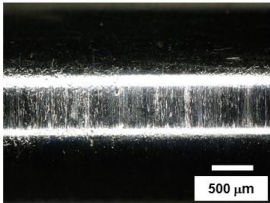
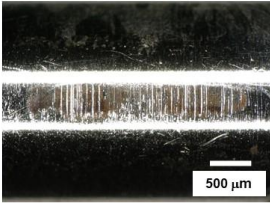
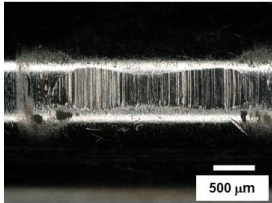
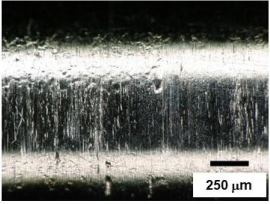
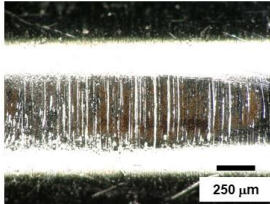
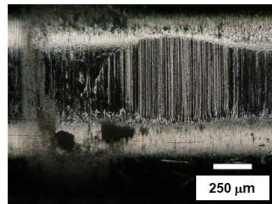
Magnification	Tested with unreinforced PA66 for 7,575 cycles	Tested with GF composite for 21,528 cycles	Tested with CF composite for 23,249 cycles
x100			
x200			
Wear volume via interferometry	-	0.0097 mm ³	0.0313 mm ³

Fig. VIII. 7 Optical microscope observations of the steel cylinder surface after the sliding tests.

Fig. VIII. 8 shows the SEM observations and SEM-EDX analysis of the cylinder tested with the GF composite or CF composite. Severe wear scars in the sliding direction, which are generally caused by two-body abrasive wear, were observed on the surface of both steel cylinders. In addition, some dark patches were observed on the surface of the cylinder tested with the GF composite; they were composed of carbon and oxygen, indicating that they originated from the PA66 and silicon (which was present in the GFs). Therefore, portions of the GF composite were strongly adhered to the steel sliding surface even after the ultrasonic washing. Carbon was detected via SEM-EDX analysis on the sliding surface of the CF composite test cylinder and the edge of the wear scar. Therefore, the CF composite also adhered to the steel surface. This indicates that the wear mode of both composites under dry conditions was adhesive wear.

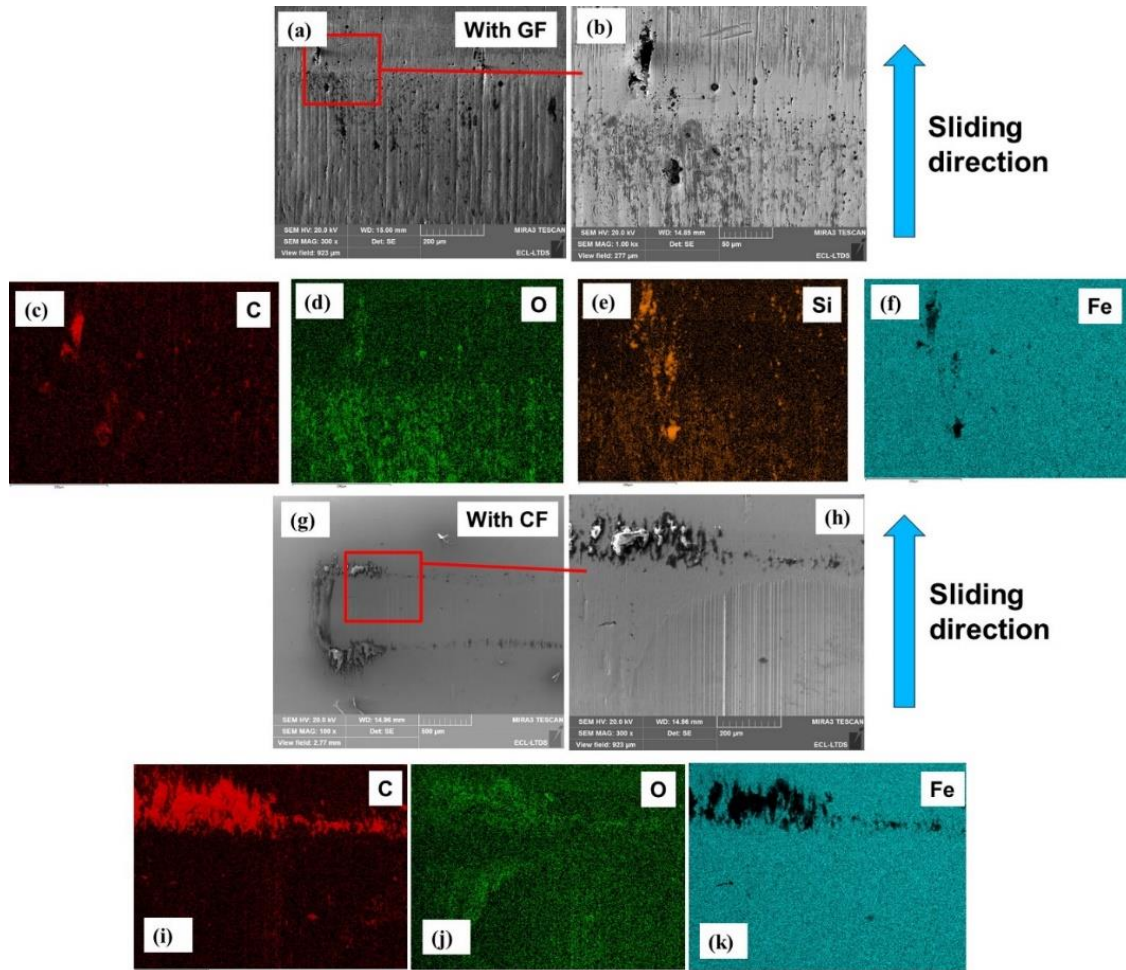


Fig. VIII. 8 (a) and (b) SEM observations of the steel cylinder tested with the GF composite after 21,528 cycles; (c)-(f) SEM-EDX images of the carbon, oxygen, silicon, and iron content at the same location as the SEM image in (b); (g) and (h) SEM observations of the steel cylinder tested with the CF composite after 23,249 cycles; and (i)-(k) SEM-EDX images of the carbon, oxygen, and iron content at the same location as the SEM image in (h).

The low friction characteristics of the CF-reinforced composite under dry conditions compared to GF composites and unreinforced PA66 were reported in several previous works [80, 99, 100, 103]. The wear mode of the polymer under dry conditions is explained primarily as adhesive wear, and the friction coefficient and wear behavior of the polymer are strongly affected by the formation of a transfer film on the metallic surface. This transfer film prevents adhesion between the polymer and metallic surface and reduces the plowing action of metallic asperities on the soft polymer surface [102]. In addition, under dry conditions, the reinforcement fibers contribute significantly to the reduction in the adhesive effect by reducing the real contact area between the metallic surface and polymeric surface. CF is a graphitized carbon with the hexagonal planes of its crystals aligned perpendicular to the fiber axis. The lubricating function of the graphitized carbon, in which the graphite debris form a thin lubrication film on the counterpart, is thought to be responsible for the reduction in the friction coefficient when CF composites slide against steel [77, 101]. Therefore, a larger reduction in the friction coefficient results in a smaller temperature increase and the smaller wear amount in the CF composite compared to the GF composite is attributed to the formation of a low friction transfer film on the counterpart steel.

In summary, the CF composite exhibited better tribological properties even under a higher contact pressure than the unreinforced PA66 or GF-reinforced PA66 composite when sliding in contact with the carbon steel under dry conditions. In addition, wear of the steel counterpart when tested with the CF composite was higher than that tested with GF composite.

3. Tribological properties under grease lubrication

Sliding tests using the GF 15% composite (no. 3) under grease lubrication were conducted with a normal load of 120 N (the same load that was used for the dry conditions presented in Section 2); however, no change in the vertical displacement (wear or creep of the composite) was observed, even after 1,200,000 cycles, as presented in Fig. VIII. 9.

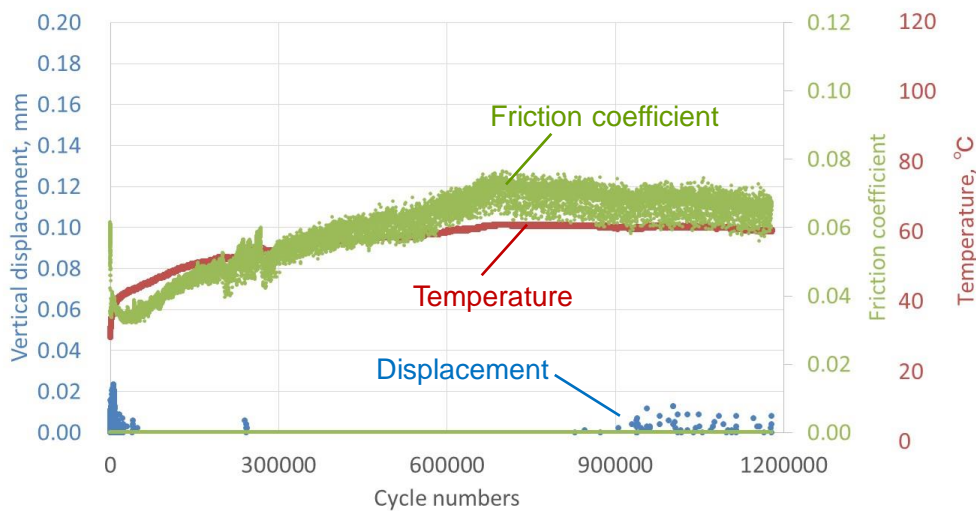


Fig. VIII. 9 Evolutions of the friction coefficient, temperature, and vertical displacement of the GF 15 % composite during the sliding test under grease lubrication and a normal load of 120 N with sliding for 10 s followed by stopping for 1 s.

For comparison, severe plastic deformation of the GF composite was observed after just 21,000-23,000 cycles under dry conditions and the same contact pressure, as presented in Fig. VIII. 4. Therefore, the grease lubrication improved the durability of the GF composite by a factor of at least 60. To compare the difference in the wear and creep resistance of the composite under grease lubrication, sliding tests with a higher normal load (350 N) were conducted (the same test conditions as used in Chapters III and VI).

Fig. VIII. 10 presents the evolutions of the friction coefficient, temperature, and vertical displacement for a normal load of 350 N under grease lubrication (during the initial 10,000 cycles and the entire test) using the same materials that were used in Section 2. The Hertzian contact pressure, calculated using Young's modulus at room temperature was 238 MPa for the CF 10% composite, 191 MPa for the GF 15% composite, and 136 MPa for the unreinforced PA66. Sliding tests were conducted at least twice for each material.

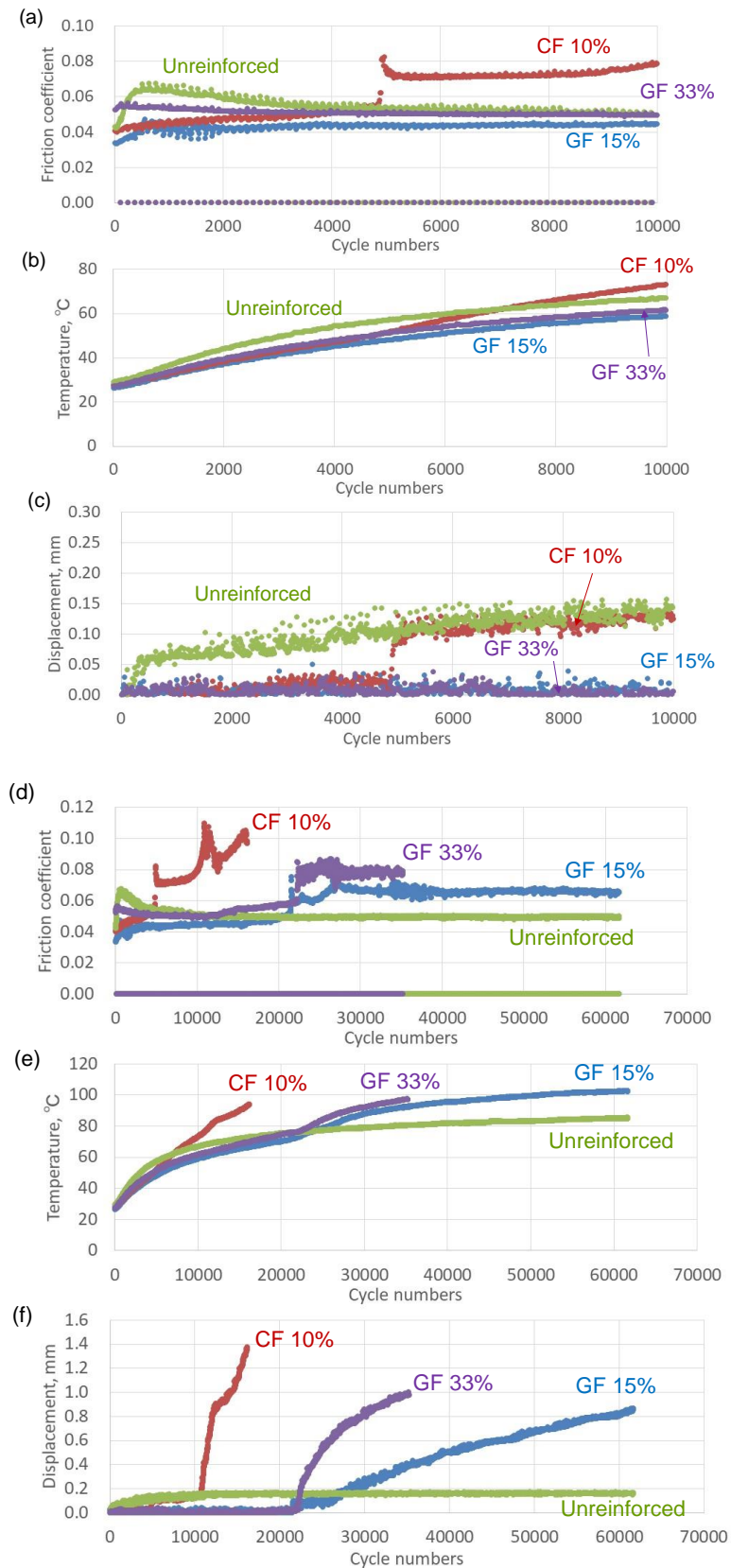


Fig. VIII. 10 Evolutions of the (a) friction coefficient, (b) temperature, and (c) vertical displacement during the first 10,000 cycles, and the (d) friction coefficient, (e) temperature, and (f) vertical displacement during the entire duration of the sliding tests under grease lubrication and a normal load of 350 N.

Completely different tribological properties were observed under grease lubrication compared to those observed under dry conditions (which were dominated by adhesion). During the initial 5,000 cycles, the friction coefficient, temperature, and vertical displacement of the unreinforced PA66 exhibited higher values than those of the GF- or CF-reinforced composites. However, sudden increases in the vertical displacement and the friction coefficient were observed in the fiber-reinforced composites, as described in Section 2.1 in Chapter III. Unlike under dry conditions, the tribological properties of the CF 10% composite were poorer than those of the GF 15% composite; the sudden increases in the friction coefficient and the vertical displacement occurred earlier for the CF 10% composite, and the rate of the increase in the displacement was higher. The volume fraction of fibers in the GF 15% composite and CF 10% composite was similar, while the Young's modulus of the CF 10% composite was higher than that of the GF 15% composite. Therefore, the higher Young's modulus and contact pressure of the CF 10% composite might induce the deterioration in the tribological properties. Thus, a sliding test with the GF 33% composite (no. 5), which had a Young's modulus (10.7 GPa) similar to the one of the CF 10% composite (9.5 GPa), was also conducted to compare the tribological properties under similar contact pressures, as presented also in Fig. VIII. 10. The Hertzian contact pressure of the GF 33% composite at room temperature was 252 MPa, which was slightly higher than that of the CF composite. The sudden increase in the vertical displacement in the GF 33% composite (10,000-21,000 cycles) occurred earlier than in the GF 15% composite (19,000-23,000 cycles), and the rate of the increase in the displacement was higher (confirming the effect of the contact pressure). Nevertheless, the sudden increase in the vertical displacement in the GF 33% composite still occurred later than it did in the CF 10% composite (9,000-11,000 cycles), and the rate of the increase in the vertical displacement and absolute value of the displacement in the GF 33% composite were lower than those in the CF 10% composite. This indicates that the tribological properties of the CF composite were also poorer than those of the GF 33% composite, even under a similar contact pressure. The wear mode of the composite under dry conditions was adhesive wear, and the addition of the CFs prevented the adhesion to the steel counterpart and provided lubrication. However, the effect of adhesion was weak under grease lubrication because direct contact between the PA66 and steel counterpart was prevented, and low friction was ensured by the grease, not by the presence of fibers. Then, the advantage of CF addition was lost, and effect of two-body abrasive wear which was observed in the GF composite is supposed to become severe in CF composite also.

Fig. VIII. 11 presents the optical microscope observations of the sliding surface of the ring specimens and the wear/creep/total height loss of the ring specimens estimated using the method explained in Section 4.2.3 in Chapter II. In contrast to dry conditions, the height loss due to wear of the unreinforced PA66 was relatively small, and 75% of the total height loss was due to creep. No severe wear on the sliding surface was observed. However, for the CF and GF composites, entire sliding surface was severely damaged and wear and creep were very important. CF composite was more damaged than GF composites. The damage mode of the GF composite, which is two-body abrasive wear related to peeled fibers that detach and scratch the PA66, was reported in Section 4 in Chapter III, and the same wear mode was observed for the CF composite, including the exposure of fibers (peeling) on the sliding surface. To understand the difference in the tribological properties between the GF composite and CF composite under grease lubrication more deeply, the effect of the PA66 molecular mass, hardness of the steel counterpart, and temperature were investigated in the following sections.

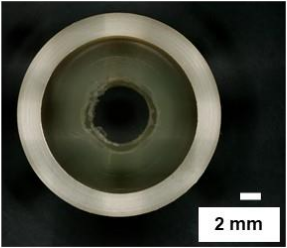
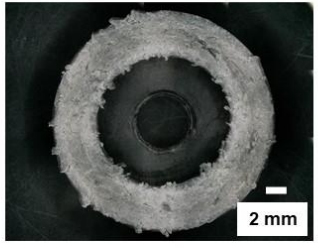
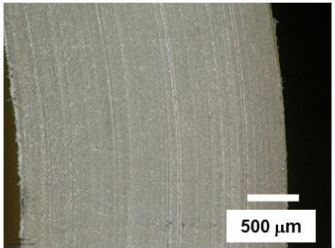
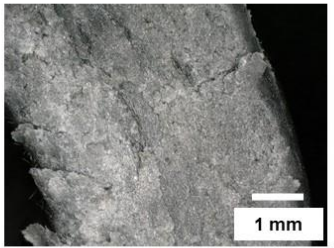
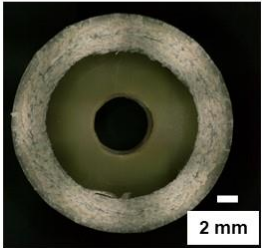
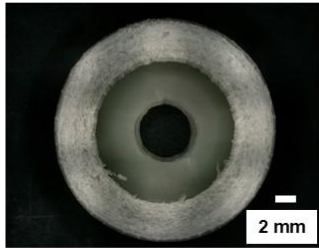

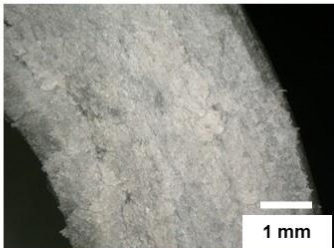
	Unreinforced PA66 after 61,704 cycles	CF 10% composite after 16,186 cycles
Entire sliding surface		
Magnified image		
Wear height loss	0.023 mm	0.501 mm
Creep height loss	0.062 mm	0.765 mm
Total Height loss	0.085 mm	1.266 mm
	GF 15% composite after 61,665 cycles	GF 33% composite after 35,242 cycles
Entire sliding surface		
Magnified image		
Wear height loss	0.575 mm	0.521 mm
Creep height loss	0.242 mm	0.465 mm
Total Height loss	0.817 mm	0.986 mm

Fig. VIII. 11 Optical microscope observations of the sliding surface and the wear/creep/total height loss after the sliding tests.

4. Effects of the molecular mass on the tribological properties of the CF composite and steel counterpart

The effects of the PA 66 molecular mass on the tribological properties of the CF-reinforced PA66 composite / steel contact were investigated.

4.1 Wear and creep resistance of the composite with different values of PA66 molecular mass

Fig. VIII. 12 presents the evolutions of the friction coefficient, temperature, and vertical displacement for composites containing PA66 with different molecular masses (indicated by VN) and 10% CF (samples no. 1 and no. 2) under a normal load of 350 N and sliding for 10 s followed by stopping for 1 s using the steel cylinder with a hardness of 4.5 GPa. The sudden increases in the displacement occurred later with the higher molecular mass CF composite. In addition, the rate of the increase in temperature was reduced owing to the lower friction coefficient.

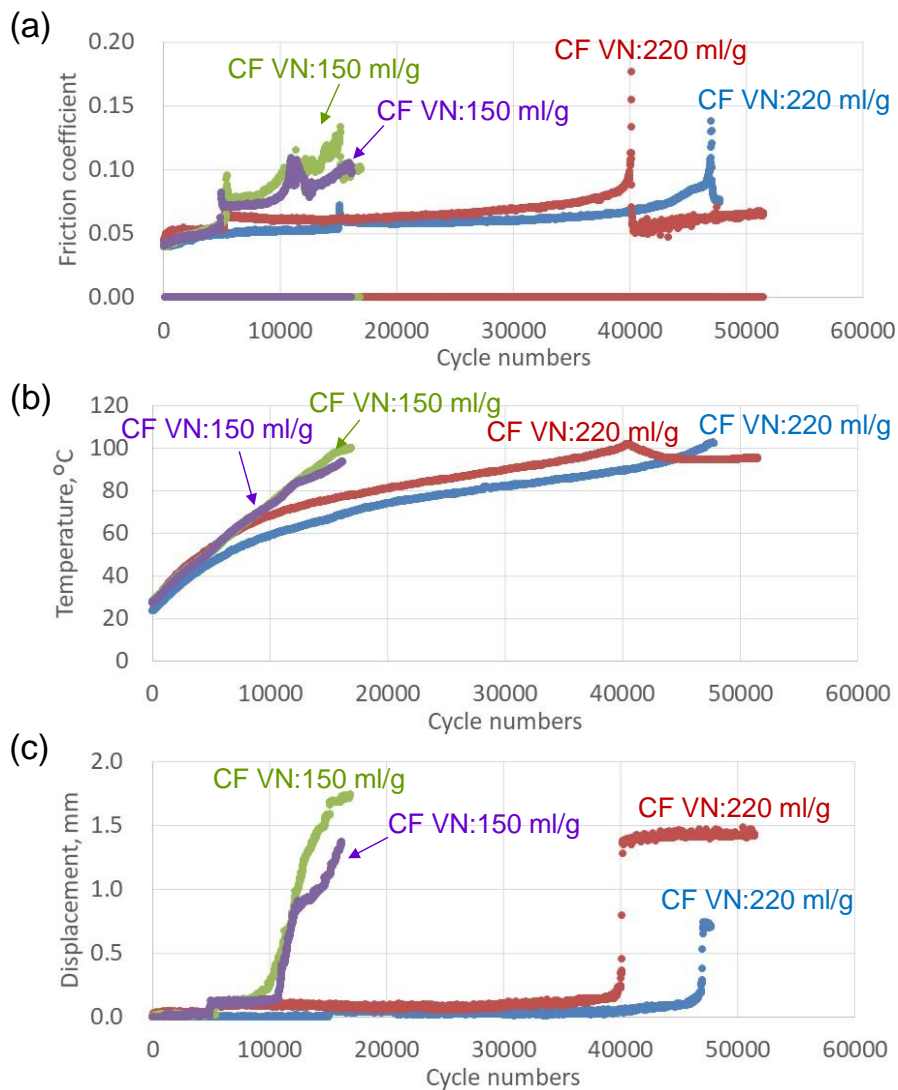


Fig. VIII. 12 Evolutions of the (a) friction coefficient, (b) temperature, and (c) vertical displacement with the composites containing PA66 with different molecular masses (VN) and 10% CF.

To clarify the effect of the PA66 molecular mass in the CF 10% composite on the tribological properties, the sliding tests were stopped intentionally after 10,946 cycles (just before the sudden increase in the vertical displacement for sample no. 1) using both composite samples, and the sliding surfaces of the composites were observed. Fig. VIII. 13 presents the optical microscope observations of the sliding surfaces of the composite rings with different molecular masses (VNs) after 10,946 cycles (samples no. 1 and no. 2). The composite with a VN of 150 ml/g exhibited partial peeling in the center region of the surface, as well as the exposure of the reinforcing CFs. In contrast, severe damage, including peeling of the surface or fiber exposure, was not observed on any part of the sliding surface of the CF composite with a VN of 220 ml/g, even when the sliding surface underwent the same number of contacts.

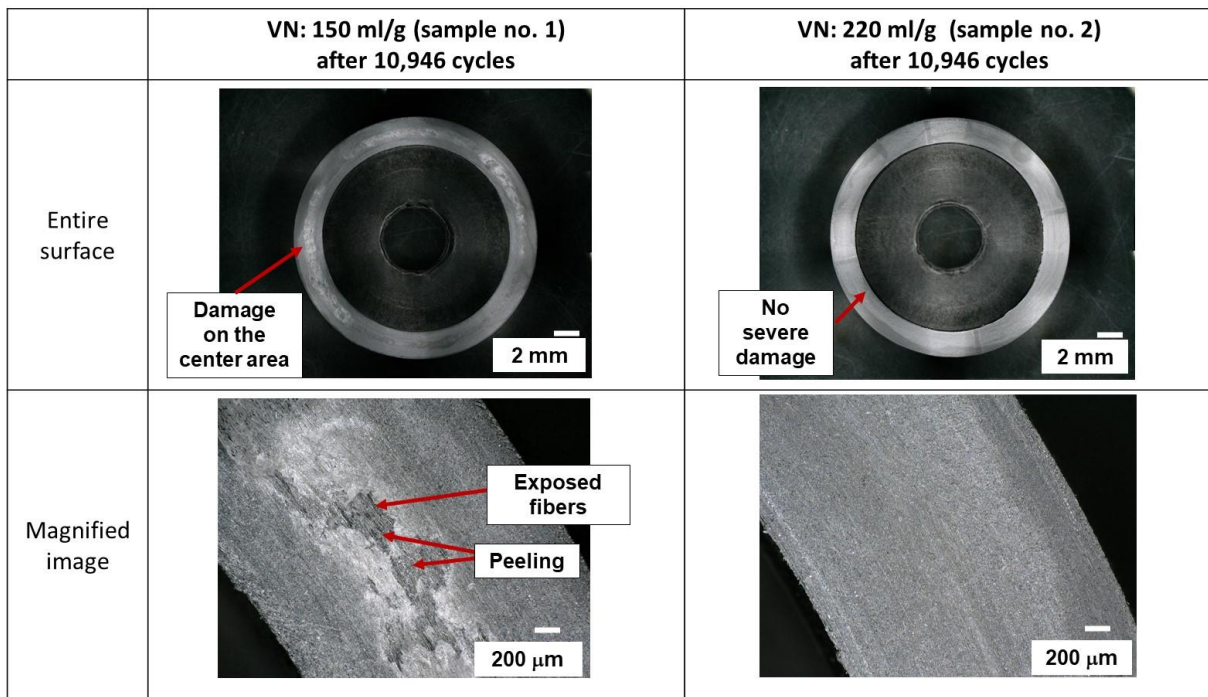


Fig. VIII. 13 Optical microscope observations of the sliding surfaces of the CF composites with different PA66 molecular masses (VNs) after 10,946 cycles (samples no. 1 and no. 2).

Fig. VIII. 14 shows a comparison of the evolutions of the friction coefficient, temperature, and vertical displacement between the CF and GF composites with higher molecular mass PA66 (samples no. 2 and no. 4, respectively) in the same conditions. The average value of the friction coefficient during the initial 40,000 cycles using the high molecular mass GF composite was 0.0419 ± 0.0007 , and that of the high molecular mass CF composite was 0.0561 ± 0.0059 . Therefore, the friction coefficient for the CF composite was 33.9% higher than that for the GF composite. The sudden increases in the vertical displacement and the friction coefficient were observed after 40,000-47,000 cycles for the high molecular mass CF composite. In contrast, no marked increase in the friction coefficient and the vertical displacement was observed until 81,000 cycles for the high molecular mass GF composite. Therefore, the CF composite also demonstrated inferior tribological properties compared to the GF composite under grease lubrication for the composites with high molecular mass PA66. The reason the GF composite exhibited better tribological properties than the CF composite will be explained in Section 5.

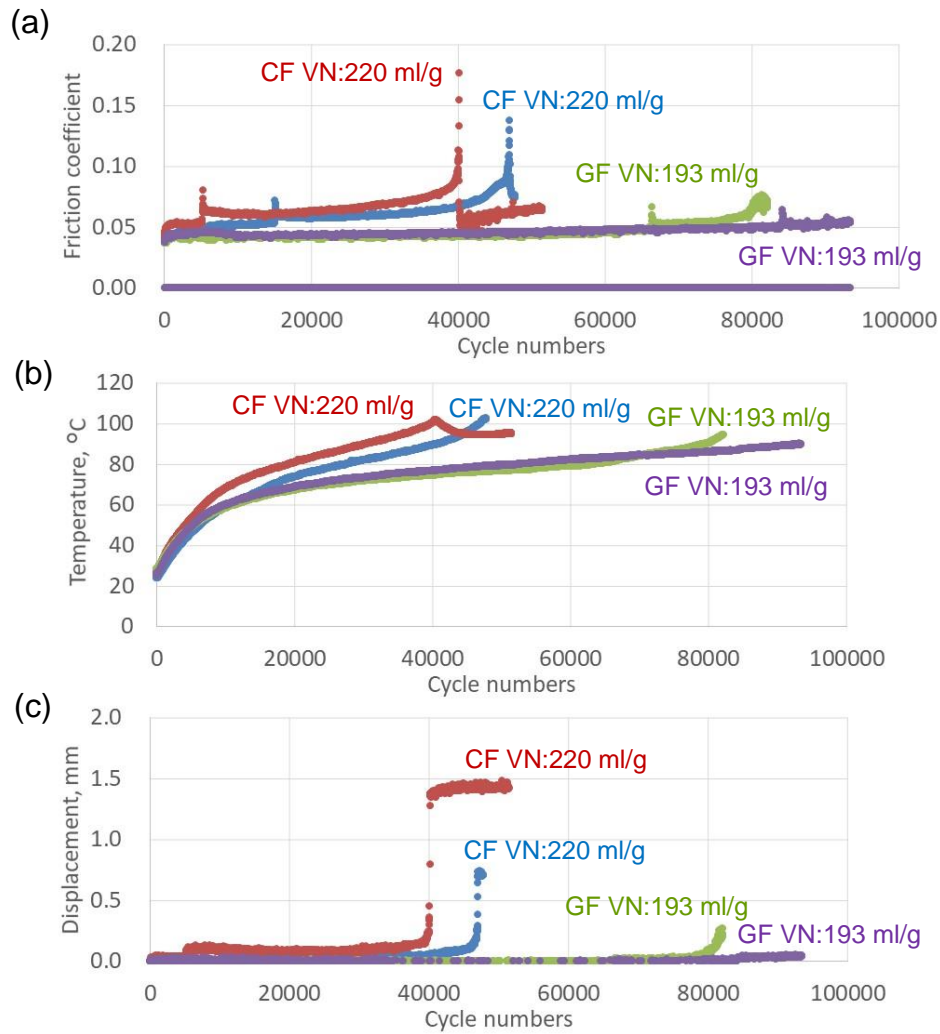


Fig. VIII. 14 Evolutions of the (a) friction coefficient, (b) temperature, and (c) vertical displacement with GF 15% composite and CF 10% composite with the high molecular mass.

The observations of the sliding surfaces of the composites and the wear/creep/total height loss are shown in Fig. VIII. 15. All of the sliding surfaces are severely damaged, and peeling of the surface and fiber exposure are observed. Sliding surface of the CF composite seems to have more damage than that of the GF composite despite shorter sliding cycle numbers. This tendency coincides with the actually measured wear and creep of the composite.

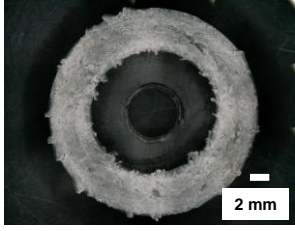
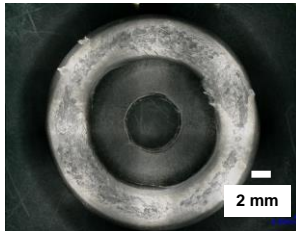
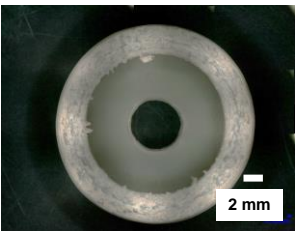
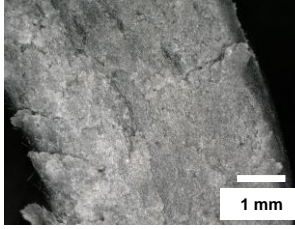
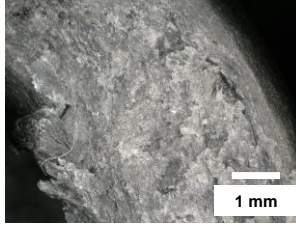
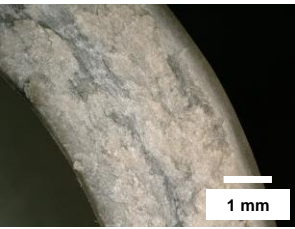
	CF composite VN: 150 ml/g after 16,186 cycles	CF composite VN: 220 ml/g after 51,497 cycles	GF composite VN: 193 ml/g after 93,440 cycles
Entire surface			
Enlarged image			
Wear height loss	0.501 mm	0.236 mm	0.083 mm
Creep height loss	0.765 mm	1.265 mm	0.154 mm
Total height loss	1.266 mm	1.501 mm	0.237 mm

Fig. VIII. 15 Sliding surfaces of the composite rings with different fibers and PA66 molecular masses after the sliding test under a normal load of 350 N with sliding for 10 s followed by stopping for 1 s, along with the corresponding wear/creep/total height loss.

4.2 Effect of PA66 molecular mass on the wear resistance of the counterpart steel

The effect of the PA66 molecular mass on the wear resistance of steel counterpart was also investigated. Fig. VIII. 16 shows the relationship between number of cycles and wear volume of the steel cylinders (total wear volume of the four steel cylinders) tested with the CF 10% composites with different PA66 molecular masses. The wear volume of the counterpart steel was significantly lower throughout cycling when the high molecular mass CF composite was used. This result shows that increasing the molecular mass of the CF composite can improve not only the wear resistance of the CF composite but also the wear resistance of the steel counterpart, and the wear of the steel counterpart is not determined solely by the fiber hardness. Fig. VIII. 17 shows the optical microscope and interferometer observations (3D images after the removal of the cylindrical shape, and central 2D profile) of the steel cylinders tested with the CF 10% composite with different PA66 molecular masses after different numbers of cycles. Unlike the steel cylinders tested under dry conditions, no adhesion of the wear debris nor change in the color on the steel cylinder surface was observed, and wear scratches in the sliding direction, which generally come from two-body abrasive wear (as observed with the GF composite), were observed. When the CFs were oriented in the perpendicular direction (relative to the sliding direction), the number of edges of the fibers, which are considered to have more destructive effects on the steel, was higher than when the CFs were oriented in the parallel direction. This can explain why the wear of the steel where

it was in contact with the inner or outer area of the composite ring can be larger than that in contact with the center area, as presented in Fig. VIII. 17 (after 10,946 cycles).

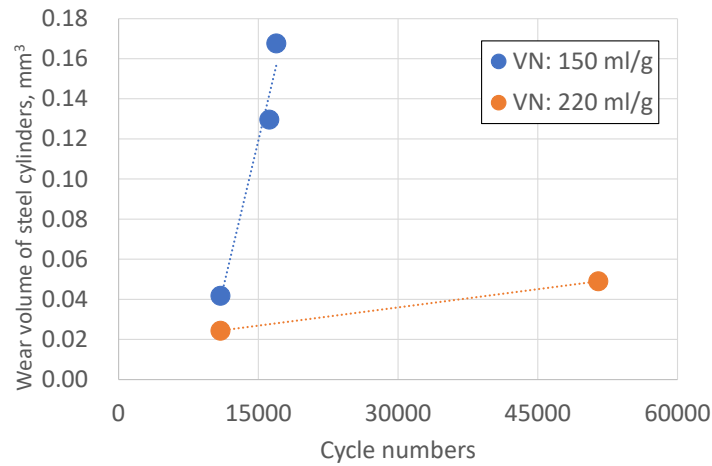


Fig. VIII. 16 Relationship between number of cycles and wear volume of the steel cylinders (total wear volume of the four steel cylinders) tested with the CF 10% composites with different PA66 molecular masses.

	VN: 150 ml/g (sample no. 1) after 10,946 cycles	VN: 220 ml/g (sample no. 2) after 10,946 cycles	VN: 150 ml/g (sample no. 1) after 16,186 cycles
Optical microscope images			
3D interferometer images			
2D profiles			
Wear volume	0.0418 mm ³	0.0244 mm ³	0.1297 mm ³

Fig. VIII. 17 Optical microscope and interferometer observations (3D images after the removal of the cylindrical shape, and central 2D profiles) of the steel cylinder tested with the CF 10% composites with different PA66 molecular masses after different numbers of cycles.

These improving effects on the tribological properties by increasing PA66 molecular mass were also observed in GF composite, as presented in Section 3 in Chapter VI. Therefore, this difference can be explained by the difference in the toughness due to the different molecular masses of the PA66, as explained in the case of GF composite. A high molecular mass (VN) of the PA66 led to a high toughness (high values of the elongation at break), whereas the Young's modulus and tensile strength did not change significantly with the molecular mass of the PA66. These results explain why a higher molecular mass of the PA66 in the CF composite can decrease the wear and creep of the composite as well as the wear of the steel cylinders. By using PA66 with a high molecular mass (therefore a high toughness), the PA66 can follow the

deformation through the shear stress due to sliding in the weakest interfaces between the PA66 and CFs. Therefore, the scratching of the PA66 that originated from the weakest interface between the PA66 and CFs becomes hard to initiate and propagate, and the wear and creep of the composite can be reduced. In addition, the higher interfacial shear strength prevents the exposure of the gap between the PA66 and CFs, which has more destructive effects on the counterpart steel, and the two-body abrasive wear of the steel counterpart can be reduced. Fig. VIII. 18 summarizes the differences in the sliding of the steel and CF composites with different PA66 molecular masses.

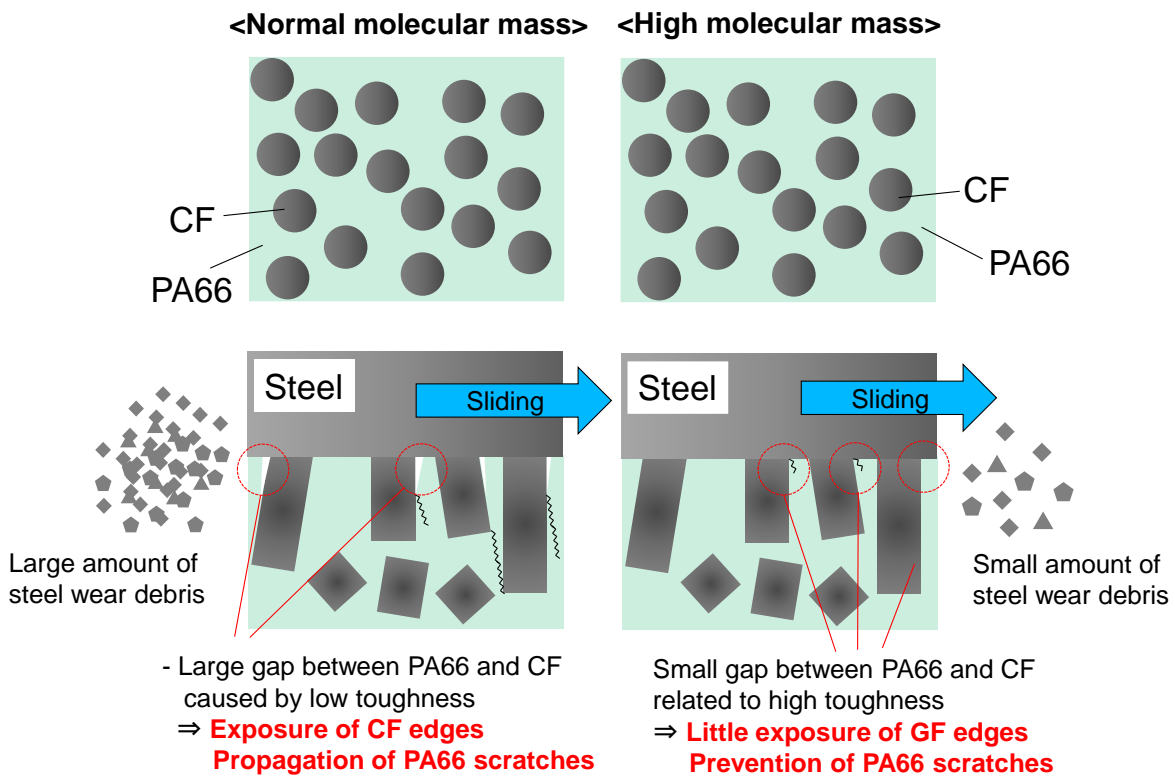


Fig. VIII. 18 Schematics of the differences in the sliding of the steel and CF composites with different PA66 molecular masses.

5. Effects of the hardness of the counterpart steel on the tribological properties

The effect of the hardness of the counterpart steel on the tribological properties was also investigated.

5.1 Effect of the hardness of the counterpart steel on the wear and creep resistance of the composite and wear resistance of the steel

Fig. VIII. 19 presents the effect of the hardness of the counterpart steel on the wear and creep height loss of the composite as well as the wear volume of the steel cylinder measured via interferometry for a normal load of 220 N (lower than the conditions presented in Sections 3 and 4) after 61,700 cycles (sliding for 10 s followed by stopping for 20 s) under grease lubrication using the CF 10% composite (no. 1) and GF 15% composite (no. 3). The Hertzian contact pressure at room temperature was 189 MPa for the CF 10% composite and 151 MPa

for the GF 15% composite. As the hardness of the steel increased, the wear of the composite increased and the wear of the steel decreased. This trend coincides with that observed in GF composite for a normal load of 350 N as presented in Section 5 in Chapter III, and it was explained by the relationship between the relative hardness of the steel and GFs; using steel with a hardness lower than the hardness of the GFs increased the wear of the steel counterpart, whereas the wear of the GF composite decreased. The wear and creep of the CF composite were higher than those of the GF composite regardless of the steel hardness; this is the same trend observed in the results from the tests with a normal load of 350 N (as explained in Sections 3 and 4). In addition, the steel wear decreased as the steel hardness increased, and the steel wear was 4.5 to 67 times higher when tested using the CF composite than it was when tested using the GF composite. This trend completely differs from the other works presented in Chapter I.

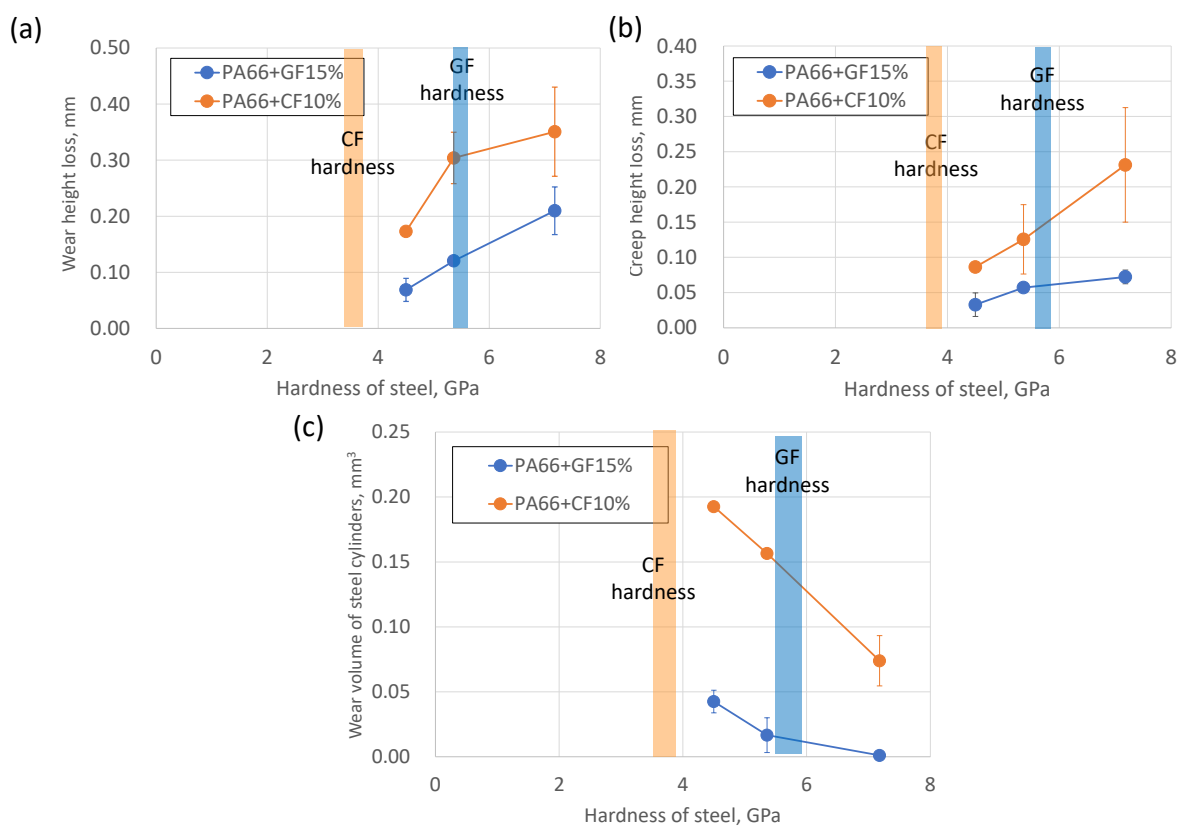


Fig. VIII. 19 Relationship between the hardness of steel cylinders and (a) the decrease in the weight of the composite ring; (b) the creep height loss of the composite ring; and (c) wear volume of the steel cylinders after 61,700 cycles of a sliding test for a normal load of 220 N with sliding for 10 s followed by stopping for 20 s.

Fig. VIII. 20 shows the evolutions of the friction coefficient, temperature, and vertical displacement in the sliding tests using the GF and CF composites and steel cylinders with a hardness of 4.5 GPa as a representative example. The friction coefficient and vertical displacement began to increase at 5,000 cycles for the CF composite, whereas no sudden increase was observed up to 35,000-40,000 cycles for the GF composite. In addition, the friction coefficient, temperature, and vertical displacement in the CF composite exhibited higher values than those of the GF composite after 5,000 cycles until the end of the test.

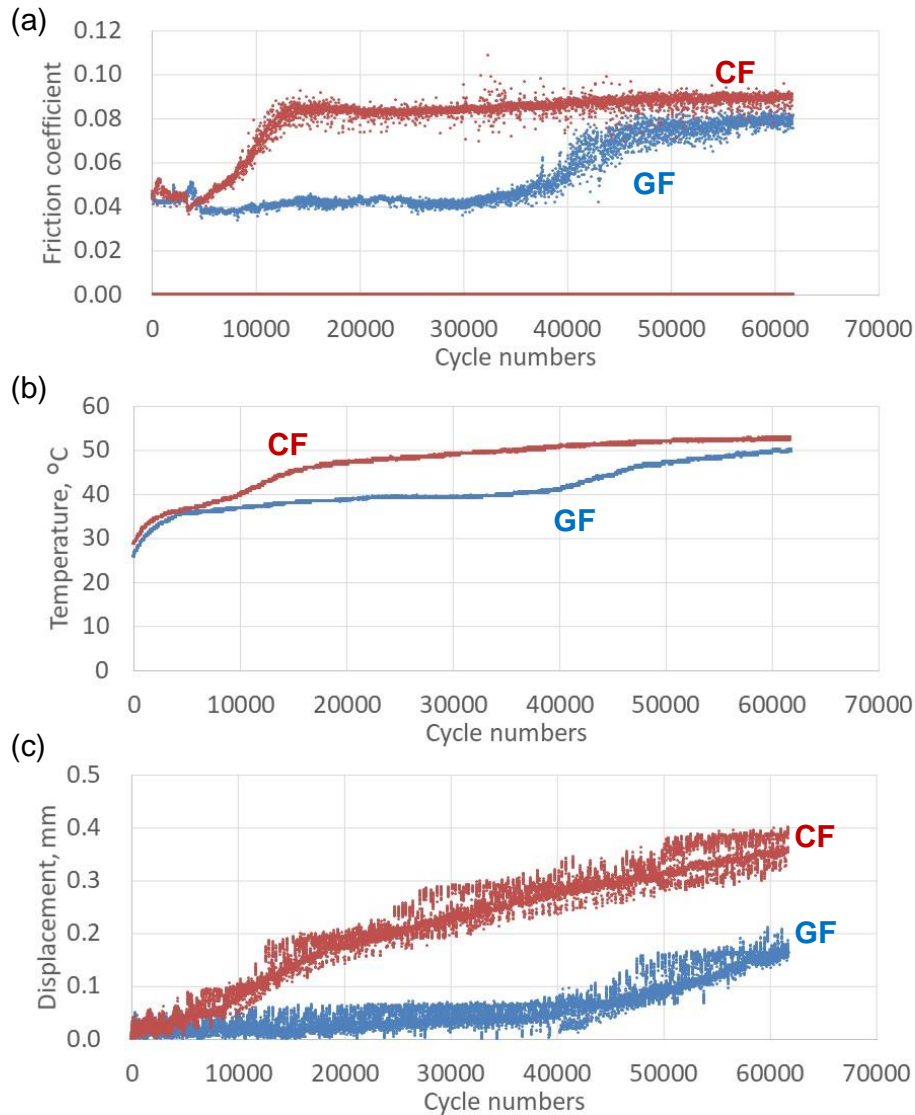


Fig. VIII. 20 Evolutions of the (a) friction coefficient, (b) temperature, and (c) vertical displacement in the sliding tests under grease lubrication for a normal load of 220 N with sliding for 10 s followed by stopping for 20 s using steel cylinders with a hardness of 4.5 GPa.

Fig. VIII. 21 shows the optical microscope observations of the ring surface after 61,700 cycles for the tests using steel counterparts with different values of the hardness and composites with different fibers. The damage to the ring sliding surface increased as the hardness of the steel increased.

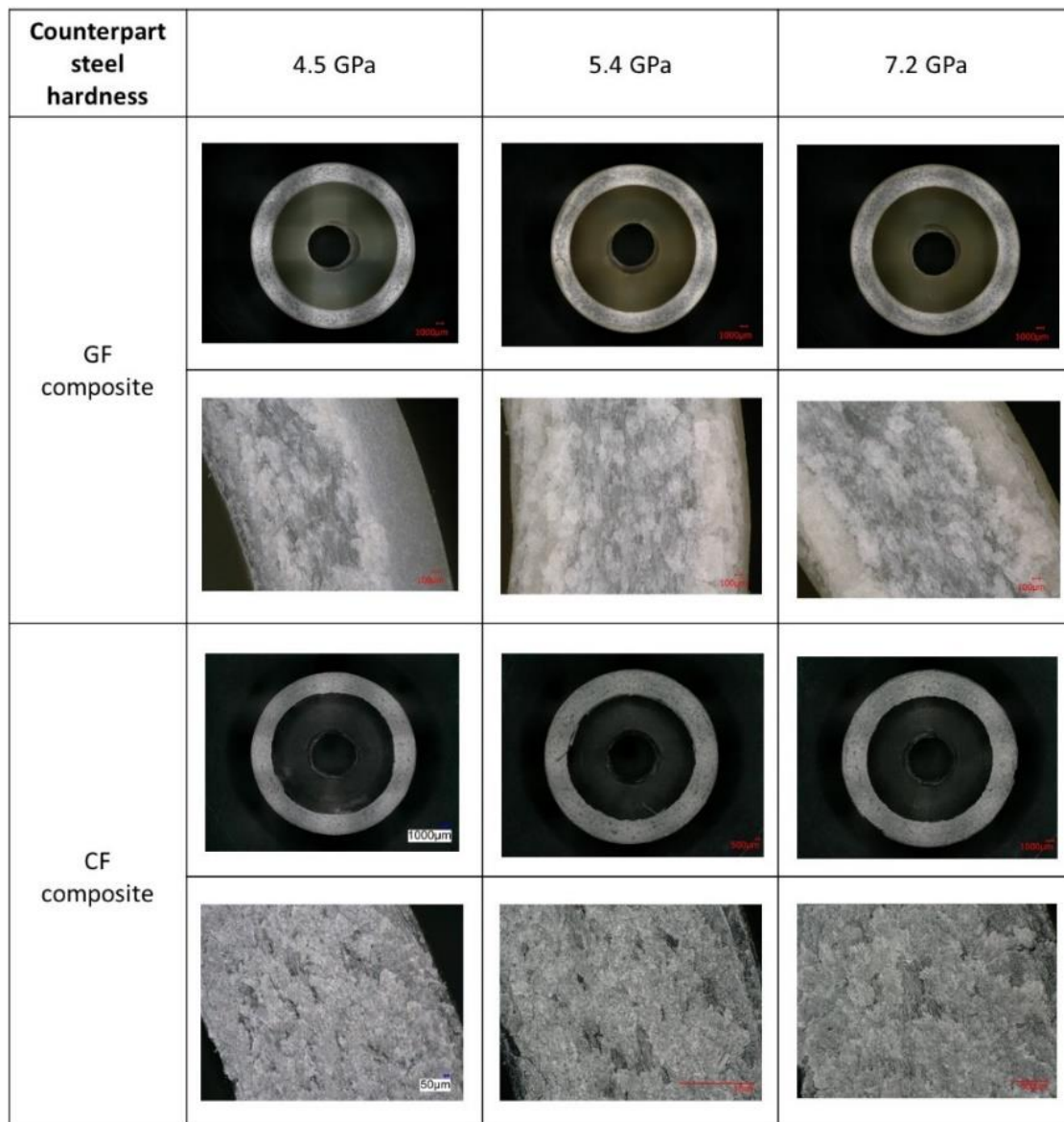


Fig. VIII. 21 Optical microscope observations of the ring surfaces after 61,700 cycles of the sliding test using steel counterparts with different hardness and composites with different fibers.

5.2 Hardness of fibers and wear mechanism of steel counterpart

To understand the effect of the steel hardness on the tribological properties, the hardness of the GFs and CFs were measured using the method presented in Section 4.5 in Chapter II. Fig. VIII. 22 shows an atomic force microscope (AFM) image of the steel surface after the hardness measurements for a normal load of 13,000 μN , the hardness of the GFs and CFs measured at various positions for a normal load of 4,000 μN , and the effect of the normal load used for the nano indentation on the measured hardness of the CFs oriented in the perpendicular direction. The indentations were not clearly visible on the surface of the CF, even those made under the maximum load of 13,000 μN . The hardness of the CFs oriented in the perpendicular direction was 3.9 ± 1.0 GPa for a normal load of 4,000 μN , and minimal variation in the hardness was observed for different normal loads. This value is similar to that reported in [187] (i.e., 2.5 – 5 GPa). The hardness of the GFs in the perpendicular direction for

a normal load of $4,000 \mu\text{N}$ was $5.7 \pm 0.2 \text{ GPa}$; therefore, the hardness of the CFs was 35% lower than that of the GFs in the perpendicular direction. In addition, anisotropy in the hardness of the CFs was observed, whereas the measured direction did not affect the hardness of the GFs. The hardness of the CFs in the perpendicular direction for a normal load of $4,000 \mu\text{N}$ was 1.61 times higher than that in the horizontal direction. The anisotropy of the mechanical properties (the Young's modulus and the hardness) of the CFs was also presented by Sun et al. [188], and the mechanical properties of the CFs in the transverse section (perpendicular direction) were higher than those in the longitudinal section (horizontal direction). The difference in the anisotropy between the GFs and CFs is due to the differences in the molecular structure of the fibers. CFs have high crystallinity, and the c axis of the graphite crystallites is perpendicular to the fiber axis [99]; therefore, the hardness of the CF in the perpendicular direction is higher than in the horizontal direction. In contrast, GFs have an amorphous structure, which has no anisotropy; therefore, the measurement position does not affect the hardness of the GFs.

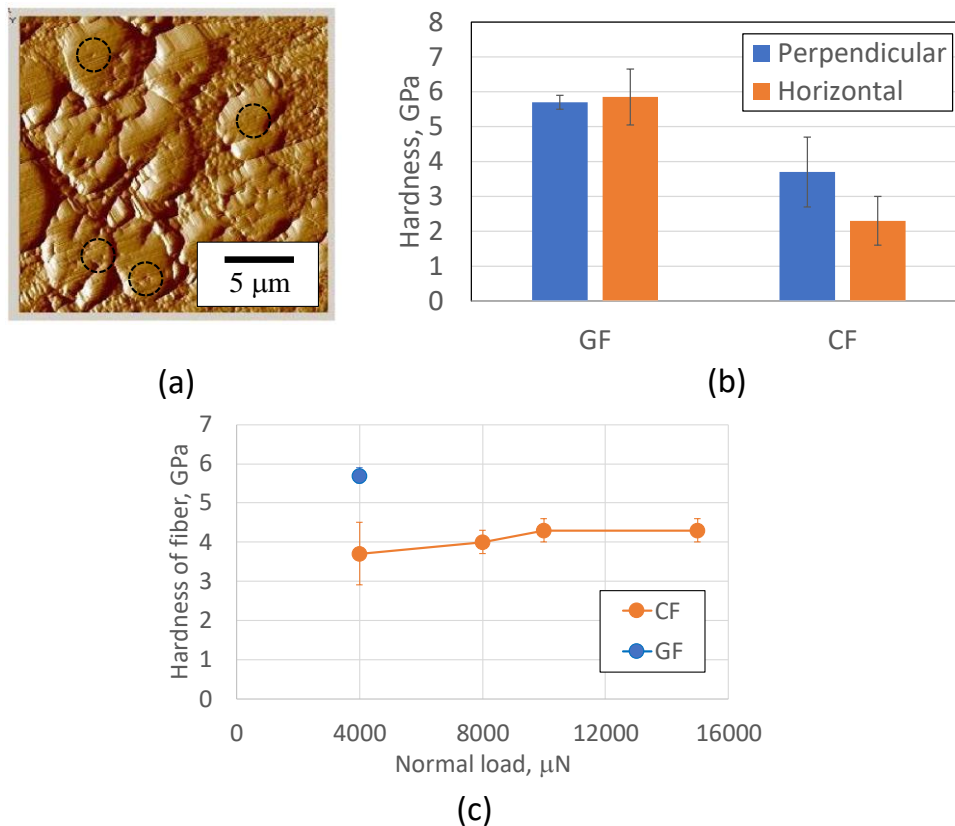


Fig. VIII. 22 (a) AFM image of the CFs after the hardness measurements with a normal load of $13,000 \mu\text{N}$; (b) the hardness of the GFs and CFs measured at various positions with a normal load of $4,000 \mu\text{N}$; and (c) the effect of the normal load of the nano indentation on the measured hardness of the CFs oriented in the perpendicular direction.

The results of the sliding tests and hardness of the fibers indicate that the CFs were softer than the steel cylinder with the lowest hardness (4.5 GPa measured by micro indentation), even after considering the anisotropy of the CF hardness. In addition, there were no significant differences in the fiber area on the sliding surface of the composite ring between the CF 10% composite (sample no. 1) and GF 15% composite (sample no. 3), as presented in Fig. VIII. 2. This indicates that the destructive effects of the composite on the counterpart steel under grease lubrication were not determined solely by the difference in the hardness of the fibers

and steel because the destructive effects of the CF composite on the counterpart steel were higher than those of the GF composite for each steel hardness. Therefore, the wear resistance of the counterpart steel is related to the wear resistance of the composite, which is related to the interfacial adhesion between the PA66 and fibers (considering that increasing the molecular mass of the PA66 in the CF composite improved the wear resistance of both the composite and the counterpart steel, as presented in Section 4). Hence, the difference in the adhesion between the fibers and PA66 was investigated.

The fracture surface on the composite in the tensile test was observed to compare the interfacial adhesion between the fibers and the PA66. Fig. VIII. 23 presents the SEM observations of the fracture surfaces from the tensile tests at 120°C with the GF 15% and CF 10% composites (samples no. 4 and no. 2, respectively). The elongation at break at 120°C of the GF composite was 3.5 times higher than that of the CF composite ($21.3 \pm 0.6\%$ and $6.4 \pm 0.3\%$, respectively). In the GF composite, few gaps between the PA66 and GFs in the perpendicular direction were observed, and the GFs strongly adhered to the entire surface of the PA66. In contrast, numerous gaps between the CFs and PA66 were observed in the CF composite, and the CFs were exposed without the adhesion to the PA66, even when the PA66 could undergo further elongation. These observations clearly demonstrate the difference in the interfacial adhesion between the PA66 and the GFs and CFs, and the difference in the elongation at break between the GF and CF composites. The schematics in Fig. VIII. 24 illustrate the differences in the sliding behavior of the CF and GF composites in contact with the carbon steel counterpart considering the differences in the interfacial adhesion between the PA66 and the fibers. The weak interfacial shear strength between the CFs and PA66 induces the gap between the CFs and PA66 on the sliding surface, leading to the exposure of the acute CF edges (which exhibit greater destructive effects on the steel than the smooth surface of the CF) and the wear of the steel counterpart. In addition, scratches on the PA66 propagate from the gap between the PA66 and CF, leading to an increase in the amount of wear on the composite. In contrast, the good interfacial adhesion between the GFs and PA66 prevents the exposure of the GF edges, which have highly destructive effects on the steel counterpart, and reduces the wear of the steel. In addition, the fewer gaps between the GFs and PA66 prevent the generation of scratches on the PA66, leading to a smaller amount of wear on the composite. In summary, one cause of the difference in the wear resistance between the GF composite and CF composite is the difference in the interfacial adhesion between the fibers and PA66.

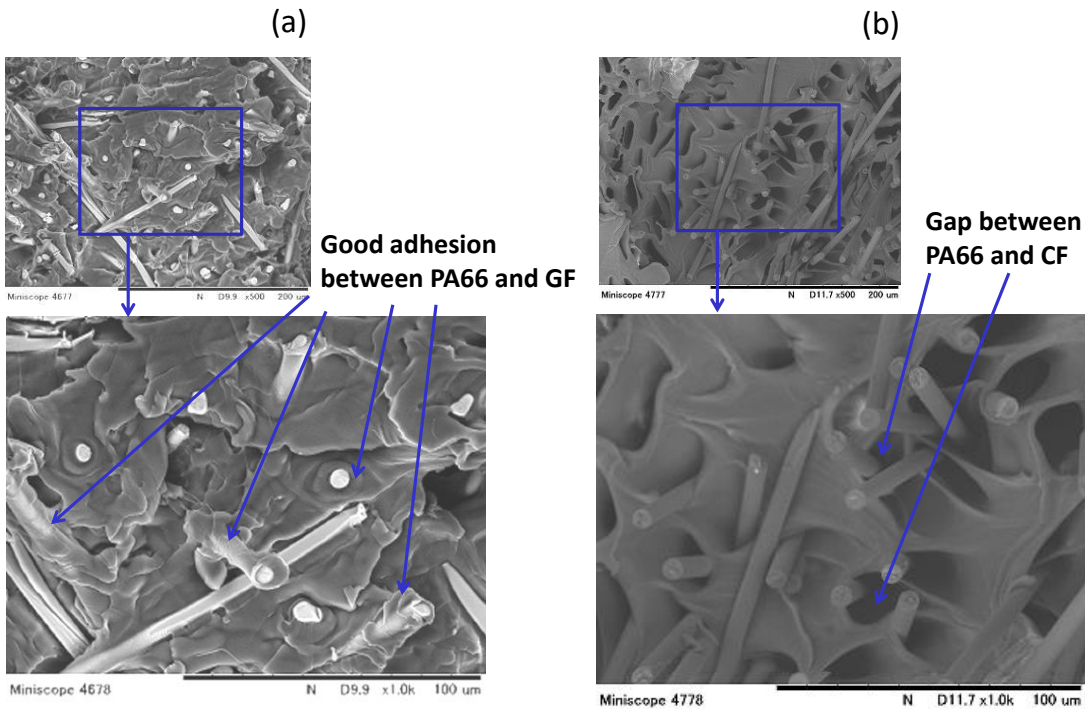


Fig. VIII. 23 SEM observations of the fracture surfaces from the tensile tests at 120°C of the (a) PA66 composite with 15% GF and (b) PA66 composite with 10% CF.

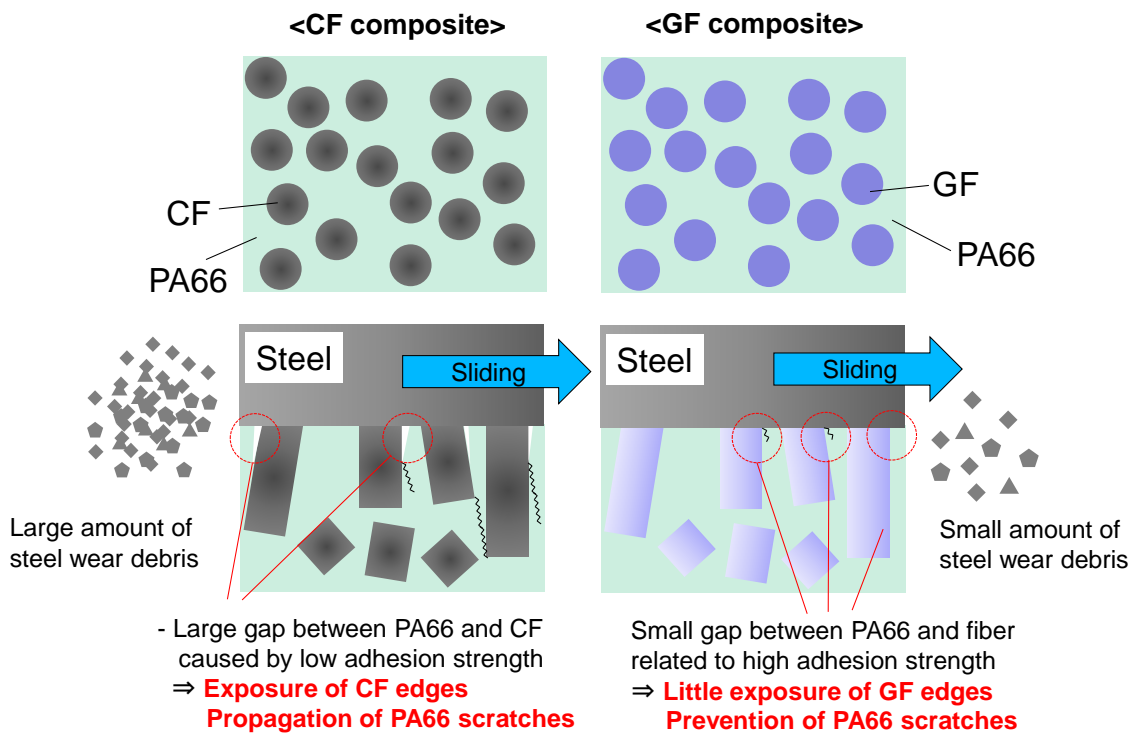


Fig. VIII. 24 Schematics of the differences in the sliding behavior of the GF and CF composites.

6. Differences in the temperature dependence of the tribological properties and tribochemistry between the CF and GF composites

In Chapter IV, the effects of additives in the grease (zinc carboxylate and sulfur type anti-oxidation agents) on the tribological properties of GF-reinforced PA66 in contact with steel were investigated. In the present section, the tribochemistry of the CF-reinforced composite was investigated and compared to the reported mechanism in the GF-reinforced PA66 composite.

6.1 Temperature dependence of the tribological properties of the CF composite and comparison to the GF composite

Fig. VIII. 25 presents the evolutions of the friction coefficient and vertical displacement using the normal molecular mass CF 10% composite (no. 1) and GF 15% composite (no. 3) with the grease containing zinc carboxylate (sample no. 1 in Table VIII. 2) under a normal load of 350 N with sliding for 10 s followed by stopping for 200 s (the test was performed at a stable temperature by preventing sliding heat generation with the introduction of a long stopping phase) at room temperature and 80°C. Optical microscope observations of the sliding surfaces after the sliding tests are shown in Fig. VIII. 26. The GF composite generally exhibited better tribological properties at 80°C than at room temperature (i.e., GF composite shows the tendency to lower friction coefficient and vertical displacement, and later cycle numbers in the sudden increase in the vertical displacement, as explained in Section 3.2 in Chapter IV; however, we cannot say it is a significant difference considering the variations in the test results). In contrast, the CF composite exhibited the opposite trend: the tribological properties at room temperature were better than those at 80°C, and the sudden increases in the friction coefficient and displacement occurred after more cycles at room temperature than at 80°C. Fig. VIII. 27 shows the wear and creep of the composite and wear of the steel cylinders (the total of the wear of the four steel cylinders). No significant differences in the wear and creep of the GF composite nor in the wear of the steel cylinders tested with the GF composite were observed between room temperature and 80°C. In contrast, the wear and creep of the CF composite at 80°C were considerably higher than those at room temperature, and the wear volume of the steel cylinders tested with the CF 10% composite at 80°C was 1.9 times higher than that at room temperature. Considering the difference in the tribological properties between the GF 15% composite and CF 10% composite, the wear of the GF 15% composite was much lower than that of the CF 10% composite at both room temperature and 80°C, and this trend is the same as that observed in Section 4. The wear of the steel cylinders tested with the CF 15% composite was also 3.5 and 6.5 times higher than those tested with the GF 10% composite at room temperature and 80°C, respectively, even though the hardness of the CF itself was much lower than that of the GFs. This trend is also the same as that observed in Section 4, and these results also explain why the wear of the counterpart steel cannot be determined solely by the hardness of the reinforcement fibers for sliding under grease lubrication.

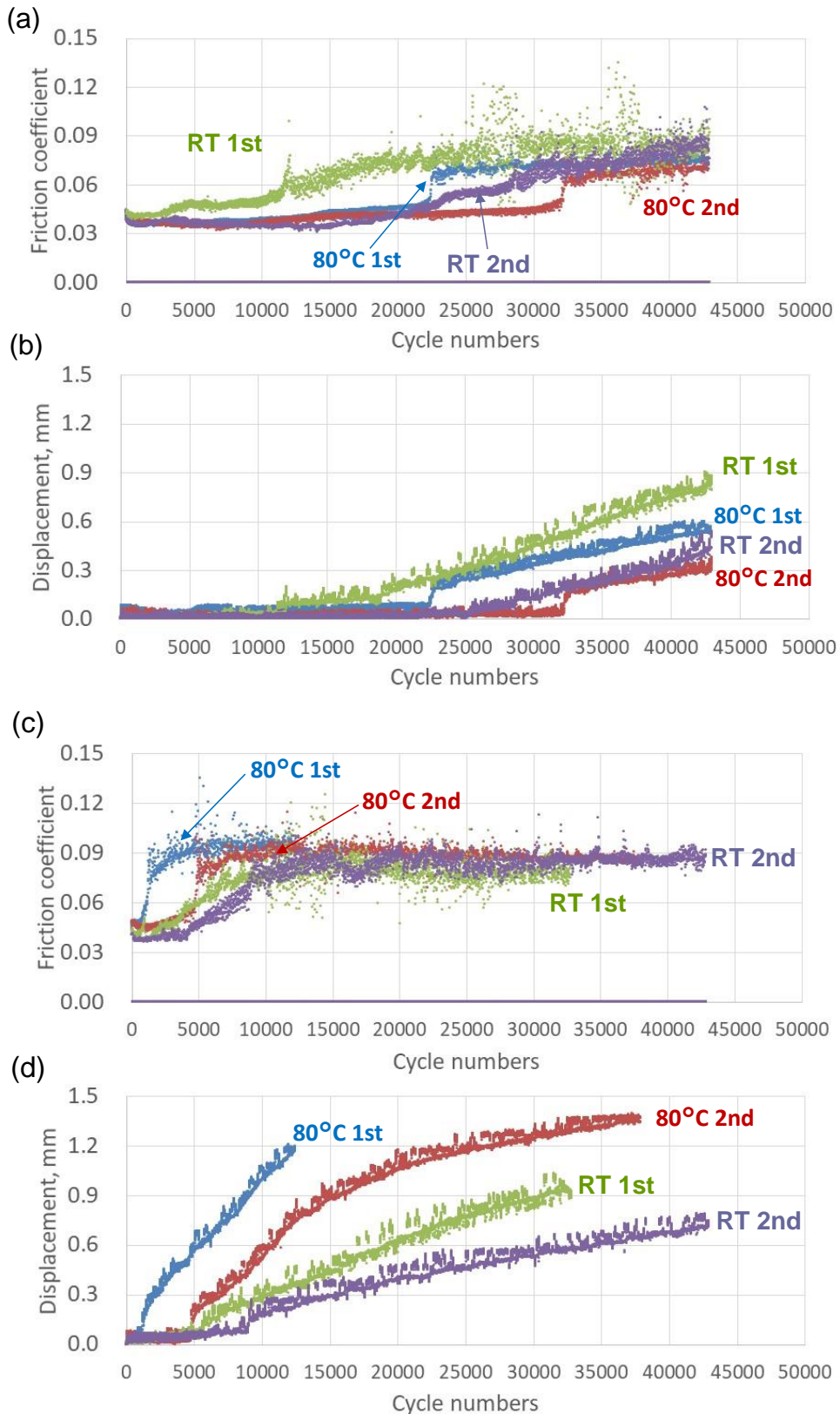


Fig. VIII. 25 Evolutions of (a) the friction coefficient using the GF composite, (b) the vertical displacement of the GF composite, (c) the friction coefficient using the CF composite, and (d) the vertical displacement of the CF composite at room temperature (RT) and 80°C under a normal load of 350 N with sliding for 10 s followed by stopping for 200 s.

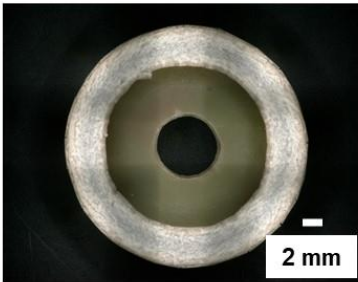
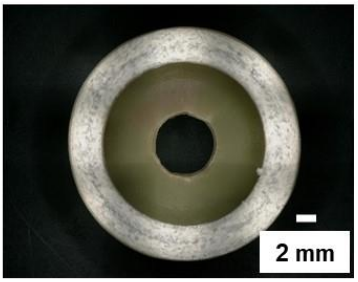
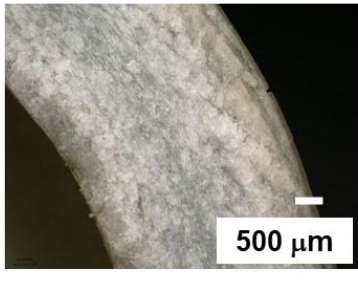
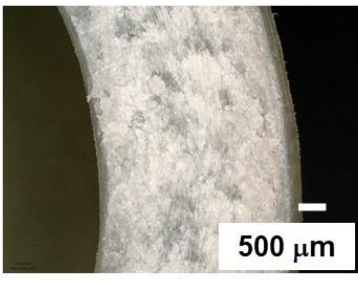
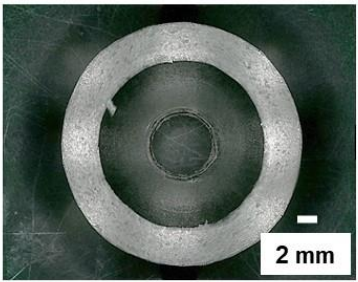
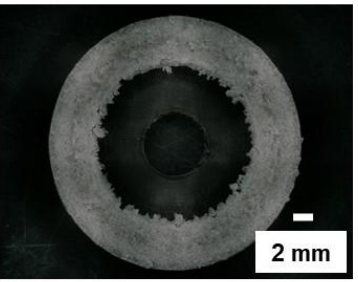
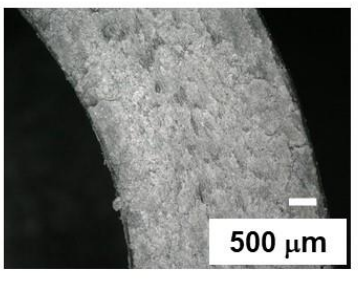
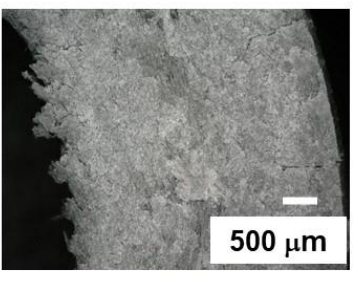
	GF 15% composite RT 42,990 cycles	GF 15% composite 80°C 42,964 cycles
Entire surface		
Magnified image		
	CF 10% composite RT 42,903 cycles	CF 10% composite 80°C 37,985 cycles
Entire surface		
Magnified image		

Fig. VIII. 26 Optical microscope observations of the sliding surfaces after the sliding tests under a normal load of 350 N with sliding for 10 s followed by stopping for 200 s at room temperature or 80°C using the GF 15% composite and CF 10% composite.

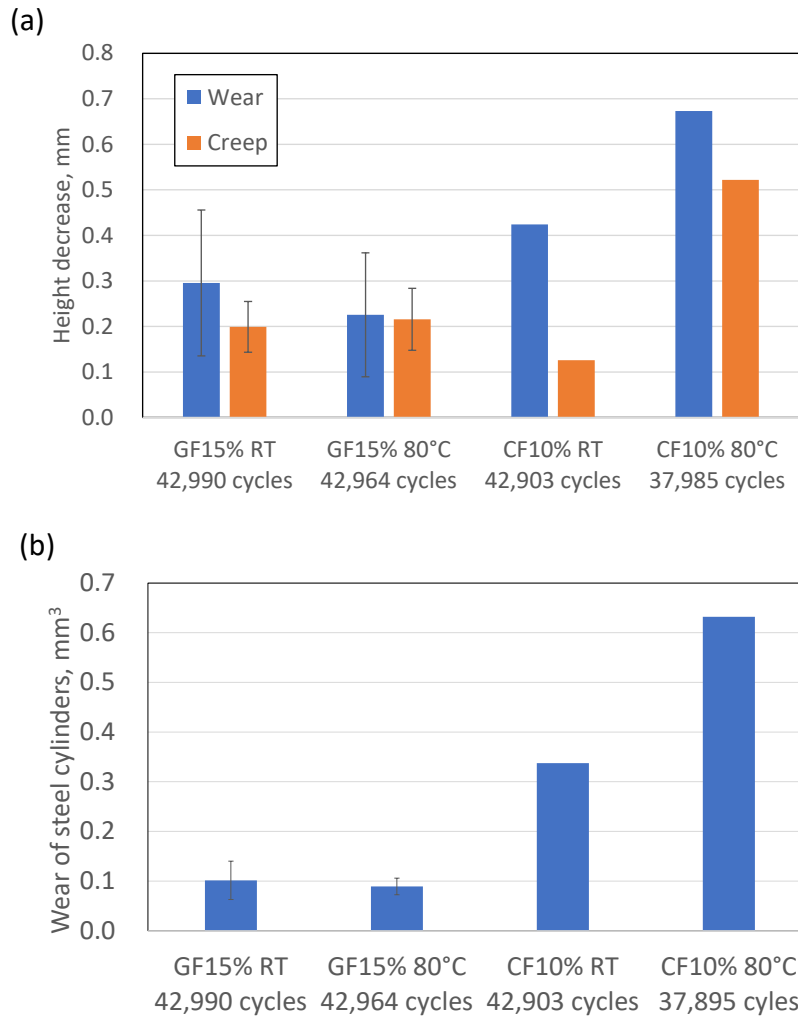


Fig. VIII. 27 (a) Wear and creep height loss of the composite and (b) wear of the steel cylinders after the sliding tests under a normal load of 350 N with sliding for 10 s followed by stopping for 200 s. The values for the GF composite are the average values for two different sliding tests.

6.2 Discussion on the tribofilm formation and effect of zinc carboxylate

To discuss the difference in the temperature dependence of the tribological properties between the GF composite and CF composite, tribofilm formation, which is related to the tribochemical reaction of the grease additives, was investigated. The sliding tests that were intentionally stopped before the sudden increases in the friction coefficient and vertical displacement were conducted for the same normal load of 350 N at 80°C with sliding for 10 s followed by stopping for 200 s, and the sliding surfaces of the steel cylinders and composite ring were observed and analyzed. The sliding tests using the GF 15% composite were stopped after 1,018 cycles and 12,595 cycles, and the sliding tests using the CF 10% composite were stopped after 4,752 cycles and 12,477 cycles. Fig. VIII. 28 shows the SEM observations of the sliding surfaces of the steel cylinder after ultrasonic washing. For the cylinders tested with the GF composite, randomly distributed dark patches were observed on the sliding surface after both sliding cycles; however, dark patches were rarely visible on the sliding surface of the steel cylinders tested with CF composite. As discussed in Section 4.1.3 in Chapter IV, ToF-SIMS analysis of the steel cylinder tested with the GF composite for 12,595 cycles revealed that a

tribofilm containing carboxylate (including stearate or palmitate), which was related to the tribochemical reaction of the zinc carboxylate added to the grease, formed on the steel surface. This carboxylate tribofilm had a significant effect on the improvement of the tribological properties at 80°C, and supplemented the degradation of the tribological properties related to the reduced mechanical properties of the GF composite compared to those at room temperature. In addition, the presence of Zn and S was detected on the sliding surface of both the GF composite and CF composite through the SEM-EDX analysis, as shown in Fig. VIII. 29. The Zn and S were present in a ZnS reactive film, which was detected through XPS analysis of the GF composite surface; however, the ZnS reactive film had less effect on the improvement of the tribological properties, as presented in Sections 4.2 and 5 in Chapter IV. Therefore, the difficulty in forming a tribofilm on the steel surface tested with the CF composite can explain why the tribological properties of the CF composite were inferior at 80°C compared to those at room temperature.

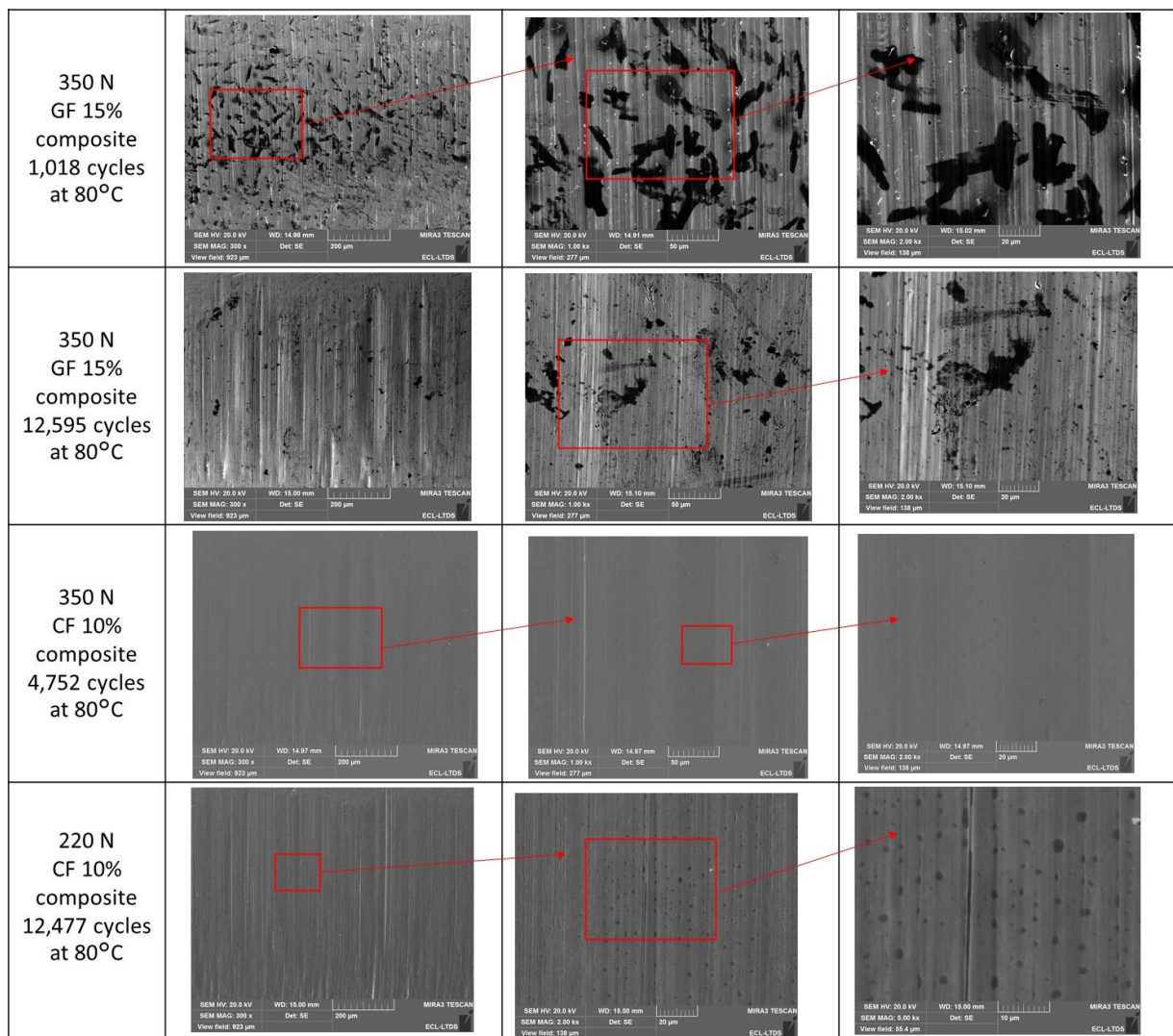


Fig. VIII. 28 SEM observations of the steel sliding surfaces after the sliding tests under different normal loads after different numbers of cycles with sliding for 10 s followed by stopping for 200 s at 80°C.

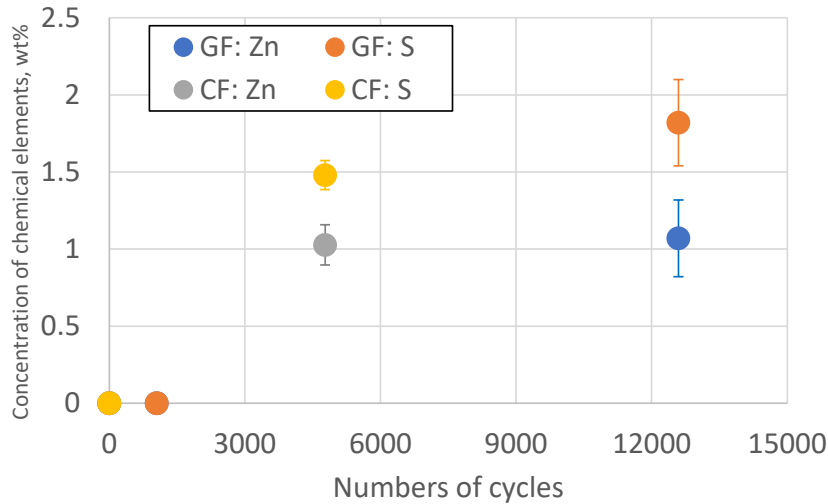
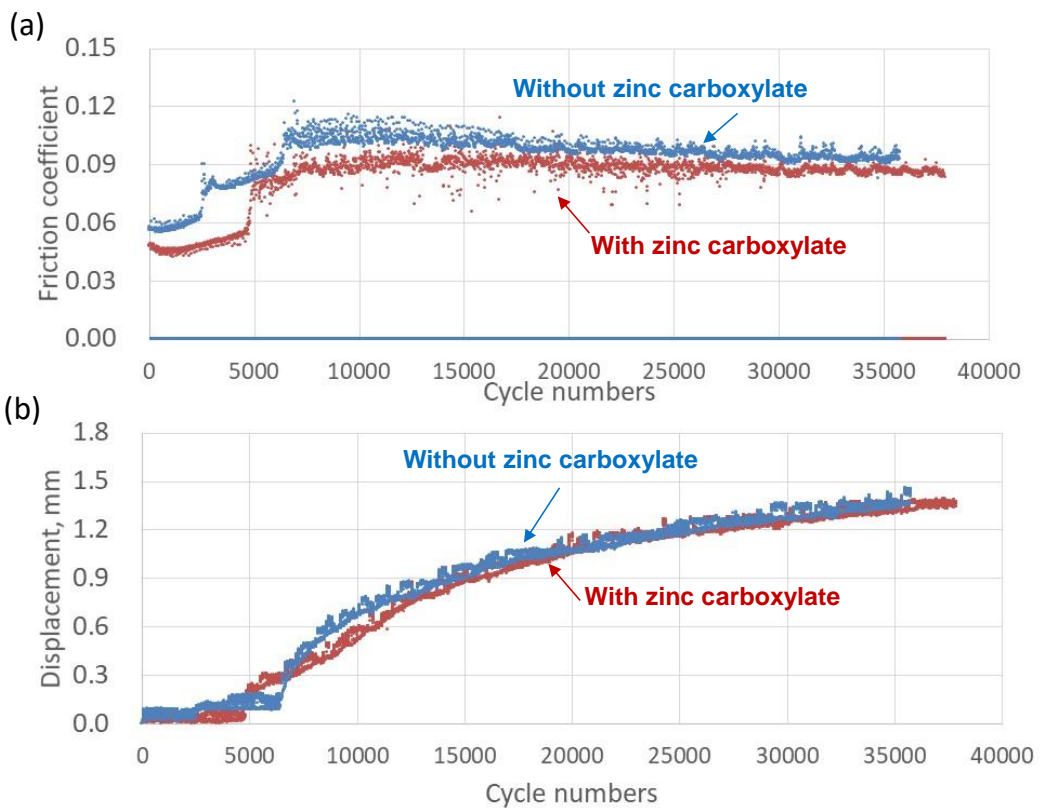


Fig. VIII. 29 Concentrations of Zn and S on the composite surface measured via SEM-EDX.

To better understand the difference in the tribochemistry between the CF composite and GF composite, the grease that did not contain zinc carboxylate as a low friction additive (grease no. 2 in Table VIII. 2) was prepared, and sliding tests were conducted under the same test conditions. Fig. VIII. 30 shows the difference in the evolutions of the friction coefficient and the vertical displacement using the CF 10% composite (sample no. 1) and GF 15% composite (sample no. 3) under a normal load of 350 N with sliding for 10 s sliding followed by stopping for 200 s at 80°C.



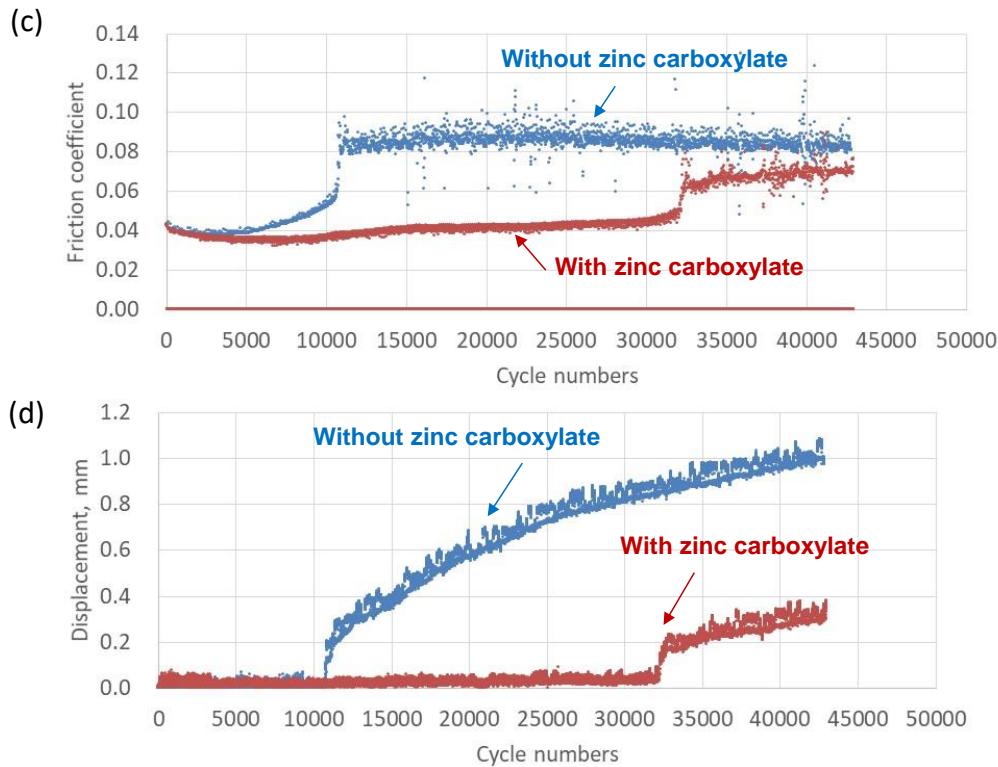


Fig. VIII. 30 Evolutions of the friction coefficient and the vertical displacement using (a, b) the CF 10% composite and (c, d) the GF 15% composite and grease with or without zinc carboxylate in the sliding tests under a normal load of 350 N with sliding for 10 s followed by stopping for 200 s at 80°C.

The zinc carboxylate addition to the grease did not significantly influence the tribological properties of the CF composite; only a slight decrease in the friction coefficient was observed. In contrast, the addition of zinc carboxylate significantly improved the tribological properties of the GF composite; a sudden increase in the friction coefficient and vertical displacement was observed after several cycles with the zinc carboxylate, and the displacements (wear and creep of the composite) were lower, as we discussed in Chapter IV. These results indicate that zinc carboxylate was not effective at improving the tribological properties when the CF composite was used under this test condition, unlike the GF composite. In addition, these results coincide with the inferior tribological properties exhibited by the CF composite at 80°C compared to those at room temperature, as presented in Fig. VIII. 25, and the formation of the tribofilm on the steel surface was not observed, as shown in Fig. VIII. 28.

6.3 Effect of the contact pressure on the tribofilm formation and temperature dependence of the tribological properties

The difference in the formation of the tribofilm on the steel cylinder surface and the effect of the zinc carboxylate under a normal load of 350 N at 80°C may be attributed to the difference in the contact pressure due to the difference in the Young's moduli of the composites or the difference in the tribochemical reaction mechanism related to the fiber type. To clarify the effects of the difference in the contact pressure on the tribochemical reaction mechanism, sliding tests were conducted using the CF composite (sample no. 1) under a normal load of 220 N (at room temperature and 80°C), with sliding for 10 s followed by stopping for 200 s; the reduced contact pressure was the same as that in the previous

sliding test of the GF composite for a normal load of 350 N (191 MPa calculated at room temperature using Hertz's law). Fig. VIII. 31 presents the evolutions of the friction coefficient, temperature, and vertical displacement from the two sliding tests after 43,044 and 104,114 cycles, respectively. Optical microscope observations of the sliding surfaces after the sliding tests are shown in Fig. VIII. 32. Unlike the evolutions under a normal load of 350 N (Fig. VIII. 25), the vertical displacements (wear and creep) and the rate of the increase in the displacement after the sudden increase were lower at 80°C than those at room temperature.

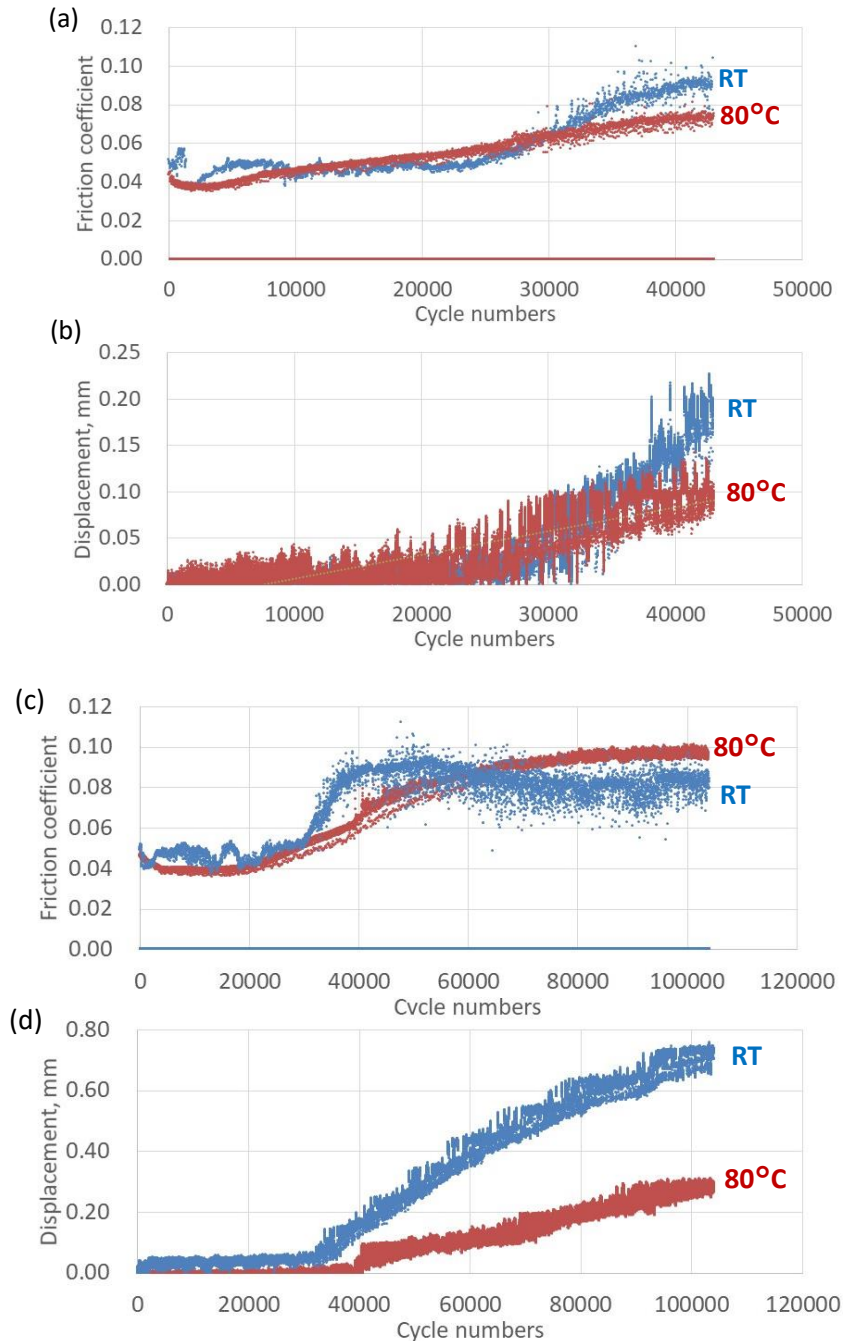


Fig. VIII. 31 Evolutions of the friction coefficient and vertical displacement using the CF 10% composite and grease with zinc carboxylate in the sliding tests under a normal load of 220 N with sliding for 10 s followed by stopping for 200 s at room temperature and at 80°C (a, b) during 43,044 cycles and (c, d) during 104,114 cycles.

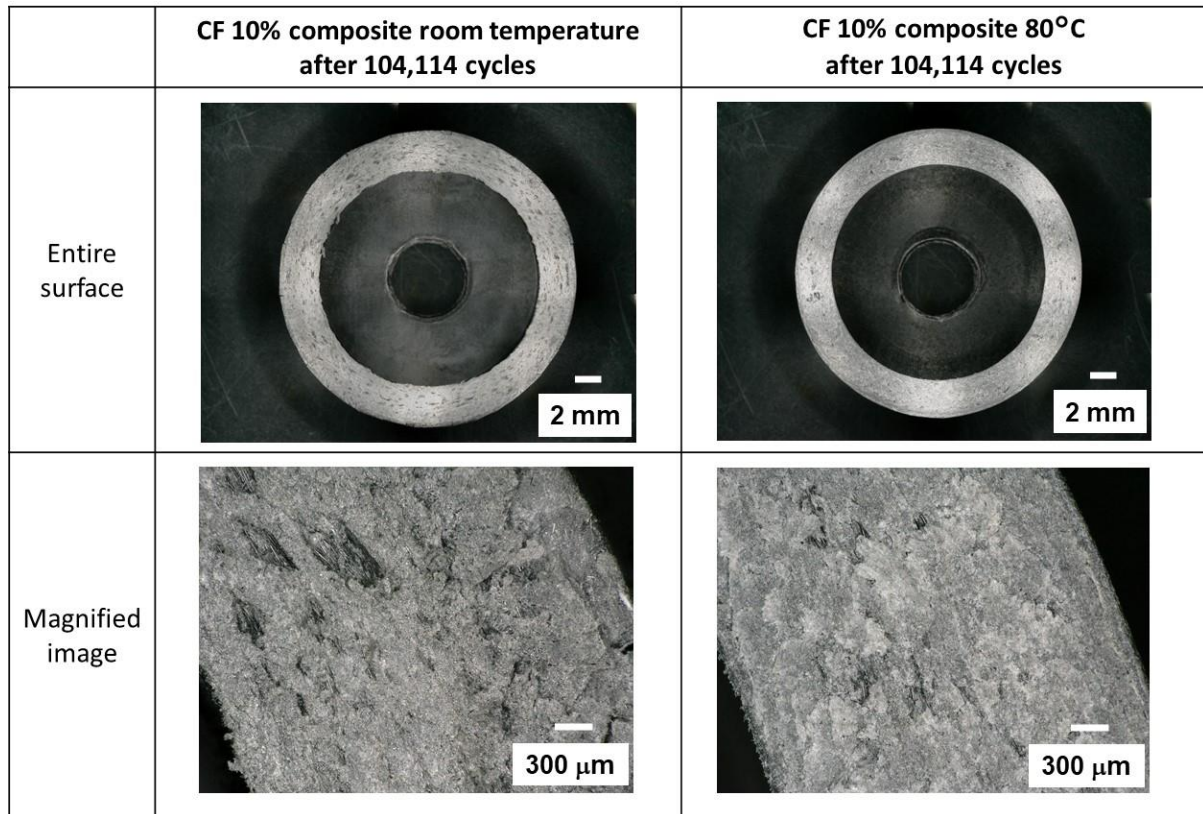


Fig. VIII. 32 Optical microscope observations of the sliding surface after 104,114 cycles of the sliding tests under a normal load of 220 N with sliding for 10 s followed by stopping for 200 s at room temperature and 80°C using the CF 10% composite.

Fig. VIII. 33 presents the wear and creep of the CF composite and wear volume of the steel cylinders (total wear volume of the four cylinders) after the sliding tests during both tests. The wear height loss of the CF composite was clearly higher at room temperature than that at 80°C. The wear height loss was higher than the creep height loss at both room temperature and 80°C, particularly after 104,114 cycles, and no significant difference in the creep height loss was observed between room temperature and 80°C. The wear volume of the steel cylinders at room temperature was also higher than that at 80°C. This trend for the wear resistance of the CF composite and steel counterpart was completely opposite to the results under a normal load of 350 N presented in Fig. VIII. 27. Therefore, the effect of the contact pressure (normal load) on the tribofilm formation on the steel surface was analyzed via SEM observations to elucidate the difference in the tribological properties between the normal loads of 220 N and 350 N.

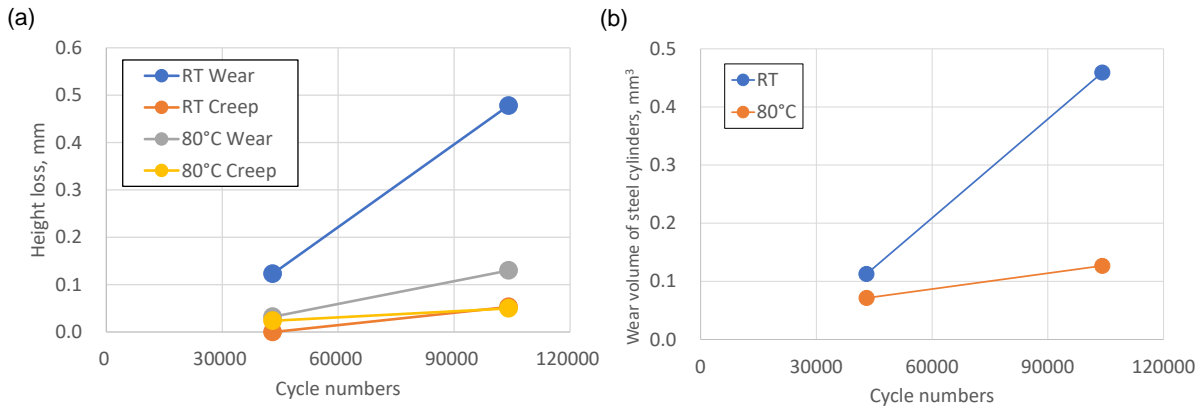


Fig. VIII. 33 (a) Wear and creep height loss of the CF composite and (b) wear volume of the steel cylinders after the sliding tests for 43,004 and 104,114 cycles under a normal load of 220 N (at room temperature and 80°C) with sliding for 10 s followed by stopping for 200 s.

Fig. VIII. 28 also presents the SEM observations of the steel cylinder sliding surface after 12,477 cycles (before the sudden increase in the friction coefficient and vertical displacement) under a normal load of 220 N with sliding for 10 s followed by stopping for 200 s at 80°C. Compared to the observations for a normal load of 350 N (also shown in Fig. VIII. 28), a larger number of dark patches were observed on the steel cylinder surface, but the surface area of the dark patches on the steel tested with the GF composite under a normal load of 350 N was much larger. These results can explain the difference in the tribological properties of the CF composite at 80°C between the normal loads of 220 N and 350 N. In the sliding test under 350 N, the contact pressure was too high to form or to keep a carboxylate tribofilm on the steel surface (the tribofilm was not formed or the rate of removal of the tribofilm was much higher than the rate of formation); therefore, the wear of the CF composite increased as the mechanical properties of the composite decreased at high temperature. In contrast, in the sliding test under 220 N, the contact pressure was appropriate for the formation of the tribofilm (the contact pressure was closer to that of the GF 15% composite under a normal load of 350 N), and the carboxylate tribofilm formation on the steel surface improved the tribological properties, as observed in the GF 15% composite.

In addition, the effect of the contact pressure on the tribological properties under grease lubrication was investigated for the GF 33% composite (sample no. 5), which had a higher Young's modulus that induced a higher contact pressure (252 MPa at room temperature) than the GF 15% composite under the same normal load. Fig. VIII. 34 presents the evolutions of the friction coefficient and the vertical displacement from the sliding test under a normal load of 350 N with sliding for 10 s followed by stopping for 200 s using the GF 33% composite and grease with/without zinc carboxylate at room temperature and 80°C.

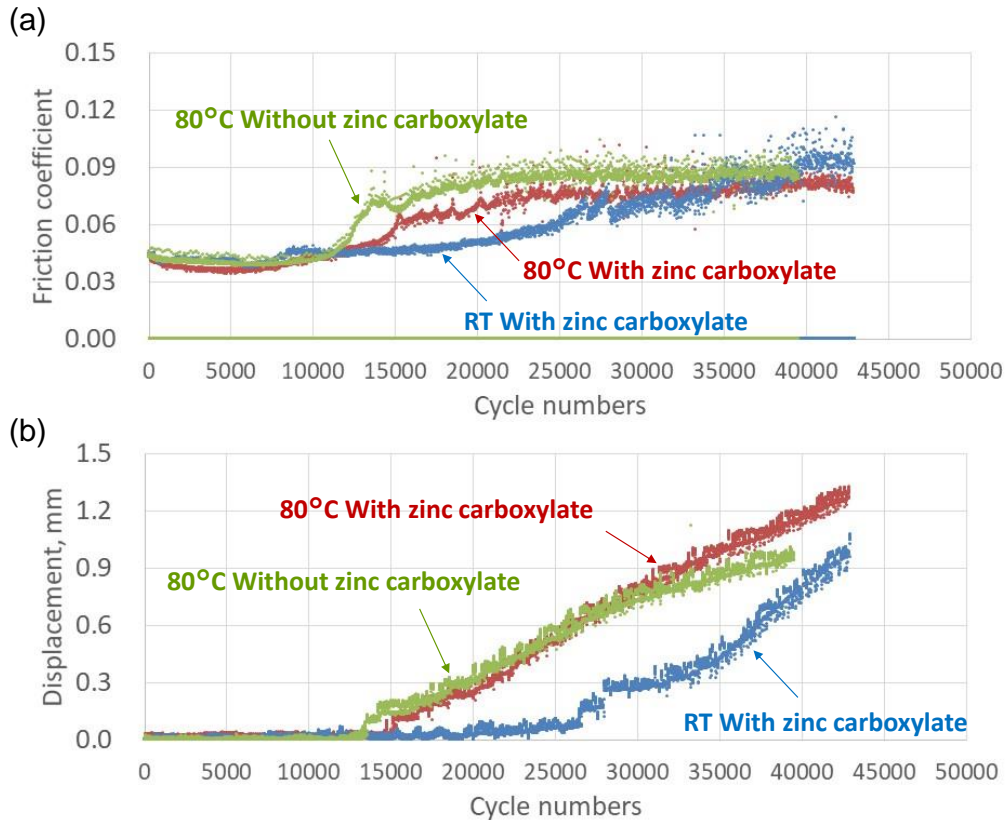


Fig. VIII. 34 Evolution of (a) the friction coefficient and (b) the vertical displacement during the sliding tests using the GF 33% composite and grease with/without zinc carboxylate, under a normal load of 350 N (at room temperature and 80°C), with sliding for 10 s followed by stopping for 200 s.

Unlike the GF 15% composite (as presented in Fig. VIII. 25 and Fig. VIII. 31), the tribological properties at 80°C were inferior to those at room temperature (a higher vertical displacement at 80°C than at room temperature), and the addition of zinc carboxylate to the grease did not produce any discernable improvements in the tribological properties at 80°C. These results follow the same trend that was observed for the CF composite under a normal load of 350 N, as presented in Fig. VIII. 25. As for the GF 15% composite, the sliding test was intentionally stopped before the sudden increase in the friction coefficient and vertical displacement; the sliding surfaces on the steel cylinder were observed via SEM to investigate the tribofilm formation relationship with the sliding test results. Fig. VIII. 35 presents the SEM observations of the steel surface tested with the GF 33% composite after 4,745 cycles using the grease with zinc carboxylate under a normal load of 350 N at 80°C with sliding for 10 s followed by stopping for 200 s. Some dark patches, which were attributed to the carboxylate film, were observed; however, the total area of the patches was markedly lower than that for the cylinders tested with the GF 15% composite under the same test conditions, as presented in Fig. VIII. 28. Therefore, similar to the CF 10% composite under a normal load of 350 N, the contact pressure was too high to form or to keep the tribofilm on the sliding surface of the steel counterpart. Therefore, the improvement in the tribological properties provided by the carboxylate tribofilm was not obtained, and the tribological properties were inferior at 80°C compared to those at room temperature, exhibiting the same evolution of the displacement (wear and creep of the composite) with and without the zinc carboxylate.

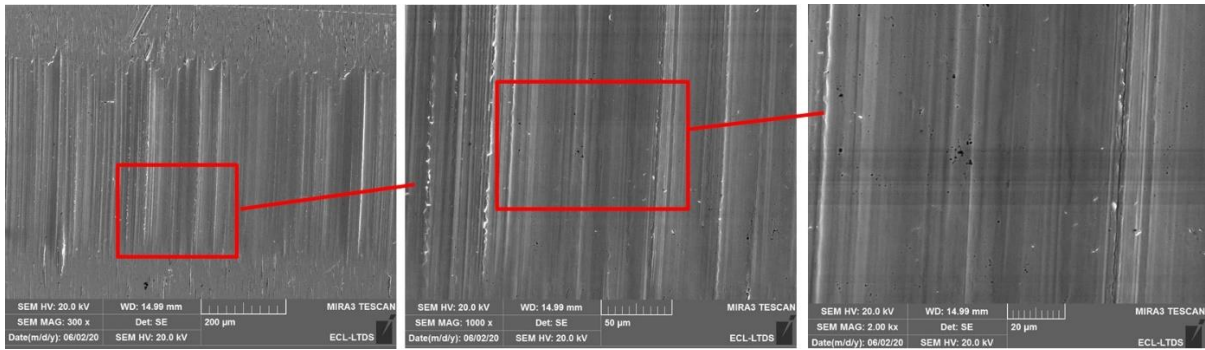


Fig. VIII. 35 SEM observations of the steel surface tested with the GF 33% composite after 4,745 cycles under a normal load of 350 N with sliding for 10 s followed by stopping for 200 s using the grease with zinc carboxylate at 80°C.

7. Conclusions

The tribological properties of CF-reinforced PA66 composites in contact with steel under grease lubrication were investigated and compared to those of GF-reinforced PA66. The following conclusions were drawn.

1) Tribological properties without lubrication

Under dry conditions, fiber reinforcement led to reduced friction and improved wear resistance compared to unreinforced PA66. The CF composite exhibited lower friction as the adhesive wear resulted in the formation of a low friction transfer film, which was composed of a graphite structure related to the CFs.

2) Tribological behavior under grease lubrication

Under grease lubrication, the CF composite presented inferior tribological properties compared to the GF composite, regardless of the molecular mass of PA66 and taking into account the contact pressure difference related to the difference in Young's moduli. The insufficient interfacial adhesion between the PA66 and CFs induced fiber peeling, which scratched the PA66 at much earlier cycles.

3) Effects of the hardness of the counterpart steel on the tribological properties and clarification of the wear mechanism of the steel counterpart

The destructive effects of the CF composite on the steel counterpart were much higher than those of the GF composite, even though the hardness of the CFs (measured through nanoindentation) was much lower than that of the GFs. The destructive effect is not determined solely by the fiber hardness, and insufficient interfacial adhesion between the CFs and PA66 also led to an increase in the wear of the steel counterpart.

4) Differences in the temperature dependence of the tribological properties and tribochemistry between the CF and GF composites

The difference in the temperature dependence of the tribological properties between the CF composite and GF composite was due to the difference in the tribofilm formation related to the grease additives. The tribofilm formation was dominated by contact pressure, regardless of fiber type, and contributed to the improvement of the tribological properties at 80°C.

In previous chapters including present chapter, tribological properties of the PA66 or fiber-reinforced composite were investigated without considering the effect of water absorption by using the test specimens in which specimens were heat-dried before conducting the sliding tests. However, PA is well-known to show the hygroscopicity, and it is necessary to take into account the effect of water absorption, considering the actual use of polymer sliding parts including the worm wheel in the worm reducer of EPS. Therefore, in the next chapter, the effect of the water absorption of GF-reinforced PA66 on the tribological properties will be investigated.

CHAPTER IX

EFFECTS OF WATER ABSORPTION ON
THE MECHANICAL AND
TRIBOLOGICAL PROPERTIES OF GF-
REINFORCED PA66 IN CONTACT
WITH STEEL UNDER GREASE
LUBRICATION CONDITIONS

CHAPTER IX: EFFECTS OF WATER ABSORPTION ON THE MECHANICAL AND TRIBOLOGICAL PROPERTIES OF GF-REINFORCED PA66 IN CONTACT WITH STEEL UNDER GREASE LUBRICATION CONDITIONS

1. Introduction.....301

2. The effect of water absorption on the mechanical properties301

3. The effect of water absorption on the tribological properties302

4. Conclusions.....307

CHAPTER IX: EFFECTS OF WATER ABSORPTION ON THE TRIBOLOGICAL PROPERTIES OF GF-REINFORCED PA66 IN CONTACT WITH STEEL UNDER GREASE LUBRICATION CONDITIONS

PA is well-known to show hygroscopicity, and it is necessary to take into account the effect of water absorption, considering the actual use of polymer sliding parts (including the worm wheel in the worm reducer of EPS). In this chapter, the effect of the water absorption of GF-reinforced PA66 on the tribological properties will be investigated.

1. Introduction

In previous chapters, tribological properties of the PA66 and fiber-reinforced composite were investigated without considering the effect of water absorption by performing tests in which specimens were heat-dried before conducting the sliding tests. PA66, however, shows hygroscopicity because of its molecular structure, as stated in Section 3.1.4 in Chapter I. Few studies investigated the effects of the water absorption on the tribological properties under grease lubrication, and mechanism has not been clarified sufficiently. Therefore, in this chapter, we focused on the understanding of the effects of the hygroscopicity of PA66 on the tribological properties with the consideration of the use of the automotive components exposed to humid conditions.

In this chapter, GF 15% composite with high molecular mass (sample no. 2 in Table II. 3) was used. In the sliding tests, single type of barium complex grease which was presented in Section 2.3.2 in Chapter II and bearing steel cylinders with the Vickers hardness of HV 789 as explained in Section 2.2 in Chapter II were used. In addition, the sliding tests in this chapter were conducted using the tribometer in JTEKT Corporation as explained in Section 4.3 in Chapter II.

2. The effect of water absorption on the mechanical properties

First, the effect of water absorption on the tensile mechanical properties of GF-reinforced composite was investigated. Fig. IX. 1 presents the relationship between the water absorption rate and tensile mechanical properties. Water absorption to the tensile test specimens was conducted using humidity chamber at 50°C, as explained in Section 2.1.5 in Chapter II. The tensile strength and Young's modulus decrease with the increase in the water absorption rate. On the other hand, tensile elongation at break exhibits almost the same value between 0% and 3.1%, and afterwards increases with the increase in the water absorption rate. These results show the same tendency as the one observed in previous works [73], and the effect of

the water absorption rate on the change in the mechanical properties is the same as the effect when the amounts of GF decrease. The effect on the mechanical properties can be explained by the inhibition of the hydrogen bonding between each molecule of PA66 through the presence of the water molecules.

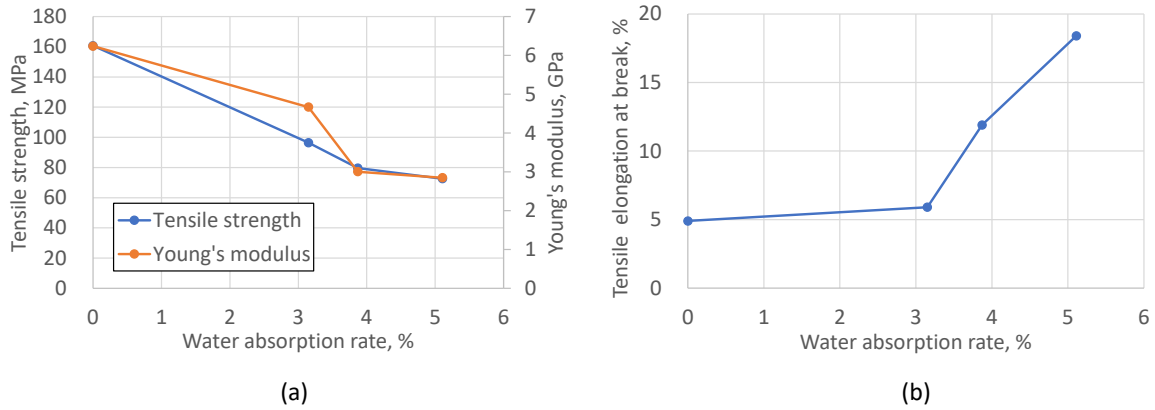


Fig. IX. 1 Relationship between the water absorption rate and (a) tensile strength and Young's modulus; (b) tensile elongation at break.

3. The effect of water absorption on the tribological properties

Next, the effect of the water absorption on the tribological properties was investigated. Fig. IX. 2 shows the relationship between soaking time at 50°C in humidity chamber as explained in Section 2.1.5 in Chapter II and water absorption rate of the ring specimens, and relationship between the water absorption rate and dimensional change in the ring specimens. Water absorption rate was calculated by the weight of the specimens after each water absorption test, and dimensional change was calculated by the change in the height of the composite ring. Linear increase in the water absorption rate is observed until 3%, and the rate of the increase in the water absorption rate decreased after 3%. The dimensional change increases almost proportionally with the increase in the water absorption rate.

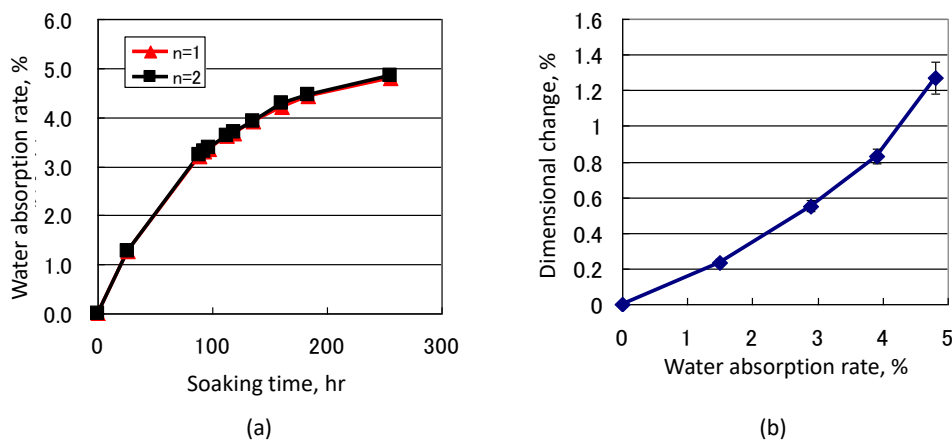


Fig. IX. 2 (a) Relationship between soaking time in the stable temperature and humidity chamber and water absorption rate of the ring specimens; (b) relationship between the water absorption rate and dimensional change in the specimens.

To clarify the effect of the water absorption on the tribological properties of GF-reinforced PA66, sliding tests were conducted for a normal load of 220 N with an intermittent contact which includes 10 s sliding and 20 s stopping phase at room temperature under grease lubrication. To measure the M_{wear} during the sliding tests correctly, it is necessary to measure the amount of the water evaporated to the atmosphere during the sliding tests, as presented in the following equation.

$$M_{total} = M_{wear} + M_{water} \quad (IX. 1)$$

where M_{total} is the total of weight decrease after the sliding tests, and M_{water} is the weight decrease related to the evaporation of the water during the sliding tests. The water absorption rates before and after sliding tests were measured in the Karl Fischer titration method as explained in Section 2.1.5 in Chapter II to estimate the M_{water} , and M_{wear} was estimated by the subtraction of the M_{water} from the M_{total} . Table IX. 1 lists the water absorption rate before and after the sliding tests which was measured in Karl Fischer titration. And h_{wear} can be calculated as it was in other chapters (see Section 4.2.3 in Chapter II). In addition, the height decrease related to the evaporation of the water h_{water} during the sliding tests was also calculated with the value of the M_{water} as the following equation.

$$h_{water} = \frac{M_{water}}{ds} \quad (IX. 2)$$

Then, the real creep height loss h_{creep} was estimated by the subtraction of h_{wear} and h_{water} from the total height decrease h_{total} , as shown in the following equation.

$$h_{creep} = h_{total} - h_{wear} - h_{water} \quad (IX. 3)$$

Table IX. 1 Water absorption before and after the sliding tests.

Water absorption rate before sliding test, %	0	1.5	2.7	3.5	4.8
Water absorption rate after sliding test, %	0	1.4	2.6	3.4	4.5

Fig. IX. 3 presents the relationship between the water absorption rate (before sliding tests) and the wear height loss, creep height loss, and height loss by water evaporation after sliding tests, which were estimated with the method explained above. Wear decreases with the increase in the water absorption rate. This can be considered to be due to the decrease in the Hertzian contact pressure owing to the decrease in the Young's modulus related with the increase in the water absorption. To interpret these results, the effect of the contact pressure on the wear height loss was investigated through the sliding tests using the same GF-reinforced composite without water absorption, steel cylinders, and grease for different normal load of 150 to 450 N (Hertzian contact pressure ranging from 129 to 222 MPa). Other test conditions were the same. As presented in Fig. IX. 4, wear of the GF-reinforced composite decreases with the decrease in the contact pressure, and it is supposed to become almost zero when the contact pressure is under 120 MPa. On the other hand, when water absorption is between 3 and 4%, Hertzian contact pressure estimated by the Young's modulus as presented in Fig. IX. 1 would be 107 to 137 MPa. Therefore, this value coincides with the contact pressure in which wear rate is supposed to be zero, and the decrease in the wear of the water-absorbed GF-reinforced composite can be related to the decrease in the contact pressure.

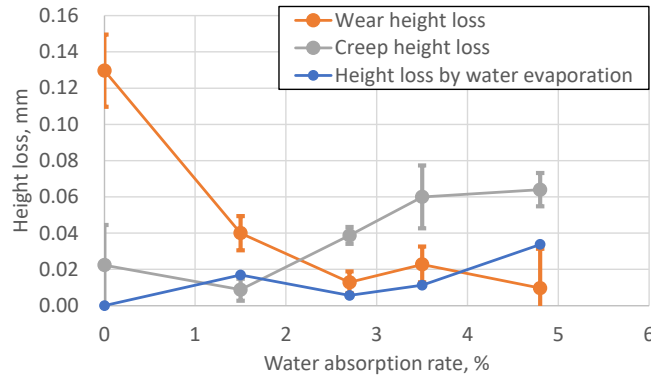


Fig. IX. 3 Relationship between the water absorption rate and the total height loss, wear height loss, and creep height loss.

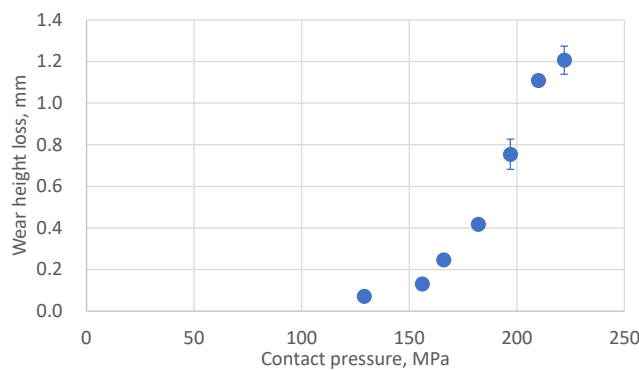


Fig. IX. 4 Relationship between the contact pressure and wear height loss for specimens without water absorption.

On the other hand, creep exhibits the same range of value until 1.5%, and increases with the increase in the water absorption rate until 4.8%. This is considered to be attributed to the decrease in the Young's modulus. Fig. IX. 5 presents the ratio of the wear and creep in the total height decrease for different values of the water absorption rate. Typical tendency in the ratio of wear and creep is observed. Over 80% of the height loss is wear in the water absorption of 0%. The ratio of the creep increases gradually with the increase in the water absorption rate, and almost 90% of the total height loss is creep when the water absorption rate is 4.8%. In addition, no wear of the steel cylinders was observed after each test and there was no change of the color of the grease.

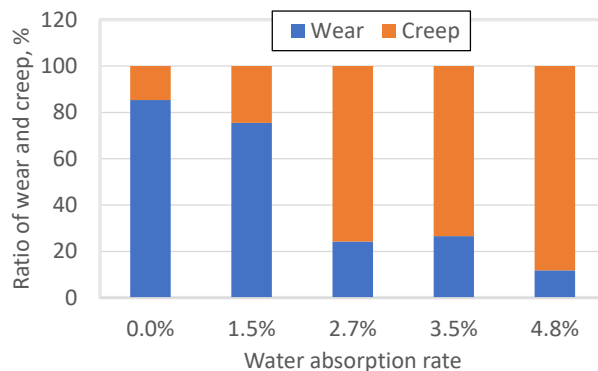


Fig. IX. 5 Ratio of the wear and creep in the total height decrease with different values of the water absorption rate.

Fig. IX. 6 presents the average values of the friction coefficient from 46,125 cycles to 61,500 cycles, and evolutions of the temperature for different values of the water absorption rate during the sliding test. No significant difference in the friction coefficient is observed with different values of the water absorption rate. Temperature decreases with the increase in the water absorption rate. This is attributed to the decrease of the sliding heat generation owing to the decrease in the contact pressure with the increase in the water absorption rate.

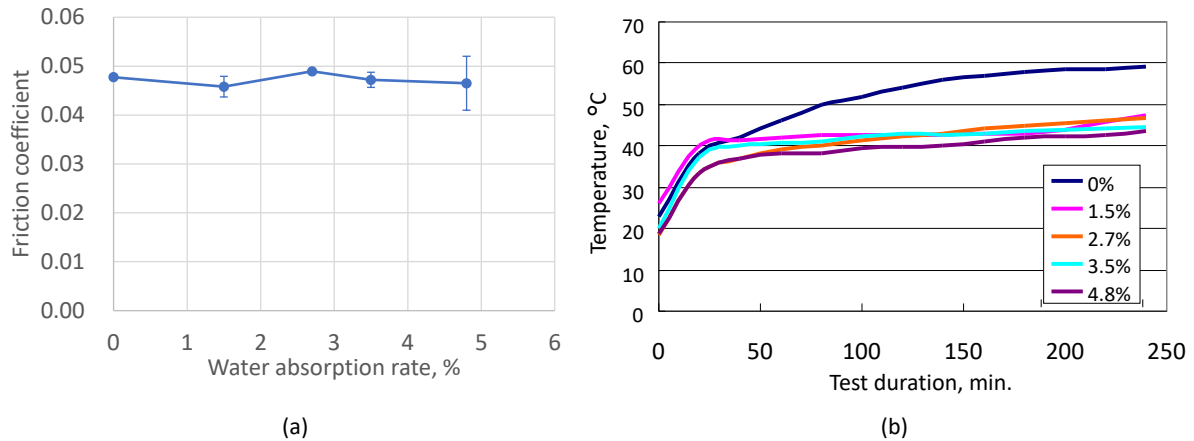


Fig. IX. 6 (a) average value of the friction coefficient from 46,125 cycles to 61,500 cycles; (b) evolutions of the temperature at different values of the water absorption rate.

The effect of the water absorption on the wear of the GF composite under grease lubrication is different from the effect under dry conditions presented in [73]. This is considered to be attributed to the difference of the wear mode. In many previous studies [65, 66, 74, 91], the wear mode of the GF-reinforced PA in contact with steel under dry conditions is reported as the adhesive wear, and the increase in the adhesive force to the steel counterpart (with the increase in the temperature, increase in the molecular mass of PA, or increase in the water absorption rate, for example) increases the friction and deteriorates the wear resistance of the GF composite. On the other hand, the 2-body abrasive wear mode dominates the wear resistance of the GF composite under grease lubrication with less effect of the adhesion, as presented in Section 4 in Chapter III, rather than under dry conditions. Therefore, the decrease in the contact pressure reduced the 2-body abrasive wear with the increase in the water absorption rate.

Fig. IX. 7 presents the optical microscope observation of the sliding surface after the sliding tests using GF composite with different values of the water absorption rate. Entire sliding surface can be worn in the sample with 0% in the water absorption rate, as observed in Section 2 in Chapter III. However, the wear on the sliding surface can decrease with the increase in the water absorption rate, and almost no wear can be observed in the sample with 4.8% in the water absorption rate. These observations correspond with the wear amounts observed in the sliding tests. Fig. IX. 8 shows the SEM images of the sliding surface in the GF composite with 0% and 2.7% in the water adsorption rate. Peeling of PA66, damaged and exposed GFs can be observed on the entire surface of the sample with 0% in the water absorption rate. On the other hand, less damage can be observed in the sample with water absorption rate higher of 2.7%, as previously mentioned.

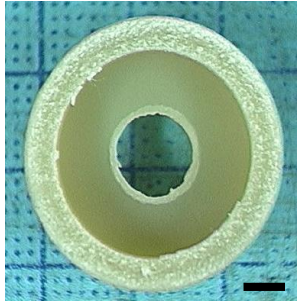
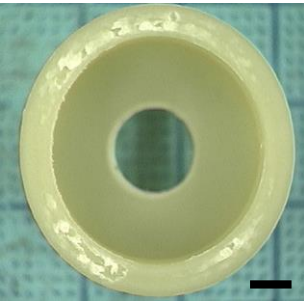
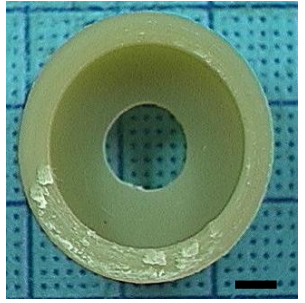



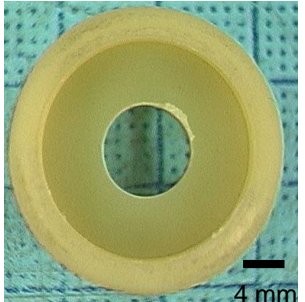
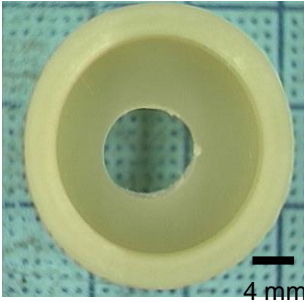
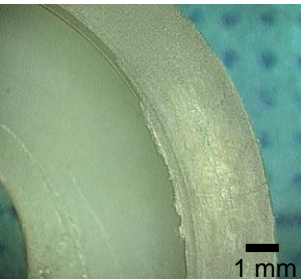
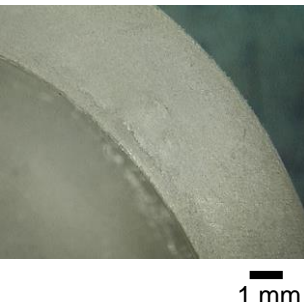
Water absorption rate	0%	1.5%	2.7%
Entire surface			
Enlarged image			
Water absorption rate	3.5%	4.8%	
Entire surface			
Enlarged image			

Fig. IX. 7 Optical microscope observations of the sliding surfaces after the sliding tests using GF composite with different values of the water absorption rate.

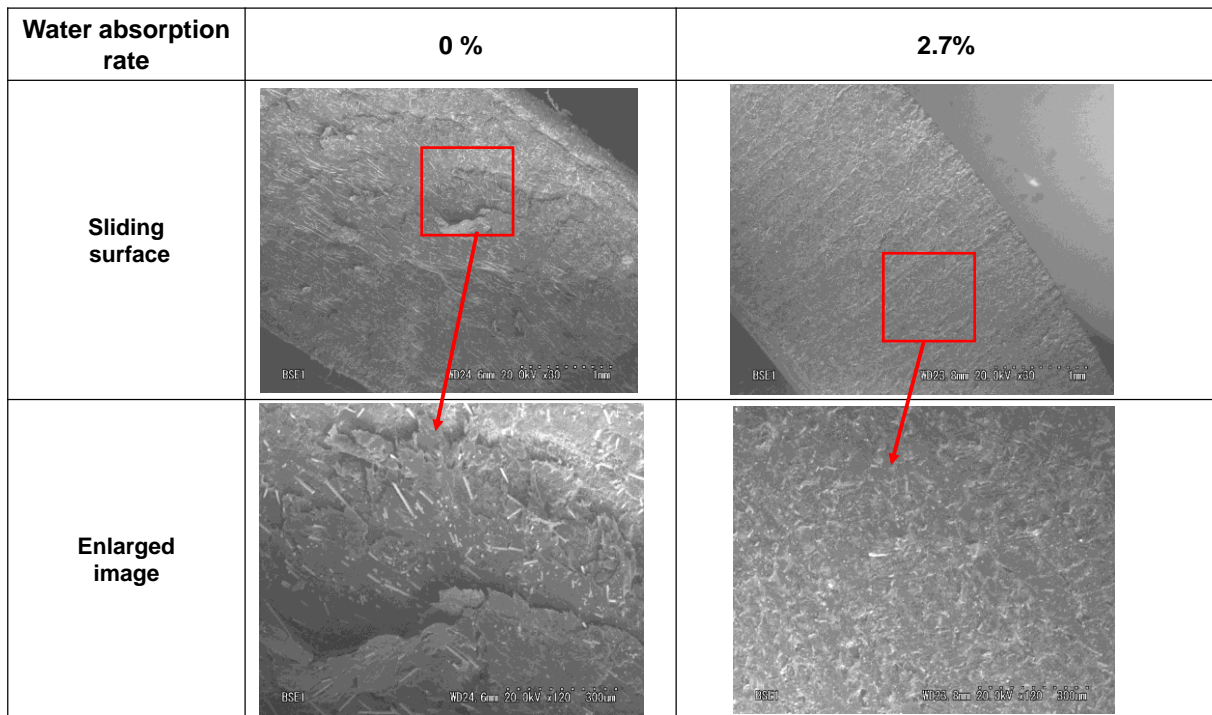


Fig. IX. 8 SEM observations of the sliding surface after the sliding tests using GF composite with 0% and 2.7% of the water absorption rate.

4. Conclusions

PA66 is known to show hygroscopicity owing to its hydrophilic molecular structure. In this chapter, the effect of the water absorption on the tribological properties of GF-reinforced composite in contact with steel under grease lubrication was investigated. Wear of the GF composite decreased and creep increased with the increase in the water absorption rate of the composite. This is related to the decrease in the Young's modulus and Hertzian contact pressure.

GENERAL CONCLUSIONS

Engineering plastics are widely used for sliding parts including worm wheel in worm reducer used in the automotive EPS. To apply the EPS to much larger vehicles or downsize the worm reducer, the development of polymer material and the design of the worm reducer which can ensure good durability and lower friction are requested. Thus, the objective of this thesis was to clarify the tribological properties of unreinforced and fiber-reinforced PA66 in contact with steel counterpart under grease lubrication to improve the tribological properties of polymer sliding parts including worm reducer in the automotive EPS.

Before the start of my PhD study, bibliography survey was carried out considering the following points: the contact geometry of worm reducer in automobile EPS, tribology of PA66 and fiber-reinforced composite material in contact with metallic material especially under lubricated conditions (with oil or grease), influence of different parameters on the tribological behavior, and lubrication theories of contacts. It was revealed that several works on the worm reducer performance or basic tribological properties of the PA66 or composite material were conducted focusing on various different experimental parameters; however, it could not be stated that sufficient research works on the typical tribological properties of PA66 or fiber-reinforced composite existed especially under high contact pressure, at various range of the temperature, at high sliding speed, and under lubricated conditions. In addition, the effect of the material parameters, including polymer or fiber types, which is significant to develop new materials, on the tribological properties under typical sliding mode has not yet been clarified enough. Therefore, the significance of clarification of the tribological behavior under lubricated conditions was proposed in the present study.

My PhD study was conducted globally in two steps: first, we focused on the clarification of the tribological behavior of PA66 and PA66-based composite in contact with steel under lubricated conditions. Next, we focused on the clarification of the effects of the composite material parameters on the tribological properties.

In the part of the clarification of the tribological behavior, the tribological mechanisms of GF-reinforced PA66 in contact with steel counterpart under high contact pressure in grease lubricated conditions were first clarified, using a basic sliding test which simulates the contact geometry of worm reducer in EPS, as presented in Fig. concl. 1.

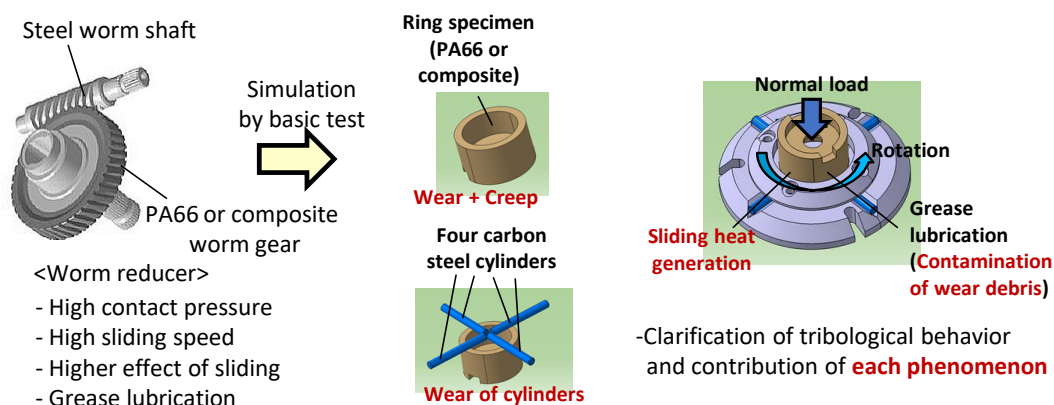


Fig. concl. 1 Basic sliding test which simulates the contact geometry of worm reducer in EPS.

An initial sudden increase in the vertical displacement during sliding tests was observed and it was related to the creep of the composite ring. After this sudden increase, the wear of the composite increased linearly with increasing number of cycles, as presented in Fig. concl. 2. The mechanical properties of the sliding surface changed over time according to the damage on the sliding surface of the composite, and the damage to the sliding surface induced the increase in creep and friction coefficient. Conversely, wear of the unreinforced PA66 was not observed, whereas initial creep was larger than that of the GF composite. An important effect regarding the fiber orientation on the sliding surface of the GF composite was observed on the wear resistance of the counterpart steel and the composite itself. The aggressive effects observed on the counterpart steel were much greater when fibers were oriented in the perpendicular direction. By contrast, wear of the composite increased when the fibers were aligned parallel to the sliding direction. In addition, the effect of the counterpart steel hardness on the tribological properties was investigated. The relative hardness between the steel and fibers is important in understanding the wear induced in the steel and composite. The wear resistance of the composite was improved when the hardness of the counterpart steel is lower, as presented in Fig. concl. 3, because aggressive effects on a composite that has harder fibers were reduced when the steel was softer, while the wear on a steel cylinder reduced the contact pressure (through an increase in contact area).

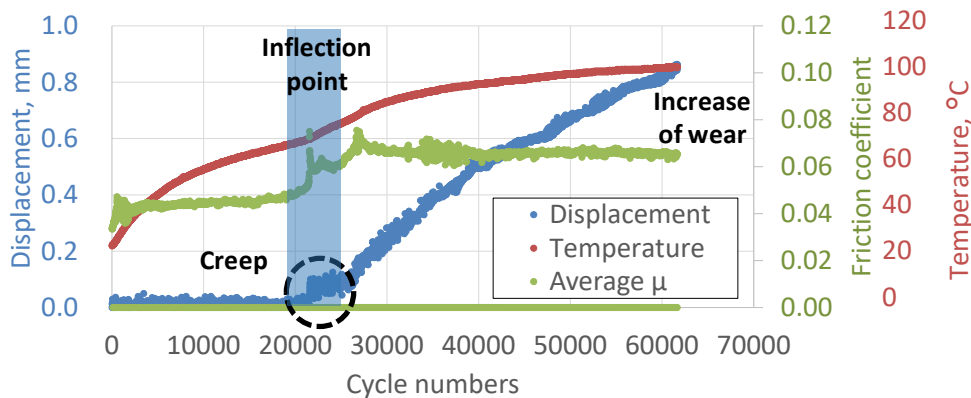


Fig. concl. 2 Evolutions of the displacement, friction coefficient, and temperature in the sliding test using GF composite in contact with steel under grease lubrication.

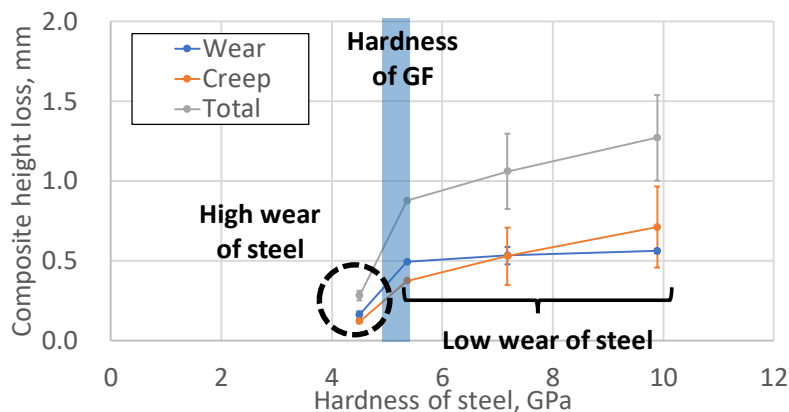


Fig. concl. 3 Effects of the steel hardness on the wear and creep resistance of the GF composite.

Next, the effects of temperature and the addition of zinc carboxylate to grease on the tribological properties of PA66 in contact with carbon steel were clarified. The tribological properties were described by considering the temperature dependence of both the mechanical properties of PA66 and the tribochemistry. Wear and creep resistance of GF-reinforced PA66 deteriorated with an increase in temperature using grease without the addition of zinc carboxylate. This was explained by the temperature dependence of the mechanical properties on the sliding surface of the composite (hardness and Young's modulus) as measured based on the micro indentation procedure. In addition, the effects of the addition of zinc carboxylate to grease were investigated at each temperature. The effects of the improvement of the tribological properties were not observed at room temperature. Conversely, significant effects of the addition of zinc carboxylate in the grease, such as a decrease in the friction coefficient, a decrease in the wear and creep of the composite, and a decrease in the wear of the steel counterpart, were observed at 80°C. The decrease in the friction coefficient was observed at 120°C. However, the effect of the decrease in the wear and creep was not confirmed at high temperature. Fig. concl. 4 shows the schematic of tribochemical reaction on the sliding surface. A ToF-SIMS analysis of the steel surface after the sliding test at 80°C revealed the formation of a heterogeneous tribofilm composed of carboxylates. An XPS analysis of the GF-reinforced PA66 composite surface showed the presence of a ZnS reactive tribofilm related to the tribochemical reaction between zinc carboxylate and sulfur-type anti-oxidation agent on the polymer surface only. The contribution of the formation of the carboxylates tribofilm on the steel surface in the improvement of the tribological properties is greater than that of the formation of a ZnS tribofilm on the PA66 surface.

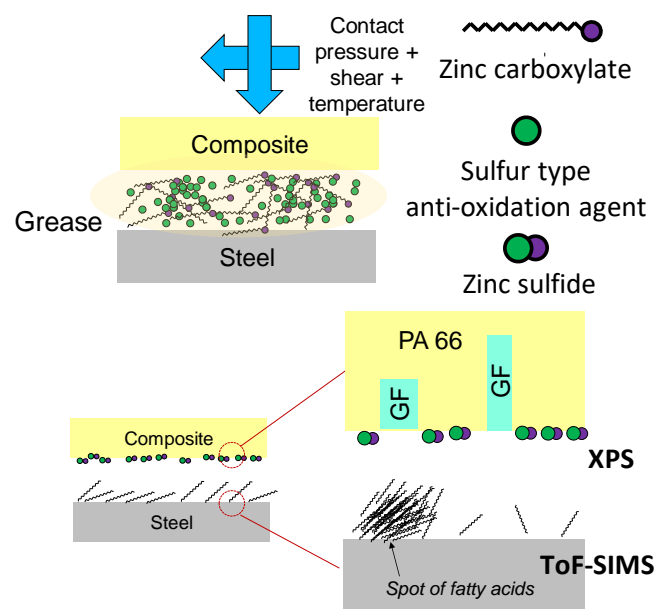


Fig. concl. 4 Schematic of tribochemical reaction on the sliding surface.

Furthermore, the friction mechanisms of the unreinforced and GF-reinforced PA66 in contact with carbon steel under PAO8 oil or PAO8-based urea grease lubrication were also elucidated in less severe conditions. At first, friction mechanism under PAO8 oil lubrication was discussed. The friction coefficient increased with increasing surface roughness of PA66

ring specimens sliding surface, decreasing sliding speed, and increasing temperature. Theoretical minimum oil film thickness was estimated using the equation for soft EHL. Λ - μ master curve (wherein the friction coefficient decreased with increasing Λ) was presented, as presented in Fig. concl. 5. The normal load dependence of the friction coefficient can also be explained by the proposed Λ - μ curve when the initial surface roughness is lower. The Bowden and Tabor law, on the other hand, explained the normal load dependence well, and the results did not coincide with the proposed Λ - μ curve when the initial surface roughness was higher because the effect of the direct contact between the PA66 and steel became more remarkable than the influence of the oil film formation, as presented in Fig. concl. 6.

The effects of the sliding speed, initial sliding surface roughness, and temperature on the friction coefficient were investigated for the GF composite, and they showed the same tendencies as observed for the unreinforced PA66. The Λ - μ master curve was obtained for the GF composite and compared to that obtained for the unreinforced PA66, thereby confirming that a lower friction coefficient can be obtained using the GF composite compared to the unreinforced PA66 for the same Λ .

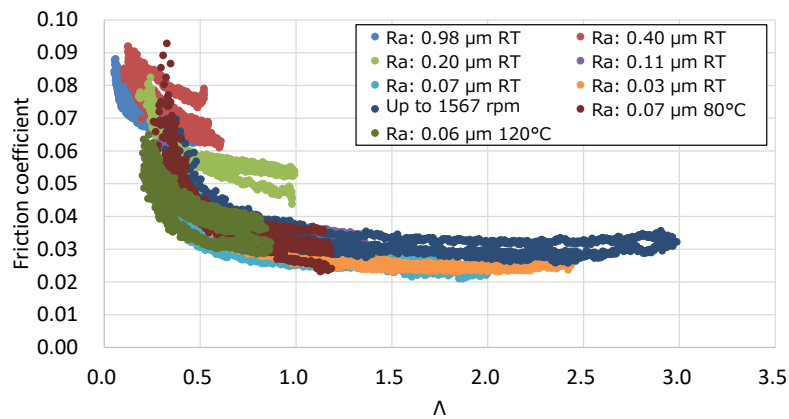


Fig. concl. 5 Obtained Λ - μ master curve.

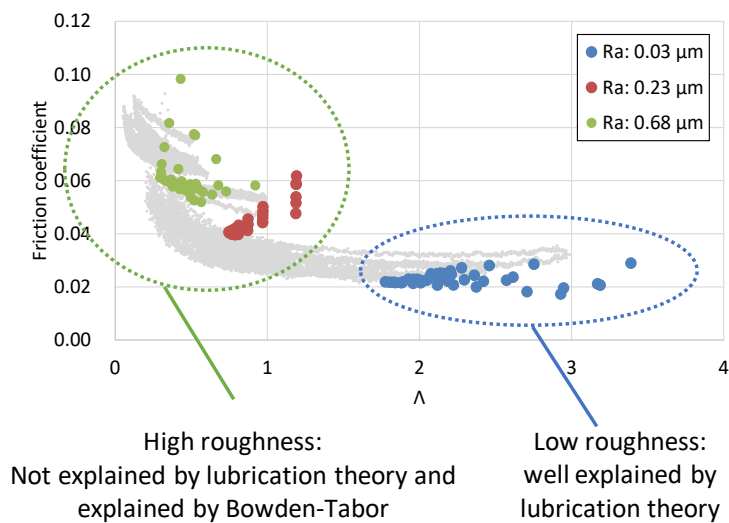


Fig. concl. 6 Relationship between Λ and friction coefficient with different values of the PA66 sliding surface roughness superimposed on Λ - μ master curve.

Finally, friction mechanism under grease lubrication was discussed. In the case where oil film is formed easily, such as under lower normal load or with lower sliding surface roughness, effect of solid contact can be reduced even under PAO8 oil lubrication (with lower viscosity than grease). And low friction coefficient, which was identical as the one under grease lubrication, can be obtained. On the other hand, in the case of high normal load or high sliding surface roughness, grease with higher viscosity can reduce the solid contact in comparison to PAO8 oil lubrication, and thus lower friction coefficient can be obtained. Therefore, the difference in the friction behavior between PAO8 oil lubrication and grease lubrication depends on the severity of the contact. The addition of zinc carboxylate to grease provided adverse effect on the friction coefficient at room temperature because zinc carboxylate does not soften and prevents the good oil film formation. By contrast, the zinc carboxylate leads to lower friction coefficient by the tribochemical reaction without prevention of oil film formation at 80°C.

In the part of the clarification of the effects of the composite composition on the tribological behavior, at first, the tribological properties of different GF-reinforced PA66 composites were studied under grease lubricated conditions. High interfacial shear strength between the PA66 and GFs reduced the composite wear. Good adhesion between PA66 and GF prevented the degradation of the mechanical properties during sliding. The wear resistance of the steel counterpart was also enhanced by increasing the interfacial shear strength. The difference in the interfacial shear strength was discussed quantitatively using a modified Kelly–Tyson model that accounts for the length and orientation of the fibers. The wear resistances of both the GF-reinforced PA66 composite and the steel counterpart were improved by increasing the PA66 molecular mass. The high elongation of the high molecular mass PA66 reduced the interfacial peeling between GF and PA66 due to the shear stress induced by sliding and prevented the exposure of the GF edges, which have a strongly aggressive effect on the steel. Additionally, the high toughness of the high molecular mass PA66 reduced the propagation of scratches on PA66, which originated at the interface between PA66 and the GFs, and enhanced the wear and creep resistance of the composite. The wear of the steel counterparts reduced with decreasing GF diameter because surfaces with high total interfacial adhesion energy can bear higher sliding energies without interfacial peeling between GF and PA66. The wear and creep resistances of the composite also improved when smaller diameter GFs were used because the strength and toughness of the composite were enhanced by the increase in the interfacial adhesion area. Fig. concl. 7 presents the schematics of the effects of the PA66 molecular mass (M_m) and GF diameter on the tribological properties.

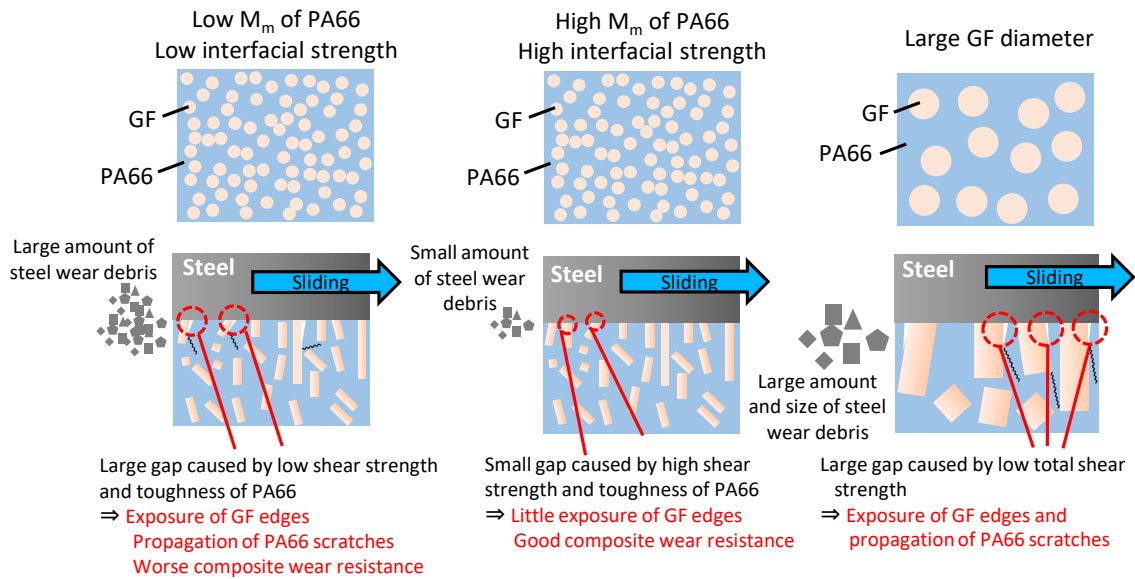


Fig. concl. 7 Schematics of the effects of the PA66 molecular mass (M_m) and GF diameter on the tribological properties.

Next, as a way to increase the PA66 molecular mass of fiber-reinforced composite, the reaction mechanism for a fiber-reinforced PA66 with added carbodiimide during extrusion as presented in Fig. concl. 8 was clarified, and the mechanical properties and tribological behavior were investigated. Addition of carbodiimide compounds to GF-reinforced PA66 increases the molecular mass of the PA66 and improves the toughness. Using aromatic carbodiimide contributes to controlling the reaction velocity, allowing the carbodiimide to remain partially unreacted in the extruded pellets. In addition, a much higher toughness was obtained with side-feeding of the carbodiimide compounds in the twin screw extruder, and therefore the toughness generally increased with increasing unreacted carbodiimide in the pellets. As shown in Fig. concl. 9, the wear resistance of GF- or AF-reinforced PA66 materials under high contact pressure and grease-lubricated conditions is improved significantly by the addition of carbodiimide compounds and the increase in molecular mass.

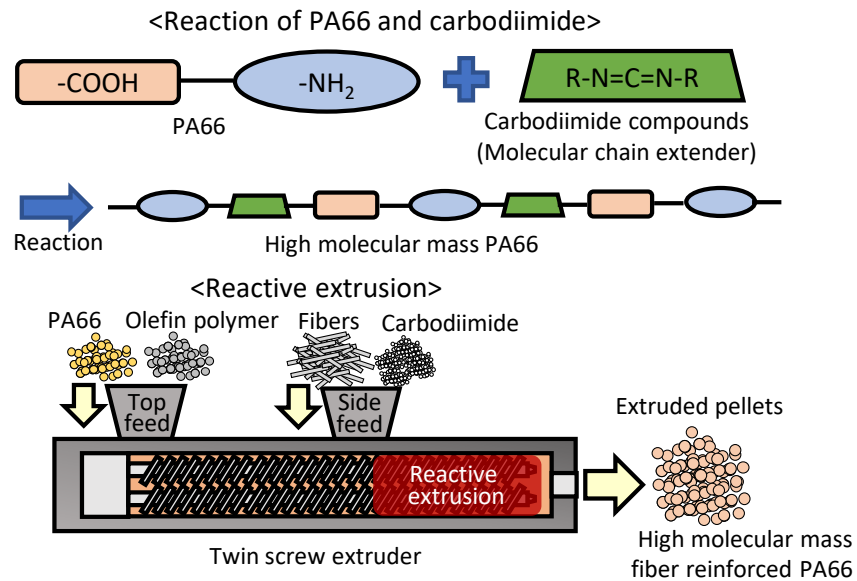


Fig. concl. 8 Reactive extrusion of PA66 with added carbodiimide.

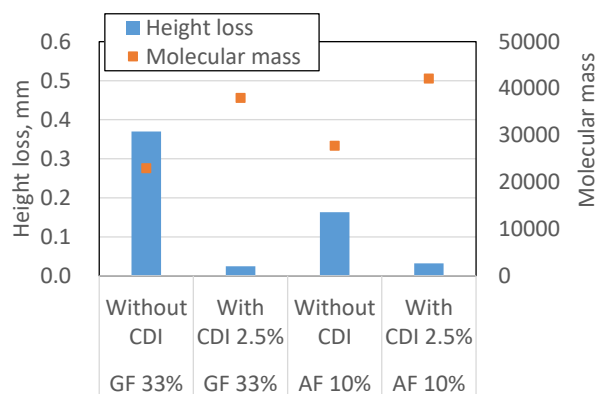


Fig. concl. 9 Poly-carbodiimide (CDI) addition effect on the wear resistance of GF- and AF-reinforced PA66 composite.

In addition to GF-reinforced PA66, the tribological properties of CF-reinforced PA66 composites in contact with steel were investigated and compared to those of GF-reinforced PA66. Under dry conditions, fiber reinforcement led to reduced friction and improved wear resistance compared to the unreinforced PA66. In particular, the CF composite exhibited lower friction because the adhesive wear. Under grease lubrication, the CF composite presented inferior tribological properties compared to the GF composite, regardless of the PA66 molecular mass and after considering the difference in the contact pressure related to the difference in the Young's moduli. Insufficient interfacial adhesion between the PA66 and CFs induced the peeling of the fibers, which scratched the PA66 at much lower numbers of cycles. The destructive effects of the CF composite on the steel counterpart were much higher than those of the GF composite, even though the hardness of the CFs was much lower than that of the GFs. The destructive effect is not determined solely by the fiber hardness, and the insufficient interfacial adhesion between the CFs and PA66 also led to an increase in the wear of the steel counterpart. Fig. concl. 10 shows the schematic of the difference in the tribological behavior between the CF composite and GF composite. The difference in the temperature

dependence of the tribological properties between the CF composite and GF composite was caused by the difference in the tribofilm formation related to the grease additives. The tribofilm formation was dominated by the contact pressure, regardless of the fiber type, and contributed to the improvement of the tribological properties at 80°C when the contact pressure was not too high.

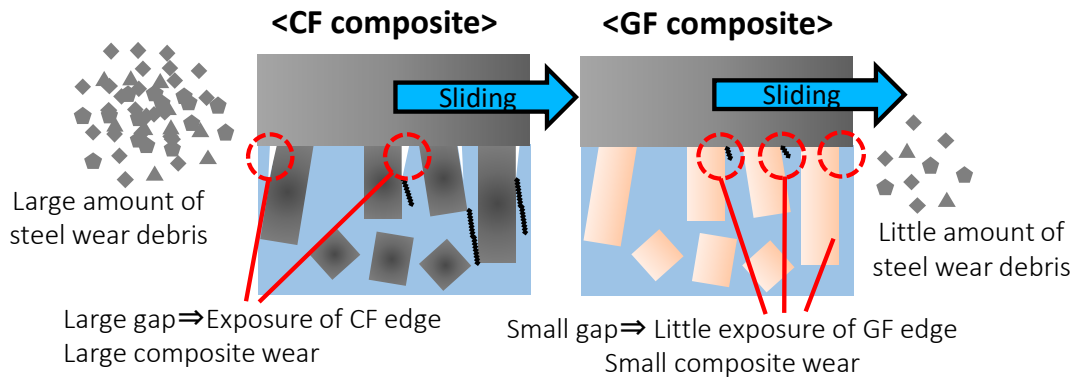


Fig. concl. 10 Schematic of the difference in the tribological behavior between the CF composite and GF composite.

Finally, the effect of water absorption was investigated. PA66 is known to show hygroscopicity owing to its hydrophilic molecular structure. The effect of the water absorption on the tribological properties of GF-reinforced composite in contact with steel under grease lubrication was investigated. Wear of the GF composite decreased and creep increased with the increase in the water absorption rate of the composite. This is related to the decrease in the Young's modulus and Hertzian contact pressure.

This PhD thesis clarified the tribological mechanisms of PA66 and fiber-reinforced composite in contact with carbon steel under lubricated conditions. The developed scientific approach and the obtained results can contribute to downsize and use the EPS which equips the worm reducer under severer conditions. In the actual EPS worm reducer durability tests, GF composite worm wheel developed based on the present study exhibited better tribological properties than widely used unreinforced PA66 worm wheel. It is expected that knowledge acquired in the present PhD study will be introduced to any polymer sliding parts widely as well as worm reducer in the EPS.

REFERENCES

- [1] M. Kurokawa, Y. Uchiyama, S. Nagai, Performance of plastic gear made of carbon fiber reinforced polyether-ether-ketone: Part 2, *Tribol. Int.* 33 (2000) 715-721.
[https://doi.org/10.1016/S0301-679X\(00\)00111-0](https://doi.org/10.1016/S0301-679X(00)00111-0)
- [2] R. J. Tappera, M. L. Longanaa, A. Nortonb, K. D. Pottera, I. Hamertona, An evaluation of life cycle assessment and its application to the closed-loop recycling of carbon fibre reinforced polymers, *Compos. Part B* 184 (2020) 107665.
<https://doi.org/10.1016/j.compositesb.2019.107665>
- [3] V. S. Balakrishnana, T.H. Rawungb, J. Buhl, H. Seidlitz, M. Bambachb, Impact and damage behaviour of FRP-metal hybrid laminates made by the reinforcement of glass fibers on 22MnB5 metal surface, *Compos. Sci. Technol.* 187 (2020) 107949.
<https://doi.org/10.1016/j.compscitech.2019.107949>
- [4] R. Nakata, Grease lubrication technology for sliding automobile parts, *JTEKT Eng. J. English Ed.* 1011E (2014) 25–30.
http://eb-cat.ds-navi.co.jp/enu/jtekt/tech/ej/img/no1011e/1011e_06.pdf
- [5] S.W. Zhang, State-of-the-art of polymer tribology, *Tribol. Int.* 31 (1998) 49–60.
[https://doi.org/10.1016/S0301-679X\(98\)00007-3](https://doi.org/10.1016/S0301-679X(98)00007-3)
- [6] S. Senthilvelan, R. Gnanamoorthy, Damage Mechanisms in injection molded unreinforced, glass and carbon reinforced nylon 66 spur gears, *Appl. Compos. Mater.* 11 (2004) 377–397.
<https://doi.org/10.1023/B:ACMA.0000045313.47841.4e>
- [7] S. Senthilvelan, R. Gnanamoorthy, Fiber reinforcement in injection molded nylon 6/6 spur gears, *Appl. Compos. Mater.* 13 (2006) 237–248.
<https://doi.org/10.1007/s10443-006-9016-9>
- [8] S. Kirupasankar, C. Gurunathan. R. Gnanamoorthy, Transmission efficiency of polyamide nanocomposite spur gears, *Mater. Des.* 39 (2012) 338-343.
<https://doi.org/10.1016/j.matdes.2012.02.045>
- [9] B. Sarita, S. Senthilvelan, Effects of lubricant on the surface durability of an injection molded polyamide 66 spur gear paired with a steel gear, *Tribol. Int.* 137 (2019) 193–211.
<https://doi.org/10.1016/j.triboint.2019.02.050>
- [10] H. İmrek, Performance improvement method for Nylon 6 spur gears, *Tribol. Int.* 42 (2009) 503-510.
<https://doi.org/10.1016/j.triboint.2008.08.011>
- [11] J. Tavčar, G. Grkman, J. Duhovnik, Accelerated lifetime testing of reinforced polymer gears, *J. Adv. Mec. Des., Sys., and Man.* 12 (2018) 1-13.
<https://doi.org/10.1299/jamdsm.2018jamdsm0006>
- [12] Y. Zhang, C. Pursell, K. Mao, S. Leigh, A physical investigation of wear and thermal characteristics of 3D printed nylon spur gears. *Tribol. Int.* 141 (2020) 105953.

<https://doi.org/10.1016/j.triboint.2019.105953>

[13] D. Walton, A.B. Cropper, D.J. Weale, P.K. Meuleman, The efficiency and friction of plastic cylindrical gears Part 1: Influence of materials, Proc. Inst. Mech. Engineers., Part J: J. Eng. Tribol. 216 (2002) 75-78.

<https://doi.org/10.1243/1350650021543915>

[14] N. M. Mehat, H. M. Noor, S. Kamaruddin, Optimization of multiple quality characteristics for injection moulded polyamide helical gear via integration of Taguchi method and Grey relational analysis, Mater. Sci. Eng. 932 (2020) 012122.

<https://doi.org/10.1088/1757-899X/932/1/012122>

[15] A.L. Gasparin, L.L. Corso, E.K. Tentardini, R.C.R. Nunes, M.M de C. F, R.V.B de Oliveira, Polyamide worm gear: manufacturing and performance, Mater. Res. 15 (2012) 483-489.

<https://doi.org/10.1590/S1516-14392012005000056>

[16] N. Tsukamoto, H. Maruyama, A study for the development of plastic worm gears: Plastic worm gears filled with fiber and solid lubricant, JSME Int. J. Ser. 3 34 (1991) 260-264.

<https://doi.org/10.1299/jsmec1988.34.260>

[17] S. Yousef, T.A. Osman, A.H. Abdalla, G.A. Zohdy, Wear characterization of carbon nanotubes reinforced acetal spur, helical, bevel and worm gears using a TS universal test rig, JOM. 67 (2015) 2892–2899.

<https://doi.org/10.1007/s11837-014-1268-5>

[18] S.C. Tung, W.W. Cheng, Simulation test of grease-lubricated steel-polymer interface of worm gear, Tribol. Trans. 41 (1998) 537-542.

<https://doi.org/10.1080/10402009808983780>

[19] W.W. Cheng, W. Tu, Tribological study of grease lubricated plastic wormgear for automotive applications, Tribol. Trans. 45 (2002) 563-567.

<https://doi.org/10.1080/10402000208982588>

[20] R.A.E. Wood, Rolling bearing cages, Tribol. 5 (1972) 14-21.

[https://doi.org/10.1016/0041-2678\(72\)90181-9](https://doi.org/10.1016/0041-2678(72)90181-9)

[21] D. Scott, J. Blackwell, P.J. McCullagh, G.H. Mills, Composite materials for rolling bearing cages, Wear 15 (1970) 257-269.

[https://doi.org/10.1016/0043-1648\(70\)90016-5](https://doi.org/10.1016/0043-1648(70)90016-5)

[22] H. Oh, M.H. Azarian, C. Morillo, M. Pecht, E. Rhem, Failure mechanisms of ball bearings under lightly loaded, non-accelerated usage conditions, Tribol. Int. 81 (2015) 291–299.

<https://doi.org/10.1016/j.triboint.2014.09.014>

[23] J. Kohout, Strength changes of moulded polyamide composite caused by thermal oxidation, J. Mater. Sci. 34 (1999) 843-849.

<https://doi.org/10.1023/A:1004593417901>

[24] D.V. Butorin, N.G. Filippenko, A.V. Livshits, S.I. Popov, Analysis of failures of bearings of axle box unit with polyamide cages and prospects of increasing their service life, IOP Conference Series: Mater.

Sci. Eng. 760 (2020) 012010.

<https://doi.org/10.1088/1757-899X/760/1/012010>

[25] Z. Wenhua, D. Sier, C. Guoding, C. Yongcun, Impact of lubricant traction coefficient on cage's dynamic characteristics in high-speed angular contact ball bearing, *Chin. J. Aeronaut.* 30 (2017) 827-835.

<https://doi.org/10.1016/j.cja.2016.08.019>

[26] K. Ishihara, Highly lubricated polymer interfaces for advanced artificial hip joints through biomimetic design, *Polym. J.* 47 (2015) 585–597.

<https://doi.org/10.1038/pj.2015.45>

[27] J.H. Dumbleton, Wear and its measurement for joint prosthesis materials, *Wear* 49 (1978) 297-326.

[https://doi.org/10.1016/0043-1648\(78\)90094-7](https://doi.org/10.1016/0043-1648(78)90094-7)

[28] Y. Sawae, Handbook of polymer tribology: chapter 3: Wear of UHMWPE for joint prosthesis, (2018) 81-109.

[29] D.C. Evans, G.S. Senior, Self-lubricating materials for plain bearings, *Tribol. Int.* 15 (1982) 243-248.

[https://doi.org/10.1016/0301-679X\(82\)90077-9](https://doi.org/10.1016/0301-679X(82)90077-9).

[30] S.S. Kim, H. J. Hwang, M.W. Shin, H. Jang, Friction and vibration of automotive brake pads containing different abrasive particles, *Wear* 271 (2011) 1194-1202.

<https://doi.org/10.1016/j.wear.2011.05.037>

[31] M. Harrass, K. Friedrich, A.A. Almajid, Tribological behavior of selected engineering polymers under rolling contact. *Tribol. Int.* 43 (2010) 635–646.

<https://doi.org/10.1016/j.triboint.2009.10.003>

[32] J. Chen, H. Xu, C. Liu, L. Mi, C. Shen, The effect of double grafted interface layer on the properties of carbon fiber reinforced polyamide 66 composites. *Compos. Sci. Technol.* 168 (2018) 20-27.

<https://doi.org/10.1016/j.compscitech.2018.09.007>

[33] M. Bondy, W. Rodgers, W. Altenhof, Tensile fatigue characterization of polyamide 66/carbon fiber direct/in-line compounded long fiber thermoplastic composites. *Compos. Part B: Eng.* 173 (2019) 106984.

<https://doi.org/10.1016/j.compositesb.2019.106984>

[34] J.H. Fonseca, G. Han, L. Quagliato, Y. Kim, J. Choi, T. Keum, S. Kim, D.S. Han, H. Lee, Design and numerical evaluation of recycled-carbon-fiber-reinforced polymer/metal hybrid engine cradle concepts, *Int. J. Mec. Sci.* 163 (2019) 105115.

<https://doi.org/10.1016/j.ijmecsci.2019.105115>

[35] K. Friedrich, Polymer composites for tribological applications, *Adv. Ind. Eng. Polym. Res.*, 1 (2018) 3-39.

<https://doi.org/10.1016/j.aiepr.2018.05.001>

[36] K. Sakata, Outlook for steering system technology aimed at self-driving, *JTEKT Eng. J. English Ed.*, 1017E (2020) 9-15.

http://eb-cat.ds-navi.co.jp/enu/jtekt/tech/ej/img/no1017e/1017e_03.pdf

[37] T. Takahashi, H. Suzuki, T. Nakayama, K. Fujiyama, S. Yamaguchi, M. Yamashita, T. Goto, T. Saito, Application technology of high-power electric power steering system, JTEKT Eng. J. English Ed. 1006E (2009) 47-52.

http://eb-cat.ds-navi.co.jp/enu/jtekt/tech/ej/img/no1006e/1006e_09.pdf

[38] S.H. Kim, Worm gear efficiency model considering misalignment in electric power steering systems, Mech. Sci., 9 (2018) 201–210.

<https://doi.org/10.5194/ms-9-201-2018>

[39] T. Sugiura, Backlash adjustment mechanism for reducer of electric power steering system, JTEKT Eng. J. English Ed. 1001E (2006) 65–69.

http://eb-cat.ds-navi.co.jp/enu/jtekt/tech/ej/img/no1001e/1001e_15.pdf

[40] Y. Nagahashi, A. Kawakubo, T. Tsujimoto, K. Kagei, J. Hasegawa, S. Kakutani, Development of high power column-type electric power steering system, JTEKT Eng. J. English Ed. 1003E (2007) 35–39.

http://eb-cat.ds-navi.co.jp/enu/jtekt/tech/ej/img/no1003e/1003e_07.pdf

[41] H. C. Ahn, Wear of glass fiber reinforced polyamide worm gear according to the direction of the glass fiber, Technical paper presented at SAE 2010 World Congress & Exhibition.

<https://doi.org/10.4271/2010-01-0917>

[42] M. Sadeghi, S. Hamid, Calculation and simulation of column electric power steering system, Int. J. Mec., Aerosp., Ind., Mechatro. Manuf. Eng. 11 (2017) 153-160.

<http://porto.polito.it/2663803/>

[43] P. Poirel, Prospects for electric power steering, ATZ Worldwide 114 (2012) 10–14.

<https://doi.org/10.1007/s38311-012-0170-4>

[44] G.H. Kim, J.W. Lee, T.I. Seo, Durability characteristics analysis of plastic worm wheel with glass fiber reinforced polyamide, Mater. 6 (2013) 1873–1890.

<https://doi.org/10.3390/ma6051873>

[45] S.H. Kim, M.C. Shin, J.W. Byun, K.H. O, C.N. Chu, Efficiency prediction of worm gear with plastic worm wheel. Int. J. Precis. Eng. Manuf. 13 (2012) 167–174.

<https://doi.org/10.1007/s12541-012-0021-7>

[46] T. Kunishima, K. Miyake, T. Kurokawa, H. Arai, Clarification of tribological behavior on tooth surface of resin worm gear for electric power steering, JTEKT Eng. J. English Ed. 1013E (2016) 27–33.

http://eb-cat.ds-navi.co.jp/enu/jtekt/tech/ej/img/no1013e/1013e_05.pdf

[47] J.Y. Youn, B.J. Park, K.H. Noh, Polyamide 6,6 resin composition having toughness, abrasion resistance and frictional resistance, U.S. Patent US 2018 / 0044519 A1.

[48] L. Congqing, D. Shijie, L. Shuzhong, The test for withstanding fracture capacity of worm gear made of antifriction composite material of polymer matrix, Proceedings of the 6th WSEAS Int. Conference on Robotics, Control and Manuf. Technol. 2006 1-5.

<http://www.wseas.us/e-library/conferences/2006hangzhou/papers/531-471.pdf>

[49] H. Arai, K. Higashida, T. Tsuda, N. Nishihata, Gear, speed reducer using the same, and electric

- power steering apparatus including the same, Japanese patent JP4475879B24427B2.
- [50] T. Murakami, T. Takajo, Research work for the improvement of the durability of glass fiber-reinforced nylon 66 by modifying the glass fiber diameter, SAE Tec. Pap. 32 (2006).
<https://doi.org/10.4271/2006-32-0032>
- [51] S. Arakawa, T. Ogawa, Polyamide resin composition containing glass fiber, U.S. Patent US 2007/0293607 A1.
- [52] Z. Jiaying, K. Ilie, Static shear strength calculation of plastic helical gears mating with steel worm, Int. J. Precis. Eng. Manuf. 15 (2014) 235–239.
<https://doi.org/10.1007/s12541-014-0330-0>
- [53] Y. Hashimoto, High Strength Resin Gear Materials, Shin-Kobe Tec. Rep. 16 (2006) (in Japanese)
- [54] K. Watanabe, Y. Shimizu, Y. Terada, A study of worm gear to size reduction and performance enhancement for EPS, SAE Tec. Pap. 01-1177 (2006).
<https://doi.org/10.4271/2006-01-1177>
- [55] A. Bormuth, J. Zuleeg, C. Schmitz, R. Schmitz, M. Pfadt, H. Meven, Lubrication of plastic worm gears, Power Transm. Eng. Aug. (2019) 42-47.
- [56] J.P. Robert, F. Künzner, Lubrication of plastic components in the steering system and brakes, ATZ worldwide eMagazine 113 (2011) 24–27.
<https://doi.org/10.1365/s38311-011-0016-5>.
- [57] M. Asakura, K. Uchiyama, S. Inour, Development of spacer balls for rack parallel type electric power steering, JTEKT Eng. J. English Ed. 1015E (2018) 47–51.
http://eb-cat.ds-navi.co.jp/enu/jtekt/tech/ej/img/no1015e/1015e_08.pdf
- [58] R.J. Palmer, Encyclopedia of polymer science and technology; Polyamides, Plast. (2001) 618-643.
<https://doi.org/10.1002/0471440264.pst251>
- [59] J. Wesołowski, K. Płachta, The Polyamide Market, Fibres & textiles in eastern Europe 120 (2016) 12-18.
<https://doi.org/10.5604/12303666.1215537>
- [60] J.J. Rajesh, J. Bijwe, U.S. Tewari, Abrasive wear performance of various polyamides, Wear 252 (2002) 769-776.
[https://doi.org/10.1016/S0043-1648\(02\)00039-X](https://doi.org/10.1016/S0043-1648(02)00039-X).
- [61] J.J. Rajesh, J. Bijwe, Investigations on scratch behaviour of various polyamides, Wear 259 (2005) 661-668.
<https://doi.org/10.1016/j.wear.2004.12.018>.
- [62] J.J. Rajesh, J. Bijwe, U.S. Tewari, B. Venkataraman, Erosive wear behavior of various polyamides, Wear, 249 (2001) 702-714.
[https://doi.org/10.1016/S0043-1648\(01\)00695-0](https://doi.org/10.1016/S0043-1648(01)00695-0)
- [63] D.W. Gebretsadik, J. Hardell, B. Prakash, Friction and wear characteristics of PA 66 polymer composite/316L stainless steel tribopair in aqueous solution with different salt levels, Tribol. Int. 141 (2020) 105917.

<https://doi.org/10.1016/j.triboint.2019.105917>

[64] M. Schnoor, P. Kronewald, K. Friedrich, M. Evstatiev, S. Fakirov, Effects of molecular weight and thermal treatment on wear behavior of Polyamide 6, *Int. J. Polym. Mater. Polym. Biomater.* 46 (2000) 361-376.

<https://doi.org/10.1080/00914030008054867>

[65] M.W. Shin, S.S. Kim, H. Jang, Friction and wear of polyamide 66 with different weight average molar mass, *Tribol. Lett.* 44 (2011) 151–158.

<https://doi.org/10.1007/s11249-011-9833-3>

[66] N. Myshkin, A. Kovalev, *Handbook of polymer tribology: chapter 1: Adhesion and friction of polymers and polymer composite*, (2018) 3-45.

[67] M. Kurokawa, Y. Uchiyama, T. Iwai, S. Nagai, Performance of plastic gear made of carbon fiber reinforced polyamide 12, *Wear* 254 (2003) 468–473.

[https://doi.org/10.1016/S0043-1648\(03\)00020-6](https://doi.org/10.1016/S0043-1648(03)00020-6)

[68] R. Feulner, Z. Brocka, A. Seefried, M.O. Kobes, G. Hülder, T.A. Osswald, The effects of e-beam irradiation induced cross linking on the friction and wear of polyamide 66 in sliding contact, *Wear* 268 (2010) 905-910.

<https://doi.org/10.1016/j.wear.2009.12.025>

[69] D.P.N. Vlasveld, S.G. Vaidya, H.E.N. Bersee, S.J. Picken, A comparison of the temperature dependence of the modulus, yield stress and ductility of nanocomposites based on high and low MW PA6 and PA66, *Polym.* 46 (10) (2005) 3452-3461.

<https://doi.org/10.1016/j.polymer.2005.02.094>

[70] J. Benz, C. Bonten, Reactive extrusion of PA6 - different ways to increase the viscosity, *Pap. presented at the AIP Conf. Proc.* 2055 (2019) 020004.

<https://doi.org/10.1063/1.5084805>

[71] S.C. Ozmen, G. Ozkoc, E. Serhatli, Thermal, mechanical and physical properties of chain extended recycled polyamide 6 via reactive extrusion: Effect of chain extender types, polymer degradation and stability, *Polym. Degrad. Stab.* 162 (2019) 76-84.

<https://doi.org/10.1016/j.polymdegradstab.2019.01.026>

[72] M. Buccella, A. Dorigato, E. Pasqualini, M. Caldara, L. Fambri, Chain extension behavior and thermo-mechanical properties of polyamide 6 chemically modified with 1,1'-carbonyl-bis-caprolactam, *Polym. Eng. Sci.* 54 (1) (2014) 158-165.

<https://doi.org/10.1002/pen.23547>

[73] J.W. Kim, H. Jang, J.W. Kim, Friction and wear of monolithic and glass-fiber reinforced PA66 in humid conditions, *Wear* 309 (2014) 82-88.

<https://doi.org/10.1016/j.wear.2013.11.007>

[74] S.S. Kim, M.W. Shin, H. Jang, Tribological properties of short glass fiber reinforced polyamide 12 sliding on medium carbon steel, *Wear* 274-275 (2012) 34-42.

<https://doi.org/10.1016/j.wear.2011.08.009>

- [75] M. Botan, A.E. Musteata, T.F. Ionescu, C. Georgescu, L. Deleanu, Adding aramid fibers to improve tribological characteristics of two polymers, *Tribol. Ind.* 39 (2017) 283-293.
<https://doi.org/10.24874/ti.2017.39.03.02>
- [76] Y.K. Chen, O.P. Modi, A.S. Mhay, A. Chrysanthou, J.M. O'Sullivan, The effect of different metallic counterface materials and different surface treatments on the wear and friction of polyamide 66 and its composite in rolling-sliding contact, *Wear* 255 (2003) 714–721.
[https://doi.org/10.1016/S0043-1648\(03\)00054-1](https://doi.org/10.1016/S0043-1648(03)00054-1)
- [77] S.N. Kukureka, C.J. Hooke, M. Rao, P. Liao, Y.K. Chen, Effect of fibre reinforcement on the friction and wear of polyamide 66 under dry rolling-sliding contact, *Tribol. Int.* 32 (1999) 107–116.
[https://doi.org/10.1016/S0301-679X\(99\)00017-1](https://doi.org/10.1016/S0301-679X(99)00017-1)
- [78] S. Zhou, Q. Zhang, C. Wu, J. Huang, Effect of carbon fiber reinforcement on the mechanical and tribological properties of polyamide6/polyphenylene sulfide composites, *Mater. Des.* 44 (2013) 493–499.
<https://doi.org/10.1016/j.matdes.2012.08.029>
- [79] D.H. Gordon, S.N. Kukureka, The wear and friction of polyamide 46 and polyamide 46/aramid-fibre composites in sliding-rolling contact, *Wear* 267 (2009) 669–678.
<https://doi.org/10.1016/j.wear.2008.11.026>
- [80] G. Srinath, R. Gnanamoorthy, Effect of short fibre reinforcement on the friction and wear behaviour of Nylon 66, *Appl. Compos. Mater.* 12 (2005) 369–383.
<https://doi.org/10.1007/s10443-005-5824-6>
- [81] <https://www.nittobo.co.jp/business/glassfiber/about/composition.htm>
- [82] M. Clerico, V. Patierno, Sliding wear of polymeric composites, *Wear* 53 (1979) 279-297, 299-301.
[https://doi.org/10.1016/0043-1648\(79\)90083-8](https://doi.org/10.1016/0043-1648(79)90083-8)
- [83] F.V.D. Velde, P.D. Baets, The friction and wear behaviour of polyamide 6 sliding against steel at low velocity under very high contact pressures, *Wear* 209 (1997) 106-114.
[https://doi.org/10.1016/S0043-1648\(96\)07500-X](https://doi.org/10.1016/S0043-1648(96)07500-X)
- [84] C.J. Hooke, S.N. Kukureka, P. Liao, M. Rao, Y.K. Chen, Wear and friction of nylon-glass fibre composites in non-conformal contact under combined rolling and sliding, *Wear* 197 (1996) 115-122.
[https://doi.org/10.1016/0043-1648\(95\)06828-7](https://doi.org/10.1016/0043-1648(95)06828-7)
- [85] F. Ramsteiner, R. Theysohn, The influence of fibre diameter on the tensile behaviour of short-glass-fibre reinforced polymers, *Compos. Sci. Technol.* 24 3 (1985) 231-240.
[https://doi.org/10.1016/0266-3538\(85\)90075-2](https://doi.org/10.1016/0266-3538(85)90075-2)
- [86] K. Ozawa, T.S. Kim, D. Tsunoda, Y. Arao, N. Taniguchi, T. Nishiwaki, A. Hosoi, H. Kawada, Influence of fiber diameter on impact tensile properties of injection-molded long glass fiber reinforced polyamide, *Trans. JSME* 82 839 (2016) 1-17.
<https://doi.org/10.1299/transjsme.15-00657>
- [87] S. Yu, K.H. Oh, J.Y. Hwang, S.H. Hong, The effect of amino-silane coupling agents having different molecular structures on the mechanical properties of basalt fiber-reinforced polyamide 6,6 composites,

Compos. Part B: Eng. 163 (2019) 511-521.

<https://doi.org/10.1016/j.compositesb.2018.12.148>

[88] D. Frihi, A. Layachi, S. Gherib, G. Stoclet, K.M. Varlot, H. Satha, R. Seguela, Crystallization of glass-fiber-reinforced polyamide 66 composites: Influence of glass-fiber content and cooling rate, *Compos. Sci. Technol.* 130 (2016) 70-77.

<https://doi.org/10.1016/j.compscitech.2016.05.007>

[89] M. Liao, Y. Yang, H. Hamada, Mechanical performance of glass woven fabric composite: Effect of different surface treatment agents, *Compos. Part B: Eng.* 86 (2016) 17-26.

<https://doi.org/10.1016/j.compositesb.2015.08.084>

[90] D. Zhao, H. Hamada, Y. Yang, Influence of polyurethane dispersion as surface treatment on mechanical, thermal and dynamic mechanical properties of laminated woven carbon-fiber-reinforced polyamide 6 composites, *Compos. Part B: Eng.* 160 (2019) 535-545.

<https://doi.org/10.1016/j.compositesb.2018.12.105>

[91] N.G. Karsli, T. Yilmaz, O. Gul, Effects of coupling agent addition on the adhesive wear, frictional and thermal properties of glass fiber-reinforced polyamide 6,6 composites, *Polym. Bull.* 75 (2018) 4429-4444.

<https://doi.org/10.1007/s00289-018-2278-1>

[92] N.G. Karsli, S. Demirkol, T. Yilmaz, Thermal aging and reinforcement type effects on the tribological, thermal, thermomechanical, physical and morphological properties of poly (ether ether ketone) composites, *Compos. Part B* 88 (2016) 253-263.

<https://doi.org/10.1016/j.compositesb.2015.11.013>

[93] M. Sharma, J. Bijwe, Influence of fiber–matrix adhesion and operating parameters on sliding wear performance of carbon fabric polyethersulphone composites, *Wear* 271 (2011) 2919-2927.

<https://doi.org/10.1016/j.wear.2011.06.012>

[94] M. Sharma, J. Bijwe, P. Mitschang, Wear performance of PEEK–carbon fabric composites with strengthened fiber–matrix interface, *Wear* 271 (2011) 2261-2268.

<https://doi.org/10.1016/j.wear.2010.11.055>

[95] X. Huang, Fabrication and properties of carbon fibers, *Mater.* 2 (2009) 2369-2403.

<https://doi.org/10.3390/ma2042369>

[96] D.A. Baker, T.G. Rials, Recent advances in low-cost carbon fiber manufacture from lignin, *J. Appl. Polym. Sci.* (2013) 713-728.

<https://doi.org/10.1002/app.39273>

[97] S.V. Joshi, L.T. Drzal, A.K. Mohanty, S. Arorac, Are natural fiber composites environmentally superior to glass fiber reinforced composites?, *Compos. Part A: Appl. Sci. Manuf.* 35 (2004) 371-376.

<https://doi.org/10.1016/j.compositesa.2003.09.016>

[98] K. Friedrich, G. Theiler, P. Klein, Handbook of polymer tribology: chapter 9: Polymer composites for tribological applications in a range between liquid helium and room temperature, (2018) 307-343.

https://doi.org/10.1142/9781848162044_0011

- [99] J.K. Lancaster, The effect of carbon fibre reinforcement on the friction and wear of polymers, *J. Physics D: Appl. Phys.* 1 5 (1968) 549-559.
<https://doi.org/10.1088/0022-3727/1/5/303>
- [100] J. Theberge, B. Arkles, Wear characteristics of carbon fiber reinforced thermoplastics, *Lubr. Eng.* 30 12 (1974) 585-589.
- [101] J. Li, Y.C. Xia, The reinforcement effect of carbon fiber on the friction and wear properties of carbon fiber reinforced PA6 composites, *Fibers. Polym.* 10 (2009) 519–525.
<https://doi.org/10.1007/s12221-009-0519-5>
- [102] B. Suresha, K.S. Kumar, S. Seetharamu, P.S. Kumaran, Friction and dry sliding wear behavior of carbon and glass fabric reinforced vinyl ester composites, *Tribol. Int.* 43 (2010) 602-609.
<https://doi.org/10.1016/j.triboint.2009.09.009>
- [103] U.S. Tewari, J. Bijwe, J.N. Mathur, I. Sharma, Studies on abrasive wear of carbon fibre (short) reinforced polyamide composites, *Tribol. Int.* 25 (1992) 53-60.
[https://doi.org/10.1016/0301-679X\(92\)90121-3](https://doi.org/10.1016/0301-679X(92)90121-3)
- [104] Y. Yamamoto, T. Takashima, Friction and wear of water lubricated PEEK and PPS sliding contacts, *Wear* 253 (2002) 820-826.
[https://doi.org/10.1016/S0043-1648\(02\)00059-5](https://doi.org/10.1016/S0043-1648(02)00059-5)
- [105] J. Li, X.H. Cheng, Friction and wear properties of surface-treated carbon fiber-reinforced thermoplastic polyimide composites under oil-lubricated condition, *Mater. Chem. Phys.* 108 (2008) 67-72.
<https://doi.org/10.1016/j.matchemphys.2007.09.003>
- [106] F. Zhao, G. Li, G. Zhang, T. Wang, Q. Wang, Hybrid effect of ZnS sub-micrometer particles and reinforcing fibers on tribological performance of polyimide under oil lubrication conditions, *Wear* 380–381 (2017) 86-95.
<https://doi.org/10.1016/j.wear.2017.03.007>
- [107] M. Kurokawa, Y. Uchiyama, S. Nagai, Performance of plastic gear made of carbon fiber reinforced poly-ether-ether-ketone, *Tribol. Int.* 32 (1999) 491-497.
[https://doi.org/10.1016/S0301-679X\(99\)00078-X](https://doi.org/10.1016/S0301-679X(99)00078-X)
- [108] R. Ramani, T.M. Kotresh, R.I. Shekar, F. Sanal, U.K. Singha, R. Renjith, G. Amarendra, Positronium probes free volume to identify para- and meta-aramid fibers and correlation with mechanical strength, *Polym.* 135 (2018) 39-49.
<https://doi.org/10.1016/j.polymer.2017.11.064>
- [109] L. Xu, Z. Zhu, G. Chen, C. Qu, Effect of load and sliding velocity on tribological behaviors of aramid fiber reinforced PA1010 composites, *Indus. Lubr. Tribol.* 62 (2010) 46-51.
<https://doi.org/10.1108/00368791011012461>
- [110] A. Bolvari, S. Glenn, R. Janssen, C. Ellis, Wear and friction of aramid fiber and polytetrafluoroethylene filled composites, *Wear* 203–204 (1997) 697-702.
[https://doi.org/10.1016/S0043-1648\(96\)07446-7](https://doi.org/10.1016/S0043-1648(96)07446-7)

- [111] A. Horovistiz, S. Laranjeira, J.P. Davim, Influence of sliding velocity on the tribological behavior of PA66GF30 and PA66 + MoS₂: an analysis of morphology of sliding surface by digital image processing, *Polym. Bull.* 75 (2018) 5113–5131.
<https://doi.org/10.1007/s00289-018-2314-1>
- [112] D. Li, Y. Xie, W. Li, Y. You, X. Deng, Tribological and mechanical behaviors of polyamide 6/glass fiber composite filled with various solid lubricants, *Sci. World J.* (2013) 320837.
<https://doi.org/10.1155/2013/320837>
- [113] D.X. Li, Y.L. You, X. Deng, W.J. Li, Y. Xie, Tribological properties of solid lubricants filled glass fiber reinforced polyamide 6 composites, *Mater. Des.* 46 (2013) 809-815.
<https://doi.org/10.1016/j.matdes.2012.11.011>
- [114] Y.L. You, D.X. Li, G.J. Si, X. Deng, Investigation of the influence of solid lubricants on the tribological properties of polyamide 6 nanocomposite, *Wear* 311 (2014) 57-64.
<https://doi.org/10.1016/j.wear.2013.12.018>
- [115] Y.L. You, D.X. Li, X. Deng, W.J. Li, Y. Xie, Effect of solid lubricants on tribological behavior of glass fiber reinforced polyamide 6, *Polym. Compos.* (2013) 1783-1793.
<https://doi.org/10.1002/pc.22582>
- [116] M.T. Lates, R. Velicu, C.C. Gavrila, Temperature, pressure, and velocity influence on the tribological properties of PA66 and PA46 Polyamides, *Mater.* 12 (20) (2019) 3452.
<https://doi.org/10.3390/ma12203452>
- [117] K.D. Dearn, S.N. Kukureka, D. Walton, Handbook of polymer tribology: chapter 13: Eng. Polym. Compos. Mach. Elem. (2018) 441-479.
- [118] A. El-Faham, F. Albericio, Peptide coupling reagents, more than a letter soup, *Chem. Rev.* 111 (2011) 6557–6602.
<https://doi.org/10.1021/cr100048w>
- [119] A.H.M. Schotman, Mechanism of the reaction of carbodiimides with carboxylic acids, *Recl. Trav. Chim. Pays-Bas* 110 (1991) 319.
<https://doi.org/10.1002/recl.19911100704>
- [120] S. Shinichiro, Cyclic carbodiimide compound, WO 2011155624 A1 (2011).
- [121] V. Melcova, R. Prikryl, P. Mencik, J. Tochacek, Processing stabilization of poly (3-hydroxybutyrate)/poly (lactic acid) blends with oligomeric carbodiimide, *Mater. Sci. Forum* 955 (2019) 7–12.
<https://doi.org/10.4028/www.scientific.net/MSF.955.7>
- [122] K. Lee, P. Huh, B. Kim, Anti-hydrolysis of PBT as functions of carbodiimide types and contents, *Polym.* 39 (4) (2015) 611-620.
<https://doi.org/10.7317/pk.2015.39.4.611>
- [123] P. Frey, M. Heinle, C. Leisen, D. Drummer, M. Merklein, Influence of metal inserts with microformed edged on subsequent injection injection assembly moulding for media tight electronic systems, *MATEC Web Conf.* 21 (2015) 1-7.

- <https://doi.org/10.1051/mateconf/20152109013>
- [124] F. Kimura, S. Kadoya, Y. Kajihara, Effects of molding conditions on injection molded direct joining under various surface fine-structuring, *Int. J. Adv. Manuf. Technol.* 101 (2019) 2703-2712.
- <https://doi.org/10.1007/s00170-018-3154-8>
- [125] A.E. Jahromi, H.R.E. Jahromi, F. Hemmati, M.R. Saeb, V. Goodarzi, K. Formela, Morphology and mechanical properties of polyamide/clay nanocomposites toughened with NBR/NBR-g-GMA: A comparative study, *Compos. Part B: Eng.* 90 (2016) 478-484.
- <https://doi.org/10.1016/j.compositesb.2015.12.042>
- [126] M. Mert, U. Yilmazer. Processing and properties of modified polyamide 66-organoclay nanocomposites, *J. Appl. Polym. Sci.* 108 (2008) 3890-3900.
- <https://doi.org/10.1002/app.27974>.
- [127] D.X. Li, X. Deng, J. Wang, J. Yang, X. Li, Mechanical and tribological properties of polyamide 6–polyurethane block copolymer reinforced with short glass fibers, *Wear* 269 (2010) 262-268.
- <https://doi.org/10.1016/j.wear.2010.04.004>
- [128] S. Zhang, C. Cui, G. Chen, Tribological behavior of MC Nylon6 composites filled with glass fiber and fly ash, *J. Wuhan University of Technol. Mater. Sci. Ed.* (2012) 290-295.
- <https://doi.org/10.1007/s11595-012-0455-x>
- [129] T. Kochi, R. Ichimura, M. Yoshihara, D. Dong, Y. Kimura, Film thickness and traction in soft EHL with grease, *Tribol. Online* 12 (4) (2017) 171-176.
- <https://doi.org/10.2474/trol.12.171>
- [130] M. Ando, J. Sukumaran, Effect on friction for different parameters in roll–slip of polyamide–steel nonconformal contacts, *Tribol. Trans.* 55 (2012) 109-116.
- <https://doi.org/10.1080/10402004.2011.636170>
- [131] B. Zabala, X. Fernandez, J.C. Rodriguez, A. L-Ortega, E. Fuentes, R. Bayón, A. Igartua, F. Girot, Mechanism-based wear models for plastic injection moulds, *Wear* 440–441 (2019) 203105.
- <https://doi.org/10.1016/j.wear.2019.203105>
- [132] B.H. Stuart, Surface plasticisation of poly (ether ether ketone) by chloroform, *Polym. Test.* 16 (1997) 49-57.
- [https://doi.org/10.1016/S0142-9418\(96\)00026-8](https://doi.org/10.1016/S0142-9418(96)00026-8)
- [133] L. R. Rudnick, *Lubricant additives: Chemistry and applications second editions*; 23. Additives for grease applications, (2009) 585-597.
- [134] P.M. Lugt, Modern advancements in lubricating grease technology, *Tribol. Int.* 97 (2016) 467-477.
- <https://doi.org/10.1016/j.triboint.2016.01.045>
- [135] S.J. Wilson, Traction and wear evaluation of a number of plastic materials and greases under combined rolling and sliding contact conditions, Master degree thesis in the Graduate School of The Ohio State University (2012).
- http://rave.ohiolink.edu/etdc/view?acc_num=osu1337191253
- [136] J. Shu, K. Harris, B. Munavirov, R. Westbroek, J. Leckner, S. Glavatskih, Tribology of polypropylene

- and Li-complex greases with ZDDP and MoDTC additives, *Tribol. Int.* 118 (2018) 189-195.
<https://doi.org/10.1016/j.triboint.2017.09.028>
- [137] Y. Kanazawa, R.S. Sayles, A. Kadiric, Film formation and friction in grease lubricated rolling-sliding non-conformal contacts, *Tribol. Int.* 109 (2017) 505-518.
<https://doi.org/10.1016/j.triboint.2017.01.026>
- [138] Y. Kanazawa, N.D. Laurentis, A. Kadiric, Studies of friction in grease-lubricated rolling bearings using ball-on-disc and full bearing tests, *Tribol. Trans.* 63 (2020) 77-89.
<https://doi.org/10.1080/10402004.2019.1662147>
- [139] D. Evans, J. B. Matthews, The structure of aluminum stearate grease, *J. Colloid Sci.* 9 1 (1954) 60-69.
[https://doi.org/10.1016/0095-8522\(54\)90086-0](https://doi.org/10.1016/0095-8522(54)90086-0)
- [140] B. Bhushan, Introduction of Tribology second edition, (2013) 508-510.
- [141] A. Adhvaryu, C. Sung, S.Z. Erhan, Fatty acids and antioxidant effects on grease microstructures, *Ind. Crops Prod.* 21 3 (2005) 285-291.
<https://doi.org/10.1016/j.indcrop.2004.03.003>
- [142] N. Kumar, V. Saini, J. Bijwe, Performance properties of lithium greases with PTFE particles as additive: Controlling parameter- size or shape?, *Tribol. Int.* 148 (2020) 106302.
<https://doi.org/10.1016/j.triboint.2020.106302>
- [143] R. G. Duque, Z. Wang, D. Duell, D. E. Fowler, ToF-SIMS analysis of anti-fretting films generated on the surface of ball bearings containing dithiocarbamate and dithiophosphate grease additives, *Appl. Surf. Sci.* 231-232 (2004) 342-347.
<https://doi.org/10.1016/j.apsusc.2004.03.088>
- [144] R. Lu, M. Morimoto, H. Tani, N. Tagawa, S. Koganezawa, Tribological properties of alkyldiphenylethers in boundary lubrication, *Lubr.* 7 (2019) 112.
<https://doi.org/10.3390/lubricants7120112>
- [145] M. Miyajima, K. Kitamura, K. Matsumoto, Characterization of tribochemical reactions on steel surfaces, *Nippon steel & Sumitomo metal Tec. Rep.* 114 (2017) 101-107.
- [146] G. Tatsumi, M. Ratoi, Y. Shitara, K. Sakamoto, B.G. Mellor, Effect of lubrication on friction and wear properties of PEEK with steel counterparts, *Tribol. Online* 14 (2019) 345-352.
<https://doi.org/10.2474/trol.14.345>
- [147] G. Tatsumi, M. Ratoi, Y. Shitara, K. Sakamoto, B.G. Mellor, Effect of organic friction modifiers on lubrication of PEEK-steel contact, *Tribol. Int.* 151 (2020) 106513.
<https://doi.org/10.1016/j.triboint.2020.106513>
- [148] F.P. Bowden, D. Tabor, Friction, lubrication and wear: a survey of work during the last decade, *British J. Appl. Phys.*, 17 (1966) 1521-1544.
<https://doi.org/10.1088/0508-3443/17/12/301>
- [149] Y. Yamaguchi, *Tribology of plastic materials: Their characteristics and applications to sliding components*, Elsevier (1990) 1.

- [150] M.M. Hossain, H.J. Sue, Handbook of polymer tribology: chapter 6: FEM modeling of Scratch-induced Deformation in Polymers, (2018) 183-219.
- [151] I.L. Singer, R.N. Bolster, J. Wegand, S. Fayeulle, Hertzian stress contribution to low friction behavior of thin MoS₂ coatings, Appl. Phys. Lett. 57, (1990) 995.
<https://doi.org/10.1063/1.104276>
- [152] P. Samyn, G. Schoukens, I.V. Driessche, J.V. Craenenbroeck, F. Verpoort, Softening and melting mechanisms of polyamides interfering with sliding stability under adhesive conditions, Polym. 47 (2006) 5050-5065.
<https://doi.org/10.1016/j.polymer.2006.05.034>
- [153] A. Mimaroglu, H. Unal, T. Arda, Friction and wear performance of pure and glass fibre reinforced poly-ether-imide on polymer and steel counterface materials, Wear 262 (2007) 1407-1413.
<https://doi.org/10.1016/j.wear.2007.01.015>
- [154] H. Unal, A. Mimaroglu, U. Kadioglu, H. Ekiz, Sliding friction and wear behaviour of polytetrafluoroethylene and its composites under dry conditions, Mater. Des. 25 (2004) 239-245.
<https://doi.org/10.1016/j.matdes.2003.10.009>
- [155] J. Takabi, M.M. Khonsari, On the dynamic performance of roller bearings operating under low rotational speeds with consideration of surface roughness, Tribol. Int. 86 (2015) 62-71.
<https://doi.org/10.1016/j.triboint.2015.01.011>
- [156] B.J. Hamrock, D. Dowson, Minimum film thickness in elliptical contacts for different regimes of fluid-film lubrication, NASA Tech. Pap. 1342 (1978) 1-22.
- [157] N. Marx, J. Guegan, H.A. Spikes, Elastohydrodynamic film thickness of soft EHL contacts using optical interferometry, Tribol. Int., 99 (2016) 267-277.
<https://doi.org/10.1016/j.triboint.2016.03.020>
- [158] M. Esfahanian, B.J. Hamrock, Fluid-film lubrication regimes revisited, Tribol. Trans. 34 (1991) 628-632.
<https://doi.org/10.1080/10402009108982081>
- [159] B.J. Hamrock, D. Dowson, Elastohydrodynamic lubrication of elliptical contacts for materials of low elastic modulus I—fully flooded conjunction, J. Lubr. Technol. 100 (1978) 236-245.
<https://doi.org/10.1115/1.3453152>
- [160] J. Vicente, J.R. Stokes, H.A. Spikes, The frictional properties of Newtonian fluids in rolling–sliding soft-EHL contact. Tribol. Let. 20 (2005) 273–286.
<https://doi.org/10.1007/s11249-005-9067-3>
- [161] T. Joyce, Handbook of polymer tribology: chapter 4: Biopolymer Tribology, (2018) 111-152.
- [162] C. Myant, H.A. Spikes, J.R. Stokes, Influence of load and elastic properties on the rolling and sliding friction of lubricated compliant contacts, Tribol. Int. 43 (2010) 55-63.
<https://doi.org/10.1016/j.triboint.2009.04.034>
- [163] B. Stoimenov, V. Fridrici, P. Kapsa, H. Kosukegawa, M. Ohta, Bioengineering materials and conditions for obtaining low friction with PVA hydrogels, Tribol. Online 8 (2013) 140-152.

<https://doi.org/10.2474/trol.8.140>

[164] K.D. Dearn, T.J. Hoskins, L. Andrei, D. Walton, Lubrication regimes in high-performance polymer spur gears, *Adv. Tribol.* 2013 (2013) 987251.

<https://doi.org/10.1155/2013/987251>

[165] P. Cann, E. Ioannides, B. Jacobson, A.A. Lubrecht, The lambda ratio — a critical re-examination, *Wear* 175 (1994) 177-188.

[https://doi.org/10.1016/0043-1648\(94\)90181-3](https://doi.org/10.1016/0043-1648(94)90181-3)

[166] N.D. Laurentis, A. Kadiric, P. Lugt, P. Cann, The influence of bearing grease composition on friction in rolling/sliding concentrated contacts, *Tribol. Int.* 94 (2016) 624-632.

<https://doi.org/10.1016/j.triboint.2015.10.012>

[167] K. Song, Y. Wang, B. Huang, and M. Wang, “Study on EHL of plastic pinion engaging with steel gear, *Lubr. Eng.* 1 (2005) 50–54.

http://en.cnki.com.cn/Article_en/CJFDTotol-RHMF20050100K.htm

[168] R. Wongpajan, S. Mathurosemontri, R. Takematsu, H.Y. Xu, P. Uawongsuwan, S. Thumsorn, H. Hamada, Interfacial shear strength of glass fiber reinforced polymer composites by the modified rule of mixture and Kelly-Tyson model, *Energy Procedia* 89 (2016) 328-334.

<https://doi.org/10.1016/j.egypro.2016.05.043>

[169] Y. Yamamoto, M. Hashimoto, Friction and wear of water lubricated PEEK and PPS sliding contacts: Part 2. Composites with carbon or glass fibre, *Wear* 257 (2004) 181-189.

<https://doi.org/10.1016/j.wear.2003.12.004>

[170] X. Chen, R. Jiao, K.S. Kim, On the Ohno–Wang kinematic hardening rules for multiaxial ratcheting modeling of medium carbon steel, *Int. J. Plast.* 21 (2005) 161-184.

<https://doi.org/10.1016/j.ijplas.2004.05.005>

[171] S.K. Paul, Prediction of non-proportional cyclic hardening and multiaxial fatigue life for FCC and BCC metals under constant amplitude of strain cycling, *Mater. Sci. Eng.: A*, 656 (2016) 111-119.

<https://doi.org/10.1016/j.msea.2016.01.029>

[172] M. Okane, T. Shitaka, M. Ishida, T. Chaki, T. Yasui, M. Fukumoto, Fatigue properties of butt welded aluminum alloy and carbon steel joints by friction stirring, *J. Phys.: Conf. Ser.* 843 (2017).

<https://doi.org/10.1088/1742-6596/843/1/012040>

[173] J.E.F. Rico, A.H. Battez, D.G. Cuervo, Rolling contact fatigue in lubricated contacts, *Tribol. Int.* 36 (2003) 35-40.

[https://doi.org/10.1016/S0301-679X\(02\)00097-X](https://doi.org/10.1016/S0301-679X(02)00097-X)

[174] H. Kuwabara, Material analysis technology R&D efforts, *JTEKT Eng. J. English Ed.* 1006E (2009) 41–46.

http://eb-cat.ds-navi.co.jp/enu/jtekt/tech/ej/img/no1006e/1006e_08.pdf

[175] R. Rabe, J.M. Breguet, P. Schwaller, S. Stauss, F.J. Haug, J. Patscheider, J. Michler, Observation of fracture and plastic deformation during indentation and scratching inside the scanning electron microscope. *Thin Solid Films* 469–470 (2004) 206-213.

<https://doi.org/10.1016/j.tsf.2004.08.096>

[176] J.M. Wheeler, J. Michler, Elevated temperature, nano-mechanical testing in situ in the scanning electron microscope. *Rev. Sci. Instrum.* 84 (2013) 045103.

<https://doi.org/10.1063/1.4795829>

[177] W.C. Oliver, G.M. Pharr, An improved technique for determining hardness and elastic-modulus using load and displacement sensing indentation experiments. *J. Mater. Res.* 7 (1992) 1564–1583.

<https://doi.org/10.1557/JMR.1992.1564>

[178] B.N. Lucas, W.C. Oliver, G.M. Pharr, J-L. Loubet, Time dependent deformation during indentation testing, Proc. 1996 MRS Spring Meeting, April 8, 1996 - April 12, 1996, vol. 436, San Francisco, CA, USA: (1996) 233–238.

[179] A.H.W. Ngan, B. Tang, Viscoelastic effects during unloading in depth-sensing indentation. *J. Mater. Res.* 17 (2002) 2604–2610.

<https://doi.org/10.1557/JMR.2002.0377>

[180] K. Laajalehto, I. Kartio, P. Nowak, XPS study of clean metal sulfide surfaces, *Appl. Surf. Sci.* 81 (1994) 11-15.

[https://doi.org/10.1016/0169-4332\(94\)90080-9](https://doi.org/10.1016/0169-4332(94)90080-9)

[181] X. Deng, D.C. Sorescu, J. Lee, Single-layer ZnS supported on Au (111): A combined XPS, LEED, STM and DFT study, *Surf. Sci.* 658 (2017) 9-14.

<https://doi.org/10.1016/j.susc.2016.12.003>

[182] S. Loehlé, C. Matta, C. Minfray, T. Le Mogne, R. Iovine, Y. Obara, A. Miyamoto, J.M. Martin, Mixed lubrication of steel by C18 fatty acids revisited. Part I: Toward the formation of carboxylate, *Tribol. Int.* 82 (2015) 218-227.

<https://doi.org/10.1016/j.triboint.2014.10.020>

[183] D.M. Laura, H. Keskkula, J.W. Barlow, D.R. Paul, Effect of glass fiber surface chemistry on the mechanical properties of glass fiber reinforced, rubber-toughened nylon 6, *Polym.* 43 (2002) 4673-4687.

[https://doi.org/10.1016/S0032-3861\(02\)00302-6](https://doi.org/10.1016/S0032-3861(02)00302-6)

[184] A. Kelly, W.R. Tyson, Tensile properties of fiber-reinforced materials: Copper/tungsten and copper/molybdenum, *J. Mech. Phys. Solids* 13 (1965) 329–350.

[https://doi.org/10.1016/0022-5096\(65\)90035-9](https://doi.org/10.1016/0022-5096(65)90035-9)

[185] H. Fukuda, T. Chou, A probability theory of the strength of short-fibre composites with variable fibre length and orientation, *J. Mater. Sci.* 17 (1982) 1003-1011.

<https://doi.org/10.1007/BF00543519>

[186] G. Wypych, *Handbook of Fillers* (Fourth Edition), (2016) 252-255.

<https://doi.org/10.1016/B978-1-895198-91-1.50004-X>

[187] A. Leatherbarrow, H. Wu, Mechanical behaviour of the constituents inside carbon-fibre/carbon-silicon carbide composites characterised by nano-indentation, *J. Eur. Ceram. Soc.* 32 (2012) 579-588.

<https://doi.org/10.1016/j.jeurceramsoc.2011.09.026>

[188] Y. Sun, G. Zhao, F. Yang, Anisotropic behavior of the nanoindentation of single carbon fibers, *Nanosci. Nanotechnol. Lett.* 6 (2014) 596-600.

<https://doi.org/10.1166/nnl.2014.1809>

PUBLICATIONS GENERATED FROM THIS WORK**Publication:**

- 1) T. Kunishima, Y. Nagai, T. Kurokawa, G. Bouvard, J.-C. Abry, V. Fridrici, Ph. Kapsa, Tribological behavior of glass fiber reinforced-PA66 in contact with carbon steel under high contact pressure, sliding and grease lubricated conditions, *Wear* 456-457 (2020) 203383.
<https://doi.org/10.1016/j.wear.2020.203383> (Chapter III)
- 2) T. Kunishima, S. Nagai, T. Kurokawa, J. Galipaud, G. Guillonnet, G. Bouvard, J.-C. Abry, C. Minfray, V. Fridrici, Ph. Kapsa, Effects of temperature and addition of zinc carboxylate to grease on the tribological properties of PA66 in contact with carbon steel, *Tribo. Int.* 153 (2021) 106578.
<https://doi.org/10.1016/j.triboint.2020.106578> (Chapter IV)
- 3) T. Kunishima, G. Bouvard, J.-C. Abry, V. Fridrici, Ph. Kapsa, Soft EHL based friction mechanism of unreinforced and GF-reinforced PA66 in contact with steel under PAO8 oil lubrication, *Tribology Lett.* under review.
(Chapter V)
- 4) T. Kunishima, Y. Nagai, S. Nagai, T. Kurokawa, G. Bouvard, J.-C. Abry, V. Fridrici, Ph. Kapsa, Effects of glass fiber properties and polymer molecular mass on the mechanical and tribological properties of a polyamide-66-based composite in contact with carbon steel under grease lubrication, *Wear* 462-463 (2020) 203500.
<https://doi.org/10.1016/j.wear.2020.203500> (Chapter VI)
- 5) T. Kunishima, T. Kurokawa, H. Arai, V. Fridrici, Ph. Kapsa, Reactive extrusion mechanism, mechanical and tribological behavior of fiber reinforced polyamide 66 with added carbodiimide, *Mater. Des.* 188 (2020) 108447.
<https://doi.org/10.1016/j.matdes.2019.108447> (Chapter VII)
- 6) T. Kunishima, Y. Nagai, G. Bouvard, J.-C. Abry, V. Fridrici, Ph. Kapsa, Comparison of the tribological properties of carbon/glass fiber reinforced PA66-based composites in contact with steel, with and without grease lubrication, *Wear* (2021) 203899.
<https://doi.org/10.1016/j.wear.2021.203899> (Chapter VIII)

Presentation in an international conference:

- 1) T. Kunishima, T. Kurokawa, H. Arai, Clarification of reactive extruding mechanism and tribological behavior on carbodiimide added fiber reinforced PA resin material, WTC 2017 6th World Tribology Congress, Beijing, China, September 17-22, 2017 (Chapter **VII**).
- 2) T. Kunishima, Y. Nagai, T. Kurokawa, H. Arai, V. Fridrici, Ph. Kapsa, Tribological behavior of fiber reinforced PA66 material under high surface pressure, sliding and grease lubricated conditions, JIFT 2019, Tours, France, April 24-26, 2019 (Chapter **III**).
- 3) T. Kunishima, Y. Nagai, T. Kurokawa, H. Arai, V. Fridrici, Ph. Kapsa, Tribological behavior of fiber reinforced PA66 material under high contact pressure, sliding and grease lubricated conditions, 46th Leeds Lyon Symposium on Tribology, Lyon, France, September 2-4, 2019 (Chapter **III**).
- 4) T. Kunishima, Y. Nagai, T. Kurokawa, H. Arai, V. Fridrici, Ph. Kapsa, Tribological behavior of fiber reinforced PA66 material under high contact pressure, sliding and grease lubricated conditions, 2019 STLE Tribology Frontiers Conference, Chicago, USA, October 20-23, 2019 (Chapter **III**).
- 5) T. Kunishima, Y. Nagai, G. Bouvard, J.-Ch. Abry, V. Fridrici, Ph. Kapsa, Comparison of the tribological properties of carbon/glass fiber reinforced PA66-based composites in contact with steel, with and without grease lubrication, 23rd International Conference on Wear of Materials, Online, April 26-28, 2021 (Chapter **VIII**).
- 6) T. Kunishima, J. Galipaud, G. Guillonneau, G. Bouvard, J.-C. Abry, C. Minfray, V. Fridrici, Ph. Kapsa, Effects of temperature and addition of zinc carboxylate to grease on the tribological properties of PA66 in contact with carbon steel, 2021 STLE Virtual Annual Meeting and Exhibition, Online, May 17-20, 2021 (Chapter **IV**).

AUTORISATION DE SOUTENANCE

Vu les dispositions de l'arrêté du 25 mai 2016,

Vu la demande du directeur de thèse

Monsieur P. KAPSA

et les rapports de

M. M. KALIN

Professeur - University of Ljubljana - Laboratory for Tribology and Interface Nanotechnology
Faculty of Mechanical Engineering - Bogisiceva 8 - 1000 Ljubljana - Slovénie

et de

M. F. VILLE

Professeur - INSA Lyon - Bâtiment Sophie Germain - 27 bis avenue Jean Capelle
69621 Villeurbanne cedex

Monsieur KUNISHIMA Takeshi

est autorisé à soutenir une thèse pour l'obtention du grade de **DOCTEUR**

Ecole doctorale MATERIAUX

Fait à Ecully, le 26 mai 2021

P/Le directeur de l'E.C.L.
Le directeur des Etudes

Grégory VIAL

Directeur des formations
École Centrale de Lyon

Grégory VIAL

